TalentDetector

TalentDetector2025_Winter
INTERNATIONAL STUDENTS SCIENTIFIC CONFERENCE

Scientific editor:
Mirosław Bonek

Department of Engineering Materials and Biomaterials,
Faculty of Mechanical Engineering,
Silesian University of Technology
31th January 2025
Gliwice, Poland

Katedra Materiałów
Inżynierskich i Biomedycznych

Katedra Materiałów Inżynierskich i Biomedycznych
Wydział Mechaniczny Technologiczny
Politechnika Śląska
ul. Konarskiego 18a, 44-100 Gliwice tel. +48 (32) 2371322

Redakcja techniczna i skład komputerowy:
dr h.c. dr hab. inż. Mirosław Bonek, prof. PŚ

Recenzenci:
M. Bonek, W. Borek, A. Czupryński, S. Dinescu, A. Drygała, B. Gitolendia, K. Gołombek, A. Kania, M. Kciuk, A. Kloc-Ptaszna, M. Kremzer, M. Król, B. Krupińska, L. Kuchariková, S. Lesz, G. Matula, C. Meran, M. Musztyfaga-Staszuk, D. Pakuła, O. Polishchuk, M. Polok-Rubiniec, M. Spilka, M. Sroka, M. Staszuk, M. Szindler, A. Śliwa, E. Tillová, M. Uhríčik, A. Włodarczyk-Fligier, B. Ziębowicz

Materiały są opublikowane na podstawie oryginałów dostarczonych przez Autorów, zaopiniowanych przez Zespół Recenzentów.

Wydano za zgodą:
Kierownika Katedry Materiałów Inżynierskich i Biomedycznych
Wydziału Mechanicznego Technologicznego
Politechniki Śląskiej

Wydawca:
Katedra Materiałów Inżynierskich i Biomedycznych
Wydział Mechaniczny Technologiczny
Politechnika Śląska
Gliwice 2025

Seria wydawnicza:
Prace Katedry Materiałów Inżynierskich i Biomedycznych
Wydział Mechaniczny technologiczny
Politechnika Śląska
Publikacja: styczeń 2025

ISBN 978-83-65138-42-2

INTERNATIONAL STUDENTS SCIENTIFIC CONFERENCE

TALENTDETECTOR2024_WINTER

SILESIAN UNIVERSITY OF TECHNOLOGY, GLIWICE, POLAND

31TH JANUARY 2025

The International Student Scientific Conference TalentDetector2025_Winter aims to integrate the student and scientific community dealing with topics related to material technologies. It is a place that gives the opportunity to exchange experiences, knowledge, skills and present current scientific achievements, developing and expanding students' interests in the field of materials engineering, surface engineering, biomaterials and biomedical engineering, nanotechnology, pro-ecological technologies and computer materials science. The conference allows for the presentation of projects conducted with the industry as part of the activities of Student Scientific Circles, doctorates, projects implemented in the form of PBL - Project Based Learning as part of the Excellence Initiative - Research University at the Silesian University of Technology, projects in the framework of EURECA PRO/European University in Responsible Consumption and Production and international bilateral cooperation between Universities.

CONFERENCE ORGANIZER

Materials Science Circle of the Association of Alumni of the Silesian University of Technology, Gliwice, Poland

CONFERENCE CO-ORGANIZER

Department of Engineering Materials and Biomaterials, Faculty of Mechanical Engineering, Silesian University of Technology, Gliwice, Poland

TalentDetector HISTORY

The International Student Scientific Conferences TalentDetector from 10 edition (since 2018) have been a place for the exchange of experience, knowledge, skills and presentation of students' current scientific achievements in the field of materials engineering, surface engineering, biomaterials and biomedical engineering since the 8th edition. As part of the conference, two international scientific monographs, TalentDetector_Summer and TalentDetector_Winter, are published annually, which already contain over 600 scientific articles resulting from the implementation of PBL, EURECA PRO, Students Scientific Cyrcles projects and projects with secondary school students with international authors. Participation in the form of presentations and posters in TalentDetector International Student Scientific Conferences allows members of the project teams to integrate the student and scientific community of the Silesian University of Technology as well as young staff from foreign research centres in Austria, Czech Republic, Ethiopia, Ghana, Georgia, Iran, Romania, Slovakia, Ukraine and Turkey, dealing with topics related to materials technologies.
Scientific monographs are prepared based on articles, mostly with international authors, reviewed by an international scientific committee.
The initiative of the cyclical organization of the International Student Scientific Conference TalentDetector significantly expands activities in the field of student education, organizational and popularization activities for the scientific community related to materials engineering at the national and international level.

Thanks to extensive international cooperation, over 180 articles were published free of charge.

The history of TalentDetector in numbers:

2018
TalentDetector 2019 (Gliwice)
Number of articles: 59
Number of authors: 206
Number of countries: 1

2021
TalentDetector2021_Winter (Gliwice)
Number of articles: 37
Number of authors: 134
Number of countries: 2

TalentDetector2021_Summer (Zawiercie)
Number of articles: 57
Number of authors: 173
Number of countries: 3

2022
TalentDetector2022_Winter (Gliwice)
Number of articles: 79
Number of authors: 179
Number of countries: 4

TalentDetector2022_Summer (Wisła)
Number of articles: 79
Number of authors: 176
Number of countries: 4

2023
TalentDetector2023_Winter (Gliwice)
Number of articles: 73
Number of authors: 143
Number of countries: 6

TalentDetector2023_Summer (Brenna)
Number of articles: 105
Number of authors: 173
Number of countries: 9

2024
TalentDetector2024_Winter (Gliwice)
Number of articles: 82
Number of authors: 135
Number of countries: 7

TalentDetector2024_Summer (Gliwice-Zilina)
Number of articles: 84
Number of authors: 147
Number of countries: 8

Number of cooperating universities: 12

Gazi University, Ankara, Turkey
Gebze Technical University, Gebze, Turkey
Georgian Technical University, Tbilisi, Georgia
Khmelnitskyi National University, Khmelnitskyi, Ukraine
Laserinstitut Hochschule Mittweida, Mittweida, Germany
Pamukkale University, Denizli, Turkey
Silesian University of Technology, Gliwice, Poland
Slovak Technical University in Bratislava, Trnava, Slovakia
Technical University in Zvolen, Zvolen, Slovakia
University of Petroșani, Petroșani, Romania
University of Pristina, Pristina, Kosovo
University of Zilina, Zilina, Slovakia

TalentDetector

31th January 2025
Gliwice, Poland

DEPARTMENT OF ENGINEERING MATERIALS AND BIOMATERIALS
FACULTY OF MECHANICAL ENGINEERING
SILESIAN UNIVERSITY OF TECHNOLOGY

INTERNATIONAL STUDENTS SCIENTIFIC CONFERENCE

Contents

VOLUME 1

VOLUME 2

TalentDetector
31th January 2025
Gliwice, Poland
DEPARTMENT OF ENGINEERING MATERIALS AND BIOMATERIALS
FACULTY OF MECHANICAL ENGINEERING
SILESIAN UNIVERSITY OF TECHNOLOGY
INTERNATIONAL STUDENTS SCIENTIFIC CONFERENCE

Structure of CoCrFe, CoFeNi, CoCrNi medium entropy alloys obtained by induction melting

Sandra Nadolna[a], Bartosz Żary[a], Miłosz Ferdyn[a], Michał Podgórski[a], Maxymilian Żukowski[a], Katrarzyna Młynarek-Żak[b], Monika Spilka[c], Rafał Babilas[c]

[a] Student of Silesian University of Technology, Faculty of Mechanical Engineering, Department of Engineering Materials and Biomaterials
[b] Silesian University of Technology, Faculty of Mechanical Engineering, Department of Engineering Processes Automation and Integrated Manufacturing Systems
[c] Silesian University of Technology, Faculty of Mechanical Engineering, Department of Engineering Materials and Biomaterials
email: rafal.babilas@polsl.pl

Abstract: Medium entropy alloys consist of at least three elements with equal atomic content. Their chemical composition prevents the dominance of one element. The article discusses medium entropy alloys containing cobalt, chromium, iron and nickel: CoCrFe, CoFeNi, and CoCrNi. Microscopic examinations were performed using a scanning electron microscope and a light microscope. Based on the element distribution maps obtained by the EDS method, it was found that the alloys are characterized by high chemical homogeneity. Additionally, a qualitative analysis was carried out on selected areas of microstructures. The content of elements in these alloys was close to equal atomic.

Keywords: medium entropy alloys, induction melting, microstructure, EDS mapping

1. INTRODUCTION

Medium entropy alloys (MEAs) are a new class of metallic materials that consist of at least three chemical elements in almost equal proportions, without any one of them dominating quantitatively [1,2]. Medium entropy alloys also show differences compared to metallic glasses with an amorphous structure. In metallic glasses with a non-crystalline structure, the elements are distributed in a disordered manner and do not exhibit long-range atomic order. Elements in medium- and high-entropy alloys are also distributed randomly but form a highly ordered crystalline structure in the form of solid solutions [3,4].

Medium entropy alloys can be produced by various methods depending on the desired properties and applications. One of the most commonly used methods is casting, which allows obtaining large-volume materials, which are then subjected to mechanical processing, which allows further forming of the alloys. Other methods include high-pressure sintering, friction welding, and advanced additive technologies such as selective laser melting (SLM). The latter

method, in which a laser beam is used to selectively melt and join materials, allows precise control of the alloy's chemical composition and its structure at the micro and nano levels. This technology is one of the most effective, especially in the production of elements with very specific structural and material requirements [5].

The aim of the work was to develop ternary alloys of medium entropy consisting of cobalt, chromium, nickel, and iron: CoCrFe CoFeNi, and CoCrNi with equal atomic shares. The authors present a method of producing these alloys by induction melting and also discuss the results of microscopic examinations using scanning electron microscopy and light microscopy. The chemical composition of the alloys was also examined by the EDS method using element distribution maps and point analysis, which allowed for a precise characterization of the chemical composition.

2. MATERIALS AND METHODS

The CoCrFe, CoFeNi, and CoCrNi alloys in the form of ingots were produced in an induction heater type NG-40 in a controlled protective atmosphere of argon to avoid oxidation reactions. The masses of individual elements (Co, Cr, Fe, Ni) were selected to obtain equal atomic shares and then melted in a ceramic crucible made of alumina (Fig. 1).

The ingots were cut on a circular saw to prepare samples for further tests. The samples were mounted hot in resin using Struers CitoPress-30. The metallographic samples were ground using abrasive papers of grit from 220 to 2000 and polished on polishing wheels on a Struers Tegramin-25 machine.

The structure of the metallographic sections was characterized using a Phenom ProX scanning microscope. Observations were performed in backscattered electron (BSE) mode. In addition, qualitative analysis of the chemical composition was performed using energy-scattering X-ray spectrometry (EDS). In addition, observations were performed using a Zeiss Axio Observer light microscope (LM).

Figure 1. Induction melting of pure elements in a ceramic crucible

3. RESEARCH RESULTS

The structure of CoCrFe, CoFeNi, and CoCrNi alloys was studied using a scanning electron microscope with EDS analysis of the chemical composition. The chemical composition distribution maps with the marked points selected for EDS analysis are presented in Figures 2-4 for CoCrFe, CoFeNi, and CoCrNi alloys, respectively. Tables 1-3 list the shares of individual elements.

The CoCrFe alloy (Fig. 2, Table 1) was characterized by a dendritic structure and the atomic fraction of the individual elements was: Co 33.21%, Fe 32.94%, and Cr 33.85%, indicating that similar atomic fractions were obtained during induction remelting. However, spot analysis revealed differences in the chemical composition in individual phases. In spot 1, the atomic fraction of Co increased to 42.81%, while the fraction of Fe was 31.55% and Cr 25.64%. In spot 2, the atomic fraction of Co was 41.67%, Fe 31.82% and Cr 26.51%. In spot 3, the atomic fraction of Co was lower at 35.34%, while Fe reached 33.83% and the Cr fraction increased to 30.83%.

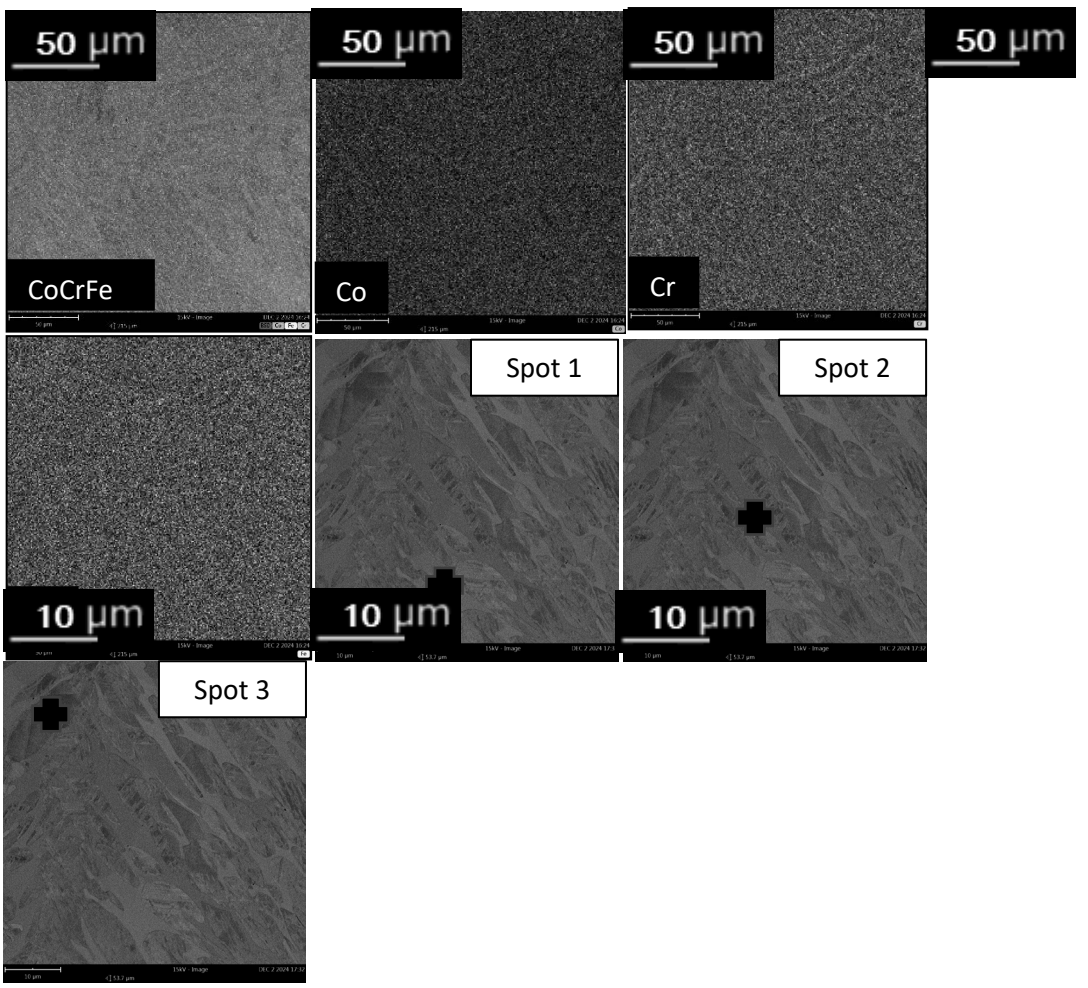

Figure 2. EDS maps with SEM images of spot analysis (spots 1-3) for the CoCrFe alloy

Table 1. Mass and atomic content of cobalt, iron and chromium from the examined microstructure area and in the EDS point analysis (spot 1-3) for the CoCrFe alloy

CoCrFe	Combined map		Spot 1		Spot 2		Spot 3	
Element symbol	Atomic %	Weight %	Atomic %	Weight %	Atomic %	Weight %	Atomic %	Weight %
Co	33.21	35.22	42.81	40.48	41.67	39.35	35.34	37.35
Fe	32.94	33.10	31.55	32.04	31.82	32.28	33.83	33.89
Cr	33.85	31.67	25.64	27.48	26.51	28.37	30.83	28.76

The results indicate microsegregation of Cr, which locally shows lower values in the point analysis, which may suggest structural inhomogeneity of the material and a potential tendency of chromium to diffuse into specific areas. Cobalt, on the other hand, shows a clear variability in the point analyses, which also emphasizes the local inhomogeneity of the chemical composition.

In the case of the CoFeNi alloy (Fig. 3, Table 2), the analysis of the chemical composition of the entire area showed atomic shares at the level of: Co 33.94%, Fe 32.89%, and Ni 33.17%. The point analysis in spot 1 shows very similar values: Co 33.61%, Fe 33.08%, and Ni 33.31%. In spots 2 and 3, the shares of individual elements were similar. Minimal differences between the results of the point analysis indicate the chemical homogeneity of the alloy. The lack of clear deviations in the composition indicates that the elements were evenly distributed in the structure.

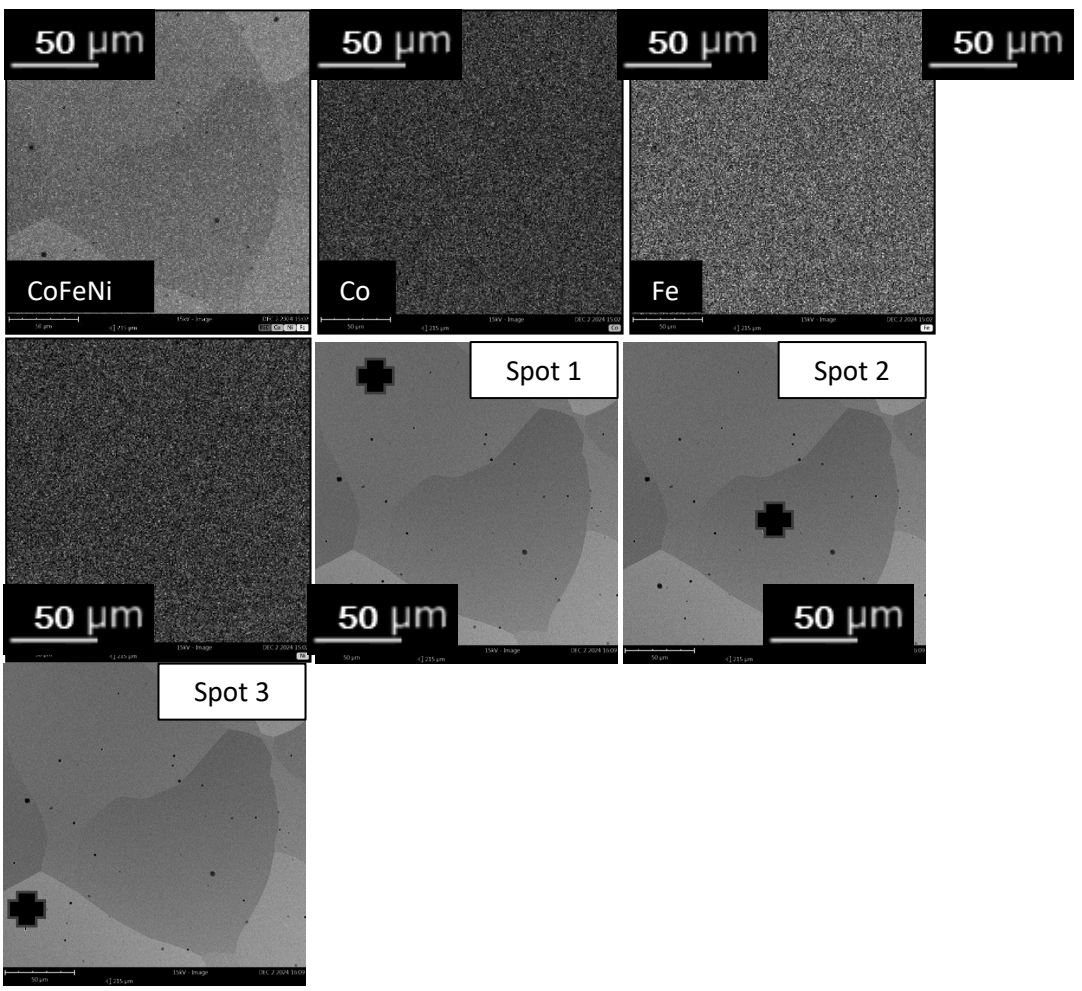

Figure 3. EDS maps with SEM images of spot analysis (spots 1-3) for the CoFeNi alloy

Table 2. Mass and atomic content of cobalt, iron and nickel from the examined microstructure area and in the EDS point analysis (spot 1-3) for the CoFeNi alloy

CoFeNi	Combined map		Spot 1		Spot 2		Spot 3	
Element symbol	Atomic %	Weight %	Atomic %	Weight %	Atomic %	Weight %	Atomic %	Weight %
Co	33.94	34.59	33.61	34.25	33.64	34.29	34.73	35.38
Fe	32.89	33.38	33.08	33.57	32.90	33.39	32.25	32.72
Ni	33.17	32.03	33.31	32.17	33.46	32.32	33.03	31.89

The results of the analyses for the CoCrNi alloy (Fig. 4, Table 3) indicate relatively small differences between the studied area and the spot measurements, especially for Cr and Ni. More pronounced differences are observed in the case of cobalt, the content of which in some points (spot 2 and spot 3) increases to the level of 34.98% and 34.06%, respectively. Such an increase may suggest local enrichment of cobalt in some areas, which is probably due to microsegregation. Despite these differences, the deviations are small compared to those of the CoCrFe alloy. This means that the CoCrNi alloy is characterized by a homogeneous chemical composition.

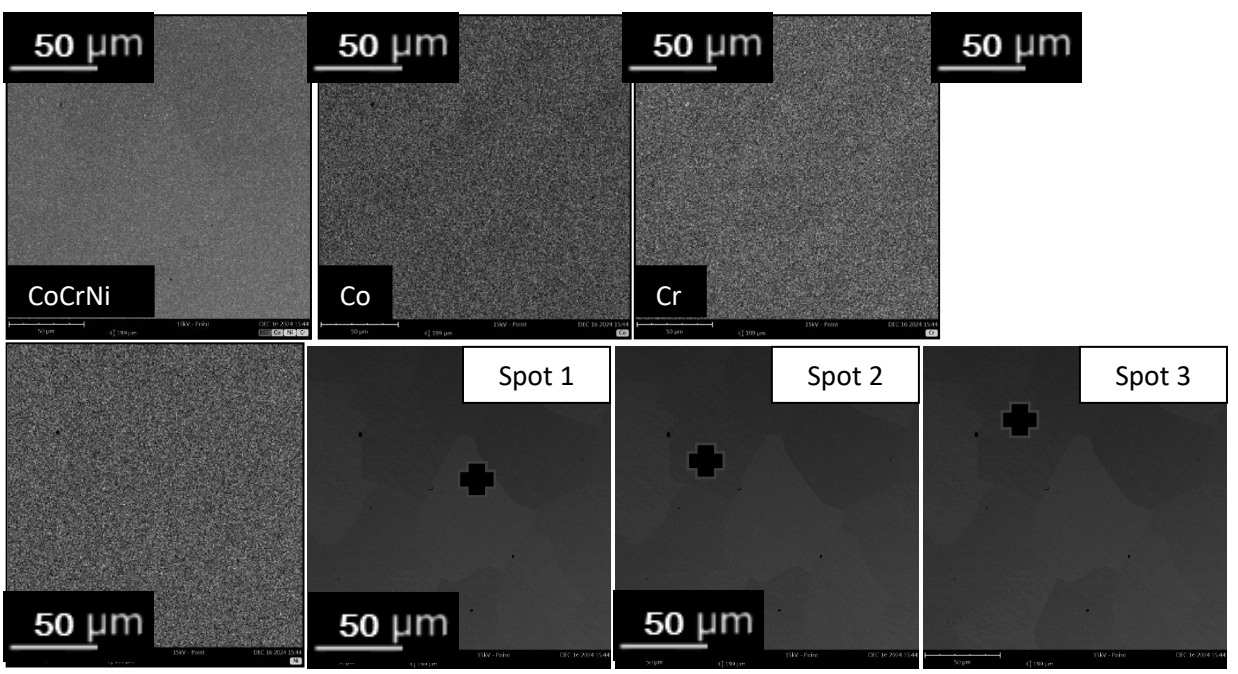

Figure 4. EDS maps with SEM images of spot analysis (spots 1-3) for the CoCrNi alloy

Tabela 3. Mass and atomic content of cobalt, chromium and nickel from the examined microstructure area and in the EDS point analysis (spot 1-3) for the CoCrNi alloy

CoCrNi	Combined map	Spot 1	Spot 2	Spot 3

Element symbol	Atomic %	Weight %	Atomic %	Weight %	Atomic %	Weight %	Atomic %	Weight %
Co	33.46	34.88	33.42	34.86	34.98	36.41	34.06	35.50
Cr	33.05	34.31	32.59	33.86	32.73	33.93	32.62	33.86
Ni	33.50	30.81	33.99	31.28	32.29	29.66	33.33	30.65

The microstructure images of the alloys observed at two magnifications using light microscopy are presented in Figures 5-7. The CoCrFe alloy (Fig. 5) was characterized by a dendritic structure, while for the CoFeNi (Fig. 6) and CoCrNi (Fig. 7) alloys, an equiaxed grain structure was observed. The CoCrNi alloy showed greater refinement of the structure compared to CoFeNi. In the work of Xue et al. [6] the results of microstructure studies for the $CrCoNiAl_{0.014}$ alloy were presented. According to the authors [6], the microstructure of the tested alloy with medium entropy consisted of cellular crystals. On the other hand, black particles may indicate oxides or gaps in the stage of preparation of microsections. According to Xue et al. [6], the matrix of the $CrCoNiAl_{0.014}$ alloy is the FCC phase. Yin et al. [7] described, among others, the effect of carbon addition on the size and shape of grains in the microstructure of medium entropy alloys based on NiCoFe. According to the authors, the microstructure of the NiCoFe alloy without carbon addition is characterized by the occurrence of coarse columnar grains with an average size of 769 µm.

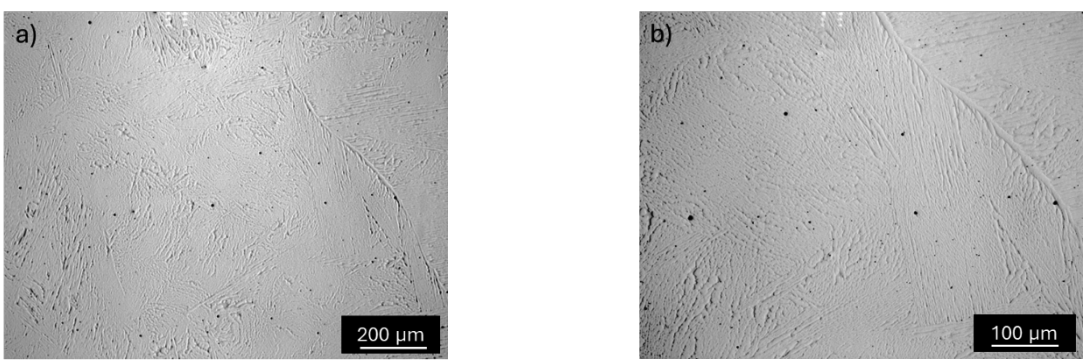

Figure 5. LM structure of the CoCrFe alloy at 50x (a) and 200x (b) magnification

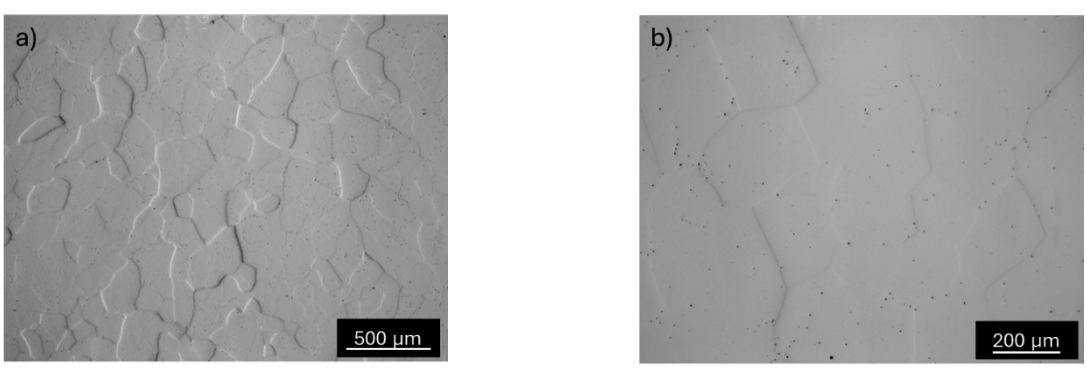

Figure 6. LM structure of the CoFeNi alloy at 50x (a) and 200x (b) magnification

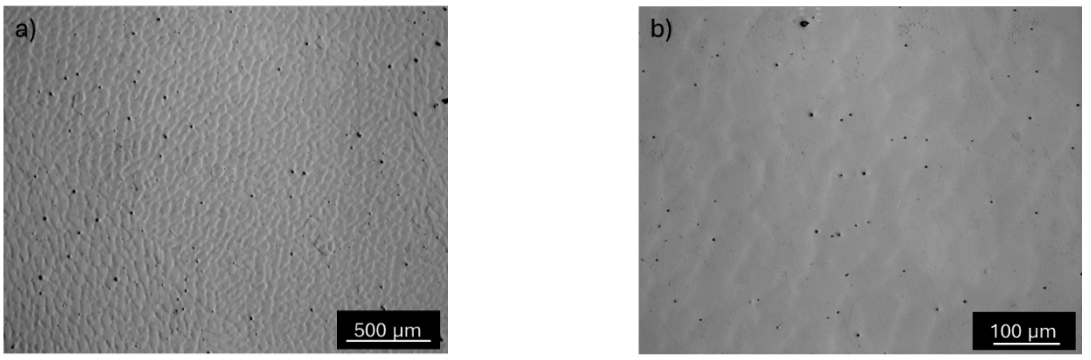

Figure 7. LM structure of the CoCrNi alloy at 50x (a) and 200x (b) magnification

4. SUMMARY

On the basis of the element distribution maps using the EDS method, it was shown that the CoFeNi and CoCrNi alloys were characterized by high chemical homogeneity, while the CoCrFe alloy showed very slight inhomogeneity. Qualitative chemical analysis of selected areas and microstructure spots confirmed that a chemical composition of tested MEAs was close to equiatomic.

BIBLIOGRAPHY

1. C. Wang, R. Sheng, D. Zhou, W. Li, S. Chen, F. Meng, G. Velisa, D. Chao, L. Jiang, P.K. Liaw, Y. Tong, Achieving an excellent combination of strength and ductility in a single-phase metastable medium-entropy alloy, Journal of Materials Research and Technology 27 (2023) 3914-3922.
2. J. Li, Y. Wang, D. Yan, J. Li, Effects of nanotwins and stacking faults on the mechanical properties of CrCoNi medium-entropy alloys, Journal of Materials Research and Technology 27 (2023) 3447-3458.
3. W. Zhou, F. Cao, Z. Yang, T. Li, Y. Niu, Y. Chen, H. Wang, L. Dai, Polymorphic phase transition in CoCrNi medium-entropy alloy under impact loadings, Journal of Materials Research and Technology 28 (2024) 3583-3596.
4. X. Zheng, H. Chen, T. Lu, N. Yao, Y. Wang, Y. Liu, K. Kosiba, Laser additive manufacturing of CoCrNi medium entropy alloy composites reinforced by in-situ nanoprecipitations: Microstructure formation and mechanical properties, Materials Characterization 207 (2024) 113500.
5. Z. Zhang, T. Yuan, R. Li, Corrosion performance of selective laser-melted equimolar CrCoNi medium-entropy alloy vs its cast counterpart in 3.5 wt% NaCl, Journal of Alloys and Compounds 864 (2021) 158105.
6. B. Xue, Z. Feng, J. Chen, C. Zhang, T. Li, J. Tan, C. Li, J. Yi, Mechanism of aluminum element segregation in as-cast medium-entropy alloy $CrCoNiAl_{0.014}$: A hybrid MD/MC simulation and experimental study, Metals 13 (2023) 331.
7. Z.H. Yin, X.W. Liu, N. Gao, S.R. Li, J.Q. Yao, Z.T. Fan, W.B. Zhang, Y.Z. Wang, Grain refinement of a NiCoFe medium entropy alloy: composition design from a solute interaction perspective, Journal of Alloys and Compounds 951 (2023) 169966.

TalentDetector
31th January 2025
Gliwice, Poland
DEPARTMENT OF ENGINEERING MATERIALS AND BIOMATERIALS
FACULTY OF MECHANICAL ENGINEERING
SILESIAN UNIVERSITY OF TECHNOLOGY
INTERNATIONAL STUDENTS SCIENTIFIC CONFERENCE

Corrosion resistance and hardness of CoCr(Fe,Ni) and CoFeNi medium entropy alloys

Sandra Nadolna[a], Bartosz Żary[a], Miłosz Ferdyn[a], Michał Podgórski[a], Maxymilian Żukowski[a], Katarzyna Młynarek-Żak[b], Monika Spilka[c], Rafał Babilas[c]

[a] Student of Silesian University of Technology, Faculty of Mechanical Engineering, Department of Engineering Materials and Biomaterials
[b] Silesian University of Technology, Faculty of Mechanical Engineering, Department of Engineering Processes Automation and Integrated Manufacturing Systems
[c] Silesian University of Technology, Faculty of Mechanical Engineering, Department of Engineering Materials and Biomaterials
email: rafal.babilas@polsl.pl

Abstract: The study presents selected properties of CoCrFe, CoCrNi, and CoFeNi medium entropy alloys, produced by induction melting of pure elements. The corrosion resistance in a 3.5% NaCl solution was examined using the potentiodynamic method. Vickers hardness measurements were also performed. The results indicate that the CoFeNi alloy exhibits the lowest average Vickers hardness. The best electrochemical parameters were obtained for the CoCrNi alloy. The CoFeNi alloy had lower open-circuit potential and corrosion potential values, however in terms of polarization resistance and corrosion current density, it demonstrated better resistance than the CoCrFe alloy.

Keywords: medium entropy alloys, corrosion resistance, hardness

1. INTRODUCTION

Medium entropy alloys (MEAs) represent a new class of metallic materials consisting of at least three chemical elements with comparable contents so that none is dominant in quantity [1,2]. This composition leads to advantageous mechanical and physicochemical properties. Research on MEAs has gained significant attention among scientists and engineers in recent years. This interest is primarily due to their excellent properties, surpassing those achievable with conventional alloys such as steel, aluminum, and titanium based alloys. MEAs are characterized by high corrosion resistance, thermal stability and wear resistance. Additionally, these alloys can exhibit superior mechanical properties in various industrial applications [3,4].

The proper selection of chemical elements, such as iron (Fe), cobalt (Co), nickel (Ni), or chromium (Cr), enables the production of alloys with high ductility, which means the ability to undergo deformation under load without fracture or cracks. This combination of properties allows for broad engineering applications, particularly under demanding operating conditions,

such as in the aerospace, automotive, and energy industries [5]. Medium entropy alloys are also suitable for chemically aggressive environments, such as those found in the chemical or marine industries. Furthermore, their radiation resistance makes them viable for use in nuclear-related technologies, where materials must withstand damage caused by ionizing radiation [6].

Furthermore, research into the hydrogen embrittlement of medium entropy alloys indicates their potential future use in energy infrastructure and hydrogen-based technologies [7]. The properties of medium entropy alloys have made them the subject of intensive research, aiming for their widespread application as structural and load-bearing materials. In particular, these alloys show potential for use in the fabrication of advanced components, such as engine parts, turbines, or devices operating under extreme conditions.

The objective of this work was to investigate selected properties of CoFeNi, CoCrNi, and CoCrFe medium entropy alloys in terms of corrosion resistance and hardness.

2. MATERIALS AND METHODS

The medium entropy alloy samples with chemical compositions expressed in weight percentages such as Co35.3Cr31.2Fe33.5, Co34.7Cr30.6Ni34.7, and Co33.9Fe32.2Ni33.9 were selected. These samples were produced by melting pure elements using an NG-40 induction generator. The remelting process of 25 g samples was carried out in ceramic crucibles under a protective argon atmosphere with 99.999% purity, preventing oxidation reactions of the material being melted.

Corrosion resistance studies of the CoCrNi, CoCrFe, and CoFeNi alloys were carried out in a 3.5% sodium chloride solution at 25 °C using an Autolab 302N potentiostat. Measurements were recorded and analyzed using NOVA 1.11 software. The surface area of the samples was approximately 1 cm^2. Electrochemical potentiodynamic measurements were performed in a cell equipped with a three-electrode system with a water jacket. A saturated calomel electrode (SCE) served as the reference electrode, a platinum rod as the counter electrode, and the sample as the working electrode. Corrosion resistance was evaluated by monitoring the open circuit potential (OCP) relative to the calomel electrode. The corrosion potential and the corrosion current density were determined using the Tafel extrapolation method. Measurements were conducted after stabilizing the open circuit potential for 3600 seconds with a scanning rate of 1 mV/s^{-1}.

Vickers hardness testing was performed using a Future Tech FM-700 hardness tester with loads of 100 g and 500 g applied for 15 seconds. Samples for testing consisted of metallographic cross sections that were not subjected to etching.

3. RESEARCH RESULTS

The evaluation of the corrosion resistance of the CoCrNi, CoCrFe, and CoFeNi medium entropy alloys was conducted by electrochemical tests with the potentiodynamic method. The results of the open circuit potential measurements as a function of time (a) and the polarization curves (b) are presented in Figure 1. The values of the open circuit potential (E_{OCP}), corrosion potential (E_{corr}), corrosion current density (j_{corr}) and polarization resistance (R_p) are summarized in Table 1.

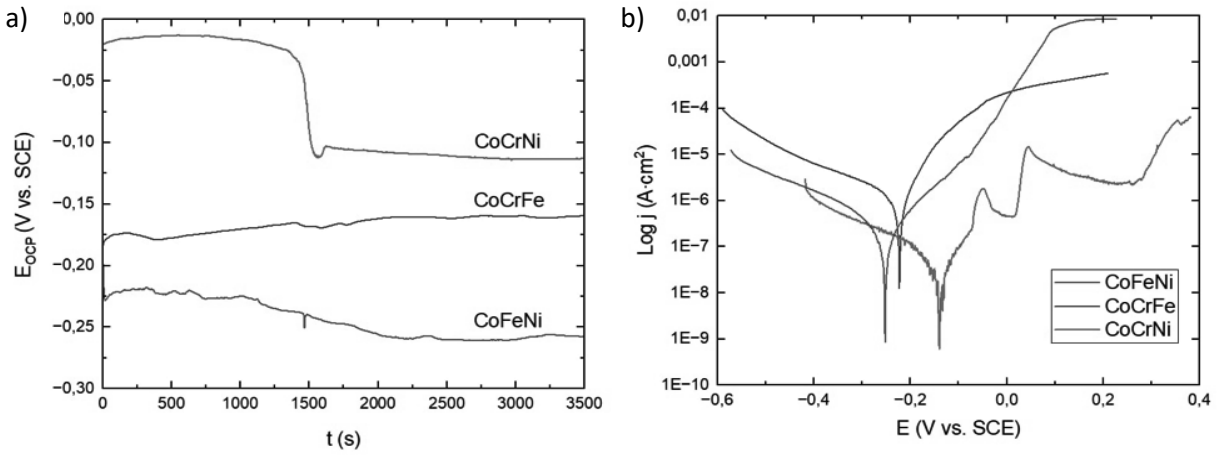

Figure 1. Changes of the open-circuit potential with time (a) and polarization curves (b) in 3.5% NaCl solution at 25 °C of CoCrNi, CoCrFe and CoFeNi medium entropy alloys

Table 1. Results of the electrochemical parameters of CoCrNi, CoCrFe, CoFeNi MEAs

Sample	E_{OCP} [V] (±0.01)	E_{corr} [V] (±0.01)	j_{corr} [μA/cm^2] (±0.01)	R_p [kΩcm^2] (±0.1)
CoCrNi	−0.113	−0.140	0.05	530.4
CoCrFe	−0.159	−0.222	1.33	17.4
CoFeNi	−0.258	−0.252	0.26	114.8

The open circuit potential of the tested samples displayed varied values during the measurement period. After 3600 seconds, more positive E_{OCP} values were recorded for the CoCrNi (−0.113 V) and CoCrFe (−0.159 V) alloys. Additionally, the CoCrNi alloy exhibited a corrosion potential shifted toward positive values (−0.140 V), the highest polarization resistance (530.4 kΩ·cm²), and the lowest corrosion current density (0.05 μA/cm²) compared to the other alloys. On the contrary, the CoFeNi alloy reached the most negative open-circuit potential (−0.258 V) and corrosion potential (−0.252 V). However, in terms of polarization resistance and corrosion current density, it achieved better values than that of the CoCrFe alloy.

Wetzel et al. [8] compared the corrosion resistance of the CrCoNi medium entropy alloy, the CrMnFeCoNi high-entropy alloy (HEA), and the AISI 304 stainless steel. The authors demonstrated that the medium entropy alloy exhibited superior corrosion resistance compared to HEA and AISI 304 in aqueous H_2SO_4 and NaCl solutions. This finding suggests that the CrCoNi alloy possesses the best corrosion resistance, primarily due to its chemical composition and chemically homogeneous structure.

The mechanical properties of the medium entropy alloys CoCr(Fe,Ni) and CoFeNi were determined based on Vickers hardness measurements under loads of 100 and 500 g. The average hardness values, calculated from 25 measurements along with the standard deviation are presented in Figure 2 and Table 2.

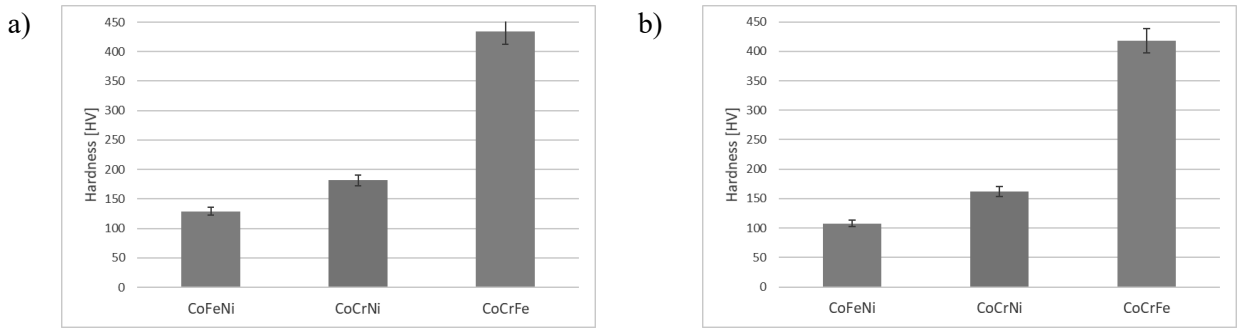

Figure 2. Average values of hardness measurements of CoCrNi, CoCrFe, and CoFeNi alloys at a load of 100 g (a) and 500 g (b)

Table 2. Average Vickers hardness of the tested alloys with standard deviation

Alloy	Vickers hardness [HV] under load:	
	100 g	500 g
CoCrNi	181.8 ±5,1	163.2±4,5
CoCrFe	433.9±20,3	417.9±18,6
CoFeNi	128.9±3,8	107.9±2,6

Based on the conducted measurements, it can be observed that among the tested materials, the highest average hardness values were recorded for alloys containing chromium. The CoCrFe alloy achieved a hardness of 433.9 HV under 100 g load and 417.9 HV under a 500 g load. A reduction in hardness was observed for the CoCrNi alloy (181.8 HV at 0.1; 163.2 HV at 0.5), likely due to the presence of nickel. In a study described in the publication [9], the hardness of 200.1 HV under a 500 g load with a measurement time of 10 seconds. These results were compared with the data from the publication [10], where the hardness of the CoCrNi alloy was determined to be 187.5 HV. For the CoFeNi alloy, the lowest hardness values were observed among the tested samples. The replacement of chromium with iron resulted in a decrease in the average hardness of the CoFeNi alloy at 128.87 HV and 107.9 HV under loads of 100 g and 500 g, respectively.

4. SUMMARY

The results of the electrochemical studies revealed varying levels of corrosion resistance among the alloys tested in a 3.5% NaCl solution. The CoCrNi alloy exhibited the best corrosion resistance, characterized by the most positive values of open circuit potential and corrosion potential (E_{corr}), as well as the lowest j_{corr} (0.05 μA/cm^2) and the highest polarization resistance (530.4 kΩcm^2).

The discrepancy between the values of E_{corr} and j_{corr} indicates better corrosion resistance of the CoFeNi alloy compared to that of the CoCrFe alloy. This is because the potential is a thermodynamic value, whereas the corrosion current density is a kinetic parameter related to the corrosion rate. It can be assumed that, despite its higher potential, the CoCrFe alloy is likely to corrode more rapidly in a 3.5% aqueous NaCl solution.

Mechanical tests of the medium entropy alloys revealed that the CoCrFe alloy has the highest hardness, which may be attributed to the presence of intermetallic phases in its structure. The lowest hardness was recorded for the CoFeNi alloy.

BIBLIOGRAPHY

1. C. Wang, R. Sheng, D. Zhou, W. Li, S. Chen, F. Meng, G. Velisa, D. Chao, L. Jiang, P.K. Liaw, Y. Tong, Achieving an excellent combination of strength and ductility in a single-phase metastable medium-entropy alloy, Journal of Materials Research and Technology 27 (2023) 3914-3922.
2. J. Li, Y. Wang, D. Yan, J. Li, Effects of nanotwins and stacking faults on the mechanical properties of CrCoNi medium-entropy alloys, Journal of Materials Research and Technology 27 (2023) 3447-3458.
3. W. Huo, S. Wang, F. Fang, S. Tan, Ł. Kurpaska, Z. Xie, H.S. Kim, J. Jiang, Microstructure and corrosion resistance of highly <111> oriented electrodeposited CoNiFe medium-entropy alloy films, Journal of Materials Research and Technology 20 (2022) 1677-1684.
4. W. Li, D. Xie, D. Li, Y. Zhang, Y. Gao, P.K. Liaw, Mechanical behavior of high-entropy alloys, Progress in Materials Science 118 (2021) 100777.
5. H. Yao, J.-W. Qiao, M.C. Gao, J.A. Hawk, S.-G. Ma, H. Zhou, MoNbTaV medium-entropy alloy, Entropy 18 (2016) 289.
6. Z. Cheng, J. Cui, D. Chen, X. Gao, J. Ren, T. Wang, H. Chang, P. Tai, J. Sun, Studies on high-temperature stability and strengthening mechanisms of high/medium-entropy alloys for potential nuclear applications: The case of FeCrV-based alloys, Materials Science and Engineering: A 870 (2023) 144858.
7. H. Luo, S.S. Sohn, W. Lu, L. Li, X. Li, .C.K. Soundararajan, W. Krieger, Z. Li, D. Raabe, A strong and ductile medium-entropy alloy resists hydrogen embrittlement and corrosion, Nature Communications 11 (2020) 3081.
8. A. Wetzel, M. Au, P.M. Dietrich, J. Radnik, O. Ozcan, J. Witt, The comparison of the corrosion behavior of the CrCoNi medium entropy alloy and CrMnFeCoNi high entropy alloy, Applied Surface Science 601 (2022) 154171.
9. M.-D. Xie, W.-T. Ye, Q. Zhou, L. Jia, B. Chen, M.-Q. Zhang, H.-F. Wang, A novel CoCrNi-based medium-entropy alloy self-lubricating composite with superior wear performance, Rare Metals (2024).
10. N. Li, G. Ji, B. Gan, Q. Qiao, S. Ni, M. Song, Effects of Mo-doping on the microstructure and mechanical properties of CoCrNi medium entropy alloy, Journal of Materials Research 35 (2020) 2726-2736.

TalentDetector

31th January 2025
Gliwice, Poland

DEPARTMENT OF ENGINEERING MATERIALS AND BIOMATERIALS
FACULTY OF MECHANICAL ENGINEERING
SILESIAN UNIVERSITY OF TECHNOLOGY

INTERNATIONAL STUDENTS SCIENTIFIC CONFERENCE

Symbiosis of AI and material science: ChatGPT as a catalytic factor in advanced material processing and analysis

Nicoleta Negru[a]

[a] University of Petroșani, Faculty of Mechanical and Electrical Engineering
email: nicoletanegru@upet.ro

Abstract: The symbiosis between artificial intelligence (AI) and materials science has ushered in a new era of advanced material processing and analysis. This study explores the integration of AI as a catalytic factor in optimizing machining processes, enhancing precision, and advancing the characterization of materials. By leveraging state-of-the-art tools like 3-axis CNC plasma jet cutting machines and Hexagon Absolute Arms, this paper highlights how AI, exemplified by ChatGPT, can support parameter optimization, real-time data analysis, and continuous process improvement. Through practical simulations, we demonstrate AI's role in proposing ideal cutting parameters, predicting outcomes, and facilitating rapid adjustments for improved quality and reduced waste. The findings underscore AI's ability to process complex datasets, detect subtle manufacturing deviations, and optimize laser-based processes. This synergy between AI and modern manufacturing technologies paves the way for unprecedented innovations in materials science, reshaping traditional workflows and expanding the frontiers of industrial applications.

Keywords: artificial intelligence, material processing, CNC, laser treatment, polymers

1. INTRODUCTION

In an era of technological advancement, where precision and innovation are fundamental values, materials science is at a transformative crossroads. The 3-axis CNC (Computer Numerical Control) plasma jet cutting machine is an outstanding example of technology that is transforming the way structural materials and their surfaces are processed and optimized. By using plasma beams to cut and shape materials, this equipment brings a level of precision and versatility essential to modern applications.

In the field of structural materials, the CNC machine facilitates the use of advanced alloys such as heat-resistant steels and light alloys, providing customized solutions for the needs of each industry. At the same time, surface engineering benefits from the possibility of advanced treatment, either through traditional finishes or through innovative methods, such as laser treatments or coatings made through technologies such as PVD (Physical vapor deposition) and CVD (Chemical vapor deposition).

This paper explores how artificial intelligence (AI), through ChatGPT, can support the processes of optimizing cutting parameters, analyzing generated data and implementing continuous improvement solutions. For example, in the context of plasma jet processing applications, ChatGPT can suggest ideal settings for different materials, reducing waste and maximizing process efficiency. Thus, artificial intelligence is not just a passive tool, but an active collaborator facilitating discoveries and innovations in real time.

By integrating advanced technologies, the CNC plasma jet machine redefines the limits of manufacturing processes, and artificial intelligence helps to harness the full potential of these equipments. With this combination, every challenge becomes an opportunity to push conventional boundaries, whether we are talking about structural materials, surface engineering or advanced manufacturing methods such as Directed Energy Deposition (DED) or metal powder modification.

This paper sits at the intersection of cutting-edge technology and materials science, providing insight into how modern equipment and artificial intelligence are radically transforming traditional processes, paving the way for breakthrough innovations.

The integration of artificial intelligence (AI) into laser material processing processes has become a topic of major interest in contemporary research. Recent studies highlight how AI can optimize and control laser machining processes, improving their quality and efficiency.

A notable example is the research carried out by Velli et al. (2020), which explores the use of AI in laser material processing. The study demonstrates how software agents, through machine learning, can select optimal processing parameters to achieve minimal surface roughness and a reduced number of defects. This approach enables continuous and automatic adaptation to new process situations and changed target parameters, providing increased flexibility and efficiency in material processing [1].

Also, Behbahani et al. (2022) investigated the monitoring of plasma surface pretreatment processes using AI and Machine Learning. By combining optical methods - spectroscopic or imaging - with AI, an automated and high-precision control of processes has been achieved. This method allows real-time adjustment of the laser parameters, ensuring an optimal interaction with the treated material and improving the processing results [2].

In addition, a study published by Shang et al. (2024) reviews the impact of digital engineering on photonic technologies, with a focus on advances in laser processing through digital models and AI. The article highlights the essential role of digital models in predicting and optimizing thermal effects in laser processing, reducing material deformations and defects. The integration of AI refines these models, improving productivity and quality in applications such as micromachining and cladding [3].

Article [4] explores the use of machine learning models such as Random Forest and neural networks to predict the mechanical properties of ultra-high temperature ceramics (UHTC) such as carbides. The method reduces experimental time and cost by providing accurate predictions of Young's modulus, flexural strength and fracture toughness. The results highlight the effectiveness of machine learning in optimizing materials for extreme applications such as aerospace.

Article [5] presents a machine learning based approach to predict peak temperature, residual stresses and distortions during laser welding of stainless steel. Using kernel ridge regression (KRR), the model was trained on data obtained from numerical simulations, including welding parameters and material properties. The KRR model demonstrated high accuracy with R^2 values of 0.968 for peak temperature, 0.951 for peak residual stress, and 0.928 for degree of distortion. The analysis revealed the significant influence of the physical properties of the

materials on the maximum temperature, while the residual stresses and distortions were influenced by both mechanical and physical factors. These findings highlight the potential of machine learning techniques in optimizing laser welding processes for stainless steels.

Article [6] explores the integration of machine learning in laser material processing (LMP) processes for e-mobility applications [7], [9], [10], with the aim of optimizing manufacturing and reducing material waste [8]. Techniques such as laser beam welding (LBW) and direct energy deposition (DED) are reviewed, and a proposed framework demonstrates the use of artificial neural networks (ANN) [8] for weld bead size prediction. The study highlights the potential of machine learning in reducing defects and improving industrial efficiency.

All these studies presented above highlight the significant potential of AI [11] in the transformation of laser processing processes or with other technologies, offering innovative solutions for optimizing process parameters, real-time monitoring and improving the quality of final products. Integrating AI into these processes not only increases efficiency, but also opens new directions for research and development in the field of materials processing.

2. PRESENTATION OF STUDY EQUIPMENT AND THEIR CLASSICAL USE

The 3-axis CNC plasma jet cutting machine represents a benchmark in modern material processing technologies, being designed to meet the varied demands of the industry, from the manufacture of structural components to the detailed machining of advanced alloys (Fig.1).

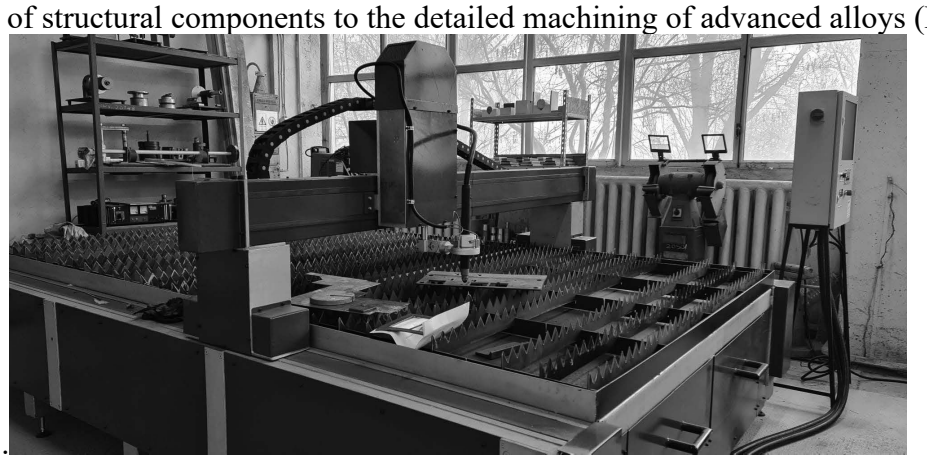

Figure 1. CNC plasma jet cutting machine with 3 axes (University of Petrosani)

This machine uses a plasma generation process by creating an electric arc between an electrode and the target material, which, under the action of an ionized gas, reaches temperatures of up to 20,000°C. This plasma jet not only melts the material, but also removes it through the gas pressure, generating clean and precise edges. CNC control allows three-axis movement (X, Y, Z), which facilitates the manufacture of complex structures.

The machine combines a high voltage power supply (400V for the plasma module) with a working gas such as compressed air or argon to produce the plasma required for the cutting process. The thicknesses of the cut materials vary depending on the type of material: up to 20 mm for mild steel, 15 mm for aluminum and 12 mm for stainless steel. The machine also offers a precision tolerance of ±0.05 mm, ensuring optimal results in industrial production.

The 83 Series Hexagon Absolute Arm represents a technological breakthrough in advanced measurement, integrating touch and 3D laser scanning capabilities to meet the diverse needs of modern industry. This equipment is designed to provide exceptional accuracy in component

inspection and material characterization, and is widely used in applications that require tight tolerances and detailed verification of surfaces and shapes.

Figure 2. Hexagon Absolute Arm (University of Petrosani)

The working principle of the Hexagon Absolute Arm is based on the use of absolute encoders, which allow precise positioning of the arm without the need for re-initialization, regardless of moving or stopping the device. It combines tactile measurements, made by a high-sensitivity probe, with three-dimensional laser scanning, providing a complete picture of the analyzed parts. The laser scanning system is capable of capturing both geometric details and complex surface textures, making it ideal for analyzing complex parts in fields such as the automotive, aerospace or medical industries.

The Hexagon Absolute Arm is not just a measuring tool, but an essential element in the optimization of modern manufacturing and characterization processes. Its contribution to increasing quality and efficiency makes this equipment indispensable in materials engineering, where precision and innovation are decisive factors for the success of industrial and scientific projects.

3. THE REVOLUTION BROUGHT BY CHATGPT

The integration of ChatGPT into the workflows associated with advanced equipment such as the Hexagon Absolute Arm and the CNC plasma jet machine represents a paradigm shift in the field of materials engineering. Its ability to process and analyze massive amounts of data, propose rapid technical solutions and facilitate detailed documentation redefines the way materials processing and characterization processes are approached.

ChatGPT, using advanced natural language processing algorithms and machine learning techniques, can quickly interpret this data to generate complex analytics. For example, for a scanned part, AI can detect subtle deviations that would not be observable manually and correlate these deviations with potential manufacturing errors or equipment wear.

In the case of the CNC plasma jet machine, data collected on cutting parameters such as feed rate, gas flow and amperage can be analyzed to identify optimizations. For example, ChatGPT can perform predictive simulations to estimate the impact of parameter changes on cut quality and equipment life. This predictive ability allows for reduced downtime, increased efficiency and prevention of material loss.

Industrial processes frequently face unforeseen problems, such as excessive surface roughness, burr formation, or excessive energy consumption during cutting. In such situations, ChatGPT can act as a virtual expert, accessing extensive databases of technical information and scientific publications to provide well-founded solutions. For example, if the edges of plasma-cut parts show defects, the AI can suggest precise adjustments, such as increasing gas pressure or reducing feed speed, based on similar scenarios in the literature.
ChatGPT can also simulate the effects of proposed adjustments, giving users a clear picture of the outcome before the changes are implemented. This not only saves time, but also minimizes the risks associated with direct experimentation on equipment.

The revolution brought by ChatGPT lies not only in its ability to rapidly process data, but also in its deep integration into the manufacturing chain, from processing and characterization to analysis of results and continuous process improvement. Through this holistic approach, ChatGPT becomes a catalyst for progress in materials engineering, providing innovative solutions that transform both processes and outcomes.

4. SIMULATION OF CHATGPT INTEGRATION IN A TECHNOLOGICAL PROCESS

To demonstrate the applicability of ChatGPT in the optimization of machining and metrological verification processes, we present a fictitious experiment based on the part observed in the images. The piece has overall dimensions of 300mm x 250mm, with two important cutouts: one 100mm x 150mm and another 100mm x 100mm. The purpose of the simulation is to optimize the cutting process to achieve clean edges and perfect dimensional compliance using the CNC plasma jet machine and the Hexagon Absolute Arm.

Stage 1: Machining the part with the CNC plasma jet machine

The process begins with the integration of ChatGPT into the CNC machine control software. The part's geometric data is fed into the system via a CAD model, and ChatGPT analyzes this data along with material properties (15mm thick steel) and design specifications. Based on this analysis, ChatGPT suggests a set of ideal parameters for pruning:

- Arc voltage: 150 V for full penetration.
- Cutting current: 180 A to reduce burrs.
- Feed speed: 900 mm/min to minimize thermal deformations.
- Gas flow: 100 l/min for plasma arc stability.

These settings are communicated directly to the CNC machine via a digital control system. Throughout the cutting process, ChatGPT receives real-time data from integrated sensors such as arc temperature, plasma jet stability and effective feed rate. Upon detecting instability in the large cutout area, the AI immediately adjusts the feed speed to 850 mm/min, transmitting these changes in real time to the machine controller. The process completes successfully and the part edges are reported as nearly compliant.

Step 2: Inspect the part with the Hexagon Absolute Arm

After the cut is complete, the part is transferred to the inspection table, where the Hexagon Absolute Arm is used for dimensional checking and surface analysis. ChatGPT is connected to the metrology software of the arm, coordinating the 3D scanning process. AI identifies critical areas of the part, such as corners and inside edges of cutouts, and configures the arm for a detailed scan.
The captured data is instantly analyzed by ChatGPT, which generates a three-dimensional map of the part (fig.3). Initial results indicate the following:
• Overall dimensions: 300.04mm x 250.02mm, conforming to ±0.05mm tolerance.
• Surface roughness: 0.85 µm, slightly above the specification of 0.8 µm.
• Deviation at the corner of the large cutout: 0.07 mm, exceeding the tolerated limit.

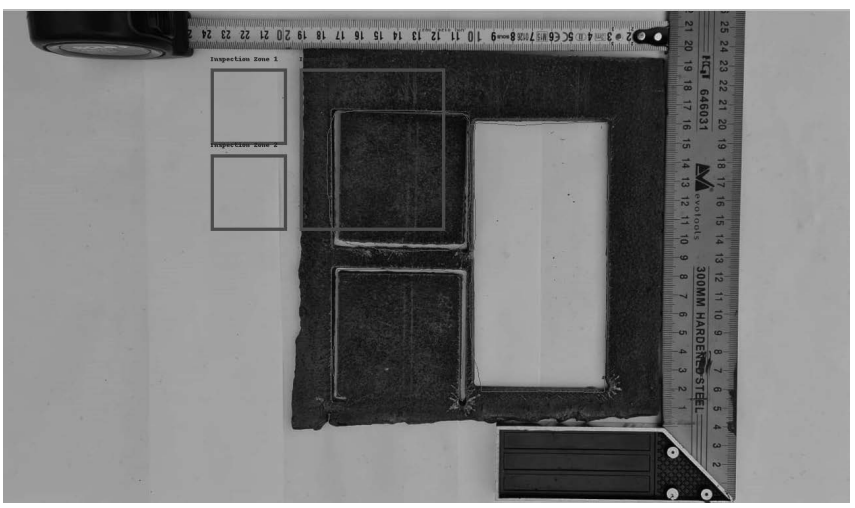

Figure 3. Minimal inspection of cuts made with ChatGPT

Based on these observations, ChatGPT proposes specific adjustments. Recommendations are sent back to the CNC machine via an automated interface, indicating the need for a localized recut. AI suggests reducing the feed rate to 800mm/min and increasing the cutting current to 185A to improve accuracy in the problem area.

Step 3: Implement adjustments and re-verify

The CNC machine implements the proposed changes and the part is recut in the corner area of the large cutout. After recutting is complete, the part is reanalyzed with the Hexagon Absolute Arm. This time, the dimensions and surface quality are fully in line with the specifications:
• Overall dimensions: 300.00 mm x 250.00 mm.
• Surface roughness: 0.78 µm, according to requirements.
• Absence of critical deviations at corners or edges.

ChatGPT acts as an intermediary between physical equipment and associated software, processing data in real time and providing adaptive solutions. Its integration is done through APIs that enable two-way communication. The AI analyzes the raw data generated by sensors and metrology software, correlates it with its knowledge base and sends precise instructions to

the machines involved. This interaction ensures a smooth workflow, eliminating human error and reducing processing time.

The simulation demonstrates how ChatGPT can simultaneously optimize processing and verification processes, integrating information from multiple sources and providing accurate solutions in real time. Its ability to interact directly with equipment and adjust operating parameters brings significant value to the field of advanced manufacturing, completely transforming the way high-precision components are made.

The results obtained from the simulation of the CNC plasma cutting process reflect a significant improvement in the process parameters and the quality of the manufactured parts. Early in the process, values for dimensional deviations and surface roughness indicated that the initial parameter settings were not optimized for the accuracy requirements. The average edge deviation was close to the specified tolerance limit of ±0.05 mm, and the surface roughness exceeded the target of 0.8 µm, hovering around 0.9 µm. These preliminary results highlighted the need for adjustments to better control the cutting process.

The optimization of the process (fig.4) started by adjusting the feed rate and the cutting current, which are essential parameters for controlling the interaction between the plasma arc and the material. Reducing the feed rate had the main effect of improving the mechanical stability of the system. By slowing down the movement of the cutting head, more interaction time between the plasma arc and the material was allowed, resulting in reduced deformations caused by thermal and mechanical forces. In parallel, the increase in the cutting current ensured a better penetration of the plasma arc, thus reducing the unevenness in the cutting area.

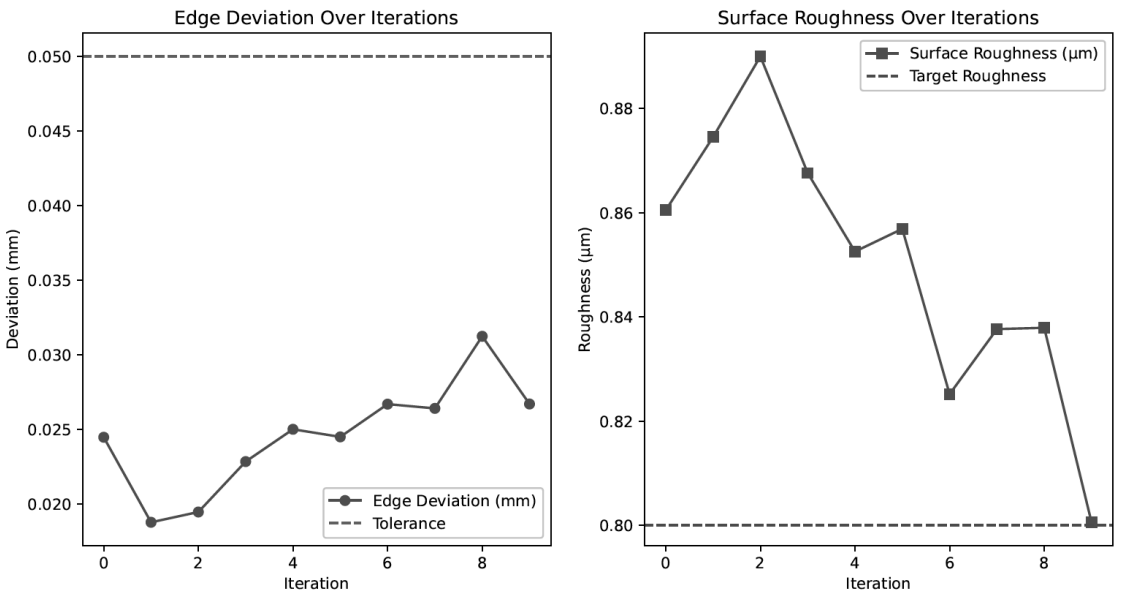

Figure.4 Edge deviation and surface roughness

After the first few iterations, the average deviation of the edges started to decrease substantially. At each iteration, the simulations showed a gradual reduction of the dimensional deviations, until they stabilized at a value of about 0.027 mm. This value is significantly lower than the tolerance limit, demonstrating an increased accuracy of the optimized process. Graphical analysis of dimensional deviations shows a clear convergence to stable and controlled values without large fluctuations between iterations.

Regarding the surface roughness, it was initially higher than the target of 0.8 μm, indicating the presence of more pronounced asperities. Successive adjustments led to a gradual improvement in surface quality as plasma arc stability improved due to increased current and reduced feed rate. In the last iteration, the average roughness reached 0.801 μm, almost identical to the specified target. This reduction in roughness indicates a significant reduction in microdefects and unevenness, resulting in a smoother and better finished surface.

CONCLUSIONS

This harmonious symbiosis between humans and AI will lead to a qualitative leap in technological innovation. Humans will continue to be the source of ideas and vision, while artificial intelligence will serve as an indispensable partner capable of turning these ideas into reality with unprecedented efficiency. As AI becomes more advanced and its integration into laboratories deepens, today's technological barriers will become tomorrow's solved challenges. Thus, the future holds for us a world in which the current limits of technology are overcome, and the possibilities for innovation become practically unlimited.

ACKNOWLEDGEMENTS

The work was created as a result of the project as part of project based learning - PBL, in the 11th competition under the Initiative of Excellence - Research University, Silesian University of Technology, Gliwice, Poland.

BIBLIOGRAPHY

1. Velli, M. C., Tsibidis, G. D., Mimidis, A., Skoulas, E., Pantazis, Y., & Stratakis, E. (2020). Predictive modeling approaches in laser-based material processing. *Journal of Applied Physics*, *128*(18).
2. Behbahani, R., Sarvestani, H. Y., Fatehi, E., Kiyani, E., Ashrafi, B., Karttunen, M., & Rahmat, M. (2022). Machine learning-driven process of alumina ceramics laser machining. *Physica Scripta*, *98*(1), 015834.
3. Shang, X., Li, E., Talbot, A., Wen, H., Lyu, T., Zhang, J., & Zou, Y. (2024). Accurate Inverse Process Optimization Framework in Laser Directed Energy Deposition.
4. Sun, J., Zhang, Z., Zhang, Y., Zhang, X., Guo, J., Fu, Q., & Wu, L. (2025). High-temperature ablation resistance prediction of ceramic coatings using machine learning. *Journal of the American Ceramic Society*, *108*(1), e20136.
5. Yang, Y., Patil, N., Askar, S., & Kumar, A. (2025). Machine learning-guided study of residual stress, distortion, and peak temperature in stainless steel laser welding. *Applied Physics A*, *131*(1), 44.
6. Ndeda, R., Botes, A., & Olakanmi, E. O. (2024). Framework for Incorporating Machine Learning (ML) Driven Optimisation into Laser Materials Processing (LMP) Technologies for e-Mobility Applications towards Attaining Zero-Material Waste. Lasers in Manufacturing and Materials Processing, 11(1), 77-108.

7. Rus, C., Leba, M., Risteiu, M., & Sibisanu, R. (2024). The Impact of Intelligent Parking Systems on Urban Mobility and the Role of Innovations in the Spectrum of Artificial Intelligence in the Electric Vehicle Industry. *ENTRENOVA-ENTerprise REsearch InNOVAtion*, *10*(1), 553-566.
8. Panaite, F. A., Rus, C., Leba, M., Ionica, A. C., & Windisch, M. Enhancing Air-Quality Predictions on University Campuses: A Machine-Learning Approach to PM2. 5 Forecasting at the University of Petroșani. *Sustainability*, *16*(17).
9. Rus, C., & Leba, M. (2022, October). Autonomous Smart Electric Vehicle Integrated into a Smart Grid Type System. In *EURECA-PRO Conference* (pp. 45-50). Cham: Springer International Publishing.
10. Marcus, R., Rus, C., Leba, M., & Risteiu, M. (2022, May). Electric Vehicles Between Recycling and Sustainable Development-@. ro. In *International Conference on Computers Communications and Control* (pp. 47-62). Cham: Springer International Publishing.
11. Rus, C., Leba, M., & Sibisanu, R. (2024, March). SOS-My Grandparents: Using the Concepts of IoT, AI and ML for the Detection of Falls in the Elderly. In *World Conference on Information Systems and Technologies* (pp. 164-173). Cham: Springer Nature Switzerland.

TalentDetector
31th January 2025
Gliwice, Poland
DEPARTMENT OF ENGINEERING MATERIALS AND BIOMATERIALS
FACULTY OF MECHANICAL ENGINEERING
SILESIAN UNIVERSITY OF TECHNOLOGY
INTERNATIONAL STUDENTS SCIENTIFIC CONFERENCE

Revolutionizing industrial energy management: low-cost IoT solutions for sustainable optimization and enhanced efficiency

Nicoleta Negru[a]

[a] University of Petroșani, Faculty of Mechanical and Electrical Engineering
email: nicoletanegru@upet.ro

Abstract: The increasing energy costs in industrial environments have driven the need for advanced and cost-effective energy monitoring solutions. This paper presents the design, development, and implementation of a low-cost, modular energy consumption monitoring system tailored for industrial halls. Leveraging open-source hardware platforms such as Arduino, accessible sensors, and IoT technologies, the proposed solution addresses the constraints of traditional monitoring systems, making it suitable for small and medium-sized enterprises (SMEs). The system integrates components such as high-precision current and voltage sensors, data transmission modules, and a web-based interface for real-time data visualization and analysis. The methodology involves real-time data acquisition from various industrial consumers, including CNC plasma cutting machines, air compressors, and lighting systems, with data aggregated and processed to provide actionable insights. Predictive analytics, enabled by IoT and machine learning algorithms, facilitate the identification of consumption patterns, inefficiencies, and optimization opportunities. The hardware implementation progresses through iterative stages, culminating in a compact and optimized system architecture for seamless integration into industrial processes. A key innovation is the deployment of a web-based platform that consolidates energy data, presenting it in a user-friendly format. The platform features interactive graphs and dynamic controls for monitoring consumption over customizable time intervals, supporting strategic decision-making. This study demonstrates the feasibility of employing affordable technologies for precise energy management, offering significant operational and economic advantages. The proposed system sets a benchmark for scalable and efficient energy monitoring, providing a pathway for sustainable practices in industrial operations.

Keywords: energy monitoring, industrial halls, low-cost systems, energy management, open-source hardware, industrial sustainability, modular systems.

INTRODUCTION

In an industrial context characterized by the accelerated growth of electricity and fuel costs, optimizing energy consumption has become a strategic priority for companies. In contemporary industry, efficient energy management is a determining factor in reducing operational costs,

increasing competitiveness and achieving sustainability goals. This necessity requires the development of advanced but also affordable technological solutions that allow real-time monitoring and control of energy consumption, even in complex industrial environments. Recent advances in microelectronics, Internet of Things (IoT) technologies, and artificial intelligence (AI) have opened up new opportunities for the development of efficient, modular, and low-cost energy monitoring systems.

The implementation of an energy monitoring system in industrial halls requires the use of a flexible and scalable hardware infrastructure.

Modern solutions include:

- Arduino or Raspberry Pi development boards: these open-source platforms enable easy programming and rapid integration with sensors and communication modules.
- high precision current and voltage sensors: the use of sensors such as the ACS712 or CT current transformers allows accurate measurement of electrical parameters in real time.
- communication modules: ethernet (such as W5100) or Wi-Fi network modules ensure continuous data transmission to servers or databases for storage and analysis.

These hardware components, combined with data processing algorithms, can generate detailed reports on energy consumption, identifying areas of inefficiency and proposing optimization solutions.

IoT technologies provide a complete insight into energy consumption, facilitating:

- real-time data collection from multiple measurement points distributed in industrial halls.
- data transmission to cloud platforms for advanced processing.
- predictive analysis of energy consumption through machine learning algorithms, which can identify consumption patterns and propose corrective measures.

In an industrial hall, energy consumption is not limited to a single piece of equipment, such as a CNC plasma cutter, but includes a variety of consumers:

- main equipment: CNC machines, hydraulic presses, robotic welding systems.
- auxiliary systems: air compressors, ventilation systems, hydraulic pumps.
- lighting and other passive consumption: Industrial lighting systems and office equipment.

The integration of these consumers in a centralized monitoring system allows the correlation of individual consumptions with the global performance of the industrial hall.

Monitoring systems based on low-cost equipment offer numerous advantages:

- financial accessibility: low implementation and maintenance costs make them ideal for SMEs or companies exploring energy optimization solutions.
- flexibility and modularity: possibility to expand the system by adding new sensors and hardware modules according to the specific requirements of the installation.
- advanced data analysis: using open-source software and machine learning algorithms to identify deviations and optimize operating parameters.

LITERATURE REVIEW ON ENERGY MONITORING SYSTEMS

In recent years, the increasing global emphasis on energy efficiency and sustainability has driven the evolution of energy monitoring systems, with particular attention to their application in industrial and renewable energy domains. These systems are now pivotal for optimizing energy consumption, ensuring reliability, and reducing operational costs while contributing to environmental sustainability.

The industrial sector, a major consumer of global energy, faces persistent challenges in balancing production efficiency with energy consumption. Advanced energy monitoring systems (EMS) have emerged as essential tools for addressing these challenges. Traditional supervisory control and data acquisition (SCADA) systems have been widely employed for energy monitoring; however, their high implementation and maintenance costs limit their adoption by small and medium-sized enterprises (SMEs). To bridge this gap, recent advancements have leveraged affordable and scalable technologies, such as open-source platforms like Arduino and Raspberry Pi, to develop cost-effective EMS for industrial applications [1].

These systems utilize a combination of sensors, communication modules, and data analytics platforms to provide real-time monitoring and actionable insights. For instance, IoT-enabled EMS, as detailed in recent studies, integrate high-precision current and voltage sensors with centralized data collection systems to monitor diverse industrial equipment, including CNC machines, air compressors, and lighting systems. By correlating energy consumption with production metrics, these systems identify inefficiencies and enable data-driven decision-making to optimize energy usage [2].

The integration of renewable energy sources, such as solar and wind, into industrial operations has further accentuated the need for robust energy monitoring solutions. Renewable energy monitoring systems must address unique challenges, including variable generation rates and integration with conventional energy grids. Advanced IoT platforms now facilitate real-time tracking of power generation, storage, and consumption, ensuring seamless integration of renewable energy into industrial and commercial applications [3].

A significant innovation in this domain is the use of battery energy storage systems (BESS) in conjunction with renewable sources. BESS plays a critical role in stabilizing energy supply by storing excess energy during peak production periods and discharging it during low production or high demand periods. Recent studies highlight the integration of IoT-based BESS monitoring systems, which enable continuous tracking of parameters such as state-of-charge (SoC), voltage, and temperature. These systems employ predictive analytics and machine learning algorithms to forecast energy needs, extend battery life, and ensure operational reliability [4].

The Internet of Things (IoT) has revolutionized energy monitoring by enabling decentralized data collection and analysis. IoT-based systems integrate various sensors and devices to provide a comprehensive view of energy usage across facilities. In industrial settings, these systems not only monitor conventional energy consumption but also facilitate the adoption of green energy solutions [4].

One exemplary application is the monitoring of solar photovoltaic (PV) systems. IoT-enabled PV monitoring systems track real-time metrics such as irradiance, panel efficiency, and energy output, optimizing energy generation and reducing maintenance costs. Furthermore, IoT platforms allow for remote monitoring and maintenance of PV systems, ensuring maximum uptime and efficiency [3].

Studies also explore the role of energy monitoring in disaster management and public infrastructure. For instance, solar-powered multi-functional portable charging devices (SPMFPCD) with IoT-based monitoring capabilities have demonstrated their utility in emergency scenarios and public spaces. These devices integrate renewable energy sources with advanced monitoring systems, providing reliable and sustainable energy solutions for critical applications [5].

The deployment of advanced energy monitoring systems aligns with global sustainability goals by reducing energy wastage, minimizing carbon footprints, and promoting the use of renewable energy. The environmental benefits of these systems are underscored by their ability to integrate renewable energy sources seamlessly, thereby reducing dependence on fossil fuels. Moreover, the economic advantages, including cost savings and enhanced energy efficiency, make these systems indispensable for both industrial and renewable energy sectors.
The evolution of energy monitoring systems, driven by technological advancements in IoT, renewable energy integration, and data analytics, has transformed the landscape of energy management. By enabling real-time monitoring, predictive maintenance, and seamless integration of renewable energy sources, these systems contribute significantly to energy efficiency and sustainability. Future research should focus on enhancing the scalability, affordability, and adaptability of these systems to ensure their widespread adoption across diverse industrial and commercial settings.

PRACTICAL IMPLEMENTATION

This study aims to develop an integrated solution for monitoring energy consumption in an industrial hall, using accessible hardware components and IoT technologies. The aim is to create a system capable of collecting, processing and analyzing energy data from an industrial environment, providing detailed reports and proposing solutions to reduce energy consumption. Also, this work contributes to the development of knowledge regarding the use of low-cost technologies in industrial environments and demonstrates the feasibility of using them to obtain significant economic and operational benefits.
The current and voltage consumed will be measured instantly as well as over a set time interval which will be displayed in a web page in the form of a graph.
Used materials:
- a UNO or NANO or Mini development board.

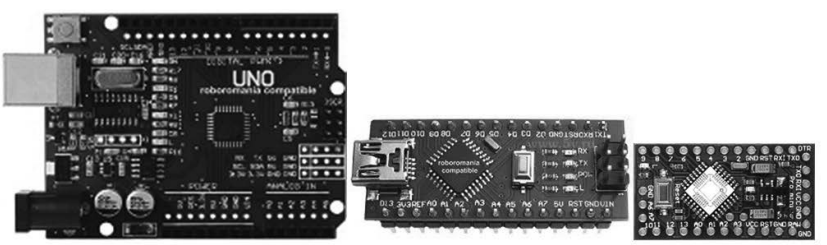

Figure 1. Arduino

- a current sensor (preferably 30A).

Figure 2. Current sensors

- a stabilized source of 5v and minimum 1A.

Figure 3. 5V stabilised source

- a circuit to rectify the alternating current read by the current sensor (coil variant).
The circuit is actually a precision rectifier with a gain of about 40.
The output with negative peaks from the current sensor is converted into a continuous voltage of approximately 0...5v in a range of approximately 0 - 50A, with a linearity and precision of approximately 0.1A.

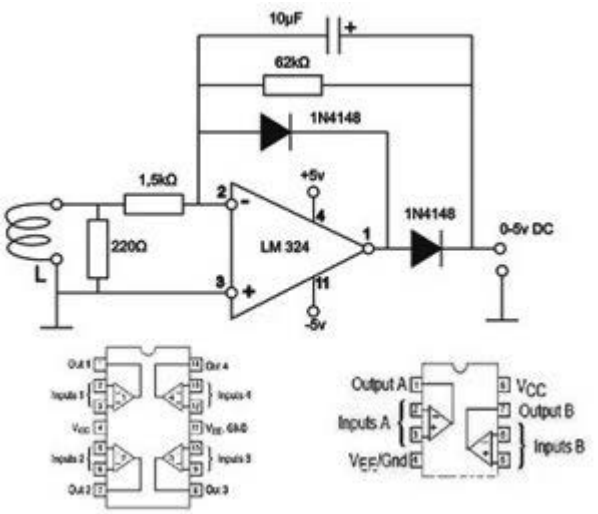

Figure 4. Rectify circuit

- a memory for the database, in which the data recorded for at least 4 weeks can be stored.

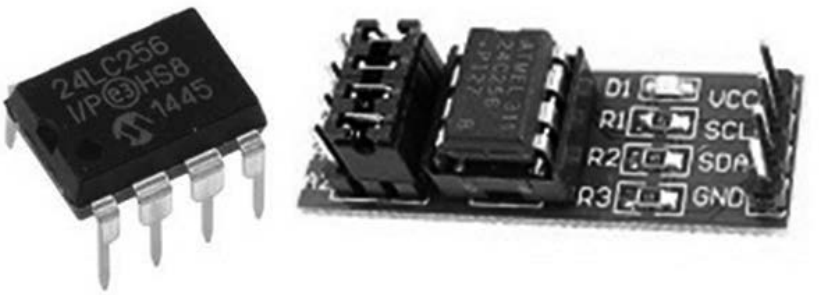

Figure 5. Memory chip

and obviously an Arduino W5100 or ENC28J60 network board. The Arduino W5100 network card will be used because it is much more stable.

Figure 6. Network extension board

The image from figure 7 illustrates the first stage of development of the energy consumption monitoring system based on open-source platforms and accessible hardware components. This initial setup demonstrates the implementation of a working prototype for energy data collection and transmission using modular electronics.

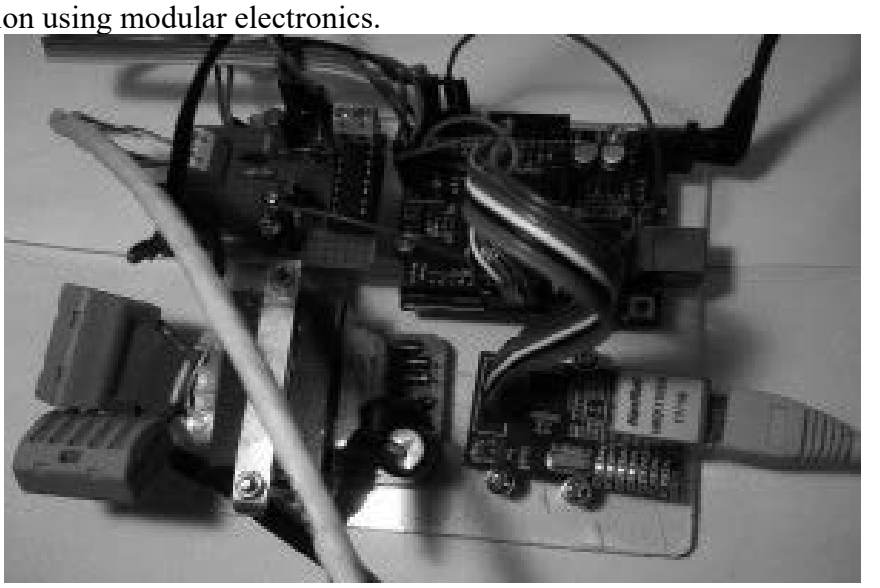

Figure 7. First stage of system

The figure 8 illustrates the final stage of development of an advanced energy consumption monitoring system. This configuration represents a compact and optimized version of the initial prototype, with full integration of hardware and software components for practical use and implementation in industrial applications.

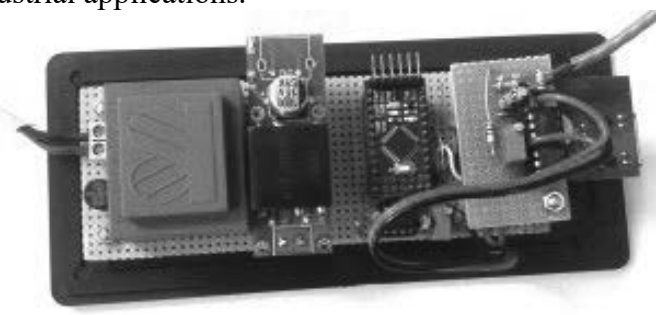

Figure 8. Final stage of system

The web page created for the system represents an intuitive and functional solution for monitoring energy consumption in real time, adapted for complex industrial environments. The user interface is simple and organized, allowing quick visualization of the main energy consumption parameters for different industrial consumers, such as CNC plasma cutting machines, air compressors and general lighting in a production hall.

At the top of the page is a centralized table that displays essential data such as current, voltage, power and energy consumed, giving users an overview of the performance of each consumer. Data is displayed in clear and standardized units, making it easy to interpret and compare.

The graph in the center of the page provides a visual representation of energy consumption over time in the form of a dynamic graph. This graphical representation allows users to observe energy consumption fluctuations over a 10-minute period, providing detailed information on consumption trends and identifying possible anomalies. Interactive buttons located below the chart provide options for viewing data over different time frames, from one minute to four weeks, allowing users to tailor the analysis to their specific needs. Also, a dedicated reset button allows a quick return to the initial settings, simplifying the use of the application.

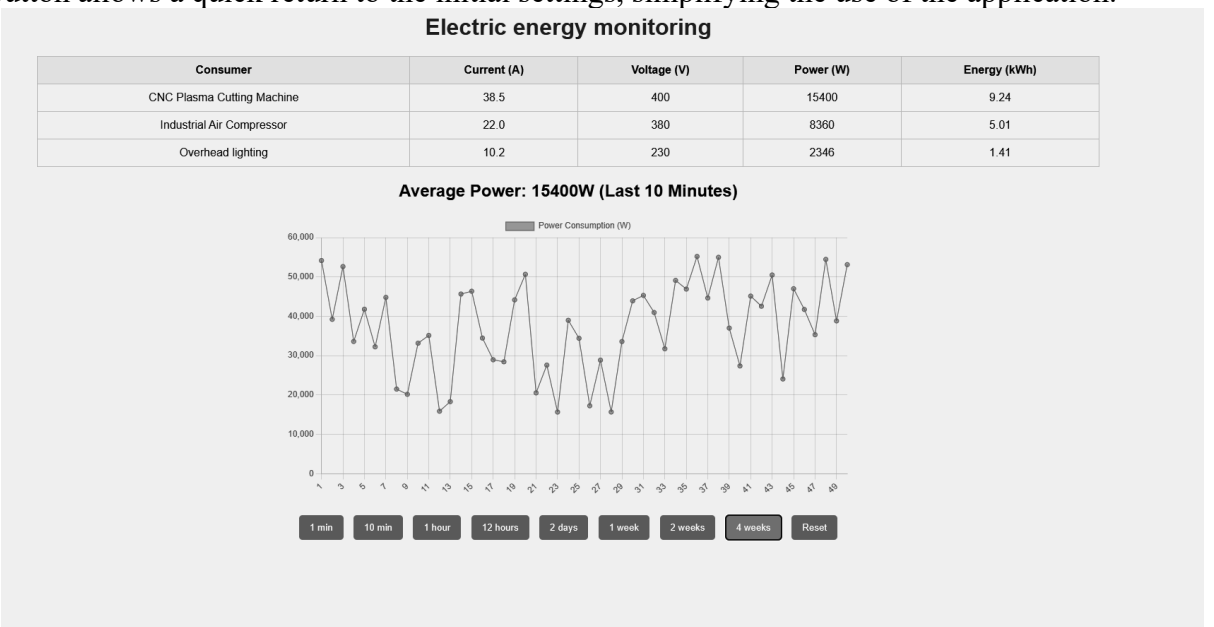

Figure 9. Web page app

The overall design of the page is modern and optimized, using distinct colors to highlight active buttons, which improves navigation and user experience. Overall, this web platform is a valuable tool for efficient energy management in industrial environments, providing quick access to critical information and support for accurate data-driven decision-making.

CONCLUSIONS

The evolution of modern industry is inextricably linked to the adoption of technological solutions that simultaneously meet economic, operational and ecological requirements. The present study demonstrates that the use of accessible platforms such as Arduino in combination with IoT technologies and advanced data processing algorithms can radically transform the way energy consumption is managed in industrial environments. These systems, designed with low cost and high flexibility, not only bring significant financial benefits, but play a crucial role in achieving sustainability goals.

The paper highlights that detailed and real-time monitoring of energy consumption provides the ability to identify patterns, anomalies and opportunities for optimization that would otherwise go unnoticed. This perspective opens the way to a proactive energy management, where decisions are based on concrete data and where the waste of resources becomes an aspect that can be effectively managed. Moreover, the applicability of these technologies in diverse environments, from main equipment such as CNC machines to ancillary systems and lighting, underscores their transformative potential.

Integrating these systems into a broader industrial strategy emphasizes the importance of correlating energy consumption with operational performance indicators. Thus, the proposed technologies not only optimize processes, but also contribute to redefining traditional industrial operation paradigms, promoting an approach in which efficiency becomes a central value.
Beyond the economic and operational benefits, this approach supports the transition to a more sustainable industry, where technological progress harmonizes with environmental responsibility. The ability to implement modular and scalable solutions without compromising performance redefines the limits of technology accessibility and democratizes access to innovation for all types of organizations.

In conclusion, this research highlights the urgent need to adopt advanced energy management as a fundamental pillar of industrial sustainability. Digital transformation through accessible technologies offers a unique opportunity to balance the economic imperative with ecological responsibility, paving the way for an industry adapted to the global challenges of the future.

ACKNOWLEDGEMENTS

The work was created as a result of the project as part of project based learning - PBL, in the 11th competition under the Initiative of Excellence - Research University, Silesian University of Technology, Gliwice, Poland.

BIBLIOGRAPHY

1. Patrascoiu, N., & Rus, C. (2022). Industrial area environmental monitoring based on transducers with MODBUS communication. In MATEC Web of Conferences (Vol. 354, p. 00069). EDP Sciences.
2. Rus, C., Negru, N., & Patrascoiu, N. (2019). Low-cost system to acquire environmental parameters in urban areas in the context of IoT. *Journal of Environmental Protection and Ecology*, *20*(3), 1451-1461.
3. Negru, N., Radu, S. M., & Soica, A. (2024, May). Air Quality Monitoring and Photovoltaic Impact Assessment in Valea Jiului. In *2024 25th International Carpathian Control Conference (ICCC)* (pp. 1-6). IEEE.
4. Rus, C., Leba, M., Negru, N., Marcuş, R., & Rîsteiu, M. (2021). Electric vehicles in smart grid and smart city for Petroşani case. In *MATEC Web of Conferences* (Vol. 342, p. 05002). EDP Sciences.
5. ur Rehman, A., Alblushi, I. G. M., Zia, M. F., Khalid, H. M., Inayat, U., Benbouzid, M., ... & Hussain, G. A. (2025). A solar-powered multi-functional portable charging device (SPMFPCD) with internet-of-things (IoT)-based real-time monitoring—An innovative scheme towards energy access and management. *Green Technologies and Sustainability*, *3*(1), 100134.
6. Pătrășcoiu, N., Rus, C., & Negru, N. (2020, October). A Solution to Monitor Environmental Parameters in Industrial Areas. In 2020 21th International Carpathian Control Conference (ICCC) (pp. 1-6). IEEE.

TalentDetector

31th January 2025
Gliwice, Poland

DEPARTMENT OF ENGINEERING MATERIALS AND BIOMATERIALS
FACULTY OF MECHANICAL ENGINEERING
SILESIAN UNIVERSITY OF TECHNOLOGY

INTERNATIONAL STUDENTS SCIENTIFIC CONFERENCE

Stabilization of electric power networks

Kamil Oleksy[a], Bartosz Nikiel[a] , Kajetan Kojm[a] , Łukasz Lomania[a] , Sszymon Szeja[a] , Kacper Krysiak[a], Cezary Zach[a]

[a] Silesian University of Technology, Faculty of Electrical Engineering, Department of Elektrotechnics
email: kamiole249@student.polsl.pl; bartnik681@student.polsl.pl;
kajekoj367@student.polsl.pl; lukalom979@student.polsl.pl; szymsze085@student.polsl.pl;
kacpkry923@student.polsl.pl

Abstract: The development of Poland's energy networks has evolved significantly since the 19th century but faces numerous challenges, including outdated infrastructure and modernization neglect. High- and extra-high-voltage networks are crucial for transmitting electricity over long distances, while medium- and low-voltage networks handle final distribution to end-users. The increasing integration of renewable energy sources (RES) demands substantial investments and modernization to ensure stability, reliability, and efficiency. Modern solutions, such as Smart Grids, provide advanced control and energy flow management, minimizing losses and enhancing efficiency. These systems enable two-way communication between producers and consumers, better aligning production with demand and reducing reliance on large energy reserves. The rise of distributed energy generation, driven by RES, marks a shift from centralized to decentralized systems, creating new opportunities and challenges. Adapting Poland's infrastructure to support renewable energy and meet growing demand requires significant investment in both transmission and distribution networks. Addressing these challenges will depend on innovative financing, transparent processes, and stronger regulatory frameworks.

Keywords: Power networks; High-voltage transmission; Distribution networks; Renewable energy sources (RES); Smart Grid; Energy efficiency; Energy demand; Distributed energy generation; Network modernization; Rotating reserves; Infrastructure investment; Energy system reliability

1. INTRODUCTION

Electricity is an indispensable component of our world. Both private individuals, such as each of us, and major players in the capital market depend on it in many aspects.

The first public utility power plant in Polish territories was built in Szczecin at the end of the 19th century. Subsequently, the rapid implementation of additional power installations shaped the industrial landscape of Polish cities. Naturally, electricity generated in the energy process

had to be delivered to homes, factories, and public utility buildings. Thus, alongside the development of coal-fired power plants, transmission networks emerged—distinct from those currently responsible for transmitting electrical energy.

Modern power systems are primarily based on three-phase alternating current systems. Initially, local direct current networks were developed, which are now mainly used in specific technical and environmental conditions for transmitting large amounts of power.

The initial voltage levels would not have met the needs of contemporary society in Poland. The first three-phase alternating current networks operated at a voltage of around 60 kV, later increasing to 150 kV. It was only in the 1950s that 220 kV voltage was introduced, integrating networks with varying voltage levels into a single national power system. Until 1964, when the first 400 kV line was built, the system relied mainly on lines with significantly lower voltages. Today, the 400 kV sector continues to expand, despite the introduction of a line reaching 750 kV in 1984.

Why mention all this information? From the perspective of the end-user, the history of power transmission network development in Poland may not seem relevant. However, the challenges of power networks and their stabilization in our country stem mainly from the diversity of centrally-based networks and neglect in their earlier modernization. Transmission losses, which pose a significant challenge in Poland's energy transition, have their roots in this "disarray," resulting from the rush to expand the power grid without planning for the possibility of decentralized energy systems. As the saying goes, "the road to hell is paved with good intentions." However, Poland's energy "hell" must come to an end, and the networks must be stabilized. Without this, neither nuclear energy nor renewable energy sources will save Poland's energy mix or fill the gap left by coal. How can we overcome this deadlock? It will not be an easy task. It must be remembered that shifting energy production predominantly to renewables involves the need to electrify practically every sector of the country's operation. The question of which energy sources we will use is crucial for the future development of the power grid.

2. DISTRIBUTION NETWORKS VS. HIGH-VOLTAGE NETWORKS

The development of the networks described above pertains to only one of the two components of the energy environment: high-voltage networks, also known as transmission networks. What is their purpose?

Their primary function is to transmit large quantities of energy over long distances, connecting power generation units (such as power plants) to distribution areas. These networks must be highly optimized for efficiency, meaning they must minimize energy losses during transmission. Within the transmission network system, there are two main variants: High-Voltage Networks (HV) and Extra-High Voltage Networks (EHV). While networks can also be classified based on construction characteristics or other factors, here we focus on their nominal voltage— the maximum electrical current voltage that can be continuously applied to the conductors.

Thus, the transmission networks carry electricity, which is then delivered to distribution areas. Near the consumer zones, substations are located where the voltage is gradually reduced to levels safe for distribution networks, the second essential component of the energy environment. Distribution networks are responsible for transferring electricity from substations to end users. To prevent fires, electric shocks, or severe damage to household electrical

appliances, the voltage must be drastically reduced, which occurs in substations. It can be said that energy transmission through distribution networks constitutes the final stage of its journey.

Distribution networks are divided into: Medium-Voltage Networks (MV): These transfer energy from smaller generation units or transmission substations to distribution substations, which supply electricity to localized areas such as residential neighborhoods or industrial zones. Low-Voltage Networks (LV): These networks then deliver energy from substations directly to our homes. To summarize this overview, the key voltage categories are:

- Extra-High Voltage Networks (EHV): Voltage differences between phase conductors are 200 kV or more.
- High-Voltage Networks (HV): Voltage between phases ranges from 60 to 200 kV.
- Medium-Voltage Networks (MV): Voltage between phases ranges from 1 to 60 kV.
- Low-Voltage Networks (LV): Standard phase voltage is 230 V.

Both high-voltage transmission networks and medium- and low-voltage distribution networks play a crucial role in Poland's energy infrastructure. Unfortunately, the challenges posed by the energy transition are not identical for these systems. It is essential to treat these networks as complementary and interdependent components of the electrical system, while acknowledging that they are distinct entities. The goal of grid transformation and modernization is to ensure the reliability of energy supply. Poland's energy landscape is evolving daily, mainly due to the increasing presence of renewable energy sources (RES). Amid these changes, the reliability of energy delivery remains highly uncertain. Let us then consider what factors pose obstacles and challenges for the development of both transmission and distribution networks in Poland.

3. NETWORK CHALLENGES AND SOLUTIONS - DISTRIBUTED SYSTEMS

The development of network infrastructure is essential to adapt the system for the electrification of additional sectors and to accommodate energy from renewable sources (RES) and nuclear power. Of course, methods such as improving energy efficiency and advancing energy storage systems can help slow the exponential growth of demand as electrification expands across the economy. Nevertheless, the International Energy Agency (IEA) predicts that global electricity demand will increase by about 4% annually until 2026.

On January 9th of this year, a record electricity demand was set in Poland, reaching 28,216 MW. This figure represents the average hourly national power demand, heavily influenced by low temperatures. Skeptics may argue that this was a temporary spike in demand. However, examining annual demand over the past few years paints a clearer picture. Annual Energy Demand and Production Trends:

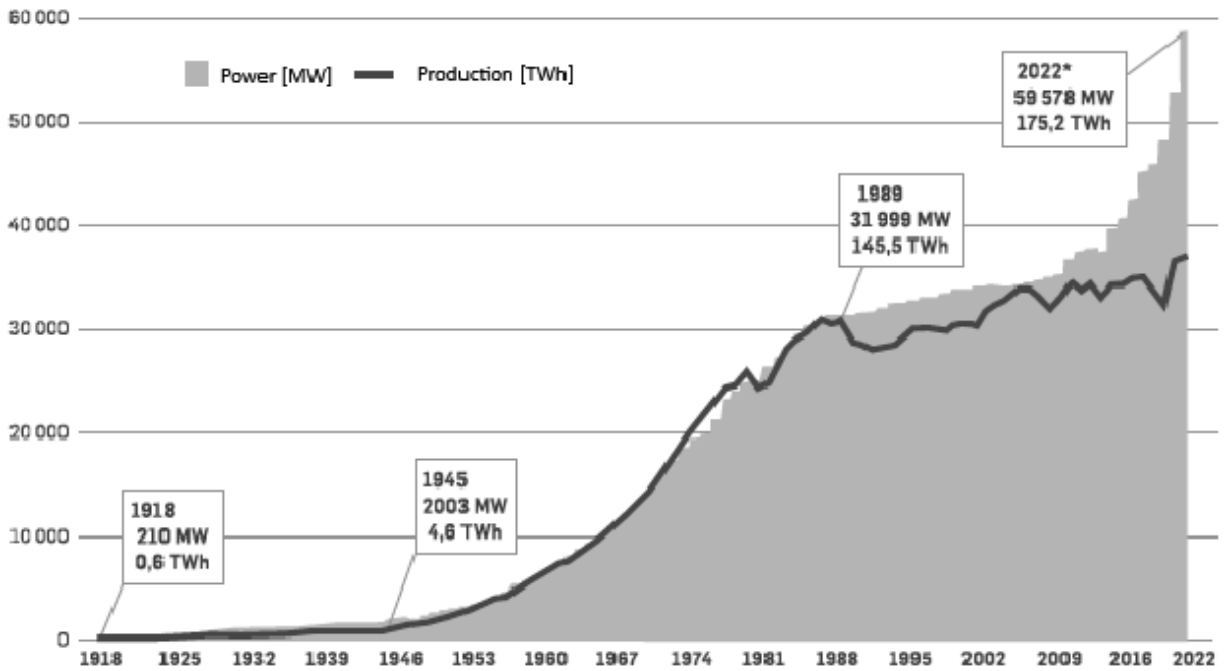

Fig. 1. Power plant capacity and electricity production in Poland from 1918 to 2022

A notable situation occurred in 2023 when Poland's annual electricity demand decreased compared to the previous year, totaling 166,082.923 TWh compared to 172,382.311 TWh in 2022. This reduction can be partially attributed to the growing self-consumption by prosumers, though this only explains part of the phenomenon. A more evident decrease in energy consumption by end-users is linked to effective energy efficiency measures and, most significantly, economic factors (refer to reports on energy poverty). In 2022, electricity production increased to 175.2 TWh despite declines in coal and gas power generation, which provided 7 TWh less energy than in 2021. Renewable energy sources (RES) compensated for this, contributing an additional 9 TWh from low-emission sources. This positive trend, while paving the way for investment opportunities, introduces challenges as the energy system transitions from centralized to distributed and from controllable to weather-dependent.

By March 31, 2024, there were 1,432,917 micro-installations connected to Poland's energy grid, with a combined capacity of over 11.5 GW. RES, primarily micro-installations with low individual capacities, exemplify distributed energy sources. This represents a revolution in energy production, moving away from centralized systems dominated by large generating units like professional power plants. The new model relies on distributed installations across the country, inherently tied to the growth of RES—a key part of the energy sector's future.

Managing Distributed Energy Networks: Distributed generation primarily involves units with low nominal power compared to traditional emission-heavy energy sources. These are connected directly to substations or integrated into low- and medium-voltage networks. Efficiently managing such a decentralized grid requires innovation in energy and heat storage technologies, with a particular focus on Smart Grid systems.

A Smart Grid is an intelligent energy system built on an advanced measurement framework. It aims to improve energy efficiency by minimizing losses and integrating all participants in the energy system—from producers to distributors to end-users. The Smart Grid measurement system leverages intelligent informational and predictive algorithms displayed at "decision

points," which also rely on algorithms. Key features of Smart Grids include: Real-time monitoring of energy consumption at specific times and locations. Identification of peak and off-peak usage periods.

Bidirectional communication between energy producers and consumers, enabling supply adjustments to actual demand and reducing the need to maintain large generating units in standby mode. Additional advantages include remote meter readings, monitoring of energy losses, remote connection and disconnection of users, tariff adjustments, and automated invoicing. The Role of Rotating Reserves: An inherently related issue in network development and energy system management is the provision of rotating reserves, a term used in energy system management.

Rotating reserves represent the power that generators already operating on the network can instantly provide but are running below their maximum capacity. This ensures system stability and reliability. Rotating reserves: Are synchronized with the grid and can immediately increase energy production.

Can be supplied by various energy sources, including RES, if equipped with appropriate storage technologies. Offer continuous energy delivery since they are sourced from already active units. Given the weather-dependent nature of sources like wind and solar power, rotating reserves are essential to offset sudden drops in renewable energy production. In cases of disturbances or failures, these reserves can quickly supply the missing power, crucial for maintaining frequency stability and preventing power outages.

Future Evolution: As renewable energy plays a more prominent role, rotating reserves will need to evolve to address challenges associated with higher shares of RES. Energy storage technologies, such as lithium-ion batteries and pumped-storage plants, are expected to become integral components of rotating reserves, ensuring reliability and stability in a decentralized energy system.

4. CONCLUSIONS

The development of Poland's power networks has come a long way since the first installations in the 19th century, yet many challenges remain unresolved. Outdated infrastructure and past neglect of modernization have led to stability and efficiency issues in the current energy system. The energy transition requires significant investments and upgrades to meet growing energy demand, particularly with the increasing role of renewable energy sources (RES).

High- and extra-high-voltage transmission networks play a critical role in delivering energy over long distances, while medium- and low-voltage distribution networks are responsible for the final stage of energy delivery to consumers. The efficiency and reliability of these networks are essential for the stability of the entire energy system. Modernizing these networks is crucial to integrate the growing number of RES micro-installations and ensure energy reaches the areas where it is most needed.

The rising electricity demand and increasing number of RES micro-installations necessitate modern solutions such as Smart Grids. These systems allow for better energy flow control and management, minimizing losses and improving energy efficiency. Smart Grids enable two-way communication between energy producers and consumers, facilitating a better alignment of production with demand and reducing the need for large energy reserves.

The key challenge for developing Poland's power networks lies in adapting the infrastructure to the new reality, where RES will play a dominant role. This requires substantial investments in both transmission and distribution networks to ensure supply reliability and efficient energy use. Financing these investments poses a significant challenge, especially in the context of rising costs and public acceptance of higher energy bills. Solutions such as increasing transparency in connection processes and strengthening the role of regulators could help overcome these challenges.

ACKNOWLEDGEMENTS

The work was created as a result of the project as part of project based learning - PBL, in the 11th competition under the Initiative of Excellence - Research University, Silesian University of Technology, Gliwice, Poland.

BIBLIOGRAPHY

1. Chmielniak T.: Technologie energetyczne. WNT, Warszawa 2008.
2. Korab R.: Optymalizacja operatorstwa przesyłowego w krajowym systemie elektroenergetycznym. Wydawnictwo Politechniki Śląskiej, Gliwice 2011.
3. Wood A.J., Wollenberg B.F.: Power Generation, Operation and Control. J. Wiley & Sons Inc., New York 1996.

TalentDetector

31th January 2025
Gliwice, Poland

DEPARTMENT OF ENGINEERING MATERIALS AND BIOMATERIALS
FACULTY OF MECHANICAL ENGINEERING
SILESIAN UNIVERSITY OF TECHNOLOGY

INTERNATIONAL STUDENTS SCIENTIFIC CONFERENCE

Möbius strip-shaped track for superconductor levitation: design and prototyping

Emil Pająk [a], Wiktoria Łowczecka [a], Alicja Jankiewicz [a], Błażej Tomiczek [b]

[a] Student, High School No. 5 with Bilingual Units in Gliwice
email: emilpajak.edu@gmail.com, wiki.lowczecka@gmail.com, alicja.jankiewicz@op.pl
[b] Silesian University of Technology, Faculty of Mechanical Engineering
email: blazej.tomiczek@polsl.pl

Abstract: This article presents the design and development process of a prototype track in the shape of a Möbius strip for superconductor levitation. The study focuses on creating uniform magnetic field along the curved path to enable high-temperature superconductor the stable levitation and suspension. The model, made using 3D printing technology, demonstrates the potential for controlled movement of superconductors in magnetic fields.

Keywords: superconductor, levitation, Meissner effect, quantum locking, 3D printing

1. INTRODUCTION

1.1. Superconductivity

Superconductivity is a state of matter in which material conducts electricity without resistance after being cooled down below its critical temperature. This phenomenon is caused by electric charge carriers pairing into - behaving as bosons - Cooper pairs and allows for energy-efficient applications in particle accelerators, superconducting magnets, and power systems. Most superconductors to exhibit superconductivity need to be cooled down to temperatures achievable only with using liquid helium. This study utilises high-temperature superconductors (HTS) due to their practicality with liquid nitrogen cooling.

1.2. Quantum locking and the Meissner effect

The phenomenon of superconductivity is accompanied by the Meissner effect, which results in the expulsion of the magnetic field from the superconductor. There are two types of superconductors [1]: Type I, which expels the magnetic field entirely from its volume (up to a specific critical field strength), and Type II, which allows the magnetic field to penetrate the material, leading to the creation of magnetic flux vortices. This enables quantum locking - a phenomenon where a superconductor becomes locked in a specific spatial position relative to a magnetic field, allowing for stable levitation at a fixed position or controlled motion along

magnetic field lines. When a superconductor transitions into its superconducting state in the presence of an external magnetic field, it effectively "remembers" the field configuration through the arrangement of flux vortices, permitting only specific movements. Therefore, in the case of a Möbius strip-shaped track, the arrangement of magnets and the orientation of their poles must be carefully considered along with the magnetic field present during the transition into the superconductive state.

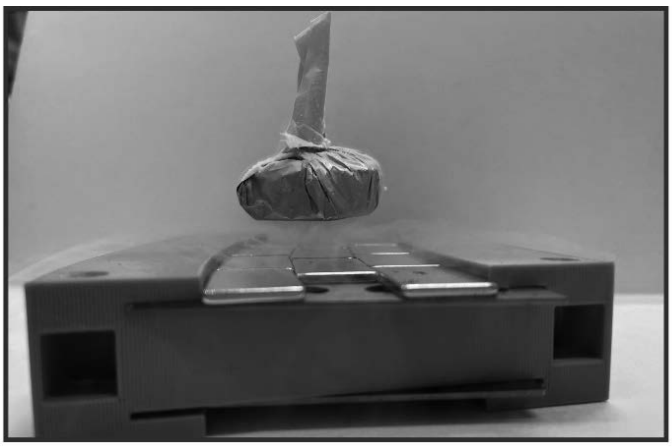

Figure 1. An insulated superconductor quantum locked above a flat track, created by three rows of neodymium magnets.

1.3. The Möbius strip geometry

A Möbius strip, as a mathematical object, is a surface having only one edge and one side. Engineering the model resembling this shape allows the track to loop itself, offering a unique path for objects that, during one complete revolution, will both levitate above and suspend below it. A typical Möbius strip is created by half-twisting a normal strip and connecting its ends. However, in this project, a 3π Möbius strip geometry was selected as it is more spectacular [2] and requires a smaller amount of unique parts to be designed, meaning that the levitating HTS before coming back to the starting position will hover above and suspend below the track three time.

2. MATERIALS AND METHODOLOGY

2.1. Shaping the magnetic field created by neodymium magnets

Grade N38 neodymium magnets were selected for this study to ensure a sufficient magnetic field for stable superconductor levitation. The magnet's dimensions (25×15×2 mm) were chosen to maximise surface area while minimising cost. All magnets were purchased from the magnes.com.pl company. A single magnet (Fig. 2a) creates a magnetic field (Fig. 2b) that decreases with the distance from its surface, whose magnetic flux density is presented in Figure 2c. However, after the steel backbone is attached to it (Fig. 2d), the field becomes focused on one side of the magnet and weakened on the other (Fig. 2e, 2f). This phenomenon allows for increasing the magnetic flux density on the exterior of the track and significantly decreasing it on the inside. Moreover, using steel elements to which magnets are attracted simplifies fixing magnets to the 3D-printed parts.

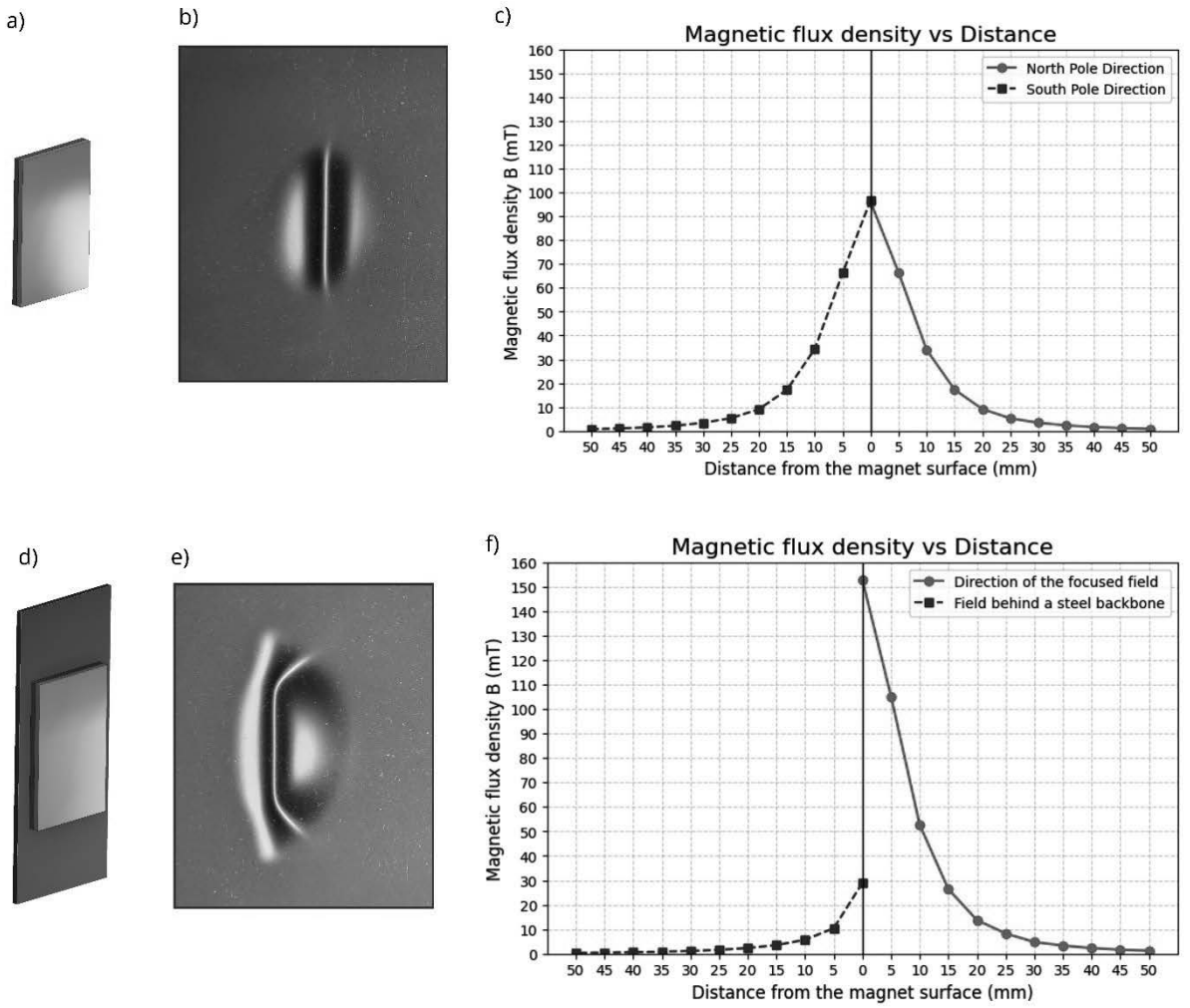

Figure 2. Diagram showing a) neodymium magnet and d) neodymium magnet attached to piece of steel; with side view of magnetic fields b) and e) observed with magnetic viewing film; and c) and f) graphs illustrate the relationship between magnetic flux density and the distance from the surface of the magnet or steel piece– measurements were made using UNI-T Gauss Meter UT335A.

Creation of the uniform magnetic field along the track was possible due to the particular arrangement of the magnets (Fig. 3a, 3b) so that while moving in the longitudinal direction, the poles of magnets are not alternating (Fig. 3c, 3d). This creates an additional repulsion force (between magnets 1-3 and 2-4 in Fig. 3a) that can be overcome by the force of attraction (between magnets 1-2, 1-4, 3-4 and 3-5 in Fig. 3e as well as attraction to the steel backbone) if the magnets are shifted properly (Fig. 3e, 3f). Moreover, while designing a Möbius strip-shaped track, the number of magnets in the transverse direction should also be considered due to the interactions between magnets on the top and bottom of a given 3D-printed part. Therefore, it is recommended to choose an even number – then magnets on the opposite sites of the printed part will be attracted to each other and remain securely in place instead of detaching and being ejected.

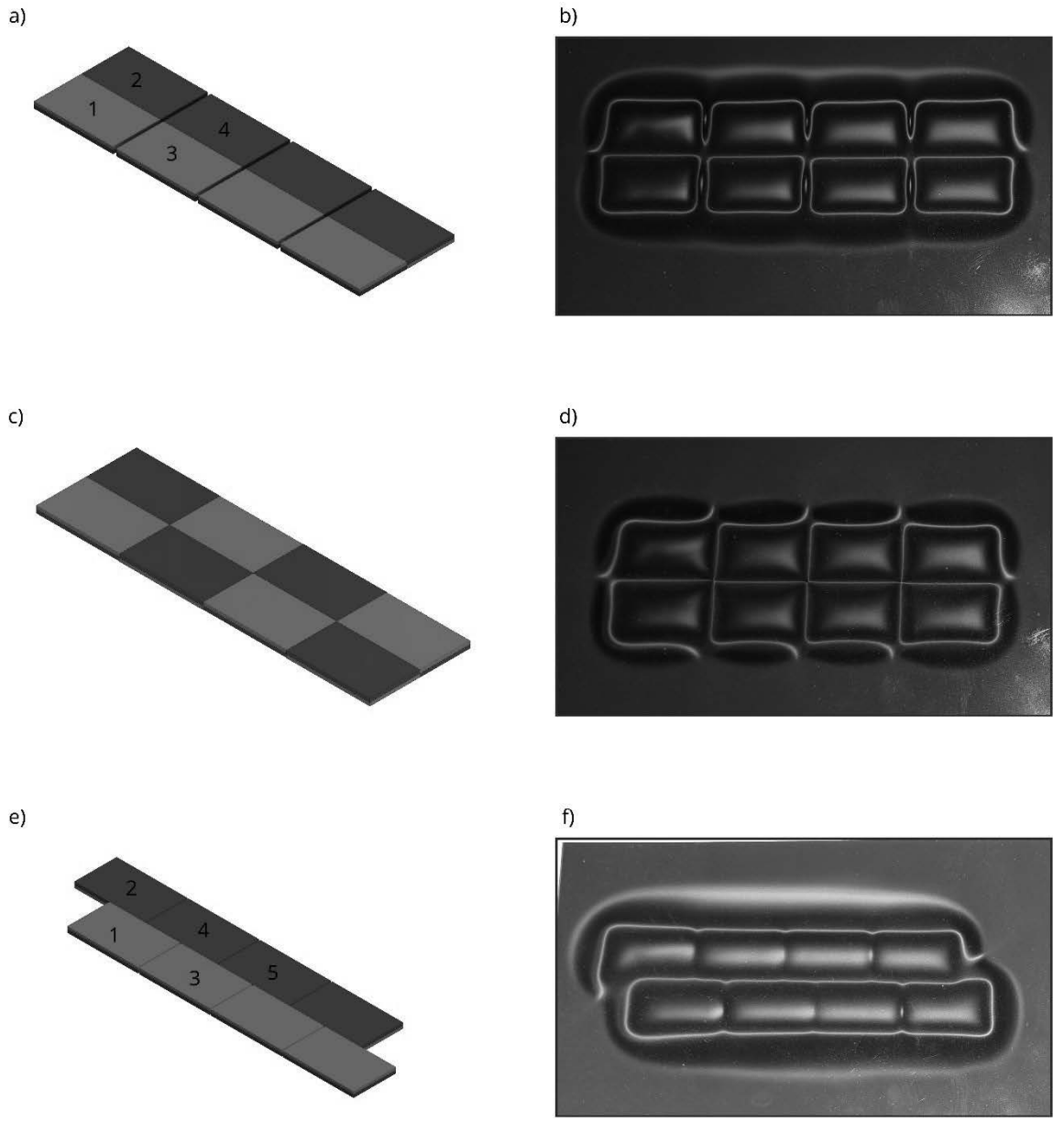

Figure 3. Diagram showing a), c), e) different alignments of the magnets and b), d), f) their corresponding magnetic fields observed using magnetic viewing film.

2.2. Suppression of HTS heating

The high-temperature superconductor (HTS) used in this study was yttrium barium copper oxide (YBCO) disk with 30 mm diameter and 10 mm thickness (Fig. 4a) supplied by CAN Superconductors company. The cooling process was performed by submerging the HTS into the Styrofoam cup filled with liquid nitrogen (LN_2). It was found that the uninsulated disk after being cooled down below its critical temperature T_C and then after being taken out from LN_2 is sustained in the superconducting state (levitation time t_L) on average for 10 seconds. Multiple measurements were performed for different cooling durations t_c: 3 min, 5 min, 8 min, and it was

observed that there is no increase of t_L with an increase in t_c after the HTS is cooled properly. Cooling time t_c was measured from the moment when the HTS had heated above the critical temperature and then was immersed in liquid nitrogen, rather than being cooled from room temperature T_R to T_C (the first cooling from T_R to T_C usually was longer to ensure the proper temperature of the whole bulk material, and not only the surface of it).

To prolong the levitation time [3], the HTS was wrapped in a thermal blanket (Fig. 4b), initially with two layers of insulation and afterwards by three layers. This approach allowed for an extension of its tL to more than 70 seconds on average, which made it possible for HTS to complete the entire loop of the 5-meter Möbius strip-shaped track multiple times before heating over the TC. However, the insulation also increased the minimal necessary cooling time to about 8 minutes. Precise tL differed across different insulation patterns, possibly caused by LN2 getting trapped between the thermal blanket layers, prolonging the levitation time. No difference in the tL was observed in terms of which side of the thermal blanket (gold or silver coloured) was facing the HTS. Furthermore, the insulated HTS was inserted into the 3D-printed PLA protective cover (Fig. 4c) to decrease the risk of HTS cracking after falling off the track when it heats up.

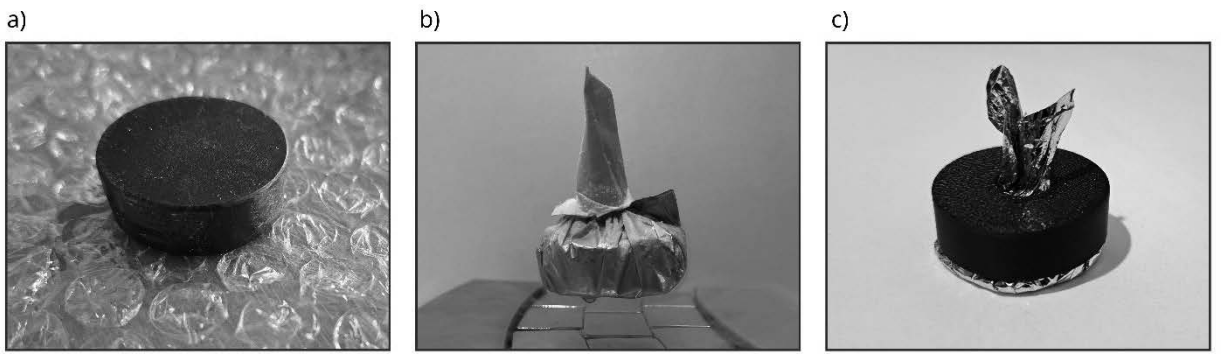

Figure 4. View of a) uninsulated YBCO disk; b) HTS wrapped in a thermal blanket in a candy-like shape to simplify grabbing it and pulling it out of the LN_2; c) insulated HTS inside the PLA protective cover

2.3. Influencing the distance between the magnetic track and superconducting HTS

While the HTS passes through the TC and becomes superconducting, it “has a memory” of the magnetic field in which it has transitioned between states. Utilising it increases and decreases the distance that separates the HTS from the track. In this study, the HTS was cooled above the pattern of magnets portrayed in Figure 3e with varying amounts of magnet layers stacked onto each other. When the multiple layers were used, the magnets of a particular layer were shifted by their half-length with respect to magnets on the layer below to overcome the force of repulsion. During the cooling process, the Styrofoam cup-filled LN2 was located directly above the outermost layer of magnets. The HTS was carefully lowered to the cup to be located right above the middle of two magnets.

It was observed that the HTS cooled above one layer of magnets was weakly bound to the track and detached after being located below the magnetic path. The levitation distance between the HTS and the track was optimum for two magnet layers. However, the HTS cooled above three or more layers of magnets was too firmly bound to the track and exhibited frictional contact with the 3D-printed material.

2.4. Design of the levitation track

The model of the whole track was divided into 36 parts. The 3π Möbius strip geometry allowed to the design of only 12 of them, as each (Fig. 5) of the twelve elements repeats three times along the path. To elevate the whole model and to enable the HTS to suspend underneath it, the circular supports were designed, whose geometry does not restrict the amount of supports that can be inserted into the Möbius strip (Fig. 6). The model of the whole track was created in Autodesk Inventor PRO and each track element was carefully designed to ensure the precise placement of neodymium magnets, enabling the track to achieve the correct 3π Möbius strip geometry.

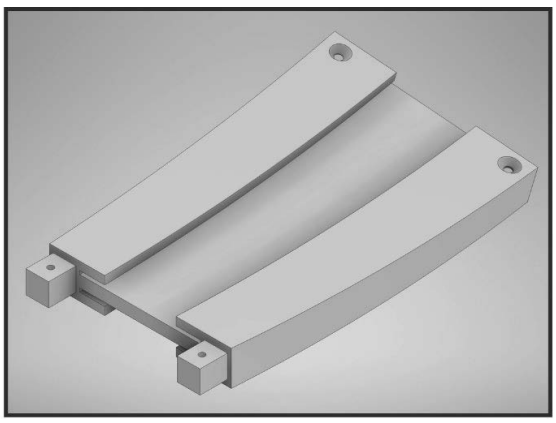

Figure 5. A computer model of one of the segments building the entire track.

Figure 6. An insulated with thermal blanket superconductor levitating above the track

2.5. Construction of the model

The track model was fabricated using 3D printing technology, which enabled the creation of elements with the desired geometry and a relatively high level of precision. The total printing time for the entire Möbius strip, including supports, exceeded 100 hours, and more than 1 km of PLA filament was consumed throughout the project.

Accurately 3D printed parts made it possible to curve the magnetic track consisting only of two adjacent magnets, minimizing the total width of the magnetic surface to 30 mm. This optimization and the use of nearly 1,000 neodymium magnets allowed for constructing a track exceeding 5 meters in length. The great advantage of 3D printing the model in many parts is that it can be easily disassembled and moved to different locations in segments.

3. RESULTS AND DISCUSSION

The final model allowed stable superconductor levitation and continuous movement along the track when external energy was applied. Preliminary tests indicated that the optimal magnet pattern and alignment were critical for maintaining consistent levitation height and minimising energy loss due to magnetic friction (Fig. 7).
Using precisely designed and 3D-printed models allowed for achieving an almost perfect curvature of the 3π Möbius strip. Moreover, due to the utilisation of a substantial number of

supports, the track does not require a perfectly flat surface to be mounted on and remains rigid even when some of the supports are not touching the ground (Fig. 8).

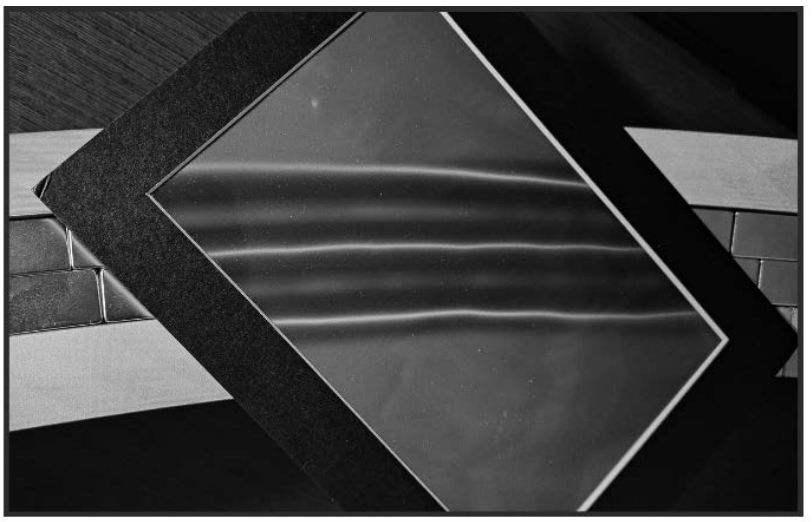

Figure 7. Uniform magnetic field above the Möbius strip-shaped track shown with magnetic viewing film

a)

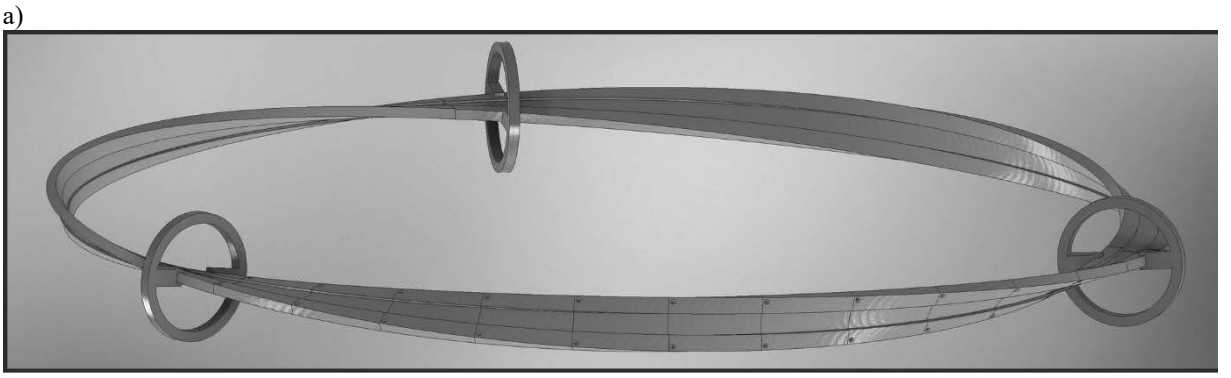

b)

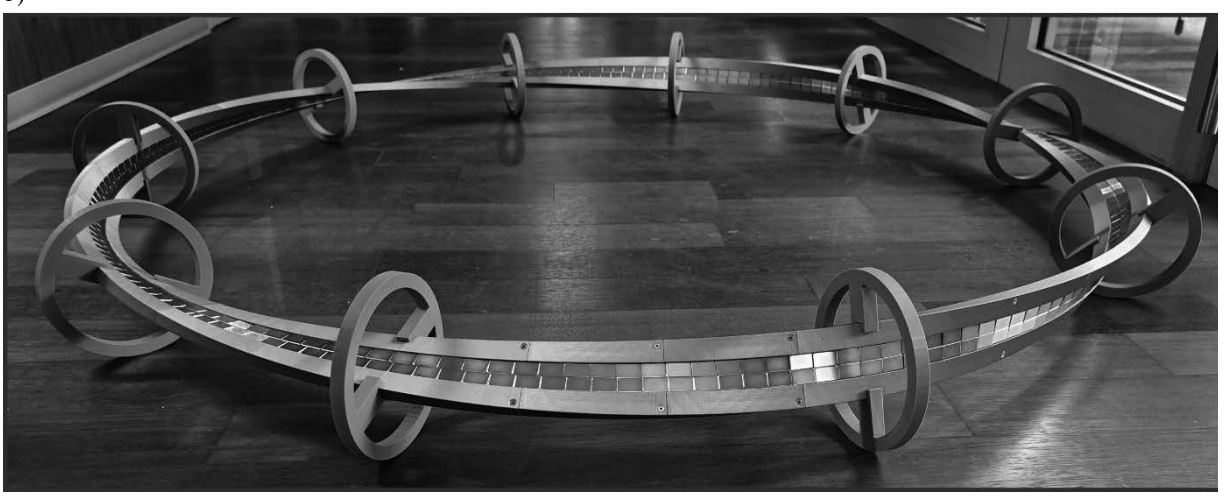

Figure 8. Comparison of a) the computer model of the 3π Möbius strip-shaped track and b) the constructed track

4. CONCLUSIONS

This project successfully demonstrated the feasibility of constructing a levitation system based on the Meissner effect and quantum locking. The Möbius strip design, combined with precise 3D printing and magnet placement, offers significant potential for future applications in magnetic levitation technologies.

ACKNOWLEDGEMENTS

The publication contains the results of research carried out within the third edition of the "POLITECHNIKA" Project, a program implemented at the Silesian University of Technology in cooperation with high school students as part of the "Excellence Initiative - Research University" project.

BIBLIOGRAPHY

[1] A. Szewczyk, A. Wiśniewski, R. Puźniak, and H. Szymczak, Magnetyzm i nadprzewodnictwo, 1st ed. Warsaw, Poland: Wydawnictwo Naukowe PWN, 2012.
[2] Ithaca College Physics (2016) „Superconducting Quantum Levitation on a 3π Möbius Strip" [online] Available: https://www.youtube.com/watch?v=Vxror-fnOL4
[3] Strehlow, Charles & Sullivan, Matthew. (2008). A Classroom Demonstration of Levitation and Suspension of a Superconductor over a Magnetic Track. American Journal of Physics. 77. 10.1119/1.3095809.

TalentDetector

31th January 2025
Gliwice, Poland

DEPARTMENT OF ENGINEERING MATERIALS AND BIOMATERIALS
FACULTY OF MECHANICAL ENGINEERING
SILESIAN UNIVERSITY OF TECHNOLOGY

INTERNATIONAL STUDENTS SCIENTIFIC CONFERENCE

Analysis of the influence of technological parameters of the laser cutting process of steel on the quality of finished large-size products

Mateusz Paluch[a], Piotr Bąk[a], Szymon Jędrzejewski[a], Hubert Przybyszewski[a], Szymon Szeja[a], Wiktoria Wanczura[a], Mirosław Bonek[b], Eva Tillova[c], Oleh Polishchuk[d]

[a] Silesian University of Technology, Faculty of Mechanical Engineering, Department of Engineering Materials and Biomaterials
[b] Silesian University of Technology, Faculty of Mechanical Engineering, Department of Engineering Materials and Biomaterials
[c] Žilinská univerzita v Žiline, Strojnícka fakulta, Katedra materiálového inžinierstva, Slovakia
[d] Khmelnitskyi National University, Faculty of Engineering, Transport and Architecture, Ukraine

Abstract: This study investigates the influence of technological parameters in the laser cutting process on the quality, efficiency, and cost-effectiveness of machining large-scale steel components. The analysis focuses on factors such as laser beam power, cutting speed, assist gas type, and material properties. It categorizes laser cutting methods, including oxygen cutting, inert gas cutting, vaporization, and cold cutting, while evaluating their specific applications and advantages. Advanced laser systems, including laser robots, are discussed for their precision and adaptability in industrial contexts. The findings provide practical guidelines for industrial applications and lay the foundation for further research into advanced materials and techniques.

Keywords: laser cutting, advanced manufacturing, laser robots, precision engineering, cutting quality

1. INTRODUCTION

Laser cutting has undergone significant advancements in the last decade, becoming a widely adopted technology in industrial manufacturing. Over 40,000 high-power laser cutting systems are in operation globally, alongside numerous low-power systems for plastics and paper cutting. Its applications span various industries, including automotive, aerospace, and household manufacturing. Key uses include the cutting of hydro-formed parts, tubes, and thin sheet metals, as well as precision cutting of thick materials [1][6].

The process's success lies in continuous innovations, such as improvements in beam quality and motion control systems, alongside enhanced gas technologies. These advancements have enabled higher efficiency, better precision, and reduced costs. Laser cutting’s versatility and

cost-effectiveness make it a cornerstone of modern manufacturing, capable of handling diverse materials with intricate geometries while requiring minimal maintenance [2][7].

2. THE PROCESS

Laser cutting operates by directing a highly focused laser beam onto a material's surface, causing the material to melt, vaporize, or combust. This process involves several critical components, including the laser source, beam guidance systems, focusing optics, and assist gases. These elements work together to ensure precise and efficient material removal [3].
The assist gas, which is typically coaxial with the laser beam, plays multiple roles, such as cooling optics, protecting them from heat damage, and expelling molten material from the cutting zone. This results in clean cuts with minimal thermal damage to the surrounding material [4]. Another advantage of laser cutting is its non-contact nature, which eliminates tool wear and mechanical stress, preserving the integrity of the workpiece [5].
A notable feature of laser cutting is its ability to achieve extremely narrow kerf widths, reducing material waste and enabling the production of parts with tight tolerances. The combination of precision, speed, and adaptability allows the technology to excel in applications that demand intricate and complex cuts [6]. The following diagram illustrates the fundamental elements and mechanism of the laser cutting process, including the interaction of the laser beam, assist gas, and the material being cut.

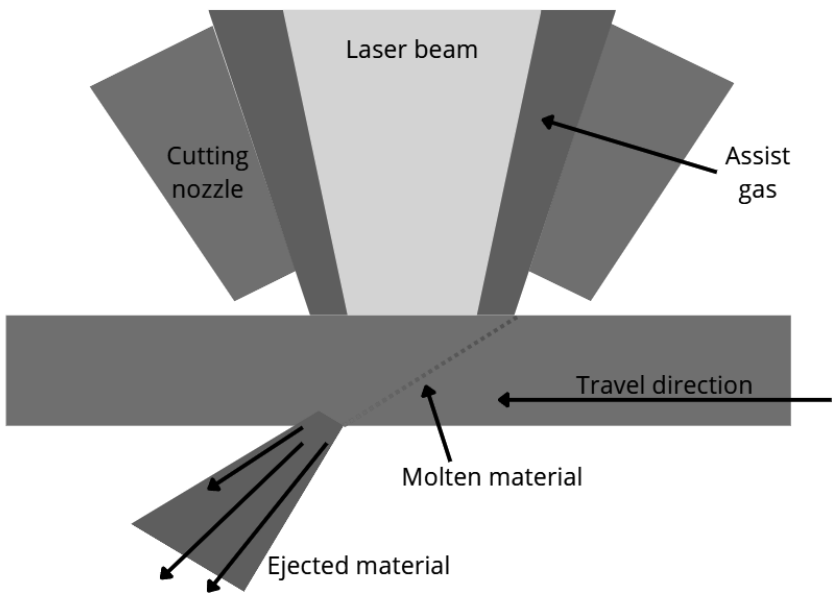

Figure 1. Laser cutting

3. METHODS OF LASER CUTTING

Laser cutting techniques can be categorized based on the type of assist gas used and the way the laser interacts with the material. The most common methods include oxygen cutting, inert

gas cutting, and specialized techniques like vaporization cutting and cold cutting. Each method offers distinct advantages tailored to specific applications [7][8].

Oxygen cutting
Employs oxygen as an assist gas to create an exothermic reaction that enhances cutting efficiency, particularly for thick ferrous metals. This method accelerates the cutting process and enables deeper penetration but may leave oxide layers on the cut edges [8].
Inert gas cutting, which uses gases like nitrogen or argon, is preferred for applications where clean cuts are essential. Since these gases do not chemically interact with the material, they prevent the formation of oxides. However, this method requires higher laser power, as the laser's energy alone must melt the material [9].

Vaporization cutting
Involves converting solid material directly into vapor without passing through the liquid phase. This method is ideal for achieving clean cuts in materials that are sensitive to thermal damage, such as certain polymers and composites. However, it demands higher laser power and precise control of gas flow [10].

Cold cutting
Uses ultraviolet lasers or ultrashort pulses to break chemical bonds without significant heating. This approach minimizes thermal damage and is particularly suited for delicate materials used in the medical and electronics industries [11].

Reactive Fusion Cutting
Reactive fusion cutting takes the fusion cutting process a step further by introducing an exothermic gas, typically oxygen, into the mix. As the laser melts the material, the oxygen reacts with it to produce additional heat, further enhancing the cutting process. This chemical reaction can lead to the formation of an oxide layer on the cut edges, which can affect the material properties. For metals like titanium, this oxide layer can make the material harder and more prone to cracking. However, for materials like mild steel, the effect is less pronounced, and the oxide layer is thin and easily removed. The key advantage of reactive fusion cutting is that it allows for faster cutting of thick materials, making it an efficient option for certain industrial applications. [9-11]

4. ADVANCED LASER CUTTING SYSTEMS

Modern laser cutting systems are designed with advanced features that enhance their performance and adaptability. Key components include:

- Laser Source: Generates a high-intensity beam that determines the system's power and efficiency [12].
- Beam Guidance System: Ensures precise delivery of the laser beam to the cutting head [12].
- Focusing Optics: Concentrates the beam for maximum cutting efficiency [12].
- Control Systems: Synchronize all components and allow for automation and process optimization [13].

Technological innovations, such as the integration of CNC systems and modular machine designs, have significantly improved the functionality of laser cutting systems. The adoption of fiber lasers, known for their high efficiency and low maintenance requirements, has further enhanced the capabilities of these machines. Applications include precision cutting of metals, composites, and plastics, as well as the production of prototypes and components for aerospace and medical industries [13]. This diagram presents the key components of a modern laser cutting machine, depicting the laser beam's path from its source to the material, including beam guidance systems and focusing optics.

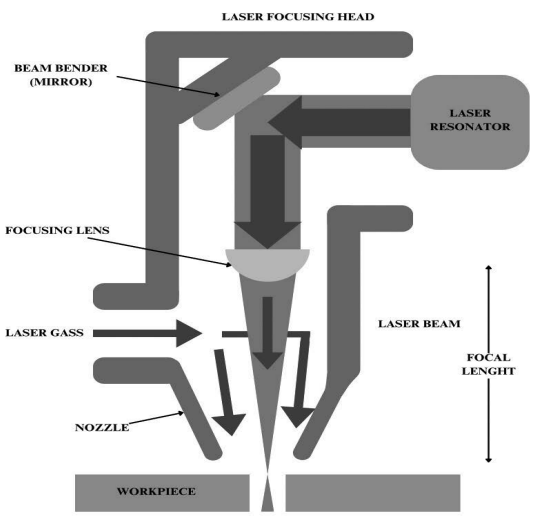

Figure 2. Laser cutting machine diagram

5. LASER ROBOTS AND THEIR APPLICATIONS

Laser robots represent the next evolution in laser cutting technology, offering unparalleled flexibility and precision. These systems utilize flying optics configurations to guide the laser beam in three-dimensional space. Their compact design and high operating speeds make them ideal for complex cutting tasks in confined or hard-to-reach areas [14].
Applications of laser robots are diverse, ranging from prototyping in automotive and aerospace industries to small-batch production of luxury items and custom components. They are also used for advanced manufacturing processes, such as precision cutting of turbine blades and injection-molded parts. Despite their advantages, challenges remain, including high integration costs and the need for regular calibration to maintain accuracy [15].

6. METODOLOGY

The goal of laser cutting parameter analysis is to understand how various technical factors affect the quality, speed, and efficiency of the process. The comparison aims to optimize the cutting process by adjusting parameters such as:

- Beam power
- Beam speed

- Properties of the gas and material

By analyzing these parameters, we can:

- Identify optimal solutions for different types of materials (e.g., metals, plastics).
- Assess the impact of parameters on cutting quality, including kerf width, burr formation, and the depth of the heat-affected zone.
- Optimize cost and process efficiency by selecting methods tailored to specific industrial applications.
- Compare technologies based on their limitations (e.g., difficulty in processing reflective materials or maximum thickness of cut components).
- Develop guidelines for industrial applications, such as cutting thin sheets, thick-walled materials, or complex-shaped components.

The table categorizes materials based on their reflective properties and other physical characteristics relevant to laser cutting or processing.

Table 1 Behaviour of different materials to laser cutting

Property	**Material**
High Reflectivity (need for fine focus)	Au, Ag, Cu, Al, brass
Medium/high reflectivity	Most metals
High Melting point	W, Mo, Cr, Ta, Ti, Zr
low Melting point	Fe, Ni, Sn, Pb
High oxide melting point (dross problems)	Cr, Al., Zr
Low reflectivity	Most nonmetals
Organics	
Tendecy to char	PVC, epoxy, leather, wood, rubber, wool, cotton
Less tendency to char	Arcylics, polythene, polypropylene, polycarbonate
Inorganics	
Tendecy to crack	Glass Natural stones
Less tendency to crack	Quartz, alumina, china, asbestos, mica

An additional indicator defining the efficiency of machining is the cutting performance parameter **S**. It takes into account the cutting speed **v**, material thickness **t**, kerf width k, and surface roughness R. The relationship between these quantities is described by the formula [16]:

$$S = v \cdot t \cdot k \cdot R$$

- S – Cutting performance,
- v – cutting speed,
- t – material thickness,
- k – kerf width,
- R – surface roughness

6.1 Purpose of the Analysis

The purpose of this analysis is to understand how various technological parameters of the laser cutting process impact the quality of large-scale steel products, as well as the efficiency and cost of production. The study focuses on factors such as laser beam power, cutting speed, the type and pressure of shielding gas, and material properties. By analyzing these parameters, the research aims to determine the optimal process conditions for various industrial applications, particularly in the context of machining large steel components. Optimization seeks to improve cutting quality by reducing kerf width, eliminating burrs, minimizing thermal deformations, and limiting the depth of the heat-affected zone (HAZ).

6.2 Scope of Research

The scope of research encompasses the analysis of the influence of technological parameters on the laser cutting process of steel, taking into account the specific requirements of large-scale products. The study investigates the characteristics of various steel grades, such as carbon steel, stainless steel, and alloy steel, focusing on their mechanical, structural, and thermal properties. The research considers the impact of material thickness and thermal conductivity on process quality. Additionally, the effects of parameters such as laser beam power on the capability to cut thicker materials and cutting speed on machining precision were examined. The type and pressure of shielding gas, such as oxygen, nitrogen, and argon, were analyzed concerning their effect on chemical reactions and the quality of the cutting edge.

6.3 Research Methodology

The research methodology is based on experimental approaches, statistical analysis, and computer simulations. During the experiments, steel samples of varying thicknesses and properties were prepared and subjected to laser cutting using different technological parameters. The process was monitored using optical and scanning electron microscopy (SEM), enabling detailed evaluation of kerf width, burr presence, and the depth of the heat-affected zone (HAZ). Statistical analysis, including experimental design (DOE), was used to identify key correlations between parameters and process outcomes. Computational modeling facilitated real-time simulation of temperature distribution and thermal deformations, providing a deeper understanding of the processes occurring during cutting.

6.4 Guidelines for Results Interpretation

The obtained results were compared with industry standards and simulation outcomes to comprehensively evaluate the impact of parameters on process quality. The analysis also considered economic aspects, such as operational costs associated with different shielding gases and the effect of parameter optimization on production time. Conclusions were formulated with the limitations of laser cutting technology in mind, such as challenges in processing reflective materials and restrictions on the thickness of the material that can be cut.

6.5 Expected Outcomes

The research is expected to result in the development of universal guidelines for optimal laser cutting parameters for large-scale products, considering both material diversity and the specifics of industrial applications. These guidelines aim to improve the quality of finished products, minimize material waste, and enhance the efficiency of the production process. Additionally, the results will serve as a foundation for further research and industrial

implementations, enabling the advancement of laser cutting technology to meet increasingly demanding technical and quality requirements.

7. CONCLUSIONS

The conducted analysis demonstrates the significant impact of laser cutting parameters on the quality, efficiency, and cost-effectiveness of machining large-scale steel components. Optimizing factors such as laser power, cutting speed, assist gas type, and material properties can greatly improve cutting precision, reduce waste, and minimize thermal damage. The research findings provide a solid foundation for establishing universal guidelines tailored to industrial applications, enhancing the overall performance of laser cutting technologies. Further studies could expand on these results, exploring advanced materials and cutting-edge techniques to meet the growing demands of modern manufacturing.

ACKNOWLEDGEMENTS

The work was created as a result of the project as part of project based learning - PBL, in the 11th competition under the Initiative of Excellence - Research University, Silesian University of Technology, Gliwice, Poland and as part of project of Students Scientific Circle of Laser Surface Treatment under the Initiative of Excellence - Research University, Silesian University of Technology, Gliwice, Poland.

BIBLIOGRAPHY

1. Smith, J., & Johnson, R. Controlled Fracture in Laser Cutting. ScienceDirect. 2003.
2. Brown, A., & Davis, M. Laser Scribing for Silicon Wafers. SpringerLink. 2013.
3. Green, T. Femtosecond Laser Ablation. Nature. 2024.
4. Taylor, P., & White, S. Laser-Assisted Oxygen Cutting. MDPI. 2022.
5. Wikipedia contributors. Laser Cutting. Wikipedia. Retrieved January 6, 2025, from https://en.wikipedia.org/wiki/Laser_cutting.
6. Mac-Tech team. Understanding Laser Cutting: Techniques and Applications. Retrieved January 3, 2025.
7. Thomas, L., & O'Connor, E. Flying optic vs fixed optic machines for CO2 laser cutting. TWI Global. 2023.
8. Lee, H., & Zhou, Q. Optimization and Design of a Laser-Cutting Machine using Delta Robot. Arxiv.org. 2022.
9. Tomosemi team. Laser Scribing Technology. Retrieved January 3, 2025.
10. Miller, K., & Adams, J. Avoiding Material Damage with Cold Laser Cutting. MDDI Online. 2024
11. https://stock.adobe.com/images/laser-cutting-technology-principle-explanation-and-machine-structure-outline-diagram-labeled-educational-metal-work-tool-for-high-precision-vector-illustration-inner-beam-resonator-and-nozzle-parts/465037803
12. Dubey, A. K., & Yadava, V. Laser beam machining—A review. International Journal of Machine Tools and Manufacture, 2008.

13. Klotzbach, A., et al. Laser processing of carbon fiber reinforced polymers and carbon fiber reinforced plastics. Physics Procedia, 2011.
14. Riveiro, A., et al. Laser cutting of aluminum alloys: Influence of process parameters in CO2 and fiber lasers. Procedia Manufacturing, 2017.
15. GoPhotonics. High-Quality Cutting of Polymers with Femtosecond Lasers. GoPhotonics, 2023.
16. Paweł Adamczyk, Małgorzata Słomion, Andrzej Wojciechowski, Maciej Matuszewski, Oleg Polishchuk, Wybrane Zagadnienia technologii cięcia laserem, nr 3/2021 www.obrobkametalu.tech

TalentDetector
31th January 2025
Gliwice, Poland
DEPARTMENT OF ENGINEERING MATERIALS AND BIOMATERIALS
FACULTY OF MECHANICAL ENGINEERING
SILESIAN UNIVERSITY OF TECHNOLOGY
INTERNATIONAL STUDENTS SCIENTIFIC CONFERENCE

Laser cutting

Roksana Pałczyńska[a], Norbert Klęk[a], Mirosław Bonek[a]

[a] Silesian University of Technology, Faculty of Mechanical Engineering

Abstract: This article describes the concept and characteristics of laser cutting. A brief history of the invention of this processing method is presented, along with the construction of the laser and the mechanism of the cutting process. The advantages and disadvantages of laser cutting, as well as its applications in various branches of industry, are also discussed.

Keywords: laser cutting, materials, subtractive machining

1. INTRODUCTION

Laser cutting is a digital manufacturing method classified as subtractive machining. It involves focusing a significant amount of energy, produced by a laser, onto a small, precise area to cut a material. The technique operates by channeling the laser's high-power output through specialized optics, which concentrate the beam onto a specific section of the material. This intense energy causes the material to either melt, burn, vaporize, or be blown away by a gas jet, resulting in a clean and high-quality edge.

In the 1960s, Peter Houldcroft, serving as the Deputy Scientific Director at The Welding Institute in Cambridge, became one of the trailblazers in exploring the potential of laser cutting. He discovered that combining a concentrated laser beam with an oxygen assist gas could significantly enhance the accuracy and efficiency of thermal cutting methods. In 1967, Houldcroft conceived the groundbreaking concept of a "laser cutting nozzle." This design included a pressurized oxygen chamber to supply a gas stream precisely at the laser beam's focal point.

More than four decades after Houldcroft’s invention, laser cutting has become ubiquitous. The technology is no longer limited to metals; it is now used on plastic, wood, paper, cardboard, textiles, and ceramics. Today’s lasers feature high-quality, precise beams capable of cutting materials up to 20 mm thick with clean, narrow edges, eliminating the need for additional finishing. The industrial sector remains the largest user of laser cutting, especially in automotive manufacturing. [1]

2. LASER CUTTING METHOD OF OPERATION

The laser beam consists of a narrow column of highly concentrated light with a single wavelength, or color. For a typical CO2 laser, this wavelength falls within the infrared range of

the light spectrum, making it invisible to the human eye. The beam starts at about 1.9 centimetre in diameter as it travels from the laser resonator, which generates it, through the machine's beam path. Along the way, the beam may be redirected by several mirrors or "beam benders" before being precisely focused onto the material. Just before reaching the plate, the focused laser beam passes through the bore of a nozzle. Along with the beam, compressed gases like oxygen or nitrogen flow through this nozzle.

The laser beam is focused using either a special lens or a curved mirror, and this process occurs within the laser cutting head. It's crucial for the beam to be accurately focused so that the focal spot is perfectly round, with a consistent energy density, and centered within the nozzle. By concentrating the large beam into a tiny pinpoint, the heat concentration at that spot becomes extremely high. It's similar to using a magnifying glass to concentrate sunlight onto a leaf, which can ignite a fire.

he high power density causes the material to heat up quickly, leading to melting and partial or complete vaporization. When cutting mild steel, the laser's heat is sufficient to trigger a typical "oxy-fuel" burning process, with pure oxygen used as the cutting gas, similar to an oxy-fuel torch. However, when cutting stainless steel or aluminum, the laser beam melts the material, and high-pressure nitrogen is used to blow the molten metal out of the cut area.

In a CNC laser cutter, the cutting head moves across the metal plate following the shape of the desired part, effectively cutting it out. A capacitive height control system ensures a precise distance between the nozzle tip and the plate being cut. This distance is crucial because it determines the position of the focal point relative to the plate's surface. The quality of the cut can be impacted by adjusting the focal point, whether it's positioned just above the surface, at the surface, or slightly below it. [2]

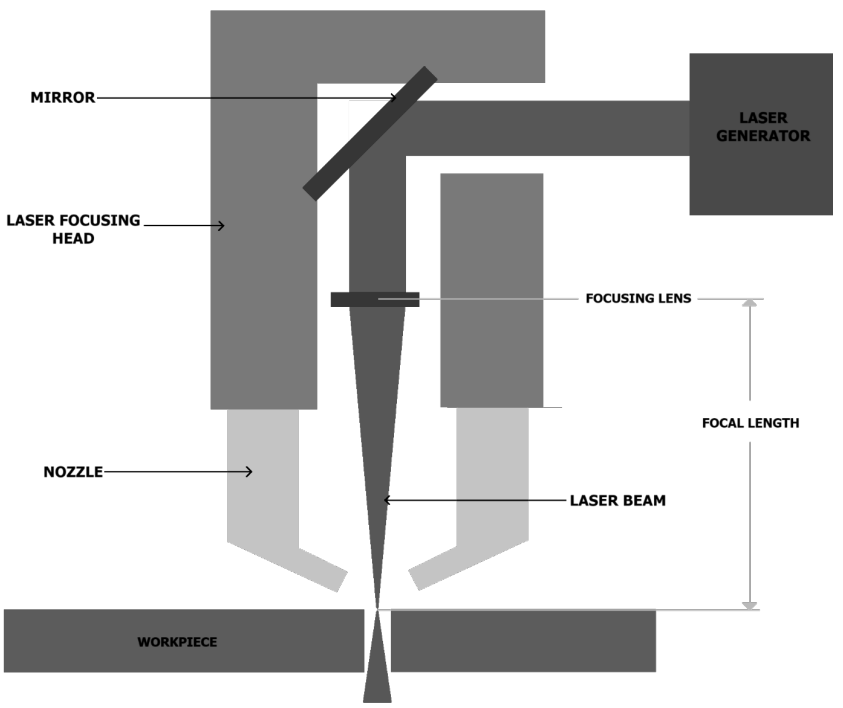

Figure 1. Laser construction scheme

3. TYPES OF LASER CUTTING

3.1 Fusion Cutting (Melting and Blowing)

Fusion cutting utilizes a high-power laser beam to melt material and an inert gas to expel the molten substance from the cut. The assisting gas, commonly nitrogen or argon, does not interact chemically with the material. Instead, it generates a strong pressure stream that efficiently clears away the melted material, producing smooth, oxidation-free edges. [3]
The main steps involved in fusion cutting are:

- Material Melting**:** The laser concentrates energy on a small point, quickly heating and liquefying the material.
- Molten Material Removal**:** The inert gas pushes the melted material out of the cut, preventing it from solidifying back into place and ensuring smooth edges.
- Continuous Operation**:** The laser moves along the predefined path, repeatedly applying this process to form a continuous cut. [3]

Suitable Materials for Fusion Cutting

Fusion cutting is particularly effective for materials that demand precise, clean edges without oxidation. These materials include:

- Stainless Steel**:** Often processed with nitrogen to avoid the formation of oxides.
- Aluminum and Its Alloys**:** Require more laser power due to their reflective surface and high thermal conductivity.
- Titanium and Nickel Alloys**:** Frequently used in aerospace and medical fields, where material strength and purity are essential.
- Non-Ferrous Metals**:** Such as copper and brass, though their reflective properties may necessitate specialized laser systems. [3]

Benefits of Fusion Cutting

- Oxidation-Free Results**:** Inert gases prevent oxidation, eliminating the need for additional cleaning of the cut edges.
- Exceptional Precision and Quality**:** Delivers neat and accurate cuts with minimal heat-related deformation.
- Reduced Finishing Requirements**:** Minimizes the need for post-cut processing.
- Capable of Complex Designs**:** Allows for the accurate creation of intricate shapes and fine details. [3]

Applications of Fusion Cutting

- Aerospace Sector**:** Producing high-precision parts with superior finishes.
- Medical Industry**:** Manufacturing surgical instruments and implants that meet strict hygiene and precision standards.
- Electronics**:** Crafting components for devices where exactness is critical.
- Automotive Field**:** Fabricating parts with clean edges, improving assembly efficiency and appearance. [3]

3.2 Flame Cutting (Reactive Cutting)

Flame cutting, also known as reactive fusion or oxygen laser cutting, utilizes laser-generated heat combined with a chemical reaction to optimize the cutting process. Oxygen serves as the

assisting gas in this technique. The laser heats the material to its ignition point, triggering an exothermic reaction between the oxygen and the metal (commonly steel), which produces additional heat to aid the cutting process. [3]

The primary steps in flame cutting are:

- Material Heating**:** The laser elevates the material's temperature to its ignition level.
- Combustion Reaction**:** Oxygen reacts with the heated metal, causing it to ignite and release more heat.
- Material Clearance**:** The molten oxide is expelled by the oxygen stream, creating a clean cut. [3]

Ideal Materials for Flame Cutting

Flame cutting works best with ferrous metals that are prone to oxidation, including:

- Carbon Steel**:** A widely used material due to its strong reaction with oxygen.
- Low-Alloy Steels**:** Metals with minimal alloying elements.
- Mild Steel**:** Frequently employed in construction and manufacturing. [3]

Benefits of Flame Cutting

- Capability to Cut Thick Materials**:** Handles thicker materials more effectively than fusion cutting at equivalent laser power.
- Efficient Laser Power Usage**:** The exothermic reaction amplifies the laser's cutting ability, reducing the power required.
- Faster Cutting Speeds**:** Especially efficient for cutting through thick steel sections.
- Lower Operating Costs**:** Oxygen is more economical compared to inert gases like nitrogen or argon. [3]

Common Applications of Flame Cutting

- Heavy Industry**:** Fabricating structural components like beams and plates.
- Shipbuilding**:** Cutting large steel sections for hulls and other ship structures.
- Construction Equipment Manufacturing**:** Producing components for heavy machinery.
- Steel Processing Facilities**:** Preparing steel sheets and plates for various industries. [3]

3.3 Sublimation Cutting (Vaporization Cutting)

Sublimation cutting, also referred to as vaporization cutting, involves the direct transformation of a material from its solid state to a gaseous state, bypassing the liquid phase entirely. A high-powered laser heats the material to its vaporization temperature, causing it to evaporate. An assisting gas, typically an inert gas like nitrogen, is used to clear the vaporized material from the cutting zone.[3]

The main steps of sublimation cutting are:

- Material Vaporization**:** The laser beam heats the material intensely, causing it to evaporate rapidly.
- Removal of Vaporized Material**:** The assisting gas flushes away the vaporized material from the cut.
- Accurate Cutting**:** With no molten residue involved, the process achieves precise cuts with minimal thermal impact.[3]

Suitable Materials for Sublimation Cutting
Sublimation cutting works best with materials that melt at lower temperatures or those that burn or melt inefficiently. Examples include:

- Wood and Paper**:** Used for intricate cuts and engraving.
- Plastics and Polymers**:** Such as acrylic, polycarbonate, and other thermoplastics.
- Fabrics and Textiles**:** Allows cutting without fraying or damaging the edges.
- Ceramic and Composite Materials**:** Ideal for brittle or high-temperature materials.
- Thin Metal **Sheets:** Used when exceptional accuracy is required.[3]

Benefits of Sublimation Cutting

- Exceptional Accuracy**:** Allows for detailed designs and fine features with very narrow kerf widths.
- Smooth Edges**:** Produces clean, burr-free cuts with no molten residue.
- Minimal Heat Damage**:** Reduces the size of the heat-affected zone for better material integrity.
- Broad Material Compatibility**:** Can handle a variety of non-metallic materials effectively.
- Non-Contact Operation**:** Avoids physical stress or deformation on delicate materials.[3]

Applications of Sublimation Cutting

- Electronics Manufacturing**:** Cutting and drilling tasks on printed circuit boards (PCBs).
- Signage and Displays**:** High-precision cutting of acrylic and plastic for premium display materials.
- Medical Component Fabrication**:** Producing parts with clean edges and strict dimensional accuracy.
- Textiles and Fashion**:** Cutting fabrics for apparel and accessories with no fraying.
- Creative Arts and Crafts**:** Crafting detailed designs from materials like wood, paper, and more. [3]

4. ADVANTAGES AND DISADVANTAGES OF LASER CUTTING

4.1 Advantages of laser cutting

- Flexibility: No need to switch tools for different cuts. A single setup handles various shapes and intricate designs with ease.
- Precision: Delivers accuracy of +/-0.1 mm, often eliminating the need for additional finishing or tolerances.
- Repeatability: Ensures consistent, identical parts with a repeatability of +/-0.05 mm.
- Automation: Highly automated machines require minimal labor, reducing costs and improving efficiency.
- Quality: Produces minimal burr and a small heat-affected zone, resulting in durable, reliable parts.
- Contactless **c**utting: Only the laser beam touches the material, avoiding tool wear.
- Versatility: Suitable for a wide range of shapes, materials, and applications, making it a highly adaptable technology. [4]

4.2 Disadvantages of laser cutting

- Expertise **r**equired**:** A skilled operator is essential to optimize a laser cutter's performance and ensure high-quality results.
- Metal thickness limitations: Laser cutting is less effective for very thick metals. Typically, it's used for materials up to 15–20 mm, depending on the equipment and expertise.
- High initial investment: Laser cutters can cost several tens of thousand of dollars, making them more expensive than waterjet or plasma cutters, though long-term efficiency can offset the high upfront cost.
- Hazardous fumes: While versatile, laser cutting produces harmful fumes, especially when cutting plastics. A good ventilation system is necessary, though it can be expensive. [4]

5. SUMMARY

Laser cutting is an advanced technology widely used in various industries. Methods such as fusion cutting, gas cutting, and sublimation cutting are selected based on the specific production requirements. Laser cutting is particularly valued in mass production due to its speed, precision, and cost-effectiveness, which are critical for clients. However, in single-unit production, or when working with thick materials, this method becomes less cost-efficient. Additional limitations include the range of materials that can be processed depending on the type of laser used, and the need for skilled specialists to operate the machines. In certain cases, alternative methods like waterjet cutting may be more suitable. Waterjet technology allows for the processing of virtually any material, eliminates heat-affected zones, and enables cutting significantly thicker materials compared to lasers. Ultimately, the choice of cutting technology is strongly influenced by various factors, such as the material's characteristics, required precision, and project budget.

ACKNOWLEDGEMENTS

The work was created as part of as part of project of Students Scientific Circle of Laser Surface Treatment under the Initiative of Excellence - Research University, Silesian University of Technology, Gliwice, Poland.

BIBLIOGRAPHY

1. https://www.sculpteo.com/media/ebook/Sculpteo_ultimate_guide_laser_cutting.pdf
2. https://esab.com/us/nam_en/esab-university/blogs/how-does-laser-cutting-work/
3.https://www.accteklaser.com/pl/jakie-sa-trzy-glowne-rodzaje-ciecia-laserowego/?srsltid=AfmBOoqX3sUDdbm-JfT6al3PahKV6T2XN-rbsNrxgKHLHmJOTG6RpDFV
4. https://fractory.com/laser-cutting-advantages-disadvantages/

TalentDetector

31th January 2025
Gliwice, Poland

DEPARTMENT OF ENGINEERING MATERIALS AND BIOMATERIALS
FACULTY OF MECHANICAL ENGINEERING
SILESIAN UNIVERSITY OF TECHNOLOGY

INTERNATIONAL STUDENTS SCIENTIFIC CONFERENCE

Metal determination methods, cyto- and genotoxicity assays for $PM_{2.5}$

Jakub Pawlikowski[a], Krzysztof Będkowski[c], Karolina Wołoszyn[b], Nikola Ochman[b], Paweł Kolak[c], Paweł Wranik[c], Elwira Zajusz-Zubek[d], Małgorzata Adamiec-Organiściok[e], Magdalena Węgrzyn[e], Magdalena Skonieczna[e], Jacek Nowak[f], Anna Mainka[d]

[a] Student of Faculty of Automatic Control, Electronics and Computer Science
email: jp300858@student.polsl.pl
[b] Students of IV Secondary School of General Education Orląt Lwowskich
email: karolina.woloszyn.32@gmail.com, nikola.ochman222@gmail.com
[c] Students of Faculty of Energy and Environmental Engineering
email: kb302264@student.polsl.pl, pk302273@student.polsl.pl, pw302307@student.polsl.pl
[d] Silesian University of Technology, Faculty of Energy and Environmental Engineering, Department of Air Protection
email: anna.mainka@polsl.pl, elwira.zajusz-zubek@polsl.pl
[e] Silesian University of Technology, Faculty of Automatic Control, Electronics and Computer Science, Department of Systems Biology and Engineering
email: magdalena.skonieczna@polsl.pl, malgorzata.adamiec-organisciok@polsl.pl, magdalena.wegrzyn@polsl.pl
[f] Silesian University of Technology, Faculty of Mining, Safety Engineering and Industrial Automation, Department of Applied Geology
email: jacek.nowak@polsl.pl

Abstract: The study highlights differences between two advanced analytic methods used for determination of metals in PM $_{2.5}$ samples, as well as cytoto- and genotoxicity assays using the BEAS-2B human bronchial epithelial cell line. In $PM_{2.5}$ samples collected in Gliwice city we analysed the concentrations of related elements by EDXRF technique, cytotoxicity of PMs was measured using cell viability, while genotoxic effects of PMs were determined using DNA damage and activation of proinflamatory cytokines IL6 and IL8 genes expression.

Keywords: $PM_{2.5}$, metals determination, cytotoxicity, cell culture, genotoxicity

1. INTRODUCTION

Environmental monitoring and air pollution assessment are essential to protect human health and environmental. Among air pollutants, fine particulate matter with a diameter <2.5 μm ($PM_{2.5}$), is recognized as one of the leading environmental health risk factors due to its ability to penetrate deep into the lungs and enter the bloodstream, [1]. Long-term exposure to $PM_{2.5}$ has been linked to premature mortality attributed to cardiovascular diseases and lung cancer. Short-

term exposure has shown a positive association with hospital admissions or emergency room visits for cardiovascular or respiratory effects [2]. In addition to respiratory and cardiovascular diseases, increasing attention has been devoted to the genotoxic and cytotoxic effects of $PM_{2.5}$. Genotoxicity refers to the potential of chemical constituents in particulate matter to damage cellular genetic material, which may lead to mutations, carcinogenesis, and other irreversible genetic changes [3]. Cytotoxicity, in contrast, reflects the ability of particulates to damage cells, resulting in dysfunction, inhibition of proliferation, or cell death [4]. Evaluating genotoxicity is particularly significant, as it represents a potential intermediate step in the carcinogenic process. Thresholds, such as the inhibitory concentration (IC_{50}), are often used to evaluate the biological activity of particles. The IC_{50} denotes the concentration at which a biological process is inhibited by 50%, providing valuable insights into the mechanisms of PM toxicity [1]. Urban $PM_{2.5}$ samples have been found to exhibit higher toxicity than suburban samples, predominantly due to traffic-related emissions. Among non-organic compounds, metals although contain only 1–2% of $PM_{2.5}$ demonstrate high toxicity and carcinogenic potential, even at low concentrations [5].

2. DETERMINATION OF METALS

2.1. Inductively Coupled Plasma-Mass Spectrometry (ICP-MS)

ICP-MS is a method of detecting naturally occurring elements at trace level. ICP-MS is widely used to determine hazardous substances present in the environment, which makes it essential to monitoring, assessing and understanding our environment [6]. Unlike other methods of detecting metal elements, such as volumetry and spectrophotometry, ICP-MS is a method capable of accurately determining multiple elements at once. With its wide detection range and high sensitivity, it is the most appropriate method of determining and analyzing trace metal concentrations in air [7]. PM samples must be diluted in order to be analyzed, as the ICP-MS method is designed to analyze liquid samples. The sample is aerosolized, and the larger aerosol droplets are filtered out in order to be properly ionized. The droplets then enter a stream of high-temperature plasma, where the sample is vaporized, and the elements present in the sample form ions. After ionization, the sample passes through a set of lenses (known as ion optics) which prevent photons from entering the mass analyzer. Photons present in the mass analyzer may cause signal instability [8]. The samples in the mass analyzer are then filtered according to their mass/charge ratio in order to be properly analyzed. To accurately assess the concentration of each element present in the sample, several reference solutions with known concentrations must be prepared in order to create a calibration curve. The data acquired by the ICP-MS analysis is then compared to the calibration curve formed by the reference solutions, allowing to accurately determine the concentration of each trace element present in the sample [9].

2.2. Energy-Dispersive X-ray Fluorescence Spectrometry (EDXRF)

EDXRF is a powerful analytical technique that finds wide application in many fields of science and industry. This method has the ability to quickly and accurately analyze the elemental composition of a variety of materials, from metals to environmental samples. XRF is becoming an increasingly popular tool in laboratories and manufacturing plants due to its versatility and non-invasive nature [10]. In the case of EDXRF, the sample is excited by an X-ray tube directly or through a filter or indirectly using so-called intermediary elements, which are polarizers or second anodes. The semiconductor detector analyzes the fluorescent X-ray radiation coming

directly from the sample. The detector and associated electronics count and sort, depending on energy, all the photons that are absorbed by it. This creates a pulse height spectrum indicating the number of photons or pulses for a given energy. The detector usually has only a few μs to process, so processing is limited to about 100,000 pulses per second. Using filters or polarizers, some of the excitation radiation can be removed to avoid overloading the detector [11].

2.3. $PM_{2.5}$ sampling and elemental composition

$PM_{2.5}$ samples were collected and analyzed in accordance with the reference procedure PN-EN 12341:2014 [12]. Sampling was conducted over 24-hour intervals between 21 and 28 November 2024 using quartz microfiber filters (QM-A Whatman, 47 mm in diameter). These filters were mounted on Atmoservice PNS-15 aspirators, operating with the flow rate of 2.3 m^3/h. The elemental composition of $PM_{2.5}$ was determined using EDXRF (BRUKER's S2 PUMA X-ray Fluorescence Spectrometer). The analysis, conducted under vacuum, covered a measurement range from sodium to americium. Table 1 presents the concentrations of $PM_{2.5}$ and metals with levels exceeding the limit of detection (LOD).

Table 1. $PM_{2.5}$ and metal concentration

Filter No.	$PM_{2.5}$	Al	Cr	Mn	Fe	Cu	Zn	Mo	Pb	Sr
	μg/m^3	ng/m^3								
1	13.4	695	LOD	12	403	285	38	6	LOD	LOD
2	16.0	LOD	LOD	LOD	261	272	30	LOD	LOD	LOD
3	13.7	LOD	LOD	LOD	223	269	34	LOD	LOD	LOD
4	24.2	453	LOD	LOD	404	285	53	LOD	LOD	LOD
5	14.5	2085	LOD	LOD	581	275	59	LOD	LOD	LOD
6	36.5	215	32	137	1063	343	128	15	343	137
7	33.1	2083	LOD	181	2066	315	127	LOD	344	LOD

Samples 4, 6, and 7 exceeded the WHO-recommended daily average concentration of $PM_{2.5}$, set at 15 μg/m^3. The highest total concentrations of metals were observed in filters 5–7. Correlation analysis revealed that the metals most strongly correlated with $PM_{2.5}$ concentrations were Mn, Fe, Cu, and Zn. These trace elements are likely derived from the re-suspension of contaminated soil and road dust, originating from coal combustion and vehicle emissions, including tire abrasion [13].

3. DETERMINATION OF CYTO- AND GENOTOXICITY

3.1. BEAS-2B Cell Line and $PM_{2.5}$ Samples Preparation

The cytotoxicity of $PM_{2.5}$ was evaluated using the BEAS-2B human bronchial epithelial cell line (from ATTC collection). Filters containing particulate matter were collected from seven monitoring stations across Gliwice, dried, and stored at room temperature. To extract adsorbed compounds, filters were washed in 5 mL of DMEM-F12 medium for 1 hour at room temperature with agitation (600 rpm, 21°C; Fig. 1). Each round filter was divided into quarters, with 2 mL of medium used per quarter, corresponding to final concentration of 0.5mL/cm^2. Two dilutions of the filter extract were prepared for cytotoxicity testing:

- **Dilution 1:1** – 200 μL of filter extract in culture medium (0.5mL/cm^2).

- **Dilution 1:2** – 100 µL of filter extract in 200 µL of culture medium (0.25mL/cm²).

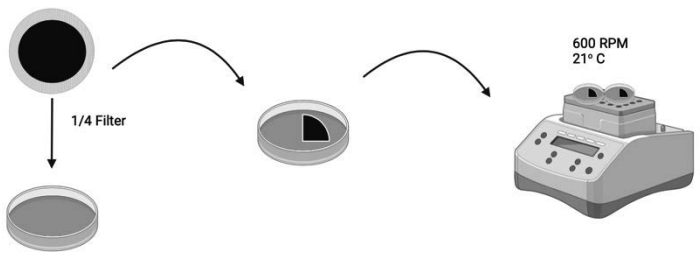

Figure 1. Samples preparation for biological activity evaluation.

3.2. BEAS-2B Cell Culture

BEAS-2B cells were seeded into 96-well plates at a density of 10,000 cells per well. Cells were trypsinized from flasks using standard protocols, including rinsing with 1 mL of trypsin (0.25 mg/mL; Sigma, in physiological saline, 1 x PBS; PAA), a brief incubation with 3 mL of trypsin, and neutralization with an equal volume of complete medium (DMEM-F12 + 12% FBS; PAA and EURx) [14]. The cell suspension was adjusted to achieve the desired concentration and plated in volume of 200 µL per well. Untreated cells, in complete medium served as the control group. Plates were incubated for 72 hours under standard conditions (37°C, 5% CO_2).

3.3. Biological evaluation of samples

Alamar Blue and MTT Assays for cells viability

Tested samples of filter extracts (No's 1-7) were added to the cells for 72 hours of incubation. At the time points of 24, 48 and 72 hours for 5 samples the viability was assessed, using the Alamar Blue dye (Thermo Scientific Fisher). Additional, at the end of the incubation, medium was removed, and cells were rinsed with 100 µL of cold PBS for MTT viability (Promega), confluency, microscopic observation and real-time qPCR for proinflammatory cytokines genes expression assays. The viability assays were performed:

- **Alamar Blue Assay**: Alamar Blue reagent (volume to be determined) was added to each well and incubated until a colour change from blue to pink; observed in the control wells. Absorbance was measured at 570 nm with a reference wavelength of 600 nm using Varioscan apparatus (Thermo Scientific Fisher) [15]. The measurements were performed after 24, 48 and 72 hours for 5 samples.
- **MTT Assay**: An MTT solution (concentration to be determined) was added to each well, and incubation continued until purple formazan crystals formed in the control wells. Absorbance was measured at 550 nm with a reference wavelength of 655 nm [16]. The measurements were performed for all 7 samples after 72 hours of incubation.

Cell viability was calculated by comparing absorbance values of treated samples to those of the untreated control group; expressed as fold changes. Each sample was tested in triplicate, and results were presented as the mean of three independent experiments.

The microscopic observations were performed directly on the plates with the samples before viability assays, using the Juli Fl apparatus (NanoEntec), at specific time-points (72 hours); with magnification 40x with visible channels under phase contrast. The collected images enabled

automatic confluency calculation, after exposing the cells to the tested filters extracts. Untreated cells were used as the control.

The toxicity of the tested filter's extracts was also evaluated for pro-inflammatory cellular pathway activation, with evaluation of specific interleukins (IL6 and IL8) genes expression level. The cells samples, after 72 h of incubation were collected and total RNA was extracted for the next, reverse transcription and real-time qPCR reactions (according to the manufacturer protocols from Eurx and A@A Biotechnology, respectively). The relative mRNA levels were determined following Livak and Schmittgen [17].

Micronucleus Assay for genotoxicity evaluation of tested samples

The micronucleus test detects genotoxic damage by identifying cells with micronuclei formed during mitosis due to chromosome fragments or miss-segregation. Conducted *in vitro* with cytochalasin B to block cytokinesis, it differentiates mononucleated (non-dividing) from binucleated (dividing) cells. Binucleated cells with micronuclei indicate DNA damage and mutation potential. Procedures followed ISO 10993-3 guidelines for genotoxicity evaluation of medical materials, with 1% hydrogen peroxide used as a positive control. Materials or samples inducing less than 30% change, compared to the untreated controls are deemed as non-genotoxic [18].

4. RESULTS AND OBSERVATIONS

4.1. BEAS-2B Survival Fraction (Alamar Blue Assay)

Alamar Blue assay results illustrate the survival fraction (SF) of BEAS-2B cells after 72 hours of exposure to filter extracts, collected from seven different locations (Figure 2). Survival data for each filter are presented separately, with sample dilutions starting at 0.5 ml/cm^2, and untreated cells serving as the control (CTR).

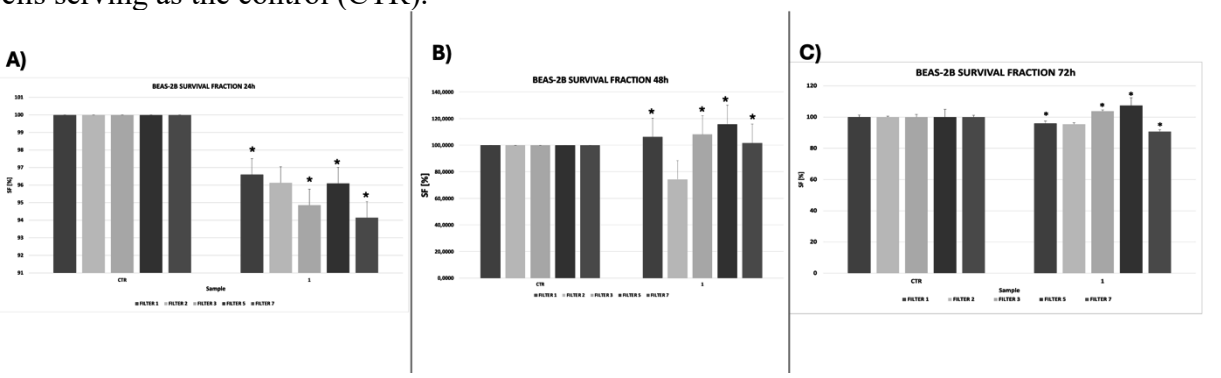

Figure 2. Survival fraction (%) of BEAS-2B cells exposed to $PM_{2.5}$ filters extracts after 24h (A), 48h (B), 72h (C). Data represent mean ± standard deviation from three independent experiments. The star (*) indicate the statistical significance, in comparison to the untreated controls (t-test, p value ≤ 0.05).

4.2. Cell Viability (MTT Assay)

The MTT assay was conducted to further assess cell viability after exposure to filter's extracts (Fig. 3A). Additionally, hydrogen peroxide (H_2O_2) at concentration of 3 µM, was used for 5 min of incubation, and served as a positive control - to induce cellular damage and showed high agent's cytotoxicity. The assay was performed using a dye, at the 0.5 mg/mL of a final

concentration (Promega). The cells were then incubated at 37°C for 2-3 hours for colorimetric reaction development.

4.3. Cells Confluency

Before treatment, BEAS-2B lung epithelial cells were cultured to approximately 80% of confluency, to ensure uniformity across experimental conditions. This level of confluency was chosen to maintain healthy cell morphology and prevent overgrowth of the population, which could interfere with the accuracy of cytotoxicity and gene expression assays. Cells at this confluency provide optimal conditions for consistent exposure to $PM_{2.5}$ filter's extracts and reliable RNA extraction for RT-qPCR analysis (Figure 3B). Figure 3D presents the samples of taken images from the treated and control plates, during the microscopic observation and for confluency calculations.

4.4. Micronucleus Test (Mn assay)

In the BEAS-2B lung epithelial cell line, DNA damage after 72 hours ranged from 2% in controls up to 20% in the positive control (1% hydrogen peroxide). With $PM_{2.5}$ filter fluids causing DNA damage between 4.5% and 13%, and total DNA damage did not exceeding 10% for most filters (Fig. 3C).

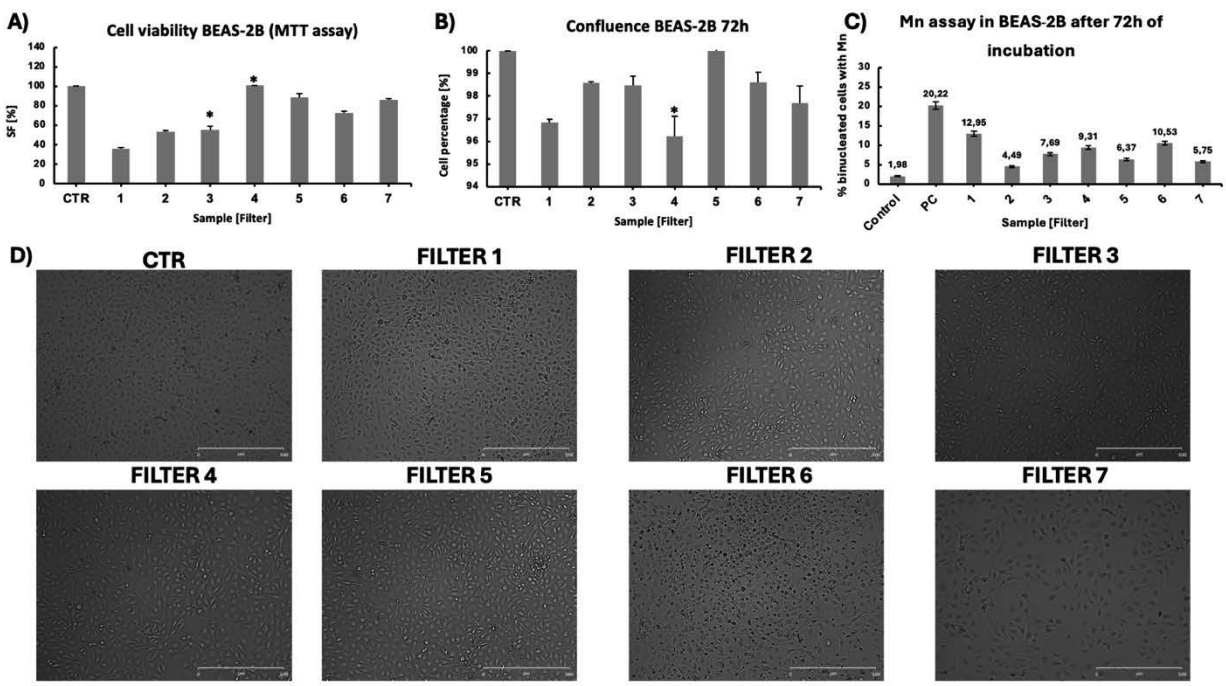

Figure 3. Viability (%) of BEAS-2B cells exposed to PM2.5 filter extracts (A). Confluence of cells at 72 h (B). DNA damage, 72 hMn assay (C). Images of BEAS-2B cells at 72 h (D). Results are expressed as mean ± standard deviation from three independent experiments. The star (*) indicate the statistical significance, in comparison to the untreated controls (t-test, p value ≤ 0.05).

4.5. RT-qPCR (quantitative Real Time Polymerase Chain Reaction)

RT-qPCR was used to evaluate IL6 and IL8 genes expression after 72 hours of exposure to $PM_{2.5}$ filter's extracts (Fig. 4). Total RNA was isolated, reverse-transcribed, and amplified using specific primers, with RPL41 as the reference gene. Calculations after Livak and Schmittgen [17].

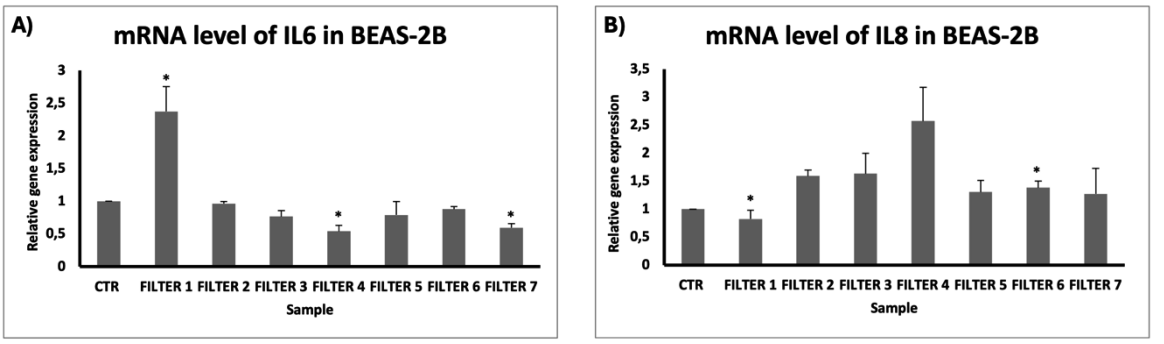

Figure 4. Gene expression of IL6 (A) and IL8 (B) in BEAS-2B after 72h of incubation. Results are expressed as mean ± standard deviation from three independent experiments. The star (*) indicate the statistical significance, in comparison to the untreated controls (t-test, p value ≤ 0.05).

5. DISSCUSION

The conducted studies demonstrated that cytotoxicity and genotoxicity assays can be effective tools for evaluating the harmful impact of $PM_{2.5}$ particulates on BEAS-2B lung epithelial cells. Results from the MTT and Alamar Blue assays, revealed a dose-response relationship, where higher concentrations of filter extracts significantly reduced cell viability, indicating the presence of toxic substances in certain samples. Filters 3 and 4 showed the highest toxicity, potentially linked to higher concentrations of organic compounds or heavy metals. In contrast, Filters 5 and 6 exhibited relatively low toxicity, suggesting fewer harmful substances in these samples. The micronucleus test (Mn assay) enabled precise analysis of genetic damage in binucleated cells. DNA damage induced by $PM_{2.5}$ filters did not exceed 10% in most samples, indicating a limited genotoxic potential compared to the positive control (H_2O_2 – 20%). Gene expression analysis of IL6 and IL8 using qPCR revealed differences in the inflammatory responses triggered by various samples. Filter 1 caused the highest increase in IL6 expression, indicating a strong pro-inflammatory effect. Meanwhile, Filter 4 exhibited the highest IL8 expression, reflecting diverse cellular responses to airborne pollutants.

6. SUMMARY

$PM_{2.5}$ particulates demonstrate a significant cytotoxic potential, posing a risk to respiratory epithelial cells. Although genotoxic effects are limited, they vary among filters, indicating compositional differences in $PM_{2.5}$ samples. IL6 and IL8 expression analysis reveals that these particulates can induce inflammatory responses, potentially contributing to chronic airway inflammation.

$PM_{2.5}$ pollutants are a major component of urban air pollution, and their impact on human health is of increasing concern, particularly in highly industrialized regions such as Silesia. Prolonged exposure to these particulates may elevate the risk of developing chronic respiratory conditions, such as asthma and chronic obstructive pulmonary disease (COPD). The observed variations among filter samples highlight the necessity for further investigation into other specific components of $PM_{2.5}$ that are associated with adverse health effects for example polycyclic aromatic hydrocarbons (PAHs), and its biological impacts. Such research could inform public health policies and support the development of targeted interventions aimed at mitigating the

health risks associated with $PM_{2.5}$ exposure, and contributing to the formulation of effective long-term mitigation strategies.

ACKNOWLEDGEMENTS
This work was supported by the 10th Project-Based Learning - PBL funding competition within the "Excellence Initiative – Research University" programme of Silesian University of Technology

BIBLIOGRAPHY

1. L. Miller, X. Xu, Ambient $PM_{2.5}$ Human Health Effects – Findings in China and Research Directions. Atmosphere, 9, 424, 2018.
2. A. Mainka, M. Żak, Synergistic or Antagonistic Health Effects of Long- and Short-Term Exposure to Ambient NO_2 and $PM_{2.5}$: A Review. *Int J Environ Res Public Health*, *19*, 14079, 2022.
3. A.R. Collins, The comet assay for DNA damage and repair. *Mol Biotechnol* 26, 249–261, 2004.
4. T. Mosmann, Rapid colorimetric assay for cellular growth." J Immunol Method,. 1983.
5. A. Mainka, P. Fantke, Preschool Children Health Impacts from Indoor Exposure to PM2.5 and Metals. *Environ Int*, *160*, 107062, 2022.
6. D. Pröfrock, A., Prange Inductively Coupled Plasma – Mass Spectrometry (ICP-MS) for Quantitative Analysis in Environmental and Life Sciences: A Review of Challenges, Solutions, and Trends. Applied Spectroscopy,66(8), 843–868, 2012.
7. S. Lu, H. Zhang, W. Du, J. Deng, Determination of Metal Elements in Workplace Air by ICP-MS, MATEC Web Conf. 319 02005, 2020.
8. S.C. Wilschefski, MR., Baxter Inductively Coupled Plasma Mass Spectrometry: Introduction to Analytical Aspects. Clin Biochem Rev. Aug, 40 (3),115–133, 2019.
9. https://www.agilent.com/en/product/atomic-spectroscopy/inductively-coupled-plasma-mass-spectrometry-icp-ms/what-is-icp-ms-icp-ms-faqs
10. https://www.laboratoria.xtech.pl/produkty/spektrometry-fluorescencji-rentgenowskiej-edxrf-11604-
11. https://www.anitepo.pl/fluxana-technika-xrf-i-oes/technika-xrf
12. Polish Committee for Standardization. PN-EN12341 Ambient Air – Standard Gravimetric Measurement Method for the Determination of the PM_{10} or $PM_{2.5}$ Mass Concentration of Suspended Particulate Matter; Polish Committee for Standardization: Warszawa, Poland, 2014.
13. A. Mainka, E. Zajusz-Zubek, K. Kaczmarek, PM2.5 in Urban and Rural Nursery Schools in Upper Silesia, Poland: Trace Elements Analysis. Int J Environ Res Public Health 12, 7990–8008, 2015
14. P. S. Hiemstra, G. Grootaers, A. M. van der Does, C.A.M. Krul, I.M. Kooter, Human lung epithelial cell cultures for analysis of inhaled toxicants: Lessons learned and future directions, Toxicology in Vitro, Volume 47, 137–146, 2018.
15. J. O'Brien, I. Wilson, T. Orton, F. Pognan, Investigation of the Alamar Blue (resazurin) fluorescent dye for the assessment of mammalian cell cytotoxicity. Eur J Biochem. Sep, 267(17), 5421-6, 2000.

16. J. van Meerloo, G.J. Kaspers, J. Cloos, Cell sensitivity assays: the MTT assay. Methods Mol Biol., 731, 237–45, 2011.
17. K.J. Livak, T.D. Schmittgen, Analysis of relative gene expression data using real-time quantitative PCR and the 2(-Delta Delta C(T)) Method. Methods. Dec, 25 (4), 402–8, 2001.
18. M. Fenech, The in vitro micronucleus technique. Mutat Res. Nov 20, 455 (1-2), 81–95, 2000.

TalentDetector
31th January 2025
Gliwice, Poland
DEPARTMENT OF ENGINEERING MATERIALS AND BIOMATERIALS
FACULTY OF MECHANICAL ENGINEERING
SILESIAN UNIVERSITY OF TECHNOLOGY
INTERNATIONAL STUDENTS SCIENTIFIC CONFERENCE

Characterization of crystalline solar cells using various microscopes

Mateusz Pfeifer[a], Dominik Szendzielorz[a], Jakub Rusek[a], Małgorzata Musztyfaga-Staszuk[b], Aleksandra Drygała[c], Krzysztof Wiśniewski[d], Marcin Staszuk[c]

[a] Pupil, Complex of Communication Schools, Warszawska 35, 44-100 Gliwice, Poland
[b] Silesian University of Technology, Faculty of Mechanical Engineering, Welding Department, Konarskiego 18a, 44-100 Gliwice, Poland
[c] Silesian University of Technology, Department of Engineering Materials and Biomaterials, Konarskiego 18a, 44-100 Gliwice, Poland
email: malgorzata.musztyfaga@polsl.pl
[d] Łukasiewicz Research Network – Institute of Non Ferrous Metals, Centre of Advanced Material Technologies
email: krzysztof.wisniewski@imn.lukasiewicz.gov.pl

Abstract: The study aims to compare the microstructural properties of mono-crystalline silicon solar cells. The samples were made with different conductive pastes. One was commercial, while the second one was produced experimentally. Both pastes were deposited using the screen printing method, but each was manufactured using a different technique. Co-firing in a belt furnace for front metallization is a classic manufacturing method, whereas selective laser sintering is a modern technique. The work presented in this paper is an extension of the ongoing project titled "*Selected research methods used in the characterization of photovoltaic materials (Part II)*".

Keywords: mono-crystalline silicon solar cells, front contact, screen printing, selective laser sintering, structural investigations

1. INTRODUCTION

The article describes the significance of selected microscopes in the development of photovoltaic technology, highlighting their crucial role in the analysis and optimization of components used in solar cells. They enable a better understanding of the structure of materials, which is essential for improving photovoltaic technologies.

Three types of microscopes that are part of the equipment in the laboratory of the Faculty of Mechanical Technology have been described. The scanning electron microscope, by utilizing a beam of electrons, allows for the examination of, for example, nanostructures of materials. The atomic force microscope enables imaging of surfaces at the atomic scale, allowing for detailed studies of topography as well as material properties. The optical microscope, although its resolution is limited by the wavelength of light, is used for quick

analysis and preliminary observations.

The Scanning Electron Microscope (SEM) (Fig. 1) is a type of electron microscope that produces an image of a sample by scanning its surface with a focused beam of electrons emitted by the microscope's electron-optical system [1]. The SEM allows for the acquisition of information about the chemical composition of the investigated material. This is made possible through characteristic X-ray radiation. Secondary electrons are used to obtain information about the topology of the studied material. In SEM microscopy, signals from secondary electrons, backscattered electrons, and characteristic X-ray radiation are most commonly utilized [2].

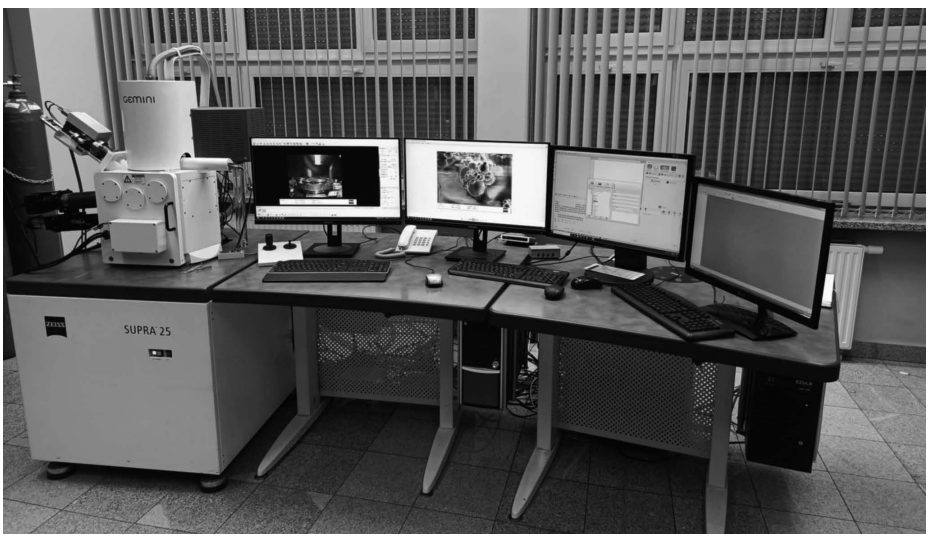

Fig. 1. The scanning electron microscope

The Atomic Force Microscope (AFM), as shown in Figure 2, operates by examining the surface of a sample using a tip mounted on a flexible lever. Interactions occur between the atoms of the tip and the atoms of the sample, which include Coulombic and Van der Waals forces, forming the basis for AFM functionality [3,4]. The atomic force microscope can operate in several modes:

1. **Contact mode**: In this mode, the tip is placed at a very close distance to the sample surface, allowing repulsive forces to act on the tip, resulting in deformation of the lever arm and providing information about the surface of the sample [3].
2. **Non-contact mode**: Here, the tip does not physically touch the sample surface, but instead moves above it at a distance of 10-100 nm while being oscillated. During scanning, as the sample moves beneath the tip, the resonance frequency of the lever's oscillations changes due to the varying force acting on the tip as the distance between the tip and the surface changes [3].
3. **Tapping mode**: This semi-contact mode combines features of both contact and non-contact modes. The lever is oscillated, and its frequency changes with the distance between the tip and the sample surface. As the tip approaches the surface of the material being studied, the amplitude of oscillations increases, and when the tip makes contact with the surface, the amplitude of oscillations decreases [4].

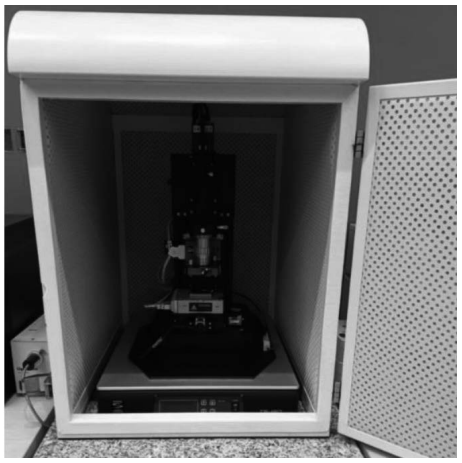

Fig. 2. The atomic force microscope

An optical microscope (Fig. 3) is a device that allows for the magnification and examination of objects that are not visible to the human eye using visible light and a combination of lenses. Its operation involves passing light through a sample and focusing it through the objective lens, followed by further magnification through the eyepiece to create a clear image. The basic components of microscopy include the light source, condenser, objective lens, and eyepiece. Optical microscopes can be equipped with various techniques, such as fluorescence microscopy or polarized light microscopy, which enable the analysis of processes in much clearer images and even at the molecular level. A limitation of optical microscopy is the phenomena of interference and diffraction, which result in the ability to clearly observe only objects that are significantly larger than the wavelength of the light used.

Fig. 3. The optical microscope

2. MATERIAL

The investigations were conducted on monocrystalline silicon wafers produced by Deutsche Solar AG using the Czochralski method. The material characteristics of silicon utilized in this study are outlined in Table 1. The front electrode was created using both commercially available silver paste PV19B and an experimentally developed silver nano-paste, applied through the screen-printing technique. Subsequently, it was co-fired at 920°C in a belt furnace for sample A, while sample B underwent selective laser sintering in an Eosint M 250 Xtended machine, utilizing a laser beam feed rate of 100 mm/s and a laser power of 49 W.

Table 1. Basic parameters of crystalline silicon

Conductivity	type p
Dopant	bor
Wafer thickness	200 ± 15 μm
Surface area	25 cm^2
Resistivity	~1 Ω·cm
Oxygen concentration	≤1x10^{18} atoms/cm^3
Carbon concentration	≤2x10^{17} atoms/cm^3

3. METHODOLOGY

During the investigation, the conveyor IR furnace was equipped with tungsten filament lamps that heated both the top and bottom of the conveyor, with a conveyor belt feed rate of 190 cm/min. Additionally, the Eosint M 250 Xtended device was used to produce front metallization. The basic parameters of the device consist of the following: laser beam feed rate (maximum 3 m/s), laser beam output power (270 W), laser beam diameter (300 μm), wavelength (10640 nm), and shielding gas (nitrogen).The topography of both the surface and cross-section of the front contacts was analyzed using a Zeiss Supra 35 scanning electron microscope (SEM) with secondary electron detection and an accelerating voltage ranging from 5 to 20 kV. Microchemical analysis of selected areas of solar cells was conducted using a scanning electron microscope with an energy-dispersive X-ray (EDS) spectrometer. Moreover, the topography of the front metallization was analyzed using both an atomic force microscope (Park Systems XE 100) in non-contact mode and a Leica DVM6 digital optical microscope.

4. RESULTS

Figures 4 and 5 present observations obtained with a scanning electron microscope (SEM) of the front electrode of solar cells, which were produced using silver paste via screen printing and selective laser sintering techniques

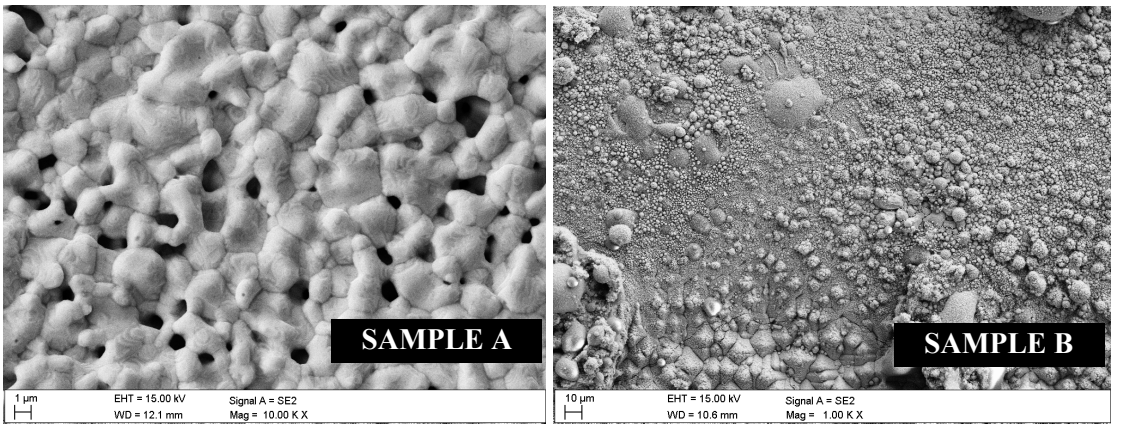

Figure 4. Topography of the front contact made from silver a) commercial and b) experimental paste (SEM)

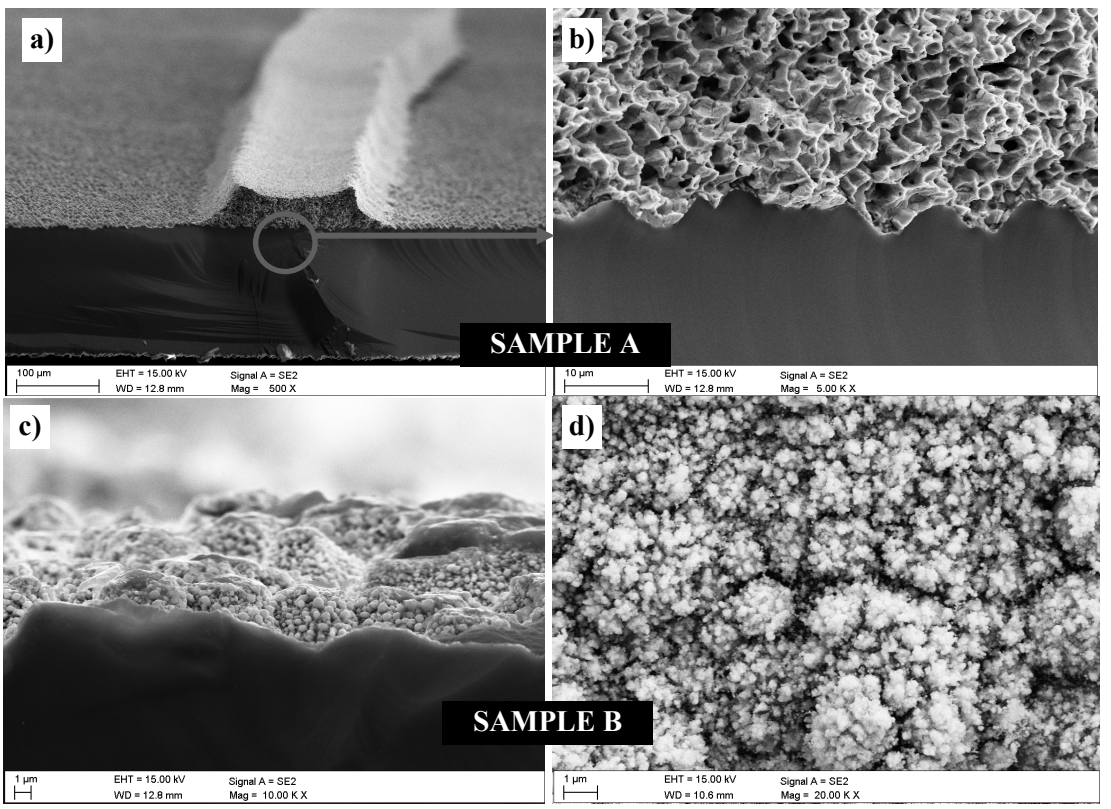

Figure 5. Cross-section of the front contact made from commercial paste (a, b) and experimental paste (c, d) (SEM)

The topographical observations in the SEM indicate that the morphology of a front contact deposited from commercial paste and co-fired in the furnace exhibits a porous structure (Fig. 4a). In contrast, the morphology of a front electrode deposited from experimental paste and selectively laser-sintered shows high heterogeneity (Fig. 4b), with various spheres of different sizes observed. The electrode layer establishes numerous uniform connections with the silicon substrate, approaching a nearly continuous link (Fig. 5a). Fractographic

observations of silicon solar cells featuring a front contact made from experimental paste and selectively laser-sintered revealed that the electrode fabrication process results in well-consolidated layers, free of pores or discontinuities, which adhere effectively to the silicon (Fig. 5b).

Microscopic observations with chemical composition analysis confirm the presence of elements suitable for the Si with deposited layers (Figure 6).

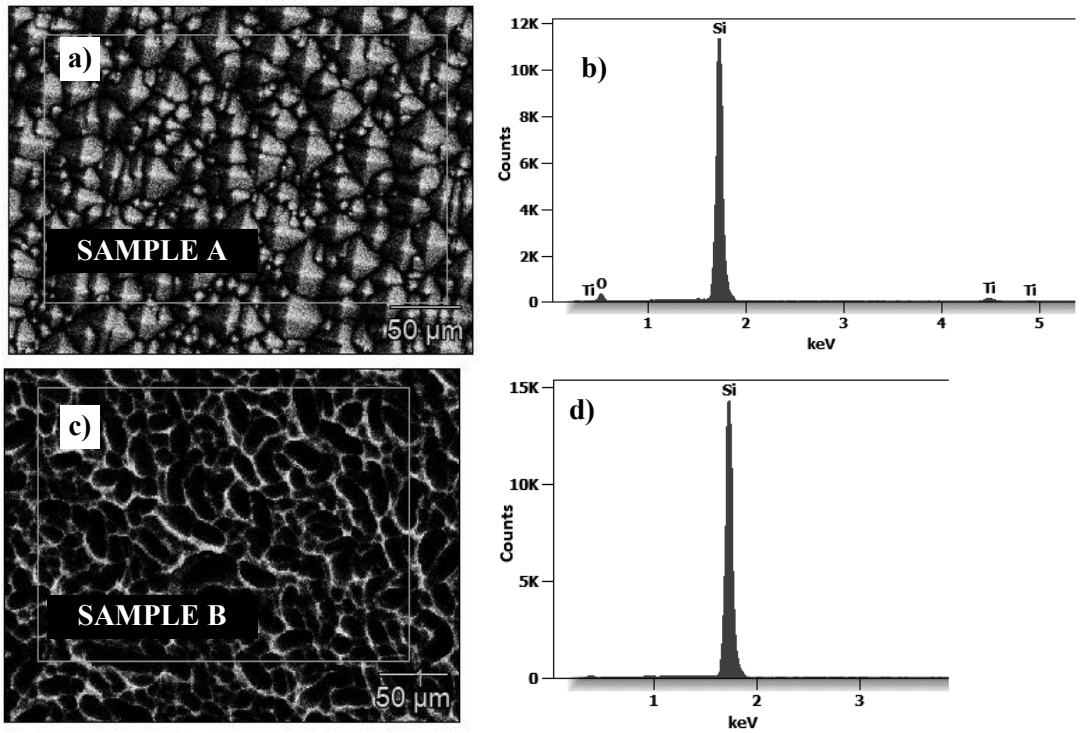

Figure 6. a, c) Topography of samples and b, d) EDS microanalysis from the area (silicon with deposited layers)

Figure 7 illustrates the topology of the textured surface of monocrystalline silicon. Based on the studies conducted using an atomic force microscope, it was determined that the average height of the pyramids on the textured surface is approximately 2 µm.

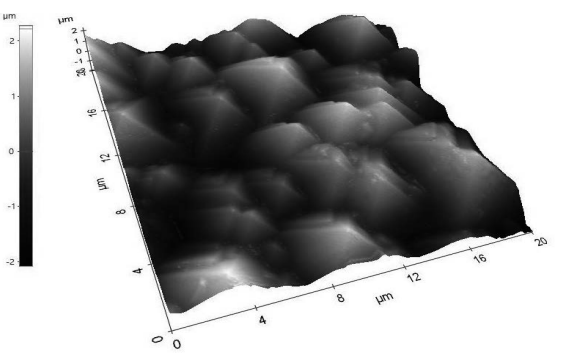

Figure 7. The topography of the textured surface of a 200 µm thick single-crystal silicon sample A (AFM)

Figure 8 presents the topography observations from the optical microscopy of the samples. Using this microscope, the finger height of the investigated samples was measured. In the case of sample A, the busbar was 7.37 mm, while for sample B it was 7.04 mm.

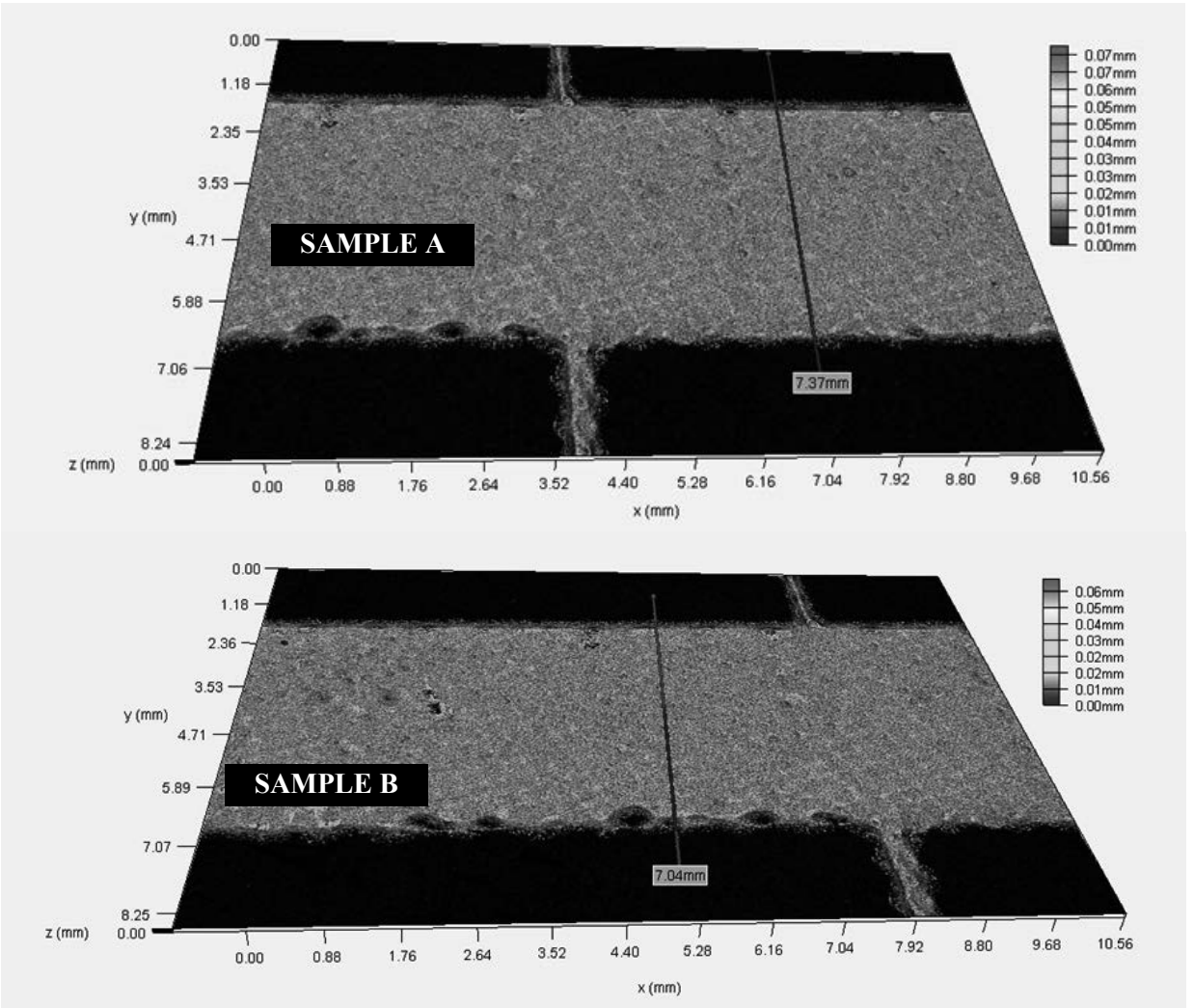

Figure 8. The three-dimensional topography of the front electrode made of a) commercial paste on a textured surface with an applied antireflective layer, b) experimental paste on a not textured surface with an applied antireflective layer.

The electrode layer forms numerous uniform connections with the silicon substrate, resembling nearly continuous connections in the case of front contacts that are co-fired in a belt furnace. Based on fractographic investigations, the electrode layer selectively laser sintered adhered well to the silicon substrate. The analysis of chemical composition verified the presence of elements appropriate for the silicon substrate. According to the research carried out with an atomic force microscope, it was found that the average height of the pyramids on the textured surface is around 2 μm. The thickness of the front contacts was determined by examining the height profile of the three-dimensional surface topography measured using

an optical microscope. Based on the analysis, there was a slight difference in the thickness of the samples investigated.

ACKNOWLEDGEMENTS

This work was produced as part of the project implemented within the framework of project-oriented education - PBL project implemented with secondary school students, in the IV competition under the Excellence Initiative - Research University program, at the Silesian University of Technology.

BIBLIOGRAPHY

1. A. Barbacki, R. Czajka, K. Jóźwiak, T. Kachlicki, R. Lubawy. Mikroskopia elektronowa. Wydawnictwo Politechniki Poznańskiej. Wydanie III poprawione pod redakcją Andrzeja Barbackiego, 2007, str. 85-92.
2. G. Słowik: Podstawy mikroskopii elektronowej i jej wybrane zastosowania w charakterystyce katalizatorów nośnikowych. Rozdział 12 w monografii Adsorbenty i katalizatory. Wybrane technologie, a środowisko. Pod redakcją Janusza Ryczkowskiego, Uniwersytet Rzeszowski, 2012, str. 219-243.
3. M. Targosz-Korecka, M. Szymoński, M. Miklaszewska, J. Pietrzyk, W. Sułowicz, R. Rumian, L. Krawentek. Nowe techniki pomiarowe w biologii i medycynie: mikroskopia sił atomowych (cz. I). Czasopismo Przegląd Lekarski, t. 60, nr 12; Instytut Fizyki Uniwersytetu Jagiellońskiego w Krakowie, 2003, str. 828-831.
4. T. Kruk, Mikroskopia Sił Atomowych (AFM), LAB Laboratoria, Aparatura, Badania. Instytut Katalizy i Fizykochemii Powierzchni im. J. Habera PAN w Krakowie, rok 18, nr 1, 2013, str. 40-50.
5. Dane na stronie: https://chem.pg.edu.pl/documents/175361/28234243/cz4.pdf

TalentDetector
31th January 2025
Gliwice, Poland
DEPARTMENT OF ENGINEERING MATERIALS AND BIOMATERIALS
FACULTY OF MECHANICAL ENGINEERING
SILESIAN UNIVERSITY OF TECHNOLOGY
INTERNATIONAL STUDENTS SCIENTIFIC CONFERENCE

Aplikácie ložiskových ocelí

Mária Pilarčíková[a], Igor Gajdáč[b]

[a] Žilinská univerzita v Žiline, Strojnícka fakulta, Katedra materiálového inžinierstva, Univerzitná 8215/1, 010 26 Žilina, Slovenská republika
[b] Žilinská univerzita v Žiline, Strojnícka fakulta, Katedra konštruovania a častí strojov, Univerzitná 8215/1, 010 26 Žilina, Slovenská republika
email: pilarcikova4@stud.uniza.sk igor.gajdac@fstroj.uniza.sk

Abstrakt: Práca sa zaoberá ložiskovými oceľami. Bližšie podáva základné informácie o ložiskových oceliach, ich využitie v priemyselnom odvetví a dôležitosť trvanlivosti a spoľahlivosti ložísk. Charakterizuje najvýznamnejšie predpoklady a požiadavky kladené na ložiskové ocele. Cieľom bolo vytvoriť stručný prehľad o aplikáciách, rozdelení a vlastnostiach ložiskových ocelí.

Kľúčové slová: ložiskové ocele, ložiská, akosť

1. ÚVOD

Ložiská sú kľúčovými komponentami umožňujúce plynulý a presný pohyb rôznych mechanických zariadení. Znižujú trenie medzi pohyblivými časťami, ako sú hriadele a osi, čím zabezpečujú ich hladké otáčanie a predlžujú životnosť. Okrem toho ložiská slúžia na presné určenie polohy jednotlivých súčastí a prenos síl a momentov medzi pohyblivými a nepohyblivými časťami mechanizmu. Vďaka týmto vlastnostiam sú ložiská nenahraditeľné v širokom spektre priemyselných odvetví [1-3].

Obr. 1 Valivé uloženia: hriadeľ podopretý dvoma ložiskami [1]
Figure 1. Rolling bearings, shaft supported by two bearings [1]

Pri vzájomnom relatívnom pohybe častí ložiskového uzla vzniká odpor proti pohybu - trenie. Trenie závisí od materiálov klzného povrchu, od množstva maziva, od klznej rýchlosti a od konštrukčného usporiadania klzného ložiska. Ložiská znižujú spotrebu energie, pretože klzný pohyb je nahradený valením s nízkym trením (obr. 1); zabraňujú poškodzovaniu a opotrebeniu tejto časti a taktiež udržiavajú správnu polohu hriadeľa [1].

Princíp činnosti ložísk spočíva v odvaľovaní valivých teliesok medzi vonkajším a vnútorným krúžkom. Podľa spôsobu, akým prenášajú zaťaženie a umožňujú pohyb, delíme ložiská na dve základné skupiny: valivé a klzné. Valivé ložiská využívajú guľôčky alebo valčeky na zníženie trenia, zatiaľ čo klzné ložiská pracujú na princípe klzných plôch.

Oba typy sa ďalej delia podľa smeru pôsobenia zaťaženia: radiálne ložiská (obr. 2b) unášajú zaťaženie kolmé na os otáčania, zatiaľ čo axiálne ložiská (obr. 2a) sú navrhnuté pre zaťaženie pôsobiace v smere osi. Existujú aj kombinované ložiská, ktoré dokážu uniesť oba typy zaťaženia, avšak ich správanie je zložitejšie a ťažšie predvídateľné [3].

Podľa tvaru valivých teliesok rozdeľujeme valivé ložiská na guľôčkové a valčekové. Guľôčkové ložiská sú charakteristické bodovým kontaktom medzi guľôčkami a ložiskovou dráhou. Valčekové ložiská vykazujú čiarový kontakt medzi valivými telieskami ako sú napríklad valčeky, ihly, kuželíky, súdky a materiálom ložiska. Prostredníctvom teliesok sa v ložiskách premieňa šmykové trenie na valenie. Ďalej sa valivé ložiská delia podľa počtu radov valivých teliesok na jednoradové, dvojradové a viacradové [1-3].

a) *b)*

Obr. 2 Ložisko: a) Axiálne jednoradové guľôčkové [4], b) Radiálne sférické klzné ložisko [5]
Figure 2. Bearing a) Axial single row ball bearing [4], b) Radial spherical sliding bearing [5]

Výhodou používania ložísk v zariadeniach je dlhšia trvanlivosť a spoľahlivosť výrobkov. V každodennom živote zohrávajú kľúčovú úlohu a práve kvôli ich dôležitosti je potrebné zabezpečiť ich odolnosť. Na výrobu vysoko odolných a trvanlivých ložísk je dôležitý výber vhodného materiálu. Ložiskové ocele sú známe najmä svojou spoľahlivosťou aj preto sú preferovaným typom materiálu na ich výrobu. Základné fyzikálne procesy pri vzájomnom relatívnom pohybe, problematika klzného a valivého trenia, opotrebovanie častí ložiskových uzlov a pod. sú predmetom skúmania samostatného vedného odboru – tribológie [1, 3].

2. CHARAKTERISTIKA LOŽISKOVÝCH OCELÍ

Za výslednou akosťou ložiska stojí správna konštrukcia ložiska, presnosť rozmerov, povrch, akosť použitej ocele a jej tepelné spracovanie. Základnými predpokladmi pre vlastnosti ložiskových ocelí je napríklad tvrdosť matrice 61-65 HRC a vysoká medza klzu. Ďalšími sú vysoká medza únavy materiálu pri kontaktnom namáhaní, vysoká pevnosť v ťahu a húževnatosť. Matrica nesmie prekročiť dovolenú hranicu obsahu oxidických inklúzií a materiál nemôže mať vnútorné chyby ako pórovitosť a bubliny. Tieto dôležité nároky na ložiskové ocele sú zahrnuté v štyroch nasledovných požiadavkách: chemické zloženie ložiskovej ocele, mikročistota, mikroštruktúra a makroštruktúra [3, 6].

2.1 Požiadavky na chemické zloženie

Ložiskové ocele sú zaraďované medzi konštrukčné ocele aj keď ich vlastnosti a chemické zloženie zodpovedajú skupine nástrojových ocelí. Ocele pre valivé ložiská sú nadeutektoidné ocele a ich charakteristickým znakom je 1% obsah uhlíka. Jednotlivé ocele sa odlišujú percentuálnym podielom chrómu, ktorý zlepšuje prekaliteľnosť materiálu [6 - 7].

Ložisková oceľ, ktorá má menší podiel chrómu sa využíva na výrobu ložiskových teliesok ako sú napríklad guľôčky a valčeky. Na súčasti sa používajú aj cementačné a koróziivzodorné ocele. Využitie rýchlorezných ocelí na ložiskové telieska je pri ložiskách, ktoré pracujú pri zvýšených teplotách. Na krúžky ložísk sa používa oceľ s vyšším obsahom chrómu. Krúžky, ktoré majú väčšiu hrúbku steny a telieska s väčším rozmerom sú vyrábané z legovaných ocelí. Tieto ocele obsahujú okrem chrómu aj mangán, dôvodom je vyššia prekaliteľnosť. Chemické zloženie je obsahom Tab.1 [6 - 8].

Tab. 1 Chemické zloženie vybraných ocelí [6]
Table 1. Chemical composition of selected steels [6]

Značka	Chemické zloženie [%]					
	≤ C	≤ Mn	≤ Si	Cr	Mo	Iné
14109	1,1	0,5	0,35	1,30-1,65	-	Cu ≤ 0,25; (Ni+Cu)≤ 0,50
14209	1,1	1,2	0,65	1,30-1,65	-	Cu ≤ 0,25; (N+Cu)≤ 0,51
80MoCrV4016	0,85	0,35	0,25	3,75-4,25	4,00-4,50	V(0,90-1,10)
100Cr6	1,1	0,45	0,35	1,35-1,65	-	-
100CrMo7	1,05	0,45	0,4	1,65-1,95	0,20-0,40	-
100CrMnMo7	1,05	0,9	0,4	1,60-1,95	0,20-0,40	-
X75WCrV1841	0,8	0,4	0,4	3,75-4,50	≤0,6	V (1,00-1,25); W (17,5-19,0)
X80WMoCrV654	0,88	0,4	0,4	3,80-4,50	4,70-5,20	V (1,70-2,00); W (6,00-6,70)

2.2 Požiadavky na mikročistotu

Mikročistota je považovaná za najdôležitejšiu vlastnosť ložiskovej ocele. Je to spôsobené trvanlivosťou - tú určuje počet, typ, tvar a veľkosť a fyzikálne vlastnosti inklúzií. Nekovové inklúzie, ktorých súčiniteľ tepelnej rozťažnosti je nižší ako súčiniteľ tepelnej rozťažnosti kovovej matrice, sú matricou stláčané pri kalení materiálu. Tým sa v materiáli vytvárajú vnútorné napätia, preto sa nekovové inklúzie, ktoré sú na funkčných ložiskových plochách alebo v ich blízkosti, stávajú zárodkami poškodenia. Takéto porušenie sa považuje za kontaktnú únavu spôsobenú

koncentrátormi kontaktného napätia. So zvyšujúcim sa počtom zaťažení dochádza na kontaktných plochách k pittingovému (jamkovitému) poškodeniu (obr. 3). Pitting je odlupovanie ocele na kontaktných vrstvách, ktoré končí zničením ložiska [3, 6, 9].

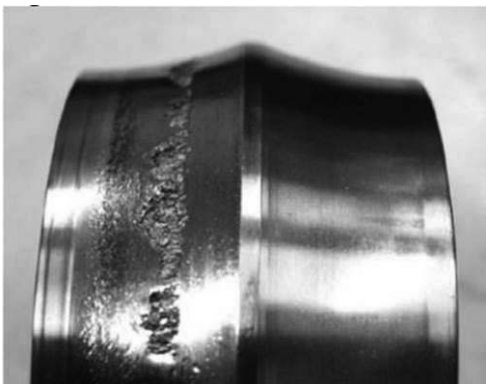

Obr. 3 Pitting, jamkové poškodenie ložiska [9]
Figure 3 Pitting in bearing [9]

Nekovové inlúzie delíme na exogénne a endogénne. Exogénne inklúzie sa do materiálu vnášajú počas tavenia či odlievania, napríklad z výmurovky pece. Aby sa tento problém zredukoval, obvykle sa vyrábajú v elektrických oblúkových peciach. Popri bežných výrobných metódach sa používa aj výroba, ako je pretavovanie trosky. Endogénne inklúzie sú produktom chemických reakcií, ktoré prebiehajú počas tavenia a odlievania - napr. deoxidácia, desulfurizácia, atď. Sú to teda oxidy a globulárne inklúzie - hlinitany, kremičitany a sulfidy [3, 6].

Obsah nekovových inklúzií sa hodnotí v súlade s normou ISO 683-17, kde sa porovnávajú vyleštené a neleptané vzorky s etalónmi. Táto norma posudzuje veľkosť, množstvo a tvar inklúzií [6]. Maximálny stupeň závisí od prierezu a je pre vybrané inklúzie uvedený v Tab. 2.

Tab. 2 Nekovové inklúzie podľa ISO 683-17 [6]
Table 2. Non-metallic inclusions according to ISO 683-17 [6]

Inklúzie	Vyrábané priemery			
	ϕ 17 - 35 mm	ϕ 36 - 70 mm	ϕ 71 - 100 mm	ϕ 101 - 140mm
Oxidy a sulfidy	K3 ≤7	K4≤6	K4≤7	K4≤8
Oxidy	K3 ≤3	K4≤2	K4≤3	K4≤3
TiC alebo TiCNi	K2≤1	K2≤1	K2 ≤ 1	K2≤1

Nekovové inklúzie majú vplyv na obrábateľnosť ocelí. Globulárne inklúzie sú tvrdé a krehké a tým zhoršujú obrábateľnosť a otupujú nástroje. Pri brúsení a superfinišovaní - dokončovacích operáciach sa vydroľujú, vytrhnú sa zo základnej hmoty a vytvárajú povrchové chyby na dotykových plochách. Ďalším negatívnym vplyvom je, že pri tvárnení sa nekovové inklúzie zhromažďujú pri hraniciach pôvodných zŕn austenitu. Typickým príkladom je FeS alebo eutektikum Fe-FeS, ktorý má nízky bod topenia a spôsobuje lámavosť materiálu v oblasti tvárniacich teplôt. Pridaním mangánu sa redukuje vznik FeS a tým sú inklúzie tvárnejšie a plastickejšie. Sulfidy a poloplastické kremičitany sú inklúzie, ktoré sú tvárne. Pri väčšom stupni

tvárnenia majú tvar pretiahnutý v smere tvárnenia. Majú vplyv na mechanické vlastnosti a spôsobujú pokles ťažnosti v materiáli.

Trvanlivosť ložiskových ocelí je daná mikročistotou a počtom cyklov zaťažovania do vzniku únavy materiálu, ktoré sa prejavujú vydrolením. Najväčší negatívny vplyv na trvanlivosť majú hlinitany. Hlinitany sú tvrdé, nedeformovateľné inklúzie s ostrými hranami a vydroľujú sa do riadkov. Ako menej škodlivé inklúzie sa prejavujú kremičitany, ktoré sú poloplastické až plastické. Nekovové inklúzie s najmenším vplyvom na ložiskovú oceľ sú sulfidy [6]. Typ inklúzií a ich jednotlivé tvrdosti sú uvedené v Tab. 3.

Tab. 3 Typ inklúzií a ich tvrdosť [3]
Table 3. The type of inclusions and their hardness [3]

Typ inklúzií	Zlúčeniny	Tvrdosť HV
oxidy	FeO	430
	Fe_2O_3	1275
kremičitany	CaO.Al2O3.5SiO2	860-880
	2FeO.SiO2	860-880
	$MnO.SiO_2$	950
hlinitany	Al2O3	2000-4500
	Cr_2O_3	1500-1700
sulfidy	FeS	160-240
	MnS	190

2.3 Požiadavky na makroštruktúru

Makroštruktúra ložiskových ocelí sa hodnotí podľa dvoch ukazovateľov. Prvým je tzv. hutnosť ocele, ktorá má vplyv na obsah pórov a hromadenie inklúzií. Hutnosť ložiskových ocelí sa dosahuje veľkým stupňom pretvárnenia. Zvyšuje sa tým medza únavy a odolnosť voči kontaktnej únave. Vlákna a ich smer, ktoré vznikli tvárnením nerovnovnorodých dendritov a nekovových inklúzií sú druhým ukazovateľom akosti ložiskových ocelí. Makroštruktúra má zásadný vplyv na trvanlivosť ložísk a dosahuje sa použitím akostného východiskového materiálu v kombinácii s vysokým stupňom pretvárnenia. Uhol, ktorý zvierajú vlákna s dotykovou plochou majú tiež významný vplyv na trvanlivosť [3, 6].

2.4 Požiadavky na mikroštruktúru

Nielen inklúzie, ale aj nerovnomerne rozložené karbidy ovplyvňujú kvalitu ložiska. Nerovnomernosť karbidov sa delí na riadkovitosť karbidov a karbidickú sieťku. Karbidická riadkovitosť sa delí na karbidické vycedeniny (obr. 4) a karbidickú pruhovitosť (obr. 5) a je spôsobená rôznou koncentráciou uhlíka v primárnej štruktúre ingotu [3, 6].

Počas tvorby dendritu sú medzidendritické pásy obohatené o segregačné prvky. Väčšie vycediny sú vo vnútri ingotu, tie sú tvorené sekundárnymi karbidmi a eutektickými karbidmi z taveniny. Pri valcovaní sú dendrity a medzidendritické pásma predĺžené v smere tvárnenia a tvar a veľkosť karbidických riadkov ovplyvňuje tepelné spracovanie ingotov. Oceľ, ktorá bola valcovaná zo žíhaných ingotov, má väčšiu karbidickú riadkovitosť v porovnaní s oceľou z nežíhaných ingotov valcovaných za rovnakých podmienok. V prípade kalenej ocele, ktorá bola

po austenitizácii ochladená nižšou teplotou ochladzovania, sa na určitých miestach v oceli vytvára tzv. sekundárna riadkovitosť [3].

Karbidická riadkovitosť spôsobuje pri obrábaní problémy a počas kalenia dochádza k zvýšeným objemovým zmenám súčiastky. Zvyškový obsah austenitu po kalení je v okolí karbidickej riadkovitosti. V dôsledku karbidov sa vytvárajú vlasové trhliny, a teda mikroštruktúra ložiskovej ocele bezprostredne ovplyvňuje ložiskovú akosť. Počas rýchleho ochladzovania po tvárnení v blízkosti karbidových riadkov, najčastejšie pozdĺž hraníc zŕn, sa vylučujú ďalšie karbidy. Tým sa vytvára karbidická sieť, ktorá sa považuje za najčastejšiu vadu ložiskových ocelí. Tieto karbidy nepriaznivo ovplyvňujú dynamickú únosnosť a vrubovú húževnatosť. Najobvyklejším miestom lomu sú totiž práve zaťažené hranice zŕn. Vznik tzv. karbidickej sieťky (obr. 6) je spôsobený zlou technologickým postupom tavenia, odlievania, kryštalizácie a tvárnenia ocele [3, 8].

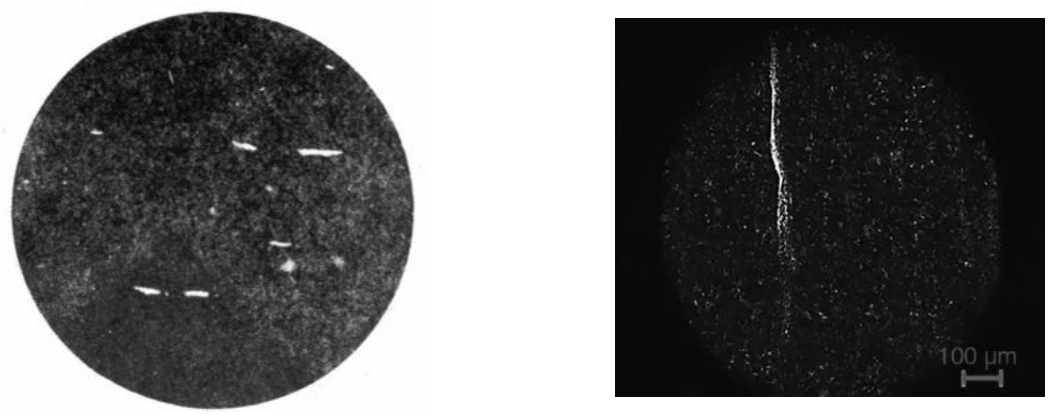

a) *b)*

Obr. 4 Karbidická riadkovitosť - karbidické vycedeniny (a) etalón [6], b) oceľ 100Cr6
Figure 4. Carbide liquation - carbide precipitates, a) norm[6], b) steel 100Cr6

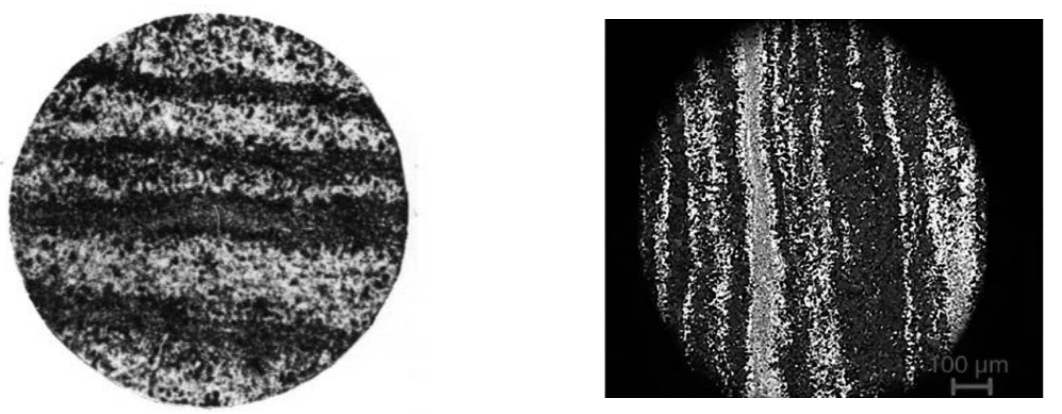

a) *b)*

Obr. 5 Karbidická riadkovitosť - karbidická pruhovitosť, a) etalón [6],b) oceľ 100Cr6
Figure 5. Carbide liquation - carbide banding, a) norm [6], (b) steel 100Cr6

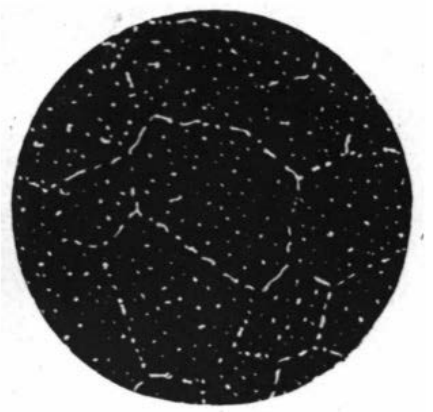

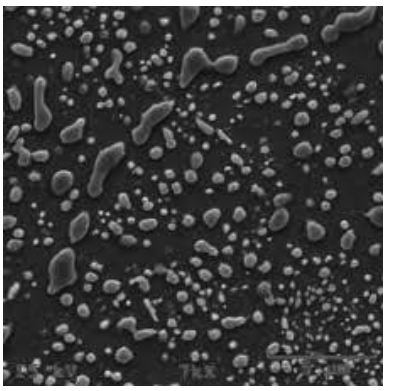

a) *b)*

Obr. 6 Karbidická sieťka, a) norma, b) oceľ 100 Cr6
Figure 6. Carbide net, a) norm [6], b) steel 100 Cr6

Rovnako sa hodnotí aj štruktúra po žíhaní na mäkko (obr. 7). Najlepšia štruktúra po tomto žíhaní je jemný globulárny perlit s rovnomerne rozloženými a rovnako veľkými globulárnymi karbidmi. Ak je v oceli lamelárny perlit, tak je oceľ menej obrobiteľná. Taktiež je zvýšená náchylnosť na vznik trhlín po kalení v materiáli a zúži sa rozsah kaliacich teplôt. Štruktúrna a objemová nestálosť ložísk je spôsobená zvyškovým austenitom po kalení. Vznik austenitu je daný prítomnosťou lamelárneho perlitu v štruktúre po žíhaní na mäkko. Rovnako aj dynamické skúšky na únavu materiálu vykazujú nižšie hodnoty, ak bol v štruktúre pred kalením lamelárny perlit. V žíhacej štruktúre sa nesmú vyskytovať zhluky jemných globulárnych karbidov, keďže pri austenitizácii sa ľahko rozpúšťajú a spôsobujú lokálne zvýšenie koncentrácie uhlíka v austenite. Takáto štruktúra po kalení vykazuje vlastnosti podobné lamelárnemu perlitu. Štruktúra po žíhaní na mäkko je hodnotená normou ISO 683-17 etalónmi pri zväčšení 500x a maximálny stupeň je 5 [6].

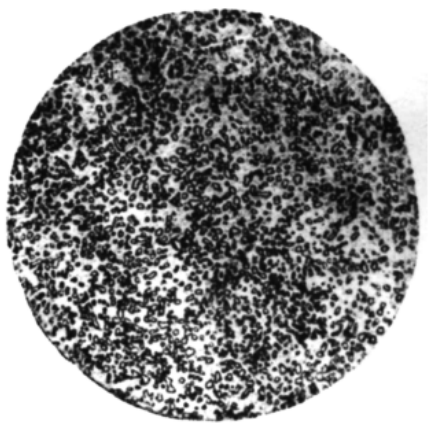

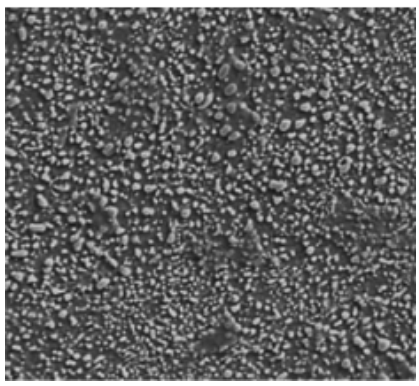

a) *b)*

Obr. 7 štruktúra po žíhaní na mäkko, a) norma [6], b) oceľ 100 Cr6
Figure 7. Microstructure after spheroidization annealing, a) norm [6], b) steel 100 Cr6

POĎAKOVANIE

Príspevok vznikol v rámci riešenia spoločného slovensko-poľského projektu Project Based Learning ako výsledok spolupráce medzi Politechnikou Slaskou, Gliwice a Žilinskou univerzitou v Žiline a projektov KEGA č. 004ŽU-4/2023 a KEGA č.009ŽU-4/2023.

BIBLIOGRAPHY

1. Bronček J., et. al, Konštruovanie 1 , Žilina : EDIS, 2015, ISBN 978-80-554-1177-4
2. Mateza, Jaké existují druhy ložisek a jaký je mezi nimi rozdíl?, [online] https://www.mateza.cz/technicke-poradenstvi/aktuality-strojirenstvi-loziska/85-jake-existuji-druhy-lozisek-a-jaky-je-mezi-nimi-rozdil, 2022
3. Kuchariková L., et al, Kontrola kvality materiálov, Žilina: EDIS,2021, ISBN 978-80-554-1782-0
4. Valivé ložiská P&M, Axiálne jednosmerné guľkové ložiská- Ložisko 51200, [online] https://loziskaeshop.sk/loziska/axialne-loziska/axialne-jednosmerne-gulkove-loziska/lozisko-51200-.html
5. Fruugo, Radiálne sférické klzné ložisko [online] https://www.fruugo.sk/ina-ge180uk2rs-radialne-sfericke-klzne-lozisko-180x260x105mm/p-48860921-97052868
6. Konečná K., et al, Materiály II, Žilina: EDIS,2020, 978-80-554-1708-0
7. Skočovský P., et al, Náuka o Materiáli, Žilina: EDIS, 2014, 978-80-554-0871-2
8. Katedra materiálového inžinierstva, Hodnotenie mikroštruktúry ložiskových ocelí, [online] http://kmi2.uniza.sk/wp-content/uploads/2010/12/kvalita5-loziskove-ocele-podklad.pdf
9. Chemtronics, CircuitWorks Silver Conductive Grease Maximizes Performance & Service Life of Roller Bearings, [online] https://www.chemtronics.com/circuitworks-silver-conductive-grease-maximizes-performance-service-life-of-roller-bearings

TalentDetector
31th January 2025
Gliwice, Poland
DEPARTMENT OF ENGINEERING MATERIALS AND BIOMATERIALS
FACULTY OF MECHANICAL ENGINEERING
SILESIAN UNIVERSITY OF TECHNOLOGY
INTERNATIONAL STUDENTS SCIENTIFIC CONFERENCE

Computer simulation of marine propeller loading

Jakub Polis[a], Jakub Bicz[a], Radosław Trojnar[a], Zuzanna Buchaj[b], Agata Śliwa[c], Marek Sroka[c]

[a] Student of Silesian University of Technology, Faculty of Mechanical Engineering
email: jakupol064@student.polsl.pl; jakubic839@student.polsl.pl; radotro676@student.polsl.pl
[b] Student of Silesian University of Technology, Faculty of Biomedical Engineering
email: zb301191@student.polsl.pl
[c] Silesian University of Technology, Faculty of Mechanical Engineering, Department of Engineering Materials and Biomaterials
email: agata.sliwa@polsl.pl

Abstract: This paper presents an FEM analysis of the distribution of stresses, displacements and deformations resulting from a specific force on a marine propeller. The analysis was carried out using SOLIDWORKS software. The areas of highest stress and displacement were determined, as well as the value of the critical force at which deformation of the component occurs.

Keywords: FEA analysis, stresses, deformations, displacements, marine propeller.

1. INTRODUCTION

The propeller is one of the key components of the ship propulsion system, substantially influencing its overall performance, efficiency and manoeuvrability. A variety of the propeller types and sizes are being used, depending on an application in specific water crafts. In case of the merchant vessels, four-bladed propellers are predominantly used, although five- and six-bladed designs are also common. The higher propeller efficiency can be achieved for the lower number of blades, however then simultaneously smaller developed surface area makes the propeller more susceptible to cavitation erosion. Concurrently, the important consideration, which must be accounted during propeller design is to minimize the propeller-induced vibrations and to avoid the superimposing of the hull, superstructure and machinery vibration frequencies. The fixed pitch (FP) and controllable pitch (CP) propellers can be distinguished, depending on the possibility of changing the blades angle of attack. The CP type propellers offer better adaptability to the changing operating conditions, allowing also to fine thrust control contributing to better manoeuvrability [1-3].
The marine propeller operates in the nonuniform flow field, connected with the wake field induced by the ship propelled – and consequently, is subjected to unsteady loadings. Furthermore, another important issue related to the propeller exploitation is the occurrence of cavitation. This phenomenon is related to the nucleation and growth of a vapor bubbles

(cavities) when the pressure of the fluid is locally decreased below its vapor pressure at that temperature. However, as the seawater contains impurities and gasses dissolved – providing the suitable nuclei, the formation of cavities may occur even above the vapor pressure at the corresponding temperature. As the pressure increases back, these bubbles collapse rapidly, within the time shorter than milliseconds. In case of the marine propellers, widely encountered type of cavitation include the so-called sheet cavitation, occurring at the propeller blade leading edges and the bubble cavitation at the mid-chord region of the blade [1,4,5].

The cavitation adversely affects the propeller performance, and will lead to vibration, noise and propeller blade erosion. The implosion of bubbles at the vicinity of the propeller blade cause the generation of high velocity microjets, directed towards its surface. In effect, erosion damage occurs – involving initially the roughening of the surface, followed by the plastic deformation and subsequently material removal. The cavitation influences also the corrosion behaviour of the propeller material, through continuous removing of the passivation layer and formation of the anodic areas, therefore causing the galvanic coupling corrosion [1,3,4,6].

Materials used for the marine propellers should meet the requirements of high resistance to corrosion and erosion, as well as ability to withstand the hydrodynamic forces subjected. In some specific applications also the low magnetic permeability is required. The most widely employed propeller materials include high tensile brasses and multicomponent aluminium bronzes, such as nickel-aluminium and manganese-aluminium bronzes. The high tensile brasses are basically the copper-zinc alloys, containing about 40% Zn, with dual-phase microstructure consisting of face-centred cubic solid solution and strengthening β′ phase. Although the high tensile brasses exhibit good resistance to corrosion, in saline solutions the dezincification can occur, leading to decrease of strength properties. In turn, the nickel-aluminium bronzes characterize with more advantageous properties, in terms of resistance to corrosion fatigue and cavitation erosion. Their composition involve 9-10% of aluminium and about 5% of nickel and iron, resulting in the dual-phase microstructure, comprised of α-phase as a matrix, with the dispersed globular precipitates of κ-phase, contributing to the advantageous mechanical properties [1,3,7]

2. MATERIALS AND METHODOLOGY

The component analysed is a four-blade fixed pitch propeller, made of the CuAl10Ni5Fe4 alloy, subjected to specific pressure values. The results obtained will be used to verify that the analysed material will meet the strength requirements and thus be suitable for use in the construction of a marine propeller. The properties of the material selected make it promising in terms of this particular application. The CuAl10Ni5Fe4 aluminium-nickel-iron bronze characterize with high strength, corrosion and erosion resistance, and can be subjected to cold working. Its applications include machine components such as shafts, bushings and worm gears [8]. The chemical composition of the selected alloy was shown in Table 1, whereas its selected properties were summarized in the Table 2.

Table 1. Chemical composition of CuAl10Ni5Fe4 alloy (accor. to the EN1652/EN12164) [8]

Element	Cu	Al	Ni	Fe	Mn	Zn	S	Sn	Pb	Others
Concen-tration	Balance*	8.5-11	4-6	3-5	≤1	≤0.4	≤0.2	≤0.1	≤0.05	≤0.2

* The percentage of copper is determined by difference and does not need to be determined or certified.

Table 2. Selected mechanical and physical properties of the CuAl10Ni5Fe4 alloy [8-10]

Specific mass [kg/m^3]	8850
Elastic modulus [N/m^2]	$1.2*10^{11}$-$1.4*10^{11}$
Ultimate tensile strenght [N/m^2]	$3.9*10^8$-$6.4*10^8$
Elongation [%]	20-10
Hardness [HV]	120-150
Thermal expansion coefficient [K]	$17.9*10^{-6}$
Thermal conduction coefficient [W/(m*K)]	95-105
Conductivity [MS/m]	12-14
Melting temperature [K]	1193-1253

3. CAD GEOMETRIC MODEL

A model of the was made using SOLIDWORKS to carry out strength analysis by means of computer simulation. The designed model is shown in Figure 1a.

4. BOUNDARY CONDITIONS

The following boundary conditions were adopted in the computer simulation:

- A finite element mesh was superimposed on the propeller model (Figure 1b),
- Five different pressures were applied to the model: 2 kPa, 2.5 kPa, 3 kPa, 3.5 kPa and 4 kPa,
- The pressure areas and immobilization geometry of the model are shown in Figure 1c.

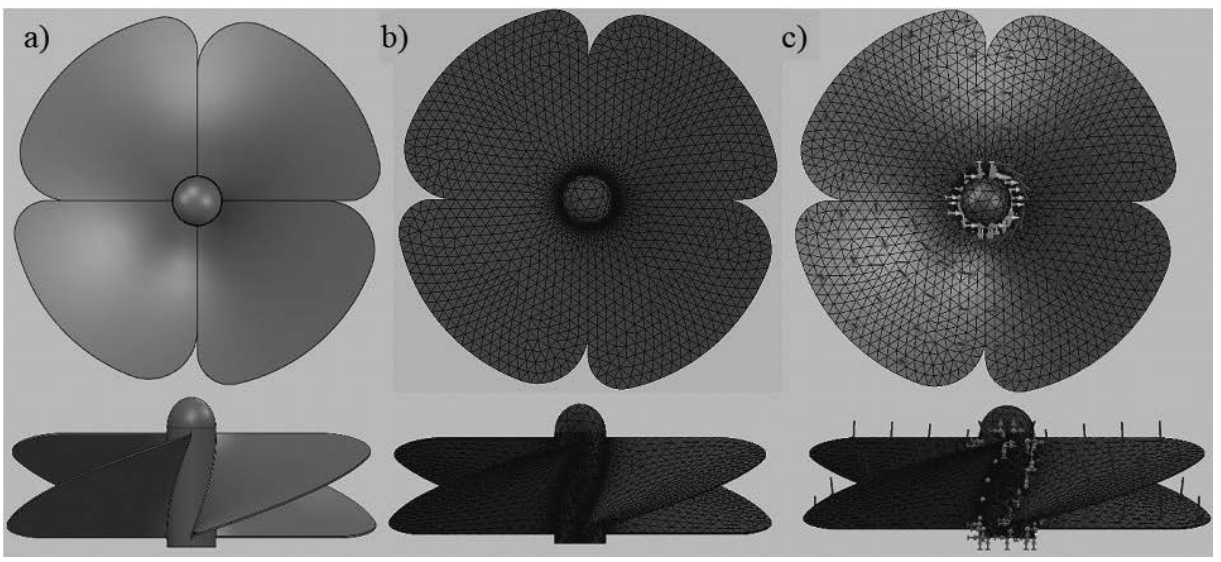

Figure 1. CAD model of marine propeller (a); with finite element mesh superimposed (b); with finite element mesh superimposed, force direction visible and geometry immobilized (c)

ANALYSIS OF RESULTS

Firstly, the numerical stress analysis was performed based on the Huber-Mises hypothesis. After loading the component, stress diagrams were obtained, the values of which are expressed in MPa (Figures 2a-6a). The highest stresses can be observed at the blade roots. The purpose of the subsequent computer simulation carried out was to determine the magnitude of the displacement under the application of a given force and to generate the displacement diagrams of the structure (Figures 2b-6b). It can be concluded, that the blade tips were subjected to largest displacements. The last simulation carried out was to determine the critical force causing the deformation. Diagrams obtained show the equivalent deformation represented by the largest force required to deform the axis (Figures 2c-6c). As it can be seen, the largest deformations occurred in the blade root area.

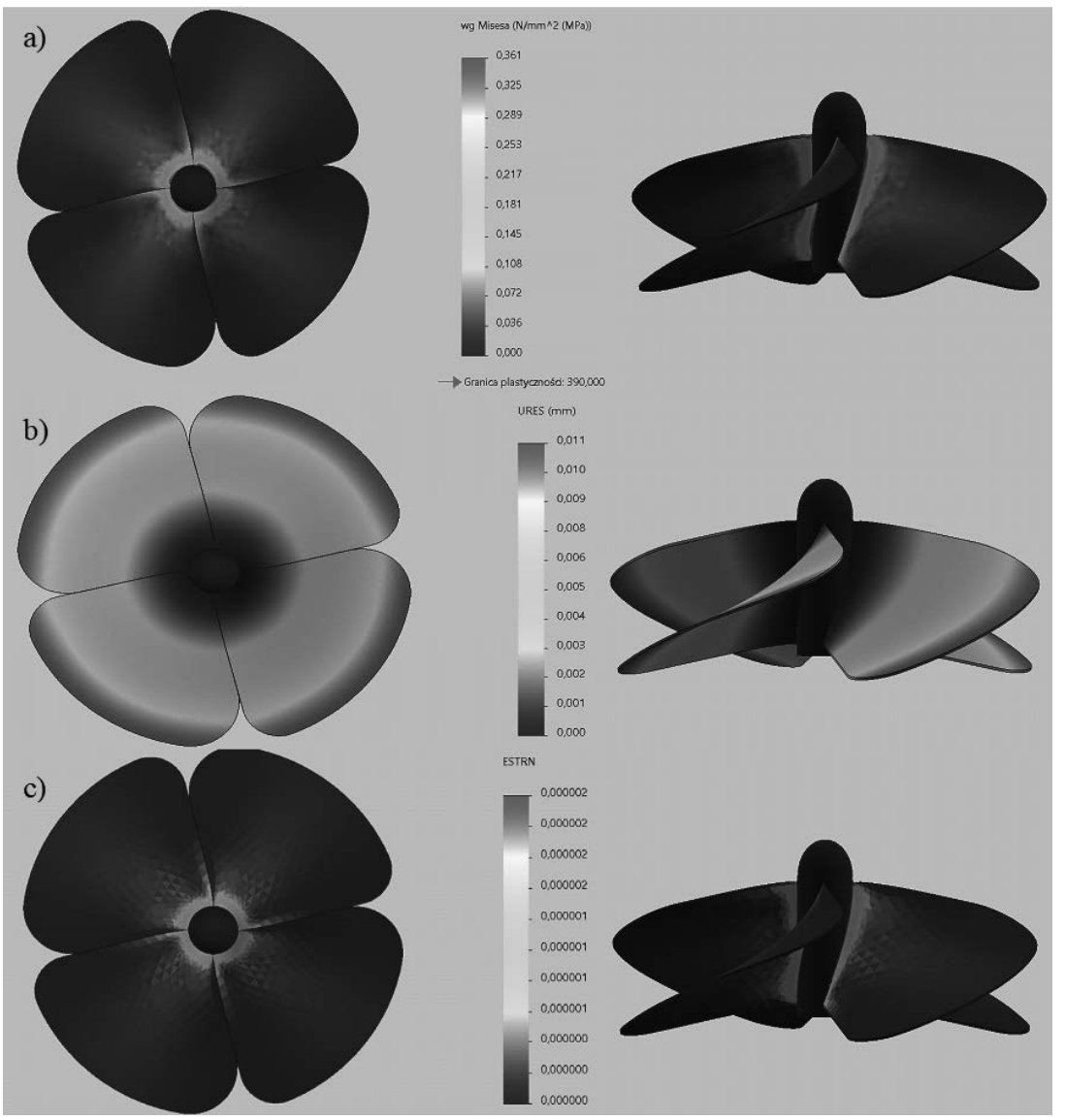

Figure 2. Huber-Mises reduced stress distribution (a), displacement distribution and equivalent deformation (c) for application of 2 kPa pressure

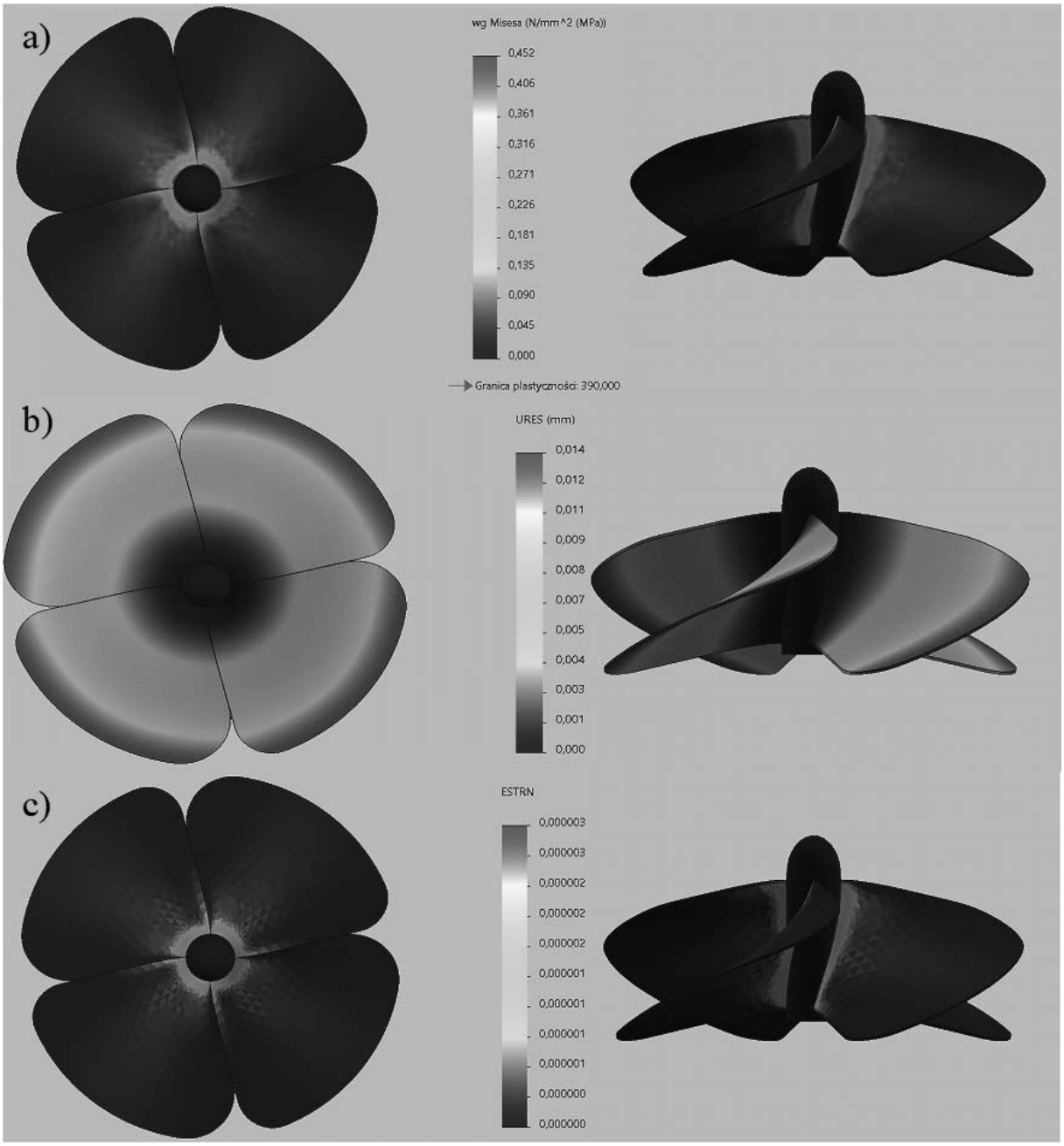

Figure 2. Huber-Mises reduced stress distribution (a), displacement distribution and equivalent deformation (c) for application of 2.5 kPa pressure

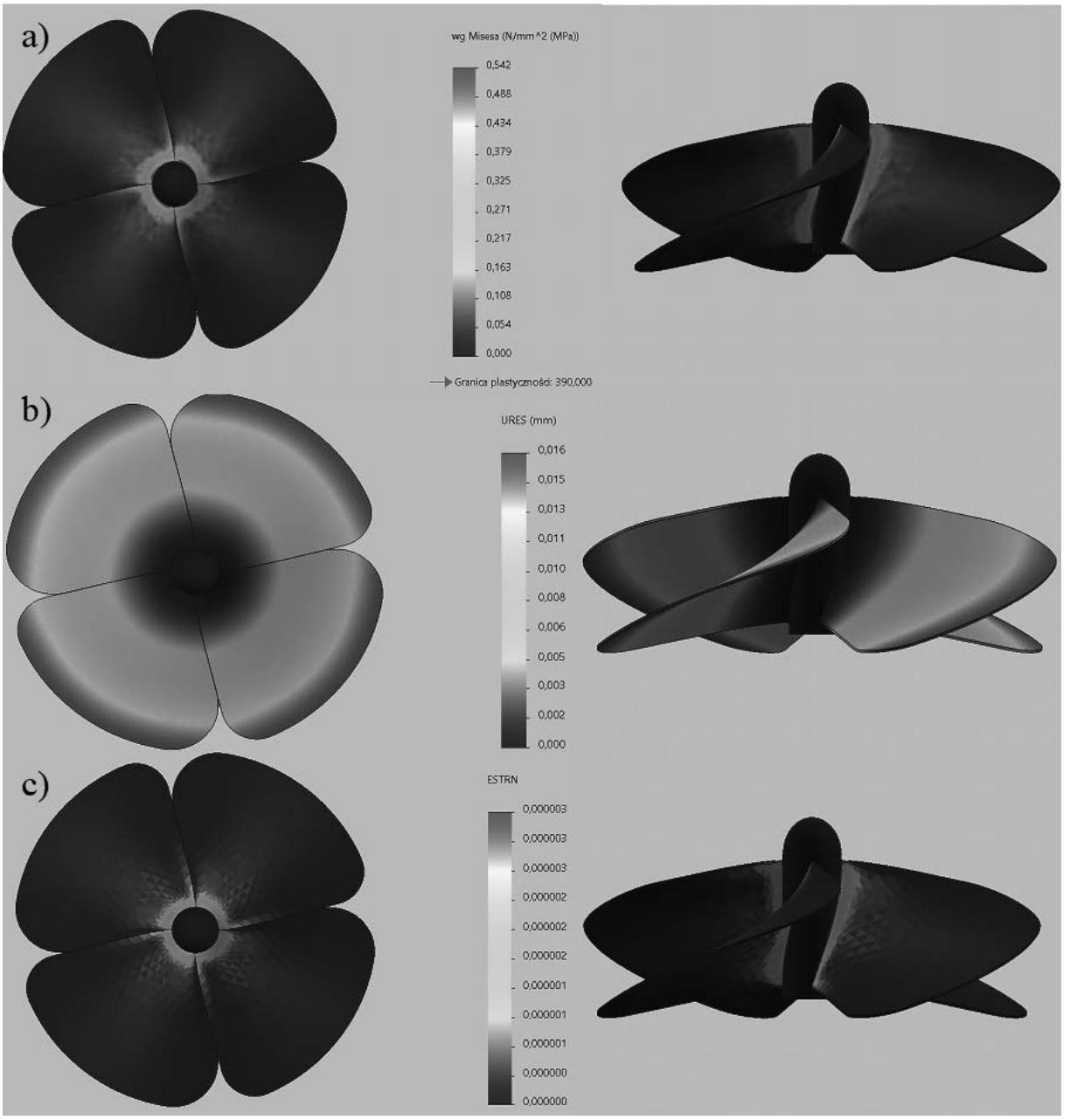

Figure 2. Huber-Mises reduced stress distribution (a), displacement distribution and equivalent deformation (c) for application of 3 kPa pressure

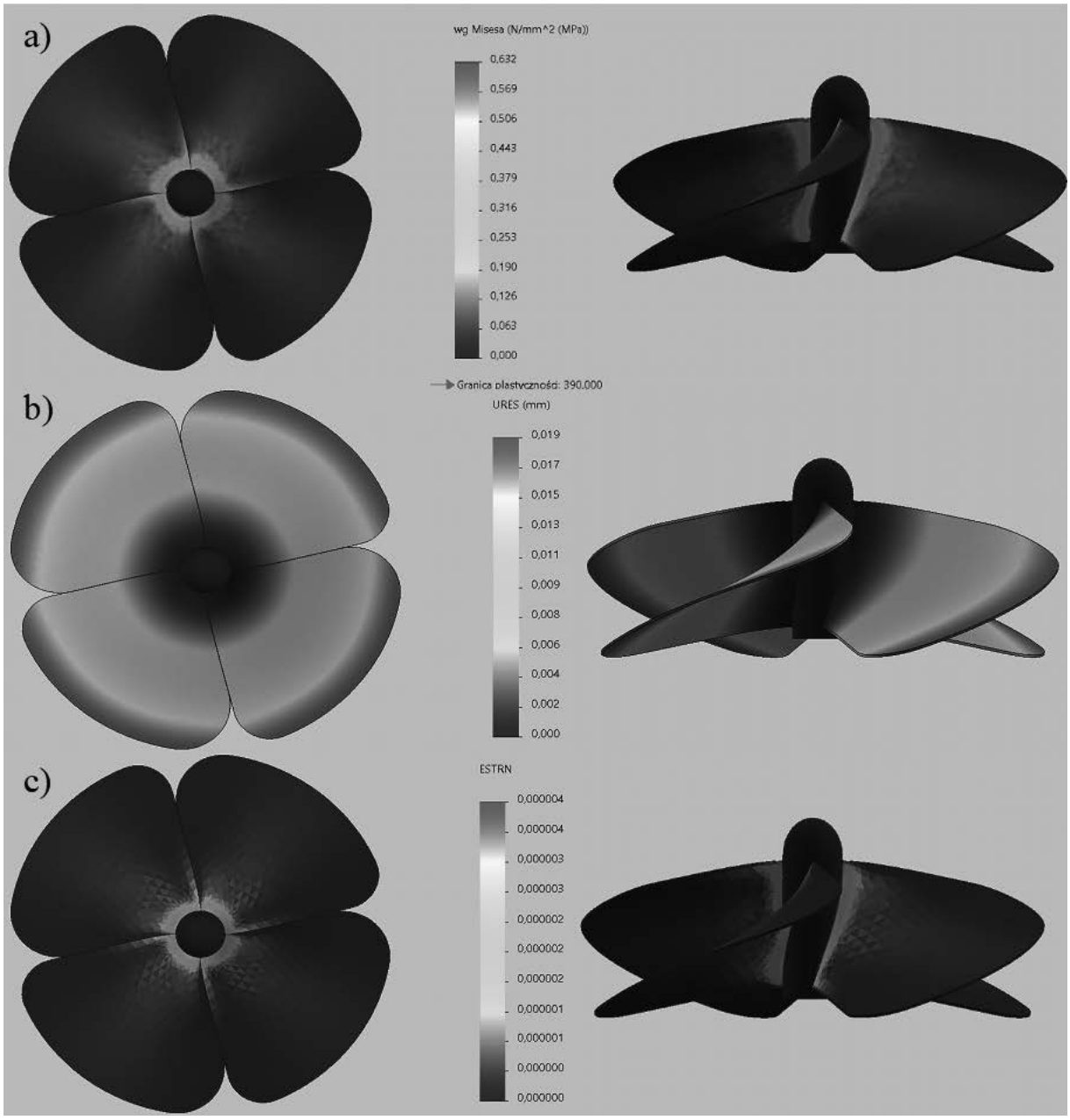

Figure 2. Huber-Mises reduced stress distribution (a), displacement distribution and equivalent deformation (c) for application of 3.5 kPa pressure

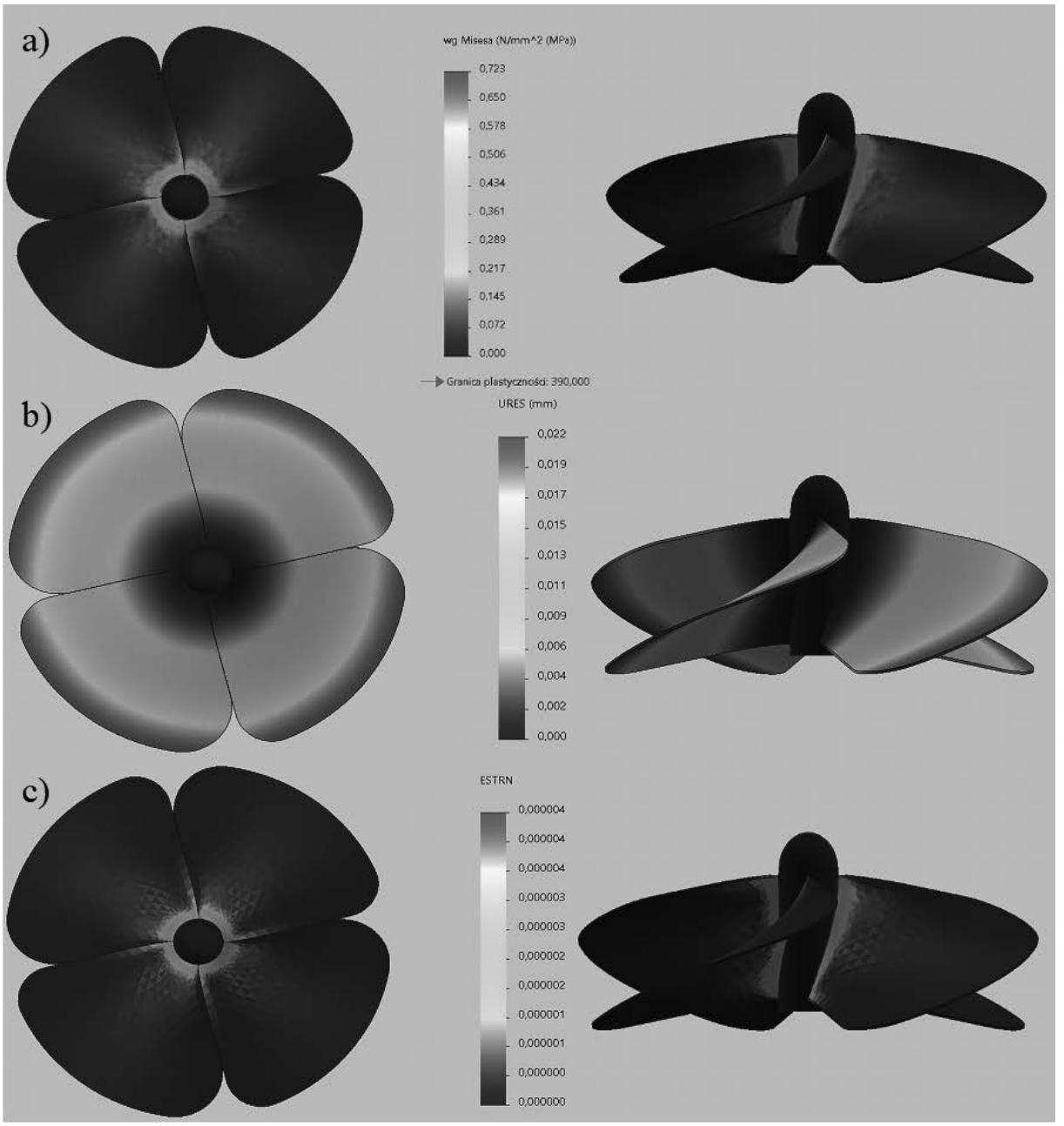

Figure 2. Huber-Mises reduced stress distribution (a), displacement distribution and equivalent deformation (c) for application of 4 kPa pressure

The overall results of the simulations performed are shown in Table 3.

Table 3. Summary of overall results from computer simulations carried out

Pressure applied [kPa]	Maximum stress value [MPa]	Maximum displa-cement value [mm]	Maximum deformation value
2	0.361	0.011	$2*10^{-6}$
2.5	0.452	0.014	$3*10^{-6}$
3	0.542	0.016	$3*10^{-6}$
3.5	0.632	0.019	$4*10^{-6}$
4	0.723	0.022	$4*10^{-6}$

5. CONCLUSIONS

In this study, the FEM analysis was employed to determine the distribution of stresses, displacement and deformation in the four-blade fixed pitch marine propeller, subjected to specific pressure values. The results allow to confirm the suitability of CuAl10Ni5Fe4 alloy as a marine propeller material, as the negligible displacement and deformation values were obtained and therefore the geometry of marine propeller was sustained. It can be also stated, that in the conditions assumed, the occurring deformations will not affect the propeller performance. The CuAl10Ni5Fe4 alloy shows a proportional response to the applied load, which is characteristic of materials with elastic properties in this load range.

The CuAl10Ni5Fe4 alloy is characterised by very good mechanical properties. The linear increase in stress, displacement and deformation with increasing pressure shows that the material operates in the elastic range and that the load values do not cause permanent deformation. This is important for a marine propeller, which is subjected to dynamic and varying loads during operation.

The maximum stress values obtained (up to 0.723 MPa) are low compared to the typical yield strength of CuAl10Ni5Fe4 alloy (approximately 240-260 MPa for this material). This indicates that in the pressure range tested, the structure is safe and has a large reserve of strength.

The minimum values of displacement (0.011-0.022 mm) and deformation ($2*10^{-6}$-$4*10^{-6}$) attest to the material's high stiffness and its ability to maintain its geometry under load. For a marine propeller, this is very beneficial, as even small changes in shape could affect the performance and efficiency of the propeller in water.

BIBLIOGRAPHY

1. J.S. Carlton, Marine Propellers and Propulsion (Second Edition), Butterworth-Heinemann, 2007.
2. Basic principles of ship propulsion – technical report, MAN Energy Solutions, 2018.
3. W. Jurczak, J. Schmidt, Badanie współczesnych materiałów przeznaczonych na pędniki okrętowe, Zeszyty naukowe Akademii Marynarki Wojennej Nr 2 (177), 2009.
4. V. Bertram, Propellers. Practical Ship Hydrodynamics, 2012, p.41-72.
5. A. Konno, H. Yamaguchi, H. Kato, M. Maeda, On the Collapsing Behavior of Cavitation Bubble Clusters, JSME International Journal Series B 45(3), 2002, p.1-8.
6. L. Wang, C. Guo, Y. Su, P. Xu, T. Wu, Numerical analysis of a propeller during heave motion in cavitating flow, Applied Ocean Research Vol. 66, 2017, p. 131-145.
7. C. Powell, P. Webster, Copper alloys for marine environments, CDA publication 206, 2011, p.1-28.
8. https://emetal.eu/braz/braz-ISO_-CuAl10Ni5Fe4-EN_-CW307G-DIN_-CuAl10Ni5Fe4-wnr_-2.0966-PN_-BA1054/ – access date: 20.12.2024 r.
9. https://neometal.pl/BA1054-CuAl10Ni5Fe4-CW307G-2.0966 – access date: 21.12.2024 r.
10. https://www.ampcometal.com/documents/CuAl10Ni5Fe_Ex_PL.pdf – access date: 21.12.2024 r.

TalentDetector

31th January 2025
Gliwice, Poland

DEPARTMENT OF ENGINEERING MATERIALS AND BIOMATERIALS
FACULTY OF MECHANICAL ENGINEERING
SILESIAN UNIVERSITY OF TECHNOLOGY

INTERNATIONAL STUDENTS SCIENTIFIC CONFERENCE

Computer simulation of dental implant loading

Jakub Polis[a], Jakub Bicz[a], Radosław Trojnar[a], Zuzanna Buchaj[b], Dominik Śliwa[c], Agata Śliwa[d], Marek Sroka[d]

[a] Student of Silesian University of Technology, Faculty of Mechanical Engineering
email: jakupol064@student.polsl.pl; jakubic839@student.polsl.pl; radotro676@student.polsl.pl
[b] Student of Silesian University of Technology, Faculty of Biomedical Engineering
email: zb301191@student.polsl.pl
[c] Student of the School in the Cloud, Warsaw
email: lightprim@gmail.com
[d] Silesian University of Technology, Faculty of Mechanical Engineering, Department of Engineering Materials and Biomaterials
email: agata.sliwa@polsl.pl

Abstract: This paper presents an FEM analysis of the distribution of stresses, displacements and deformations resulting from a specific force on a dental implant depending on the material used, such as Ti-6Al-4V alloy, steel AISI 316, polietheretherketone (PEEK). The analysis was carried out using SOLIDWORKS software. The areas of highest stress and displacement were determined, as well as the value of the critical force at which deformation of the component occurs.

Keywords: dental implant, FEA analysis, stresses, deformations, displacements.

1. INTRODUCTION

The aim of dental prosthetics is to restore proper occluding relations, by reconstructing dentition lost in effect of illness or injury. One of the most effective methods of completion of dentition deficiencies is dental implantation. Implant system used for reconstruction of missing teeth consists of an implant corresponding the tooth root, a abutment – which is supporting the prosthetic crown, and the crown itself, recreating the outer part of the tooth. The dental implant is inserted directly into the mandible or maxilla bone of the patient. Properly integrated implant forms a kind of pillar for the prosthetic crown. It is also possible to place a prosthetic bridge on it, reproducing several teeth at the same time [1-3].

One of the key criteria for the selection of implant materials is their biocompatibility and appropriate mechanical properties – allowing to transfer the loads to which the implant is subjected, while reducing the risk of bone weakening around the implant. Therefore, the mechanical properties of the implant material should be as close as possible to those

of surrounding bone tissue. A significant difference in the value of Young's modulus between the implant material and the surrounding bone results in local relief of the bone – which is referred to as "stress shielding". According to Wolff's law, bone tissue that is deprived of stimulation undergoes partial resorption, which leads to loosening of the implant [4, 5].
The key factor influencing the long-term stability of the implant is the ability to osseointegration – to form a structural, functional connection between the implant and bone tissue. The osseointegration rate is affected by roughness and wettability of the implant surface. These should have hydrophilic properties, allowing the cells to adhere and thus the development of bone tissue. Also, higher surface roughness promotes osteoblasts adhesion, accelerating osseointegration [2, 4, 6].
Conditions prevailing in the oral cavity environment are highly aggressive for metallic materials. The values of pH and temperatures during can change significantly – during mastication values of pH in range between 2 and 11 can occur, with temperature approaching to even 70°C. Implants inserted in the oral cavity are subjected also to corrosive influence of saliva and various compounds being present in comestible products. Products of corrosion released to surrounding tissues can causing inflammatory complications, which lead to aseptic loosening and, in effect implant failure. Although most of metallic implant materials exhibits ability to passivation, passive layer can be breached in effect of loads subjected, increasing release of ions and generating debris. Consequently, in order to enhance corrosion resistance, biomaterials used for implants manufacturing are being subjected to various surface modifications. Concerns associated with risk of ion release and insufficient corrosion resistance, contributed also to development of non-metallic implant materials – such as zirconia and, more recently, polyetheretherketone [7-10].

2. MATERIALS AND METHODOLOGY

The component analysed is a complete implant system, composed of implant integrated with abutment and the dental crown connected with these. The application of three different implant materials are compared: Ti-6Al-4V alloy, AISI 316 stainless steel and polyetheretherketone (PEEK). Use of dental crown made of commercially pure titanium (cp-Ti) is assumed. The main consideration is that the implant should be able to carry a load comprised of 200 N in parallel and 150 N perpendicular direction without losing its integrity. In addition, the material used should be biologically safe for the patient.

3. MATERIALS SELECTION

Ti-6Al-4V alloy

Titanium alloys are widely used in dental prosthetics, because of their biocompatibility, corrosion resistance and high specific strength. In manufacturing of dental implants, most commonly used material is the technically pure titanium – referred as cp-Ti (commercially pure titanium) and alloys with $\alpha + \beta$ structure, such as Ti-6Al-4V. Titanium alloys are also used, among others, for manufacturing of dental crowns, bridges and clasps. A key feature, which contribute to widespread use of titanium and its alloys for the manufacturing of implants is their ability to osseointegration, unique as compared to other metallic biomaterials. Important advantage of titanium alloys is their good corrosion resistance in physiological fluids,

which derives from its ability to passivation. Passivation layer starts to form almost immediately after exposure to oxygen, reaching 1.5-5 nm of thickness [5,7,9].
In comparison with technically pure titanium, Ti-6Al-4V alloy exhibits lower Young modulus value, with simultaneously higher strength properties. However, significant drawback is risk of release to the human body aluminium and vanadium ions, which have toxic and carcinogenic properties. Consequently, the use of alloys based on utilization of more biocompatible alloying elements are considered – such as niobium, zirconium, tantala and molybdenum [6, 11].
In order to enhance its osseointegration ability titanium-based implants can be subjected to surface roughening. For this purpose, mechanical surface treatments such as grit blasting and plasma spraying can be used. Other group of surface modification include chemical treatments such as anodization or chemical etching. In case of anodization – realized by oxidation of titanium in strong acids, with high potential applied – microporous oxide layer with thickness up to 1000 nm can be obtained. Laser surface treatments are also considered – allowing to obtain a surface roughness in the nanometer scale, which influences osteoblastic cell attachment [2, 4, 6].

AISI 316 steel
Austenitic stainless steels were one of the first metallic materials used to manufacturing of implants. In stomatology, their applications include orthodontic wires, dental implants and temporary dental crowns. In this purpose, chromium-nickel steel grades are commonly used – including AISI 302, AISI 304 and AISI 316. Popularity of stainless steels in the field of dentistry arise from their availability, economic reasons, good mechanical properties and acceptable corrosion resistance in the environment prevailing in the oral cavity. For their corrosion resistance, contributes presence of chromium, in concentration higher than 13%. Due to its affinity to oxygen, at the surface of steel is being developed a chromium-rich passive layer, preventing steel from further oxidation. Nickel stabilize austenitic structure – steels containing minimum 8%, with simultaneously high content of chromium, characterize with presence of austenitic structure in the room temperature. In effect, these steels exhibits higher corrosion resistance, at the same time having better mechanical properties. Stainless steels shows relatively good biocompatibility, however, in long term perspective, due to gradual degradation of the implant in the harsh conditions prevailing in human body, release of ions from their surface can occur – which concur to adverse effects [9, 11-13].
AISI 316 steel applied in simulation is a austenitic corrosion-resistant chromium-nickel steel, widely used in biomedical applications. Due to addition of molybdenum, it exhibits higher resistance to pitting corrosion. Molybdenum, characterizing with great affinity to carbon, binds carbon contained in steel, thus preventing local depassivation of surface [11, 14].

Polyetheretherketone – PEEK
Polyetheretherketone (PEEK) is a semi-crystalline thermoplastic polymer from polyaryletherketones family. Polyaryletherketones (PAEKs) features with good mechanical properties and high temperature stability. Their monomers are comprised of alternately arranged ketone and ether functional groups. Their characteristic feature is also presence of aromatic rings. Family of polyaryletherketones includes a range of polymers differentiating with mutual ratio of functional groups and consequently properties – such as melting point and glass transition temperature [15, 16].

Table 1. Comparison of selected mechanical and physical properties of materials used in simulation

Material / Property	Ti-Al6-4V	AISI 316	PEEK
Elastic modulus [N/m^2]	$1.05*10^{11}$	$1.93*10^{11}$	$3.9*10^{9}$
Poisson's ratio	0.31	0.3	0.4
Shear stress ratio [N/m^2]	$4.10*10^{10}$	-	-
Specific mass [kg/m^3]	4428.78	8000	1310
Ultimate tensile strength [N/m^2]	$1.05*10^{9}$	$5.5*10^{8}$	$9.5*10^{7}$
Yield strength [N/m^2]	$8.27*10^{8}$	$1{,}38*10^{9}$	$7.5*10^{7}$
Thermal expansion coefficient [K]	$9*10^{-6}$	$1{,}6*10^{-5}$	-
Thermal conduction coefficient [W/(m*K)]	6.7	16.3	0.24
Specific heat [J/(kg*K)]	586.04	500	1850

Table 2. Comparison of chemical composition of Ti-6Al-4V alloy and AISI 316 steel [17, 18]

Material	Ti-6Al-4V		Material	AISI 316	
Element	Min [%]	Max [%]	Element	Min [%]	Max [%]
V	3.5	4.5	Cr	16.5	18.5
Al	5.5	6.75	Ni	10	13
Fe	-	0.3	Mo	2	2.5
O	-	0.2	Mn	-	2
C	-	0.08	Si	-	1
N	-	0.05	C	-	0.07
H	-	0.015	P	-	0.045
Y	-	0.005	S	-	0.015
Ti	Balance*		N	-	0.11

* The percentage of titanium is determined by difference and does not need to be determined or certified.

Factors contributing to use of PEEK in manufacturing of dental implant is their biocompatibility and advantageous mechanical properties – close to the bone tissue. Polyetheretherketone features relatively good fatigue strenght and low friction coefficient. Furthermore, exhibits resistance for most of organic solvents, acids and bases. Due to its resistance to high-pressure water vapor and very low water absorption PEEK can be subjected to sterilization. However, polyetheretherketone is a biologically inert material – its osseointegration is also inhibited by the hydrophobic properties of their surface.

Consequently, various methods of enhancing its bioactivity are considered – in example via surface modification, such as deposition of hydroxyapatite coatings with the use of magnetron sputtering. Other way to improve their osseointegration ability is to combine of PEEK with bioactive materials, thus creating a composite [4, 15, 16].

4. CAD GEOMETRIC MODEL

A model of the hip endoprosthesis was made using SOLIDWORKS to carry out strength analysis by means of computer simulation. The designed hip endoprosthesis model is shown in Figure 1a.

5. BOUNDARY CONDITIONS

The following boundary conditions were adopted in the computer simulation:

- A finite element mesh was superimposed on the modelled implant system (Figure 1b),
- A force of 200 N in parallel and 150 N in perpendicular direction was applied,
- The location of force application and immobilization geometry of the dental implant model are shown in Figure 1c.

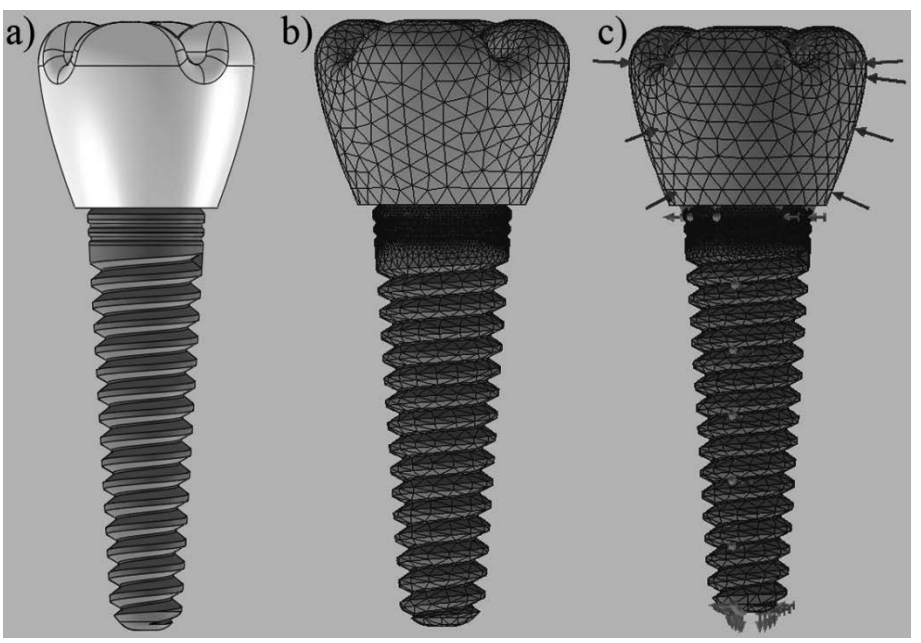

Figure 1. CAD model of analysed implant with dental crown (a); with superimposed finite element mesh (b); with superimposed finite element mesh, visible direction of forces and immobilised endoprosthesis geometry (c)

6. ANALYSIS OF RESULTS

6.1 Numerical stress analysis results

Numerical stress analysis was performed based on the Huber-Mises hypothesis. After loading the component, stress diagrams were obtained, the values of which are expressed in MPa. Figure 2 shows the distribution of stresses developed during the given loading.

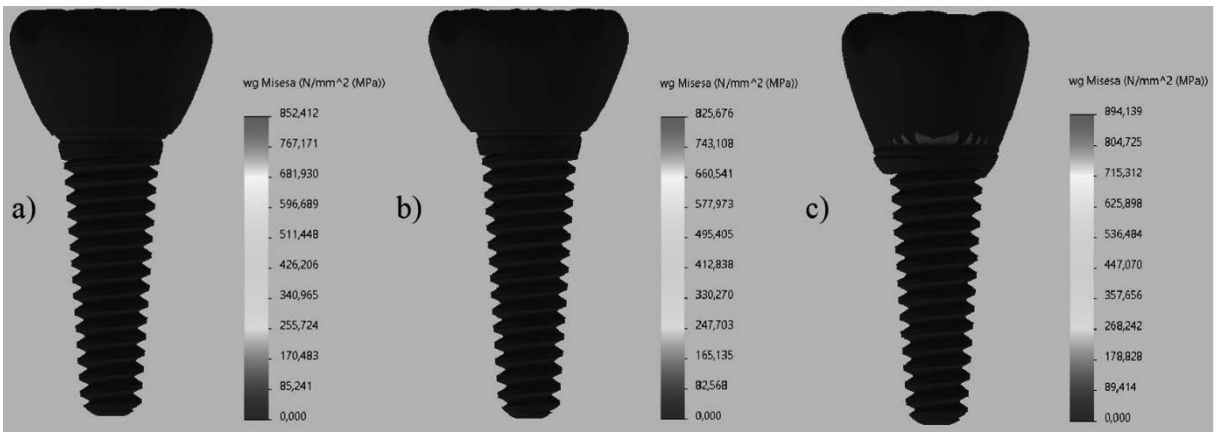

Figure 2. Huber-Mises reduced stress distribution for Ti-6Al-4V alloy (a), AISI 316 steel (b) and PEEK (c)

6.2 Numerical displacements analysis results

The purpose of the subsequent computer simulation carried out was to determine the magnitude of the displacement under the application of a given force and to generate the displacement diagrams of the structure, which are shown in Figure 3. As a result of the load, the geometric dimensions of our model can change.

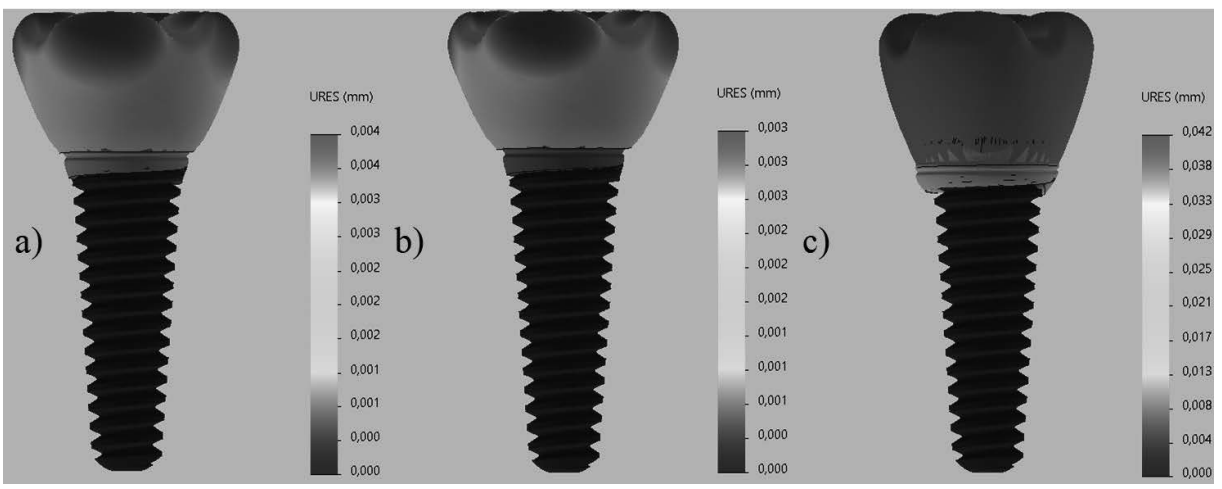

Figure 3. Displacement distributions for Ti-6Al-4V alloy (a) and AISI 316 steel (b) and PEEK (c)

6.3 Numerical equivalent deformation analysis results

The last simulation carried out was to determine the critical force causing the deformation. Figure 4 shows the equivalent deformation represented by the largest force required to deform the axis.

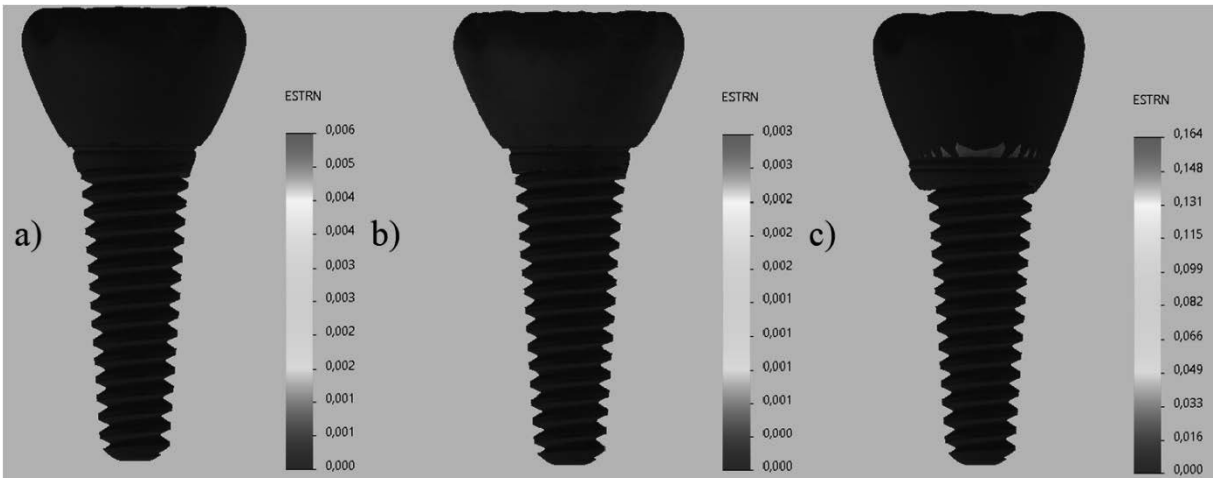

Figure 4. Equivalent deformation for Ti-6Al-4V alloy (a), AISI 316 steel (b) and PEEK (c)

The overall results of the simulations performed are shown in Table 3.

Table 3. Summary of overall results from computer simulations carried out

Material used	Maximum stress value [MPa]	Maximum displacement value [mm]	Maximum deformation value
Ti-6Al-4V alloy	852.412	0.004	0.006
AISI 316 steel	825.676	0.003	0.003
PEEK	894.139	0.042	0.164

7. CONCLUSIONS

The results of the conducted strength analysis indicate that both Ti-6Al-4V alloy and AISI 316 steel are suitable for use as a dental implant material. In case of using the polyetheretherketone as an implant material, under influence of load applied, significant deformation of material takes place, which results from the relatively low strength properties of polymeric materials. Strength properties of polyetheretherketone are even lower than these of cortical bone tissue – therefore, currently application of PEEK-based composites is being considered. Composite utilizing carbon fibers as a reinforcement allows to obtain elastic modulus value corresponding to these of cortical bone.

The highest stresses were obtained for the application of the polyetheretherketone – for the Ti-6Al-4V alloy and the AISI 316 steel these values were, respectively, over 40 MPa and nearly 70 MPa lower.

The largest displacements were obtained for the model made of PEEK – these value was one order of magnitude higher in comparison with these recorded for both metallic biomaterials.

In case of utilizing polyetheretherketone as an implant material, the largest deformation was also obtained – whereas for the AISI 316 steel deformation value was over fifty times lower. For Ti-6Al-4V alloy recorded value of deformation was slightly higher than for steel, but still over twenty-five times lower than in case of the polyetheretherketone.
Of the materials used in simulation, the steel AISI 316 can be considered as an optimal material for dental implant due to its satisfactory strength properties, resulting in the lowest values of displacement and deformation obtained for this material.

BIBLIOGRAPHY

1. A. Łagoda, Analiza wytrzymałościowa wybranych połączeń w protetyce stomatologicznej – Praca Doktorska, Wydział Mechaniczny Politechniki Opolskiej, Opole, 2019.
2. S. Najeeb, M. Mali, S. A. U. Yaqin, M. S. Zafar, Z. Khurshid, A. Alwadaani, J. P. Matinlinna, Dental implants materials and surface treatments, Advanced Dental Biomaterials, 2019, p. 581–598.
3. N. Jayakumar, G. Senthilkumar, S. Aravinda Samy, V. Karthick, T. Renganathan, Comparison of stress analysis for dental crown (FPD) for various materials, Materials Today: Proceedings, 45, 2021, p. 7939–7950.
4. Z. Khurshid, S. Hafeji, S. Tekin, S. R. Habib, R. Ullah, F. Sefat, M. S. Zafar, Titanium, zirconia, and polyetheretherketone (PEEK) as a dental implant material, Dental Implants, 2020, p. 5–35.
5. M. Kaur, K. Singh, Review on titanium and titanium based alloys as biomaterials for orthopaedic applications, Materials Science and Engineering C 102, 2019, p. 844-862.
6. Md Enamul Hoque, Nazmir-Nur Showva, Mansura Ahmed, Adib Bin Rashid, Sarder Elius Sadique, Tarek El-Bialy, Huaizhong Xu, Titanium and titanium alloys in dentistry: current trends, recent developments, and future prospects, Heliyon vol. 8 issue 11, 2022, e11300.
7. M. Walczak, Wpływ wybranych zabiegów technologicznych na trwałość użytkową układów metal-ceramika stosowanych w protetyce stomatologicznej – monografia, Politechnika Lubelska, Lublin 2014.
8. M. Özcan, C. Hämmerle, Titanium as a reconstruction and implant material in dentistry: advantages and pitfalls, Materials 5(9), 2012, p. 1528-1545.
9. M. Roach, Base metal alloys used for dental restorations and implants, Dental clinics of North America, 51(3), 2007, p. 603–627.
10. D. Chopra, A. Jayasree, T. Guo, K. Gulati, S. Ivanovski, Advancing dental implants: Bioactive and therapeutic modifications of zirconia, Bioactive Materials, volume 13, 2022, p. 161-178.
11. Q. Chen, G. A. Thouas, Metallic implant biomaterials, Materials Science and Engineering: R 87, 2015, p. 1–57.
12. L. A. Dobrzański, Podstawy nauki o materiałach i metaloznawstwo, Wydawnictwo Naukowo-Techniczne, Warszawa, 2002.
13. B. Świeczko-Żurek, Biomateriały, Wydawnictwo Politechniki Gdańskiej, 2009.
14. https://virgamet.pl/00h17n14m2-1-4404-1-4401-aisi-316-316l-tp316-tp316l-stal-nierdzewna – access date: 21.12.2024 r.
15. G. Sacks, V. Shah, L. Yao, C. Yan, D. Shah, L. Limeta, V. DeStefano, Polyaryletherketones: Properties and applications in modern medicine, Biomedical Technology 6, 2024, p. 75-89.

16. W. Wojnarowska, K. Sandecki, Polieteroeteroketon (PEEK) w zastosowaniach medycznych, Badania i rozwój młodych naukowców w Polsce – nauki techniczne i inżynieryjne część IX, 2018, p. 119-127.
17. https://emetal.eu/tytan/tytan_grade_5_R56400_Ti-6Al-4V_3.7165/ – access date: 21.12.2024 r.
18. https://virgamet.pl/00h17n14m2-1-4404-1-4401-aisi-316-316l-tp316-tp316l-stal-nierdzewna?fbclid=IwAR3jm8lSlLiiHsmVBRdc67GqJW5zNzbJJj2ugPM6vnzFemS7EU4HYcgSe-Y – access date: 21.12.2024 r.

TalentDetector
31th January 2025
Gliwice, Poland
DEPARTMENT OF ENGINEERING MATERIALS AND BIOMATERIALS
FACULTY OF MECHANICAL ENGINEERING
SILESIAN UNIVERSITY OF TECHNOLOGY
INTERNATIONAL STUDENTS SCIENTIFIC CONFERENCE

Polymer biocomposites based on biodegradable binders, reinforced with plant-derived fibers for 3D printing

Oleg Polishchuk [a], Mirosław Bonek [b], Andrii Polishchuk [c], Serhii Matiukh [d], Svitlana Lisevich[e], Artem Tolstiuk[f]

[a] Khmelnitskyi National University, Faculty of Mechanical Engineering, Transport and Architecture, Khmelnitskyi, Ukraine email: opolishchuk7l@gmail.com .
[b] Silesian University of Technology, Faculty of Mechanical Engineering, Department of Engineering Materials and Biomaterials, Gliwice, Poland email: miroslaw.bonek@polsl.pl .
[c] Khmelnitskyi National University, Faculty of Mechanical Engineering, Transport and Architecture, Khmelnitskyi, Ukraine email: andrepol215@gmail.com .
[d] Khmelnytskyi National University, Faculty of Engineering Mechanics, Khmelnytskyi, Ukraine email: matuh@khmnu.edu.ua.
[e] Khmelnitskyi National University, Faculty of Engineering Mechanics, Khmelnitskyi, Ukraine email: lisevichsv@gmail.com.
[f] Khmelnitskyi National University, Faculty of Engineering Mechanics, Khmelnitskyi, Ukraine email: tvenergetik@gmail.com.

Abstract: The article considers the relevance of creating biodegradable polymer materials capable of natural decomposition under the influence of microorganisms, moisture and temperature. The main attention is paid to the problem of environmental pollution by traditional plastic waste and the possibilities of replacing synthetic polymers with environmentally friendly analogues. The requirements for biodegradable plastics and their prospects for use in various industries are analyzed. Biocomposites based on biopolymers and natural fibers are considered, which demonstrate significant potential in reducing environmental impact and contribute to sustainable economic development. Biodegradable binders are studied as a key component of biocomposites that ensure the environmental characteristics of materials and their ability to natural decomposition. The main groups of biodegradable plastics are considered. An analysis of global production capacities of biodegradable plastics and a forecast of their growth until 2028 are conducted. Attention is paid to the prospects for the use of PLA, which demonstrates the greatest growth in global production. The development of the biodegradable plastic market in Ukraine is studied, in particular its activation due to changes in environmental standards and legislation. The results of marketing research are presented, which indicate the attractiveness of this industry for investment and further development. The growing role of polylactide (PLA) in the global production of biodegradable plastics, its physicochemical and mechanical properties, as well as the main reasons for its popularity are studied. Experimental studies of the properties of PLA in comparison with traditional polymer materials (polystyrene, polypropylene, PET) are conducted. Natural fibers of plant origin are studied as a promising material for creating environmentally friendly composites. Their

classification, chemical composition, physicomechanical properties and role in the production of biodegradable polymer materials are considered. The advantages of using such fibers are described, in particular their environmental friendliness, biodegradability and ability to be reused. The main types of fibers, such as flax, jute, sisal, coconut fiber and agricultural residues, are analyzed, as well as their applications in construction, the automotive industry, the textile industry and 3D printing.

Keywords: biocomposites, biodegradable plastics, natural fibers, plant fibers, 3D printing, polylactide, PLA.

1. INTRODUCTION

The development of biodegradable materials and composites is an important area of research, which is reflected in many scientific works. In particular, attention is paid to the creation of composite mixtures based on synthetic polymers using fibers of natural origin, as well as wood waste as fillers. The works [1-3] consider the prospects for the use of such materials, their properties and approaches to the design of technological equipment for 3D printing. These studies emphasize the importance of implementing environmental technologies in modern production.

In recent years, research efforts have focused on developing biodegradable materials that can naturally degrade in the environment. This is due to growing environmental demands that include reducing environmental impacts, in particular by reducing greenhouse gas emissions such as carbon dioxide. These measures are aimed at increasing the rate of global climate change caused by human activities, including industrial processes, transportation, and household waste.

This problem is particularly relevant in the field of the use of polymeric materials, which are the main source of pollution. Every year, millions of tons of plastic are produced in the world, a significant part of which, after use, ends up in the environment, polluting soil, water and oceans. Due to their long resistance to decomposition, plastic waste accumulates, creating serious environmental threats.

Against this backdrop, the development of biodegradable plastics that can be degraded by natural factors such as microorganisms, moisture, and temperature is of key importance. Biodegradable materials have the potential to significantly reduce environmental damage by replacing traditional synthetic plastics in many industries, including packaging, medicine, agriculture, and the production of everyday goods [4].

Research in this field focuses on creating materials that meet modern environmental standards while maintaining the mechanical, physical, and chemical properties necessary for functional tasks. Such materials not only reduce environmental impact but also contribute to sustainable economic development.

According to EN 13432:2000, the biodegradability of plastic packaging materials is assessed by aerobic and anaerobic biodegradation [5]. Under aerobic conditions, the material should decompose by 90% within 6 months compared to a reference sample. Under adequate conditions, the degree of decomposition, determined by the volume of biogas produced, should reach 50% of the dry weight of the material over the same period. The decomposition process produces environmentally friendly products such as carbon dioxide, methane, water and inorganic compounds.

Of particular interest among polymer composite materials are biocomposites consisting of a biopolymer binder reinforced with natural fibers.

When considering binders for biocomposites, attention will be focused on biodegradable plastics derived from plant raw materials, since they are the most promising in terms of meeting environmental requirements. Today, such plastics account for 75-80% of the entire bioplastics market.

2. FORMULATION OF THE PROBLEM

The object of the research is the processes of creating biodegradable polymer composites reinforced with plant fibers and their application in 3D printing technologies. To solve the problem, it is necessary to consider the chemical composition, physical and mechanical properties of the binder biodegradable polymers and plant fibers, as well as their influence on the formation of the characteristics of biocomposites.

3. PRESENTING MAIN MATERIAL

Biodegradable binders are a key component in the composition of biocomposites, after which they provide adhesion between reinforcing fibers and complement the environmental characteristics of the material. The main feature of such binders is their ability to decompose under natural conditions into environmentally safe compounds.

Biodegradable plastics, which are widely used in the production of environmentally friendly materials, are conventionally divided into three main groups. The polymers of each of these groups have unique properties that make them useful in industry and everyday life.

1. Polylactide (PLA).

Polylactic acid (PLA) is one of the most popular biodegradable plastics. It is made from lactic acid, which is obtained by lactic fermentation of sugar-containing substances such as corn starch, sugar cane or beets. The main advantages of PLA include:

- high biocompatibility;
- suitability for 3D printing (it is the most common material for additive manufacturing due to its easy processing and thermal stability);
- biodegradability (decomposes under compost conditions, forming water, carbon dioxide and organic residues).

2. Polyhydroxyalkanoates (PHAs).

Polyhydroxyalkanoates (PHAs) are produced by the fermentation of plant sugars by microorganisms. They are natural polymers that can be completely degraded in the natural environment, including seawater.

Main characteristics of PHA:

- a wide range of properties (depending on the structure, they can be both rigid and elastic);
- resistance to moisture and chemicals;
- environmental friendliness.

3. Starch-based materials.

Starch is an affordable and renewable raw material used to create biodegradable plastics. Materials based on it can be obtained by modifying natural starch or combining it with other polymer components. The main properties of such materials are:

- cheapness and availability;
- biodegradability.

Other biodegradable materials.

There are a number of other biodegradable polymers that are also used in production, namely: materials made from polyvinyl alcohol, polyvinyl acetate, polyglycolic acid (synthetic polymers), as well as lignin, cellulose, caprolactone, etc. (natural polymers).

Biodegradable plastics are the materials that lead to environmentally friendly production. Due to the variety of their properties, they have found wide application in various industries.

Based on the results of a market study of the biodegradable plastics market conducted by Pro-Consulting, a forecast of its global capacity growth was made [6]. According to European Bioplastics in cooperation with Nova-Institute, by 2025, the world will have capacity to produce 2.87 million tons of bio-based plastics, of which the biodegradable polymer market will account for 1.8 million tons (Fig. 1).

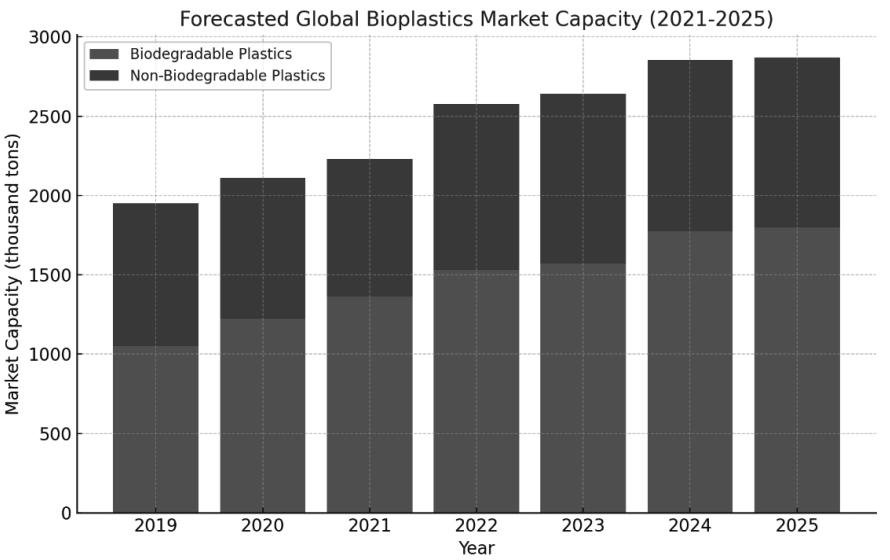

Fig. 1. Global production of bioplastics in 2021-2024 and forecast indicators for 2025

According to the latest report published by Emergen Research, the global bioplastic market is expected to reach USD 25.27 billion in 2027, and register a steady CAGR of 14.9% during the forecast period [7].

The top eight global biodegradable plastics companies by revenue are: BASF SE (Revenue US$86 Billion); Eastman Chemical Company (Revenue US$10 Billion); Plantic Technologies (Revenue US$23 Million); Futamura Group (Revenue US$1.19 Billion); NatureWorks LLC (Revenue US$1.50 Billion); Polymateria Ltd ([Revenue US$17.16 Million); TIPA Corp Ltd (Revenue US$13 Million); Biome Bioplastics Limited (Revenue US$6.40 Million) [7].

An analysis of the Ukrainian biodegradable plastic market conducted by Pro-Consulting for the period 2019 - 1st half of 2021 showed that its active growth began in 2020, when the

public began to pay more attention to reducing environmental impact through rationalization of consumption and raising environmental standards of packaging materials [6]. In 2021, development was strengthened at the state level by adopting the law "On Limiting the Volume of Plastic Bags in Ukraine". Due to favorable conditions and the presence of many raw materials bases, the biodegradable plastic market in Ukraine has become attractive for investment and development of production capacities.

Analysis of global capacities by main types of biodegradable plastics, based on the diagrams shown in Fig. 2 and 3, demonstrates significant development of the industry and strengthening of the position of PLA plastic in the world [8].

Analysis for 2020 (Fig. 2). The diagram shows the structure of global capacities by main types of biodegradable plastics. Starch mixtures and PLA have an equal contribution to the overall structure - 32.2% each, which indicates their equal popularity in 2020. PBAT occupies 23.2%, inferior to the two previous materials. Plastics such as PBS, PHA and others together occupy about 12.4% of the market, which demonstrates their lower concentration.

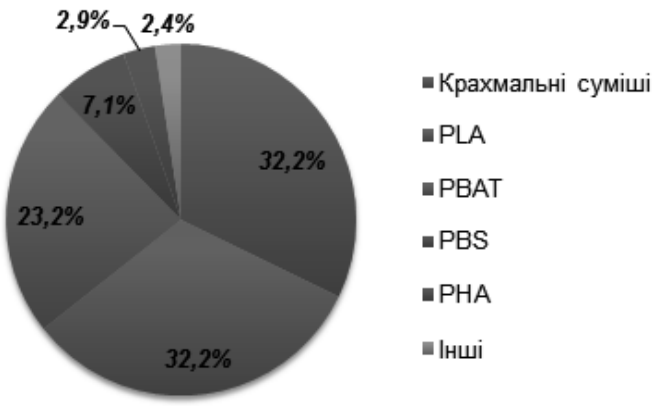

Fig. 2. Structure of world capacities by main types of biodegradable polymers, 2020 (source European Bioplastics)

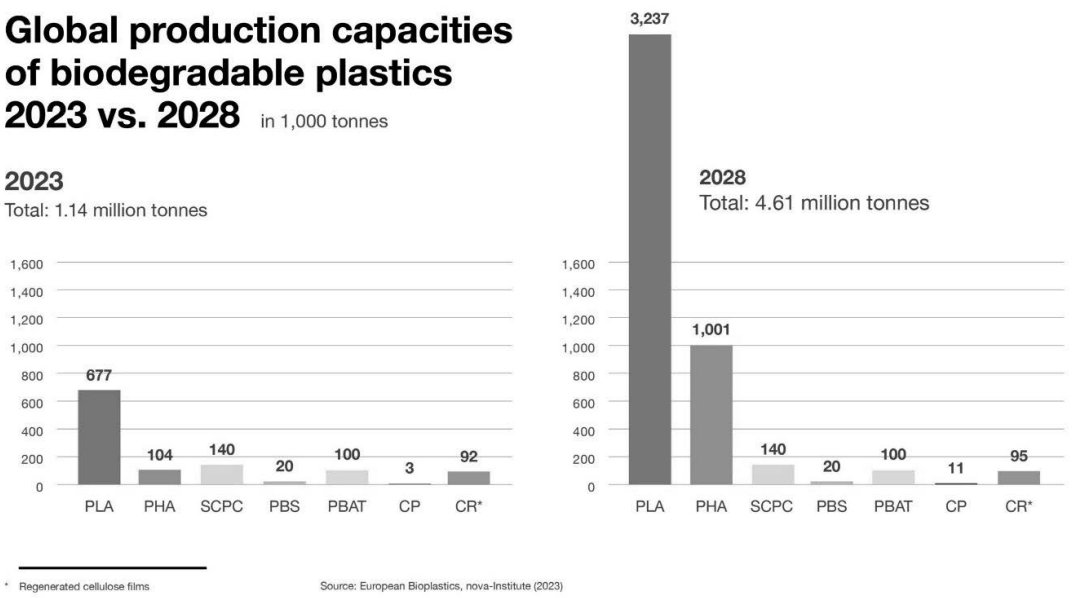

Fig. 3. Global production capacities of biodegradable plastics 2023 vs 2028

Analysis for 2023 (Fig. 3). The total capacity of biodegradable plastics in 2023 is 1.14 million tons. PLA is the undisputed leader in production with 677 thousand tons (over 59% of the total). PHA is in third place (104 thousand tons), but significantly behind PLA. Materials such as PBAT, PBS and others are used in smaller quantities (from 20 to 140 thousand tons depending on the type).

Forecast for 2028. The total capacity of biodegradable plastics will increase to 4.61 million tons. PLA production will increase more than 4 times and reach 3.237 million tons, which will account for more than 70% of the total volume. PHA will grow to 1.001 million tons, which will confirm its stable place in the market, but will remain significantly behind PLA. The production of other materials will increase slightly, and PBS and PBAT plastics will remain at the levels of 20–140 thousand tons.

The growing role of PLA plastic in the world. Monitoring the biodegradable plastic market on a global scale shows that polylactic acid occupies the largest share in it. The share of PLA in the structure of global capacities increased from 32.2% in 2020 to 59% in 2023, and in 2028 it is predicted to increase to over 70% (Fig. 2, 3).

The reasons for its popularity are as follows [6]:

- PLA is obtained from renewable raw materials (sugar cane, corn), which ensures its environmental friendliness;
- high compatibility with various technologies, including 3D printing;
- resistance to environmental influences;
- high strength characteristics, which determines a wide range of uses;
- better recyclability than PHA;
- PLA complies well with composting standards (e.g. EN 13432), making it attractive to environmentally conscious markets.

PLA is expected to become the main material for biodegradable plastics, displacing other polymers due to the availability of raw materials, versatility, and high environmental friendliness.

The world's largest producers of polylactic acid are: Total-Corbion (Thailand); NatureWorks (USA); Hitachi (Japan); Zhenjiang Hisun Biomaterials (China); Synbra Technologies (Netherlands) [6].

Polylactide is a transparent thermoplastic polymer whose physicochemical properties can be specified in advance. This can be achieved by using different optical isomers of the monomer (lactide) and/or changing the degree of polymerization. This allows materials with different characteristics of strength, water resistance and biodegradability to be obtained.

The physicochemical and mechanical properties of lactide-based polymers and copolymers are relatively similar to those of polyethylene, polypropylene (PP), polyethylene terephthalate (PET), and polystyrene (Table 1).

Polylactide products can be manufactured using standard equipment (extrusion equipment) used to process traditional synthetic polymers. This makes polylactide a promising alternative to replace conventional polymers in many industries.

In order to conduct experimental studies to establish the parameters of polylactide and compare them with the properties of traditional polymers, experimental studies were conducted. For this purpose, experimental samples were made from the following plastics: polylactide, polystyrene (PS), polyethylene terephthalate (PETF) and polypropylene (PP).

The studied parameters were divided into three main groups: density, mechanical and thermal properties.

To determine the thermal parameters of plastics, a differential scanning calorimeter model DSC 250 from TA Instruments was used. To measure the density of solids, a pycnometer model AccuPyc II 1340 from Micromeritics was used. To determine the mechanical properties of plastics such as: tensile strength, tensile modulus and relative elongation at break, an Instron 3369 machine was used, which is a universal device for testing the mechanical properties of materials. The experimental studies conducted allowed us to obtain a complete picture of the mechanical properties of the specified materials.

The obtained experimental data are given in Table 1. It demonstrates a comparison of the main parameters of polylactide (PLA) with other traditional polymer materials.

Table 1. Parameters of polylactide compared with parameters of traditional polymers

No.	Parameters	Parameter values for polymers			
		polylactide	polystyrene	PETF	polypropylene
Thermal parameters					
1	Melting point, ^{0}C	232	-	249	160
2	Glass transition temperature, ^{0}C	67	87	70	130
Physical property					
3	Density, g/cm ^{3}	1.24	1.06	1.27	0.91
Mechanical properties					
4	Tensile strength, MPa	51	38	70	23-35
5	Relative elongation at break, %	30	3	50	430
6	Tensile modulus, GPa	2.3	3.2	3.0	28

The analysis of the obtained experimental data allowed us to draw the following conclusions.

Polylactide exhibits balanced mechanical and thermal properties, making it competitive with the traditional polymers listed in Table 1 (polystyrene, polypropylene, and polyethylene terephthalate). Its high tensile strength (51 MPa) allows PLA to withstand significant loads, making it effective in industries such as rigid packaging, 3D printing parts, and biodegradable products. Its moderate stiffness (modulus of elasticity of 2.3 GPa) also makes PLA suitable for applications that require sufficient resistance to deformation.

However, one of the main limitations of polylactide is its low elongation at break (30%), which indicates its brittleness compared to polypropylene, which exhibits elongations of up to 430%. This property limits the use of PLA in products that require high flexibility, such as flexible films or elastic components. However, polylactide remains suitable for products where stiffness and shape stability are key factors.

The temperature characteristics of PLA, in particular the glass transition temperature (67 °C) and melting point (232 °C), make it an optimal material for 3D printing in medium-temperature processing conditions. Due to its relatively low melting point, polylactide is easily processed on standard 3D printing equipment, which ensures high print quality even on low-cost printers. This property makes PLA an ideal choice for printing complex geometric shapes, decorative elements, prototypes and functional parts with low thermal stability requirements.

However, the glass transition temperature of polylactide (67 °C) means that products made from this material lose their mechanical stability at elevated temperatures. For example, finished parts can deform when exposed to direct sunlight or when in contact with hot objects. This limits the use of polylactide in the production of parts that will be used in high-temperature environments, such as components for the automotive industry or kitchenware for hot drinks.

Thus, PLA is one of the most suitable materials for 3D printing, especially for creating decorative and prototype parts. At the same time, for printing products that require increased heat resistance, it is advisable to use other polymers, such as PETG or ABS, which have better resistance to high temperatures and retain their shape even in difficult operating conditions.

Overall, polylactide is a promising material that has an impact on environmental sustainability with significant mechanical and thermal properties. However, its brittleness and limited thermal stability require further improvement or modification, for example, by creating PLA-based composites reinforced with plant-derived fibers or combining them with other polymeric materials to expand its scope of use.

Natural fibers of plant origin have been used since ancient times to create textile, construction and other technical materials. This is one of the oldest areas of material culture, which continues to be relevant even in the modern era of high technology. Previously, many experts assumed that the development of artificial materials and polymers would lead to the complete replacement of natural fibers. However, practice has shown the opposite. The growing popularity of biodegradable materials and the environmental orientation of modern industry have given natural fibers a second life.

In particular, natural fibers play a key role in the production of composite materials today. They are widely used in such technologically advanced industries as the automotive industry, the aerospace industry, construction and consumer goods production. For example, in the automotive industry, natural fibers are used to create lightweight and strong panels, armrests, seats and soundproofing materials. Such composite materials help reduce the weight of the car, which has a positive effect on its fuel efficiency and reduces CO_2 emissions.

The popularity of natural fibers is due to their unique properties. Firstly, it is a cheap and accessible resource, as the fibers are obtained from renewable plant sources, such as flax, hemp, jute, coconut fiber or even agricultural waste, such as straw. Secondly, natural fibers are environmentally friendly, as they are fully or partially biodegradable, reducing the burden on the environment. For example, composite materials based on natural fibers can be recycled or returned to nature at the end of their life cycle without generating hazardous waste.

Another important advantage of natural fibers is their mechanical properties. Plant fibers, such as flax or jute, have high tensile strength, low density and good heat resistance. These properties allow the creation of lightweight, yet strong composite materials that can be used in critical structures. For example, composites with the addition of flax fibers are widely used in the manufacture of panels for aircraft and high-speed trains.

In addition, the use of natural fibers contributes to the development of a circular economy. The production of materials from plant-based fibers allows the use of agricultural residues, which reduces waste and increases economic efficiency. For example, coconut fibers, which are a by-product of the production of coconut milk, are used in the manufacture of mattresses, car panels and insulation materials.

In modern realities, the demand for natural fibers continues to grow due to their environmental friendliness, availability and unique physical and mechanical properties. Innovative technologies allow creating composite materials from them with improved

characteristics that are competitive in comparison with artificial analogues. Thus, natural fibers are becoming an integral part of sustainable industrial development and solving global environmental challenges.

Natural plant fibers are classified according to their source: stems, leaves, fruits, or other parts of plants. They have unique mechanical and physicochemical properties that make them valuable for technical uses, such as in the production of composite materials, textiles, and insulation.

The classification of natural plant fibers used for technical purposes is shown in Fig. 4. The figure illustrates the division of fibers by source: bast crops, fruit fibers, leaf fibers, perennial grasses and agricultural residues. Each type of fiber is labeled and visualized according to its category.

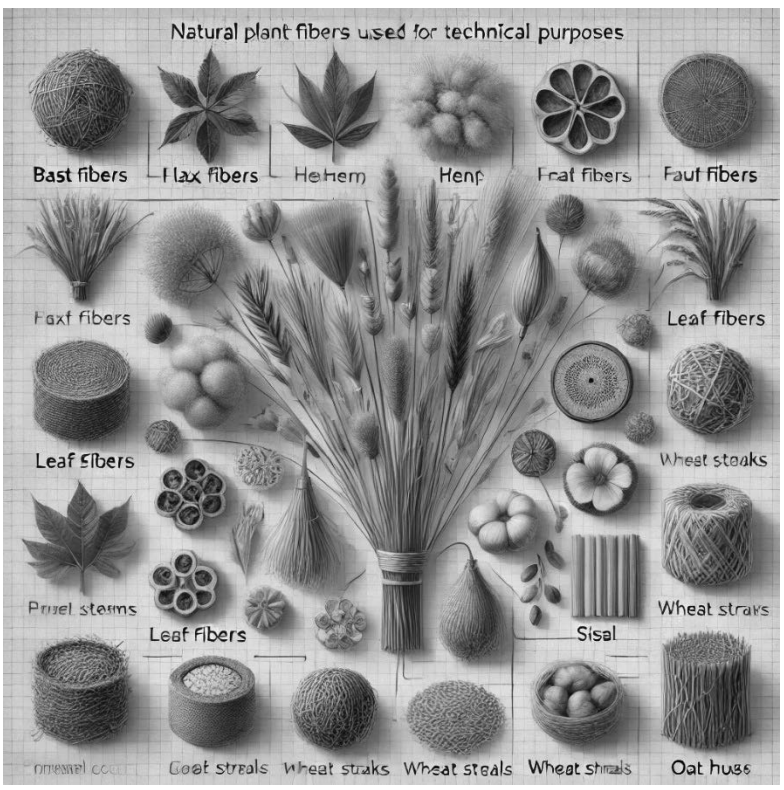

Fig. 4. Natural fibers used for technical purposes

Let's take a closer look at the categories of fibers.

1. Fibers of bast crops.

Flax. It is characterized by high strength, low density and good thermal stability. It is widely used in the textile industry, rope manufacturing and composites.

Hemp. Has high wear resistance and moisture resistance. Used in the production of ropes, fabrics, and soundproofing materials.

Kenaf. A lightweight and durable material suitable for the production of paper, textiles, and building panels.

Jute. A fiber with high strength and low cost. Used in the manufacture of bags, ropes, and carpets.

2. Fruit fibers.

Coconut fiber (coir). A stiff fiber with high moisture resistance. Used in the manufacture of mattresses, carpets, and soundproofing panels.

3. Fibers from leaves.

Mexican hemp (sisal): A tough fiber that is resistant to wear and moisture. Used in ropes, carpets, and packaging.

4. Fibers of perennial herbs.

Millet. Used in the manufacture of building materials and fillers for composites.

Chinese reed. A moisture-resistant, lightweight material used in construction and paneling.

5. Crop fibers.

Soybean, corn, wheat, and oat stalks are a byproduct of agriculture and are used to create insulation, bioplastics, and composite materials.

The chemical composition and structure of plant fibers largely depend on factors such as climatic conditions, the age of the plant and its metabolic processes. Unlike cotton, the main components of natural fibers are lignin, pectin, cellulose, hemicellulose, wax and water-soluble substances. These components determine the physicochemical and mechanical properties of the fibers, as well as their ability to biodegrade, which is an important advantage compared to artificial materials.

Cellulose is the main structural component of plant fibers, providing their strength and stiffness. Hemicellulose and pectin act as binding agents between cellulose microfibrils, while lignin gives the fibers additional stiffness and water resistance. Wax and water-soluble substances perform an auxiliary function, affecting the surface properties of the fibers, in particular their hydrophobicity.

The physical and mechanical properties of natural fibers are largely determined by the content of the main components, such as cellulose, hemicellulose and lignin. The strength of the fibers and their stiffness depend on the cellulose content, the degree of its polymerization, and the angle of orientation of the microfibrils relative to the fiber axis. For example, fibers with a high cellulose content and a small angle of axial orientation of the microfibrils have a higher modulus of elasticity and tensile strength. That is why flax and hemp fibers are considered to be among the strongest among plant fibers.

The mechanical characteristics of natural fibers vary depending on the part of the stem from which they are obtained (closer to the root or the top), as well as the extraction method. For example, fibers obtained by chemical methods are characterized by higher purity, but may lose some of their mechanical strength due to the influence of aggressive reagents.

The mechanical properties of many natural fibers, such as flax, jute, or sisal, are comparable to those of synthetic fibers traditionally used as reinforcing components in polymer composites. For example, the tensile strength of flax fibers can reach 1.0–1.2 GPa, which is similar to that of glass fibers. Unlike synthetic fibers, plant fibers are environmentally friendly. They do not produce toxic substances during decomposition and are easily biodegradable, which makes them attractive for use in environmentally friendly technologies.

The use of plant fibers in polymer composite materials helps reduce the negative impact on the environment due to their ability to absorb CO_2 during growth. This allows for the creation of environmentally friendly materials that meet the requirements of a circular economy and contribute to sustainable development.

Due to their mechanical properties, chemical composition and environmental benefits, plant fibers have a wide range of applications, including the production of biocomposites, construction materials, textiles and packaging products. They are a promising alternative to

synthetic fibers, contributing to the implementation of more sustainable and environmentally friendly technologies in industrial processes.

Plant fibers such as flax, jute, hemp or coconut fiber have significant potential as reinforcing components for biodegradable plastics, which serve as binders in the creation of environmentally friendly composites for 3D printing. Due to their unique mechanical, thermal and environmental properties, these composites can become the basis for the development of innovative materials that will find applications in various industries.

Reinforcing biodegradable plastics such as PLA with plant fibers will significantly improve their mechanical properties. The fibers will increase tensile strength, elastic modulus, and resistance to deformation due to the high cellulose content and optimal microfibril orientation. This will make such composites suitable for applications in architecture, design, the automotive industry, etc.

Plant fibers are lighter than traditional reinforcing components, such as fiberglass, which will allow for weight reduction of products. The use of renewable raw materials will contribute to reducing environmental impact and creating materials that comply with the principles of the circular economy.

4. CONCLUSIONS

The research has confirmed the importance of developing biodegradable polymer materials that are capable of natural decomposition under the influence of microorganisms, moisture and temperature. This contributes to reducing environmental pollution and replacing traditional synthetic plastics with environmentally friendly analogues.

Biocomposites based on biopolymers and natural plant-based fibers show significant potential in reducing environmental impacts. Polylactide has confirmed its leading role among biodegradable plastics due to its environmental friendliness, mechanical properties and compatibility with technologies such as 3D printing. Its share in the global production of biodegradable plastics is predicted to reach more than 70% by 2028.

Marketing research has shown the attractiveness of the biodegradable plastics market for investment, particularly in Ukraine, where the activation of this sector is associated with changes in environmental legislation and growing demand for environmentally friendly materials.

Natural plant fibers, due to their physical and mechanical properties, environmental friendliness and availability, are a promising material for creating composites in construction, transport, textile and 3D printing. The use of these fibers contributes to the implementation of the principles of a circular economy.

Further experimental studies are needed to determine the physical and mechanical properties of natural plant fibers to better understand their potential for use as reinforcing components in biocomposites.

It is necessary to conduct research aimed at improving the compositions of biocomposites, improving their production technologies, and studying the durability and stability of these materials under various operating conditions.

An important area of further research is the development of specialized 3D printing equipment that will allow for the efficient processing of biodegradable composites. Such equipment will contribute to expanding the capabilities of additive manufacturing, in particular in the creation of environmentally friendly and functional products.

ACKNOWLEDGEMENTS

The work was created as a result of the project as part of project based learning - PBL, in the 11th competition under the Initiative of Excellence - Research University, Silesian University of Technology, Gliwice, Poland.
The publication is result of cooperation within the Visegrad Scholarship Program 2024/2025.

BIBLIOGRAPHY

1. O.S. Polishchuk, A.O. Polishchuk, M.M. Rubanka. Prospects for creating composite mixtures based on synthetic polymers reinforced with fibers of natural origin. "Mechatronic systems: innovations and engineering". November 23, 2023, Kyiv National University of Technologies and Design. - R.127.
2. O. Polishchuk, A. Polishchuk, A. Tolstiuk. Use of chopper wood waste as a filler of a composite mixture for 3D printing. Technical creativity. Collection of scientific works. Khmelnytskyi. No. 7, 2024. - P. 159-161.
3. Polishchuk O., Polishchuk A., Bonek M., Musial Ja., Tolstyuk A. Justification of the product manufacturing method with composite mixtures based on thermoplastic polymers and wood waste. Actual problems of modern science. Monograph: edited by Matiukh S., Musial J., Polishchuk O., Macko M. 2024, Bydgoszcz, Poland. - R.787-792.
4. Polishchuk O., Polishchuk A., Bonek M., Musial Ja, Tolstyuk A. Justification of the product manufacturing method with composite mixtures based on thermoplastic polymers and wood waste. Actual problems of modern science. Monograph: edited by Matiukh S., Musial J., Polishchuk O., Macko M. 2024, Bydgoszcz, Poland. - R.787-792.
5. DSTU EN 13432:2015 Packaging. Requirements for packaging disposed of by composting and biodegradation. Test schemes and evaluation criteria for final acceptance of packaging (EN 13432:2000, IDT). –K.: DP "UkrNDNTS", 2016.
6. https://pro-consulting.ua/ua/pressroom/rynok-biorazlagaemogo-plastika-v-ukraine-dannye-pro-consulting [access: 01.08.2025].
7. https://www.emergenresearch.com/blog/top-8-bioplastic-companies-transforming-the-world-in-an-eco-friendly-way [access: 08.01.2025].
8. https://www.european-bioplastics.org/bioplastics/materials/biodegradable/ [access: 08.01.2025].

TalentDetector
31th January 2025
Gliwice, Poland
DEPARTMENT OF ENGINEERING MATERIALS AND BIOMATERIALS
FACULTY OF MECHANICAL ENGINEERING
SILESIAN UNIVERSITY OF TECHNOLOGY
INTERNATIONAL STUDENTS SCIENTIFIC CONFERENCE

Technologies for processing carbon fibers into finished products using extrusion

Andrii Polishchuk [a], Mirosław Bonek [b], Oleg Polishchuk [c], Serhii Matiukh [d], Svitlana Lisevich[e], Yevhen Harbar [f]

[a] Khmelnytskyi National University, Faculty of Mechanical Engineering, Transport and Architecture, Khmelnytskyi, Ukraine email: andrepol215@gmail.com.
[b] Silesian University of Technology, Faculty of Mechanical Engineering, Department of Engineering Materials and Biomaterials, Gliwice, Poland email: miroslaw.bonek@polsl.pl.
[c] Khmelnytskyi National University, Faculty of Mechanical Engineering, Transport and Architecture, Khmelnytskyi, Ukraine email: opolishchuk7l@gmail.com.
[d] Khmelnytskyi National University, Faculty of Engineering Mechanics, Khmelnytskyi, Ukraine email: matuh@khmnu.edu.ua.
[e] Khmelnytskyi National University, Faculty of Engineering Mechanics, Khmelnytskyi, Ukraine email: lisevichsv@gmail.com.
[f] Khmelnytskyi National University, Faculty of Engineering Mechanics, Khmelnytskyi, Ukraine email: garbarzhenia@gmail.com.

Abstract: The article highlights the current aspects of using carbon fiber to create finished products by extrusion, in particular 3D printing. Key technologies are analyzed, including the production of composite filament with a polymer matrix and reinforcing fibers, as well as the use of these filaments in additive manufacturing processes. The advantages of using continuous carbon fiber, which provides increased strength, lightness and stability of products, are considered in detail. The prospects for the use of high-temperature plastics, such as PEEK, PLA, PETG and ABS, in combination with carbon fibers are discussed, which makes it possible to create materials for the aviation, automotive, construction and medical industries. Special attention is paid to the innovative technology of direct extrusion of the "polymer + carbon fiber" mixture using screw extruders, which eliminates the disadvantages of two-stage melting of the polymer. The challenges associated with the implementation of these technologies are considered, in particular the high cost of equipment, the need for fine-tuning of processes, as well as the need to develop specialized extruders to ensure stable work with reinforced materials. Prospects for improving equipment and optimizing technological processes to expand the use of carbon fiber in various industries are presented.

Keywords: carbon fiber, extrusion, extruder, 3D printer, composite material, polymer.

1. INTRODUCTION

Polymer extrusion is a technological process that is widely used to form plastic products by forcing molten polymer through a molding die. [1, 2]. This method is used to produce films,

pipes, profiles, fibers, sheets, compounds and many other products. Extrusion is one of the most common and efficient ways of processing polymers, providing high productivity and versatility.

It is particularly important to note that 3D printing is also based on the principles of extrusion. In FDM/FFF (fused deposition modeling), molten polymer material is forced through an extrusion die and deposited in layers to create a three-dimensional product. This extends the capabilities of extrusion, adding the benefits of additive manufacturing, including the creation of complex geometries, rapid design modification, and reduced material costs.

The main areas of application of extrusion: production of films and sheets for food, pharmaceutical and household packaging; production of pipes, insulating materials, profiles for windows and doors in construction; creation of light and durable parts, seals, coatings and decorative elements for the automotive industry; production of cable insulation, protective casings and other insulating materials for the electrical industry; production of synthetic fibers for clothing and technical textiles for the textile industry; creation of functional prototypes, models and final products using additive technologies (3D printing); production of technological parts, semi-finished products, compounds for further processing and components for automated systems in industry, etc.

According to analytical data, the global polymer extrusion market is showing an annual growth rate of about 5%. In 2023, its volume was estimated at $80 billion. If such rates are maintained, the market is expected to grow to $113 billion in monetary terms by 2030.

Typical trends in the global market for polymer processing by extrusion are: growing demand for biodegradable polymers and the use of recycled plastics in production; optimization of extrusion processes to reduce energy consumption; development of extrusion technologies for additive manufacturing through the creation of new equipment; expansion of the range of materials through the creation of new polymers with improved characteristics, including reinforced composites, etc.

Trends in the development of polymer extrusion include the extrusion of: multilayer materials, which provides the creation of products with improved properties, such as barrier properties , heat resistance and strength; biopolymers due to the growing demand for products based on PLA, PHA eco-friendly plastics; for 3D printing, which encourages the emergence of composites with high mechanical characteristics; carbon materials for the purpose of reinforcing polymers with short or continuous carbon fibers in order to impart high mechanical properties to products, including stiffness and strength. The use of continuous carbon fiber allows you to create parts with characteristics that can compete with metals, especially in high-tech industries.

Polymer extrusion, including its integration into 3D printing technologies, is a direction of modern manufacturing. Its application in industries including automotive, medical, construction and the introduction of innovative materials such as carbon fiber contributes to expanding production capabilities, increasing environmental friendliness and reducing costs. The development of extrusion allows to meet modern market needs, making this technology a key tool in industrial evolution.

2. FORMULATION OF THE PROBLEM

The object of the research is the processes of creating polymer composites reinforced with carbon fibers and their application in 3D printing technologies. To solve the problem, it is necessary to study the chemical composition, physical and mechanical properties of carbon

fiber and thermopolymers. To list possible technologies for their processing into finished products.

3. PRESENTING MAIN MATERIAL

Carbon fiber is an innovative material that is increasingly used in industry due to its unique properties. [3]. It is made from organic polymers (most often polyacrylonitrile or bitumen) by heat treatment (Fig. 1). The basis of this material is long thin carbon filaments with a high degree of purity, which are combined into bundles and can be used independently or as a reinforcing component in composites.

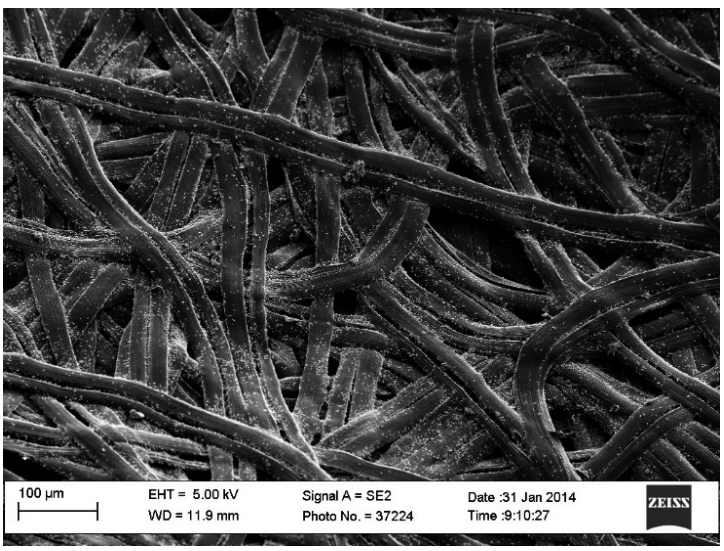

Fig. 1. Carbon fibers obtained by pyrolysis of silk cocoon. Electron micrograph — scale bar at bottom left shows 100 µm [4]

Carbon fiber is a material whose chemical composition consists almost entirely of carbon, the share of which reaches more than 90%. The remaining components are impurities that depend on the type of raw material and the processing technology used. The carbon fiber production process consists of several stages. At the first stage, stabilization, the starting polymer is subjected to heat treatment, which ensures the formation of a thermostable structure. The second stage, carbonization, involves heating the material to a temperature of 1000–3000 °C in an inert environment. This allows hydrogen, oxygen and nitrogen to be removed from the material, leaving only carbon. The next, optional stage is graphitization, which is carried out to improve the mechanical and electrical characteristics of the fiber. At the final stage, finishing, the fibers are treated with chemicals that increase their adhesion to the matrix and ensure the formation of threads. In general, the production of carbon fiber is a complex and costly process, which largely determines the high price of this material.

Carbon fiber is a modern material that is becoming increasingly popular due to its unique physical and mechanical properties [5]. The main characteristics of carbon fiber are high tensile strength, light weight, heat resistance, chemical resistance, and low coefficient of thermal expansion. These properties make the material indispensable in many industries, including aerospace, automotive, construction, medical, and others.

In the aerospace industry, carbon fiber is used to create lightweight and strong components for aircraft, satellites, and rockets. The material allows for significant weight

reduction, improving fuel efficiency and reducing operating costs. In the automotive industry, carbon fiber is used to make bodies, panels, frames, and decorative elements. The lightness and strength of the material allow for weight reduction, energy efficiency, and dynamic performance. In construction, carbon fiber is used to reinforce concrete, create lightweight panels, and facade elements. The material provides high structural strength and durability, which is part of modern construction projects. In the medical field, the fiber is used to create prostheses, surgical instruments, and radiolucent components. Due to its biocompatibility and lightness, the material has found its place in the creation of high-tech medical equipment.

It is worth noting the use of carbon fiber in sports. It is widely used to make bicycles, tennis rackets, skis and other sports products. The lightness and stiffness of the materials can increase the performance of athletes and the durability of equipment. In electronics, carbon fiber is used to make device housings, antennas and other components where strength and lightness are required.

Particular attention should be paid to the use of carbon fiber in additive manufacturing (3D printing). The use of carbon fibers allows you to create components whose strength can compete with metal counterparts, but they remain lighter. 3D printing with their use finds application in the production of prototypes, functional parts, tools and structural elements.

Despite its high cost, carbon fiber continues to conquer new industries due to its unique properties and capabilities. Therefore, research aimed at reducing the cost of production, improving processing technologies, and expanding the scope of use of this high-tech material is becoming relevant.

Carbon fiber is a material with unique physical and mechanical properties that make it one of the most promising in modern industry.

The main characteristic of carbon fiber is its high tensile strength, which reaches 7 GPa. This is 5–7 times higher than the strength of steel, which allows the use of this material in highly loaded structures, for example, in the aviation, space and defense industries.

Another significant advantage is its low density, which is 1.75–2.0 g/cm³. This makes carbon fiber approximately four times lighter than steel. This property is critical for industries where weight reduction in structures contributes to increased efficiency, such as automotive and aerospace.

The heat resistance of carbon fiber is another important factor in its popularity. The material can withstand temperatures of up to 3000 °C in an inert environment, making it suitable for high-temperature applications such as turbine components, rocket engines, and high-temperature equipment.

Carbon fiber also has high chemical resistance, meaning it is inert to acids, alkalis, and most organic solvents. This property makes the material useful in aggressive environments such as oilfields, chemical manufacturing, and marine engineering.

Another key advantage is its low coefficient of thermal expansion, which ensures dimensional stability over a wide temperature range. This is critical for high-precision structures and equipment, particularly in electronics, optics, and aerospace applications. The combination of these properties makes carbon fiber indispensable for many industries, including industry, transportation, construction, medicine, and sports.

The disadvantages of carbon fibers include their high cost. The production of the material is a complex and energy-intensive process, which significantly affects its final price. This complicates the widespread use of carbon fiber in budget or mass products.

The brittleness of the material is another drawback. Carbon fiber, although it has high tensile strength, is a brittle material under impact loads. This limits its use in structures that

require impact resistance, such as automotive parts that are subject to significant mechanical stress.

A separate problem is the complexity of processing carbon fibers. They are difficult to recycle due to the peculiarities of their structure. This is relevant in the context of modern environmental standards that require reducing the amount of waste and its effective use.

Although carbon fiber is a costly material to produce, its advantages outweigh this disadvantage. Continuous research aimed at optimizing production processes is expanding the scope of fiber applications. Given the constantly growing demand for lightweight, strong and impact-resistant materials, carbon fiber has every prospect of becoming the basis for innovative technologies of the future.

Carbon fiber is becoming increasingly popular in extrusion processes due to its unique properties that allow the creation of high-performance composite materials. In the extrusion process, carbon fiber acts as a reinforcing element, which significantly improves the mechanical, thermal and performance characteristics of the final product.

Two main types of carbon fiber are commonly used:

- short fibers, which are excreted in the form of crushed segments up to several millimeters long;
- continuous fibers that integrate into the matrix without breaking.

Short fibers are evenly mixed with the polymer matrix, providing improved mechanical properties in all directions. In contrast, the presence of continuous fibers provides maximum strength in the direction of fiber orientation, making it indispensable for creating high-strength structures.

The matrix for carbon fiber composites is thermoplastic polymers, including polylactide (PLA), polyamide (PA), polycarbonate (PC), polyethylene terephthalate (PET), acrylonitrile butadiene styrene (ABS), and high-temperature polymers such as PEEK and PEKK [6]. These materials provide an optimal combination of lightness, strength, and durability, which allows them to be used in the creation of high-performance composites for a variety of industries.

Polylactide (PLA) is one of the most environmentally friendly materials, derived from renewable raw materials such as corn starch. When combined with carbon fiber, PLA allows the creation of composites used in light industry, 3D printing, packaging and design.

Polycarbonate (PC), known for its impact and heat resistance, combined with carbon fiber creates strong and lightweight materials that find applications in the automotive and electronics industries, as well as in the production of sports equipment.

Polyamide (PA) is characterized by high chemical resistance and strength. PA and carbon fiber-based compositions are often used in aviation, the transportation industry and to create parts that operate in aggressive environments.

Polyethylene terephthalate (PET), widely used in the production of bottles and textiles, when combined with carbon fiber becomes ideal for creating lightweight structures that require high impact resistance.

Acrylonitrile butadiene styrene (ABS) is a versatile polymer that provides high mechanical strength, impact resistance, and good processability. Adding carbon fiber to ABS significantly increases its strength and stiffness, creating a material suitable for use in the automotive industry, electronics, and in the production of prototypes and parts for 3D printing.

PEEK and PEKK are high-temperature polymers that provide excellent mechanical properties even in extreme conditions. When combined with carbon fiber, they find applications in aerospace, medical (for implants) and defense industries.

The combination of thermoplastic matrices with carbon fiber allows creating composites that have not only high strength and stiffness, but also chemical resistance, low weight and durability. Due to this, they remain indispensable in the automotive, aviation, space, construction and electronics industries. In addition, such materials open up new horizons for use in the production of environmentally friendly and high-tech products that meet modern requirements for efficiency and sustainable development.

One of the main advantages of using carbon fiber in extrusion is a significant improvement in the mechanical properties of composites. Due to the high tensile strength and stiffness of carbon fibers, the final products can receive significant mechanical loads. The low density of the material ensures lightness of the structure, which is of particular importance in the transport, aviation and space industries, where every gram of weight is critical. In addition, the high thermal resistance and chemical inertness of carbon fiber can use such compounds in aggressive environments and at extreme temperatures.

In the field of 3D printing, carbon fiber composites also play an important role. Short-fiber-reinforced filaments are a material for creating lightweight and strong parts. This requires specialized extruders that can work with high-temperature polymer matrices. Continuous carbon fiber reinforcement allows you to create parts with strength that can compete with metal products, while maintaining low weight.

However, the use of carbon fiber in extrusion has its challenges. These include the high cost of the material, the need for specialized equipment to process it, and the reliability of ensuring uniform mixing of the fiber with the matrix. In addition, as already noted, carbon fiber-based composites are difficult to process, which can create difficulties in the disposal of such materials.

In general, carbon fiber is a promising material for extrusion in many industries. Its use, through the creation of innovative products with improved characteristics, opens up new opportunities for the development of modern technologies. Further improvement of carbon fiber production technologies and the development of specialized equipment for its processing can significantly reduce the cost of the material and expand the scope of its application.

Let's consider existing and possible technologies for using carbon fibers in creating finished products.

Today, the technology for manufacturing finished products using carbon fibers is known, which consists of two main stages:

- production of composite thread;
- using composite filament in 3D printers to create finished products.

In the first stage, a composite filament is created using extrusion, in which the matrix is a polymer and the reinforcing material is crushed short carbon fibers (Fig. 2).

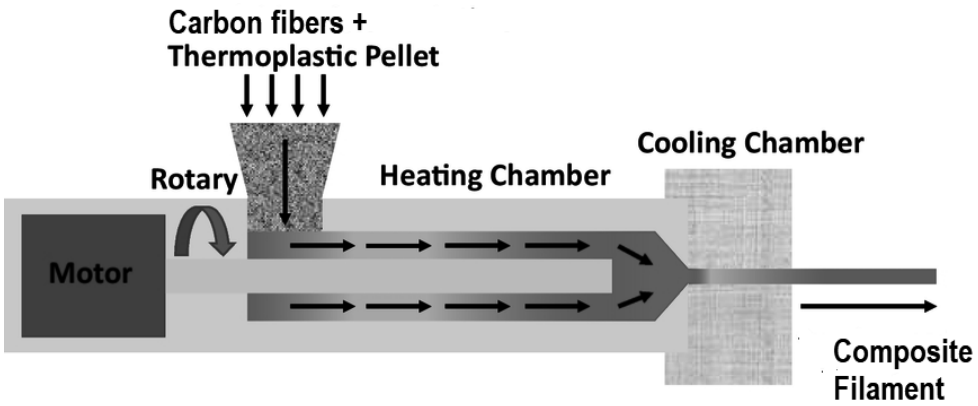

Fig. 2. Scheme of extrusion of composite filament in an extruder [7]

This process includes the following steps:

- raw material preparation. A polymer (e.g. PLA, ABS, PETG, PA or PEEK) and shredded carbon fiber are mixed in certain proportions. The composition of the components changes the final balance between strength, stiffness and processability of the filament;
- extrusion. A mixture of polymer and carbon fibers is fed to an extruder, where it is melted and evenly mixed. The extrusion process ensures a uniform distribution of fibers in the polymer matrix;
- filament formation. The molten material is extruded through a nozzle, cooled and cut or wound into coils for further use. The finished filament has high mechanical properties due to carbon fiber reinforcement.

In the second stage, the composite filament is used in the additive manufacturing process on 3D printers (Fig. 3).

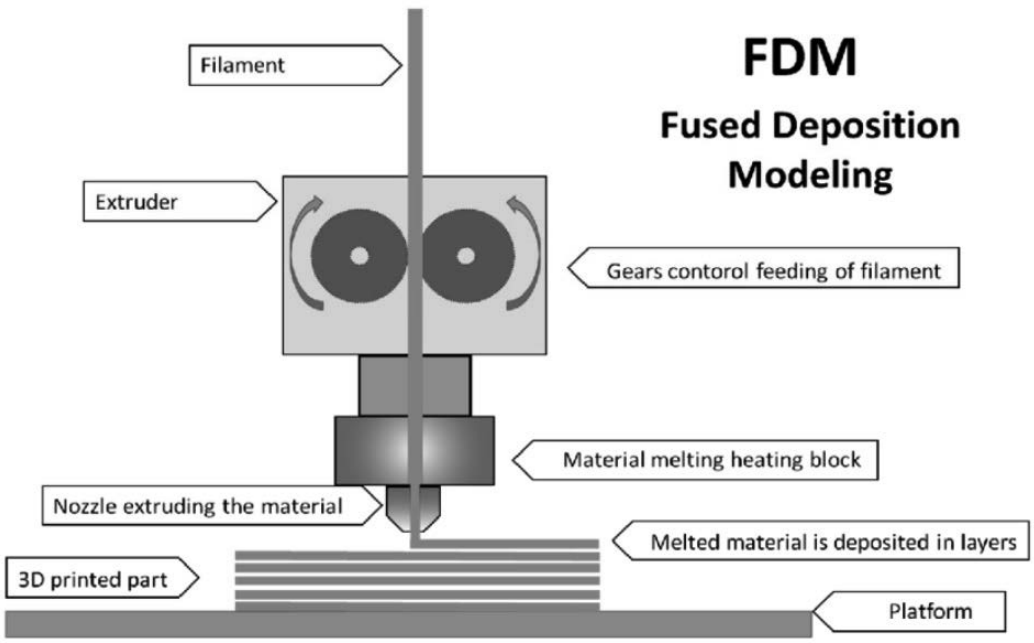

Fig. 3. Scheme of extrusion of composite polymer in a 3D printer using technology [8]

This process involves the following steps:

- filament preparation. The composite filament is loaded into a 3D printer equipped with an extruder capable of working with materials with a high melting point;
- printing of the finished product. The filament is fed to the extrusion head, where it is melted and applied layer by layer to the platform according to the given digital model. Thanks to carbon fiber reinforcement, the parts receive increased strength and rigidity;
- the finishing process. The finished product undergoes minimal post-processing, if necessary (sanding, painting, etc.).

This technology is relatively new and requires further development, including improvements in equipment and processes. To ensure optimal distribution of carbon fiber in the polymer matrix and achieve excellent mechanical properties, extruders with specialized features such as improved mixing ability and the ability to work with high-viscosity materials are required. It also requires the creation of 3D printers with extruders capable of maintaining stable temperatures up to 400 °C and ensuring high-precision printing from composite materials.

In addition, an innovative approach to the development of consumables and optimization of technological processes will be key factors in expanding the application of this technology in various industries.

One of the significant drawbacks of using the technology in question is the two-stage melting of the polymer. In the first stage, during the manufacture of the composite filament by extrusion, the polymer is melted to evenly mix with the carbon fibers. In the second stage, when using this filament in a 3D printer, the polymer is melted again to create the finished product. This double heating cycle can significantly affect the properties of the polymer.

Consequences of two-stage melting:

- polymer degradation. High temperatures and repeated heating can lead to thermal degradation of the polymer matrix, which deteriorates its mechanical and chemical properties;
- reduction of adhesion characteristics. Loss of chemical activity at the molecular level can negatively affect adhesion between the polymer matrix and carbon fibers;
- reduced strength. Remelting can reduce the uniformity of the material, which leads to reduced strength and durability of the finished product.

To eliminate two-stage melting, a new technology for processing composite polymers by extrusion is proposed, which uses 3D printers equipped with screw extruders (Fig. 4).

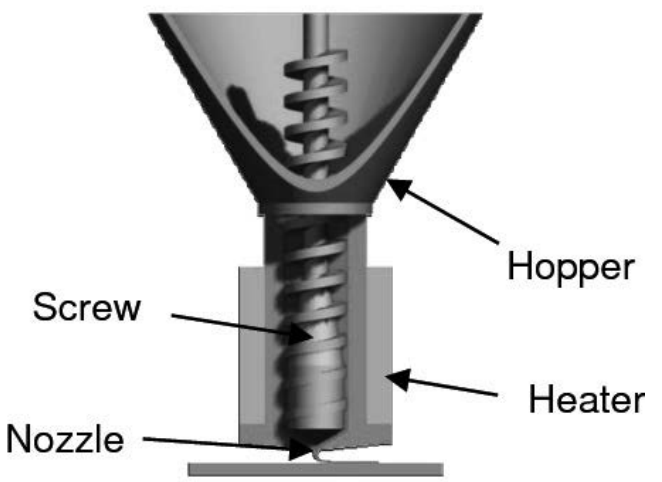

Fig. 4. Scheme of a 3D printer with a screw extruder [9]

Such devices allow processing the polymer + carbon fiber mixture simultaneously, bypassing the stage of preliminary production of the composite thread.

This technology has the following advantages:

- with one-step melting, the material is heated and extruded during the printing process, which eliminates the need for re-melting the polymer and allows it to preserve its original properties;
- reduction of thermal degradation due to lower thermal exposure, which allows preserving the chemical cellularity of the polymer matrix, improving its mechanical characteristics and increasing adhesion to carbon fibers;
- saving resources by eliminating one technological stage, which reduces electricity costs;
- using a screw extruder allows you to work with a wider range of materials, including high-viscosity polymers and specialized compositions.

The principle of operation of a 3D printer with a screw extruder for processing a "polymer + carbon fiber" mixture includes several main stages.

1. Raw material loading. A composite mixture consisting of granulated polymer (e.g. PLA, ABS, PETG, PA, PEEK) and shredded carbon fiber is fed into the printer hopper. The ratio between polymer and fiber can be selected depending on the properties requirements of the final product.

2. Feeding the prepared composite material. The mixture is fed into the screw extruder by gravity or forced feeding. The screw rotates, pushing the material into the melting zone.

3. Heating and melting. In the melting zone, the material is heated to a set temperature. The temperature is regulated depending on the polymer used for plastics: PLA — 180–220 °C; ABS — 210–250 °C; PEEK — up to 400 °C.

The screw ensures uniform mixing of the polymer matrix with carbon fiber, which allows achieving homogeneity of the composition.

4. Extrusion. The molten material is extruded through the extruder nozzle, forming a thin layer of melt, which is applied layer by layer to the worktable. Due to the high temperature and uniform distribution of fibers, high strength of the layers and good adhesion between them are ensured.

5. Product formation. The software controls the movement of the extrusion head and platform, accurately following the parameters set in the digital model of the product. Layer-by-layer printing allows you to create products with high geometric accuracy and complex shapes.

6. Cooling and stabilization. After each layer is applied, the molten material is cooled. This ensures dimensional stability and accuracy of the finished product.

The technology of processing raw materials using a screw extruder has a number of features that make it effective and versatile. First, it provides direct processing of raw materials, which eliminates the need to manufacture an intermediate filament due to the simultaneous use of polymer granules and carbon fibers. Second, this technology is extremely efficient, since the elimination of the pre-extrusion stage significantly reduces the cost of time, energy and resources. One-step melting ensures the preservation of the primary physical and mechanical properties of the polymer, while carbon fiber adds strength and rigidity to the final product. Another advantage is the versatility in the choice of materials: the printer can work with a variety of polymer matrices, including high-temperature polymers, which expands the range of its applications in various industries.

Manufacturing finished products using solid carbon fiber is an innovative technology that provides high strength, lightness and durability of final products (Fig. 5). This technology

is based on the introduction of solid carbon fiber into a polymer matrix during additive manufacturing (3D printing). The process consists of several stages.

1. Preparation of materials.

Continuous carbon fiber. A continuous filament is used that maintains its integrity and strength. The fiber is supplied in the form of bobbins or rolls.

Polymer matrix. Thermoplastic polymers such as PLA, PETG, PA, PC, or high-temperature materials such as PEEK and PEKK are used. The material provides fiber support and additional adhesion.

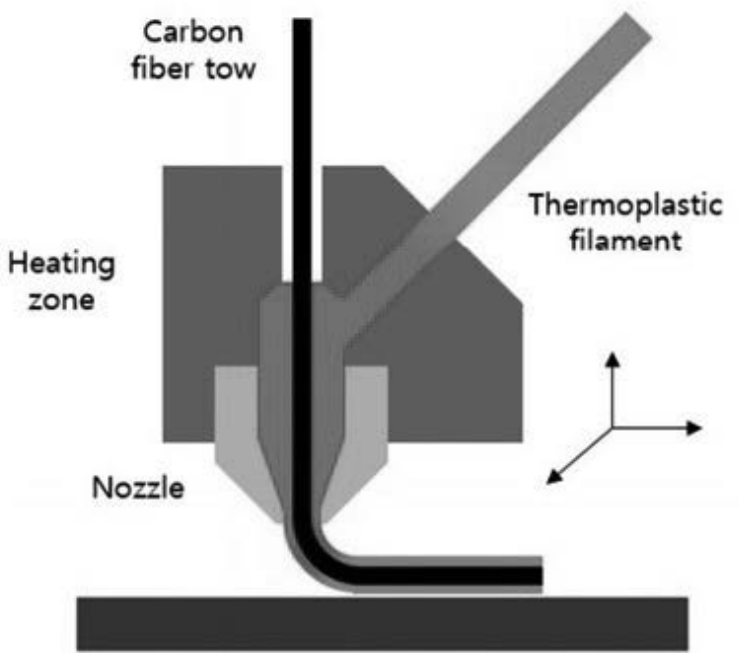

Fig. 4. Scheme of introducing carbon fiber into a polymer matrix under 3D printing time [10]

2. Material feeding. Carbon fiber and polymer are fed separately through different channels of the extrusion head. The printer is equipped with two feeding systems: one for feeding continuous carbon fiber, and the second for melting and feeding polymer.

3. Layering. The first extruder channel melts the polymer and feeds it to the work platform to create the base layer. The second extruder channel simultaneously integrates continuous carbon fiber into the polymer melt. The fiber acts as a reinforcing material, giving the product increased strength and stiffness.

4. Product formation. The printer deposits molten polymer layer by layer, integrating continuous carbon fiber into the structure of each layer. Precise software control ensures optimal fiber orientation according to the load directions.

5. Cooling and stabilization. Each layer is cooled to ensure the stability of the shape and strength of the finished product. It undergoes final processing, if necessary.

The technology of using continuous carbon fiber has a number of advantages that make it unique and promising in various industries. The main advantage is the increased strength and rigidity of products. Thanks to the use of continuous carbon fiber, the material retains its integrity and does not break into fragments, which allows it to withstand significant mechanical loads. In addition, the low density of the material ensures the lightness of finished products,

which is critically important in industries where weight restrictions are of key importance, for example, in aviation or automotive engineering.

The technology also demonstrates high adaptability. During printing, the fiber orientation can be optimized depending on the location of load zones in the structure, which significantly increases the efficiency of material use. In addition, the use of continuous fiber allows for a reduction in the volume of the polymer matrix, which not only reduces the weight of the product, but also reduces its material consumption and, accordingly, its cost.

However, the technology has certain drawbacks and challenges. One of the key ones is the complexity of the equipment. 3D printers to implement this technology require specialized extrusion heads with two feed channels: for the polymer matrix and for carbon fiber. This significantly complicates the design of the equipment and increases its cost. Another challenge is technological limitations, in particular the need for precise fiber orientation, which requires the use of sophisticated software and high-precision settings.

It is also worth noting the high cost of materials. Solid carbon fiber and high-performance polymers used as a matrix are expensive, which limits the mass introduction of this technology into production. However, given the advantages that the technology provides and the constant development of equipment and materials, it has significant potential and can become one of the foundations in high-tech industries.

4. CONCLUSIONS

As a result of the research, the following conclusions can be drawn:

There is a limited number of manufacturers of high-temperature carbon fiber reinforced plastics and specialized 3D printing equipment for the technologies in question on the market. This creates certain limitations for consumers in choosing available solutions. However, it also opens up significant prospects for the development and implementation of their own innovative products, such as reinforced plastics and specialized 3D printers to work with them.

To implement 3D printing with high-temperature plastics reinforced with carbon fibers, specialized 3D printers are required that can heat the extruder nozzle to 400 °C. Such printers must have reliable temperature control systems, a reinforced extrusion system, and reinforcing fiber feeding mechanisms to ensure printing accuracy and stability. On the other hand, printing with plastics filled with shredded fibers can be carried out even on consumer-level printers if a high-temperature extruder and a wear-resistant nozzle are installed. For example, nozzles made of stainless steel, titanium, as well as synthetic corundum or sapphire inserts can be used to work with such materials, which ensure durability and accuracy.

Given the promising materials and technologies based on the use of carbon fiber reinforced plastics, it is advisable to develop new 3D printing technologies that will include advanced extrusion systems, fiber feeding systems, and adaptive software. This will expand the possibilities of working with materials, improve product quality, and reduce production costs.

The use of high-temperature plastics reinforced with continuous carbon fibers is promising in industries such as aviation, automotive, construction and medicine. In particular, the ability to create lightweight, strong and heat-resistant parts opens up new horizons for the use of such materials in critical structures. In addition, the development of 3D printing technologies with short fibers can become the basis for the implementation of cost-effective solutions in industries with less stringent requirements for materials.

Thus, the analysis of the market situation and technical requirements for equipment indicates the significant potential of the technologies under consideration and the need for their further improvement. This will allow expanding the application of high-tech materials and strengthening competitive positions in the global additive manufacturing market.

ACKNOWLEDGEMENTS

The work was created as a result of the project as part of project based learning - PBL, in the 11th competition under the Initiative of Excellence - Research University, Silesian University of Technology, Gliwice, Poland.

The publication is the result of cooperation within the Visegrad Scholarship Program 2024/2025.

BIBLIOGRAPHY

1. Kovalenko K.G., Sokolsky O.L., Sivetsky V.I. Extrusion formation polymeric molding products taking into account viscoelastic properties: monograph. Kyiv: Igor Sikorsky Kyiv Polytechnic Institute Sikorsky, 2018. 108 p.
2. Suberlyak O.V., Bashtanyk P.V. Technology of processing of polymeric and composite materials: a textbook for students of universities. Ed. 2nd, supplemented. Lviv: Rastr-7, 2015. 454 p.
3. Polishchuk AND., Polishchuk O., Lisevich S., Urbanyuk E., Rubanka M. Compositional mixtures on basis synthetic polymers and fillers and equipment for 3D printing by them. Bulletin Khmelnytskyi national University. Technical science 2023. No. 2. Part 1. WITH. 252-262.
4. https://en.wikipedia.org/wiki/Carbon_fibers [access: 12.01.2025].
5. http://surl.li/soxgak [access: 12.01.2025].
6. Polishchuk O. S., Zozulya P. F., Polishchuk A. O. Generalized classification filaments for 3D printing. Bulletin Khmelnytskyi national University. 2017. No. 6. P. 51–59.
7. Dongyang Cao. Enhanced buckling strength of the thin-walled continuous carbon fiber–reinforced thermoplastic composite through dual coaxial nozzles material extrusion process. The International Journal of Advanced Manufacturing Technology. 2023. 128(3-4):1-11. DOI :10.1007 /s00170-023-12014-8.
8. Robert E. Przekop 1, Ewa Gabriel, Daria Pakuła and Bogna Sztorch. Liquid for Fused Deposition Modeling Technique (L-FDM) - A Revolution in Application Chemicals to 3D Printing Technology: Color and Elements. Appl. Sci. 2023, 13, 7393. https://doi.org/10.3390/app13137393.
9. H. Valkenaers, F. Vogeler, J. Kruth. Screw extrusion based 3D printing, a novel additive manufacturing technology. Engineering, Materials Science 2013.
10. https://www.unibw.de/leichtbau-en/forschung/faserverbundwerkstoff_technologien [access: 12.01.2025].

TalentDetector
31th January 2025
Gliwice, Poland
DEPARTMENT OF ENGINEERING MATERIALS AND BIOMATERIALS
FACULTY OF MECHANICAL ENGINEERING
SILESIAN UNIVERSITY OF TECHNOLOGY
INTERNATIONAL STUDENTS SCIENTIFIC CONFERENCE

Design and construction of a hydroponic chamber

Grzegorz Pośpiech[a], Estera Nawrocka, Paweł Kruczyński, Monika Kruczyńska, Karolina Hanzlik, Aneta Kania[b], Magdalena Polok-Rubiniec, Anna Włodarczyk-Fligier

[a] Student of Mechanical Engineering at the Faculty of Mechanical Engineering at the Silesian University of Technology
email: gp307818@student.polsl.pl
[b] Silesian University of Technology, Faculty of Mechanical Engineering, Department of Engineering Materials and Biomaterials
email: aneta.kania@polsl.pl

Abstract: Purpose of the following article is to describe the proces of designing and building of a hydroponic chamber. Made of easily accessible materials, including aluminum profiles for frame, MDF panels for external walls, equipped with climat control systems based on sensors to monitor proper development of cultivated plants.

Keywords: hydroponics, hydroponic chamber, sustainable agriculture

1. INTRODUCTION

Hydroponics is a method of growing plants that takes advantage of the fact, that plants are among the few organisms that can synthesize all the required metabolites from inorganic ions, water and CO_2 using the energy captured from the sun [1]. The growing interest in this field field is caused by from numerous advantages, including the ability to control nutrient levels in cultivated plants, independence from atmospheric conditions, more efficient water use, and the possibility of growing plants in areas with poor soil quality. We can identify various methods of hydroponic cultivation (Fig. 1) [2]:

- wick system hydroponics – the only method, that does not require additional pumps, water and nutriens are transported through pipes with the use of capillary acrion (process of a liquid flowing in a narrow space without the assistance of external forces),
- drip system – a network of pipes or hoses with holes or sprinklers delivers water in droplets directly to the plant. Pressure is achieved using either a pump or a gravity-fed system, where the water reservoir is placed higher than the plants,
- ebb and flow (or flood and drain) – plant roots, located in a growing medium, are rinsed at specific time intervals. Water and nutrients that are not absorbed return to the reservoir,
- deep water cultivation (DWC) – plants are placed on a floating platform above the water level. A water pump is necessary, as well as an air pump to supply oxygen to the roots. The pH,

nutrient concentration, oxygen levels and salinity must be carefully monitored to prevent algal or mold growth in the reservoir,

- nutrient film technique (NFT) – only the bottom of the roots has access to water and nutrients, while the upper part of the roots remains exposed to air, ensuring constant oxygen availability,
- aeroponics – in the closed chamber, a nutrient-rich water solution is periodically sprayed onto the hanging roots, providing them with essential nutrients and hydration while maximizing oxygen exposure.

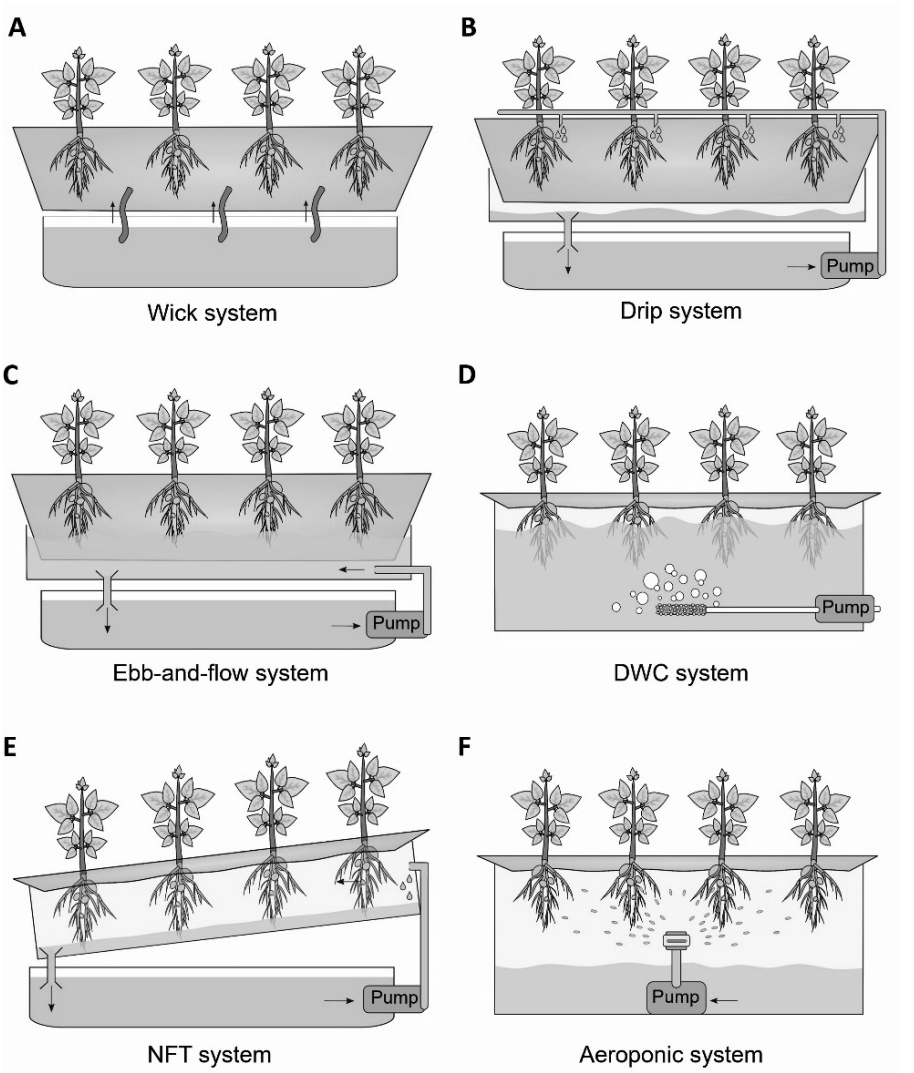

Figure 1. Types of hydroponic systems: a) wick system, b) drip system, c) ebb-and-flow system, d) deep water cultivation (DWC) system, e) nutrient film technique (NFT) system, f) aeroponic system [2]

Our chamber enables DWC system and aeroponic system.

2. DESIGN OF THE CHAMBER

The chamber, as predicted and modeled using Autodesk's Fusion 360 software, has dimensions of 1 m x 1 m x 1 m, which were successfully achieved in reality (Fig. 2).

Figure 2. 3D model of the chamber

3. CONSTRUCTION OF THE CHAMBER

The space designated for plant growth measures 1 m x 1 m x 0.8 m. The chamber's frame was constructed using 20 mm x 20 mm aluminum profiles, and the interior was tightly sealed with foil joined with glue, for hermetic closure. The profiles were connected with foil using 3D-printed connectors, while the exterior walls were build with MDF panels. Access to the inside of the chamber is possible through inspection doors.

The inside partition of chamber is equipped with (Fig. 3):

- full-spectrum LED stripes,
- LED 20 W (5, 6, 7, 8),
- ultrasound height sensor (3),
- two temperature sensors to monitor and verify consistent temperature inside of the chamber (3, 6),
- pressure sensor (3,7),
- water level sensor (7),

– water resistence sensor (7),
– atomizer (7),
– humidity sensor (6),
– oxygen sensor (6),
– CO_2 sensor (6).

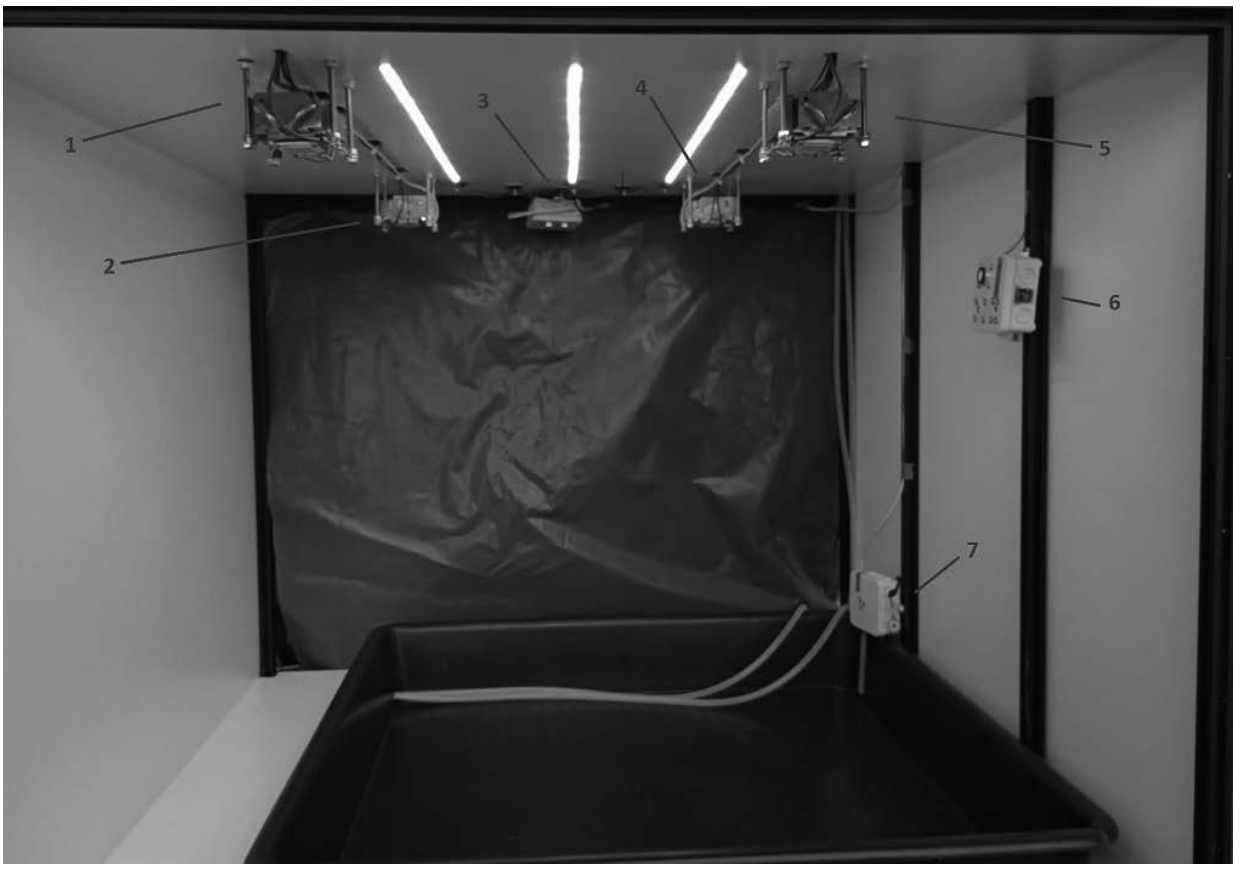

Figure 3. Inside view of the hydroponic chamber

Electrical cabinet

The upper part of the chamber, isolated from moisture from the lower section, is designated for electrical components, such as (Fig. 4):
– sensor connectors (1),
– main fuze (2),
– 12V power supply (3),
– 5V power supply (4),
– air pump (5),
– fertilizer pumps (6),
– water pump (7),
– controller – Arduino (8),
– fuze (9),
– energy meter (10).

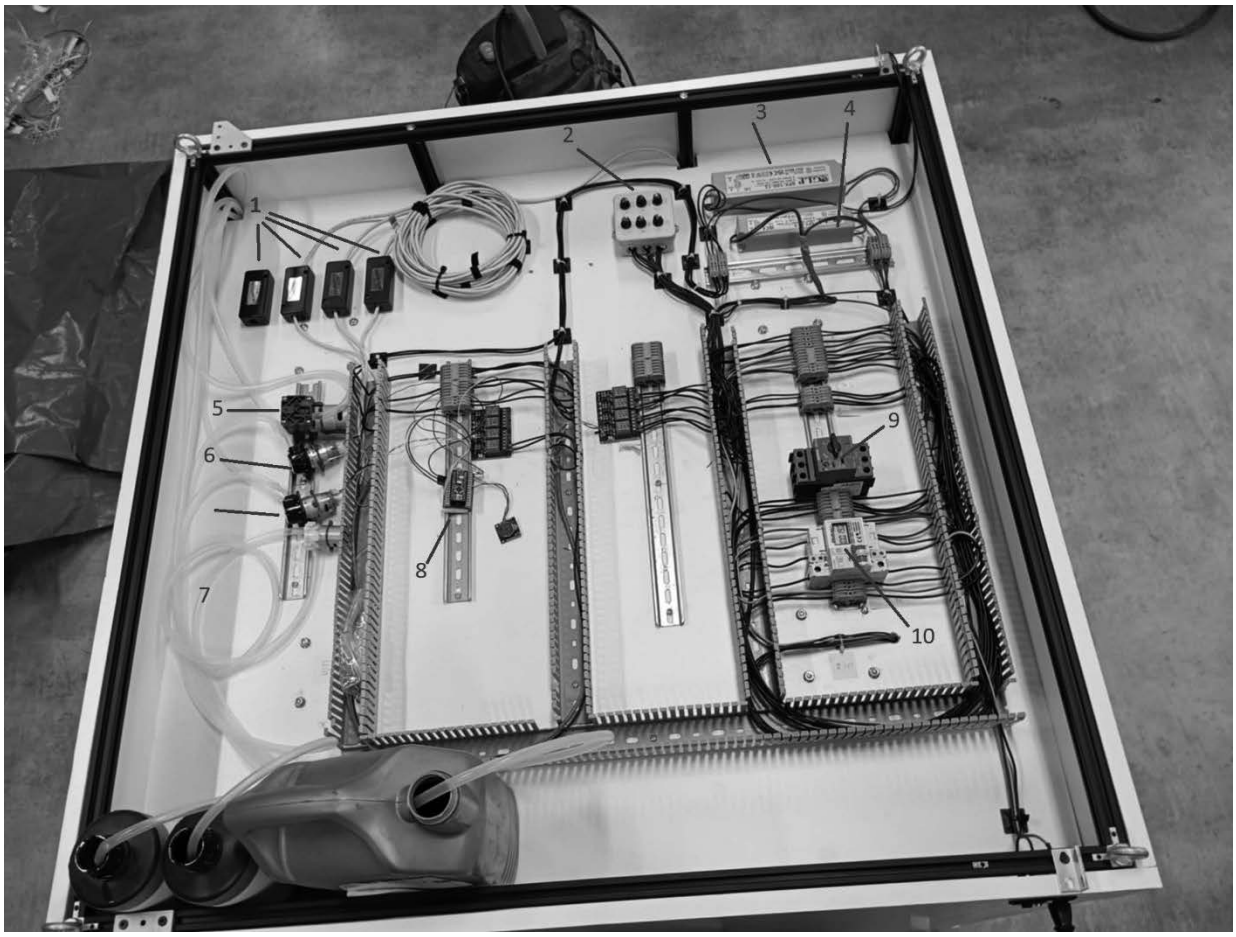

Figure 4. Electrical cabinet of the hydroponic system

4. CLIMATE CONTROL SYSTEMS

Hydration system

The water and nutrient reservoirs can be filled from the outside, without exposing the plants to the external conditions outside the chamber.

Lighting

We can control the duration of plant exposure to light along with the light wavelength in a way that mimics the day cycle and seasonal changes of the plant's natural habitat, which is achieved by using a full-spectrum LED stripes.

Ventilation and climate control

Using a fan, we simulate gentle wind, which is important for strengthening the growing plants and balancing the temperature and humidity throughout the chamber.

Plant containers

The cultivated plant will be placed in a styrofoam board, with niches filled with rocks, floating on the water surface. During cultivation in the DWC system, this setup maintains the appropriate distance between the plant and the nutrient-water solution.

Automation

Control is managed through an Arduino controller. The program cycle includes reading sensor data and activating the appropriate actuators – pumps, lights and the atomizer.

5. CONCLUSION AND PERSPECTIVE

The construction of a hydroponic chamber provides an efficient solution for plant cultivation in controlled environments. This article outlined essential components, including the irrigation system, lighting and automation, as well as process of building the chamber. One of the key advantages of this system is its potential for development. The chamber can be enlarged and addition of more precise sensors can improve quality along with quantity of nutrients in cultivated plants.

BIBLIOGRAPHY

1. S.C. McDowell, G. Akmakjian, C. Sladek, D. Mendoza-Cozatl, J.B. Morrissey, N. Saini, R. Mittler, I. Baxter, D.E. Salt, J.M. Ward, J.I. Schroeder, M.L. Guerinot, J.F. Harper, Elemental concentrations in the seed of mutants and natural variants of Arabidopsis thaliana grown under varying soil conditions, PLoS One, 6/8 (2013) 63014.
2. S. Rajendran, T. Domalachenpa, H. Arora, P. Li, A. Sharma, G. Rajauria, Hydroponics: Exploring innovative sustainable technologies and applications across crop production, with Emphasis on potato mini-tuber cultivation, Heliyon, 10/5 (2024) 26823.

This paper is the result of a Project Based Learning (PBL) entitled Development of a chamber for hydroponic plant cultivation and comparison of its efficiency to natural cultivation.

TalentDetector
31th January 2025
Gliwice, Poland
DEPARTMENT OF ENGINEERING MATERIALS AND BIOMATERIALS
FACULTY OF MECHANICAL ENGINEERING
SILESIAN UNIVERSITY OF TECHNOLOGY
INTERNATIONAL STUDENTS SCIENTIFIC CONFERENCE

History of sound recording - from the phonograph to the digital era

Katarzyna Ptasznik[a], Bogusław Zięboweicz[a], Anna Zięboweicz[b]

[a] Faculty of Mechanical Engineering, Department of Engineering Materials and Biomaterials, Silesian University of Technology, Konarskiego 18A , 44-100 Gliwice, Poland;
email: kp309682@student.polsl.pl; boguslaw.ziebowicz@polsl.pl
[b] Faculty of Biomedical Engineering, Department of Biomaterials and Medical Device Engineering, Silesian University of Technology, Roosevelta 40, 41-800 Zabrze, Poland;
email: anna.ziebowicz@polsl.pl

Abstract: The article presents the history of sound recording, which began with Thomas Edison's phonograph (1877), through Emil Berliner's gramophone and gramophone records (1887), cassette tapes and cassettes (second half of the 20th century). Its culmination in the 21st century were digital audio carriers - CD, MP3, streaming. Each stage has developed accessibility and sound quality.

Keywords: sound recording, vinyl records, turntable, gramophone, phonograph, autophonograph, magnetic tape, compact disc, MP3, streaming, digital platform, artificial intelligence

1. INTRODUCTION

Sound recording is one of the most important inventions in the history of mankind, which had a huge impact on the development of culture, music, science and technology. A breakthrough moment, in which sound became material, revolutionized the way we transmit and receive information. Before the invention of recording devices, sound was only a fleeting phenomenon – it lasted only a moment and disappeared after a while. Once sounds were recorded on various media, people gained the ability to reproduce and transmit them many times, which was of great importance for the development of art, education and science.

Sound recording technologies have changed the way knowledge and emotions are transmitted. In the case of music, they allowed for the recording of sounds in a form that could reach a wide audience, regardless of place or time. For science, sound recording has enabled more precise studies of acoustics and sound engineering, and for technology, it has opened the door to further innovation, from playback devices to modern digital systems.

The aim of this article is to present the main stages of the development of sound recording, showing the most important inventions and technologies that marked the subsequent stages of this process. Both precursor mechanical devices and breakthrough inventions that have led to the development of digital technologies.

2. THE BEGINNINGS OF SOUND RECORDING. PIONEERING INVENTIONS

Édouard-Léon Scott de Martinville - phonoautograph

The first device to record sound was the phonoautograph, invented in 1857 by Édouard-Léon Scott de Martinville. It recorded sounds on glass plates covered with soot, creating a visual record of acoustic waves. Although it did not allow for their reproduction, it was an important foundation for further research in this field. (Fig. 1) [1,4-8]

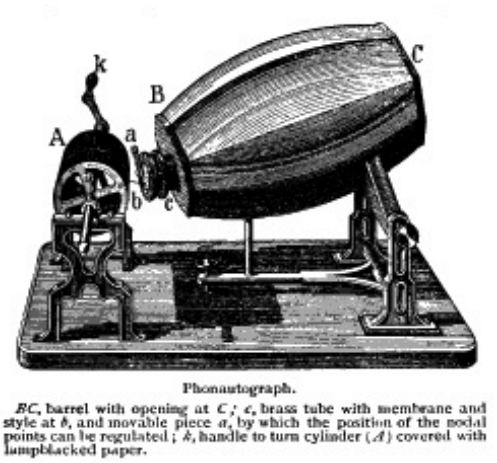

Phonautograph.

BC, barrel with opening at *C*; *c*, brass tube with membrane and style at *b*, and movable piece *a*, by which the position of the nodal points can be regulated; *k*, handle to turn cylinder (*d*) covered with lampblacked paper.

Figure 1. Phonoautograph, Édouard - Léon Scott de Martinville [8]

Thomas Edison - phonograph

A breakthrough in sound recording technology was Thomas Edison's phonograph from 1877. This device allowed for recording and reproducing sound with a needle gouging grooves on a cylinder covered with a thin layer of tin. The first recording was the rhyme "Mary had a little lamb". The phonograph not only changed the way sounds were recorded, but also revolutionized the entertainment and education industry. (Fig. 2) [1,4-8]

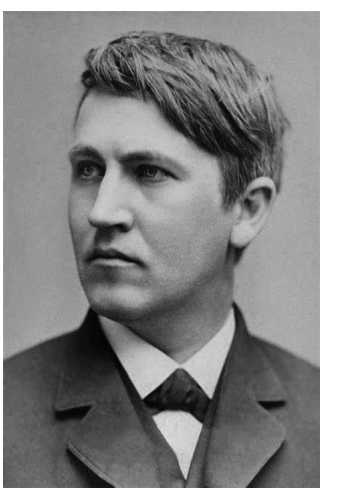

Figure 2. Phonograph - Thomas Edison [8]

Emil Berliner - gramophone

In 1887 Emil Berliner invented the gramophone, which introduced the use of flat plates instead of cylinders. Initially made of lacquered cardboard and later shellac, these records were more durable and easier to produce, which contributed to the development of the music industry. Berliner's invention enabled the mass production of recordings, changing the way we listen to music and laying the foundations for modern phonography. (Fig. 3) [1,4-8]

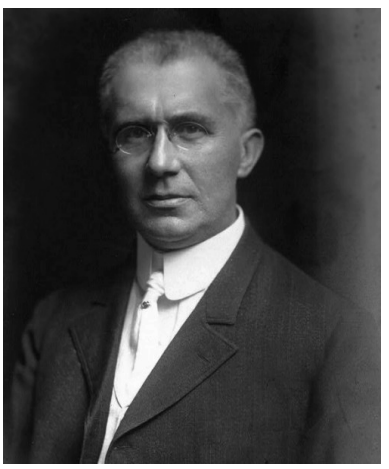

Figure 3. Gramophone - Emil Berliner [8]

2.1 The development of sound recording: From phonoautograph to turntable

Phonoautograph – the first sound recording

The first experiments related to sound recording date back to the mid-nineteenth century, when Édouard-Léon Scott de Martinville, a French inventor, created a device called the phonoautograph, which allowed for the visual recording of acoustic waves. The phonoautograph, invented in 1857, was based on a mechanism in which a sound wave caused a diaphragm to vibrate, which moved a stylus recording a trace on a cylinder covered with soot. This device, although technologically advanced, had its limitations – it could not reproduce the recorded sound. It was merely a graphic record that could be seen but not heard.

However, the phonoautograph became an important step in the history of sound recording technology, as it allowed for the first mechanical recording of sounds. Scott de Martinville drew inspiration from the structure of the human ear, which he studied in detail. Although the invention did not have the ability to play recorded sounds, its usefulness was appreciated only in the 21st century, when in 2008, using modern computer technology, it was possible to recreate one of the oldest recordings, which dates back to 1860. It contained a fragment of the French folk song "Au Clair de la Lune", marking a breakthrough moment in the history of sound recording. [1,4-8]

Phonograph – recording and playing back sound

The year 1877 brought another revolution in sound recording technology. Thomas Edison, an American inventor, demonstrated the phonograph – a device that could both record and reproduce sound. The phonograph was based on a mechanism in which sound vibrations set the

membrane in motion, and the needle on this membrane carved grooves on a thin tin foil, applied to a rotating roller. The reproduction process consisted of the needle passing through these grooves again, which caused the diaphragm to vibrate, which in turn was converted into sound coming out of the horn.

Edison's phonograph, patented in 1878, was the first device capable of playing recorded sounds. The initial version used tin foil, which, however, had its disadvantage – it was not very durable and was not suitable for mass production. In the following years, thanks to the work of Charles Tainter and Chichester Bell, the phonograph gained new improvements – tin foils were replaced with more durable wax rollers, and later celluloid rollers. Thanks to these changes, it has become possible to mass-produce copies of recordings, which was of great importance for the development of the phonographic industry. Edison's invention was a milestone in the history of sound recording, setting new possibilities for both in the field of music and communication. [1,4-8]

Turntable – the evolution of sound recording

The next important step in the development of sound recording technology was the invention of the gramophone by Emil Berliner in 1887. Although the phonograph was revolutionary, it had its limitations – it used cylinders, which were relatively expensive and difficult to store. Berliner, wanting to simplify the whole process, created a turntable that used records – instead of cylinders – to store recordings. Originally, the plates were made of zinc or glass covered with a layer of wax, and later more durable materials such as shellac began to be used.

The turntable grew in popularity because it was more economical and practical than the phonograph, and its records are easier to store. Initially, the turntable was treated as a toy device, but it quickly gained respect when improvements such as Eldridge Johnson's work on recording quality improved the sound. Soon, the turntable became the primary device for playing music, opening the way for the mass production of gramophone records.

In the 90s of the nineteenth century, turntables were already available on the market, and subsequent innovations. In their mechanisms of operation, including an improved drive mechanism and modern needles for sound reproduction, contributed to the further popularization of this device. An important moment was also the standardization of the plate format at the beginning of the 20th century, when the rotational speed was set at 78 rpm, which became an international standard. The turntable has become not only a device for playing music, but also one of the key tools for the development of the music industry, ushering in a new era of in the history of music and sound.

3. THE ANALOGUE ERA

3.1 Magnetic tape - the beginning of a new era (1898-1930)

The first steps towards recording sound with magnetic tape were taken as early as the end of the 19th century. The first invention in this field was Valdemar Poulsen's telegraphon, patented in 1898. This device, using a steel wire, allowed for the recording of sound in a magnetic form. This was the first step in the later development of magnetic tape, which was to revolutionize the music and audio industry.

In the 1930s, this technology was perfected by German engineers, which allowed the creation of the first real magnetic tapes, which gained popularity in Europe. These tapes were used in radio, television and in professional sound recording in studios. Magnetization allowed sound to be stored on materials with high durability, which was a huge advantage over earlier technologies, such as gramophone records or phonographs, which were susceptible to damage.

This technology has revolutionized the way sound is recorded and stored, opening the way to a new era in music production and sound broadcasting. [2-4]

3.2 The 40s and 50s - tape recorders and cassettes

In the 40s of the twentieth century, the development of magnetic tape technology broke the barrier of professional recording studios, becoming an accessible solution also to a wider circle of users. At the beginning of this decade, tape recorders were still large, finely complex devices, but they quickly began to gain popularity thanks to improvements in sound quality and the introduction of new, compact models.

At the same time, in the 50s of the twentieth century, tape recorders became more accessible, and mobile devices made it possible to record sound at home. In 1953, BASF introduced the first professional tape recorders, which began to dominate the recording studios. Magnetic tape allowed for multiple recording and playback of material without loss of sound quality, which was a big advantage compared to earlier technologies.

One of the breakthrough moments in the history of sound recording was the introduction of cassette tapes in 1963 by Philips. Cassettes have become easy to use and available to the general public. Thanks to them, portable recording devices and sound reproduction have become popular among the mass audience, changing the way in which how people listened to music and recorded sound. In 1965, thanks to an improved tape recorder, musicians and reporters were able to transfer their magnetic tape recordings in high quality, making it easier to work in the field and in the studio.

One of the breakthrough moments in the history of sound recording was the introduction of cassette tapes in 1963 by Philips. Cassettes have become easy to use and available to the general public. Thanks to them, portable recording devices and sound reproduction have become popular among the mass audience, changing the way in which how people listened to music and recorded sound. In 1965, thanks to an improved tape recorder, musicians and reporters were able to transfer their magnetic tape recordings in high quality, making it easier to work in the field and in the studio. [2-4]

3.3. Vinyl records (since 1948)

Simultaneously with the development of tape recorders, in 1948 LP (Long Play) records were introduced, which constituted a new quality in the world of vinyl sound carriers. Vinyl records have revolutionized the music market by offering a much longer playtime than traditional shellac records, which has made them the standard in the music industry.

Vinyl records were produced in the pressing process, thanks to which it was possible to produce and distribute them on a mass scale. With the development of pressing technology and the improvement of playback quality, LPs became a symbol of the 50s-70s, being the foundation of the musical culture of that era. The sound quality, compared to magnetic tape, was more natural and analogue, which gave the music a fuller, warm character. [6]

Vinyl records, despite the development of new technologies, remain an icon and a classic among music lovers, gaining popularity among collectors and fans of analogue sound. To this day, they are a symbol of the musical culture of the past decades.

3.4. Multitrack recorders (50s and 60s)

Multitrack recorders are one of the most revolutionary inventions in the history of music production. In the 50s and 60s of the twentieth century, the ability to record multiple soundtracks at the same time was introduced, which revolutionized the way of recording and music production. Thanks to this, musicians and music producers gained the opportunity to work on several tracks in one recording, which made it possible, for m.in, to create sound effects, mix instruments and create complex musical arrangements.

Multitrack recorders became an essential tool for professional recording studios, especially for bands like The Beatles, who used these technologies to create their legendary recordings. The recording of multiple tracks also allowed for better matching and mixing of sound, which allowed for a fuller extraction of the artistic and technical potential of the music. [2-4]

4. DIGITAL TECHNOLOGY [9,10]

4.1. Getting started with digitizing audio

The 70s of the twentieth century marked the beginning of the digitization of sound recording. The introduction of Pulse Code Modulation (PCM) made it possible to record audio in digital form, which allowed for higher sound quality and easier data storage. The first experimental digital devices began to appear at this time, but it was later technologies that revolutionized the music industry.

4.2. Compact Discs (CD, 1982)

In 1982, compact discs (CDs) were introduced, which became the new standard in storing and playing music. Thanks to the collaboration between Sony and Philips, CDs offered higher sound quality and longer media durability compared to analogue vinyl and magnetic tapes. CDs popularized digital sound recording and became the primary medium for the music industry, which resulted in the slow disappearance of magnetic tapes.

4.3. The MP3 era and the music storage revolution (1990-2000)

In the 90s of the twentieth century, compression algorithms, such as MP3, allowed large amounts of music to be stored on small media, such as hard drives and CDs. The revolution in music storage was started by MP3 players, including the iPod in 2001, which allowed you to listen to music on the go. This era marked the beginning of digital mobility and changed the way we consume music.

4.4. Streaming and the development of digital platforms

With the rise of the internet, streaming has become the most popular way to listen to music. Services such as Spotify, Apple Music, and YouTube have become major music distribution

platforms. The subscription model, in which users pay to access content instead of owning it, has changed the way people consume and consume music.

5. MODERN SOUND RECORDING TECHNOLOGIES [3-9]

5.1. Cloud Recording and Digital Collaboration

Modern technologies now allow sound recordings to be stored in the cloud, enabling remote collaboration in music production. This change has transformed the way recording studios operate, allowing artists and producers to create music regardless of their location.

5.2. Artificial intelligence and sound reconstruction

Artificial intelligence (AI) algorithms are now being used to clean up old recordings, remove interference, and reconstruct missing fragments. AI also automates the mixing and mastering process, allowing for faster and more precise preparation of musical material.

5.3. Surround sound and 3D audio technologies

Binaural recording technology and Dolby Atmos have revolutionized spatial audio, allowing for the creation of immersive soundscapes used in virtual reality, video games, and cinema. These technologies enable listeners to experience sound in a three-dimensional space, enhancing the sense of immersion and realism. Spatial sound creates a more lifelike and engaging listening experience, positioning sounds in a 360-degree field, which is increasingly becoming a key trend in modern audio production. This advancement is transforming how audiences experience music, film, and interactive media.

6. SUMMARY AND PERSPECTIVES

The journey of sound recording has come a long way, from the early mechanical inventions like the phonograph to contemporary digital technologies that enable sound storage in the cloud and the creation of virtual sound experiences. The advancements in sound quality and the accessibility of media have revolutionized how we consume music and sound, significantly impacting culture and education. As we move forward, the integration of emerging technologies like artificial intelligence, 3D audio, and cloud-based collaboration continues to shape the future of sound recording, offering even more innovative ways to create, share, and experience music in immersive environments.

In the future, we can expect further innovations such as holographic sound and even greater personalization of audio content through artificial intelligence. These technologies will enable even higher levels of interactivity and immersion in the experience of sound, offering listeners the ability to tailor their auditory environments in ways that were previously unimaginable. As advancements in AI, spatial audio, and interactive media continue, the boundaries of how we engage with music and sound will expand, creating more dynamic and individualized auditory experiences.

ACKNOWLEDGMENTS

This work is part of a Project Based Learning (PBL) project titled 'Analysis of the sound quality recorded on a vinyl record depending on its usage and the wear level of the phonograph needle,' conducted in the 2024/25 academic year at the Silesian University of Technology.

BIBLIOGRAPHY

[1] Historia gramofonu (dostęp 16.12.2024r.) https://voiceshop.pl/pl/n/16.
[2] Krótka historia audio – fonograf, fonoautograf, telegraf i gramofon (dostęp 16.12.24r.) https://www.rms.pl/aktualnosci/sprzet/1051-krotka-historia-audio-fonograf-fonoautograf-telegrafon-i-gramofon.
[3] Zapis i odtwarzanie muzyki (dostęp 16.12.24r.) https://mlodytechnik.pl/eksperymenty-i-zadania-szkolne/wynalazczosc/30029-zapis-i-odtwarzanie-muzyki.
[4] M. Kominek, Zaczęło się od fonografu, Polskie Wydawnictwo Muzyczne, Kraków, 1986.
[5] A. Fogg, Adaptery, Państwowe Wydawnictwa Techniczne, Warszawa, 1957.
[6] T. Olszewski, Książka o winylach, Wydawnictwo Polvinyl sp z o.o., 2023.
[7] M. Anniss, P. Fuller, Winyle – podręcznik miłośnika winylów, Wydawnictwo Bellona, Warszawa, 2019.
[8] https://pl.wikipedia.org/wiki. (dostęp 30.12.2024r)
[9] D.M. Huber, R. Runstein, Modern sound recording technologies, Routlege, New York, 2013.
[10] D. Morton, Sound recording, Bloomsbury Academic, 2004.

TalentDetector
31th January 2025
Gliwice, Poland
DEPARTMENT OF ENGINEERING MATERIALS AND BIOMATERIALS
FACULTY OF MECHANICAL ENGINEERING
SILESIAN UNIVERSITY OF TECHNOLOGY
INTERNATIONAL STUDENTS SCIENTIFIC CONFERENCE

Investigations of the materials structure and morphology using light microscopy

Alicja Rachubka[a], Magdalena Grabysz[a], Marta Ostaficzuk[a], Monika Kciuk[b]

[a] Student of the Academic High School of the Silesian University of Technology in Gliwice
email: alicja.rachubka@alogliwice.polsl.pl
[b] Silesian University of Technology, Faculty of Mechanical Engineering, Department of Engineering Materials and Biomaterials
email: monika.kciuk@polsl.pl

Abstract: The article presents the results of the researches on the selected living (biological) preparations using light microscopes. The analyzes were carried out using a stereoscopic light microscope and a digital light microscope. The selection of appropriate research methodology and comparison of the imaging quality of the same objects required combining knowledge and skills in its practical use in the field of physics, biology, chemistry.

Keywords: light microscopy, samples, magnification

1. INTRODUCTION

A light microscope, also known as an optical microscope, is one of the most commonly used microscopes in both research and education. It uses visible light, typically in the 400 to 700 nm wavelength range, to illuminate the specimen and create a magnified image. The image is formed by the interaction of light with the specimen, and it is magnified through glass lenses [1,2].

Light microscopes do not weigh much and, compared to scanning microscopes, they do not have large dimensions and don't require a vacuum environment, making them ideal for quick and observations. They are well-suited for viewing a variety of specimens, including live or material samples, with minimal preparation. The specimens can be stained with colored dyes for better visibility, and they don't need to be dehydrated or prepared in highly specific ways, unlike electron microscopy specimens (Fig.1) [3].

The magnification power of light microscopes typically ranges up to 1,500x and depend on the types and number of lenses that make up the microscope. There are two types of microscopes i. e simple light microscope (it has low magnification because it uses a single lens) and the compound light microscope (it has a higher magnification compared to the simple microscope because it uses at least two sets of lenses, an objective lens, and an eyepiece) [4]. The lenses are aligned in that, they can be able to bend light for efficient magnification of the image, which is enough to view cells and subcellular structures but is considered low compared

to the capabilities of electron microscopes. Focusing the image is done by adjusting the position of the lenses mechanically, and images are viewed directly through an eyepiece.
There are several types of light microscopes [2,5]:

- Dark-field microscopes: Use light-blocking techniques to create high contrast, making the subject appear brighter against a dark background.
- Bright – field microscopes: The most common and simplest form of light microscopy. It uses a bright light source beneath the sample, which illuminates the specimen, and the resulting image is formed by the contrast between the specimen and its surroundings.
- Phase-contrast microscopes: Alter the phase of light waves passing through a transparent specimen to improve image contrast without needing dyes.
- Fluorescent microscopes: Use fluorescence to highlight specific components of the specimen, offering enhanced detail by using phosphorescent light emission.

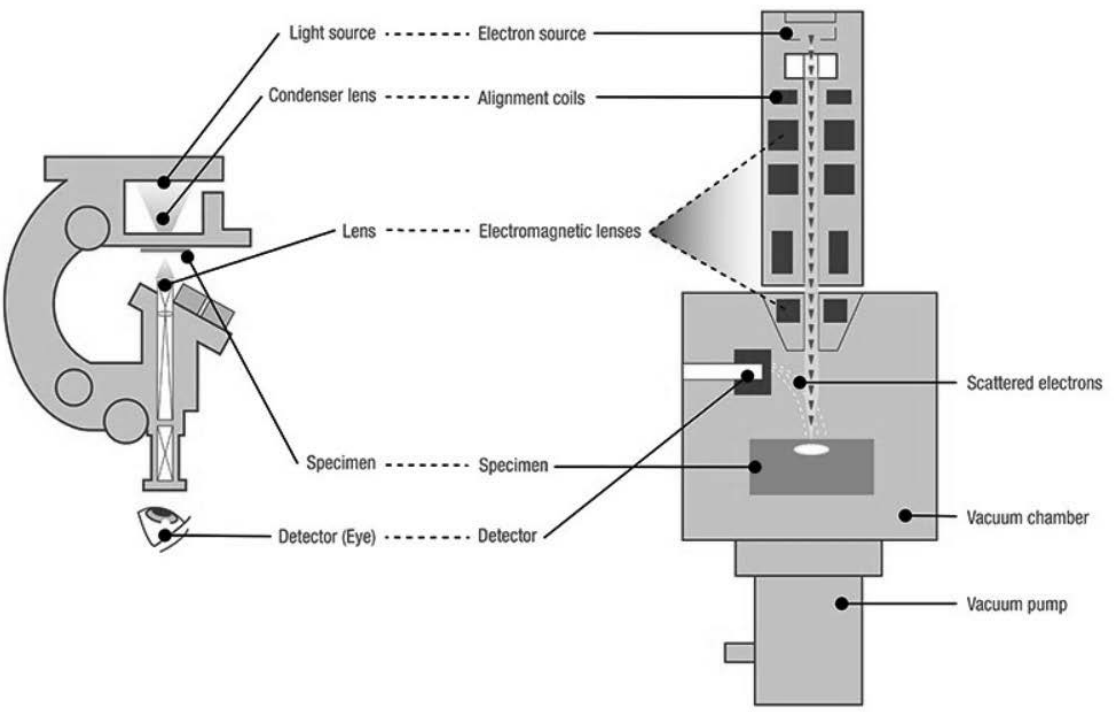

Figure 1. Differences between Light Microscope and Electron Microscope [3]

2. RESEARCH METHODOLOGY

Surface tests of the samples were carried out using a SteREO Discovery V12 stereoscopic microscope (ZEISS) at a 10÷100x magnification.

A light microscope (model DVM6 A) from Leica was used to observe the sample surfaces. The device, thanks to three interchangeable lenses, allows to observe objects on a macro and micro scale. Lenses are distinguished according to their magnification capacity [6,7]:

- low magnification – used to view the sample surface and look for characteristic areas. The maximum magnification is 190x, and the field of view is 43.75 mm,

- medium magnification – allows observation of small objects within the sample. The magnification range is from 46x to 675x and the field of view is 12.55 mm,
- with high magnification – allows the observation of very small details of the sample, up to 425 nm. The maximum magnification is 2350x, with a field of view in the range of 3.6 mm.

An additional advantage is the tilting function, thanks to which it is possible to observe the sample surface at angles of ±60°. Combined with the possibility of moving and rotating the table, this gives the opportunity to examine hard-to-reach details of the sample and complex structures, such as corrosion changes in metals.

3. EXPERIMENTAL RESULTS

As part of the research, a comparative analysis was carried out of the possibility of using two light microscopes: a stereoscopic and a digital microscope to examine the structure and morphology of selected inanimate objects and biological preparations. The test results are presented in Figures 2-4.

a) b)

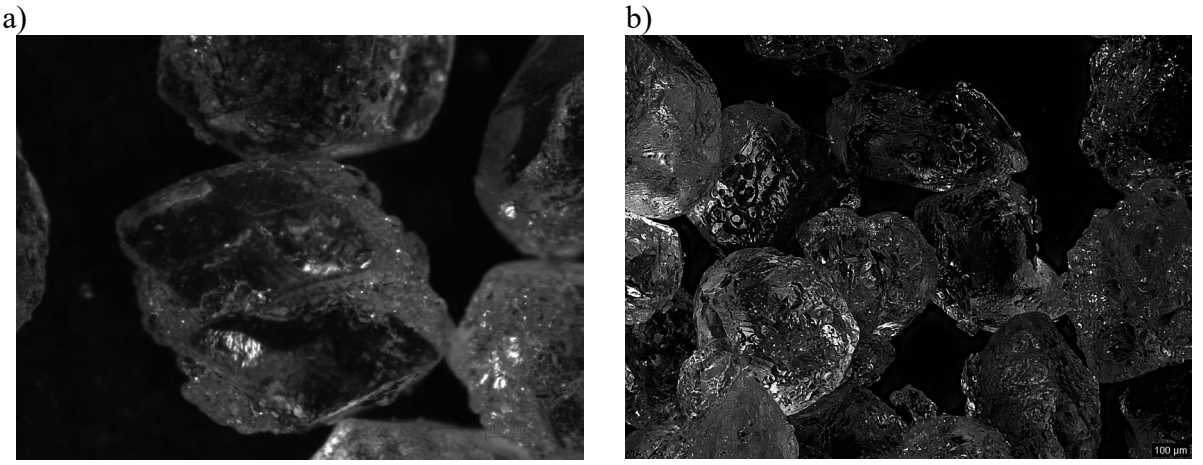

Figure 2. Surface of the citric acid crystals, a) stereoscopic microscope 50x, b) digital microscope 75x

a) b)

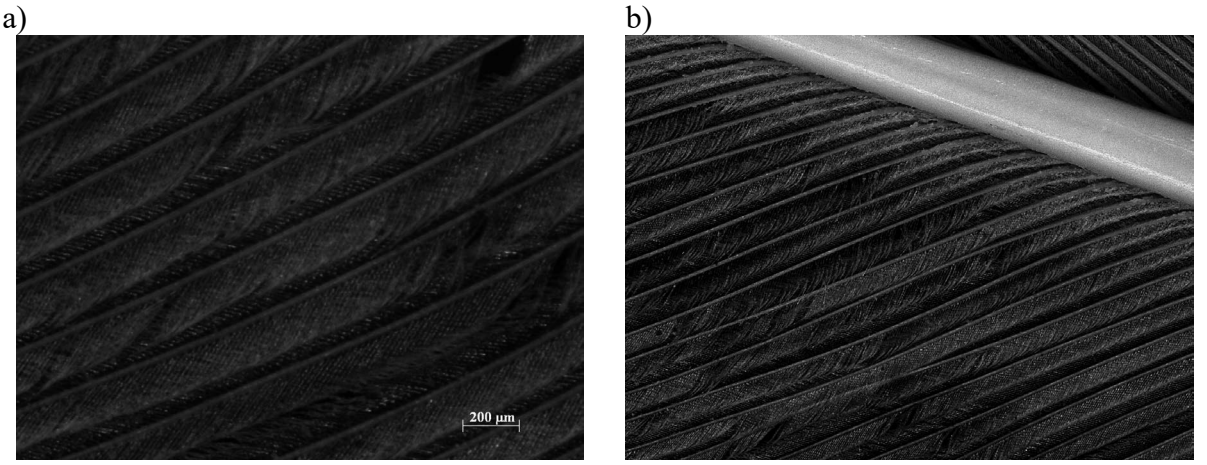

Figure 3. Morphology of bird's tail, a) stereoscopic microscope 70x, b) digital microscope 70x

a) b)

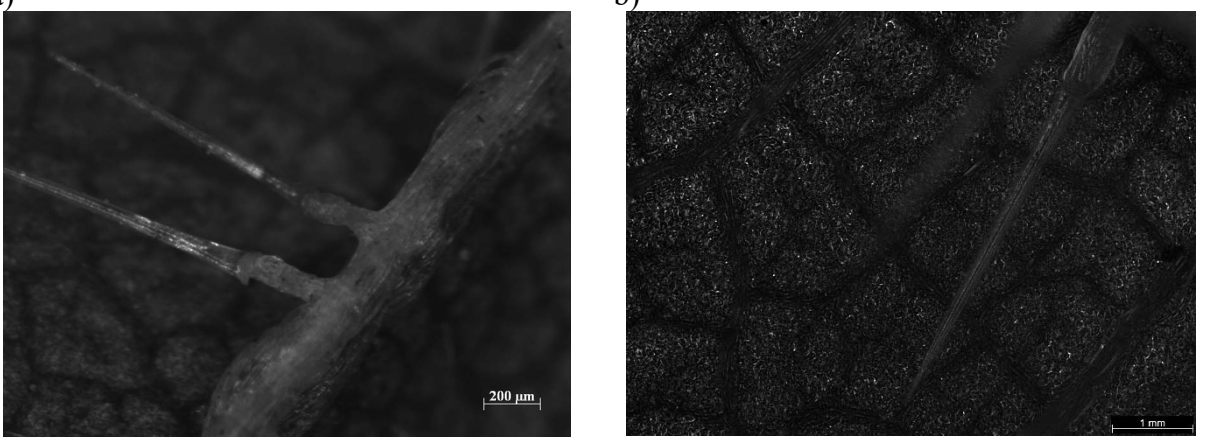

Figure 4. Nettle leaf with stinging hairs, a) stereoscopic microscope 70x, b) digital microscope 300x

Based on a comparative analysis of images obtained from two light microscopes, it can be concluded that even with the same magnification (Fig.3), the quality, colors and details of the preparation are much better in the case of a digital microscope. Using a higher magnification makes it possible to see details, e.g. polyhedral nettle plant cells (Fig. 4).

4. CONCLUSIONS

Some of the most fundamental processes in nature occur at the microscopic scale, far beyond the limits of what we can see by eye, which motivates the development of technology that allows us to see beyond this limit.

Light microscopy permits the observation of living samples, without having a negative effect on them and permits the analysis of grain structures, phase distributions and material defects such as cracks or precipitations.

BIBLIOGRAPHY

1. L.A. Dobrzański, Metody badań metali i stopów. 2. Mikroskopia świetlna i elektronowa, WNT, Warszawa 1987
2. https://www.excedr.com/blog/light-microscope-vs-electron-microscope
3. https://www.thermofisher.com/us/en/home/materials-science/learning-center/applications/sem-optical-microscopes-difference.html
4. https://microbenotes.com/light-microscope/
5. https://www.microscopeworld.com/p-4463-a-comprehensive-guide-to-the-light-microscope-how-to-use-a-light-microscope.aspx
6. https://www.leica-microsystems.com/products/digital-microscopes/
7. https://technolutions.pl/mikroskopy-cyfrowe/

This paper is the result of a project carried out with secondary school students, entitled Investigations of the materials structure from the student's environment using electron and light microscopes.

TalentDetector
31th January 2025
Gliwice, Poland
DEPARTMENT OF ENGINEERING MATERIALS AND BIOMATERIALS
FACULTY OF MECHANICAL ENGINEERING
SILESIAN UNIVERSITY OF TECHNOLOGY
INTERNATIONAL STUDENTS SCIENTIFIC CONFERENCE

Properties of Uncommon Elements Coatings (Ir, Ta, Re): A Comprehensive Overview

Karolina Rogalewska[a], Magdalena Polok-Rubiniec[b]

[a] Student of Materials Engineering and Technology, Silesian University of Technology, Faculty of Mechanical Engineering, Department of Engineering Materials and Biomaterials,
email: kr313886@student.polsl.pl
[b] Silesian University of Technology, Faculty of Mechanical Engineering, Department of Engineering Materials and Biomaterials

Abstract: This paper contains information about not as prevalent elements used in surface treatment such as Ir, Re and Ta. They belong to refractory metals group which are great in usage in elevated temperatures. Thin coatings, while lightweight, significantly enhance the properties of the substrate. Iridium's high chemical inertness at elevated temperatures makes it ideal for withstanding extreme heat and minimizing cooling requirements in spacecraft combustion chambers. Tantalum-based coatings are highly biocompatible, making them suitable for use in bone tissue engineering, where they are safe for osteoblast cells. Rhenium, with its remarkable high melting point and wear resistance, forms a protective film that extends the lifespan of many spacecraft components.

Keywords: metals and alloys, coating, properties

INTRODUCTION

The main elements being use for surface treatment in surface engineering are boron, nitride, carbon, chromium, zinc, tin and mixes of all of those. Nevertheless the need for advanced materials or simply human curiosity led to experiments of metal treatment with rare elements.
Necessity for advanced materials stems from faster and bigger vehicles and airplanes, and also space expedition dream. That fact create need for light, durable and affordable materials. Except of the desire to go higher people trying to explore the deepest depths of oceans. Eagerness to know what is hiding in deep waters as well as attempt to living or driving at the bottom of canals, seas and lakes meet the demands of high corrosion resistance.

1. Iridium coating:

Iridium stands out for its high melting point (2173 K), low oxygen permeability, and high chemical stability, which make it very resistant to harsh conditions. These characteristics make iridium suitable in applications such as rocket and nozzle coatings, glass manufacturing, ion

metal sensors, mirrors, X-ray and optical equipment for spacecraft. Additionally, iridium films serve as effective oxygen barriers and greatly enhance the durability of electrodes in corrosive marine conditions. [1]

Iridium coatings are prepared by different methods such as metal–organic chemical vapor deposition (MOCVD), molten salt electrodeposition, magnetron sputtering, the double-glow plasma method. [2] Iridium can be deposited on several materials metallic or ceramics. The method and material using to develop iridium coating have direct relationship with morphology of final coating (fig. 1 and 2). The appearance of coating is connected to their properties like durability or adhesion to the substrate. In addition crystal morphology of powder grains used to prepare iridium surface has also influence on its results. [2]

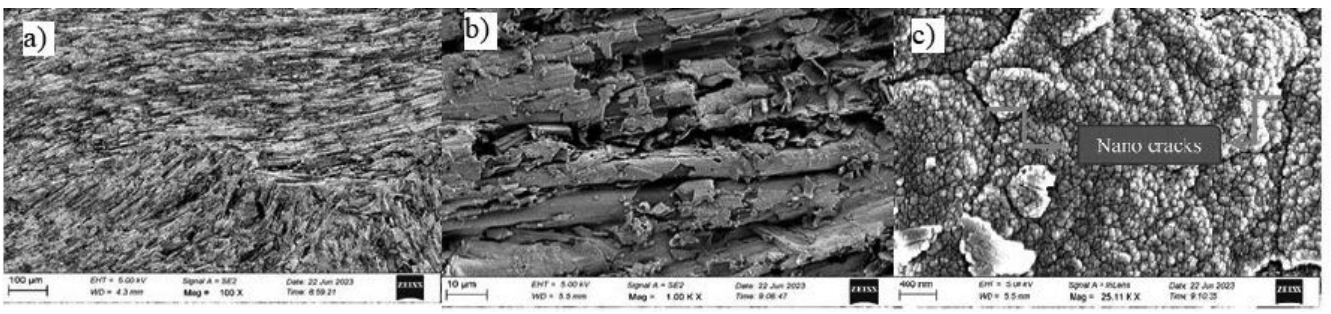

Fig. 1. SEM photos of Iridium coating on C/C composites by MOCVD method in different magnification: a) 100, b) 1K, c) 25K [1]

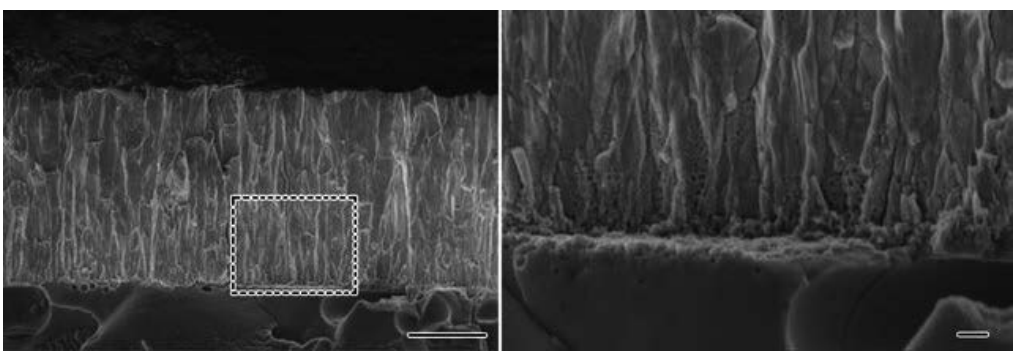

Fig. 2. FE-SEM photo of iridium coating on Ti material with 5K and 20K magnification [3]

The team of Bejin [4] works on iridium powder morphology to examine if that has any influence on final product. The outcome was expected – shape of grain powder changes the morphology of iridium coatings. They obtained two different powders – hexagonal columnar crystals and tetragonal flake crystals. The volatility of the hexagonal columnar crystals is superior to that of the tetragonal flake crystals under the experimental conditions. This is because the hexagonal columnar crystals have more exposed crystal faces, which increases their surface area in contact with the transport gas compared to the tetragonal flake crystals. The Ir coating formed from the hexagonal columnar crystals exhibited a smooth and continuous surface, whereas the coating prepared from the tetragonal flake crystals showed more pronounced cracks. Due to the precursor's volatility, hexagonal columnar crystals are preferable as a precursor in the Ir MOCVD process.

The paper published in Material Research Express [1] show some data about properties of iridium coating prepared on carbon composites. The hardness of coated sample was higher about 250 HV points than uncoated sample. Moreover the C−C substrate shows a slow increase

in displacement, indicating initial elastic deformation. In contrast, the iridium-coated sample exhibits less displacement at lower weights, suggesting greater hardness and deformation resistance.

Further tests covers corrosion resistant of presented coating. Table 1 shows that the iridium-coated sample had an resulting in a corrosion rate of 0.00307 mm/year, indicating excellent corrosion protection. In contrast, the uncoated carbon-carbon composite had a corrosion rate of 0.0743 mm/year, approximately 24 times faster than the iridium-coated sample. Additionally the oxide resistance in temperature of 1300K are great. Tests conducted on Iridium coating prepared on pure tungsten [2] indicate that oxidation are weaker. Iridium oxide forms at a much higher oxygen partial pressure compared to tungsten oxide when oxidized at 1300 K. This indicates that iridium is significantly more resistant to high-temperature oxidation than tungsten. The WO_3, formed at the tungsten surface has high volatility, making oxidation at high temperatures potentially catastrophic. In contrast, iridium forms gaseous IrO_2, but film remains highly stable, leading to minimal iridium coating loss during high-temperature oxidation, offering excellent protection for the substrate.

Tab. 1 Corrosion rate analysis[2]

Samples	E_{corr} (mV)	I_{corr}(μA)	Corrosion rate mm/year
Iridium coated	5.795	0,5	0,00307
Uncoated C-C composite	-114,682	8,006	0,0743

2. Rhenium coating:

Rhenium (Re) is a refractory metal known for its exceptional high-temperature mechanical properties, including a high melting point of 3180 °C, high modulus, and good ductility. [5] It's the only refractory metal that does not form carbides. [6] These qualities make it an ideal material for high-temperature structural applications. Furthermore, rhenium demonstrates impressive resistance to most non-oxidizing combustion gases, along with excellent wear and corrosion resistance, making it a promising material for extreme high-temperature environments, such as those found in solid and liquid rocket engine combustion chambers. Thin-walled rhenium components and coatings can be produced using techniques like electron beam physical vapor deposition (EB-PVD), chemical vapor deposition (CVD), and electrodeposition in molten salts (ED). [5]

Tests on electrodeposited Re coating shows that when deposition temperature increases, the surface morphology of the Re coatings evolves (fig. 3) from spired starfish to pyramid shapes, and then to faceted grains with noticeable grain coarsening. The roughness of the coatings reaches a minimum at 800 °C, with both higher and lower temperatures increasing roughness. This is due to increased nucleation rates and slower grain growth at lower temperatures, while grain size increases with higher deposition temperatures. XRD patterns show that Re coatings have polycrystalline structures with varying orientations, with preferred growth crystal planes changing from (100) to (110) to (002) as the temperature increases. Increasing current density leads to a proportional increase in coating thickness, significant surface roughening, and grain refinement. Surface morphology changes from faceted grains at lower currents to dendrite-like surfaces at higher currents, with grain size decreasing significantly as current density rises.

Coating structure to protect the Nb–5Mo–15W alloy from high-temperature oxidation is using a combination of electroplating and pack cementation with Cr and Al. The coating

includes a Re-based diffusion barrier with (Re, Cr) and Re(Cr) phases, and an Al reservoir in the form of an α-Cr(Al, Re) or β-NiAl layer. Uncoated Nb–5Mo–15W alloys exhibit aggressive oxidation, necessitating a compact and intact (Re–Cr) layer for effective protection. The (Re–Cr) layer demonstrated excellent oxidation resistance at 1373 K in air and also can perform as a barrier against the inward diffusion of Al, Ni, and Cr, and the outward diffusion of substrate alloying elements. The (Re–Cr) phase has exceptionally low diffusion coefficients, approximately 10^3 times smaller than those of Ni–Cr and Ni–Re systems. Results also indicate that Re in the coating reacts with Cr, W, and Co to form Re-based σ-phase alloys, while elements like Al, Ti, Ta, and Ni tend to migrate. This suggests that Re and its alloys possess a self-structuring capability, enabling the formation of an effective diffusion barrier. [7]

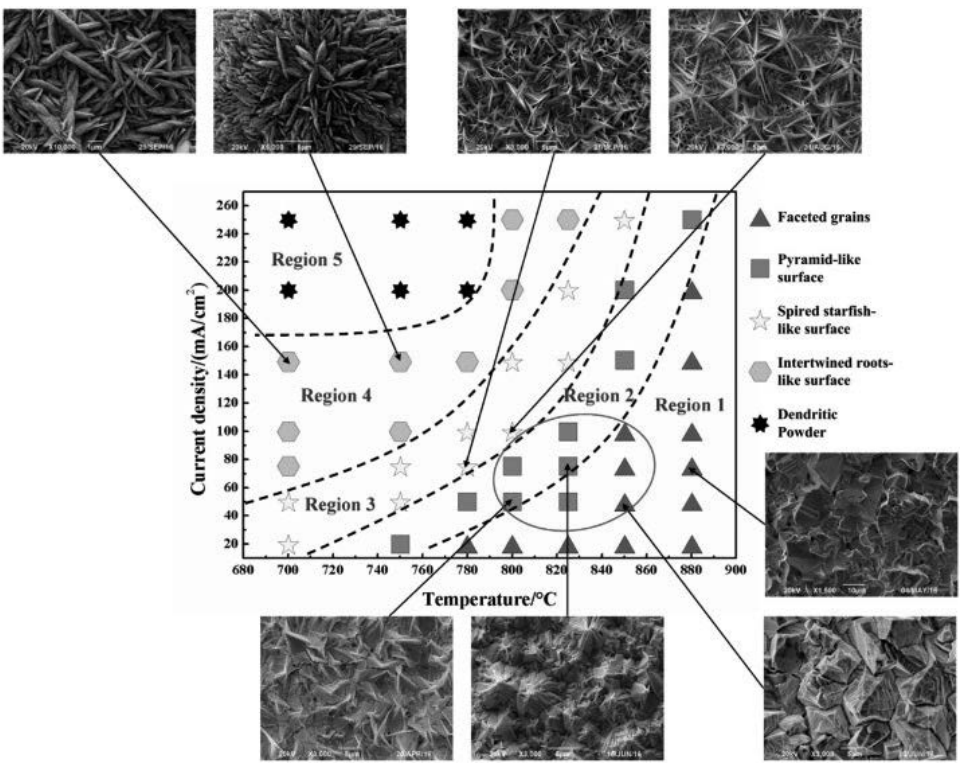

Fig. 3 Map of Re coat morphology depends on temperature and current density [5]

Rhenium has very high elastic moduli one of the biggest among metals. As the temperature increases from room temperature to 1000 K, the elastic modulus decreases to point of 20%. This indicates that structures made from rhenium will maintain excellent mechanical stability and rigidity. A high recrystallization temperature is crucial for ensuring good creep resistance, and rhenium outperforms other materials in both tensile strength and creep-rupture resistance across a wide temperature range. With about 35% ductility, measured in total elongation, and a tensile strength that decreases from 1172 MPa at room temperature to 48 MPa at 2983 K, rhenium demonstrates remarkable resistance to thermal shock. One of the key advantages of rhenium as a contact material is the excellent conductivity of its oxides, which results in minimal changes to contact resistance up to temperatures of 1300 K. Rhenium also demonstrates remarkable stability in thermionic properties across a variety of gaseous

environments, boasting a high work function and melting point. These characteristics contribute to effective ionization, high electrical resistance, and the preservation of plasticity after repeated heating. [8]

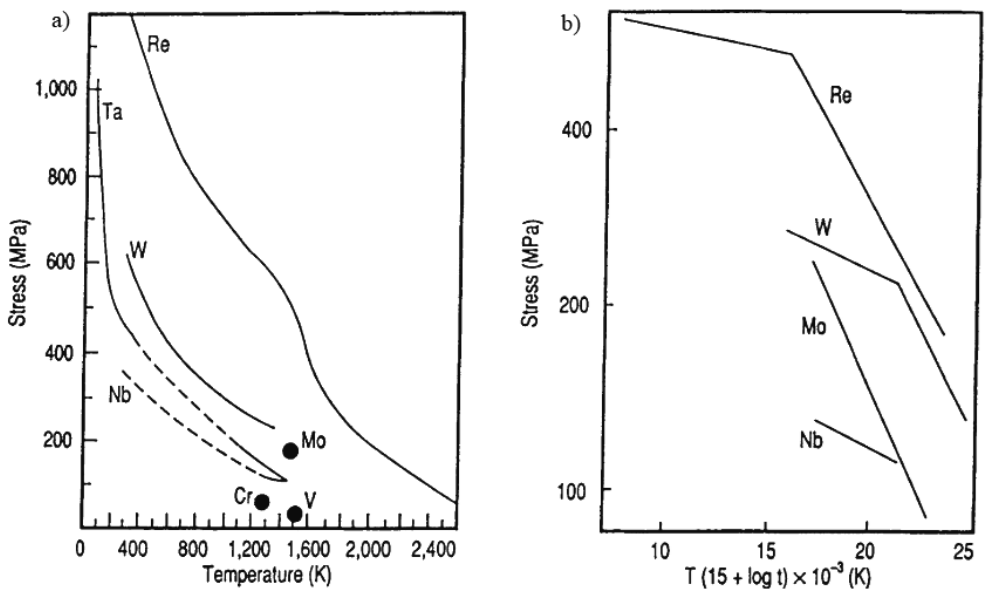

Fig. 4 Comparison properties of refractory metals: a) Ultimate Tensile Strength, b) Creep-Rupture Strength [8]

3. Tantalum coating:

The combination of chemical inertness, corrosion resistance, biocompatibility, and high-temperature stability makes tantalum extremely valuable in demanding industries such as aerospace, healthcare, and nuclear power, though its high cost limits use in chemical engineering. The strong passive layer that forms on the surface of this metal plays a significant role in its outstanding resistance to corrosion. [9] At room temperature, they are virtually immune to attack by concentrated inorganic acids (except for hydrofluoric acid) and aqua regia. In high-temperature environments, they can react with fluorine, chlorine or oxygen. [10] Tantalum is ideal for strongly corrosive acidic environments due to its durable oxide film, ensuring a corrosion rate below 254 μm/year and long equipment life. Tantalum coatings can be produced using various processing techniques, including PVD processes, magnetron sputtering technology, molten salts electrocoating, and anodization. The most effective for corrosion protection methods of tantalum coatings are: Explosion Clad (EC), Chemical Vapor Deposition (CVD), and Molten Salt Electrodeposition (MSE). EC produces thick coatings (about 1 mm) what requires significant material use. MSE offers advantages over CVD, including precise thickness control, simpler equipment, deposition rates to 100 μm/h, and excellent throwing power, that is making it a promising option for manufacturing tantalum-clad vessels.

The study demonstrated that tantalum coatings significantly improve the corrosion resistance of 316SS. Corrosion weight changes (fig. 5) in Ta-316 samples increased with exposure time, indicating the formation of adherent corrosion products providing a protective effect. Initial weight changes for 316SS and Ta-316 decreased with increasing salt

concentration but rose beyond 9%. For pure Ta, weight changes showed a slight increase from 3% to 10% salt concentration, with no salt accumulation on its surface, contrasting with significant crystallization on 316SS and Ta-316 reactors, intensifying with higher salt concentrations.

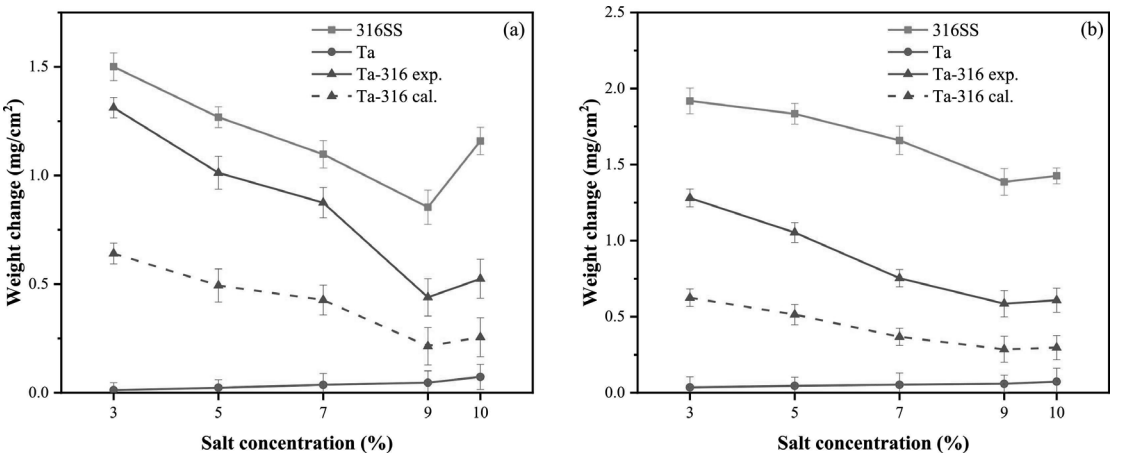

Fig. 5 Weight changes of three tested materials exposed to different concentrations of salt at 290°C for 150 h (a. NaCl, and b. NaBr). [11]

The weight changes in Ta-316SS after 150 hours at 370°C were 0.67394 mg/cm² for NaCl and 0.87569 mg/cm² for NaBr solution. Ta-316 exhibited a 67.3% lower weight change than 316SS, confirming that the tantalum coating significantly enhanced corrosion resistance. The weight gain rate at 30 and 300 h changed: 0.01023 ÷ 0.00614 $mg \cdot cm^{-2} \cdot h^{-1}$ in NaCl, 0.01504 ÷ 0.00649 $mg \cdot cm^{-2} \cdot h^{-1}$ in NaBr, indicating stabilization of surface oxide formation. No significant oxide film detachment was observed. These results demonstrate Ta-316's high stability and corrosion resistance in Cl^- and Br^- environments. [11]

The elastic modulus and hardness of SEBM Ti64, Ta, and Ta-Ti64 samples, measured using the Oliver method, were 114.6 GPa/4.87 GPa for Ti64 and 175.8 GPa/4.84 GPa for pure Ta. These results align with Mondal et al. [11], who reported 123.8 GPa and 8.08 GPa for nano tantalum coatings. At a 3 mN load**,** Ta-Ti64 showed smaller indentation depths and greater elastic recovery (tab. 2), indicating improved elastic resistance. The tantalum coating nearly doubled the surface hardness of Ti64 without significantly affecting its elastic modulus. [13]

Tab. 2 Hardness and elastic modulus of Ti6Al4V and Ta coating at load of 3 mN [13]

Samples	Hardness (GPa)	Elastic modulus (GPa)	H/M
Ti64	4.87	114.6	0.042
Ta	4,84	175,8	0,027
Ta-Ti64	8,08	123,8	0,065

CONCLUSIONS

Civil engineering has far exceeded our expectations, resulting in space expeditions that led to the demand for better surface solutions. The search for materials with high mechanical, thermal, and corrosion resistance properties prompted the use of rare elements in experimental coatings. The first element discussed is iridium, known for its high melting point, excellent oxidation resistance at elevated temperatures, and resilience in harsh chemical conditions. Research has primarily focused on its corrosion resistance, but its application on various substrates has also been explored. It has been proven that iridium coatings enhance resistance to oxide formation, even at high temperatures. The mechanical properties of carbon composites improve after being coated with iridium, with significant increases in hardness and resistance to deformation.

One of the elements meeting the criteria for excellent thermal and mechanical properties is rhenium (Re). It has an even higher melting temperature, remarkable resistance to most non-oxidizing combustion gases, great elastic moduli, and outstanding wear resistance. Rhenium is frequently used in combination with other elements or as a component in layered composites, which helps enhance properties and reduce the cost of rhenium applications.

Another rare element commonly used in aerospace and medical industries is tantalum (Ta), which forms an effective anti-corrosion coating that also improves the hardness and elastic modulus of coated titanium. Stainless steel coated with tantalum exhibits improved corrosion resistance, demonstrated by a nearly 65% reduction in weight change. Titanium shows a 60% increase in hardness when coated with tantalum.

BIBLIOGRAPHY

1. Kumar, J. V. Sai & Rajabakkiyam, Sundharesan & D T, Arunkumar & Ghadai, Ranjan., Enhancing thermal stability and corrosion resistance of carbon-carbon composites with iridium coatings deposited by electron beam physical vapor deposition, Materials Research Express (2024) 11-9.
2. Zhang, J., Chen, D., Zhang, X., Li, R., et al, Deposition of iridium coating on pure tungsten and high-temperature oxidation behavior at 1300 K. Coatings, (2022) 12-11.
3. Wu, W.; Chen, Z. Growth mechanism of polycrystalline Ir coating by double glow plasma technology. Plasma Sci. Technol 469–479 (2012) 25.
4. Shi, J., Hao, Y., Yu, X., Tan, C., et al., The crystal morphology effect of Iridium tris-acetylacetonate on MOCVD iridium coatings. IOP Conference Series: Materials Science and Engineering, (2017).
5. Zhu, L., Wang, J., Wang, Z., Ye, Y., Bai, S., Wan, H., Li, S., Tang, Y., Morphologies and textures of rhenium coatings electrodeposited in chloride molten salts, Surface and Coatings Technology, (2021) 428.
6. Yue, G., Hong-yu, X., Zeng-rong, J., Zhi-xiang, X., Mechanical Properties and Thermal Shock Resistance of Rhenium Coating in Iridium/Rhenium/Carbon-carbon Composites. Procedia Engineering 1407-1414 (2015) 99.
7. Fukumoto, M., Matsumura, Y., Hayashi, S., Sakamoto, K., Kasama, A., Tanaka, R., & Narita, T, Formation of a Rhenium-Base Coating on a Nb-Base Alloy. Oxidation of Metals 335–346 (2003) 60-3.
8. Canales, C. P., Adalsteinsson, S. M., Tryggvason, T. K., Lyu, X., Ramírez, G., Mallouk, T. E., Ingason, Á. S., Magnus, F., Serov, A., Synthesis of rhenium coatings on 316 stainless

steel and their electrochemical behavior towards water oxidation in saline environments. Electrochimica Acta, (2025) 512.
9. Cardarelli, F., Taxil, P., & Savall, A, Tantalum protective thin coating techniques for the Chemical Process Industry: Molten salts electrocoating as a new alternative. International Journal of Refractory Metals and Hard Materials 365–381 (1996) 14-6.
10. Turkowska, M., Research on methods of separating niobium and tantalum and development of methods for determining tantalum in niobium compounds. PhD thesis, Silesian University of Technology, Gliwice 2023 (in polish).
11. Wang, J., Zhang, S., Han, F., Luo, Y., Chen, J., Hu, Z.-T., Pan, Z., Hu, M., Corrosion performance and mechanisms of tantalum coatings on 316 stainless-steel in subcritical aqueous solutions of NaCl and NaBr. Corrosion Science (2024) 231.
12. Krawczenko, Y.O., Coy, L.E., Peplińska, B., Iatsunskyi, I., Załęski, K., Kempiński, M., Beresnev, V.M., Konarski, P., Jurga, S., Pogrebnjak, A.D., Nano-multilayered coatings of (TiAlSiY)N/MeN (Me=Mo, Cr and Zr): Influence of composition of the alternating layer on their structural and mechanical properties. Journal of Alloys and Compounds 483-495 (2018) 767.
13. Sui, Z., Wang, J., Wu, C., Niu, J., Zhu, J., Zhou, L., Research on the surface characterization, corrosion and bioactivity of nano-featured tantalum coating on selective electron beam melted Ti6Al4V alloy. Journal of Alloys and Compounds, (2023) 946.

This paper is the result of a Project Based Learning (PBL) project entitled Development and 3D printing of a prosthetic hand model with software for a disabled person

TalentDetector
31th January 2025
Gliwice, Poland
DEPARTMENT OF ENGINEERING MATERIALS AND BIOMATERIALS
FACULTY OF MECHANICAL ENGINEERING
SILESIAN UNIVERSITY OF TECHNOLOGY
INTERNATIONAL STUDENTS SCIENTIFIC CONFERENCE

Selected research methods for the characterization of photovoltaic materials

Bartosz Rybak[a], Paweł Pietraszek[a], Tymoteusz Tarnawski[a], Aleksandra Drygała[b], Małgorzta Musztyfaga-Staszuk[c], Jakub Budzynowski[d], Bartosz Drygała[e], Marcin Staszuk[b], Judyta Drygała[f]

[a] Pupil, Complex of Communication Schools, Warszawska 35, 44-100 Gliwice, Poland
[b] Silesian University of Technology, Faculty of Mechanical Engineering, Department of Engineering Materials and Biomaterials, Konarskiego 18a, 44-100 Gliwice, Poland
[c] Silesian University of Technology, Faculty of Mechanical Engineering, Welding Department, Konarskiego 18a, 44-100 Gliwice, Poland
[d] Student, Silesian University of Technology, Faculty of Mechanical Engineering, Konarskiego 18a, 44-100 Gliwice, Poland
[e] Student, Silesian University of Technology, Faculty of Automatic Control, Electronics and Computer Science, Akademicka 16, 44-100 Gliwice, Poland
[f] Student, Silesian University of Technology, Faculty of Architecture, Akademicka 7, 44-100 Gliwice, Poland
email: aleksandra.drygala@polsl.pl

Abstract: The research methods used in the characterization of photovoltaic materials are diverse and include the study of optical, electrical, and structural properties. Precise research not only enables the improvement of the efficiency and reliability of solar cells, but also accelerates the development of new technologies. This paper presents selected research methods used to assess the quality of photovoltaic materials and the results of surface topography and selected optoelectrical properties studies for polycrystalline silicon.

Keywords: silicon, doping, p-n junction, solar cells, optical properties, electrical properties

1. INTRODUCTION

Silicon is a basic material in semiconductor technology, key to modern electronics and photovoltaics. Its versatility results from the possibility of doping, which allows control of its electrical properties. Intrinsic silicon is a material in which the concentration of free electrons and holes is the same. Adding an element from group V of the periodic table (e.g. phosphorus, arsenic), i.e. an atom with five valence electrons, increases electronic conductivity. The fifth electron does not participate in the formation of a covalent bond, and is therefore weakly bound to the nucleus. This type of material is called an n-type semiconductor. Silicon can also be doped with elements from group III of the periodic table (e.g. gallium, boron or aluminum), which have only three valence electrons. Atoms of these elements tend to capture an electron from a neighboring silicon atom to complete four covalent bonds. In this type of material, free spaces called holes are created. At the

interface of p-type and n-type silicon, a p-n junction is formed, which is a key element of devices such as diodes, transistors, and solar cells. In the semiconductor industry, high-temperature diffusion or ion implantation are commonly used methods of silicon doping. The diffusion process uses a concentration gradient and high temperature to enable the migration of dopants into the interior of the material. During ion implantation, dopant atoms are injected into the crystal lattice of silicon using an ion accelerator [1-3]. Solar cells convert solar radiation energy into electrical energy thanks to the photoelectric effect. Their main element is the p-n junction, which is responsible for the separation of charge carriers (electrons and holes) generated by solar radiation and their flow in the device [4,5].

This paper presents selected research methods used to characterize photovoltaic materials and the results of studies on the optoelectrical properties of polycrystalline silicon. Evaluation of the quality of photovoltaic devices at each stage of their production is a key stage in the process of designing, optimizing and manufacturing solar cells. The use of appropriate research methods allows for understanding the properties of photovoltaic materials and phenomena occurring in them, which has a direct impact on their efficiency, durability and cost-effectiveness in commercial applications [5].

2. SCANNING ELECTRON MICROSCOPY

Scanning electron microscopy is a highly functional method used to obtain high-resolution images and detailed information of surface. A scanning electron microscope (SEM) equipped with an energy dispersive X-ray spectrometer (EDS) enables not only the evaluation of structure and morphology but also the analysis of the chemical composition of the surface. In SEM, information is obtained using an electron beam generated by an electron gun. The interaction between the primary electrons (incident electron beam) and the sample material generates various signals, such as secondary electrons, characteristic X-ray radiation, backscattered electrons, and cathodoluminescence [6,7].

a) b)

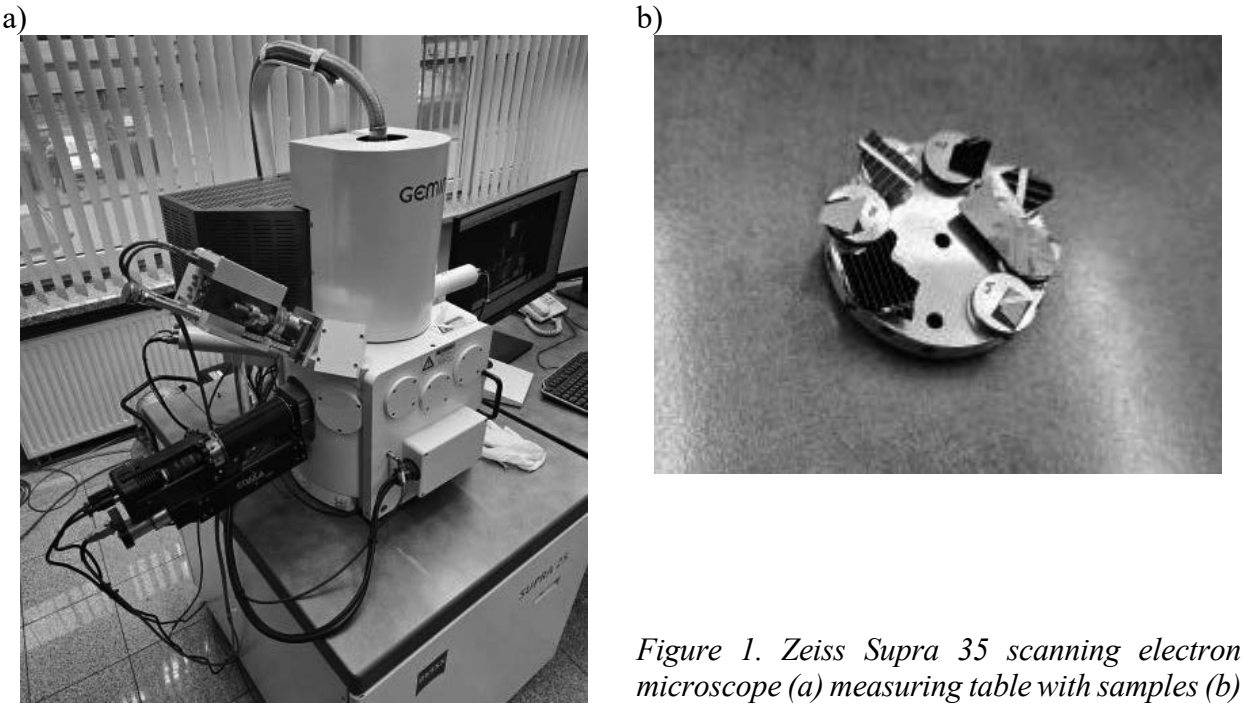

Figure 1. Zeiss Supra 35 scanning electron microscope (a) measuring table with samples (b)

In this work the topography of polycrystalline silicon after alkaline texturing were investigated using ZEISS SUPRA 25 scanning electron microscope (SEM) (Fig. 1). Silicon texturing is a chemical surface modification process that aims to reduce surface reflection and consequently increase the efficiency of the solar cell. It consists in selective etching of the silicon surface using chemical solutions. The use of alkaline solutions for texturing monocrystalline silicon with crystallographic orientation (100) results in the formation of a pyramidal structure on the surface [8,9]. Figure 2 shows the surface topography of polycrystalline silicon using potassium hydroxide. Irregularities were observed on the surface, the nature of which depends on the crystallographic orientation of the grain. It was found that alkaline etching is not as effective as in the case of monocrystalline silicon.

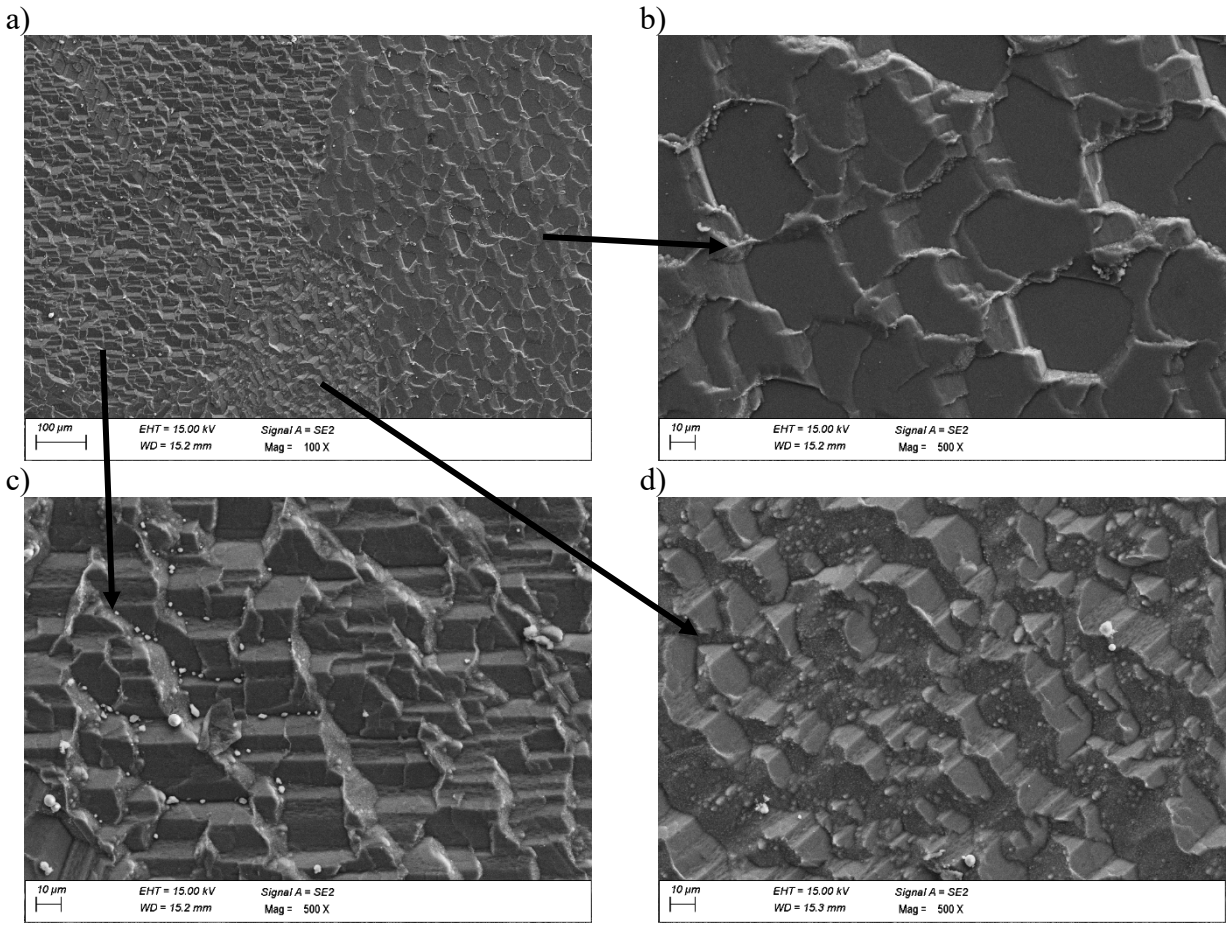

Figure 2. Topography of polycrystalline silicon surface after alkaline etching

3. SHERESCAN INSTRUMENT

The Sherescan device (Fig. 3) uses a four point probe for [10,11]:

- recognition of the P/N conductivity type of a semiconductor material (Fig. 3c),
- measurement of the surface resistivity of silicon and assessment of the quality of the produced emitter diffusion layers (Fig. 3d),
- measurement of the front electrical contact resistance of a silicon solar cell.

The measurement consists of pressing a measuring head consisting of 4 probes against a silicon wafer and then passing current through the two outer probes. As a result, a potential difference is created between the inner probes.The instrument uses an x, y, and z mechanism for precise positioning of the four-point probe, and a vacuum holds the wafer in place on the table [10,11].

In this work, the conductivity type was tested and the surface resistivity of polycrystalline silicon was measured. Based on the tests performed, it was found that the tested substrate is of the p-type and the average surface resistivity is 33,8 Ω/sq.

a) b)

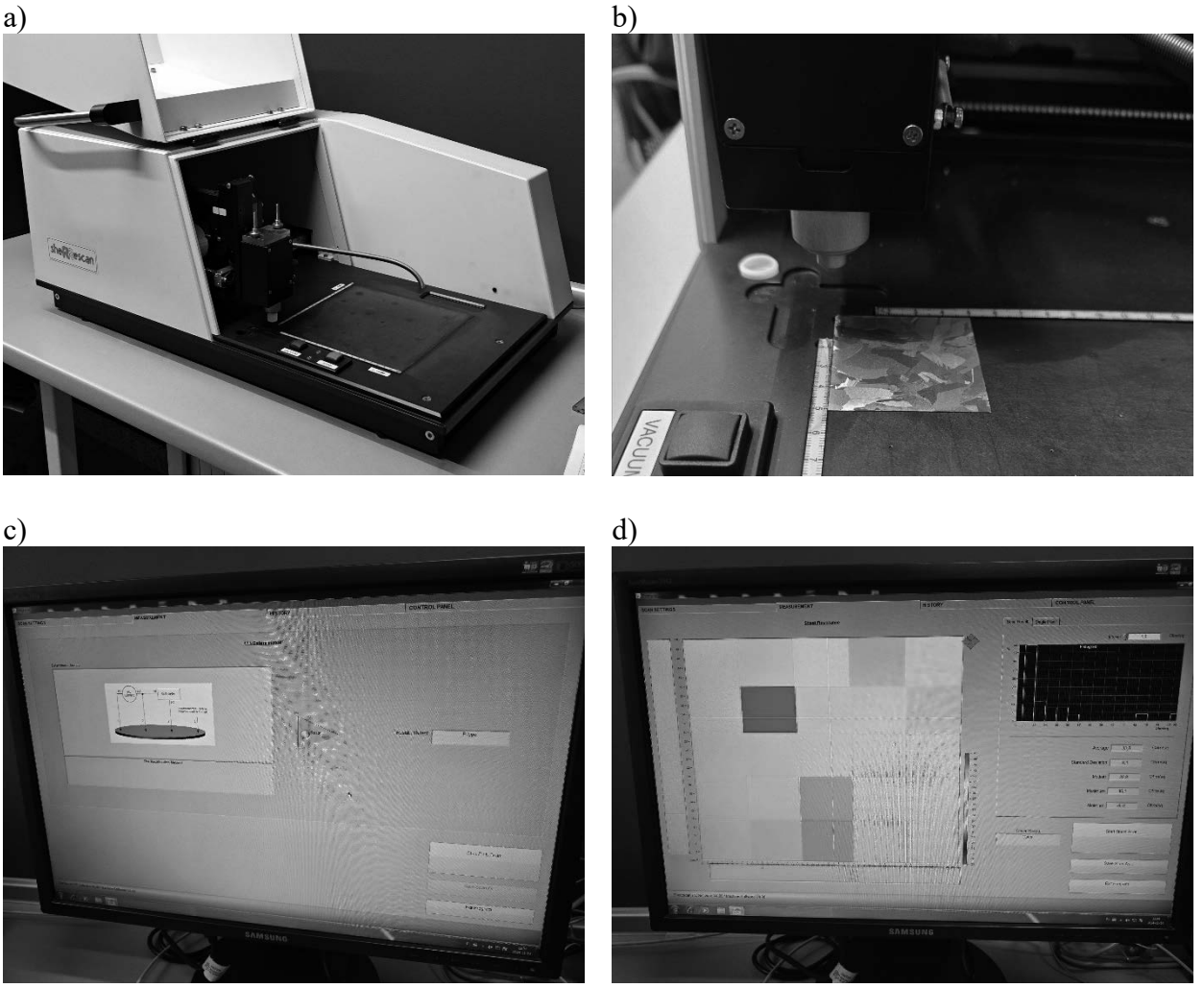

c) d)

Figure 3. SunLab Sherescan device (a), measuring head and table with placed sample (b) program window showing the device's operating principle and measurement result – p/n type recognition (c) program window with mapping of sheet resistivity for polycrystalline silicon surface (d)

4. SPECTROPHOTOMETRY

Spectrophotometer (Fig. 4) is a device used to measure the intensity of light that passes through or is reflected from a sample, allowing the analysis of its optical properties, such as absorbance, reflection, or transmission [12]. The spectrophotometer consists of five key components [13]:

- light source - produces light across multiple wavelengths,
- monochromator - isolates a specific wavelength of light,
- sample holder - holds the material being analysed,
- detector - converts transmitted light into an electronic signal.

Figure 5 shows the dependence of light reflection on wavelength for a polycrystalline silicon surface before and after alkaline texturing. The reflectance was measured by Thermo Scientific UV-Vis spectrophotometer. It was found that the use of alkaline etching significantly reduces light reflection. At wavelength of 600 nm, the light reflection from the textured polycrystalline silicon surface is about 17% lower than the untextured surface.

Figure 4. Thermo Scientific UV-Vis spectrophotometer

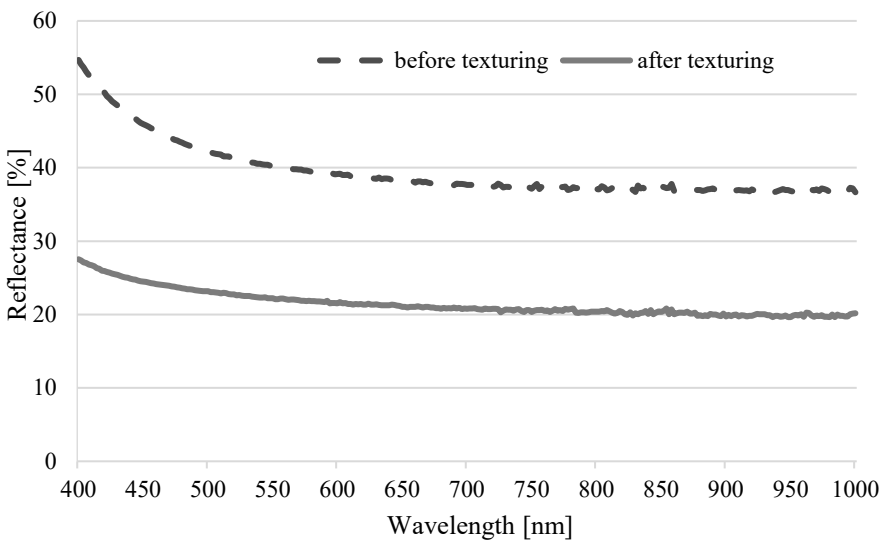

Figure 5. Reflectance for polycrystalline silicon wafer before and after alkaline texturing

5. CONCLUSIONS

Research methods play a fundamental role, enabling the assessment of the quality, efficiency and durability of solar cells. They also allow for the identification of technological problems and the development of new solutions to increase the efficiency of converting solar energy into electrical energy. The research conducted in this work allowed for the assessment of the polycrystalline silicon surface and the determination of its selected optoelectrical properties. The dynamic development of photovoltaic technologies indicates the growing role of solar energy in sustainable development.

ACKNOWLEDGEMENTS

The work was created as a result of a project carried out with secondary school pupils as a part of the Excellence Initiative - Research University program, Silesian University of Technology.

BIBLIOGRAPHY

1. S. Jang, K. Lee, Properties of silicon for electronic applications, Journal of Materials Science, 54(12) (2019) 1457-1465
2. A. Kumar, S. Meena, Silicon-based solar cells: Current status and future prospects. Renewable and Sustainable Energy Reviews, 82 (2018) 78-94
3. S. Zhang, Z. Chen, Y. Li, Recent advances in silicon-based materials for next-generation electronic devices. Advanced Materials, 32(22) (2020) 1905421
4. E. D. Dunlop, K. H. Le, Progress in high-efficiency crystalline silicon solar cells. Solar Energy Materials and Solar Cells, 193 (2019) 189-199
5. J. Meyer, P. Piwowar, Solar cell technology: Crystalline silicon and beyond. Materials Today, 38, (2020) 32-40
6. P. Boryło, L. Sozańska-Jędrasik, K. Gołombek, Zastosowanie skaningowej mikroskopii elektronowej w badaniach materiałów inżynierskich, Laboratoria Aparatura Badania 2(2019) 6-13
7. B. Vulcan, M.Salih, Recent Advances in Scanning Electron Microscopy. Microscopy Research and Technique, 77(9) (2014) 682-690
8. L. G. Chien, J. P. Chu, Effect of alkaline etching on the surface texturing of monocrystalline silicon for photovoltaic applications, Solar Energy Materials and Solar Cells (2019)
9. A. S. Yoon et al., Surface texturing of monocrystalline silicon using NaOH and KOH solutions for improved photovoltaic performance, Solar Energy (2018)
10. M. Prokopiuk vel Prokopowicz, M. Szindler, L.A. Dobrzański, A. Drygała, Wyznaczanie własności elektrycznych krzemowych ogniw fotowoltaicznych, Prace studenckich kół naukowych Sokół, 29 (2014) 63-68
11. A. Drygała, M. Musztyfaga-Staszuk, M. Szindler, M.M. Szindler, Wybrane metody badań materiałów fotowoltaicznych i ogniw słonecznych, Ochrona klimatu i środowiska, nowoczesna energetyka, S. Werle, J. Ferdyn-Grygierek (red.), Wyd. Politechniki Śląskiej, (2023) 174-189
12. A. K. Goswami. "Introduction and basics of spectrophotometry". Spectrophotometric Determination of Nickel and Cobalt: Methods and Reagents, Berlin, Boston: De Gruyter, (2023) 1-21
13. C. Burges, The basics of spectrophotometric measurement, Techniques and Instrumentation in Analytical Chemistry, 27 (2007) 1-19

TalentDetector
31th January 2025
Gliwice, Poland
DEPARTMENT OF ENGINEERING MATERIALS AND BIOMATERIALS
FACULTY OF MECHANICAL ENGINEERING
SILESIAN UNIVERSITY OF TECHNOLOGY
INTERNATIONAL STUDENTS SCIENTIFIC CONFERENCE

Activated carbon: Properties, modifications and environmental applications

Kinga Rzepiak[a], Wiktoria Kroczek[a], Karol Kukuła[a], Ewa Puszczało[b]. Anna Marszałek[b], Gabriela Kamińska[b], Grzegorz Michalski[c]

[a]Politechnika Śląska, Wydział Chemiczny, email: kr300329@student.polsl.pl
[b]Politechnika Śląska, Wydział Inżynierii Środowiska i Energetyki, email: ewa.puszczalo@polsl.pl
[c]NITROERG S.A., Bieruń, g.michalski@nitroerg.pl

Abstract: Activated carbon (AC) is a widely used adsorbent, characterised by its high porosity and large specific surface area, enabling effective removal of contaminants from water, air and soil. This paper describes the different types of AC, including granular, powdered and more specialised forms such as impregnated and plasma-modified. Activated carbon modification processes (chemical, physical, microwave, plasma, ozone and biological) that enhance its adsorption properties and adapt it to specific applications are discussed.

Keywords: activated carbon, adsorbent, adsorption, water treatment, air purification

1. INTRODUCTION

Activated carbon (AC) is a widely used adsorbent that can effectively remove a broad spectrum of contaminants from air, liquids and soil [1]. High porosity and a large specific surface area are the most important features of AC that allow it to physically adsorb gases and dissolved substances in liquids or solids, such as soil [1]. Spent AC causes additional environmental pollution and is therefore regenerated so that it can be reused [2].

2. TYPES OF ACTIVATED CARBONS

AC, which is a crude form of graphite, shows a very high adsorption capacity, which can reach up to 90%. It is a non-polar adsorbent that effectively retains mainly non-polar organic substances as well as non-electrolytes. Its adsorption properties are closely related to its preparation methods. AC can be derived from both mineral and organic raw materials. Its production is by thermal or thermochemical treatment [3]. It is produced from raw materials that have a high carbon content, for example: coal, coconut shells, wood, bamboo. The physical and chemical properties of carbon are influenced by the materials used in its production and by the time and temperature of the activation process, i.e. developing the porosity of the material. The structure of AC, consisting of graphite plates with uneven shapes, results in a large active surface area and adequate porosity, so that AC can adsorb contaminants [3].

Depending on the precursor materials and activating agents used to produce AC, several types can be distinguished. The main commercially available types are granular activated carbon (GAC) and powdered activated carbon (PAC).

Granular activated carbon (GAC) is usually extracted from waste materials such as coconut shells, palm or olive kernels during the activation process. Its granulation is carried out using soft, low-density waste materials and by adding binders. In addition to the waste materials, the moulding pressure, temperature, moisture content and activation method can also affect the quality of GAC. It is a type of AC that can be used in water treatment due to the lack of separation of carbon from the liquid mass. It effectively removes colour, odour, turbidity and microplastics, micropollutants and heavy metals [4].

Powdered activated carbon (PAC) is obtained from wood, lignite, used tyres and bio-waste materials (peanut shells). This type of AC is characterised by its large surface area and high microporosity, characteristic of its adsorption capacity. It is used in wastewater treatment and allows the removal of contaminants from water, air, liquids and gases. PAC has a higher adsorption capacity, but it cannot be regenerated due to the difficulty of separating it from the liquid phase [4].

There are also other types of activated carbon, such as:

- Extruded activated carbon (EAC) - made from powdered anthracite or charcoal with a suitable binder to form compressed granules. These are extruded under the high pressure of cylindrical moulds [5],
- Bead activated carbon (BAC) - is produced from petroleum tar and has a spherical shape. It is characterised by low impurity concentration and high mechanical strength [5],
- Impregnated activated carbon - carbon that has been saturated with a solution containing a specific metal compound and then calcined to produce a metal oxide on the carbon surface [5],
- Polymer-coated carbon - carbon coated with a polymer to produce a permeable coating that does not clog pores [5].

3. ACTIVATED CARBON MODIFICATIONS

Although activated carbon (AC) is one of the most popular materials used to remove contaminants, it is sometimes the case that it partially or completely fails to adsorb the compounds in question. There can be several reasons for this, including structural limitations or a small number of functional groups on the carbon surface. For this reason, AC has begun to undergo a modification process. This process involves changing the structure of AC or its chemical properties to improve its adsorption properties or to adapt it to the specific conditions in which it will be used. Modifications may include changing the porosity, adding functional groups or changing the hydrophilic or hydrophobic character of the AC. We distinguish between chemical, physical, impregnation, microwave, plasma, ozone and biological modification [5, 6].

3.1. Chemical modification

Chemical modification is a process that involves the introduction of different functional groups onto the surface of the AC by means of reducing or oxidising compounds. The process is usually carried out in the liquid or gas phase. In the liquid phase, the most commonly used

compounds are hydrogen peroxide, nitric(V) acid or a mixture of concentrated sulphuric(VI) and nitric(V) acids in a molar ratio (1:1). In the gas phase, on the other hand, the most commonly used compounds are oxygen from the air, nitrogen oxides, carbon dioxide or water vapour. By convention, it is preferable to carry out the process in the liquid phase rather than the gaseous phase, because modification in the liquid phase is much easier to control and more efficient than in the gaseous phase, but the gaseous phase, which causes less pollution, is just as often used because of the high pollution that the process causes in the liquid phase [7].

3.2. Physical modification

Physical modification is a process that involves changing the porous structure and physical properties of AC under the influence of physical agents. The aim of this process is primarily to improve the adsorption properties and thermal stability of AC, by influencing parameters such as specific surface area or pore volume of AC. The most common methods in this process are thermal, physical, moisture adsorption or surface modification. The greatest advantages of physical modification are the low production of impurities, the cleanliness and environmental friendliness of the process and its versatility [8].

3.3. Impregnation modification

Impregnation modification is a process that involves coating the AC surface with metal ions. This process is used to improve the adsorption properties of AC in aqueous environments for contaminants such as cyanides, heavy metals, fluorides or arsenic. The action of this modification is based on the formation of complex compounds with contaminants by means of metal aggregates. Iron salts Fe3+, copper, silver and aluminium are most commonly used for impregnation. The greatest advantages of this modification are increased durability to moisture and resistance to varying pH conditions [6].

3.4. Microwave modification

Microwave modification is a process that involves treating AC with microwave radiation. It is used to improve the absorption properties and adsorption rate in AC. It is a state-of-the-art method that is faster compared to physical modification, making it increasingly popular in industry. In addition to speed, the biggest advantages of this modification are the ease of process control and the operation at higher temperatures than in physical modification. The main disadvantages of this modification are the high cost of energy and apparatus needed to carry out the process [6].

3.5. Plasma modification

Plasma modification is a process that involves exposing AC to a plasma. It is used to improve the adsorption properties of AC in trapping metal ions. The action of this modification is to increase the acidity of the AC surface by acting with free oxygen radicals on the AC surface, which were formed during the plasma interaction and this allows the introduction of groups such as carboxyl or aldehyde groups on the AC surface. This process can be carried out under vacuum or at atmospheric pressure in the presence of a controlled gas such as air or oxygen. The greatest advantages of this modification are the precision of the process and the low damage to the AC

structure. The biggest disadvantages of this method are the high energy and equipment costs and the need for accurate process control [6].

3.6. Ozone modification

Ozone modification is a process that involves treating AC with ozone. It is used to improve the adsorption properties of AC in trapping organic compounds such as sulfonic acids or phenols and its derivatives. The action of this modification resembles that of plasma modification with the difference that the oxygen radical is formed from ozone and no acid groups are added. In addition, groups such as lactone, hydroxyl or carbonyl groups are formed on the AC surface during this process. This process is usually carried out at atmospheric pressure at 100oC. The biggest advantages of this modification are the efficiency and cost of the process. On the other hand, the biggest disadvantage is the sensitivity of the modification to atmospheric factors [6].

3.7. Biological modification

Biological modification is a process that involves exposing AC to microorganisms. It is used to improve the adsorption properties of AC in conditions where other modifications would harm the environment in which the AC is used. The action of this modification involves the interaction of micro-organisms with the surface of the AC and the subsequent biosorption of contaminants or the production of enzymes that adsorb contaminants by these organisms. The most common organisms in this modification are bacteria, algae or fungi. The biggest advantages of this modification are the fairly low cost of the process, environmental friendliness and selectivity. The biggest disadvantages of this modification are the time-consuming nature of the process and the very strict quality standards [6].

4. THE USE OF ACTIVATED CARBON IN WATER AND WASTE WATER TREATMENT

The development of the pharmaceutical, chemical and agricultural industries has led to an increase in the amount of various chemical compounds in wastewater. Consequently, the search for effective and economical solutions for their treatment has begun. AC has been recognised as a potential sorbent for wastewater treatment [10]. AC has adsorption properties, making it very suitable for the removal of contaminants found in water and wastewater. The process of sorption of contaminants from water onto AC (usually in granular form) is often used in Water Treatment Plants [11]. It is one of the last stages of the entire treatment cycle [12]. In addition to this, AC has a developed porous structure and excellent regeneration capability, which has the effect of extending the operating time and reducing the cost of the bed [13].
The main applications of AC in water treatment are:

- dechlorination,
- removal of odour and/or taste contaminants,
- removal of micropollutants from water, including: phenols, detergents, heavy metals, pesticides, carcinogens, aromatic and aliphatic hydrocarbons and viruses,
- reduction in colour.

Chlorine is used to disinfect the water, but unfortunately, due to its unpleasant odour, another water treatment process is needed to improve the water quality, for example with AC. Also other

odorous compounds in the water, such as sulphur compounds, nitrogen compounds and many organic compounds are removed with AC to improve water quality.

AC easily removes harmful organic compounds such as pesticides or aromatic compounds present in the water due to its large adsorption surface area. With the help of AC adsorption, it is also possible to effectively retain heavy metals present in wastewater. According to M. Malicka, 20-90% and 20-60% of mercury ions can be removed by adsorption onto GAC and dusty activated carbon [14].

In summary, AC is an effective adsorbent used in the treatment of wastewater from various types of pollutants. However, other equally effective and low-cost adsorbents are constantly being sought.

4. THE USE OF ACTIVATED CARBON IN AIR PURIFICATION

Gaseous pollutants in the air include: nitrogen oxides, sulphur oxide, carbon monoxide, carbon dioxide, ammonia and volatile organic compounds.
Sources of these pollutants are:

- industrial plants where, for example, the combustion of fossil fuels takes place,kotłownie domowe,
- municipal thermal power plants,
- transport by road, air, rail, sea,
- natural sources e.g. fires, volcanic eruptions, decay processes.

Cement composites with AC have been developed that allow the absorption of harmful pollutants such as nitrogen oxides from the air [15]. The activity of carbon to absorb nitrogen oxides does not require exposure of the material to harmful UV radiation, so such composites can be used, for example, in underground tunnels. The addition of a highly porous material such as AC to a cement composite has the effect of increasing and stabilising the uptake of nitrogen oxides and other pollutants from the air [16]. In a study by M. Horgnies et al. the rate of nitrogen(IV) oxygen adsorption for a reference concrete under prototype garage conditions without the addition of AC was less than 3%, and for concrete with the addition of 0.5% m.c. it was 20-26% [17]. In summary, AC is used to clean the air of many pollutants: noxious gases, odours from industry, dust, smoke, chemical vapours and other undesirable substances. Due to its wide application, it is widely used in industry.

In summary, AC is an irreplaceable material in environmental protection and the development of remanufacturing technology supports sustainable development and the conservation of natural resources.

7. CONCLUSION

Activated carbon is one of the most versatile and effective adsorbents, used for both water and wastewater treatment and air purification. Its unique properties, such as its large specific surface area and high porosity, make it an ideal material for the removal of organic pollutants, heavy metals and gases. Modification processes, including chemical, physical and biological techniques, make it possible to further increase its adsorption capacity and adapt it to specific applications. Activated carbon finds applications in water treatment, elimination of unpleasant odours and tastes, and air protection, including reduction of harmful gas emissions. Thanks to its

regenerability and wide range of modifications, it is not only an effective but also an economical solution in many industrial and environmental sectors.

Funding: This research was funded by the Polish Ministry of Science and Higher Education

BIBLIOGRAPHY

1. Mohammad-Khah A., Ansari R., Activated Charcoal: Preparation, characterization and Applications: A review article, *Int. J. Chemtech Res.*, 2009, 859-862.
2. Lim J., Okada M., Regeneration of granular activated carbon using ultrasound, *Ultrason. Sonochem.*, 2004, *12*, 277–282, doi:10.1016/j.ultsonch.2004.02.003.
3. Marko I., Stanko Š., Csicsaiová R., Comparison of the adsorbent efficiency of different types of granulated activated charcoal, *Pollack Period*., 2019, *14*, 87–95, doi:10.1556/606.2019.14.3.9.
4. Muttil N., Jagadeesan S., Chanda A., Duke M., Singh S.K., Production, Types and Applications of Activated Carbon Derived from Waste Tyres: An Overview, *Appl. Sci.*, 2022, *13*, 257, doi:10.3390/app13010257.
5. Ganjoo R., Sharma S., Kumar A., Daouda, M., Activated Carbon: Fundamentals, classification, and properties, *In the Royal Society of Chemistry eBooks*, 2022, 1–22, doi:10.1039/bk9781839169861-00001.
6. Wolak E., Vogt E., Szczurowski J., Modification of Activated Carbons for Application in Adsorption Cooling Systems, *Tech. Sci,* 2019, *1*, 87–98, doi:10.31648/ts.4350.
7. Bhatnagar A., Hogland W., Marques M., Sillanpää M., An Overview of the Modification Methods of Activated Carbon for Its Water Treatment Applications, *Chem. Eng. J.,* 2013, *219*, 499–511, doi:10.1016/j.cej.2012.12.038.
8. Zmiany właściwości węgli aktywnych po procesie ich modyfikacji, *Proc. ECOpole,* 2014, doi:10.2429/proc.2014.8(1)032.
9. http://www.os.not.pl/docs/czasopismo/1999/Choma_2-1999.pdf [dostęp dnia 03.01.2025r.].
10. Kobyłka A., Zastosowanie adsorpcji na węglu aktywnym w różnych układach technologicznych oczyszczalni ścieków, *Technical Issues,* 2016, *4*, 27-34.
11. Olesiak P., Stępniak L., Metody Intensyfikacji Procesu Sorpcji w Uzdatnianiu Wody, http://www.ekodok.pl/2014/62.pdf [dostęp dnia 03.01.2025 r.]
12. Sorbak Z., Adsorpcja i adsorbenty: teoria i zastosowanie, Wyd. Naukowe Uniwersytetu im. A. Mickiewicza, Poznań, 2000.
13. Bansal R.C., Goyal M., Adsorpcja na węglu aktywnym, WNT, Warszawa, 2009.
14. Malicka M., Metody usuwania jonów rtęci z zanieczyszczonych roztworów wodnych, Prace Naukowe GIG, Górnictwo i Środowisko, 2007, *4*, 19-30.
15. Lenart M., Gruszczyński M., Kozak A., Sowa A.I., O możliwości wykorzystania cementu z dodatkiem węgla aktywnego do oczyszczania powietrza z NOx, https://www.dnibetonu.com/wp-content/pdfs/2021/Lenart_Gruszczynski_Kozak_Sowa.pdf [dostęp dnia 03.01.2025 r.]
16. Ramakrishnan, G.; Orlov, A. Development of novel inexpensive adsorbents from waste concrete to mitigate NOx emissions, *Build. Environ.,* 2014, *72*, 28–33.
17. Horgnies M., Serre F., Dubois-Brugger I., Gartner E., NOx De - pollution Using Activated Charcoal Concrete - From Laboratory Experiments to Tests with Prototype Garages. In Proceedings of the 4th International Conference on Environmental Pollution and Remediation; Prague, Czech Republic, 2014.

TalentDetector
31th January 2025
Gliwice, Poland
DEPARTMENT OF ENGINEERING MATERIALS AND BIOMATERIALS
FACULTY OF MECHANICAL ENGINEERING
SILESIAN UNIVERSITY OF TECHNOLOGY
INTERNATIONAL STUDENTS SCIENTIFIC CONFERENCE

Analiza wytrzymałościowa klucza imbusowego wykonanego z różnych materiałów inżynierskich

Adam Schwarz[a], Łukasz Buszka[a], Łukasz Mann[b], Amadeusz Dziwis[c], Wojciech Mikołejko[c], Agata Śliwa[c]

[a] Uczniowie Zespołu Szkół Technicznych i Ogólnokształcących „Mechanik" w Tarnowskich Górach
email: misteradamowski@gmail.com, lukaszbuszka2@gmail.com
[b] Nauczyciel Zespołu Szkół Technicznych i Ogólnokształcących „Mechanik" w Tarnowskich Górach
email: l.mann@mechaniktg.pl
c Politechnika Śląska, Wydział Mechaniczny Technologiczny, Instytut Materiałów Inżynierskich i Biomedycznych
email: amadeusz.dziwis@polsl.pl, wojciech.mikolejko@polsl.pl, agata.sliwa@polsl.pl

Streszczenie: W pracy dokonano porównania kluczy imbusowych wykonanych z różnych gatunków stali na podstawie analizy naprężeń i przemieszczeń przy obciążeniu odpowiadającemu standardowej sile i momentowi skręcającemu działającej na narzędzie w czasie jego standardowego użytkowania. Analizy dokonano z wykorzystaniem Metody Elementów Skończonych w oprogramowaniu SolidWorks 2014.
Abstract: in this paper several hex keys made from different steels were compared, based on the stress and displacement analysis, corresponding the load of standard force and torque during regular using of tool. The analysis was made using Finite Elements Method in SolidWorks 2014 software.

Słowa kluczowe: klucz imbusowy, stal narzędziowa, CrV, SolidWorks, rozkład naprężeń, rozkład przemieszczeń

1. WSTĘP

Klucz imbusowy zwany potocznie imbusem jest rodzajem klucza trzpieniowego o przekroju sześciokąta foremnego (Rys. 1). Zazwyczaj występuje w postaci wygiętego w kształt litery L pręta lub wymiennych końcówek do wkrętaków automatycznych oraz ręcznych. Imbusem może też być nazywany rodzaj łba śruby o sześciokątnym otworze, przeznaczony do wkręcania takim kluczem. Śruby imbusowe stosowane są w miejscach, gdzie średnica łba jest niewiele większa niż średnica gwintu oraz w przypadku śrub bez łba. Ponadto wkręcanie i wykręcanie tego typu śruby nie wymaga dodatkowego miejsca w płaszczyźnie prostopadłej do osi śruby, co pozwala na stosowanie tego typu śrub przy ograniczonym

dostępie bocznym. Łby imbusowe stosowane są także we wkrętach do drewna. Rozwiązanie to jest bardzo często stosowane w meblach przeznaczonych do samodzielnego montażu, gdzie do zestawu dołączany jest tani klucz imbusowy o niskiej jakości, odpowiedni na ogół do skręcania mebli przez niedoświadczonego użytkownika. Łby śrub wykonanych z tych samych materiałów i o tej samej wytrzymałości mogą mieć mniejszą średnicę w przypadku zastosowania kluczy imbusowych niż w przypadku kluczy nasadowych. Wymiar sześciokąta jest zależny od średnicy śruby, które są wykonywane w standardzie metrycznym oraz calowym według europejskiej normy ISO 2936 [1,2]

Klucze imbusowe podobnie jak inne podobne narzędzia są wytwarzane ze stali narzędziowej wyróżniającej się wysoką twardością, odpornością na ścieranie i rozciąganie oraz działanie wysokiej temperatury. Dodatki stopowe tych stali wpływa na wytrzymałość narzędzi, ale także zwiększa koszty produkcji. Jednym z ważniejszych pierwiastków stopowych jest wanad, stosowany w procesie wytwarzania stali stopowej chromowo-wanadowej CrV, która jest jeszcze najczęściej dodatkowo hartowana. Elementy narzędzi ręcznych wykonane ze stali CrV charakteryzuje wysoka wytrzymałość na ścieranie. Istotną rolę odgrywają też walory ergonomiczne klucza, czyli jego dobre „trzymanie się" w dłoni. Uzyskuje się to dzięki odpowiedniemu przetłoczeniu korpusu, które decyduje o wygodnym kształcie rękojeści i o jej chropowatej, antypoślizgowej powierzchni [1,2,3]

Rysunek 1. Model 3D klucza imbusowego
Figure 1. The 3D model of Hex key

2. ZAŁOŻENIA MODELOWE

W niniejszej pracy analizie naprężeń został poddany standardowy klucz imbusowy zwymiarowany według normy ISO 2936. Do stworzenia trójwymiarowego modelu i przeprowadzenia symulacji wykorzystano program komputerowy SolidWorks 2014. Celem analizy jest sprawdzenie, która z zaproponowanych stali stosowanych do produkcji kluczy imbusowych, wykaże się najlepszymi własnościami mechanicznymi w podanym przykładzie, gdzie na dłuższe ramię działa siła o wartości 1000N. Natomiast mocowanie zostało przyłożone w miejscu kontaktu klucza ze śrubą (Rys.2.). W tym celu do stworzonego modelu zastosowano różne gatunki najpowszechniej stosowanej stali przedstawione w tablicy 1.

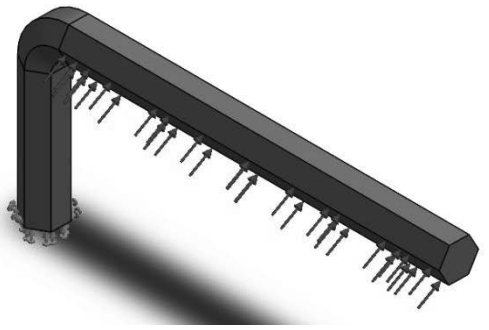

Rysunek 2. Madel klucza imbusowego z nałożonymi warunkami brzegowymi- analiza statyczna

Figure 2. Geometrical model of Hex key with applied boundary conditions- static analysis

Tablica 1. Charakterystyka zastosowanych materiałów.

Table 1. Characteristics of the materials

	Chromowa stal nierdzewna	Stal narzędziowa 1.2316 X36CrMo17	Stal narzędziowa 1.4116 X50CrMoV15
Współczynnik sprężystości (N/mm^2)	200000	207000	215000
Współczynnik Poissona	0.28	0,28	0,28
Masa właściwa (kg/m^3)	7800	7750	7700
Granica plastyczności (N/mm^2)	172.34	935	785

3. ANALIA NAPRĘŻEŃ I PRZEMIESZCZEŃ

W wyniku przeprowadzonej analizy metodą elementów skończonych przy użyciu oprogramowania SolidWorks 2014 na wykonanym modelu klucza imbusowego dokonano analizy naprężeń Von Mises oraz przemieszczenia. Symulację wykonano z użyciem siły 1000N dla wszystkich trzech materiałów. Według przeprowadzonej symulacji największe naprężenia występują w miejscu wygięcia klucza imbusowego (Rys 3-8).

W przypadku klucza imbusowego wykonanego z chromowej stali nierdzewnej maksymalne naprężenia, w miejscu wygięcia, wynoszą 895,62 [Mpa] (Rys. 2). Wartość ta maleje wraz z oddaleniem od miejsca wygięcia w stronę dłuższego ramienia, gdzie osiąga wartość ok. 80 [MPa]

W przypadku klucza nimbusowego wykonanego ze stali narzędziowej 1,2316 maksymalne naprężenia wynoszą 895,48 [MPa] (Rys. 4) i maleją w stronę dłuższego ramienia gdzie osiągają wartość ok. 42 [MPa]

W ostatnim przypadku gdzie zastosowano stal narzędziową 1,4116 naprężenia maksymalne osiągają wartość 895,35 [MPa] (Rys. 6). Natomiast najmniejsze wartość naprężenia zanotowano na dłuższym ramieniu, a ich wartość to ok. 42 [MPa]

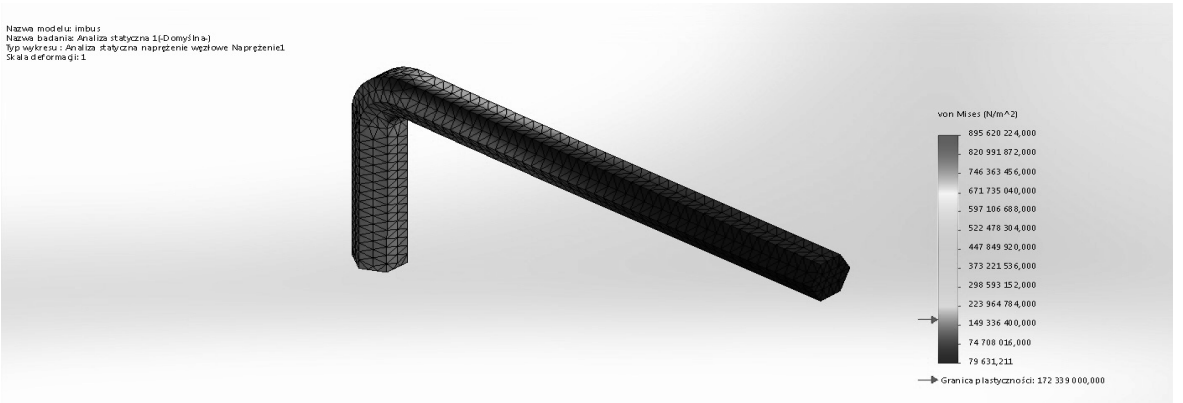

Rysunek 3. Wyniki analizy MES – naprężenia Von Mises – Chromowa stal nierdzewna
Figure 3. The FEM research results – Von Mises stress – Chrome stainless steel

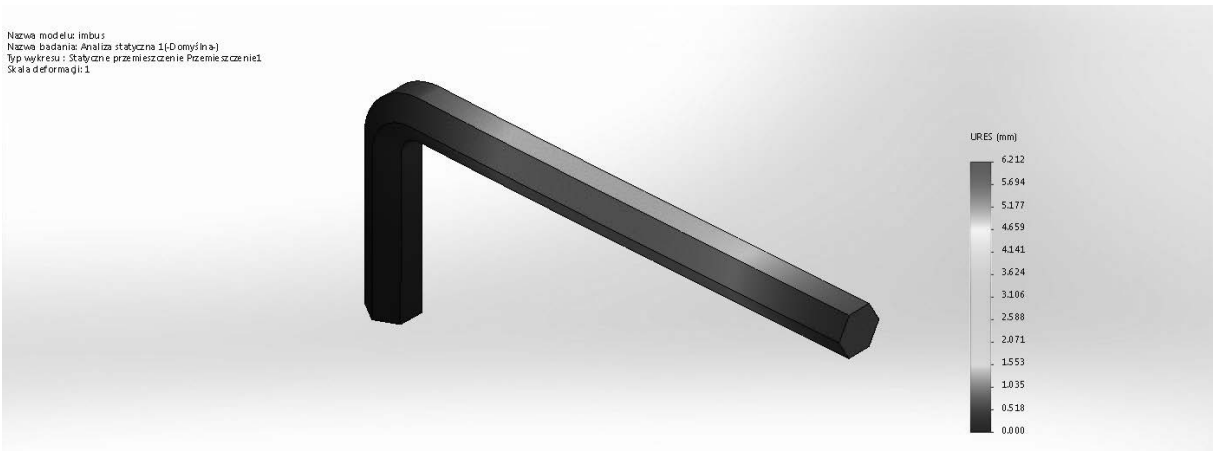

Rysunek 4. Wyniki analizy MES – przemieszczeń – Chromowa stal nierdzewna
Figure 4. The FEM research results – displacement– Chrome stainless steel

Rysunek 5. Wyniki analizy MES – naprężenia Von Mises – Stal narzędziowa 1.2316
Figure 5. The FEM research results – Von Mises stress – tool steel 1.2316

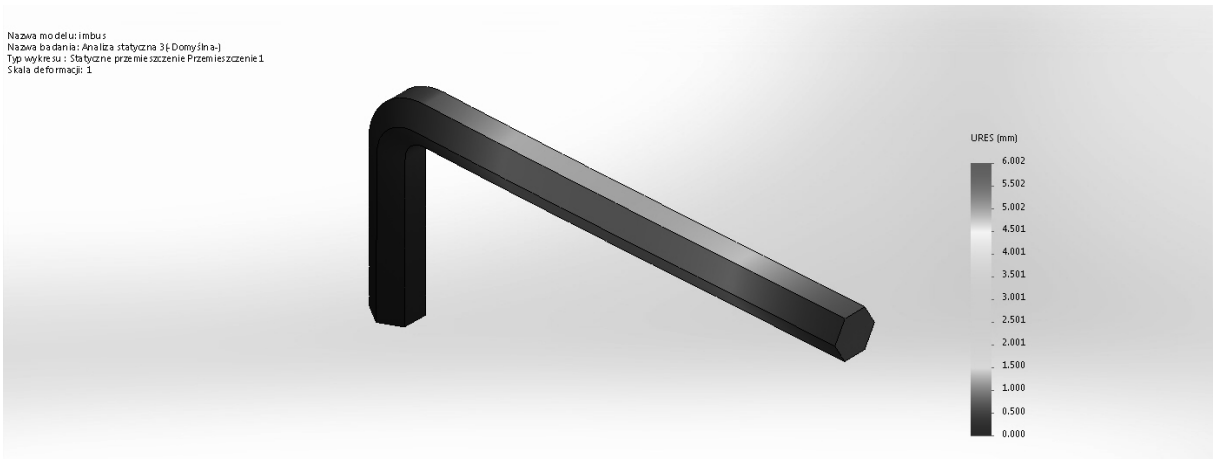

Rysunek 6. Wyniki analizyMES – przemieszczeń – Stal narzędziowa 1.2316
Figure 6. The FEM research results – displacement – tool steel 1.231

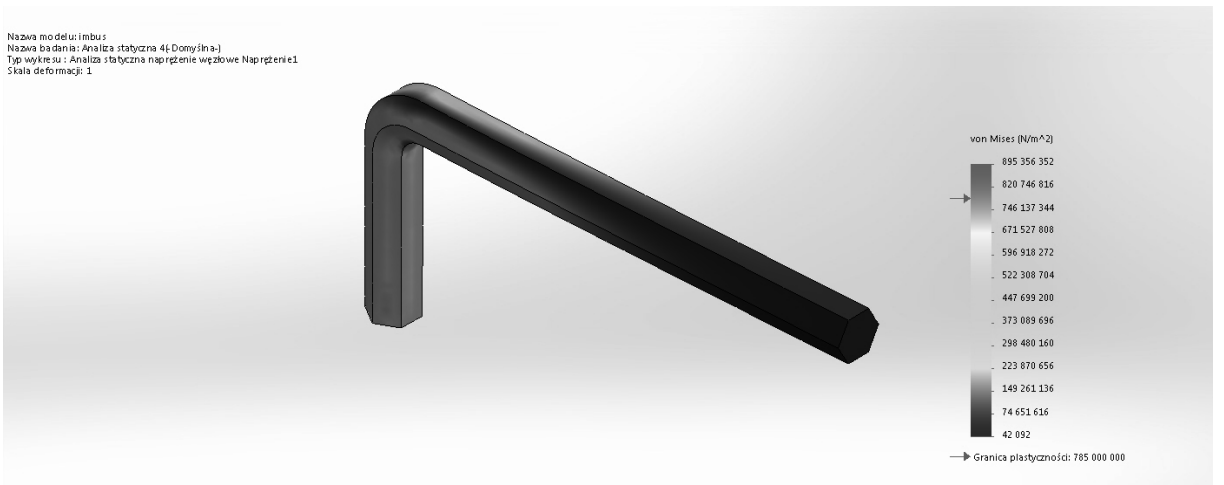

Rysunek 7. Wyniki analizy MES – naprężenia Von Mises – Stal narzędziowa 1.4116
Figure 7. The FEM research results – Von Mises stress – tool steel 1.4116

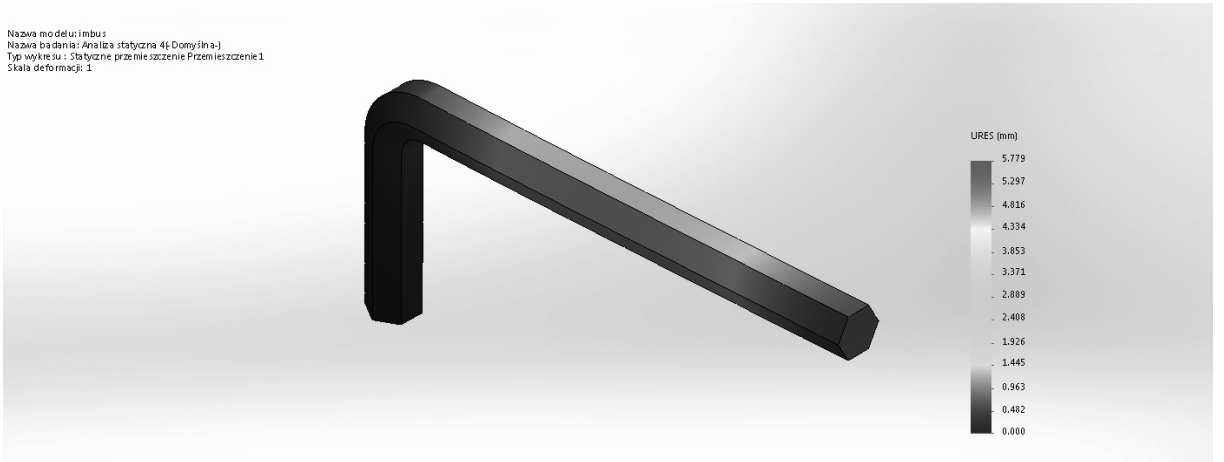

Rysunek 8. Wyniki analizy MES – przemieszczeń – Stal narzędziowa 1.4116
Figure 8. The FEM research results – displacement – tool steel 1.4116

4. PODSUMOWANIE

W pracy został przedstawiony model klucza imbusowego oraz wykonana została symulacja metodą elementów skończonych. Symulacja klucza zobrazowała rozkład występujących naprężeń i przemieszczeń pod wpływem działającej siły (1000N) dla trzech wybranych materiałów. Po przeprowadzonej symulacji wnioskujemy, że klucz wykonany ze stali narzędziowej 1.4116 charakteryzuje się najmniejszą wartością przemieszczeń.

Co raz częściej spotykamy się z zastosowaniem analizy MES, które odwzorowują rzeczywiste warunki. Duży wpływ na to ma rozwój technologii komputerowych. Projektując modele jesteśmy w stanie odwzorować najmniejsze szczegóły rzeczywistych obiektów. Wykonana analiza posiada wiele zalet. Jedną z nich jest zmniejszenie kosztów związanych z wykonywaniem prototypów do badań laboratoryjnych. Jesteśmy także w stanie wykonać analizę dla elementów o skomplikowanej geometrii, dla których obliczenia analityczne są praktycznie niemożliwe.

BIBLIOGRAFIA

1. Norma PN—ISO 2936 Narzędzia montażowe do śrub i nakrętek, Klucze trzpieniowe kątowe do wkrętów z gniazdem sześciokątnym
2. L.A. Dobrzański, Podstawy nauki o materiałach i metaloznawstwo. Materiały inżynierskie z podstawami projektowania materiałowego, Wydawnictwo NaukowoTechniczne, Gliwice,2002.
3. J. Jaworski, T. Trzepieciński, Stal stosowana na narzędzia do przeróbki plastycznej metali: z klasyfikacją i oznaczaniem stali według PN-EN, Oficyna Wydawnicza Politechniki Rzeszowskiej, Rzeszów, 2014

TalentDetector
31th January 2025
Gliwice, Poland
DEPARTMENT OF ENGINEERING MATERIALS AND BIOMATERIALS
FACULTY OF MECHANICAL ENGINEERING
SILESIAN UNIVERSITY OF TECHNOLOGY
INTERNATIONAL STUDENTS SCIENTIFIC CONFERENCE

Właściwości powłoki miedzianej nakładanej w procesie galwanizacji

Jakub Sikora[a], Krzysztof Michalik[a], Jakub Hasiński[a], Michał Nowak[a], Beata Krupińska[b], Marcin Staszuk[b]

[a]Politechnika Śląska, Wydział Mechaniczny Technologiczny, Mechanika i Budowa Maszyn
[b]Politechnika Śląska, Wydział Mechaniczny Technologiczny, Katedra Materiałów Inżynierskich i Biomedycznych

Abstract: The properties of a copper coating applied to a closed profile made of structural steel S235 were investigated using electrolytic galvanization technology. Particular focus was placed on measurements of the coating's thickness, hardness, and composition. The galvanization process was performed under controlled conditions, taking into account parameters such as current intensity, process time and abrasive gradation during surface preparation for the process. The results of the study enabled an assessment of the efficiency of the applied method and its potential applications.

Streszczenie: Zbadano właściwości powłoki miedzianej, która została naniesiona na profil o przekroju kwadratowym wykonany ze stali konstrukcyjnej S235 przy użyciu technologii galwanizacji elektrolitycznej. W szczególności skupiono się pomiarach grubości, twardości i składu chemicznego powłoki. Proces galwanizacji wykonano w kontrolowanych warunkach, z uwzględnieniem parametrów takich jak natężenie prądu, czas procesu oraz gradacja ścierniwa w trakcie przygotowania powierzchni do procesu. Wyniki badań pozwoliły na ocenę efektywności zastosowanej metody i jej potencjalnego zastosowania.

Słowa kluczowe: stal, galwanizacja, miedziowanie

1. WSTĘP

Galwanizacja to metoda wykorzystywana do ochrony elementów metalowych przed metalu na różne powierzchnie, głównie metalowe. Proces ten opiera się na zjawiskach elektrochemicznych i wymaga odpowiedniego przygotowania materiałów przed pokryciem ich nową powłoką korozją oraz poprawy ich estetyki. Polega na elektrolitycznym nakładaniu cienkich powłok. Proces odbywa się poprzez zanurzenie dwóch elektrod w roztworze elektrolitycznym, między którymi przepuszczany jest prąd stały. W wyniku różnicy potencjałów jony metalu zawarte w kąpieli przylegają do powierzchni przedmiotu poddawanego obróbce [1-4].

Celem badania było sprawdzenie własności mechanicznych powłoki miedzianej naniesionej w rożnych warunkach. Zmiennymi były chropowatości powierzchni stali, natężenie prądu podczas galwanizacji oraz czas zanurzenia próbki.

2. MATERIAŁY DO BADAŃ I METODYKA BADAWCZA

Do procesu galwanizacji zastosowano profile o przekroju kwadratowym o wymiarach 15x15x1,5 mm i długości 50 mm (rys. 1) wykonane ze stali konstrukcyjnej S235 (PN-EN 10025-2) o składzie chemicznym podanym w tabeli 1. Profile miały różną chropowatość powierzchni uzyskane za pomocą papierów ściernych o różnych gradacjach. Po oczyszczeniu próbki ze stali zostały odtłuszczone w 5% roztworze NaOH na gorąco i wytrawione w 10% roztworze HCl. Następnie profile zostały wypłukane wodą destylowaną i osuszone sprężonym powietrzem. Każda próbka po takim zabiegu była zanurzana w kąpieli zawierającej siarczek miedzi i poddana procesowi galwanizacji przy zmiennych parametrach czasu i natężenia prądu (tab.2).

Do badań powłok miedzianych użyto, mikroskop świetlny Axio Observer firmy ZEISS, wysokorozdzielczy skaningowy mikroskop elektronowy SUPRA 35 firmy ZEISS z dołączonych detektorem EDS. Do badania twardości powłok miedzianych zastosowano mikrotwardościomierz FUTURE–TECH FM–ARS9000.

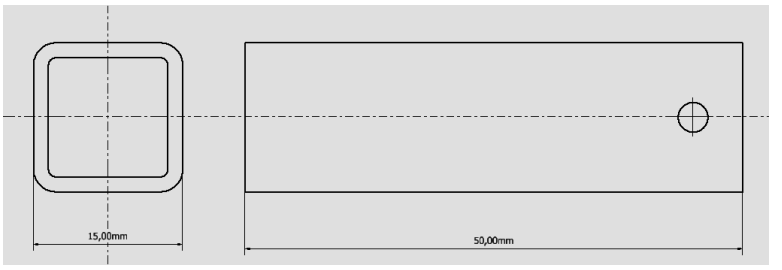

Rys.1. Wymiary profili stalowych zastosowanych do galwanizacji
Fig. 1. Dimensions of steel profiles used for galvanization

Tabela 1. Skład chemiczny stali S235 według PN-EN 10025-2
Table 1. Chemical composition of S 235 steel according to PN-EN 10025-2

C	Mn	Si	P	S	Cr	Ni	Mo	V	Nb	Ti	Al	Cu
Max 0,17	Max 1,40	-	Max 0,025	Max 0,025	-	-	-	-	-	-	-	Max 0,55

Tabela 2. Parametry procesu galwanizacji
Table 2. Parameters of the electrochemical copper galvanization process

Nr próbki	Gradacja ścierniwa	Temperatura kąpieli do odtłuszczania i trawienia [°C]	Natężenie prądu [A]	Czas galwanizacji [min]
2	1200	20	2,5	1
3	1200	20	1	1
4	1200	60	1	1
5	800	60	1	0,5

6*	1200	60	1	1,5
7	2500	60	0,6	1,5
8	2500	60	0,6	2,5
9	220	60	0,6	2,5
10*	220	60	0,6	4
11*	220	60	1	1
*próbki użyte do dalszej analizy				

3. WYNIKI BADAŃ

W wyniku analizy wszystkich uzyskanych próbek w procesie galwanizacji (2-11) do dalszych badań wybrano trzy; oznaczone nr 6,10 i 11 (tab.2). Ocenę jakości powłok miedzianych naniesionych w procesie galwanizacji wykonano za pomocą mikroskopu świetlnego i zestawiono na rysunkach 2-4.

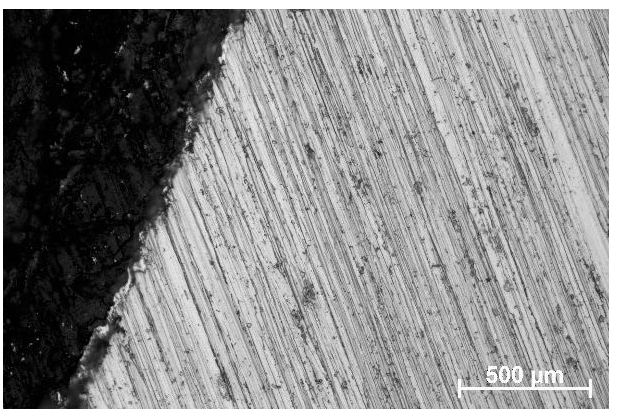

Rys. 2. Próbka 6 – przekrój poprzeczny
Fig. 2. Sample 6 - cross section

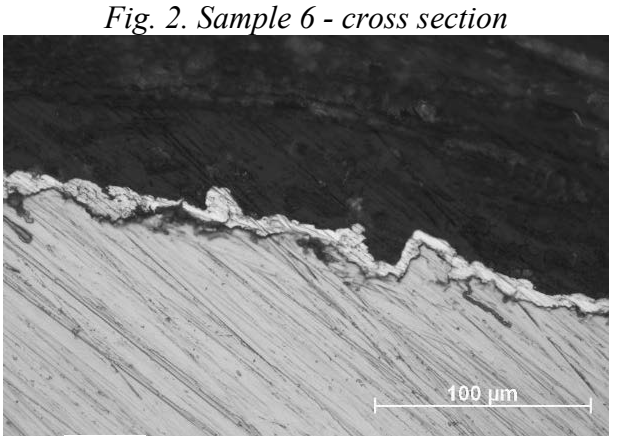

Rys. 3. Próbka 10 – przekrój poprzeczny
Fig. 3. Sample 10 - cross section

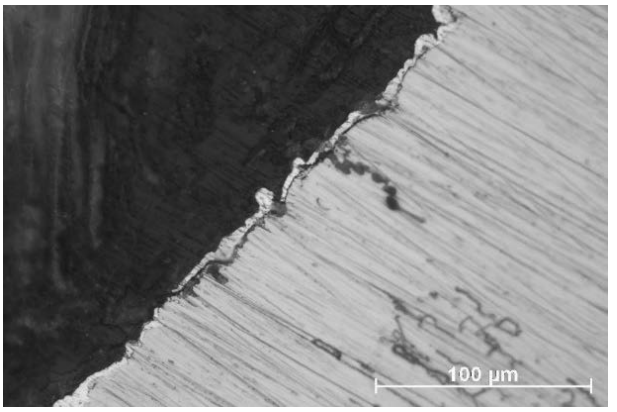

Rys. 4. Próbka 11 – przekrój poprzeczny
Fig. 4. Sample 11 - cross section

Za pomocą elektronowego mikroskopu skaningowego dokonano pomiaru grubości powłok miedzianych na profilach stalowych (rys. 5-7). Średnią wartość grubości powłoki zamieszczono w tabeli 3.

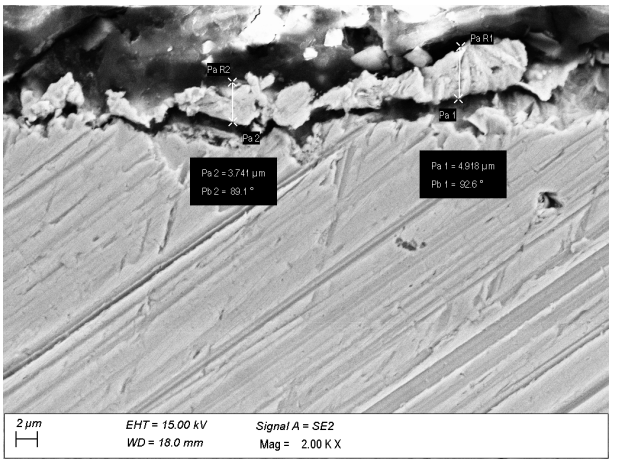

Rys. 5. Pomiar grubości powłoki miedzianej na profilu stalowym nr 6.
Fig. 5. Measurement of the thickness of the copper coating on steel profile no. 6.

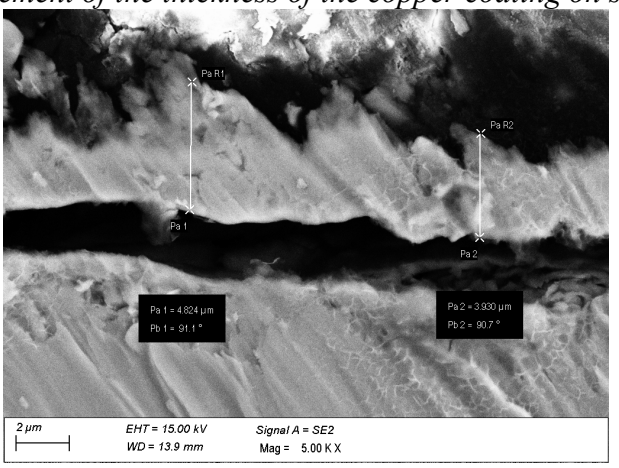

Rys.6. Pomiar grubości powłoki miedzianej na profilu stalowym nr 10.
Fig. 6. Measurement of the thickness of the copper coating on steel profile no. 10.

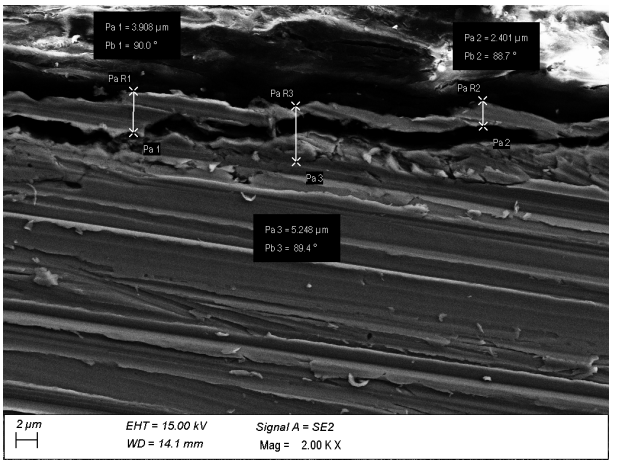

Rys.7. Pomiar grubości powłoki miedzianej na profilu stalowym nr 11
Fig. 7. Measurement of the thickness of the copper coating on steel profile no. 11.

Tabela 3. Średnia grubość powłoki Cu na profilach stalowych
Table 3. Average thickness of the Cu layer on steel profiles

Nr próbki	*Średnia grubość powłoki [µm]*
6	*4.30*
10	*4.35*
11	*3.83*

Obserwacje prowadzone za pomocą skaningowego mikroskopu elektronowego oraz badania składu chemicznego wykonane z zastosowaniem rentgenowskiej mikroanalizy ilościowej EDS potwierdzają, że pomiary grubości zostały wykonane na naniesionej w procesie galwanizacji powłoce miedzianej (Rys.8-13)

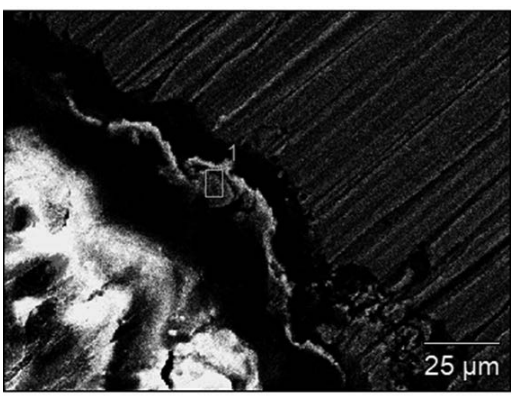

Rys. 8. Obszar badania składu powłoki próbki 6
Fig. 8. Area of coating composition analysis for sample 6

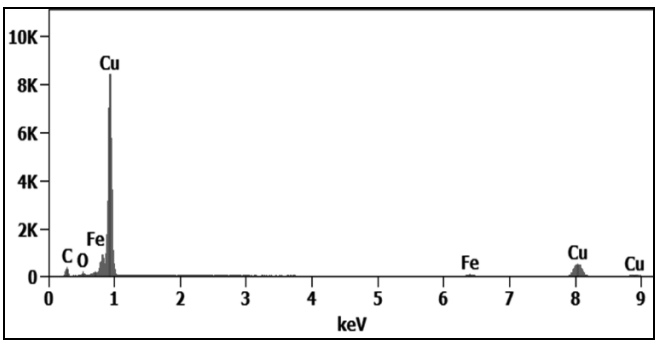

Rys. 9. Analiza składu chemicznego w mikroobszarze oznaczonym 1 na rys. 8
Fig. 9. Analysis of the chemical composition in the micro-area marked as 1 in Fig. 8.

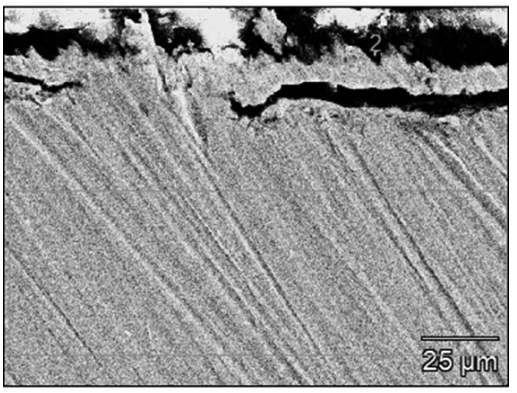

Rys. 10. Obszar badania składu powłoki próbki 10
Fig. 10. Area of coating composition analysis for sample 10

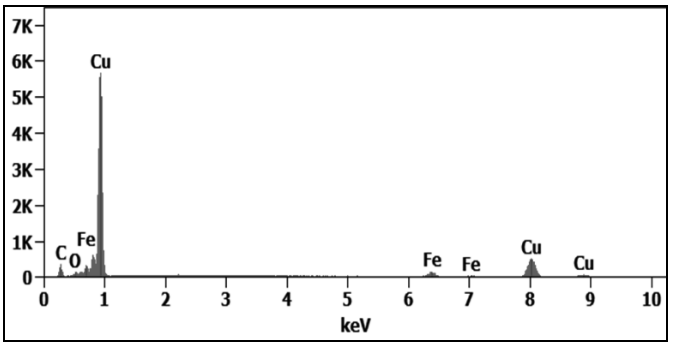

Rys. 11. Analiza składu chemicznego w mikroobszarze oznaczonym 2 na rys. 10
Fig. 11. Analysis of the chemical composition in the micro-area marked as 2 in Fig. 10

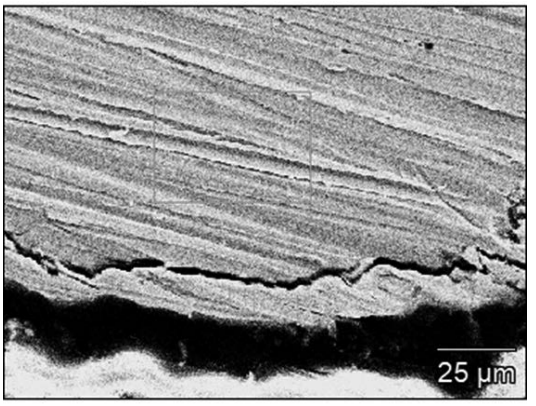

Rys. 12. Obszar badania składu powłoki próbki 11
Fig. 12. Area of coating composition analysis for sample 11

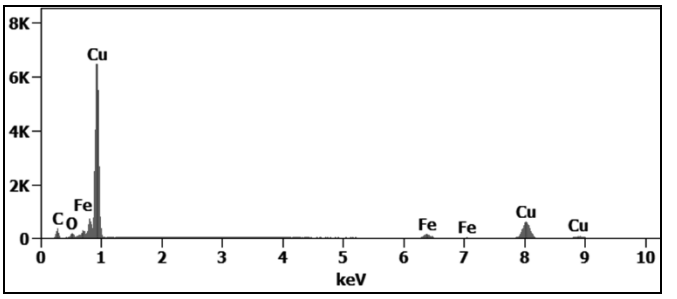

Rys. 13. Analiza składu chemicznego w mikroobszarze oznaczonym 1 na rys. 12
Fig. 13. Analysis of the chemical composition in the micro-area marked as 1 in Fig. 12

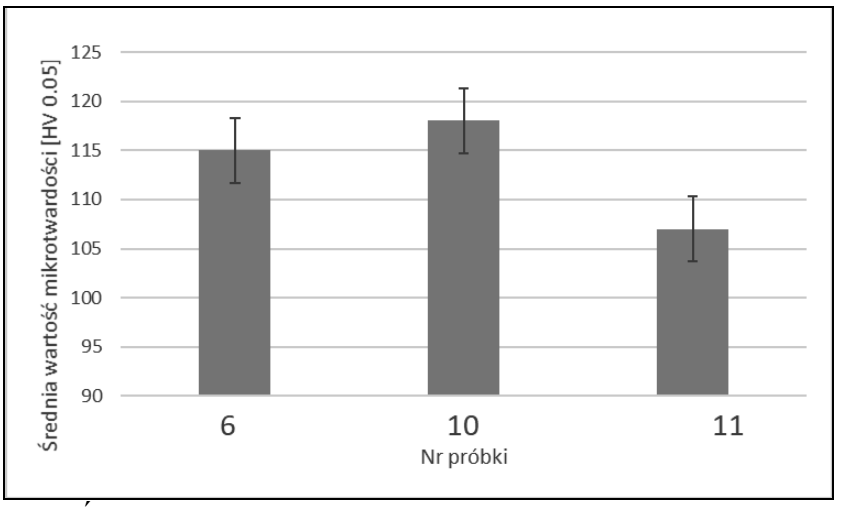

Rys. 14. Średnie wartości mikrotwardości HV0.05 powłoki miedzianej
Fig. 4. The average microhardness values HV0.05 of the copper coating

Powierzchnię profili stalowych po galwanizacji miedzią zbadano mikrotwardościomierzem FUTURE–TECH FM–ARS9000, pod obciążeniem 50 gf (ok. 0,5 N) przez 10 sekund. Średnie wyniki pomiarów mikrotwardości na powierzchni zewnętrznej zamieszczono na rysunku 14.

Analiza mikrotwardości próbek wykazała, że wartości mikrotwardości powłoki mieszczą się w zakresie od 107 do 132 HV, przy czym rozkład mikrotwardości na powierzchni próbek jest nierównomierny. Próbka 11 charakteryzuje się najniższą średnią mikrotwardością. Z kolei próbka 10 wykazuje najwyższą średnią mikrotwardość wynoszącą 132 HV.

4. PODSMOWANIE

W pracy przedstawiono wybrane własności wytworzonych powłok miedzianych na elementach stalowych przy zastosowaniu procesu galwanizacji elektrochemicznej. Wyniki badań potwierdzają, że jakość powłok miedzianych zależy od: chropowatości powierzchni, czasu galwanizacji. Odpowiedni dobór parametrów galwanizacji, takich jak natężenie prądu i czas procesu, umożliwia uzyskanie optymalnych wartości grubości oraz trwałości otrzymywanych powłok, co umożliwia efektywne zastosowanie metody w praktyce.

PODZIĘKOWANIA

Praca powstała w wyniku realizacji projektu „*Elektrochemiczne tworzenie powłok ochronnych na metalach*” w ramach kształcenia zorientowanego projektowo – PBL, w konkursie XI w ramach programu Inicjatywa Doskonałości – Uczelnia Badawcza, Wydział Mechaniczny Technologiczny, Politechnika Śląska.

LITERATURA

1. L.A. Dobrzański, A.D. Dobrzańska-Danikiewicz, Obróbka powierzchni materiałów inżynierskich, Open Access Library, Volume 5 (2011)
2. Praca zbiorowa, Poradnik Galwanotechnika, Wydawnictwo naukowo techniczne (1985)
3. W.I. Łajner, N.T. Kudriacew, Podstawy galwanostegii Tom I, Państwowe Wydawnictwo Techniczne (1955)
4. Lawrence J. Durney, Electroplating Engineering Handbook, Van Nostrand Reinhold (1984)

TalentDetector

31th January 2025
Gliwice, Poland

DEPARTMENT OF ENGINEERING MATERIALS AND BIOMATERIALS
FACULTY OF MECHANICAL ENGINEERING
SILESIAN UNIVERSITY OF TECHNOLOGY

INTERNATIONAL STUDENTS SCIENTIFIC CONFERENCE

Development of thermal spraying technology for coatings effectively protecting power plant components against high-temperature corrosion

Grzegorz Sikorski[a], Katarzyna Jędrzejczyk[a], Michał Wnętrzak[a], Julia Żuławska[a], Tomasz Harężlak[a], Mateusz Dziergas[a], Artur Czupryński[b], Waldemar Kwaśny[b]

[a] Student of Silesian University of Technology, Faculty of Mechanical Engineering
[b] Silesian University of Technology, Faculty of Mechanical Engineering, Department of Welding Engineering
email: gs302480@student.polsl.pl

Abstract: The project aimed to develop guidelines for manual flame spraying to protect boiler screen tubes in high-temperature, corrosive environments with sulfur, chlorine, and ammonia. The research included determining optimal spraying parameters, assessing coating quality, comparing microstructures, measuring atomic concentrations, and evaluating hardness and wear resistance compared to wear-resistant steel.

Keywords: powder flame spraying process, Ni-B-Si protective coatings, low-oxygen corrosion

1. INTRODUCTION

Thermal spraying methods significantly enhance the protection of machine elements exposed to abrasive, erosive, and corrosive wear [1÷4]. Coatings combine the substrate's favorable properties with wear resistance, hardness, and heat resistance, separating load transfer from environmental protection. Thermal spraying is an effective, economical process for increasing the durability of new elements and repairing worn parts [5÷8]. The SuperJet-S Eutalloy® process (Castolin Eutectic, Gliwice, Poland) is particularly effective, using an oxygen-acetylene torch for precise coating application [9]. In powder flame spraying, elements are heated to 150÷500°C, and plasticized powder particles create a mechanically bonded pre-layer, followed by additional layers applied at 600÷700°C [2,9]. Each layer is melted within the liquidus-solidus range of the alloy, enhancing adhesion. This method is ideal for elements needing high resistance to abrasion, erosion, corrosion, impact, and high temperatures [2,10÷12]. The SuperJet-S-Eutalloy® system uses self-fluxing powders, mainly based on Ni, Co, and Ni-Cr alloys.

The energy industry’s growing reliance on biomass and alternative fuels increases corrosion in boiler waterwall tubes due to chlorine and sulfur. To meet strict EU NOx emission regulations, low-emission combustion is being adopted, leading to heightened low-oxygen or high-temperature corrosion. Protective thermal spray coatings are essential for extending component lifespan by mitigating corrosion, erosion, impact, and wear, increasing the operational efficiency of energy devices.

2. OWN RESEARCH

2.1. Purpose of the research

The scientific aim of the project was to develop technological guidelines and compare manual flame spraying techniques for protective powder coatings that effectively protect the surfaces of boiler screen tubes against the effects of an aggressive gas atmosphere at high temperatures, including a reducing atmosphere containing sulfur, chlorine, and ammonia compounds. The scope of the research included, among others:

- determination of optimal parameters for the powder flame spraying process based on preliminary technological trials,
- assessment of coating quality depending on process parameters,
- comparison of the metallographic microstructure of coatings, the heat-affected zone (HAZ), and the base material,
- determination of atomic concentrations of elements present in the coating,
- measurement of the hardness of the coating, the heat-affected zone, and the base material,
- investigation of the coatings' resistance to abrasive and erosive wear in comparison to a reference material in the form of wear-resistant steel.

2.2. Equipment and materials used to perform the operation

The powder flame spraying process was carried out at a production station equipped with a modern and precise modular system for manual powder flame spraying — a SuperJet-S-Eutalloy® acetylene-oxygen torch (Fig. 1).

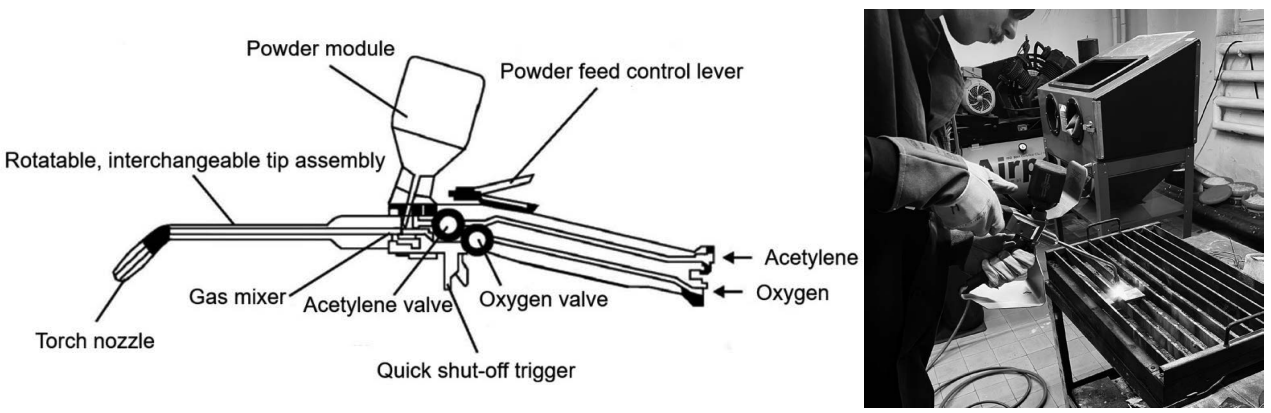

(a) (b)

Fig. 1. Build diagram of Superjet-S-Eutalloy® torch from powder flame spraying (a) [9] and the course of the spraying process of the samples (b)

The samples, shaped as rectangular prisms with dimensions of 55x47x5 mm, were made of boiler steel grade 16Mo3. The surface of the samples was subjected to abrasive blasting in a cabinet blaster, using cast iron shot with a grain size of G34 (0.8–1.2 mm), in accordance with the requirements of ISO 2063-1, prior to the spraying process. This treatment aimed to clean the external surfaces of the samples from contaminants such as rust, scale, and grease. After this step, the samples underwent additional brushing to remove any remaining shot particles, followed by chemical cleaning using tetrachloroethylene.

As the additional material for flame spraying, three types of metallic powders from Castolin Eutectic were used, namely Eutalloy® BronzoChrom 10185, Eutalloy® RW 17535, and Eutalloy® RW 12495. The chemical composition of the boiler steel and the powders used for spraying, according to the manufacturer's data, is provided in tables 1–4. The physical properties of boiler steel 16Mo3 are presented in Table 5.

Table 1. Chemical composition of 16Mo3 steel according to PN-EN 1561

Chemical composition, wt.%									
C	Mn	Si	P	S	Cr	Mo	Ni	Cu	N
0.20	0.4-0.9	<0.35	<0.025	<0.010	<0.3	0.25-0.35	<0.3	<0.3	<0.012

Table 2. Chemical composition of deposited metal according to manufacturer data (Castolin Eutectic) of powder Eutalloy® BronzoChrom 10185

Chemical composition, wt.%					
C	Cr	Fe	B	Si	Ni
≤0.1	≤0.5	≤0.5	2.5	3.0	rest

Table 3. Chemical composition of deposited metal according to manufacturer data (Castolin Eutectic) of powder Eutalloy® RW 17535

Chemical composition, wt.%					
C	Cr	Fe	B	Si	Ni
0.8	26.0	1.0	3.0	3.7	rest

Table 4. Chemical composition of deposited metal according to manufacturer data (Castolin Eutectic) of powder Eutalloy® RW 12495

Chemical composition, wt.%					
C	Cr	Fe	B	Si	Ni
0.56	13.30	2.85	1.92	3.13	rest

Table 5. Physical properties of boiler steel 16Mo3 according to PN-EN 1561

Mechanical properties			
Strength R_m, MPa	Hardness, HB 30	Melting point, °C	Thermal resistance,°C
440÷590	140÷170	1300	≤600

2.3. Parameters and technique of the powder flame spraying process

The powder flame spraying was performed in two steps. First, the sample was preheated to 300°C, and a 0.1 mm thick underlayer was applied. The torch was moved in a straight line along the sample. In the second step, the sample was reheated to 500°C, and another layer was applied and remelted. The torch moved diagonally across the sample, covering the entire surface in one pass, achieving a coating thickness over 1.0 mm. The nozzle was kept 24-30 mm from the surface, with the uncoated temperature not exceeding 550°C. No further heat treatment was applied after cooling.

The powder flame spraying tests of 16Mo3 boiler steel were conducted according to the requirements of the thermal spray coatings standard ISO 14923. The quality evaluation criteria for the sprayed coatings included appropriate thickness, good adhesion to the substrate, continuity, uniformity of coverage, absence of cracks, and low porosity. The optimal spraying parameters, determined based on preliminary technological trials, are presented in Table 6. The appearance of the samples with the sprayed coatings is shown in Fig. 2.

Table 6. Powder flame spraying of Eutalloy® BronzoChrom 10185, Eutalloy® RW 17535 and, Eutalloy® RW 12495 layers on boiler steel 16Mo3 parameters

Type of powder	Oxygen working pressure, bar	Acetylene working pressure, bar	Oxygen flow rate, l/h	Acetylene flow rate, l/h	Burner's nozzle working distance, mm
Eutalloy® BronzoChrom 10185	2	0,5	440	400	24÷30
Eutalloy® RW 17535	2	0,5	440	400	24÷30
Eutalloy® RW 12495	2	0,5	440	400	24÷30
Note: A standard modular lance with a working nozzle marked B3 S (injector Ø = 0.6 mm) was used. spraying was carried out with a normal flame					

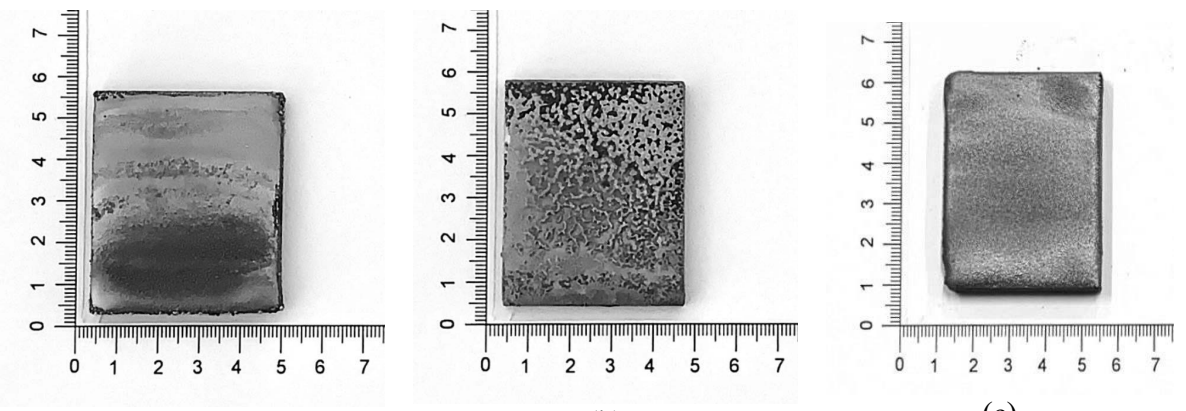

(a) (b) (c)

Fig. 2. View of sample layers after powder flame spraying of: Eutalloy® RW17535 (a), Eutalloy® BronzoChrom 10185 (b), Eutalloy® RW 12495 (c) on boiler steel 16Mo3

2.4. Research methodology and results

Non-destructive tests results

Non-destructive testing, including visual (ISO 17637 [20]) and penetrant (ISO 3452-2 [21]) tests, was conducted according to the relevant standards. Visual inspections (VT) involved assessing the surface condition without instruments, after thorough cleaning. For penetrant testing, dye penetrants (System Designation Type II, Sensitivity 2) Cd-2 PT ISO 3452-2 II Cd-2 were used.

After visual and penetration tests on the surface of Ni-B-Si coatings made by powder flame spraying, no welding incompatibilities such as cracks, surface pores, excessive convexity, wrong edges, or spatter were observed. The coatings exhibited high surface smoothness and uniform weld metal distribution. Using Eutalloy® BronzoChrom 10185, Eutalloy® RW 17535,

and Eutalloy® RW 12495 powders, with the applied technological parameters, coatings meeting the B quality level according to ISO 5817 were achieved, meeting the highest requirements for layers.

Results of phase composition and metallographic tests

Microscopic studies were conducted on prepared metallographic specimens. The samples were chemically etched with 3% ethyl alcohol, and the etching time was adjusted experimentally for each material. Observations were made using the Olympus SZX7 and GX 71 microscopes. The macroscopic images allowed for determining the coating thickness and SWC depth. Phase analysis of the coatings was performed using the X'Pert Pro PANalytical diffractometer, in the Bragg-Brentano configuration, with a copper lamp (λ=1.54056) at 40 kV and 30 mA, in the 2Θ range from 30° to 105°.

Macroscopic tests of coatings on boiler steel 16Mo3, sprayed with Eutalloy® BronzoChrom 10185, Eutalloy® RW 17535, and Eutalloy® RW 12495 powders, revealed no welding incompatibilities such as cracks, lack of fusion, excessive penetration, or gas voids. Only small gas blisters were observed on the coatings' cross-section. The absence of incompatibilities indicates proper substrate preparation and correct spraying parameters. The coatings with Eutalloy® BronzoChrom 10185 showed a diffusive connection with the native material, without partial melting. The heat-affected zone was narrow, with no significant structural changes in the native material, and the diffusion depth did not exceed 100 μm.

Tests of the phase composition of flame-sprayed coatings with Eutalloy® BronzoChrom 10185, Eutalloy® RW 17535, and Eutalloy® RW 12495 powders on boiler steel 16Mo3, mainly revealed a solid nickel solution crystallizing in a surface-centered regular system. The presence of the $Cr_{23}C_6$, Cr_7C_3 and SiO_2 phase was also found.

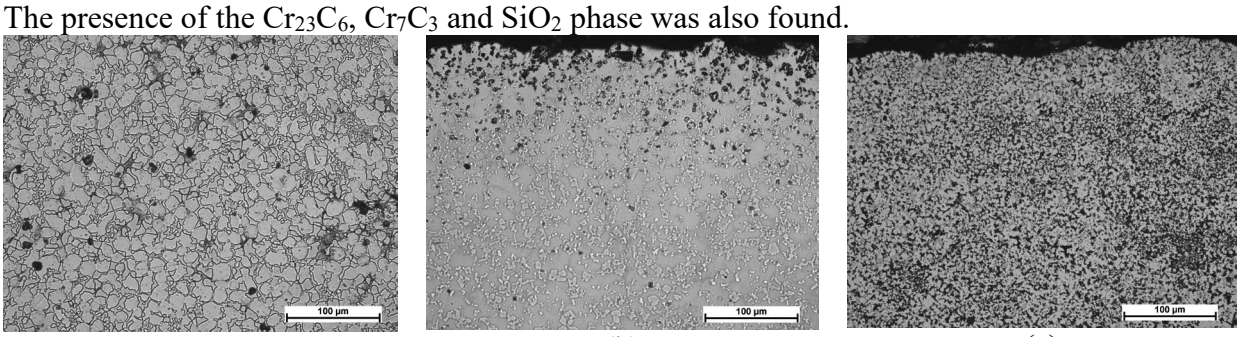

(a) (b) (c)

Fig. 3. Microstructure general view on layers powder flame sprayed on boiler steel substrate: a) Eutalloy® BronzoChrom 10185, b) Eutalloy® RW 17535, c) Eutalloy® RW 12495

Hardness measurement results

The Vickers hardness method was used for measuring the hardness of the samples, characterized by a wide measurement range, minimal invasiveness, and high precision. The tests were conducted on a Future Tech FM-810 device according to the PN-EN ISO 6507 standard. Hardness is calculated as the ratio of the applied force to the surface area of the indentation, made using a diamond indenter with a vertex angle of α=136°. The tests were performed on the sample cross-section, covering the sprayed layer, the fusion line with a small heat-affected zone, and the base material. The hardness measurement results are presented in Table 7.

Table 7. Hardness test results on surface of powder flame sprayed Eutalloy® BronzoChrom 10185, Eutalloy® RW 17535, and Eutalloy® RW 12495 layers on boiler steel substrate

Measurement point	Eutalloy® BronzoChrom 10185 [HV]	Eutalloy® RW 17535 [HV]	Eutalloy® RW 12495 [HV]
1	354	386	355
2	273	411	400
3	301	457	378
4	340	465	371
5	290	465	271
6	263	418	293
7	328	607	369
8	408	452	384
Average	319	457	352

Results of erosion resistance tests

Erosion resistance of flame-sprayed coatings on steel substrates was tested according to ASTM G76-95 [23] using the setup shown in Fig. 4. Al_2O_3 powder with particle sizes up to 50 μm was used as the abrasive material. The particle velocity was 70 ±2 m/s, the feed rate was 2.0 ±0.5 g/min, and the nozzle-to-sample distance was 10 mm. Erosion resistance tests were conducted at impact angle of incidence of 30°. Erosion resistance wear test results are presented in Table 8.

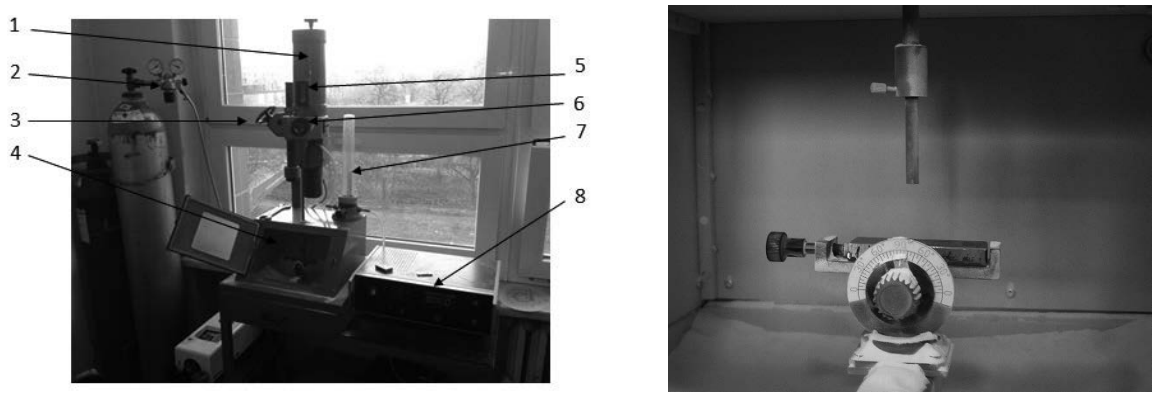

(a) (b)

Fig. 4. Erosion resistance test rig according to ASTM G 76-2: (a) general view: 1 – erodent tank, 2 – gas pressure regulator, 3 – distance adjustement of the nozzle from the sample surface, 4 – blasting chamber, 5 – window for checking the erodent level in the tank, 6 – window for checking the erodent feed into the air stream, 7 – flowmeter, 8 – control and adjustment unit , (b) the interior view of the erosion measuring chamber

Table 8. Erosion resistance wear test results of powder flame sprayed Eutalloy® BronzoChrom 10185, Eutalloy® RW 17535, and Eutalloy® RW 12495 layers on boiler steel 16Mo3 substrate in comparison to abrasion-resistant steel

Angle of incidence of the erodent,	Type of the coating's material	Mass loss, [mg]	Volume loss, [mm^3]	The speed of erosion, [mg/min]	Resistance to erosive wear, [0.001mm^3/g]	Relative erosion resistance
30°	Eutalloy® RW 17535	1.3	0.2	0.13	0.01	1.00
	Eutalloy® BronzoChrom 10185	4.5	0.6	0.45	0.03	0.33
	Eutalloy® RW12495	3.4	0.4	0.34	0.02	0.2
	Hardox 400	1.9	0.2	0.19	0.01	1.00
Note: 1) – the result was referred to samples made of Hardox® 400 wear-resistant steel plate with a nominal hardness of 400 HBW. Erosion rate, g/min = mass loss of the sample, mg: exposure time, min; Resistance to erosive wear, 0.001 mm^3/g = sample volume loss, mm^3: total mass of erodent used in the test, g. Erosion test parameters: speed – 70 ± 2 m/s, temperature 20°C, erodent – Al_2O_3, nominal particle size of the erodent – 50 μm, amount of erodent administered – 2.0 ± 0.5 g/min, test time – 10 min, distance between the nozzle and sample – 10 mm, density of coatings and reference material according to table 9, mass of erodent used in the test – 20.25 g.						

Table 9. Density of coatings and reference material

Type of the coating's material	Eutalloy® RW 17535	Eutalloy® BronzoChrom 10185	Eutalloy® RW12495	Hardox 400
Denisty [g/ cm^3]	7,16	7,26	7,73	7,87

3. SUMMARY

The flame-sprayed coatings exhibit limited erosion resistance compared to Hardox® 400 wear-resistant steel, which indicates the need for further optimization of the process parameters or materials used in environments particularly susceptible to erosive wear. Despite these limitations, the coatings effectively protect the surfaces of boiler screen tubes against high-temperature corrosion, especially in atmospheres containing sulfur, chlorine, and ammonia. By ensuring proper surface preparation and optimizing the spraying parameters, good adhesion, coating continuity, and resistance to cracking and porosity were achieved. Macroscopic examination of coatings sprayed on 16Mo3 boiler steel revealed no welding defects such as cracks, lack of fusion, excessive penetration, or gas inclusions. Only minor gas blisters were observed, indicating proper substrate preparation and correct spraying parameters. The analysis of the phase composition revealed a solid nickel solution crystallizing in a face-centered cubic structure, providing strong mechanical properties. Chromium carbides ($Cr_{23}C_6$ and Cr_7C_3) enhance hardness and wear resistance, while silica (SiO_2) improves

corrosion resistance by acting as a protective barrier. This combination of phases ensures the coatings are durable and resistant to degradation in high-temperature environments. These coatings have significant potential to increase the durability of power plant components, particularly in the context of corrosion caused by aggressive gas environments, which is important given the growing use of biomass and alternative fuels.

Pracę zrealizowano w ramach kształcenia zorientowanego projektowo – PBL, w ramach programu Inicjatywa Doskonałości – Uczelnia Badawcza w zakresie projektu pt.: *„Opracowanie technologii natryskiwania cieplnego powłok skutecznie zabezpieczających elementy instalacji energetycznych przed korozją wysokotemperaturową”.*

BIBLIOGRAPHY

1. Tobota K., Chmielewski T., Chmielewski M., Microstructure and selected properties of Ni-Cr-Re coatingsdeposited by means of HVOF thermal spraying. Welding Technology Review, 2019, Vol. 91(1), 25–30. https://doi.org/10.26628/wtr.v91i1.1000
2. Bhushan B., Principles and Applications of Tribology, 2013, New York, John Wiley & Sons, 980.
3. Marcos Sá DeSousa J., Ratusznei F., Pereira R., de Medeiros Castro R., Mercado Curib E.I., Abrasion resistance of Ni-Cr-B-Si coating deposited by laser cladding process. Tribology International, 2020, Vol. 143, 106002. https://doi.org/10.1016/j.triboint.2019.106002.
4. Shveikin G.P., Sokolova N.V., Rudenskaya N.A., Kuzmin V.I., Supersonic plasma and wear-resistant nickel alloy coatings. Доклады Академии Наук, 2015, Vol. 463(3), 309–312.
5. Ilushchenko A. F., Manoylo E. D., Andreev M. A., Onashchenko F. E., Flame spraying of coatings of self-fluxing alloys. Welding International, 2017, Vol. 31(11), 887-891. https://doi.org/10.1080/09507116.2017.1349279
6. Hejwowski T., Erosive and abrasive wear resistance of overlay coatings. Vacuum, 2008, Vol. 83(1), 166–170. DOI: 10.1016/j.vacuum.2008.03.029
7. Majewski D., Hejwowski T., Łukasik D., The influence of microstructure of arc sprayed coatings on wear resistance. Advances in Science and Technology. Research Journal, 2018, Vol. 12(1), 285–292. https://doi.org/10.12913/22998624/86210
8. Jiméneza H., Olayaa J.J., Alfonsob J.E., Pineda-Vargas C.A., Corrosion resistance of Ni-based coatings deposited by spray and fuse technique varying oxygen flow. Surface and Coatings Technology, 2017, Vol. 321, 341–349. https://doi.org/10.1016/j.surfcoat.2017.04.068.
9. http://www.castolin.com
10. Bęczkowski R., Gucwa M., Qualifying of hardfacing surfacing layers operating under conditions of the cement industry. Welding Technology Review, 2015, Vol. 87(9), 43–46. https://doi.org/10.26628/wtr.v87i9.450
11. Dorfman M.R., Thermal Spray Coatings. Handbook of Environmental Degradation of Materials (Third Edition), 2018, 469–488.
12. Kondej A., Babul T., Microstructure of the Ni-Cr-B-Si coating obtained in surfacing process. Welding Technology Review, 2016, No. 3, 23–26. Welding Technology Review – www.pspaw.pl Vol. 92(3) 2020 21

TalentDetector
31th January 2025
Gliwice, Poland
DEPARTMENT OF ENGINEERING MATERIALS AND BIOMATERIALS
FACULTY OF MECHANICAL ENGINEERING
SILESIAN UNIVERSITY OF TECHNOLOGY
INTERNATIONAL STUDENTS SCIENTIFIC CONFERENCE

Construction of an electric drive module for wheelchairs and implementation of control systems using AI and BCI

Wojciech Sikorski[a], Dominik Kłaput[a], Anastasiia Pashko[a], Julian Koterba[a]

[a] Silesian University of Technology, Faculty of Automatic Control, Electronics and Computer Science
email: ws306725@student.polsl.pl

Abstract: This article presents a prototype of an electric module designed to be mounted on a conventional wheelchair. The proposed design integrates multiple control methods, including a traditional joystick, image analysis AI, voice recognition, and a brain–computer interface (BCI). This configuration offers users a wide range of navigation options, significantly enhancing their independence and comfort. Real-world tests demonstrated notable improvements in mobility and reduced travel times compared to a standard manual wheelchair.

Keywords: brain-computer interface (BCI), electric wheelchair, assistive technology, artificial intelligence (AI), gaze and voice control

1. INTRODUCTION

People with physical disabilities face numerous difficulties in today's world related to performing such basic activities as moving around, communicating, or accessing public services. These problems often arise from architectural barriers, limited availability of assistive technologies, and challenges in social integration. In this context, the development of assistive technologies (AT) [1] and brain-computer interfaces (BCI) is becoming a key area of research aimed at improving the quality of life for people with severe motor disabilities.
More traditional assistive technologies, such as electric wheelchairs and other personal transportation devices, play an important role in improving the everyday functioning of people with mobility limitations. However, their high cost can represent a significant obstruction, which consequently limits the potential for their use by target group representatives. Such financial constraints may lead to a reduced quality of life for users [2], emphasizing the necessity of implementing more cost-effective technological solutions [3].
This study focuses on building a low-cost test platform in the form of a wheelchair with an electric drive module. The prototype integrates BCI technology, image and voice analysis based on artificial intelligence (AI), as well as traditional control methods, such as physical and remote joysticks.
The proposed test platform stands out for its universal approach, combining various control methods that can serve users with different types of disabilities. The introduction of these

features enables the creation of a system that provides the user with a high level of independence and safety while simultaneously allowing customization according to individual needs.
The tests conducted include a comprehensive analysis of existing brain-controlled wheelchair solutions and an evaluation of the proposed system's effectiveness in real-world conditions.
Brain-computer interfaces (BCIs) [4] are systems that enable direct communication between the human brain and external devices. They are particularly useful for patients with neurological disorders, such as amyotrophic lateral sclerosis (ALS) or strokes, where the use of traditional interfaces often becomes impossible.
In recent years, image and voice analysis, as important branches of artificial intelligence (AI), have been significantly developed. These technologies allow for the creation of systems that provide individuals with disabilities a more intuitive interaction with their environment. Combining them with BCIs makes it possible to design assistive solutions that enhance the independence of users with motor impairments and improve their quality of life [5]. This work aims to support the development of such solutions that enhance the independence of people with disabilities[6].

2. METHODOLOGY

2.1. Project Assumptions

The project involves creating a universal electric drive module that can be easily mounted on a traditional wheelchair, along with various control systems adapted to different types of disabilities.
The drive module consists of two motors, which will ensure high maneuverability and allow precise navigation, even in relatively confined spaces. The control systems used in the project include:
• Physical joystick
• Joystick in a mobile application
• Head movement control
• Human silhouette tracking system
• Control via EEG signals
• Voice commands
Each module implementation will maintain a high level of versatility, enabling easy testing and the addition of new functionalities. Additionally, an important assumption of the project is to keep the prototype's construction costs low to ensure its potential affordability.

2.2. System Components

2.2.1. Construction of the Electric Drive Module

The architecture of the electric drive system consists of several key components:
• Motors: The drive system consists of two three-phase motors that are independently controlled, enabling precise navigation and trajectory control.
• Controller: A controller sourced from a hoverboard was reprogrammed by uploading open-source software, which allowed the adaptation of its functionality to the project's requirements, including enabling communication via a UART interface with the ESP32 module.
• ESP32 Module: The ESP32 serves as the main communication hub. It is responsible for:
1. Communication with the hoverboard controller via UART.

2. Wireless communication through Bluetooth (BT), allowing the wheelchair to be controlled using a phone or computer.
3. Wired control via a USB cable connected to a computer.
• Joystick: A joystick is connected to the ESP32 module, enabling manual control of the wheelchair.
• Safety Button: This button can be used in emergency situations to immediately stop the vehicle.
Depending on the configuration, the system can operate manually using the joystick or integrate additional modules for more advanced control methods, such as BCI, image analysis, or voice recognition.

2.2.2. Mobile Application Control Module
A mobile application was developed for Android and iOS systems using Kotlin and Swift, enabling control of the electric wheelchair via Bluetooth. The application offers an on-screen joystick for controlling the wheelchair, allows users to select control modes, and provides diagnostic data. Communication is bidirectional, ensuring synchronization of information exchanged between the application and the wheelchair.

2.2.3. EEG Control Module (Hardware and Software)
The system utilizes electrical signals generated by the brain, which are analyzed and processed to control the wheelchair [7]. The Emotiv EPOC X headset was used to record these signals, standing out for its ease of use and affordability compared to other EEG devices.

2.2.4. Image Analysis Module
The system uses AI for image analysis to enhance the functionality of the wheelchair. The module includes:
• *Silhouette tracking* – the YOLO algorithm [8] detects and tracks human silhouettes in real-time.
• *Facial and gaze analysis* – the MediaPipe library [9] interprets facial expressions and gaze direction, allowing the system to infer the user's intended direction of travel.

2.2.5. Voice Recognition Module
The voice recognition module uses the SpeechRecognition library [10], which relies on the Google API to convert speech to text. This solution allows users to issue voice commands, further enhancing the system’s intuitiveness and ease of use [11].

3. IMPLEMENTATION

3.1. Construction of the Wheelchair Prototype
During the design of the prototype, various structural concepts were considered. One proposed solution involved using a single pivoting wheel controlled by a servomechanism, modeled after existing electric add-ons for wheelchairs. However, it was ultimately determined that this design would be difficult to implement and would not provide sufficient maneuverability. Instead, a solution was adopted that relies on two independently controlled wheels placed between the rear wheels of the wheelchair. This configuration allows the wheelchair to rotate in place and provides high precision in maneuvering.

The drive module was constructed using a welded steel frame, though plans are in place to replace it with aluminum to reduce weight. All electronic components were housed in a sealed enclosure to protect them from damage and moisture.
A custom battery was also developed for the project. Initially, lead-acid batteries were considered, but their unfavorable capacity-to-weight ratio led to the selection of Li-Ion batteries. The battery was built using 18650 cells in a 10S5P configuration, providing a voltage of 36 V. This voltage level was chosen for safety reasons and because of the wide availability of compatible components such as chargers and other accessories.
A Battery Management System (BMS) monitors the battery pack, protecting it against overcharging, excessive discharge, and current overload. The BMS's maximum instantaneous current rating of 30A was selected to be 80% of the maximum instantaneous current recommended by the cell manufacturer. This additional safety margin helps prevent the cells from overheating in the unventilated pack.
The entire module, including the battery, motors, and electronics, is attached to the wheelchair frame using screws. This enables quick removal of the module, restoring the full functionality of a traditional wheelchair (fig. 1).

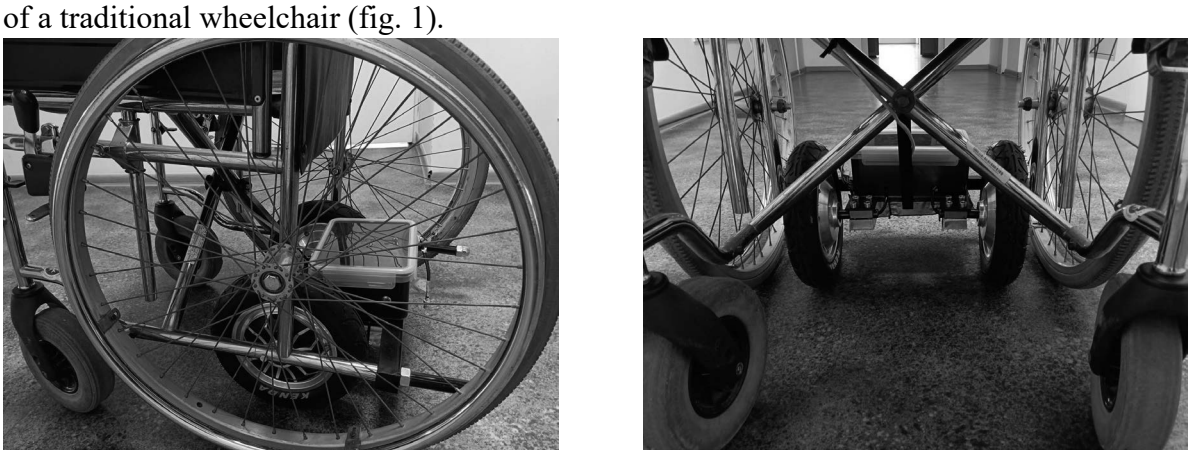

Figure 1. Prototype of a wheelchair controlled by EEG and AI

3.2. Mobile Application Control Module

The process of creating the application began with the implementation of a joystick that generates x and y coordinates based on the user's movements. These values are sent to the wheelchair as text-based commands. The communication mechanism includes the cyclic transmission of these commands and the reception of responses from the wheelchair, which are processed as diagnostic data stored in a fixed-size buffer.
The format of the returned data contains information such as direction, speed, temperature, battery voltage, and the number of lost data packets. The synchronization mechanism was based on alternating data transmission and short delays between cycles. Additionally, the functionality to select a control mode was implemented, requiring the transmission of information about the preferred mode to the wheelchair and the disabling of the joystick within the application if control is being performed from another source.
During the implementation, challenges arose related to selecting the representation of the joystick's position and ensuring stable application performance in situations where the wheelchair responded with incomplete data.

3.3. Image Analysis Algorithms

3.3.1. Image Analysis

Initially, the Haar Cascade [12] algorithm was used for tracking the human silhouette; however, its effectiveness proved insufficient, particularly during motion. This issue was resolved by employing the YOLO (You Only Look Once) algorithm, which significantly improved the reliability and enabled real-time human tracking [13].

3.3.2. Gaze Direction Analysis

For facial analysis and determining the direction of gaze, the MediaPipe library was utilized. This library includes a built-in convolutional neural network that provides coordinates for 468 facial landmarks. Key points such as the tip of the nose, the area between the eyes, the tip of the chin, and the corners of the eyes are used to measure head rotation. The measured rotation refers to the axis running between the point between the eyes and the tip of the chin.

This system requires calibration for each user to account for individual facial shapes and preferences. A challenge arises when the camera is positioned at an angle greater than 30 degrees relative to the face. The solution involves placing the camera centrally or using two cameras on either side of the wheelchair, with seamless switching between them depending on the current gaze angle.

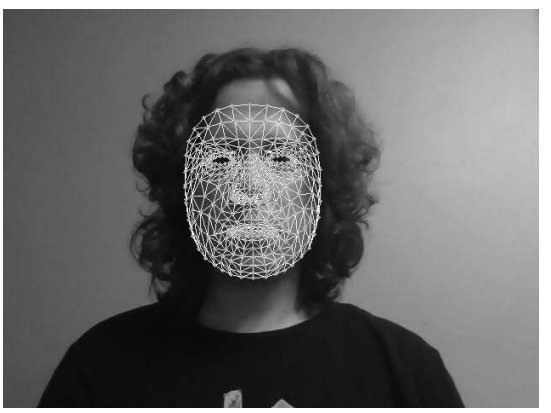

Figure 2. A grid of points on the face detected by MediaPipe

3.4. Voice Analysis Algorithms

3.4.1. Voice Recognition

Initially, OpenAI's Whisper AI model [14] was used for speech transcription. However, it proved to be too resource-intensive and struggled with short commands such as "left," "faster," and "slower." It often generated artifacts in the form of repeated words, and the response time (several seconds) was unacceptable for a real-time system.

The solution was to use the SpeechRecognition library, which utilizes the Google API for transcription, which operates quickly and accurately without generating errors. However, this solution requires a constant internet connection, increasing data transfer load. To mitigate this, preliminary analysis of audio samples was performed using the WebRTC VAD library, which detects the presence of human voice. Additionally, the MediaPipe library was used to detect lip movement, recording audio only when the user's mouth is open. Although this approach slightly slows down the transcription process, it significantly reduces the amount of data transmitted over the internet.

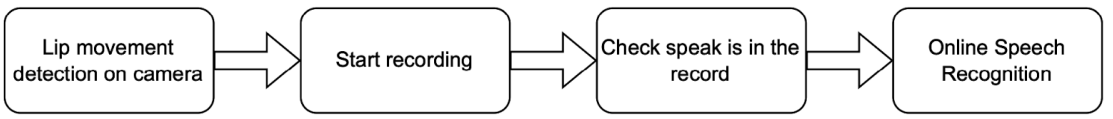

Figure 3. The graph shows the data inflow for voice command analysis

3.5. Control Using BCI

Designing a control system based on EEG signals required a comprehensive analysis and evaluation of various implementation possibilities. One of the first approaches considered was the use of visual signals, which show clear activity in the EEG recording within the range of potentials evoked by visual stimuli. The plan was to use a display where different areas would emit images with varying flicker frequencies. When the user focused on a specific section of the display, the generated EEG signal would be easy to detect and interpret. Despite the potential benefits, such as the simplicity of data analysis, this solution proved to be impractical. The need for an additional display and the difficulty of simultaneously tracking movement led to this approach being rejected due to its low user comfort.

Another concept was control using signals associated with phantom limb movements, that is, the imagined movements of limbs. For this method, the EEG helmet DSI-24 was chosen, known for its high precision in readings, which was crucial for the reliable interpretation of phantom limb movement signals. Unfortunately, this option turned out to be incompatible with the project assumptions. The very high cost of the device (24,800 USD), combined with the significant time investment required to create a comprehensive interpretative software, led to this method being ultimately rejected. The final choice was the Emotiv EPOC X helmet, which, in combination with the dedicated software from Emotiv, allowed for the training and implementation of mental control commands such as forward and backward movement or turning right or left. This helmet, thanks to the Emotiv Cortex API, was integrated with the wheelchair control system through a relatively user-friendly interfacing program. After practical tests Emotiv EPOC X helmet proved to be the ideal choice for this project. Its relatively low price (999 USD), ease of use, and user comfort were significant advantages that perfectly aligned with the project assumptions. Compared to other tested devices, the EPOC X provided sufficient quality of EEG readings while minimizing costs and the time required for system implementation and testing.

Figure .4 The DSI 24 EEG device on the left and The Emotiv EPOC X EEG device on the right, image sources: [15] [16]

3.6. Integration

In our prototype, the system architecture was designed with flexibility and easy expansion in mind. The core of the system includes the key components necessary to launch and operate the device: BLDC motors with the controller, battery, emergency switch, joystick, and the ESP32 module, which acts as a HUB. These components allow the system to be powered on with basic functionality.

Thanks to its modular design, the system can be adapted to different user needs and expanded with new functionalities in the future.

Such extensions include, among others, the aforementioned cameras for analyzing gaze direction and/or body tracking, voice control using a microphone, EEG control, as well as remote control from an application on a phone or computer.

The default system configuration assumes the joystick as the primary control method, and then, according to the selected operating mode (which can be chosen by voice or through the mobile app), it is possible to configure the system to ignore other interfaces (EEG, image analysis, mobile app, etc.) or assign them a specific priority.

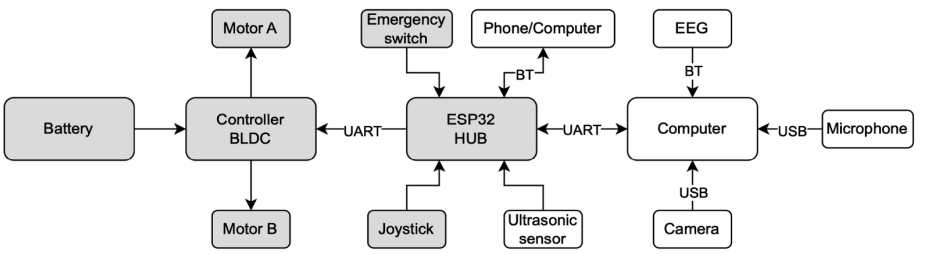

Figure 5. Graph showing the connections between project modules

4. RESULTS AND ANALYSIS

4.1. Analysis of Gaze Direction Control

To implement gaze direction control, we wrote software that estimated the user's current gaze angle based on the camera view. To prove the effectiveness of our software, an experiment was conducted, which involved repeating the measurement of the gaze angle 100 times for each established head angle. For each trial, the arithmetic mean and measurement uncertainty were calculated and presented in graphs. The measurements were performed under different lighting conditions: 10 lx, 100 lx, 150 lx oraz 300 lx. The lighting levels were measured using a lux meter available in a mobile application.

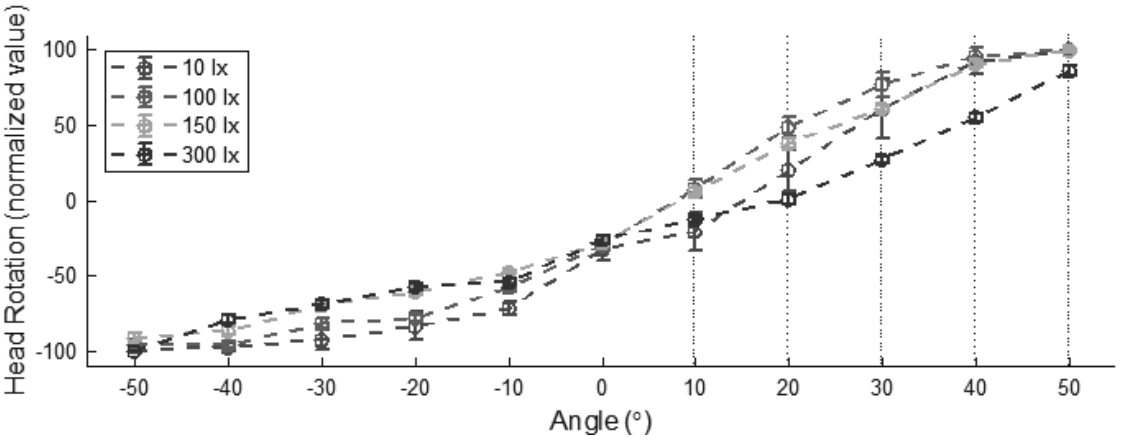

Figure 6. Comparison of head rotation angles vs normalized values measured by the program under different illumination conditions (10 lx, 100 lx, 150 lx, and 300 lx)

4.1.1. Interpretation of Results

The graphs show the relationship between the actual head rotation angle (X-axis) and the normalized value calculated by the program (Y-axis). For each lighting level, the graphs exhibit a similar pattern, which indicates a high level of consistency between the results and the expected behavior of the system.

4.1.2. Impact of Lighting Level on Measurement Accuracy

The analysis of the graphs shows that measurements taken at lower lighting levels (10 lx, 50 lx, and 100 lx) exhibit significantly greater uncertainties. At higher lighting levels, particularly from 150 lx upwards, the accuracy of the measurements improves significantly, and the measurement uncertainties become minimal. A lighting level of 150 lx, considered realistic for typical conditions when using a wheelchair, provides very high accuracy, confirming the practical usefulness of the system.

4.1.3. Consistency of Errors at Extreme Tilt Angles

In all the graphs, a deviation from a linear relationship is observed at extreme head tilt angles (angles near -40° and +40°). However, these changes are systematic, meaning that the system consistently overestimates or underestimates the result by a constant value at these extremes. The consistency of these changes allows for easy inclusion in the calibration process, which could further improve the system's accuracy.

4.2. Measurement of Voice Command Recognition Effectiveness

The experiment assessed the effectiveness of voice command recognition at different background noise levels, simulated by recording street noise. The noise level was measured using a mobile application, and for each level (0 dB, 60 dB, 70 dB, 80 dB, 90 dB, 100 dB), 50 repetitions of the commands "left", "faster", and "slower" were performed. A command was considered successful if it was correctly interpreted, and a failure if there was an interpretation error or no response. The measurement used the built-in microphone of a laptop.

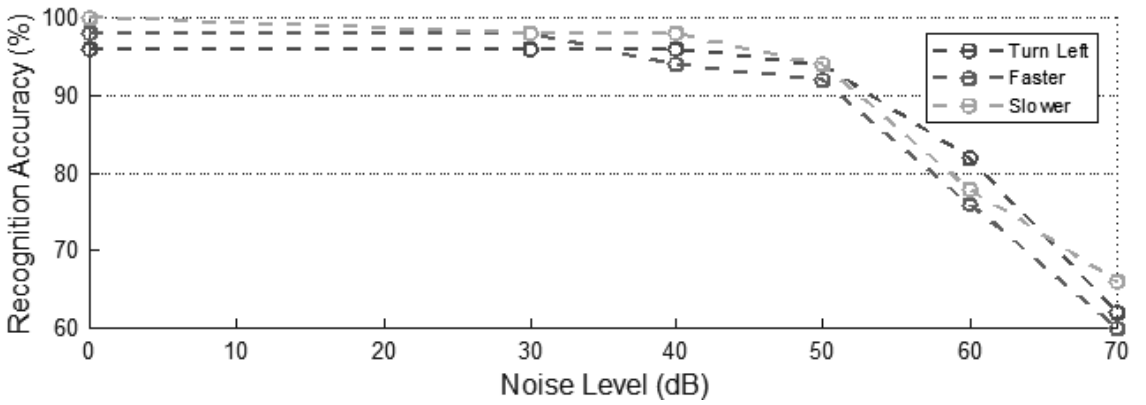

Figure 7. Chart showing the accuracy of command recognition depending on noise levels

4.2.1. Interpretation of Results

Up to a noise level of 80 dB, the system demonstrates a high effectiveness in recognizing commands (92-100%), which is sufficient for typical urban conditions, where street noise levels usually range from 70-80 dB. Such high effectiveness means that the system can be useful in everyday life, ensuring reliable operation in environments with average noise levels. However, for noise levels above 80 dB, a noticeable decrease in effectiveness was observed – for 90 dB it was around 76-82%, and for 100 dB it was only 60-66%. The greatest decrease was observed for the command "faster", which may suggest that shorter or more dynamic commands are more difficult to recognize correctly in noisy conditions. Nevertheless, the results for the commands "left" and "slower" were more stable, indicating greater resistance of the system to interpretation errors with simpler commands.

5. DISCUSSION

The creation of a prototype electric wheelchair that utilizes various control techniques while staying well within the project budget (5000 PLN) confirmed the feasibility of implementing advanced supporting technologies at relatively low costs. These results suggest that developing more affordable technological solutions is achievable, which could increase the availability of such devices to a wider range of users.

However, it should be emphasized that the wheelchair prototype developed within the project is merely a demonstration of technical capabilities. Implementing the same functionalities in a high-quality, full-fledged product with appropriate safety standards would certainly increase costs. Nevertheless, it is important to note that not all systems implemented in the prototype are necessary for every user. Combined with the potential benefits of economies of scale, it is possible to significantly reduce production costs compared to current market standards.

The project opens up broad perspectives for development in the field of assistive technology. Areas for further exploration include both the development of new control systems and the improvement of existing solutions [17].

The work carried out and the prototype created demonstrate that advanced assistive technologies can be developed and implemented in an economical manner, which is an important step toward their widespread application.

6. CONCLUSIONS

The conducted research confirmed the feasibility of using modern control techniques for wheelchair control. The system integrating image analysis, voice recognition, and EEG interfaces demonstrated high effectiveness and potential for further development. The use of image analysis to measure the user's gaze angle proved to be very effective, even under lower lighting conditions. Although accuracy decreases in challenging lighting conditions, the detection level remains satisfactory. As a result, this method is intuitive, touchless, and can enhance the user's independence.
Voice control, despite initial difficulties, was also evaluated as useful, although limited in real-time applications. The commands "left" and "slower" were more reliable than "faster." Further work is planned to improve noise reduction algorithms and speech recognition stability, as well as to select the most reliable commands. As of now errors and artifacts generated by the speech recognition system make it difficult to perform critical actions. However, voice control can successfully be used to change driving modes and operate user interface elements.
Tracking the silhouette using the YOLO algorithm also yielded promising results. The system allows for wheelchair control by tracking the movement of the person, but it requires the presence of a caregiver, limiting the potential use of this method for fully autonomous control.
During daily use of a wheelchair, controlling it with head movements and voice commands can significantly reduce travel time and increase convenience compared to a traditional wheelchair. This allows users to perform daily activities more efficiently and enhances their independence.
EEG-based wheelchair control in laboratory conditions is possible but requires refinement to be used outside the laboratory. The high sensitivity to head movements and the need to wear complex equipment are significant challenges. Despite these difficulties, the experimental results are promising and indicate great potential for this technology in the future.

ACKNOWLEDGEMENTS

The project was carried out as part of the PBL (Project Based Learning) program at the Silesian University of Technology, in connection with the university's participation in the "Initiative of Excellence - Research University" program. We would especially like to thank the scientific supervisors of the project, the main supervisor, Dr. Tomasz Moroń, and the assistant supervisor, Mgr. Tomasz Kukuczka, for all their help, dedicated time, and substantive support during the project.

LITERATURE

1. K. Tai, S. Blain, T. Chau, A review of emerging access technologies for individuals with severe motor impairments, Assistive Technology, 20(4), 204–221, 2008.
2. P. Davison, M. Sharpe, D. Wade, C. Bass, Wheelchair patients with nonorganic disease: A psychological inquiry, Journal of Psychosomatic Research, 47(1), 93–103, 1999.
3. R. A. Cooper, R. Cooper, M. L. Boninger, Trends and issues in wheelchair technologies, Assistive Technology, 20(2), 61–72, 2008.
4. R. P. N. Rao, Brain-computer interfacing: an introduction, Cambridge University Press, New York, 2013.

5. S. C. Chan, A. P. Chan, User satisfaction, community participation and quality of life among Chinese wheelchair users with spinal cord injury: a preliminary study, Occupational Therapy International, 14(3), 123–143, 2007.
6. R. E. Cowan, B. J. Fregly, M. L. Boninger, L. Chan, M. M. Rodgers, D. J. Reinkensmeyer, Recent trends in assistive technology for mobility, Journal of NeuroEngineering and Rehabilitation, 9, 1–8, 2012.
7. M. Biegaj, K. Dziedziech, M. Górski, Wykorzystanie sygnałów EEG, EOG i EMG do sterowania wózkiem inwalidzkim, Pomiary Automatyka Robotyka, 15(6) , 72–75, 2011.
8. J. Redmon, S. Divvala, R. Girshick, A. Farhadi, You Only Look Once: Unified, Real-Time Object Detection, Proceedings of the 2016 IEEE Conference on Computer Vision and Pattern Recognition (CVPR), 779–788, 2016.
9. C. Lugaresi, J. Tang, H. Nash, C. Sminchisescu, M. Elbanhawi, MediaPipe: A framework for building perception pipelines, Google, https://github.com/google/mediapipe, 2019.
10. A. Zhang, Speech Recognition (Version 3.11) [Software], https://github.com/Uberi/speech_recognition#readme, 2017.
11. J. Bilmes, X. Li, J. Malkin, K. Kilanski, R. Wright, K. Kirchhoff, et al., The Vocal Joystick: A voice-based human-computer interface for individuals with motor impairments, Proceedings of the Human Language Technology Conference and Conference on Empirical Methods in Natural Language Processing, 995–1002, 2005.
12. P. Viola, M. Jones, Rapid object detection using a boosted cascade of simple features, Proceedings of the 2001 IEEE Computer Society Conference on Computer Vision and Pattern Recognition (CVPR), 511–518, 2001.
13. A. Mazhar, P. G. Esteban, Detecting and Tracking Objects in HRI: YOLO Networks for the NAO “I See You” Function, w: Proceedings of the 2018 27th IEEE International Symposium on Robot and Human Interactive Communication (RO-MAN), 1123–1128, 2018.
14. A. Radford, J. W. Kim, T. Xu, G. Brockman, C. McLeavey, I. Sutskever, Robust Speech Recognition via Large-Scale Weak Supervision, arXiv, https://arxiv.org/abs/2212.04356, 2022.
15. NEUROSPEC, DSI-24 First Dry & Artefact Resistant EEG, https://www.neurospec.com, [access date: 02.01.2025].
16. EMOTIV, *EPOC X – 14* Channel Wireless EEG Headset, https://www.emotiv.com, [access date: 02.01.2025].
17. S. K. Sahoo, B. B. Choudhury, A Review on Human-Robot Interaction and User Experience in Smart Robotic Wheelchairs, Journal of Technology Innovations and Energy, 2(2), https://doi.org/10.56556/jtie.v2i2.576, 39–55, 2023.

TalentDetector
31th January 2025
Gliwice, Poland
DEPARTMENT OF ENGINEERING MATERIALS AND BIOMATERIALS
FACULTY OF MECHANICAL ENGINEERING
SILESIAN UNIVERSITY OF TECHNOLOGY
INTERNATIONAL STUDENTS SCIENTIFIC CONFERENCE

Effect of steel triboactivation on hardening and relaxation properties of surface layers

Yuliia Sokolan[a], Kateryna Sokolan[b], Pavlo Maidan[c], Serhii Matiukh [d], Oleg Polishchuk[e], Mirosław Bonek[f]

[a] Khmelnitskyi National University, Faculty of Mechanical Engineering, Transport and Architecture, Khmelnitskyi, Ukraine email: sokolan.julia@gmail.com.
[b] Khmelnitskyi National University, Faculty of Mechanical Engineering, Transport and Architecture, Khmelnitskyi, Ukraine email: sokolan.kateryna @gmail.com .
[c] Khmelnitskyi National University, Faculty of Mechanical Engineering, Transport and Architecture, Khmelnitskyi, Ukraine email: maidanp@khmnu.edu.ua.
[d] Khmelnytskyi National University, Faculty of Engineering Mechanics, Khmelnytskyi, Ukraine email: matuh@khmnu.edu.ua.
[e] Khmelnitskyi National University, Faculty of Mechanical Engineering, Transport and Architecture, Khmelnitskyi, Ukraine email: opolishchuk7l@gmail.com.
[f] Silesian University of Technology, Faculty of Mechanical Engineering, Gliwice, Poland email: miroslaw.bonek@polsl.pl.

Abstract: Tribological properties of steel and its resistance to wear are largely formed directly in the process of external friction as a result of dynamic substructural rearrangement of the near-surface zone of friction contact. Such rearrangement, as a rule, has a relaxation nature and can be accompanied by both hardening and de-hardening of the friction zone subjected to dynamic force influence. The steel substructure formed by external friction, as well as the load-velocity mode of contact interaction, determine the level and corresponding mechanisms of internal friction, which, in turn, determine the temperature regime, dissipative properties and dynamic stress of the friction contact. The paper shows that friction hardening of steel results in the formation of subsurface hardening zones, which, when scratch-tested, show acoustic emission activity to a greater or lesser extent, the level of which characterizes the relaxation (dissipative) properties of the structure of hardened areas. Subsurface layers formed during friction of hardened steel are characterized by high strength and significant relaxation (dissipative) ability with residual compression stresses. As a consequence, abrasion in the form of finely dispersed powder (wear by dispersion) occurs during sliding friction. During friction of medium- and high-tempered steel, the near-surface layer with a thickness of about 30 μm (400 °C tempering) and 20 μm (600 °C tempering) enters the state of nucleation with low relaxation properties. Embrittlement and reduction of fracture toughness of such a layer under sliding friction leads to its delamination in the form of finely dispersed flakes (delamination wear mechanism). Probably, the fracture center at friction of low-tempered steel (T_{temp} = 100, 200 °C) is transferred under the surface to the depth of 5-10 microns.

Keywords: acoustic emissivity, scratch testing, hardening, tempering, steel 45, internal friction, martensite, surface layer, stress relaxation.

1. INTRODUCTION

Tribological properties of steel and its resistance to wear to a significant extent are formed directly in the process of external friction as a result of dynamic substructural reorganization of the near-surface zone of friction contact. Such restructuring, as a rule, has a relaxation nature and can be accompanied by both hardening and de-strengthening of the friction zone subjected to dynamic force influence. The substructure of steel formed by external friction, as well as the load-velocity mode of contact interaction, determine the level and corresponding mechanisms of internal friction, which, in turn, determine the temperature regime, dissipative properties and dynamic stress of frictional contact [1]. In [2] it is noted that "external friction, as an independent phenomenon, does not exist, and there is a process of internal friction in the thin cover of a solid body and in the underlying surface layer, i.e., there is a two-layer internal friction, each with its own friction coefficient, manifested in a layer with a thickness of a dozen angstroms and in a layer with a thickness 2-3 orders of magnitude greater".

It is generally believed that friction of metals in the near-surface layer generates an exceptionally high density of dislocations forming an ultradisperse cellular structure with signs of amorphization [3, 4, 5].The accumulation of dislocations and their interaction leads to the formation of a large number of point defects (vacancies, dislocated atoms), resulting in the activation of diffusion processes (especially at elevated temperatures).A possible cause of "amorphization" is the growth of potential energy at friction, which promotes the growth of electrochemical and adsorption potentials of the near-surface layer. As a result, oxygen diffusion with internal oxidation is activated, which ensures the coexistence of the amorphized layer with the underlying crystalline phase. It is also assumed that in a structure with properties similar to those of the Beilby layer, the separation of wear particles with flat surfaces occurs due to fatigue phenomena [4, 6].

Nevertheless, at present, there is no unambiguous answer to the question of where frictional fracture of metals begins - on the contact surface or in the subsurface layer. According to [7], the kinetics of frictional fatigue depends on the depth of maximum tangential stresses, which varies inversely with the friction coefficient. According to some estimates, at high friction coefficients ($\mu > 0.3$) the zone of maximum tangential stresses comes to the surface, initiating predominantly the destruction of the friction contact surface. This conclusion contradicts the delamination theory of wear by peeling.

According to the delamination theory [8], the formation of wear particles is the result of the development of subsurface cracks. The distribution of stresses in the frictional contact zone leads to the fact that during sliding friction dislocations accumulate mainly at some distance from the surface, forming a zone of increased density of linear defects. In this zone plastic deformation occurs, limited from above and below by regions of elastically deformed material. The specified zone of dislocations accumulation is the area of the most probable nucleation and growth of micro voids, which coalize, leading to the formation of sub-surface microcracks, propagating parallel to the friction surface. After repeated loading of the material, the cracks reach a critical size, leading to flaking of wear particles in the form of thin petals whose thickness (about 10 microns) is several times less than their length. According to this theory, the depth of formation and the width of the dis-location accumulation zone with the formation of voids increase with the growth of the fracture coefficient, which should lead to an increase in

the thickness of the flaking particles. In other words, the thickness of wear particles is determined by the thickness of the zone with a lower concentration of mobile dislocations.

2. FORMULATION OF THE PROBLEM

Ambiguity and inconsistency of the above mentioned conclusions require further studies of the mechanism of metal wear in sliding friction.

3. PRESENTING MAIN MATERIAL

Carbon steel 45 was studied. Heat treatment: quenching in water from a temperature of 850 ºC followed by tempering (1 hour) at temperatures of 100, 200, 400, 600 ºC.

Friction tests were carried out on a friction machine (see Fig. 1) according to the scheme "finger - disk": a fixed sample (finger) with a controlled force (P = 0.3 MPa) was pressed against the plane of a rotating metal disk, on the surface of which abrasive sheets were fixed, periodically replaced in the process of triboactivation of the sample by paper with a thinner fixed abrasive. The final stage of grinding the surface of the samples was polishing.

Tribo-strength (sclerometric) and acoustic-emission properties of the subsurface layers were investigated using the RST (Revetest Scratch Tester) by CSM Instruments (Fig. 2).

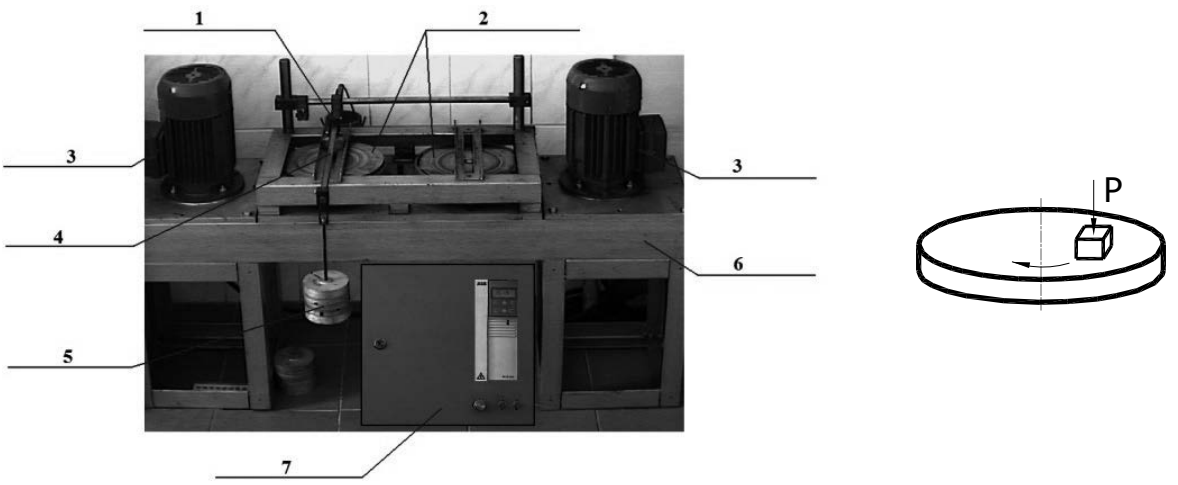

a) b)

Figure 1 – General view of the friction machine (a) for the study of wear intensity and schematic diagram (b):
1 - sample holder; 2 - control samples (disks); 3 - motor; 4 - load shoulder; 5 - load; 6 - supporting structure; 7 - control unit

During scratch testing, normal load, sclerometric force and coefficient of friction, depth and speed of Rockwell al-maz indenter penetration, as well as acoustic emission, the level of which was evaluated relative to the reference sample with titanium nitride coating, were recorded. Sclerometry (scratch-analysis) of the investigated surfaces was performed by continuous indentation of the indenter with simultaneous tangential movement of the sample relative to the indenter.

At the same selected measurement base (S = 4 mm) and constant speed of horizontal scanning (V_S = 4 mm/min), setting the program of maximum value of linearly increasing

normal load (F_n^{max} = 100, 150, 200 N) realized the modes of simultaneous growth of the speed of its impact on the indenter (V_F = 100, 150, 200 N/min).

Fig. 3 shows the results of scratch testing of hardened steel in the initial state (Fig. 3 a, b) and after friction (Fig. 3 c-e) as a function of the vertical indenter loading speed (V_F = 100, 200 N/min) and the level of acoustic emission signal amplification *S*. Tangential velocity of surface scanning Vs = 4 mm/min.

In the initial state of hardening (after electropolishing), the steel exhibits negligible acoustic-emission activity during scratch testing (Fig. 3 a, b). However, after friction, powerful acoustic pulses are registered in the near-surface layer at depths up to 10-20 μm depending on the indenter loading rate (Fig. 3 c-d).

a)

b)

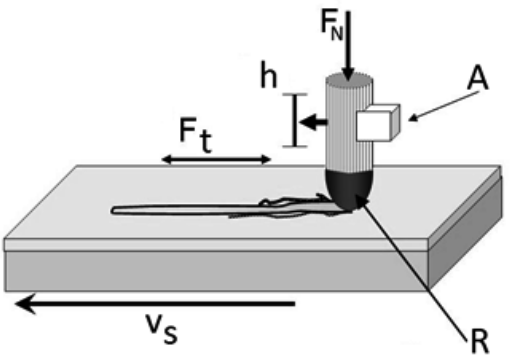

c)

Figure 2 – Installation for sclerometric studies: a - general view;
b - working unit; c - schematic diagram;
F_t - friction force sensor; *h* - embedding depth sensor; F_N - applied load (increasing);
A - acoustic sensor; V_S - sample movement speed; *R* - scratching tapered indenter (Rockwell).

Figure 4 illustrates the variation of scratch test parameters of steel after friction as a function of tempering temperature and indenter loading rate V_F (S = 5).

Low-temperature tempering (T_{temp} = 100, 200 ºC) sharply reduces the intensity of acoustic emission initiated by friction, and the near-surface localization of acoustic-emission activity is preserved (Fig. 4 a-d). At the same time, tempering at higher temperatures, in addition to a general decrease in the intensity of tribo-activated acoustic emission, leads to a shift in the areas of its manifestation to deeper layers (Fig. 4 e-h). From Figs. 3, 4 it follows that the subsurface localization of the zones of increased acoustic emission depends not only on the tempering structure of steel, but also on the indenter loading rate in the process of surface scanning: with its growth, the force range of acoustic-emission activity manifestation expands

and shifts to the region of increased values (Fig. 5). At the same time, the depth at which acoustic emission is registered changes.

4. THE RESULT OF WORK

According to Figs. 3 and 4, Fig. 6 systematizes the regularities of hardening zone formation (h_1 and h_2) in the subsurface layers as a result of friction, and also compares the results of estimation of the depth of occurrence and width of acoustic activity areas (shading) taking into account the influence of steel tempering temperature and vertical indenter loading rate during scratch testing.

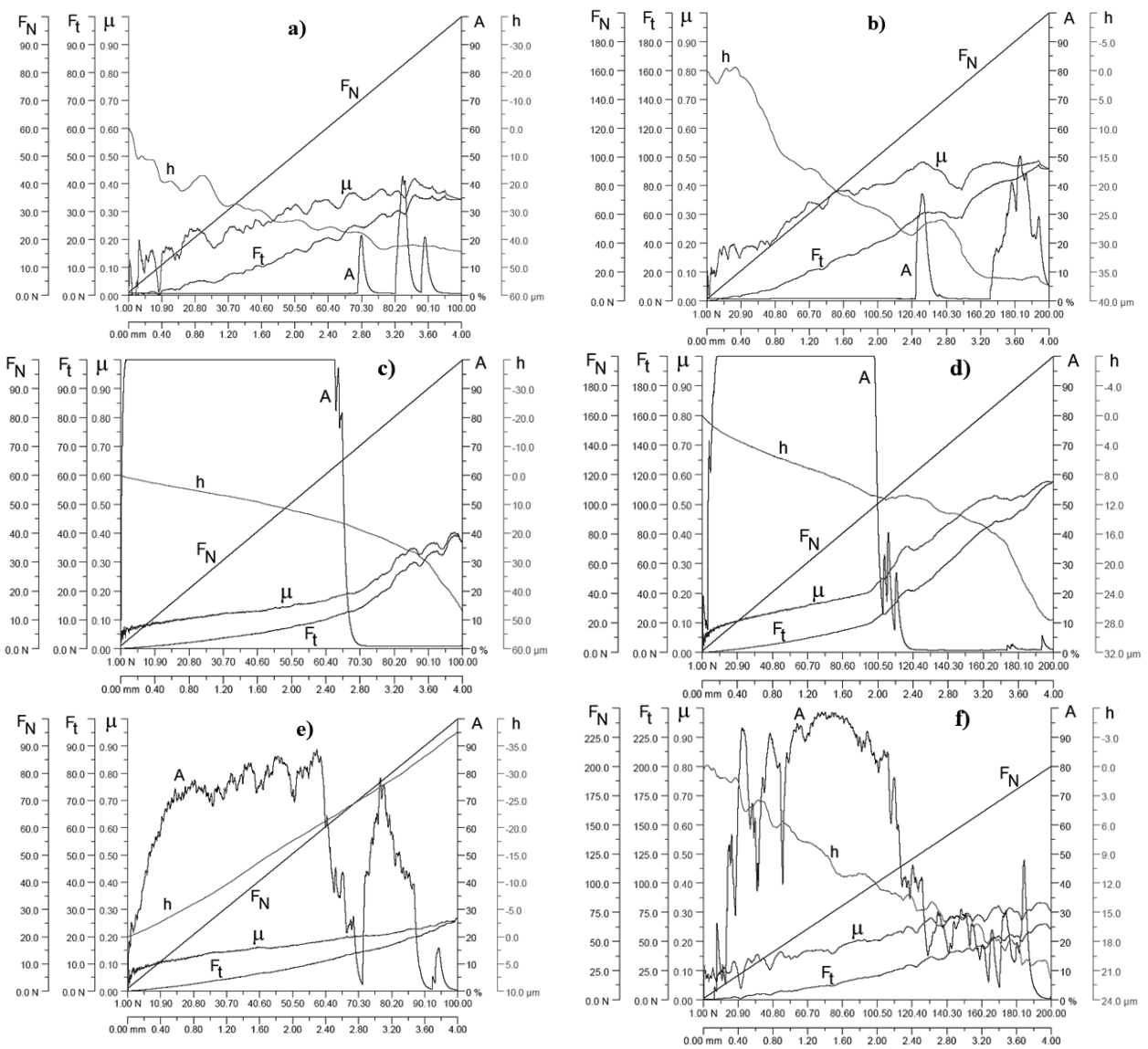

Figure 3 – Scratch testing of hardened steel:
a, b - initial state (a - V_F = 100 N/min, b - V_F = 200 N/min); c, d, e, f - after friction:
c - V_F = 100 N/min (S = 5); d - V_F = 200 N/min (S = 5); e - V_F = 100 N/min (S = 1);
f - V_F = 200 N/min (S = 1);
(F_N - normal load, N; h - indenter penetration depth, μm; μ - coefficient of friction;
F_t - friction force, N; A - acoustic emission, %)

The character of change of sclerometric friction force in all cases reveals two hardening zones (I and II), formed under the influence of external friction (zone III, not being activated by friction, refers to the original structure after the corresponding heat treatment). The localization (lower boundary) of zones I and II in Fig. 6 corresponds to the depths h_1 and h_2.

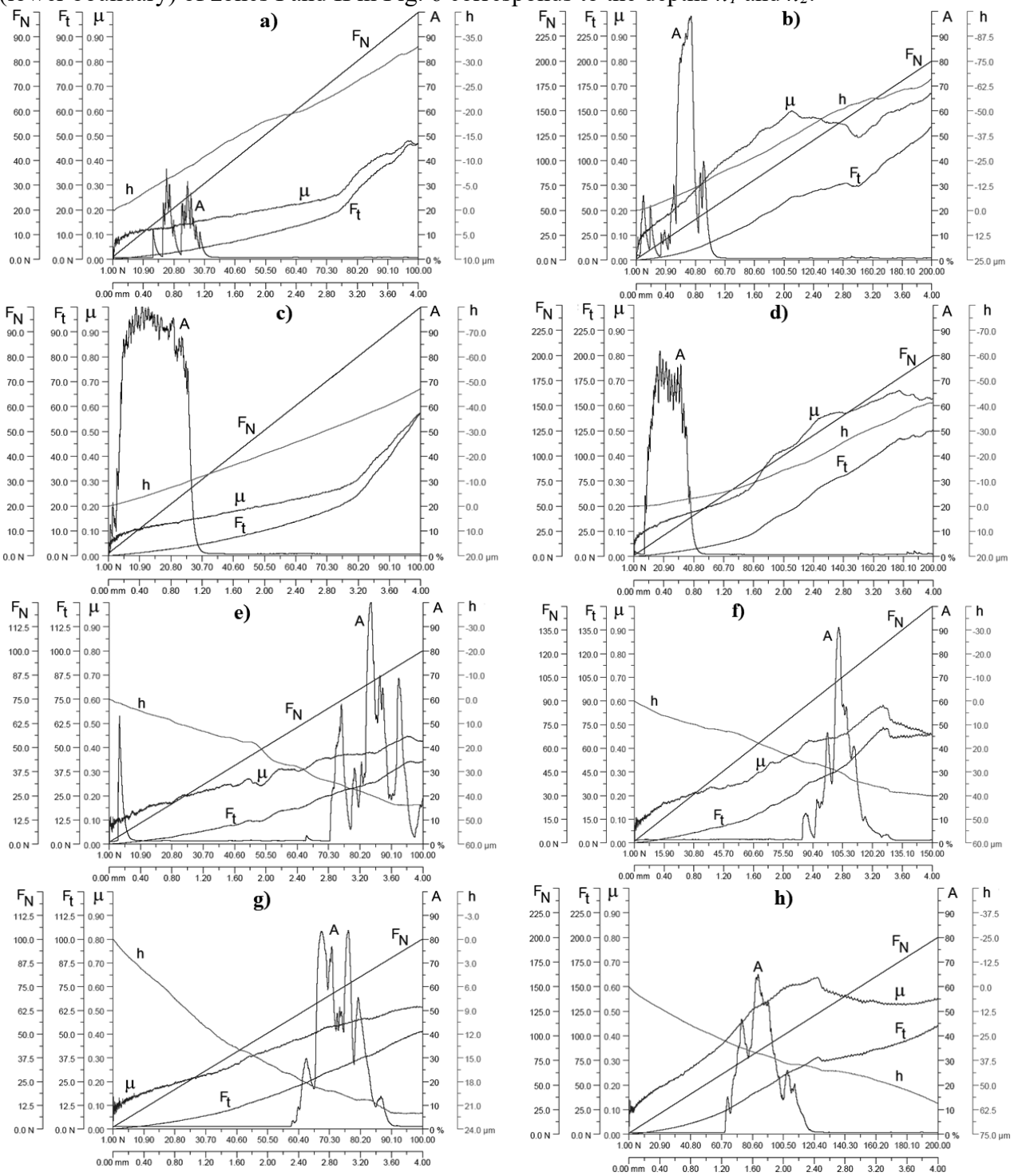

Figure 4 – Sclerometric indices of triboactivated steel depending on tempering temperature and indenter loading rate (S = 5). Tempering temperature: a, b - 100 ºC; c, d - 200 ºC; e, f - 400 ºC; g, h - 600 ºC (a, c, d, g - V_F = 100 N/min; b, d, e, h - V_F = 200 N/min)

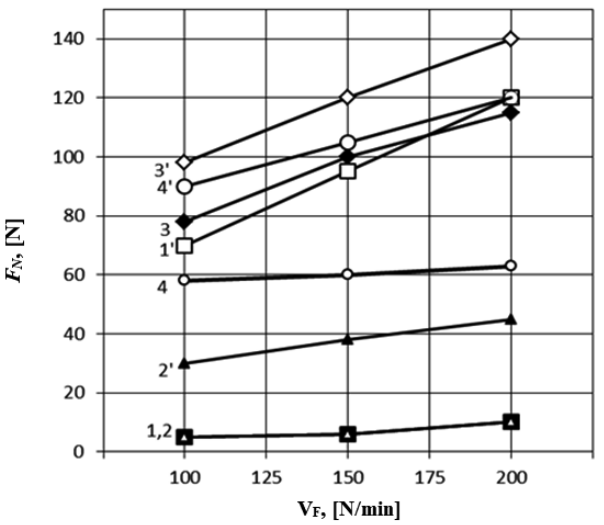

Figure 5 – Effect of indenter loading rate on the values of forces corresponding to the beginning (1, 2, 3, 4) and the end ($1^|$, $2^|$, $3^|$, $4^|$) of acoustic emission registration (after friction activation): 1, $1^|$ - hardening; 2, $2^|$ - 200ºC tempering; 3, $3^|$ - 400ºC tempering; 4, $4^|$ - 600ºC tempering.

The martensitic hardening structure is characterized by exceptionally high acoustic-emission activity within both hardening zones directly at the friction contact surface (Fig. 6 a). Low-temperature tempering (T_{temp} = 200 ºC) significantly reduces (5 times and more) the intensity of acoustic signals, which are recorded mainly within the I zone of hardening (Fig. 6 b). After friction of medium- and high-tempered steel (Fig. 6 c, d) acoustic-emission activity is manifested only at a certain depth from the contact surface and is localized near the boundary of transition from II to III zone or within II zone.

For two of the investigated structural states of steel (hardening, tempering 200 ºC) with increasing indenter loading rate, the hardening zones (h_1 and h_2) as well as the areas of acoustic-emission activity (shaded) narrow, shifting closer to the friction surface (Fig. 6 a, b). In the case of medium tempered steel (T_{temp} = 400 ºC) with increasing dynamics of indenter introduction, the width of the acoustic-emission activity area does not change much, but the hardening zones also shift to the friction contact surface (Fig. 6 c).

When testing the highly tempered steel (Fig. 6 d), the opposite picture is observed: with increasing indenter loading speed, the hardening zones and acoustic activity areas expand and are fixed at a greater distance from the friction contact surface, which is apparently characteristic of the material that has undergone the usual mechanical galling of a thin surface layer in the process of external friction. It is noteworthy that at the minimum speed load on the indenter (V_F = 100 N/min) the depth of the fixed hardening zone h_2 of this steel was the smallest in comparison with the rest of the studied structural states, which is a consequence of low microplasticity of the near-surface layer.

The above is consistent with the results of estimation of the indenter penetration rate in the hardening zones depending on the rate of force applied to it (Fig. 7). With the increase of the maximum load in the indenter insertion cycle, a natural growth of the indenter penetration rate is observed only in the case of highly tempered steel (Fig. 7 a, curve 4).

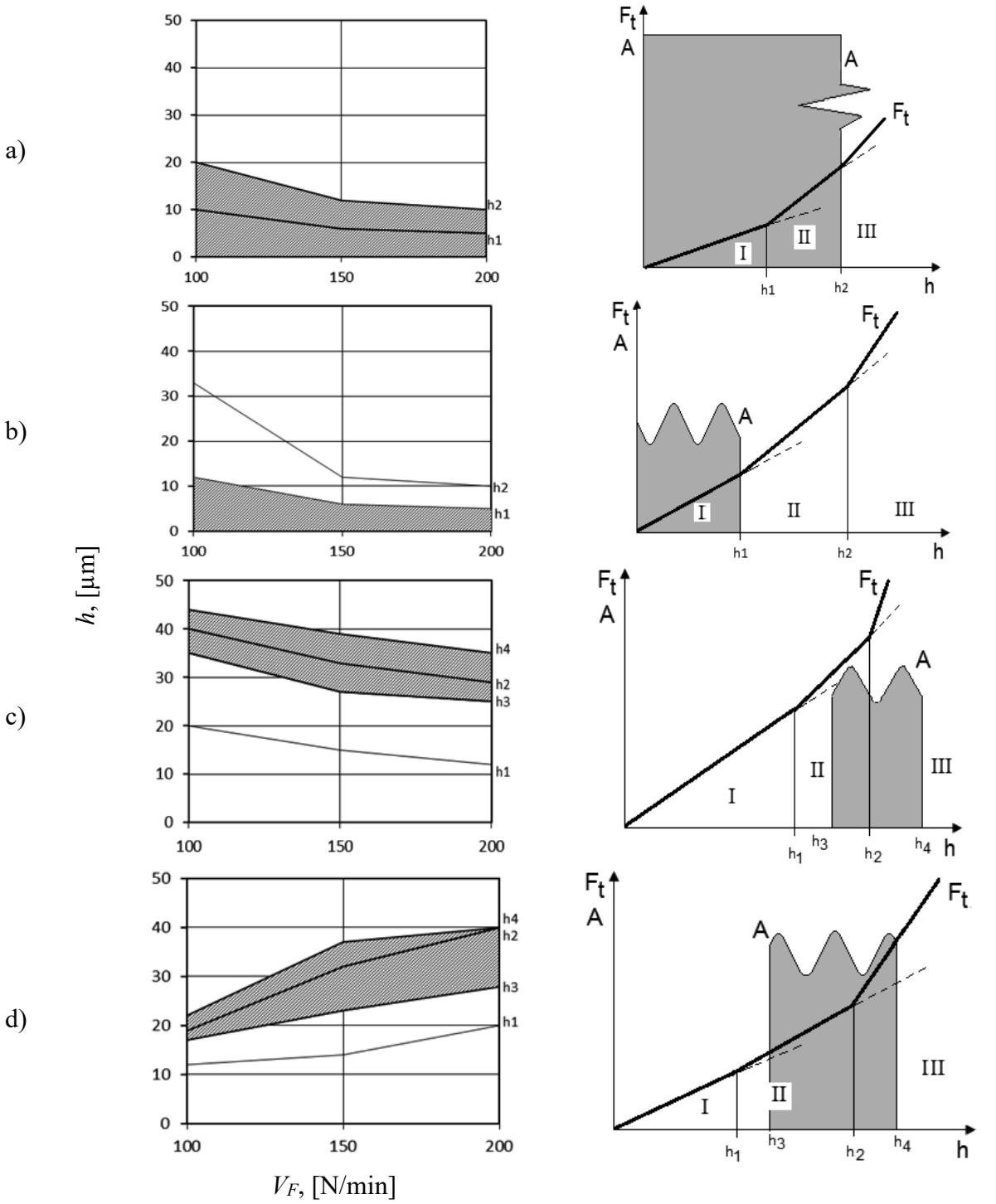

Figure 6 – Effect of indenter loading rate on localization (by depth) of hardening zones and acoustic-emission activity areas (shading) taking into account steel heat treatment: a - hardening; b-d - respectively, T_{temp} = 200, 400, 600 ºC. (on the right are schemes of change of sclerometric friction force Ft and level of acoustic emission A by depth of indenter penetration for V_F = 150 N/min).

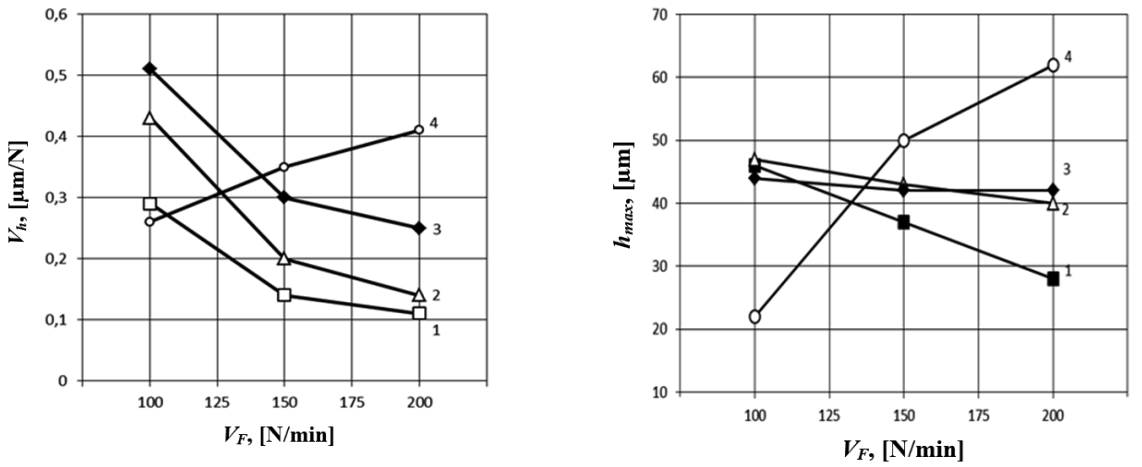

a) b)

Figure 7 – Effect of indenter loading rate on the average speed of its penetration (pliability) in the hardening zone (a) and on the maximum penetration depth within the full scanning base (b): 1 - hardening; 2, 3, 4 - respectively, T_{temp} = 200, 400, 600 ºC.

For steel in the state of hardening, as well as low and medium tempering, the opposite effect is observed (Fig. 7 a, curves 1-3): the indenter embedding rate, as well as the depth of localization of the hardening zone, decreases with increasing vertical velocity of indenter loading. Compared to highly tempered steel, these structures exhibit increased micro-elasticity (with higher initial hardness) at lower vertical scratch indentation velocity (V_F = 100 N/min). At the same time, as the indenter loading rate increases, the considered indices (h_2 and V_h) decrease, indicating the hardening effect of the sclerometry process, the efficiency of which increases in proportion to the strain rate caused by the indenter. This is an indication that strain hardening of friction contact of hardening, low and medium tempering structures differs from the hardening process of high tempered steel both in mechanism and efficiency.

This is confirmed by the dependences of the maximum indenter penetration depth along the entire length of the specimen scanning path (S = 4 mm) on the vertical loading rate (Fig. 7 b). Only highly tempered steel (Fig. 7 b, curve 4) showed a progressive growth of the indenter embedding depth with increasing loading rate, without showing signs of dynamic hardening. The greatest reaction with hardening effect on the growth of strain rate is shown by steel in the state of hardening (martensite + residual austenite). After tempering at 400 ºC, the maximum depth of indenter embedding is practically independent of the strain rate in scratch testing (Fig. 7 b, curve 3). Differences of properties of subsurface layers formed at friction, depending on load-velocity parameters of sclerometry (scratch-testing) and mode of heat treatment of steel are expressively shown by scale and character of change of signals of acoustic emission in process of removal from a friction surface. Thus, the mode of heat treatment of steel affects the ranges of indenter indentation force values and the depth of its penetration, at which an abnormal increase in the acoustic emission activity of the structure is manifested (Fig. 8). The widest range of values of these parameters corresponds to the steel in the state of hardening. The lowest values of these indices with a narrow range of their values correspond to the structures tempered at 100 and 200 ºC. Tempering of steel at 400 ºC forms such regions of acoustic-emission activity, which correspond to the highest values of both the embedding force F_N and the embedding depth h. Increasing the tempering temperature to 600 °C again lowers the ranges of values of these parameters.

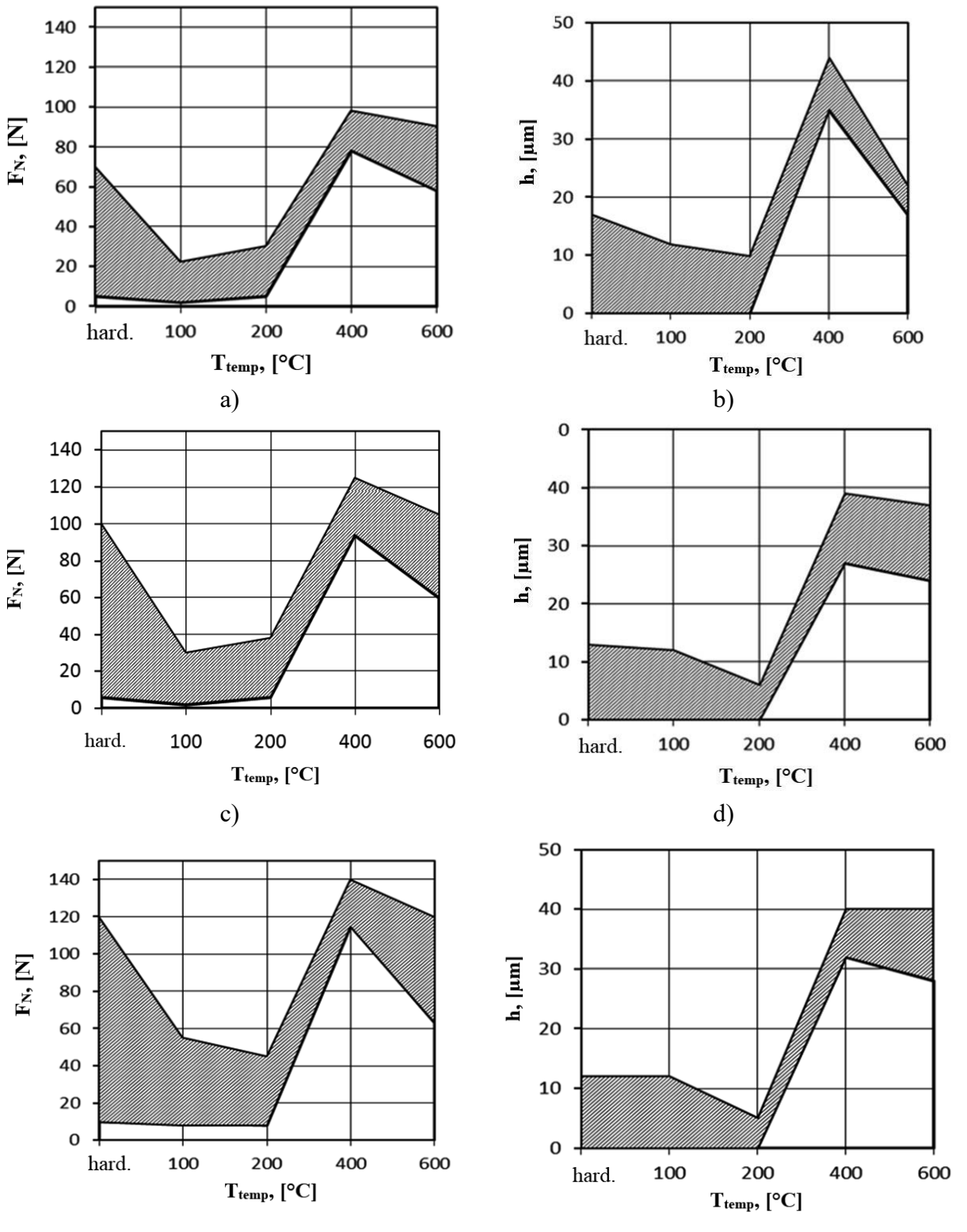

Figure 8 – Influence of steel tempering temperature on the ranges of embedding force (a-c) and indenter embedding depth (d-f), at which the acoustic emission activity of the structure is registered (shading):
a, b, c - respectively, V_F = 100, 150, 200 N/min

Acoustic emission during mechanical loading of a solid body at the microlevel is caused by local restructuring of the structure due to the development of discrete dynamic processes accompanied by relaxation of internal stresses [9, 10, 11, 12]. In this case, energy is released in the form of elastic waves with a change in the stress-strain state. In other words, the emission of acoustic pulses accompanies relaxation phenomena caused by the transformation of the metal microstructure under mechanical loading.

The level of acoustic emission depends not so much on the density of dislocations as on their mobility and free path length [10, 11]. In addition to the high density of mobile defects in the crystal structure, the factors causing high acoustic-emission activity of a solid body under force impact usually include [12, 13]:

– heterogeneity and high strength of the material;
– high strain rate;
– breakthroughs of dislocation clusters through obstacles;
– tendency to twinning;
– formation of microcracks.

When steel is quenched, the volume of martensite formed is greater than the volume of austenite. Residual compressive stresses (phase riveting) arising in this process cause preservation of residual austenite. Low acoustic-emission activity of "fresh" (not friction-activated) martensite (Fig. 3 a, b) is caused by:

– high microstresses and their large heterogeneity in separate micro-volumes, which promotes early manifestation under load of local microplasticity with lowering of the physical elastic limit;

– large tetragonality of the crystal lattice due to oversaturation of the solid solution with carbon;

– low mobility of dislocations blocked by point defects (vacancies, introduction atoms) created by phase nucleation in the process of hardening.

High acoustic-emission activity of hardened steel (martensite + residual austenite), acquired in the process of external friction (Fig. 3, c-e), is due to specific changes in the substructure in the thin surface layer, simultaneously leading, on the one hand, to the growth of relaxation capacity, and on the other hand, to the hardening of the metal. It is known [13, 14, 15, 16] that after the surface plastic deformation of over-rolled carbon steel with a significant increase in the residual compression stresses, a decrease in the physical width of X-ray interference lines is observed, indicating a decrease in local micron stresses in the surface layer. It is obvious that at external friction of hardened steel over deformation rivetins, which is usually caused by the increased density of low-moving dislocations, the processes forming the near-surface structure with high relaxation ability prevail.

In the case of low-tempered steel (T_{temp} = 100, 200 ºC), the hardening zone created by friction shows acoustic-emission activity only up to a certain depth (Fig. 4 a-d; 8 c), although several times less compared to deformed unstrained martensite. Apparently, this is due to the influence of factors controlling the density of mobile dislocations in the matrix, and hence the relaxation ability of the material. Coherent particles of ε-carbide are released already in the process of the mentioned preliminary heat treatment of steel, the number of which can increase in the process of subsequent deformation under friction. Such releases effectively block active sliding systems in the solid solution under the action of external load (strengthening effect). The greater the number of separated carbide phase particles, the smaller the intercarbide distance, the higher the resistance to dislocation movement and the lower the acoustic-co-

emission (relaxation) capacity. Such material behaves more elastically, and purely elastic deformations, as is known, do not cause acoustic emission.

Tempering of steel at 400 ºC forms a highly dispersed mixture consisting of lamellar ferrite and cementite (tempering troostite). In the initial state, such a structure has high internal friction and reduced modulus of elasticity. Due to a decrease in the concentration of carbon in the solid solution (due to its transition to carbides during heat treatment), the external friction process in the near-surface layer creates conditions for the effective operation of dislocation sources and intensive interaction of the latter, which leads to mechanical sticking, in which the structure acquires a low relaxation capacity with zero acoustic-emission activity and minimal internal friction. At the same time, a zone of acoustic-emission activity with increased relaxation capacity is formed under this layer at a depth of 20-40 μm (see Fig. 4 e, f).

After tempering at 600 ºC the steel has a sorbitic temper structure as a result of coagulation and spheroidization of cementite and recrystallization of ferrite. At friction of such steel in the near-surface layer due to low potential barrier of shear deformation a textured structure is formed, in which due to a large number of barriers the movement of dislocations is blocked and the work of their sources is suppressed. Such a structure shows zero acoustic emission activity in scratch testing. At the same time, the main type of hardening of the sorbitan structure in the near-surface layer is riveting. The dislocations released and generated by friction are additionally blocked by impurity introduction atoms already at room temperature in the process of deformation aging, when, apparently, the concentration of carbon atoms in the solid solution increases due to partial dissolution of carbides. At a depth of 20-40 μm, zones of increased acoustic-emission activity formed by external friction are detected (Fig. 8 c).

5. CONCLUSIONS

Thus, friction hardening of steel forms subsurface hardening zones, which, when scratch-tested, exhibit acoustic-emission activity to a certain degree, the level of which characterizes the relaxation (dissipative) properties of the structure of hardened areas.

Subsurface layers formed by friction hardened steel are characterized by high strength and significant relaxation (dissipative) capacity with residual compression stresses. As a consequence, abrasion in the form of finely dispersed powder (wear by dispersion) occurs in sliding friction.

During friction of medium- and high-tempered steel, the near-surface layer with a thickness of about 30 μm (400 °C tempering) and 20 μm (600 °C tempering) goes into a state of sticking with low relaxation properties. Embrittlement and reduction of fracture toughness of such a layer under sliding friction leads to its flaking off in the form of finely dispersed flakes (delamination wear mechanism). Probably, the fracture center at friction of low-tempered steel (T_{temp} = 100, 200 °C) is transferred under the surface to the depth of 5-10 microns.

ACKNOWLEDGEMENTS

The work was created as a result of the project as part of project based learning - PBL, in the 11th competition under the Initiative of Excellence - Research University, Silesian University of Technology, Gliwice, Poland.

BIBLIOGRAPHY

1. Shevelya, V. V. Rheology of viscoelastic friction contact / V. V. Shevelya, A. S. Trytek. // Problems of tribology. - 2010. - № 4. - p. 5-15.
2. Kragelskii I. V. Friction and wear in vacuum / I. V. Kragelskii, I. M. Lyubarskii, A. A. Guslyakov [and others]. – M.: Mashinostroenie, 1973. - 216 p.
3. Löhr M. In situ acoustic emission for wear life detection of DLC coatings during slip-rolling friction / M. Löhr, D. Splatmann, S. Binkowski, E. Satner, M. Woydt. // Wear. – 2006. – 260. – p. 469-478.
4. Scott D. The Particles of Wear / D. Scott, W. W. Seifert, V. C. Westcott. // Scientific American. – 1974. – v. 230, №5. – p. 88-97.
5. Valiev R. Z. Principles of equal-channel angular pressing as a processing tool for grain refinement / R. Z. Valiev, T. G. Langdon. // Progress in Material Science. – 2006. – 51. – p. 881-981
6. Bushe N. A. Compatibility of rubbing pairs / N. A. Bushe, V. V. Kopytko. – M.: Nauka, 1981. – 128 p.
7. Kragelsky I. V. Fundamentals of friction and wear calculations / I. V. Kragelsky, M. N. Dobychin, V. S. Kambalov. – M.: Mashinostroenie, 1977. - 526 p.
8. Suh N. P. The delamination Theory of Wear / N. P. Suh. // Wear. – 1973. – v. 25, №1. – p. 111-124.
9. Greshnikov V. A. Acoustic emission / V. A. Greshnikov, Y. B. Drobot. – M.: Izd. of Standards, 1976. - 272 p.
10. 66. Ivanov V. I. Acoustic-emission control of welding and welded joints / V. I. Ivanov, V. I. Belov. – M.: Metallurgy, 1981. - 184 p.
11. Novikov, N.V. On the physical nature of acoustic emission during deformation of metallic materials / N.V. Novikov, V.G. Vainberg. // Problems of Strength. - 1977. - № 12. - p. 65-69.
12. Sviridenok A. I. Acoustic and electrical methods in tribo-technology / A. I. Sviridenok, N. K. Myshkin, T. F. Kalmykova, O. V. Kholodilov. - Minsk: Science and Technology, 1987. – 280 p.
13. Balter M. A. Strengthening of machine parts / M. A. Balter. - M.: Mashinostroenie, 1978. - 184 p.
14. E. Kehl. Untersuchungen leber das Verscheissverhalten der Metalle bei gleitender Reibung / Kehl E., Siebel E. // Archiv fuer das Eisenhuettenwessen. – 1936. – V. 9, № 11. – p. 536-570
15. Kinnunen E. Developmant of a new direct quenched abrasion resistant steel / E. Kinnunen, I. Miettunen, M. Somani, D. Porter, P. Karjalainen, I. Alamattila, A. Kemppainen, T. Liimatainen, V. Ratia. // Int. J. Metall. Eng. – 2013. – 1. – p. 27-34.

TalentDetector
31th January 2025
Gliwice, Poland
DEPARTMENT OF ENGINEERING MATERIALS AND BIOMATERIALS
FACULTY OF MECHANICAL ENGINEERING
SILESIAN UNIVERSITY OF TECHNOLOGY
INTERNATIONAL STUDENTS SCIENTIFIC CONFERENCE

Additive Manufacturing of Cobalt-Chromium Dental Implants Using Selective Laser Melting (SLM)

Maryam Soleimani[a], Wojciech Sitek[b], Magdalena Szindler[c]

[a] Silesian University of Technology, Faculty of Mechanical Engineering, Department of Didactic Laboratory of Nanotechnology and Material Technologies, email: Maryam.Soleimani@polsl.pl
[b] Silesian University of Technology, Faculty of Mechanical Engineering, Scientific and Didactic Laboratory of Nanotechnology and Material Technologies
[c] Silesian University of Technology, Faculty of Mechanical Engineering, Department of Engineering Materials and Biomaterials

Abstract: Recent advancements in dental technology have enhanced patient care. The capacity of 3D printing to accurately perceive and record both soft and hard tissues allows for the creation of high-resolution models. Cobalt-chromium (Co-Cr) alloys are commonly used in dental prostheses due to their low cost and good mechanical properties. The manufacturing method significantly impacts these alloys' mechanical and metallurgical characteristics. Selective laser melting (SLM), an additive manufacturing process, is increasingly being utilized to create medical devices of Co-Cr alloys due to its advantages over traditional methods, which include improved microstructures, grain refinement, and tuned porosity. The impact of additive manufacturing more especially, SLM on the mechanical, and biological characteristics of dental implants composed of cobalt-chromium alloys are examined in this review.

Keywords: SLM, dental implants, additive manufacturing, Co-Cr alloys

1. INTRODUCTION

The most successful method for replacing lost teeth has been dental implants. Intelligence choice of material is essential for successful implantation. The surface characteristics, microstructure, constituent parts, and manufacturing process of a material can all affect the implant's performance and dependability. The implant's toughness must resemble the native bodily component as much as feasible, and the material must be biocompatible [1]. The dentistry sector has extensively used cobalt-chromium-based alloys in recent years, and this market is expected to develop steadily and reach $2.6 billion by 2030. ISO22674:2022 standard (Dentistry-Metallic materials for fixed and removable restorations and appliances) states that because of its exceptional abrasion resistance, corrosion resistance, and special mechanical qualities, this metallic alloy is used extensively in the manufacturing of dental implants [2]. Co-Cr alloys are typically alloyed with other elements like Mo and W. The passive oxide layer that

forms on the alloy's surface due to Mo's presence shields the implant from corrosion. W is also in charge of keeping the chemical composition stable. According to studies, one of the most influential factors on the microstructure of cobalt-chromium dental implants is the manufacturing method, which affects mechanical properties, corrosion resistance, and ultimately biocompatibility [3]. Among the available methods for manufacturing dental restorations and prostheses, additive manufacturing methods are the most common due to their greater accuracy, repeatability, and high processing speed. Also, in 3D printing methods such as SLM, simple and complex parts can be designed according to the needs and location of the dentures, and even personalized dental implants. Selective Laser Melting (SLM) proces (shown on Figure 1), which produces a strong structure by targeted fusion. During SLM a layer of Co-Cr alloy powder is carefully melted and solidified using a high-energy laser, which is powered by computer-aided design (CAD) software, making it possible to produce intricate and personalized dental implant frameworks semi-automatically [4]. The primary objective of this research is to comprehensively analyze the various characteristics that influence the performance and effectiveness of dental implants manufactured using selective laser melting technology. This investigation encompasses a detailed evaluation of the implants from two critical perspectives: mechanical properties, which include strength, durability, and wear resistance; and biological considerations, including biocompatibility, osseointegration, and interaction with surrounding tissues. By addressing these key factors, the study aims to provide a holistic understanding of how selective laser melting impacts the overall functionality and long-term success of dental implants [5].

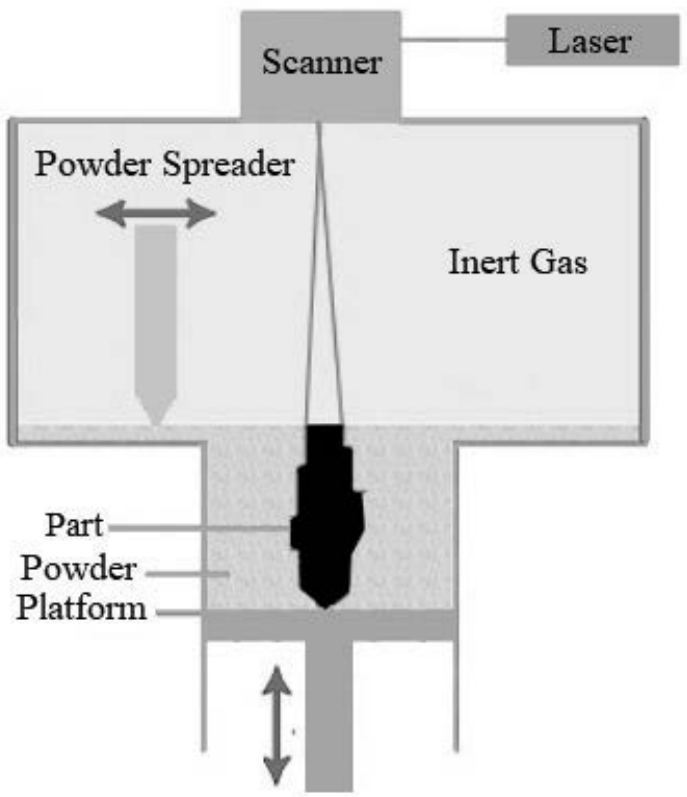

Figure 1. Illustration of the Key Steps in the Selective Laser Melting Process [6]

2. MECHANICAL PROPERTIES OF CO-CR DENTAL IMPLANTS FABRICATED BY SLM

One of the most well-known mechanical properties of the cobalt-chromium alloys is its tensile strength. On the other side, the method employed for manufacturing dental implants can directly affect the mechanical and metallurgical properties. Selective Laser Melting (SLM) is one of the most desirable additive manufacturing techniques, capable of safeguarding the tensile strength of Co-Cr alloys through the formation of unique microstructures [5]. During the SLM process, distinctive microstructures resembling "fish scales" emerge as a result of the molten pool and the stacked layers created by each laser path. When observed under high magnification, these "fish scale" patterns reveal fine microstructures accompanied by numerous columnar grains growing perpendicular to the circular, arch-shaped molten pool boundaries (MPBs). Additionally, large interlocked elongated grains with varying orientations are visible within the dendritic structures. These grains, along with the "weld lines" and their three-dimensional texture resembling woven fabrics enhance the damage tolerance of the alloy. The columnar-cellular growth of grains aligns closely with the direction of heat flow. These fine cellular or columnar-dendritic structures serve as barriers to dislocation motion, thereby improving the tensile strength of SLM Co-Cr alloys [6,7]. Co-Cr alloys fabricated through SLM exhibit improved mechanical properties, such as greater strength, hardness, and ductility, compared to their cast counterparts. According to the available data from different studies, the cobalt-chromium phase diagram well explains the exceptional mechanical properties of SLM Co-Cr alloys. The rapid cooling process in these alloys preserves much of the FCC phase at room temperature. This results in an increased solid solution limit for alloying elements, reducing precipitate and dendritic segregation while maintaining an oversaturated state. These factors contribute to solid solution strengthening and second-phase strengthening effects. Consequently, SLM Co-Cr alloys demonstrate superior strength, hardness, and ductility due to their higher FCC phase fractions and elevated solid solution limits. Another factor that plays a critical role in mechanical properties enhancement is the grain boundary. Grain refinement strengthening constitutes an essential aspect of SLM, contributing to improved mechanical properties of alloys by enhancing their strength, ductility, and toughness. Grain boundaries (GBs) act as barriers to crack propagation, and a reduction in grain size increases the GB area, thereby intensifying the grain refinement effect and further enhancing the alloy's performance. Moreover, the primary dendrite spacing in the fine microstructure of SLM Co-Cr alloys is significantly smaller (2.5 μm) than in cast Co-Cr alloys, which reduces the slip length and consequently increases the alloy's strength. In fact, the GB area of SLM Co-Cr alloy is larger than that of cast Co-Cr alloy [8].

3. BIOCOMPATIBILITY OF CO-CR DENTAL IMPLANTS

Given the widespread utilization of cobalt-chromium alloys in dental implants, various comparative studies should be undertaken to examine the biological effects of metal ions released into the body as a result of the corrosion of metallic implants. As the corrosion resistance of a device is reduced, it can negatively impact its biocompatibility. Implants can experience different types of localized corrosion, including crevice, fretting, and galvanic corrosion, which is influenced by factors such as the implant's type, material, design, shape, geometry, surface properties, mechanical function, load-bearing capacity, material interfaces,

and the in-vivo conditions at the implantation site. Depending on their form, type, size, and concentration, corrosion products can negatively impact the biocompatibility of the implant. According to the literature, the microstructure plays a significant role in determining the corrosion resistance of alloys [9]. While the biocompatibility of the Co-Cr alloy is under consideration, the chemical composition is an important factor due to different alloys based on the ASTM. Co-Cr alloys used in implants and medical devices typically adhere to specific ASTM standards which ensure their suitability for medical applications [10,11]. Examples of standards for Co-Cr alloys are listed in Table 1.

Table 1. Examples of standards for Co-Cr alloys

ASTM Standard	Alloy Type	Composition	Processing Method
ASTM F75	Co-28Cr-6Mo	28% Cr, 6% Mo	Castings
ASTM F799	Co-28Cr-6Mo	28% Cr, 6% Mo	Forgings
ASTM F90	Co-20Cr-15W-10Ni	20% Cr, 15% W, 10% Ni	Wrought
ASTM F562	35Co-35Ni-20Cr-10Mo	35%Co,35%Ni, 20%Cr,10% Mo	Wrought
ASTM F1058	40Co-20Cr-16Fe-15Ni-7Mo	40%Co,20% Cr, 16% Fe,15% Ni, 7% Mo	Wrought
ASTM F1537	Co-28Cr-6Mo	28%Cr,6% Mo	Wrought
ASTM F1091	Co-20Cr-15W-10Ni	20% Cr, 15% W, 10% Ni	Wrought
ASTM F688	Co-35Ni-20Cr-10Mo	35%Ni,20%Cr, 10% Mo	Wrought
ASTM F961	35Co-35Ni-20Cr-10Mo	35% Co,35% Ni, 20%Cr,10% Mo	Forgings
ASTM F3213	Co-28Cr-6Mo	28% Cr, 6% Mo	Additive Manufacturing

Earlier research has demonstrated that both the manufacturing process and the type of alloy play equally significant roles in influencing the amount of metal ions released from the alloys. Cell proliferation has been observed to be significantly higher on SLM samples compared to cast samples, reflecting superior biocompatibility in SLM-manufactured materials. This trend has been consistently reported in studies investigating the relationship between microstructural differences and biocompatibility. SLM samples exhibit a homogeneous and regular scale-like microstructure, while cast samples display a dendritic structure characterized by dendrites and interdendritic regions. The schematic representation of sample formation in the SLM Process was shown on figure 2. The uniform, low-porosity microstructure of SLM samples results from localized melting and rapid solidification of metal powders during the manufacturing process, where cooling rates are significantly faster (10^3–10^8 K/s). In contrast, the slower cooling rates in cast samples (20–100 K/s) contribute to the development of the dendritic microstructure. These structural differences have a profound impact on cellular behawior [12]. The homogeneous microstructure of SLM samples enhances the adhesion, viability, proliferation, and morphology of fibroblasts, outperforming cast samples. Additionally, SLM samples demonstrate a more uniform and less porous microstructure, leading to a lower rate of metal ion release, which further supports their superior biocompatibility. However, the quality of SLM

materials can be affected by the use of recycled metal powders. Although reusing leftover powder may seem economically advantageous due to the high cost of SLM manufacturing, it has been shown that SLM samples produced from recycled powders release significantly higher amounts of cobalt (Co) and chromium (Cr) ions. This increased ion release negatively impacts biocompatibility when compared to samples manufactured from fresh, unused powders. Further investigations into the cytotoxicity of Co-Cr alloys produced through various methods, including casting, milling, laser sintering, and pre-sintered milling, revealed that none of these alloys were cytotoxic under ISO 10993-5 standards. However, differences were noted in inflammatory responses. Cast and pre-sintered milled Co-Cr alloys triggered a stronger inflammatory response in human peripheral blood mononuclear cells compared to those produced by other methods. This underscores the significance of both the manufacturing process and microstructure in determining the biocompatibility and inflammatory behavior of Co-Cr alloys [9,13].

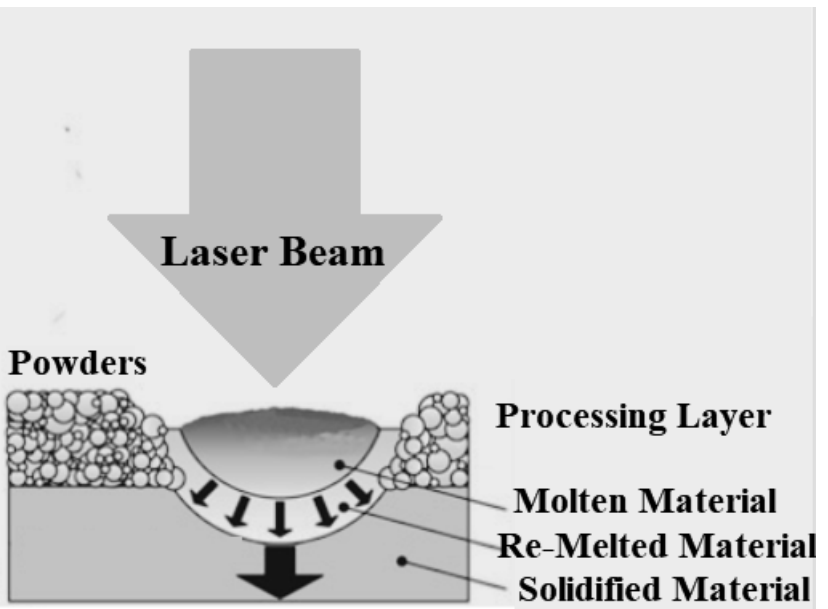

Figure 2. Schematic Representation of Sample Formation in the SLM Process [6]

4. CONCLUSION

In conclusion, while many Co-Cr alloy manufacturing processes prioritize enhancing mechanical properties, it is equally important to focus on corrosion resistance and biocompatibility for medical applications. Selective Laser Melting (SLM) stands out as a more effective method compared to traditional casting, as it allows for better control over the microstructure, which in turn improves both corrosion resistance and biocompatibility. The superior mechanical properties of SLM-manufactured Co-Cr alloys, when compared to cast alloys, are due to the microstructure created during the SLM process. The high temperatures and rapid cooling involved in SLM result in a dense, compact, homogeneous, finer, and defect-free microstructure, leading to enhanced mechanical, corrosion, and biocompatibility properties. Thus, a thorough evaluation of these factors is essential to ensure the successful use of biomaterials in medical applications.

BIBLIOGRAPHY

1. C. Sotova *et al.*, “Dental Implants: Modern Materials and Methods of Their Surface Modification,” *Mater. 2023, Vol. 16, Page 7383*, vol. 16, no. 23, p. 7383, Nov. 2023, doi: 10.3390/MA16237383.
2. D. Viderščak *et al.*, “Influence of laser powder bed fusion parameters on microstructure and mechanical properties of Co–Cr dental alloy,” *J. Mater. Res. Technol.*, vol. 30, pp. 6218–6226, May 2024, doi: 10.1016/J.JMRT.2024.05.052.
3. W. A. Uriciuc *et al.*, “Study on the Surface of Cobalt-Chromium Dental Alloys and Their Behavior in Oral Cavity as Cast Materials,” *Materials (Basel).*, vol. 15, no. 9, p. 3052, May 2022, doi: 10.3390/MA15093052/S1.
4. M. ; Jeong *et al.*, “Materials and Applications of 3D Printing Technology in Dentistry: An Overview,” *Dent. J. 2024, Vol. 12, Page 1*, vol. 12, no. 1, p. 1, Dec. 2023, doi: 10.3390/DJ12010001.
5. A. Takaichi *et al.*, “Microstructures and mechanical properties of Co–29Cr–6Mo alloy fabricated by selective laser melting process for dental applications,” *J. Mech. Behav. Biomed. Mater.*, vol. 21, pp. 67–76, May 2013, doi: 10.1016/J.JMBBM.2013.01.021.
6. MaterFlow. (n.d.). SLM (Selective Laser Melting). MaterFlow. Retrieved January 10, 2025, from https://www.materflow.com/en/slm-selective-laser-melting-2/
7. Y. Zhou, N. Li, J. Yan, and Q. Zeng, “Comparative analysis of the microstructures and mechanical properties of Co-Cr dental alloys fabricated by different methods,” *J. Prosthet. Dent.*, vol. 120, no. 4, pp. 617–623, Oct. 2018, doi: 10.1016/J.PROSDENT.2017.11.015.
8. H.-G. Kang and Dental Co-Cr alloys fabricated by selective laser melting: A review article J. Kore*an Acad. Prosthodont.*, vol. 59, no. 2, pp. 248–260, Apr. 2021, doi: 10.4047/JKAP.2021.59.2.248.
9. W. Fu *et al.*, “Wear Resistance and Biocompatibility of Co-Cr Dental Alloys Fabricated with CAST and SLM Techniques,” *Mater. 2022, Vol. 15, Page 3263*, vol. 15, no. 9, p. 3263, May 2022, doi: 10.3390/MA15093263.
10. G. Mani, D. Porter, S. Collins, T. Schatz, A. Ornberg, and R. Shulfer, “A review on manufacturing processes of cobalt-chromium alloy implants and its impact on corrosion resistance and biocompatibility,” *J. Biomed. Mater. Res. - Part B Appl. Biomater.*, vol. 112, no. 6, Jun. 2024, doi: 10.1002/JBM.B.35431.
11. J. H. Hong and F. Y. Yeoh, “Mechanical properties and corrosion resistance of cobalt-chrome alloy fabricated using additive manufacturing,” *Mater. Today Proc.*, vol. 29, pp. 196–201, Jan. 2020, doi: 10.1016/J.MATPR.2020.05.543.
12. X. zhen Xin, J. Chen, N. Xiang, and B. Wei, “Surface Properties and Corrosion Behavior of Co-Cr Alloy Fabricated with Selective Laser Melting Technique,” *Cell Biochem. Biophys.*, vol. 67, no. 3, pp. 983–990, Dec. 2013, doi: 10.1007/S12013-013-9593-9/TABLES/3.
13. X. Z. Xin, N. Xiang, J. Chen, and B. Wei, “In vitro biocompatibility of Co–Cr alloy fabricated by selective laser melting or traditional casting techniques,” *Mater. Lett.*, vol. 88, pp. 101–103, Dec. 2012, doi: 10.1016/J.MATLET.2012.08.032.

TalentDetector

31th January 2025
Gliwice, Poland

DEPARTMENT OF ENGINEERING MATERIALS AND BIOMATERIALS
FACULTY OF MECHANICAL ENGINEERING
SILESIAN UNIVERSITY OF TECHNOLOGY

INTERNATIONAL STUDENTS SCIENTIFIC CONFERENCE

Overview of materials for effective drone construction

Kinga Stępska[a], Martyna Urbańska[b], Natalia Bijok[c], Sylwia Dziwoki[d], Jan Wypiór[e], Magdalena Hulbój[f], Emilia Krzystanek[g], Krzysztof Goczoł[h], Mariusz Król[i]*,

[a] Studentka kierunku Inżynieria Produkcji i Zarządzania, e-mail: ks309686@student.polsl.pl
[b] Studentka kierunku Inżynieria Produkcji i Zarządzania, e-mail: mu309689@student.polsl.pl
[c] Studentka kierunku Inżynieria Produkcji i Zarządzania, e-mail: nb309657@student.polsl.pl
[d] Studentka kierunku Inżynieria Produkcji i Zarządzania, e-mail: sd309660@student.polsl.pl
[e] Student kierunku Inżynieria Produkcji i Zarządzania, e-mail: jw309692@student.polsl.pl
[f] Studentka kierunku Inżynieria Produkcji i Zarządzania, e-mail: mh309664@student.polsl.pl
[g] Studentka kierunku Inżynieria Produkcji i Zarządzania, e-mail: ek309672@student.polsl.pl
[h] Student kierunku Inżynieria Produkcji i Zarządzania, e-mail: kg309663@student.polsl.pl
[i] Politechnika Śląska, Wydział Mechaniczny Technologiczny, Katedra Materiałów Inżynierskich i Biomedycznych, e-mail: mariusz.krol@polsl.pl,

Abstract: Drones, also known as uncrewed aerial vehicles (UAV), are becoming increasingly important across various fields, including entertainment, industry, science, and rescue operations. They are utilized for purposes such as land monitoring, aerial photography, and agriculture. A critical aspect of drone design is the choice of materials for the frame. The frame must be lightweight, strong, and weatherproof, as it serves as the foundation of the drone and directly impacts its flight stability and safety. When designing the frame, several factors are considered, including the intended use, size, weight, and available budget. The selection of material significantly influences the drone's stability, resistance to damage, and energy efficiency. An optimal design balances lightness, rigidity, and resistance to vibrations. Additionally, the material should effectively dissipate heat generated by the motors and electronics. Durability and resistance to fluctuating weather conditions and mechanical damage are also essential attributes of the chosen material. Ultimately, the selection will depend on the user's specific needs, environmental conditions, technical requirements, and budget. Each material used for drone frames has its own advantages and disadvantages, making it crucial to carefully evaluate the options before making a decision.

Keywords: drone, frame, materials, ABS, glass fibre, carbon fibre.

1. INTRODUCTION

Uncrewed aerial vehicles, otherwise known as drones, have played an essential role in various industries in recent years, as well as in science and everyday life. Formerly used only in the military for special tasks, today, they are also used for recreational purposes, aerial

photography (so-called bird's eye view) and advanced industrial operations such as infrastructure monitoring and terrain mapping. They are becoming increasingly crucial in agriculture. They are used for spraying and soil fertility monitoring. In some countries, they are used for parcel delivery. Sometimes, drones save human and animal lives as they are used in rescue and search operations (Figure 1) [1, 2].

Drones are an indispensable tool of modern technology. However, to fulfil their functions, design teams must face the challenge of selecting the right material for their supporting components, depending on their intended use. This process requires the consideration of several technical, but also economic and environmental factors. The main requirements include mechanical strength, lightness, rigidity, and resistance to changing weather conditions. In addition, price, ease of processing and safety in case of failure are also essential considerations [3].

Figure 1. Application of drones [3]

Many modern materials, such as polymers and carbon or glass fibres, meet the necessary conditions for creating composites. Additionally, materials that enable 3D printing of frames at home are also noteworthy. Light metal alloys can be used to manufacture drone frames; however, these alloys generally have a higher specific weight compared to other materials, leading to an increase in the overall weight of the device. As a result, they are used less frequently and are mainly employed for military applications [4].

2. AIM OF THE RESEARCH

The availability of innovative methods for optimizing the shapes and sizes of drone frames using specialized computer software is substantial. However, selecting the right material is equally important, as it significantly influences the drone's functionality due to its physical and chemical properties.

This study aims to identify and characterize a suitable material for the frame of a quadcopter drone. It will compare modern high-tech materials, including carbon fiber, glass fiber, polycarbonates, polyvinyl chlorides, and various plastics commonly used in 3D printing, such as nylon and ABS. The analysis will focus on the key properties of these materials that fulfill the essential requirements for drone frames.

3. MAIN FEATURES OF THE DRONE FRAME

The drone frame should be characterised by lightness, strength and adequate stiffness. An important parameter is tensile strength, which ensures the stability of the structure during flight and allows it to withstand the forces acting on the frame. The frame material must also exhibit high impact strength to absorb energy during impacts, essential for emergency landings or hitting obstacles. In addition, the frame should be stiff enough to reduce vibrations that can affect the drone's stability and the quality of its operation, such as when taking photos or measurements. The frame's durability is also crucial, so the material must resist changing weather conditions, moisture and mechanical damage. The material must exhibit an adequate yield strength, allowing it to deform under load before breaking. Additionally, the drone's frame should be designed to allow the heat generated by the motors and electronics to dissipate efficiently, ensuring the thermal stability of the device. Optimal frame material density is also critical as low weight translates into better energy efficiency for the drone, which is crucial for its long-term operation [4-6].

4. FACTORS DETERMINING THE CHOICE OF MATERIAL FOR THE DRONE FRAME

Several important factors should be considered before choosing the right material for a drone frame.

Firstly, the purpose and application of the device should be established. This is crucial to the choice of material. For example, a drone used for photographic purposes should have a very stable frame, while a racing drone will require a lightweight, robust and aerodynamic design.

Related factors to the use of the drone are its size, weight, and intensity of use. The size of the drone must be matched to the type of propellers and motors that are planned to be fitted. The device's dimensions directly affect the material needed for the frame.

Another important aspect is weight. Lighter frames reduce energy consumption, but they must be robust enough to withstand the impact and weight of components.

The intensity and conditions of use of the drone also influence the choice of material. A drone design that will be used frequently should be more resistant to wear and tear and mechanical damage [7-10].

One key factor is the budget allocated to the project. At the beginning of the work, it is worth defining the available financial resources. Various materials are available on the market to meet the structural requirements of a drone frame, but their prices can vary considerably.

5. MATERIALS USED FOR THE DRONE FRAME

5.1. Carbon fiber

Carbon fibre consists almost entirely of stretched carbon structures, similar to graphite. It is formed by the pyrolysis of organic fibres, primarily polyacrylonitrile (PAN) lignin or artificial silk. It is most commonly found in the form of braided fabrics. Each fibre in a fabric comprises 3,000 to 12,000 threads, which are 1/10th the thickness of a hair.

There are two main types of fibre: towed (thin strands of carbon woven together) and prepeg (pulverised carbon combined with polymer resin). The structure of carbon fibres is organised,

making it mechanically very strong. It is also distinguished by its abrasion resistance, dimensional stability and good vibration damping.
As mentioned earlier, carbon fibre resembles graphite in structure, thus demonstrating infusibility and chemical resistance. It is also resistant to sudden changes in temperature. In non-oxidising atmospheres, at temperatures up to 2000°C, carbon fibre does not lose its properties, which distinguishes it extremely favourably from glass and aramid fibres. Furthermore, at 3500°C, it does not melt but sublimes. The only material that surpasses carbon fibre's heat resistance is graphite itself.
In addition, carbon fibre is characterised by its low density (1.6-2.0 g/cm^3), high tensile strength (2800-5000 MPa), fatigue and creep resistance, and high Young's modulus (230 GPa). It is a durable material that does not corrode or rust, making it resistant to the elements (Figure 2).

Unfortunately, carbon fibre also has several disadvantages. It cannot bond to the polymer matrix, so the fibre undergoes oxidation prior to resin flooding. In addition, the fibre is characterised by low thermal conductivity and lack of reusability due to its brittleness and high manufacturing price [11, 12].

Figure 2. Carbon fibre drone frame [13]

5.2. Nylon and abs

Nylon is a very durable and strong synthetic fibre belonging to the polyamide group. It is divided into three main types: aliphatic (carbon chains), aromatic (benzene rings) and block copolymers (two different types of monomers); Nylon is produced by polycondensation.

It is characterised by its high resistance to damage, stretching, creasing and abrasion, which positively affects the long service life of items made from this material. In addition, polyamide is a water-repellent material which dries quickly and wicks away moisture well, making it very resistant to weather conditions.

It is worth mentioning that nylon is a very lightweight material and simultaneously resistant to damage and abrasion. It is not harmful or toxic. Nylon can also be recycled, and its low price and general availability make it widely used in many industries.

Unfortunately, nylon has a high melting point, making it challenging to work with.

ABS (acrylonitrile-butadiene-styrene) is an amorphous plastic with high mechanical and performance properties.

This material is distinguished by its resistance to impact, vibration and wear, making it ideal for mechanical strength applications. It is very hard and is characterised by high stability and dimensional stability.
The plastic is resistant to many acids and alkalis and can be used in chemically aggressive environments.

ABS is easy to process, but to prevent quality degradation, it is recommended that it be dried at approximately 75°C for 2-4 hours.
Despite its many advantages, ABS has its limitations. The plastic is very sensitive to UV light, meaning prolonged exposure to sunlight leads to a loss of mechanical properties. In addition, ABS can emit volatile substances during processing, which can be a nuisance to health and the environment. It should also be mentioned that ABS is difficult to recycle (Figure 3) [14].

Figure 3. ABS drone frame [15]

5.3 Polyvinyl chloride

Poly(vinyl chloride) is the third most commonly produced synthetic plastic polymer. It is frequently referred to as polyvinyl chloride or PVC, for short. It is made in specialised mixing plants through the polymerisation of vinyl chloride (C_2H_3Cl). It can be obtained using various methods, including pearl polymerisation, during which suspension fixatives are used, and the finished product resembles pearls. Another method is emulsion polymerisation, for which surfactants, stabilisers and initiators are used. Another frequently used method is the so-called bulk polymerisation, which requires the reaction of pure monomers without adding a solvent in the presence of an initiator.

Polyvinyl chloride is classified as a thermoplastic polymer, so it can be repeatedly heated and moulded without losing its essential properties. It is a complex and rigid material in its simplest form, but it can be modified by adding various plasticisers and undergoing appropriate processes. In terms of mechanical and physical properties, polyvinyl chloride is divided into rigid or hard PVC and flexible or soft PVC. Hard PVC is characterised by high mechanical strength, abrasion resistance and stability at high temperatures. Soft PVC, conversely, is more flexible, easy to form and other plastic processing, and performs well in applications that require the material to be flexible. Another version of PVC has recently appeared on the market - foamed PVC, which exhibits a light and porous structure.

Poly(vinyl chloride) has a linear structure in which the vinyl chloride monomer units are repeated. The chlorine atoms give PVC good resistance to various chemical agents (acids, salts,

bases and alcohols). In addition, the chlorine present in the PVC structure results in increased UV resistance, making it durable and resistant to various atmospheric agents. Further essential characteristics of polyvinyl chloride are its low heat transfer coefficient, its resistance to both low and high temperatures and the fact that it is not easily flammable. In addition, it insulates electricity and sounds well (Figure 4) [16, 17].

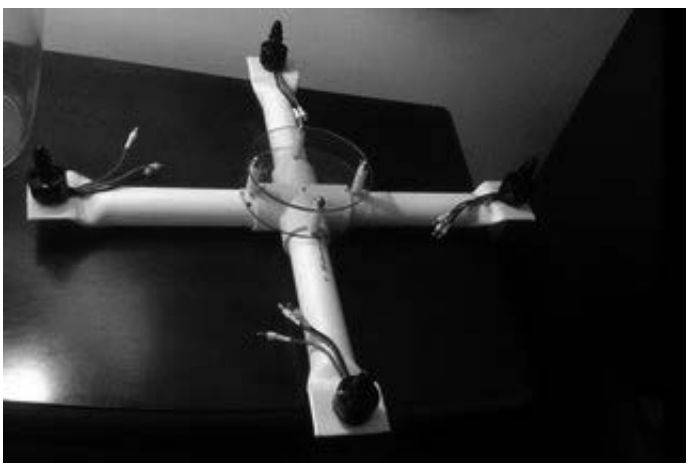

Figure 4. Polyvinyl chloride drone frame [18]

5.4. Polycarbonate

Polycarbonate is a thermoplastic polymer that has become very popular in various industries, including construction, engineering, aerospace and automotive.

It can be manufactured in various ways. The most common is made by reacting bisphenol A (previously formed from the condensation of phenol with acetone under acidic conditions) with carbonyl chloride, which produces long polymer chains that give the material high strength and flexibility.

Due to their different properties and applications, polycarbonates are divided into two varieties: chambered and solid. Chambered polycarbonates are advanced structural materials that consist of two or more layers of polycarbonate. Each layer is separated from the other by air chambers, and the structure of chambered polycarbonate itself resembles a honeycomb. This structure significantly increases the insulation efficiency (thermal and acoustic). In addition, it reduces the weight of the material, making it easy to handle and install. The cellular polycarbonate structure also provides excellent impact resistance and high light transmission (approximately 90%). Solid polycarbonate, on the other hand, is characterised by its compact glass-like structure. It is much heavier and more durable than cellular polycarbonate (but more susceptible to damage in the event of point pressure). It is characterised by better light transmission and poorer insulating properties.

In addition to high mechanical strength and high impact strength, polycarbonates also exhibit excellent thermal stability. It can be used in temperature ranges from -100°C to +135°C (with the softening point of polycarbonate being 145°C). Thus, it is not exposed due to extreme temperature changes. Polycarbonates also show resistance to UV radiation. In addition to its sensitivity to certain organic solvents, polycarbonate is resistant to various environmental conditions (Figure 5) [19, 20].

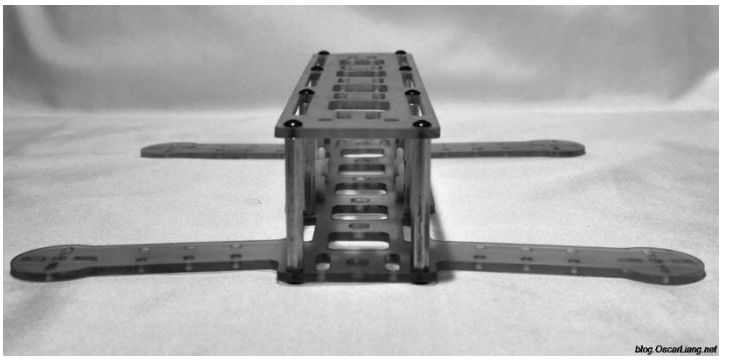

Figure 5. Polycarbonate drone frame [20]

5.5. Glass fiber

Fibreglass is a material that is very popular in various industries due to its unique properties. It is a thin fibre (0.005 to 0.01 mm in diameter) drawn from molten glass or water glass and impregnated.

The production of glass fibre begins with the melting of silica (silica sand, or silicon dioxide SiO2) at a temperature usually between 1,400°C and 1,700°C and, depending on the type, together with various mixtures that impart specific properties (e.g. with minerals containing oxides). It then flows to a refiner, where its temperature is lowered to around 1370°C, and then goes to a so-called feeder, where it is transported to heated fibreglass spinning boats. The boat contains many holes (up to 8,000) through which the molten glass is extruded. Thus, delaminated glass is cooled almost immediately to preserve the structure. The resulting fibres are coated with suitable preparations (binders and coatings). The preparations contain lubricants and adhesion promoters. This step protects the brittle glass fibres, prevents them from abrading each other and allows them to bond with various materials, including epoxies, polyamides, polyesters and polypropylenes. This is why glass fibre is used to create composite materials.

By application, glass fibres can be divided into general and special fibres. Special glass fibres are characterised by higher mechanical strength and chemical resistance and are more complex and tailored to specific applications.

The main advantage of glass fibre is its exceptional resistance to mechanical damage despite being relatively light. The high elasticity of this material makes it stretchable and does not break under heavy loads. Another essential property of glass fibre is its high resistance to chemicals and chemical corrosion, both in acid and alkaline environments. In addition, it does not change over a wide temperature range and under the influence of moisture (it is hydrophobic) and is resistant to UV radiation. Glass fibre has low thermal and electrical conductivity and a low dielectric constant, and these properties make it a good insulator (Figure 6) [21, 22].

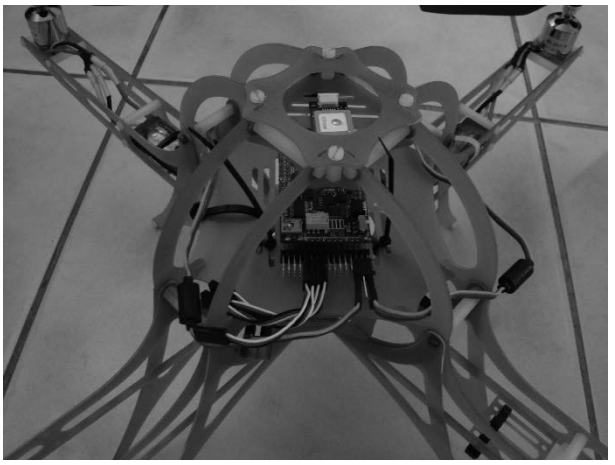

Figure 6. Glass fiber drone frame [23]

6. SELECTION OF THE FINAL MATERIAL AND ITS DETAILED DESCRIPTION

When selecting the best material for building a drone, several factors must be taken into account. First and foremost, it is essential to determine the intended use of the drone. A consumer looking to purchase a drone in a store will have different priorities compared to a scientist or researcher. Generally, consumers focus on the product's price, while scientists are more concerned with the technical specifications of the equipment. Based on this reasoning, we have chosen carbon fiber as the most suitable material for drone construction.

Carbon fiber offers a unique combination of high strength and low weight, making it an appealing choice for building drones. Its low density, ranging from 1.6 to 2.0 g/cm^3, plays a crucial role in the construction of a quadcopter, positively impacting energy efficiency and extending flight time.

Additionally, the carbon fiber structure has an exceptional ability to dampen vibrations, which is vital for aerial photography and terrain mapping. Although drones are equipped with specialized stabilization equipment known as a gimbal to minimize jitter, they still experience forces during flight. The resilience of carbon fiber enables the drone frame to endure repeated cycles of these forces without compromising its integrity, ultimately enhancing the drone's lifespan and durability.

7. SUMMARY

Selecting the appropriate materials for a drone frame is a complex and time-consuming task. It requires careful consideration of technical specifications, economic factors, and relevant regulations. Key material characteristics, including weight, strength, weather resistance, and ease of processing, were analyzed. The materials considered included carbon fiber, glass fiber, polycarbonates, polyvinyl chloride, and various plastics such as nylon and ABS. After a thorough comparison, it was determined that carbon fiber was the best choice, as it met all the necessary criteria for constructing a drone frame.

ACKNOWLEDGEMENT

The current study was conducted as part of the collaborative activities of the Student Research Group 'GYROID' at the Department of Engineering and Biomedical Materials, Faculty of Mechanical Engineering, Silesian University of Technology in Gliwice.

This thesis was developed as a result of a project focused on practical, hands-on, project-oriented education (PBL), which was part of competition VI in the Excellence Initiative—Research University program at Silesian University of Technology.

LITERATURE

1. https://flystore.pl/co-to-sa-drony-i-jakie-sa-ich-rodzaje
2. https://air-video.pl/drony/
3. https://fotisedu.com/applications-of-drones/
4. https://www.rynek-lotniczy.pl/
5. https://www.swiatdronow.pl/zrob-to-sam-dron-wyscigowy
6. https://at-machining.com/pl/drone-manufacturing/
7. L.A. Dobrzański, Podstawy nauki o materiałach, Wydawnictwo Politechniki Śląskiej 2012
8. K. Mordal, A. Szarek, Modelowanie stanu naprężeń i odkształceń w kompozycie UHMWPE – włókno węglowe, Aktualne Problemy Biomechaniki, 17/2019
9. M. Fejdyś, M. Łandwijt, Włókna techniczne wzmacniające materiały kompozytowe, Techniczne Wyroby Włókiennicze, 18/12/2010
10. https://www.kierunekchemia.pl
11. https://pl.custom-composite.com
12. Paulina Mayer, Jacek W. Kaczmar, Właściwości i zastosowania włókien węglowych i szklanych, Tworzywa Sztuczne i Chemia, 6/2008
13. https://pl.impact-fibers.com/
14. https://inzynieria.com
15. https://www.euroextrusions.com/abs/
16. https://www.thyssenkrupp-materials.pl
17. https://www.products.pcc.eu/
18. https://www.instructables.com/The-Ultimate-PVC-Quadcopter/
19. https://www.armetpolska.pl/poliweglan
20. https://www.d-pos.pl/blog/poliweglan-lity-co-to/
21. https://oscarliang.com/polycarbonate-mini-quad-frame-chaney-aerospace/
22. https://blog.polymernanocentrum.cz
23. https://www.instructables.com/Quadcopter-frame-design-fiberglass/

TalentDetector
31th January 2025
Gliwice, Poland
DEPARTMENT OF ENGINEERING MATERIALS AND BIOMATERIALS
FACULTY OF MECHANICAL ENGINEERING
SILESIAN UNIVERSITY OF TECHNOLOGY
INTERNATIONAL STUDENTS SCIENTIFIC CONFERENCE

Analysis of reactive power compensation in a 100/15kV station

Szymon Szeja

Silesian University of Technology, Faculty of Electrical Engineering
email: szymsze085@polsl.pl

Abstract: The article describes the compensation of reactive power of one of the power stations in southern Poland. The feasibility of connecting or disconnecting the capacitor bank was analyzed.

Keywords: reactive power, transformer, capacitor bank

1. INTRODUCTION

This article focuses on the analysis of reactive power compensation in a 110/15 kV station in southern Poland. The presented data are true, provided by the power grid operator Tauron dystrybucja SA. Unfortunately, this data cannot be public, therefore for the purposes of presenting the article the name of the station has been changed (working name: GLIWICE (GLW)).

2. COMPENSATION ANALYSIS

110/15 kV Gliwice (GLW) station operates as a two-section. A BKR1 capacitor bank is installed in section S1, which is powered by a 16 MVA 2-winding 110/15 kV transformer TR1.

A BKR2 capacitor bank is installed in section S2, which is powered by a 16 MVA 2 - winding 110/15 kV transformer TR2, but the bank is not working.

The analysis of the transformer load in the 110/15 kV Gliwice (GLW) station in SCADA WN shows that since 01.08.2022, transformers TR1 and TR2 have been operating in hidden reserve (both transformers TR1 and TR2 are loaded, and the 15 kV clutch is switched off).

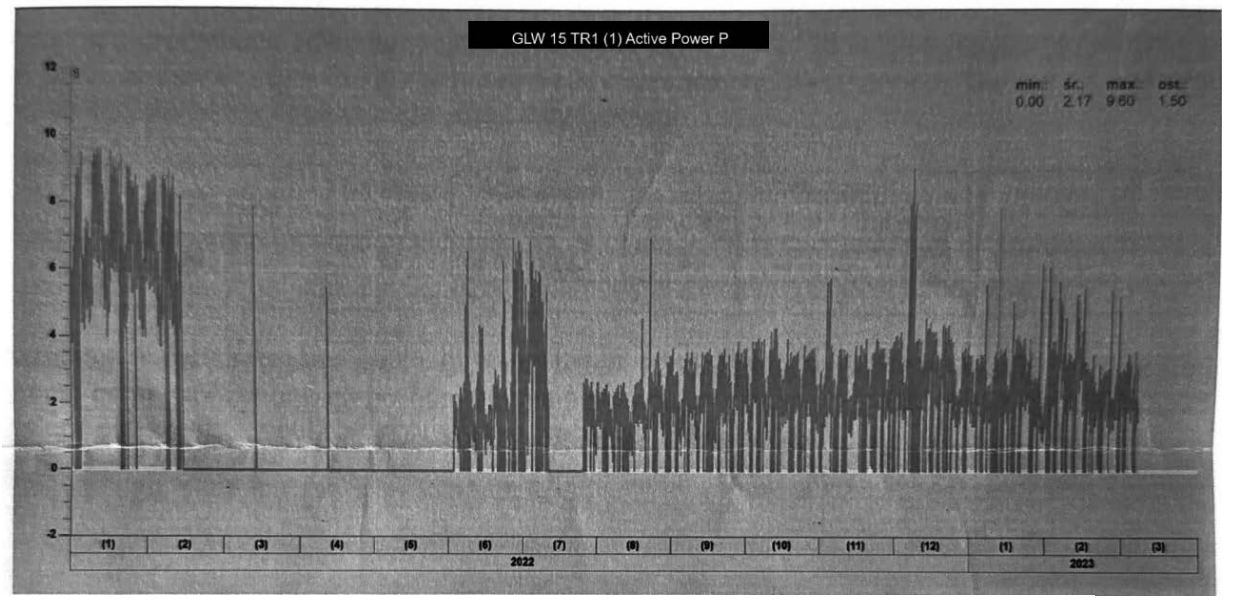

Chart 1. P=f(t) graph in the period from 01.01.2022 to 07.03.2023 - transformer TR1

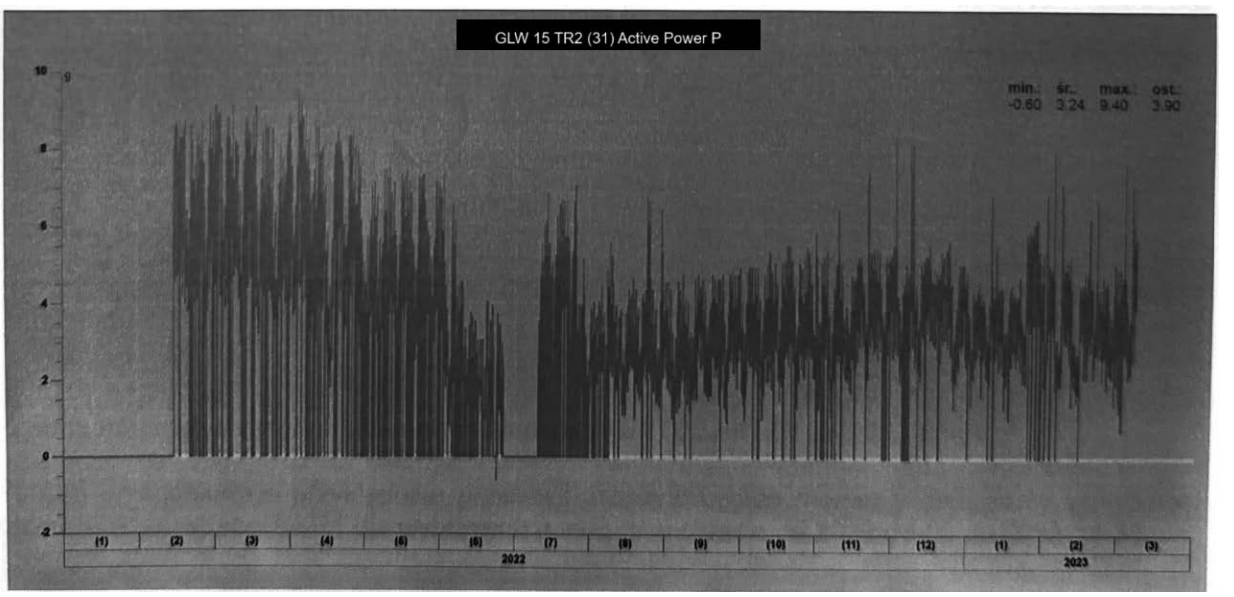

Chart 2. P=f(t) graph in the period from 01.01.2022 to 07.03.2023 - transformer TR2

Therefore, the analysis was carried out for a 7-month operating cycle of the above-mentioned transformers in the period from 01.08.2022 to 28.02.2023.

2.1. S1 SECTION

According to the operation program of the 110 kV power grid of Tauron Dystrybucja SA for the summer of 2022, the BKR1 capacitor bank with a power of Q_{BKR1} = -1.08MVAr should operate continuously throughout the week.

station name	voltage [kV]	battery power [Mvar]	work schedule		
			6.00-22.00	22.00-6.00	days off
Gliwice	15	Nr 1 1,08	+	+	+
		Nr 2 0	+	-	-

Table 1. Work schedule – summer 2022

According to the operation program of the 110 kV power grid of Tauron dystrybucja SA for the winter of 2022/23, the BKR1 capacitor bank with a power of Q_{BKR1} = -1.08MVAr should operate continuously throughout the week.

station name	voltage [kV]	battery power [Mvar]	work schedule		
			6.00-22.00	22.00-6.00	days off
Gliwice	15	Nr 1 1,08	+	+	+
		Nr 2 0	+	-	-

Table 2. Work schedule – winter 2022/23

However, the current waveforms IBKR1 = f(t) of the BKR1 capacitor bank indicate that the operation of this bank deviated from the adopted work schedule. In the period from 01.08.2022 to 28.02.2023, the battery operated continuously, but did not work on weekends.

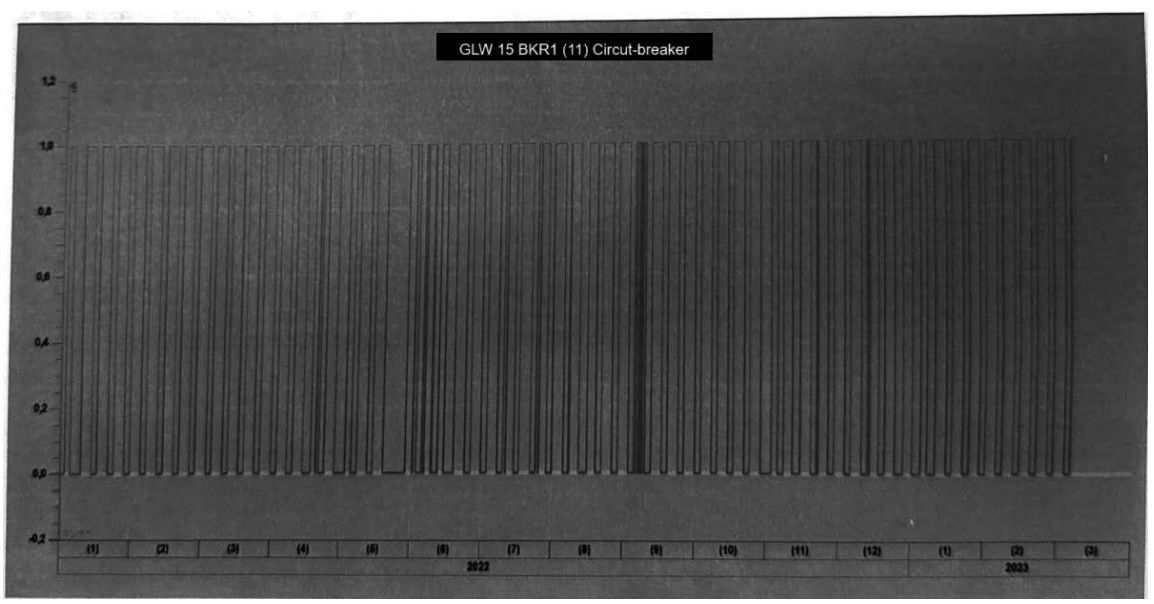

Chart 3. Circuit breaker BKR1 = f(t) engagement graph in the period from 01.01.2022 to 07.03.2023

Below are example waveforms showing the switching moments of the BKR1 capacitor bank

circuit breaker for selected months in the period from 01/08/2022 to 31/12/2022.

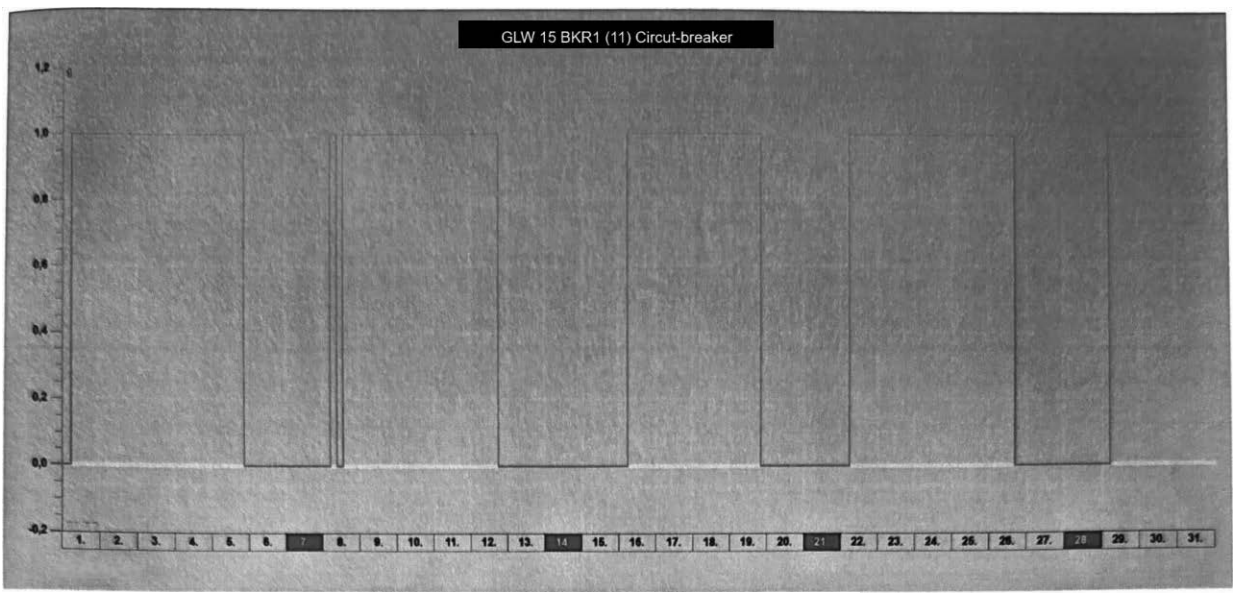

Chart 4. Circuit breaker BKR1 = f(t) engagement graph – 08.2022

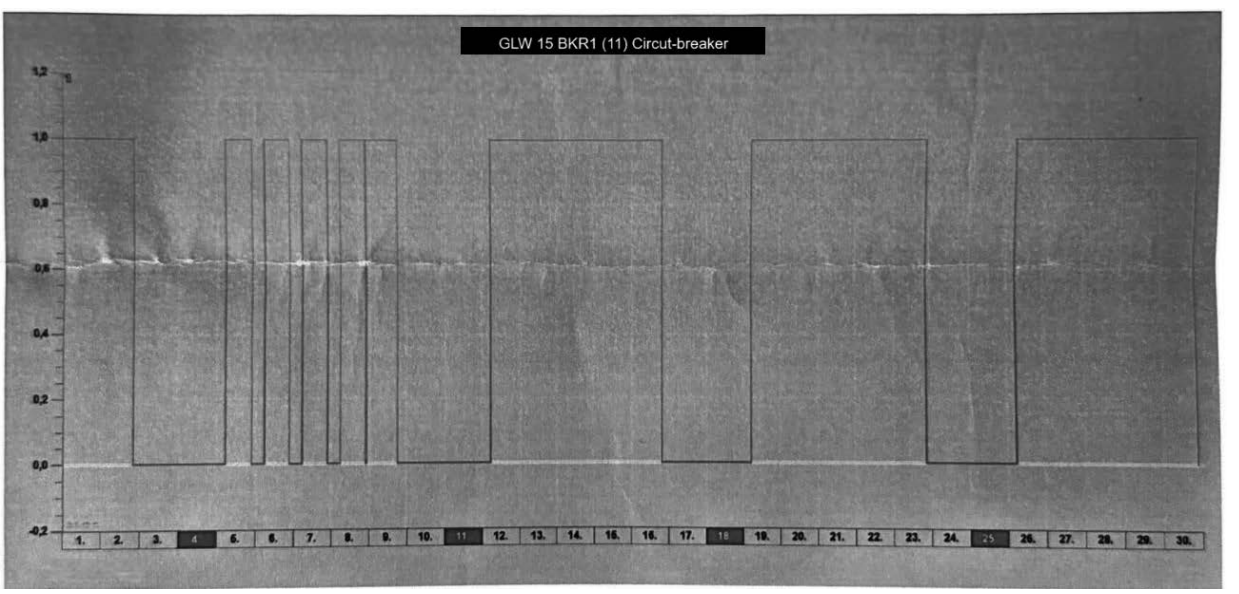

Chart 5. Circuit breaker BKR1 = f(t) engagement graph – 09.2022

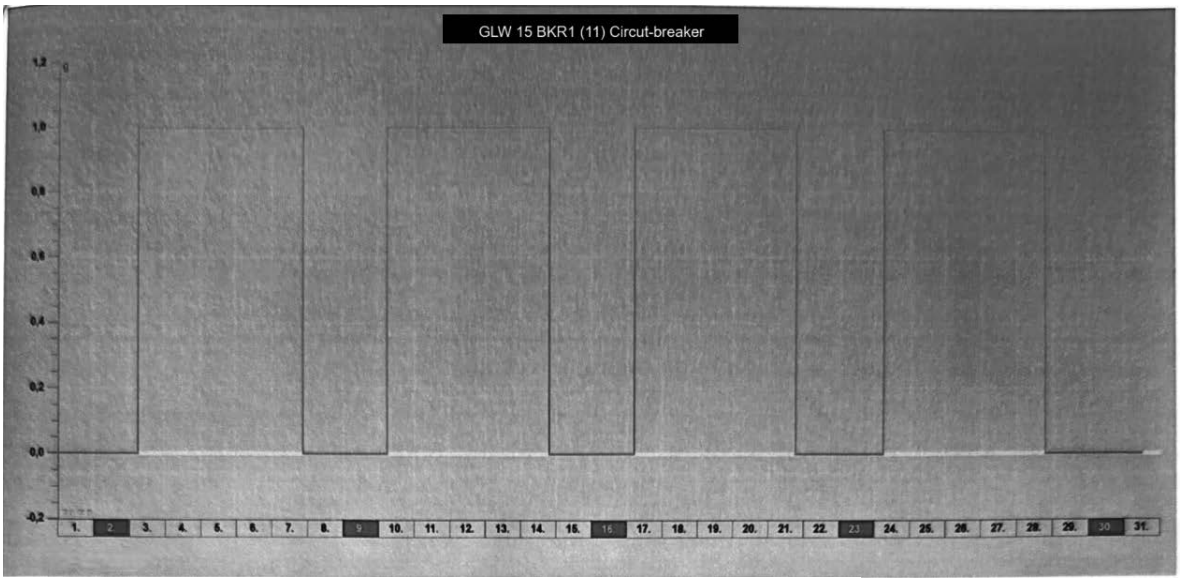

Chart 5. Circuit breaker BKR1 = f(t) engagement graph – 10.2022

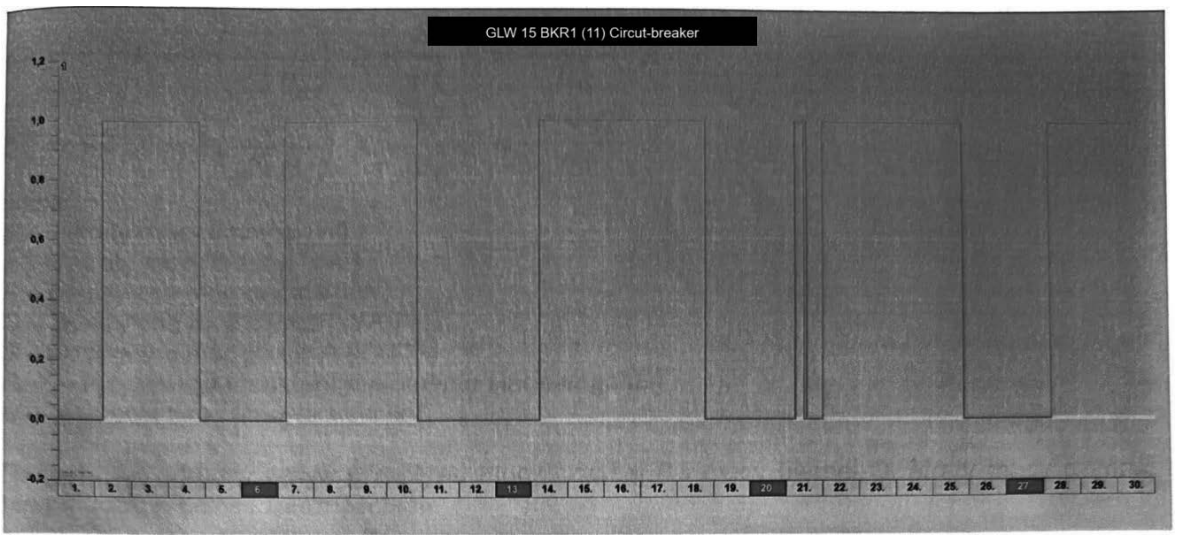

Chart 6. Circuit breaker BKR1 = f(t) engagement graph – 11.2022

The reactive power load graphs of section S1 in the period from 01.08.2022 to 28.02.2023 show that the section is loaded with reactive power Q of a capacitive nature. During this period, section S1 was loaded with reactive power with an average value of Q1 = -0.75 MVAr.

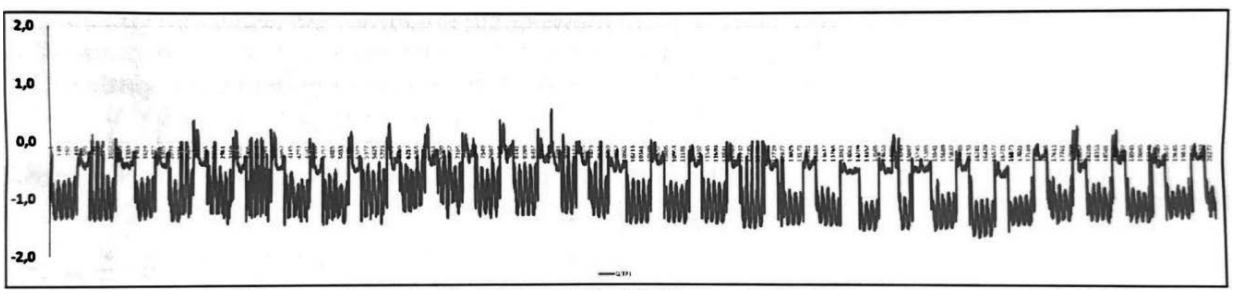

Chart 7. Q1 = f(t) graph in the period from 01.08.2022 to 28.02.2023 - section S1 (actual mileage)

Below is a simulation of the load of section S1 with reactive power Q1sym = f(t) in the period from 01.08.2022 to 28.02.2023 in the event that the capacitor bank used was disconnected (average value Q1symsr = -0.08 MVAr).

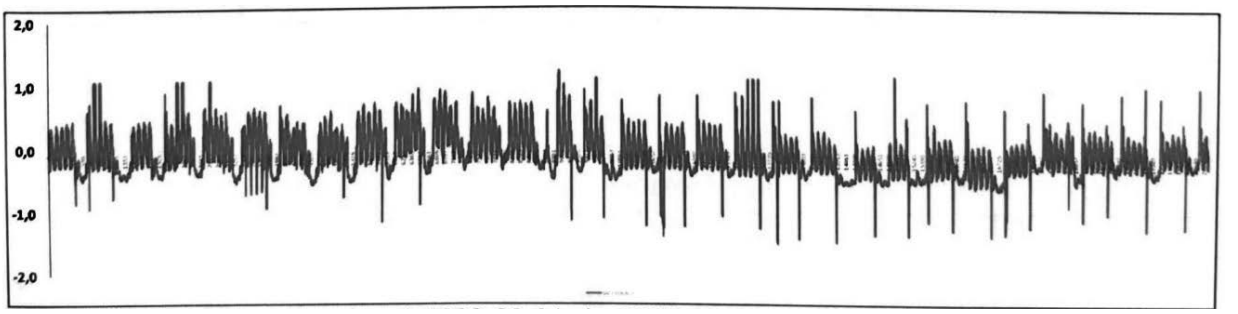

Chart 8. Q1 = f(t) graph in the period from 01.08.2022 to 28.02.2023 - section S1 (capacitor bank shutdown simulation)

3. THE INFLUENCE OF REACTIVE POWER OF THE USED CAPACITOR BATTERY ON POWER LOSSES

The load losses of active and reactive power occurring in the network element are:

$$\Delta P = 3I^2R = 3(\frac{S}{\sqrt{3}U_n})^2 R = \frac{S^2}{U_n^2}R = \frac{P^2+Q^2}{U_n^2}\ R$$

$$\Delta Q = 3I^2X = 3(\frac{S}{\sqrt{3}U_n})^2 X = \frac{S^2}{U_n^2}X = \frac{P^2+Q^2}{U_n^2}\ X$$

ΔP - active power losses [W]
ΔQ - reactive power losses [Var]
P - Transmitted active power [kW]
Q - Transmitted reactive power [kVAr]
S - Transmitted apparent power [kVA]
R, X - Resistance and reactance of the network element [Ω]
U_n - rated network voltage [kV]

Considering the separate influence of the active power flow P and reactive power flow Q, the active and reactive power losses can be described by the following relations:

$$\Delta P = \frac{P^2+Q^2}{U_n^2}\ R = \frac{P^2}{U_n^2}R + \frac{Q^2}{U_n^2}R = \Delta P_a + \Delta P_r$$

$$\Delta Q = \frac{P^2+Q^2}{U_n^2}\ X = \frac{P^2}{U_n^2}X + \frac{Q^2}{U_n^2}X = \Delta Q_a + \Delta Q_r$$

ΔP_a - Active power losses due to active power flow [W]
ΔP_r – Active power losses caused by reactive power flow [W]
ΔQ_a - Reactive power losses caused by active power flow [Var]
ΔQ_r – Reactive power losses due to reactive power flow [VAr]

Considering power losses originating only from reactive power flow, they can be defined as:
active power losses caused by reactive power flow:

$$\Delta P_r = \frac{Q^2}{U_n^2} R$$

Reactive power losses caused by reactive power flow:

$$\Delta Q_r = \frac{Q^2}{U_n^2} X$$

Since in our case U, R, X are constant, the level of losses is determined only by the reactive power flow Q and in particular Q^2.

4. SIMULATION FOR SECTION S1

The table below presents the analysis results for different variants of the capacitor bank operation. For each variant, the sum of the reactive power values in each quarter of time $\sum Q^2$ was calculated in order to determine the most advantageous variant, generating the lowest active and reactive power losses on the transformer.

Table 3. Analysis results for different variants of the capacitor bank operation

Variant description	**Battery power [MVAr]**	**Battery schedule**	**∑Q2 (value affecting active power losses)**
Current status (according to the recorded battery operation in SCADA WN)	1,08	Actual (based on recorded measurements)	15 026
When the battery is completely disconnected	-	battery disconnected	2 410
Status with existing battery operating according to the schedule specified in the network operation program	1,08	On weekdays: continuous work On weekends: continuous work	29 813
Condition with existing battery - working according to the new schedule (optimal, generating the lowest active power losses)	1,08	On weekdays: 7-15 On weekends: continuous work	5 658
Status when changing battery power and schedule (selection of optimal battery power and schedule)	0,216	On weekdays: 7-15 On weekends: continuous work	2 123

5. CONCLUSIONS

During the majority of the operating time in the period from 01.08.2022 to 28.02.2023, section S1 was loaded with reactive power Q of a capacitive nature with an average value of Q_1 = - 0.75 MVAr, which indicates overcompensation with capacitive reactive power of this section.

The simulation results indicate that in the analyzed period with the recorded load in section S1, active and reactive power losses would be smaller with a significantly reduced capacitor bank power and the adoption of a new work schedule or when disconnecting the battery.

In connection with the above, it is recommended to disconnect the capacitor bank as the simplest solution.

BIBLIOGRAPHY

1. B. Witek, Projektowanie elektroenergetycznych układów przesyłowych, Gliwice 2013,
2. S. Bolkowski, Elekrotechnika, Warszawa 1994,
3. W. Orlik, Badania I pomiary elektroenergetyczne dla praktyków, Krosno 2015,
4. K. Żmuda, Elektroenergetyczne układy przesyłowe i rozdzielcze, Gliwice 2016.

TalentDetector
31th January 2025
Gliwice, Poland
DEPARTMENT OF ENGINEERING MATERIALS AND BIOMATERIALS
FACULTY OF MECHANICAL ENGINEERING
SILESIAN UNIVERSITY OF TECHNOLOGY
INTERNATIONAL STUDENTS SCIENTIFIC CONFERENCE

Analiza numeryczna własności mechanicznych wspornika architektonicznego

Mateusz Szojda[a] , Bianka Wyrobek[a] , Wojciech Mikołejko[b], Amadeusz Dziwis[b], Agata Śliwa[b], Marek Sroka[b]

[a] Akademickim Liceum Ogólnokształcące Politechniki Śląskiej w Gliwicach
email: matiszojda@icloud.com, wyrobek.bianka@gmail.com
[b] Silesian University of Technology, Faculty of Mechanical Engineering, Department of Engineering Materials and Biomaterials
email: wojciech.mikolejko@polsl.pl, amadeusz.dziwis@polsl.pl, agata.sliwa@polsl.pl, marek.sroka@polsl.pl

Streszczenie: W pracy przedstawiono analizę MES rozkładu naprężeń i przemieszczeń powstałych w wyniku obciążenia wspornika stalowego ciężarem 1kg. Określono miejsca o najwyższej wartości naprężeń oraz przemieszczeń. Następnie zaproponowano propozycję zminimalizowania naprężeń oraz przemieszczeń w analizowanym elemencie.

Abstract: The paper presents the MES analysis of stress distribution and displacements in steel bracket caused by the load equivalent to weight of 1kg. Locations with the highest value of stresses and displacements were specified. Later the proposition of minimalizing the stress distribution and displacements in tested element was proposed.

Keywords: MES, rozkład naprężeń, rozkład przemieszczeń

1. WPROWADZENIE

Wspornikiem nazywamy element architektoniczny pełniący funkcję podpierającą. Jego zadaniem jest podtrzymanie elementu wystającego przed lico ściany wewnątrz. Takimi elementami mogą być żebra sklepienia, posągi lub przykładowo po prostu parapet lub półka. Dawniej wsporniki wykonywano z cegły lub kamienia, często również z drewna. Poza zadaniem czysto funkcjonalnym – podtrzymywaniem, często, w droższych budowlach ich zadaniem było także pełnienie funkcji dekoracyjnych stąd były one z reguły bogato dekorowane i profilowane. Przykład ozdobnego wspornika widoczny jest na rysunku 1. Aktualnie wsporniki wykonuje się ze stali lub żelbetu, zaś jako elementy zdobnicze (np. w sztukaterii) - ze styropianu [1].

Rys.1. Dekoracyjny wspornik pod balkonem [1]
Fig. 1. Decorative cantilever under the balcony [1]

Wsporniki stosuje się także poza architekturą, w konstrukcjach mechanicznych, przykładowo w maszynach, urządzeniach i pojazdach. Wykonywane są wówczas głównie z metali przy pomocy tłoczenia lub odlewania, a także z tworzyw sztucznych. Obecnie do formowania polimerowych wsporników wykorzystuje się głównie metody wtryskowe lub odlewanie. Wszędzie tam mają podobne zadanie i podobny wygląd, jak w zastosowaniach architektonicznych [1]. Wspornikami nazywane są także elementy, najczęściej wykonywane z metalu używane do trwałego zamocowania półki do ściany. Cechuje je przede wszystkim łatwość w montażu oraz nierzadko estetyczny wygląd, w zależności od potrzeb klienta. Ze względów materiałowych wspornik taki musi cechować się wysoką odpornością na odkształcenia pod wpływem działającej na niego siły. Negatywnym wynikiem takich odkształceń w najgorszym wypadku może być przesuwanie się elementów ustawionych na półkach co jest wynikiem niepożądanym. Obecnie na rynku istnieje wiele możliwych wariantów takich wsporników, które można klasyfikować zarówno ze względu na zastosowany do ich stworzenia materiał, ale także ze względu na ich wielkość, kształt, metodę mocowania oraz stopień dekoracyjności [1].

W poniższej pracy skupiono się na wsporniku wykonanym ze stali konstrukcyjnej niskostopowej. Jest to stal o niskiej zawartości węgla maksymalnie do 0,22% posiadająca dodatki stopowe w ograniczonych ilościach, nie przekraczających w sumie 3,5% [2,3].

Stale niskostopowe używane są do budowy konstrukcji narażonych na działanie warunków atmosferycznych takich jak mosty, maszty, wagony kolejowe czyli wszędzie tam, gdzie zastosowanie jej jest uzasadnione ekonomicznie. Charakteryzują się większą wytrzymałością od stali konstrukcyjnych wyższej jakości oraz większą odpornością na korozję.

W celu analizy rozkładu naprężeń występujących we wsporniku stalowym podczas obciążenia wykorzystano metodę elementów skończonych (MES). Jest to jedno z podstawowych narzędzi komputerowych stosowanych w obliczeniach inżynierskich i naukowych. Obliczenia MES polegają na podzieleniu obszaru na elementy skończone i wykonanie obliczeń tylko dla wyróżnionych punktów – węzłów [3-5].

2. ZAŁOŻENIA MODELOWE

W poniższej pracy skupiono się na wsporniku wykonanym ze stali 1.0037 (S235JR). Przy pomocy oprogramowania Solidworks wykonano symulację komputerową dwóch wsporników [2,4]:

1. Na rysunku 2 przedstawiono geometrię oraz wymiary analizowanego wspornika nr 1, a następnie odebrano wszystkie stopnie swobody na bocznej powierzchni, która docelowo ma zostać przykręcona do ściany oraz określono kierunki przyłożenia siły do konstrukcji w miejscach na których opiera się półka, co zostało przedstawione na rysunku 6.
2. Na rysunku 3 przedstawiono geometrię oraz wymiary analizowanego wspornika nr 2. Wspornik ten został dodatkowo wyposażony w poprzeczkę, która miałaby za zadanie zmniejszenie naprężeń powstałych w trakcie pracy. Następnie odebrano wszystkie stopnie swobody na bocznej powierzchni, która docelowo ma zostać przykręcona do ściany oraz określono kierunki przyłożenia siły do konstrukcji w miejscach na których opiera się półka, co zostało przedstawione na rysunku 8.

Oba przypadki rozpatrywane są dla takiego samego obciążenia wynoszącego 1kg (10N), co ma symulować podporę lekkiej półki, przeznaczonej na niewielkie elementy dekoracyjne.

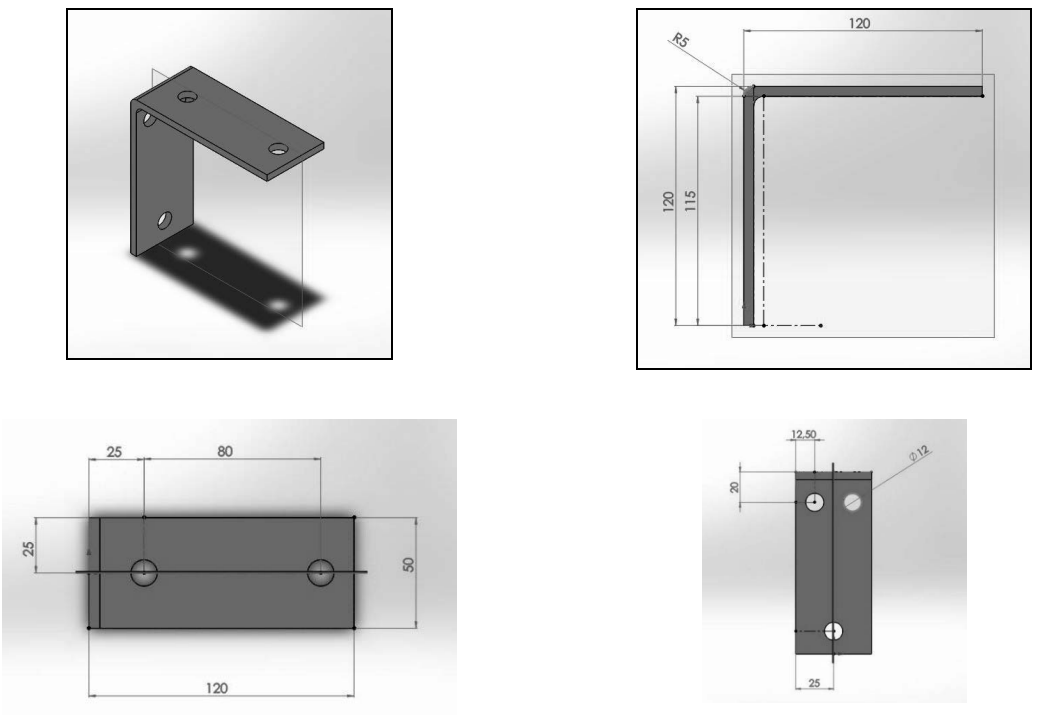

Rys. 2. Geometria i wymiary analizowanego wspornika bez poprzeczki.
Fig. 2. The geometry and dimensions of analyzed cantilever without crossbar.

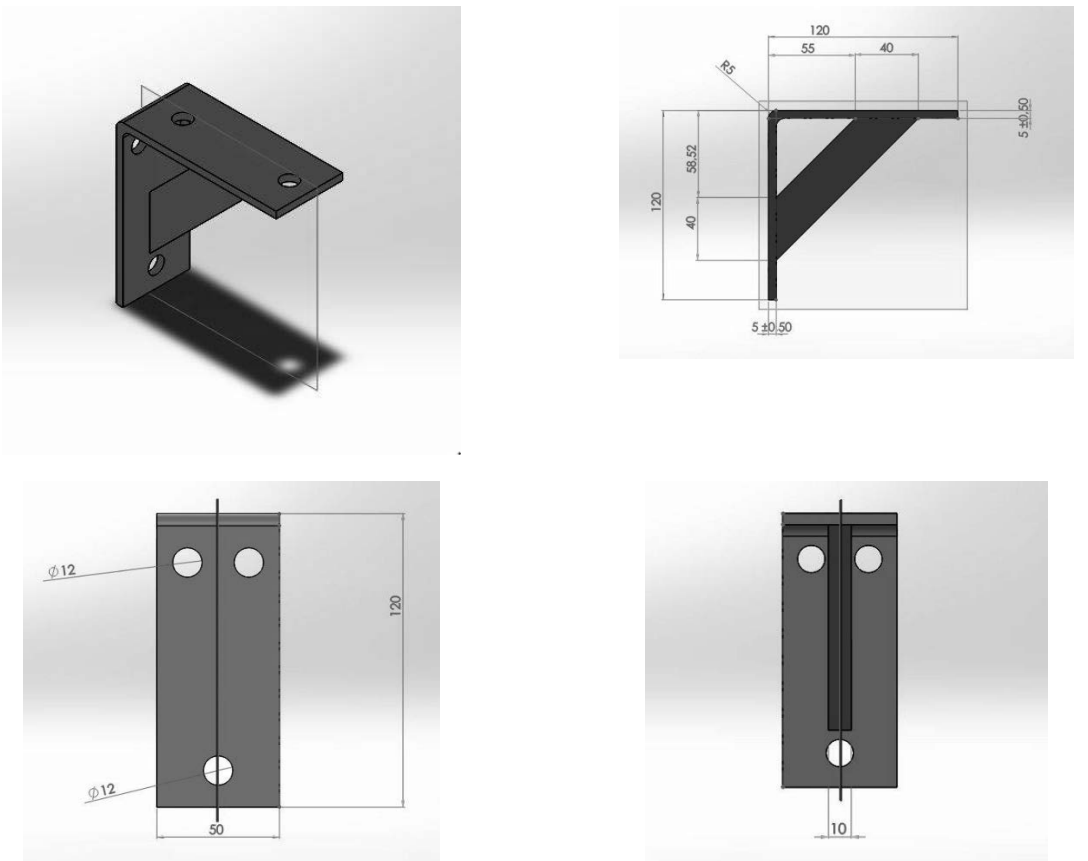

Rys. 3. Geometria i wymiary analizowanego wspornika z poprzeczką.
Fig. 3. The geometry and dimensions of analyzed cantilever with crossbar.

3. ANALIZA ROZKŁADU NAPRĘŻEŃ I PRZEMIESZCZEŃ

Na rysunkach 4-5 przedstawiono dane materiałowe oraz masowe odnośnie analizowanego wspornika. Wybrano stal 1.0037, czyli stal, z której najczęściej wykonane są tego typu elementy. Na rysunkach 6-7 przedstawiono rozkład naprężeń oraz przemieszczeń powstających we wsporniku przy obciążeniu 1kg obliczonych przy wykorzystaniu oprogramowania SolidWorks. Wyraźnie można zauważyć, że największe naprężenia powstają w miejscu występowania otworu przeznaczonego do przykręcenia półki do wspornika. Jest to obszar najbardziej narażony na uszkodzenie podczas użytkowania wspornika. Występuje też bardzo duże przemieszczenie, wygięcie części wspornika, która ma za zadanie przenosić obciążenie półki.

Jak widać na powyższych rysunkach 6-7 projekt wspornika jest niewłaściwy ponieważ przy obciążaniu półki może wystąpić zniszczenie i pękanie wspornika. Poniżej, na rysunkach 8-9 przedstawiono rozkład naprężeń oraz przemieszczeń we wsporniku, do którego dodana została poprzeczka, która ma za zadanie polepszyć działanie tego elementu.

Jak widać w drugim przypadku obliczone naprężenia we wszystkich przypadkach nie zbliżają się nawet do granicy plastyczności analizowanej stali, co przy uwzględnieniu niedokładności przybliżeń zdefiniowanych własności materiału oraz uproszczeń modelu daje podstawy do uznania iż dodanie poprzeczki do projektu znacznie polepsza jej pracy oraz

umożliwia zastosowanie go praktyce bez możliwości iż zostanie on zniszczony lub uszkodzony w trakcie użytkowania.

Właściwości masy Część1
Konfiguracja: Domyślna
System współrzędnych: -- domyślny --

Gęstość = 0.01 gramy na milimetr sześcienny

Masa = 654.60 gramy

Objętość = 83922.57 milimetry sześcienne

Obszar powierzchni = 32726.80 milimetry kwadratowe

Środek masy: (milimetry)
X = 35.06
Y = 85.03
Z = 0.00

Osie główne bezwładności i momenty główne bezwładności: (gramy * milimetry kwadratowe)
Pobrane w środku ciężkości.
Ix = (0.71, 0.71, 0.00) Px = 377608.23
Iy = (-0.71, 0.71, 0.00) Py = 1294631.42
Iz = (0.00, 0.00, 1.00) Pz = 1480815.87

Momenty bezwładności: (gramy * milimetry kwadratowe)
Mierzony w środku masy i wyrównany z wyjściowym układem współrzędnych.

Lxx = 837662.99	Lxy = 458509.00	Lxz = 0.00
Lyx = 458509.00	Lyy = 834576.66	Lyz = 0.00
Lzx = 0.00	Lzy = 0.00	Lzz = 1480815.87

Momenty bezwładności: (gramy * milimetry kwadratowe)
Mierzone w wyjściowym układzie współrzędnych.

Ixx = 5570076.55	Ixy = 2409749.97	Ixz = 0.00
Iyx = 2409749.97	Iyy = 1639100.88	Iyz = 0.00
Izx = 0.00	Izy = 0.00	Izz = 7017753.65

Rys 4. Dane dotyczące analizowanego wspornika
Fig.4. Data regarding analyzed cantilever

Materiał przypisany do tej części jest:

1.0037 (S235JR)

Moduł Younga:
2.1e+011N/m^2

Granica plastyczności:
2.35e+008N/m^2

Rys 5. Dane materiałowe analizowanego wspornika.
Fig.5. Material data regarding analyzed cantilever

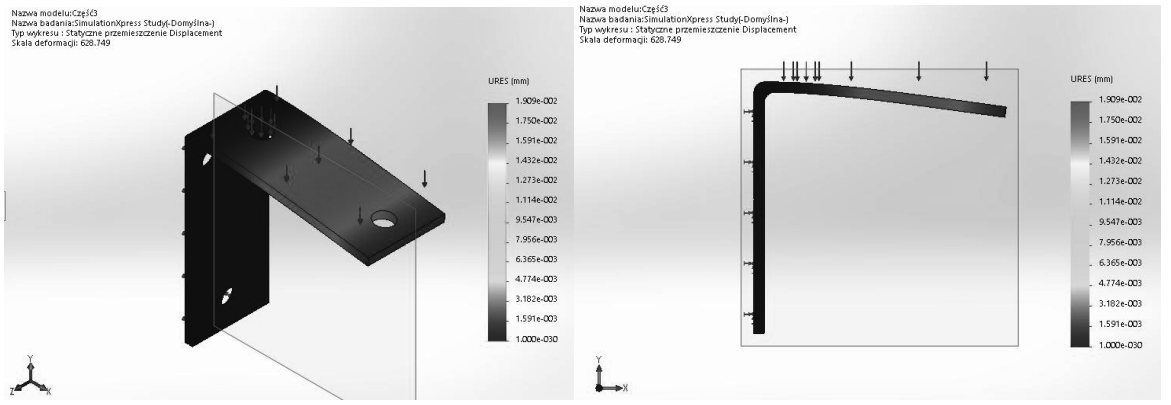

Rys. 6. Rozkład przemieszczeń przy obciążeniu 1kg we wsporniku bez poprzeczki. Różne rzuty.
Fig. 6. Displacement distribution in the cantilever without the crossbar with load of 1kg. Different Angles.

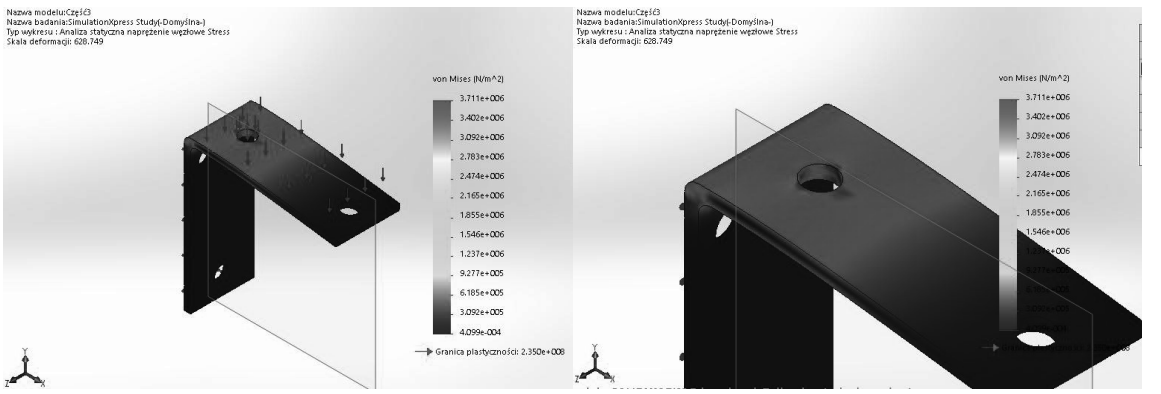

Rys. 7. Rozkład naprężeń zredukowanych wg. Huberta-Minesa przy obciążeniu 1kg we wsporniku bez poprzeczki. Różne rzuty.
Fig. 7. Distribution of Hubert-Mises stress with a load of 1kg in the cantilever without the crossbar. Different Angles

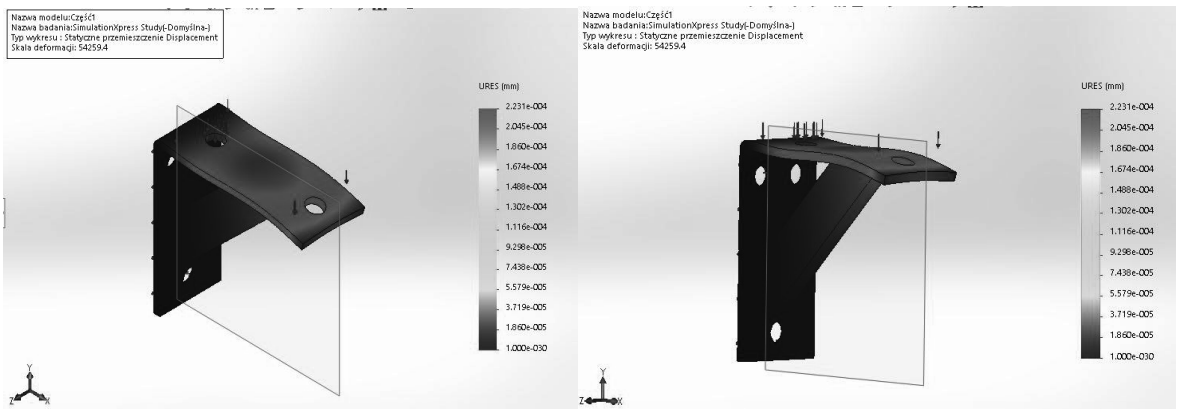

Rys. 8. Rozkład przemieszczeń przy obciążeniu 1kg we wsporniku z poprzeczką. Różne rzuty.
Fig. 8. Displacement distribution in the cantilever with the crossbar with load of 1kg. Different Angles.

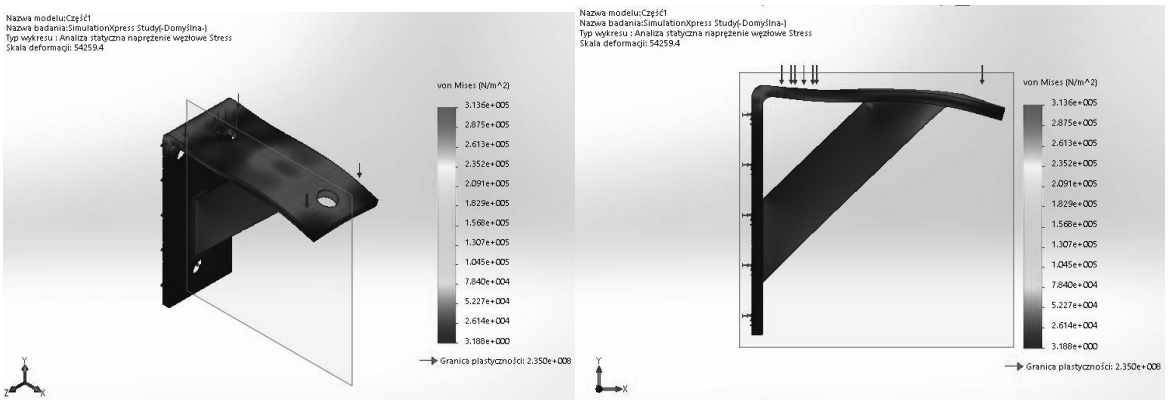

Rys. 9. Rozkład naprężeń zredukowanych wg. Huberta-Minesa przy obciążeniu 1kg we wsporniku z poprzeczką. Różne rzuty.
Fig. 9. Distribution of Hubert-Mises stress with a load of 1kg in the cantilever with the crossbar Different Angles

4. PODSUMOWANIE

W pracy przedstawiono analizę MES rozkładu naprężeń i przemieszczeń powstałych w wyniku obciążenia wspornika stalowego ciężarem 1kg.Określono miejsca o najwyższej wartości naprężeń oraz przemieszczeń. Następnie zaproponowano propozycję zminimalizowania naprężeń oraz przemieszczeń w analizowanym elemencie. Otrzymane wyniki rozkładu naprężeń nie przekraczają granicy plastyczności zadanego stopu stali 1.0037 co przy uwzględnieniu uproszczeń modelu pozwala sądzić, iż dla analizowanej geometrii oraz wymiarów dopuszczalne jest użytkowanie wspornika po dodaniu do projektu poprzeczki.

LITERATURA

1. Witold Szolginia: *Architektura*. Warszawa: Sigma NOT,1992,s.178. ISBN 83-85001-89-1
2. https://metaltech.sklep.pl/c/32297/wsporniki-zlacza-budowlane-art-metalowe.html
3. *Classification of Carbon and Low-Alloy Steels :: Total Materia Article*, www.keytometals.com
4. Międzynarodowa internetowa baza materiałoznawcza, http://www.matweb.com/search/DataSheet.aspx?MatGUID=de59918cfd3c48ae9ad2f70032c6b4ab
5. A.Z. Fortuna, B. Macukow, J. Wąsowski, Metody numeryczne, WNT, Warszawa, 1993.
6. A. Budzyński, Krótki wstęp do zastosowania Metody Elementów Skończonych do numerycznych obliczeń inżynierskich, http://www.knse.pl/publikacje/65.pdf

TalentDetector
31th January 2025
Gliwice, Poland
DEPARTMENT OF ENGINEERING MATERIALS AND BIOMATERIALS
FACULTY OF MECHANICAL ENGINEERING
SILESIAN UNIVERSITY OF TECHNOLOGY
INTERNATIONAL STUDENTS SCIENTIFIC CONFERENCE

Influence of laser modification on structure and properties of hot-work tool steel

Dominik Towarnicki[a], Bartosz Nikiel[b], Kamil Oleksy[b], Cezary Zach[b], Antonina Olszewska[a], Karolona Rogalewska[a], Mirosław Bonek[a], Oleh Polishchuk[c], Boris Gitolendia[d]

[a] Silesian University of Technology, Faculty of Mechanical Engineering, Department of Engineering Materials and Biomaterials
email: domitow239@student.polsl.pl
[b] Silesian University of Technology, Faculty of Electrical Engineering
[c] Khmelnitskyi National University, Faculty of Engineering, Transport and Architecture, Ukraine
[d] Georgian Technical University, Faculty of Transport Systems and Mechanical Engineering, Tibilisi, Georgia

Abstract: The article presents the results of research on the structure and properties of laser-alloyed hot-work tool steel X40CrMoV5-1. The experiments used a high-power diode laser and tungsten carbide as an additive. The influence of key technological parameters, such as the thickness of the applied tungsten carbide paste layer, the shielding gas used, and laser intensity, on the structure and mechanical properties of the surface layer was discussed. The relationship between microhardness and laser beam intensity on the sample surface was also analyzed.

Keywords: High-power diode laser (HPDL), X40CrMoV5-1 tool steel, tungsten carbide (WC), laser alloying, surface layer, melt zone, microhardness, dendritic structure, heat-affected zone (HAZ), surface modification.

1. INTRODUCTION

In recent years, the development of laser technologies has opened new possibilities for modifying material properties. High-power diode lasers (HPDL) are gaining popularity due to their high energy efficiency and effectiveness, particularly compared to traditional CO_2 gas lasers and pulsed Nd:YAG lasers. HPDLs are characterized by a higher absorption coefficient (20-40% for steel), making them suitable for surface treatment applications.
The surface condition of the material, including its roughness, plays a significant role in the process, as it affects the energy distribution of the laser. In HPDL technology, energy is evenly distributed over the focal spot of the laser beam, enabling precise surface layer modification. Structural changes occurring in the material's microstructure during laser remelting are schematically shown in Figure 1.
The main aim of this study was to determine the optimal technological conditions for alloying the surface layer of hot-work tool steel X40CrMoV5-1 with tungsten carbide using a high-power

diode laser. Particular attention was paid to analyzing the influence of laser processing parameters on the mechanical properties of the surface layer, crucial for extending the durability of hot-work tools.

2. METHODOLOGY

The research material consisted of hot-work tool steel X40CrMoV5-1 samples supplied in the form of vacuum-melted bars with a diameter of 75 mm. The chemical composition of the material is presented in Table 1. Samples were machined from the softened material into discs with a diameter of 70 mm and a thickness of 6 mm. The samples were subjected to austenitization in a salt bath furnace at 1060°C for 30 minutes and then rapidly quenched in hot oil. Final processing included double tempering at 510°C for 2 hours each time.

Tabele 1 Chemical composition of X40CrMoV5-1 Steel

Type of Steel	C	Mn	Si	Cr	W	Mo	V	P	S
X40CrMoV5-1	0.41	0.44	1.09	5.40	0.01	1.41	0.95	0.015	0.010

Tabele 2 Selected properties of tungsten carbide powder

Powder	Average grain size, μm	Melting temperature, °C	Density, g/cm³	Hardness, HV30
Tungsten carbide WC	2-3	2730-2870	15.6	1550

Tabele 3 Technical specifications of the HPDL ROFIN DL 020 diode laser

Radiation wavelength, nm	808 ± 5
Laser beam output power, W	2500
Power range, W	100-2500
Laser beam focal length, mm	82 / 32
Laser beam focal dimensions, mm	1.8 × 6.8 / 1.8 × 3.8
Power density range in the beam focus plane, kW/cm²	0.8-36.5

On the prepared samples, layers of paste containing tungsten carbide powder were applied with different thicknesses (0.06 mm and 0.11 mm). The surfaces were processed with a high-power diode laser (HPDL), as specified in Table 3. Experiments were conducted at a constant remelting speed while varying the laser beam power from 0.5 kW to 1.9 kW.

The steel samples were sandblasted and polished on magnetic grinders to achieve a sufficiently smooth surface. Subsequently, degreased surfaces were coated with a tungsten carbide paste layer, the properties of which are described in Table 2. The laser processing was performed using an HPDL Rofin DL 020, enabling two remelt tracks on each sample with different radii (12 and 22 mm). The laser beam was adjusted to ensure even energy distribution on the material surface, enabling stable remelting results.

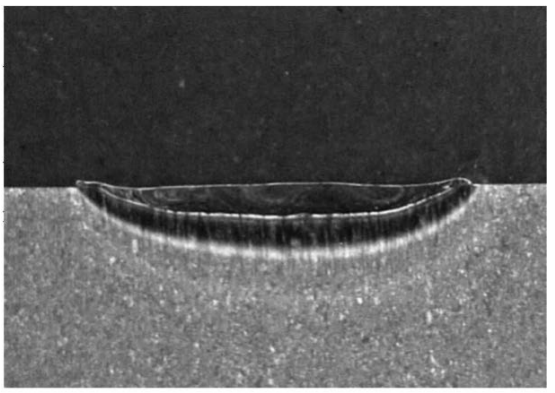

Figure. 1 Cross-section of the laser-alloyed zone with characteristic capillary lines after HPDL laser alloying; WC coating thickness - 0.06 mm, beam scanning speed - 0.5 m/min, laser power - 1.9 kW.

The remelt zone was protected by an argon stream with a flow rate of 20 l/min to prevent material oxidation. The surfaces of the samples were prepared for metallographic examination by polishing with diamond pastes and then etching in nital at room temperature.

Structural analyses were performed using light and scanning electron microscopes to examine the cross-sections of the surface layers and measure grain sizes and dendrite lengths. The results of the analyses were presented graphically and statistically, taking into account the variable process parameters.

3. RESULTS

The results of the experiments demonstrated that process parameters such as laser beam power, the thickness of the tungsten carbide paste layer, and scanning speed significantly influenced the structure and properties of the remelted layers. Increasing laser power and the thickness of the tungsten carbide layer resulted in noticeable changes in the geometry of the melt track, including increased roughness and surface waviness.

During alloying, it was observed that tungsten carbide grains, due to their high melting temperature, were partially embedded in the molten steel substrate. The remelting process caused dynamic structural changes, including the formation of a fine-grained dendritic structure in the remelted layer. It was also noted that the laser power influenced the depth of remelting—from 0.02 mm for a 0.5 kW beam to 0.47 mm at 1.9 kW.
Structural changes in the remelted layer were closely linked to the applied laser parameters. For instance, increasing laser power resulted not only in deeper remelting but also in more pronounced morphological differences in the layer. Intense circulation of liquid metal was observed in the remelted zones, leading to the formation of surface tension gradients. In areas of highest temperature, the material flowed to the edges, causing irregularities.

When tungsten carbide was used as the alloying material, its high melting temperature led to partial embedding of undissolved grains in the molten steel substrate. The rapid solidification of metal following laser beam passage “froze” the structure, which was particularly evident in the

remelted layer. As a result, different zones were formed: the remelted zone (RZ), the heat-affected zone (HAZ), and the surface layer (SL).

Structural analysis

The remelted layer exhibited a fine-grained dendritic structure with a regular orientation of crystal axes consistent with heat flow. At the boundary between the remelted zone and the heat-affected zone, elongated grains formed as a result of recrystallization caused by rapid cooling. In the central part of the remelted zone, fine, equiaxed crystals surrounded by a carbide network were observed.

Depending on the process parameters (e.g., laser power), the grain size in the remelted zone ranged from 6.11 to 28 μm². In the heat-affected zone, the grain size was larger, reaching 7.93 to 30.36 μm², while the base material exhibited significantly larger grains of 221.45 to 284.07 μm².

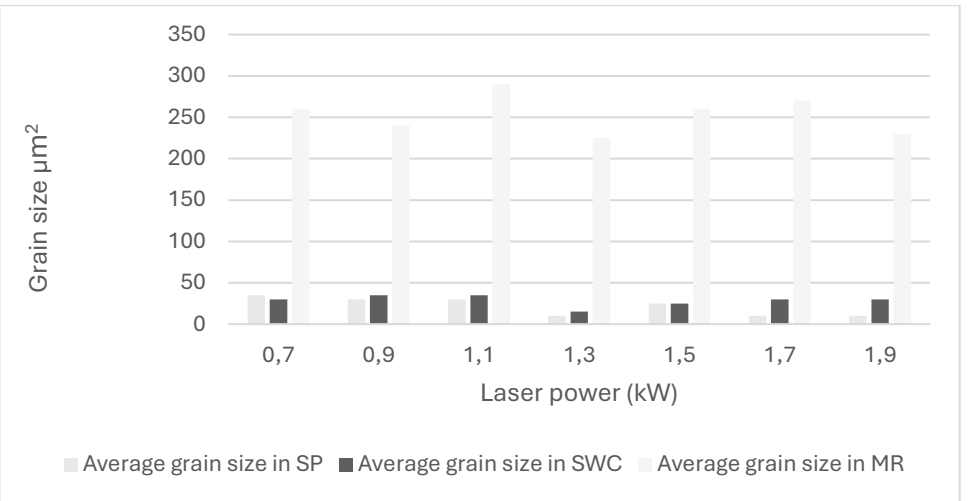

Fig. 3. Average grain size in individual zones of the steel surface layer after laser alloying.

Microhardness and mechanical properties

Microhardness testing revealed significant differences between the zones. The remelted layer exhibited the highest microhardness, reaching approximately 1300 HV0.05, attributed to the presence of tungsten carbide and the fine-grained dendritic structure. The heat-affected zone showed lower hardness (approximately 800 HV0.05) due to partial tempering of the steel. Beyond the heat-affected zone, hardness returned to the level characteristic of the base material (approximately 900 HV0.05).

The relationship between microhardness and laser power was linear, with higher power resulting in proportionally increased hardness in the remelted zone, as shown in Figure 4.

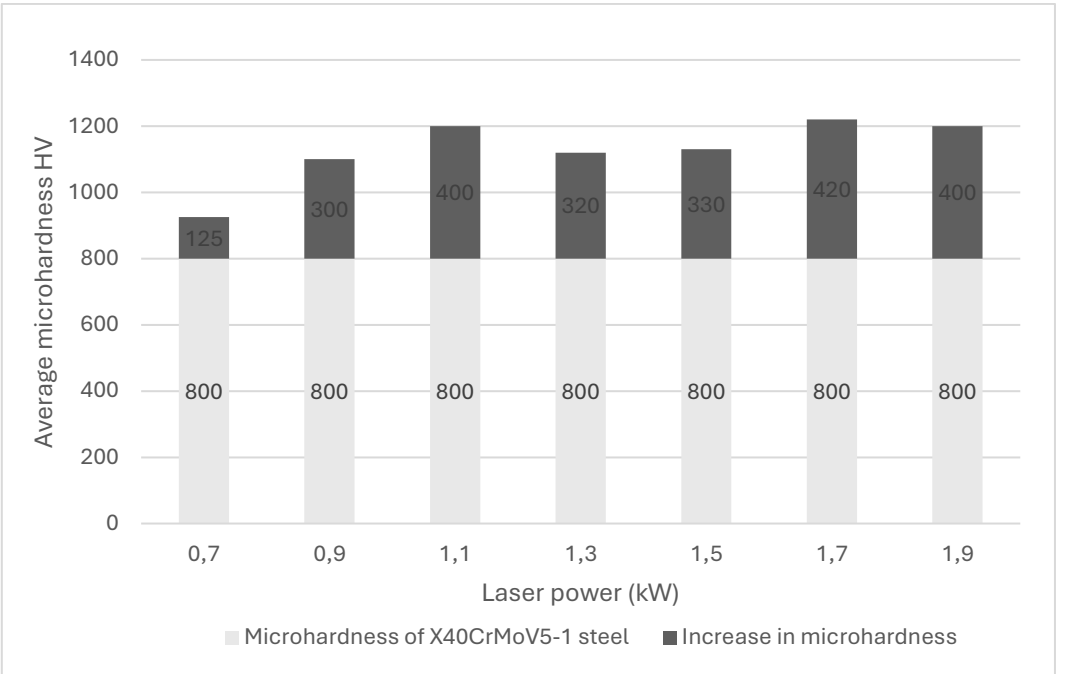

Fig. 4. Changes in microhardness in the tungsten carbide-alloyed surface layer of steel; WC coating thickness – 0.11 mm, beam scanning speed – 0.5 m/min.

Geometry of the Melt Zone

The results of geometric studies confirmed that the depth and width of the melt zone strongly depend on the laser parameters. At a power of 0.5 kW, the melt depth was approximately 0.02 mm, while at the maximum power of 1.9 kW, it reached 0.47 mm. A similar dependency was observed for the heat-affected zone (HAZ), whose thickness increased proportionally with the laser beam power, ranging from 0.15 mm to 0.8 mm.

The remelting process remained stable at a scanning speed of 0.5 m/min, and the use of argon shielding allowed for uniform remelting without cracks or surface defects.

Mechanisms of Material Mixing

Various mechanisms of material mixing were observed during laser alloying, which depended on the laser's intensity. At lower laser energy levels, capillary lines in the melt zone remained separate, resulting in a relatively uniform structure. As the laser power increased, vortex patterns in the capillary lines began to form and merge, leading to a more complex structure. At the highest beam power, the bottom of the melt zone exhibited undulations, caused by the intense movement of liquid metal within the melt zone.

Relationship Between Melt Depth and Laser Parameters

The depth of the melt zone increased with the laser beam power, which can be attributed to the higher energy delivered to the material's surface. The melted layer formed primarily as a result

of heat conduction, which is proportional to the laser's power. High energy application intensified thermal processes, leading to deeper melting.

Characteristics of the Melt Zone

The melt zone was dominated by fine-grained dendritic structures that developed along the direction of heat flow. In the central area, where heat dissipation occurred in all directions, equiaxed crystals surrounded by a fine carbide network were formed. The boundary between the melt zone and the heat-affected zone showed varied grain morphology, with grains in this region being elongated and partially remelted.

Grain Morphology and Dendrite Size

As a result of laser alloying with tungsten carbide, the grain size in the melt zone was significantly smaller than in the base material. The average grain size in the melt zone ranged from 12.48 to 28.38 μm² for a WC coating thickness of 0.06 mm, while the base material exhibited grain sizes between 221.45 and 284.07 μm². The dendrite length in the melt zone ranged from 16.56 to 20.74 μm, indicating the fine-grained nature of the remelted area.

Microhardness and Variability in the Melt Zone

Measurements of microhardness across the cross-section of the melt zone revealed significant differences between the zones. The microhardness of the melt zone averaged 1300 HV0.05, which was significantly higher compared to the heat-affected zone (800 HV0.05) and the base material (900 HV0.05). The variability in microhardness within the melt zone was attributed to chemical inhomogeneity and fluctuations in the composition of tungsten carbide within this region.

The studies showed that with appropriately selected process parameters (laser power, scanning speed, and shielding gas type), it is possible to achieve a high-quality melted layer. The surface was smooth, and the number of defects, such as cracks or inclusions, was minimized.

4. CONCLUSIONS

The conducted research on laser alloying of X40CrMoV5-1 tool steel using a high-power diode laser (HPDL) demonstrated that this technology has significant potential for improving the mechanical properties and durability of hot-work tools. By utilizing tungsten carbide as an alloying material, a surface layer was obtained with enhanced microhardness, better wear resistance, and a fine-grained structure.

The process analysis showed that the proper selection of technological parameters, such as laser beam power, scanning speed, and shielding gas type, allows for precise control over the geometry and quality of the melt zone. The melted layer, with a thickness of up to 0.47 mm, consisted of a fine-grained dendritic structure, significantly improving its mechanical properties compared to the base material.

The results of metallographic studies and microhardness measurements indicate that:

- The microhardness of the melted layer increased by approximately 50% compared to the material subjected to traditional heat treatment, reaching around 1300 HV0.05.
- The presence of tungsten carbide in the melted layer structure effectively enhanced its wear resistance, which is critical for tools operating in high temperatures and demanding conditions.
- The thickness of the heat-affected zone changed proportionally with the laser power, ranging from 0.15 mm to 0.8 mm, confirming the ability to precisely control the process.

Additionally, the use of argon shielding minimized oxidation and ensured a high-quality melted surface. Defects such as cracks or excessive roughness were successfully avoided, which is essential for the industrial application of this technology.

The proposed laser alloying technology has broad potential in the tooling industry, particularly in the production of components subjected to intense mechanical and thermal wear. Improving mechanical properties, such as microhardness, wear resistance, and operational durability, opens opportunities for producing tools with extended service life.

However, to fully implement this technology in industrial applications, further studies are necessary, including:

1. Durability tests of tools manufactured using this technology under industrial conditions.
2. Optimization of the process in terms of production costs and processing time.
3. Further analysis of structural stability under dynamic changes in temperature and mechanical loads.

In conclusion, laser alloying of tool steel with tungsten carbide using a high-power diode laser is a promising method for improving surface properties. This approach has the potential to revolutionize production processes in the tooling industry and related fields, ensuring higher efficiency and durability of tools in demanding operating environments.

ACKNOWLEDGEMENTS

The work was created as part of project based learning - PBL, in the 11th competition under the Initiative of Excellence - Research University, Silesian University of Technology, Gliwice, Poland and as part of project of Students Scientific Circle of Laser Surface Treatment under the Initiative of Excellence - Research University, Silesian University of Technology, Gliwice, Poland.

BIBLIOGRAPHY

1. Dobrzański L.A., Hajduczek E., Marciniak J., Nowosielski R.: Metaloznawstwo i obróbka cieplna materiałów narzędziowych. WNT, Warszawa, 1990.

2. Klimpel A.: Przegląd Spawalnictwa, Nr 6 (2001) s. 1-6.
3. Major B., Ebner R.: Inżynieria Powierzchni, Nr 1, 1996, 53-65.
4. Kusiński J.: Lasery i ich zastosowanie w inżynierii materiałowej. WN „Akapit", Kraków, 2000.
5. Dobrzański L.A., Bonek M., Klimpel A., Lisiecki A.: Proc. 10th Int. Sc. Conf. AMME 2001, Cracow - Zakopane, 2001, s. 133-136.
6. Dobrzański L.A., Bonek M., Klimpel A., Lisiecki A., Bugliosi S.: Proc. 11th Int. Sc. Conf. AMME'2002, Gliwice - Zakopane, 2002, s. 77-82.
7. Dobrzański L.A., Bonek M., Klimpel A., Lisiecki A.: Materials Science Forum, T. 437-438, (2003) s. 69-72.
8. Dobrzański L.A., Bonek M., Klimpel A.: 4th Int. Conf. on Ind. Tools, Bled-Celje, 2003, s. 723-728.
9. Dobrzański L.A., Bonek M., Hajduczek E., Klimpel A., Lisiecki A.: International Conference on Advanced Materials & Processing Technologies, AMPT 2003, Dublin, 2003, s. 77-80.

TalentDetector
31th January 2025
Gliwice, Poland
DEPARTMENT OF ENGINEERING MATERIALS AND BIOMATERIALS
FACULTY OF MECHANICAL ENGINEERING
SILESIAN UNIVERSITY OF TECHNOLOGY
INTERNATIONAL STUDENTS SCIENTIFIC CONFERENCE

Investigation and analysis of electrical and structural parameters of multicrystalline silicon solar cells

Julia Urbanek[a], Kacper Jakubowski[a], Bartosz Lemański[a], Mikołaj Wąsik[a], Christian Sanquedolce[b], Małgorzata Musztyfaga-Staszuk[c], Wojciech Filipowski[d]

[a] Silesian University of Technology, Faculty of Automatic Control, Electronics and Informatics, Department of Automatic and Robotics, Akademicka 16, 44-100 Gliwice, Poland
[b] Silesian University of Technology, Faculty of Transport and Aviation Engineering, Zygmunta Krasińskiego 8, 40-019 Katowice, Poland
[c] Silesian University of Technology, Department of Engineering Materials and Biomaterials, Konarskiego 18a, 44-100 Gliwice, Poland
email: malgorzata.musztyfaga@polsl.pl
[d] Silesian University of Technology, Faculty of Automatic Control, Electronics and Informatics, Department of Telecommunications end Teleinformatics, Akademicka 16, 44 - 100 Gliwice, Poland
email: wojciech.filipowski@polsl.pl

Abstract: This article presents the results of research and analysis on the parameters of multicrystalline silicon solar cells conducted to evaluate the reproducibility of manufacturing processes. The study involved measuring efficiency based on illuminated current-voltage characteristics, line contact resistance, and contact resistance. Additionally, the chemical composition (EDS) of the front contacts, their topography, and fractography were examined.

Keywords: solar cell, photovoltaics, EDS, current-voltage characteristic, line contact resistance, contact resistance

1. INTRODUCTION

1.1. Global trends in photovoltaic development

The photovoltaic industry is a rapidly evolving sector that utilizes advanced technological solutions. According to a report by the Renewable Energy Institute [1], photovoltaics account for 60% of the installed capacity from renewable energy sources in Poland, with a total capacity of 17 GW at the end of 2023 - an increase of 4.662 GWp compared to the previous year. This positions Poland 6th in Europe for total installed photovoltaic capacity and 4th for annual growth.

Currently, approximately 97% [2] of photovoltaic (PV) solar cell production relies on crystalline silicon, with monocrystalline silicon being the dominant type. Innovations such

as larger silicon wafer formats (e.g., M10 and G12) and bifacial module technologies have led to a 52% reduction [2] in the weighted average market price of crystalline silicon modules by the end of 2023 compared to the previous year. These cost reductions are also attributed to the decreased use of silver- and aluminum-based metallization pastes, which, after silicon, represent the most significant material cost components. Additionally, advancements aimed at lowering reflectivity have further enhanced module efficiency. Laboratory tests have achieved photovoltaic conversion efficiencies of 27.3% for monocrystalline silicon cells and 24.4% for multicrystalline silicon cells [3].

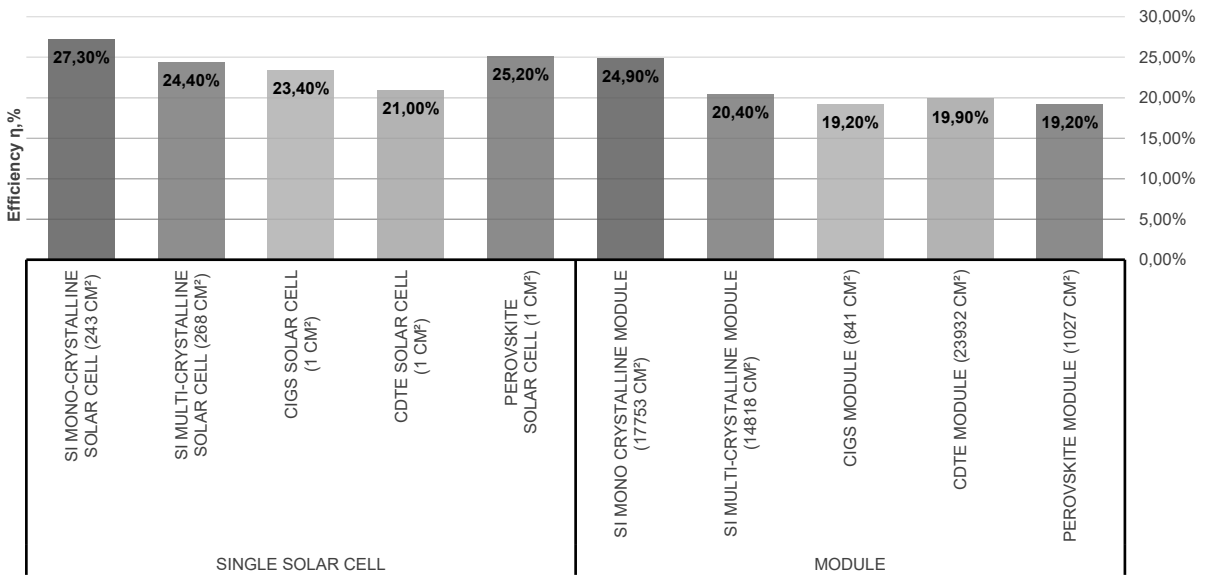

Fig. 1. Comparison of the highest efficiency results of PV solar cells and modules based on the base material and the technology used for their production under laboratory conditions [3]

It is predicted that tandem perovskite-silicon solar cells will achieve average efficiencies of approximately 27% by 2028 and 30% by 2034, surpassing the efficiency limits of single-junction silicon-based solar cells imposed by physical constraints [2]. Intensive research is being conducted on perovskite solar cells, particularly focusing on the long-term stability of their performance.

1.2. Silicon solar cell manufacturing technology

This section outlines the typical steps involved in the production of silicon solar cells. Initially, p-type base wafers are cleaned and etched to create an anti-reflective structure. The wafers then undergo phosphorus diffusion from a phosphorus oxychloride source in a resistive reaction furnace. Subsequent steps include the removal of dopant glass and etching of the p-n junction on the rear surface and edges. The silicon surface is passivated through thermal oxidation, followed by the deposition of an antireflective layer. Electrical contacts are applied using screen printing method, typically with a silver-based paste for the front electrode and aluminum for the rear. Both electrodes are then subjected to drying and co-firing processes. [4]

A schematic of the crystalline silicon solar cell manufacturing process is illustrated in Figure 2.

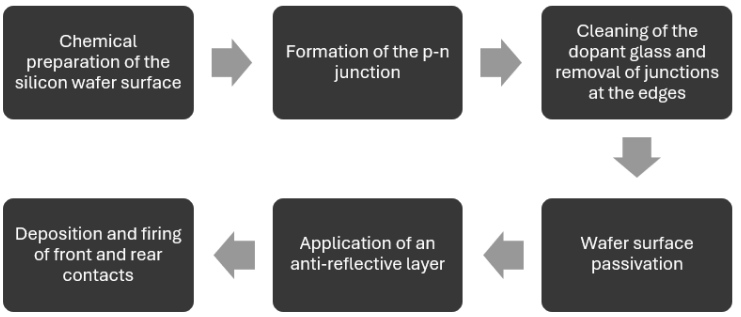

Fig. 2. Manufacturing of crystalline silicon solar cells

2. MATERIALS USED FOR RESEARCHES

The study utilized six identical solar cells, one of which (solar cell no 6) was damaged during testing. Table 1 presents the main properties of multicrystalline silicon, while Figure 3 illustrates an example of a solar cell used in the research.

Table 1. Properties of multicrystalline silicon

Conductivity	p-type
Admixture	boron
Thickness	175µm±17,5 µm
Area	100 mm×100 mm ± 0.25 mm

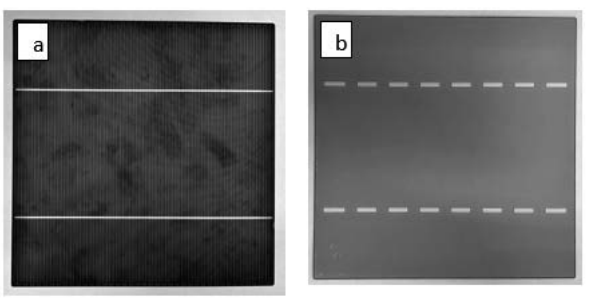

Fig. 3. Solar cell: a) front view, b) back view

3. METHODOLOGY

The Correscan device, developed by SunLab in collaboration with Mechatronics, was utilized to measure the parameters of solar cell contacts. Two modes were employed: 1) the Core scan, 2) the LBIC scan. The LBIC mode identified current density, while the Core scan analyzed electrical contact parameters, resulting in the destruction of solar cells during the Core scan testing [5]. Efficiency and fill factor were determined using a setup equipped with the SS150AAA solar simulator from Photo Emission Tech. The following parameters were measured: U_{oc} (open-circuit voltage), I_{sc} (short-circuit current), V_m (voltage at maximum power), I_m (current at maximum power), P_m (maximum power), FF (fill factor), and E_{ff} (conversion efficiency).

4. RESULTS ANALYSIS

4.1. Electrical properties analysis

Table 2 summarizes the distribution of current density induced by a light beam across the surfaces of the analysed solar cells. The average values were calculated from three measurements for each solar cell.

Table 2. Obtained results

Solar cell number	J, mA/cm^2
1	66.30
2	66.90
3	69.93
4	67.86
5	68.83
6	68.84

Based on Table 2, it can be concluded that all the analysed solar cells exhibit a uniform current distribution within the material under study, ranging from 58 to 75 mA/cm^2.

Figure 4 presents a graphical interpretation of the obtained results. Although solar cell number 6 was damaged during testing, the measurements from its undamaged portion remained unaffected.

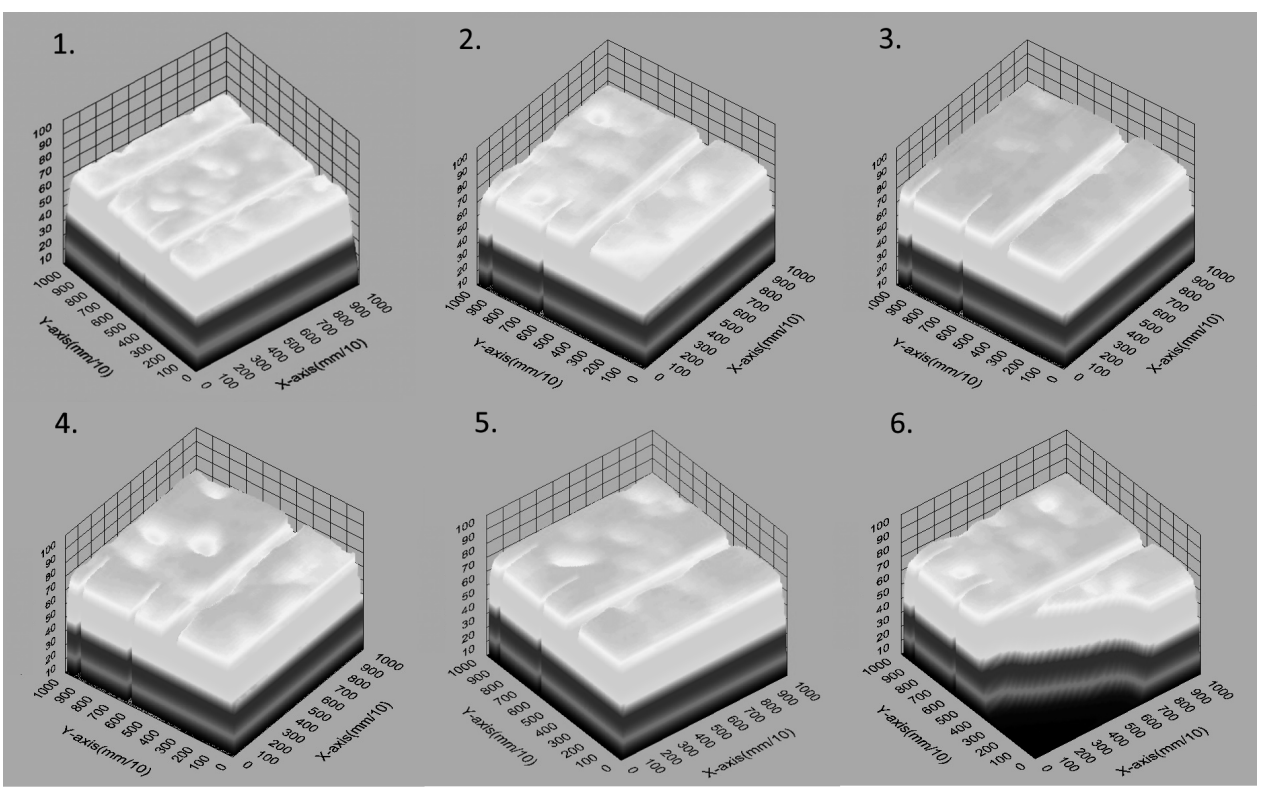

Fig. 4. 3D images of measured current in analysed solar cells, where the numbers 1 to 6 correspond to respective solar cells

Table 3 presents the line contact resistance (R_{cl}) and contact resistance (R_c) data (defined by Correscan device) for the analyzed solar cells. These values were obtained from the average of three measurements for each solar cell, using the Core scan mode of the Correscan device [5].

Table 3. Obtained results of chosen electrical parameters

Solar cell number	U, mV	R_{cl}, Ωcm	R_c, mΩ cm^2
1	22.46	6.73	80.6
2	19.56	5.86	70.3
3	16.43	4.93	59.0
4	15.13	4.53	54.3
5	17.86	5.36	64.3
6	17.40	5.20	62.6

Figure 5 illustrates the electrical measurements (in three dimensions) for the analyzed samples.

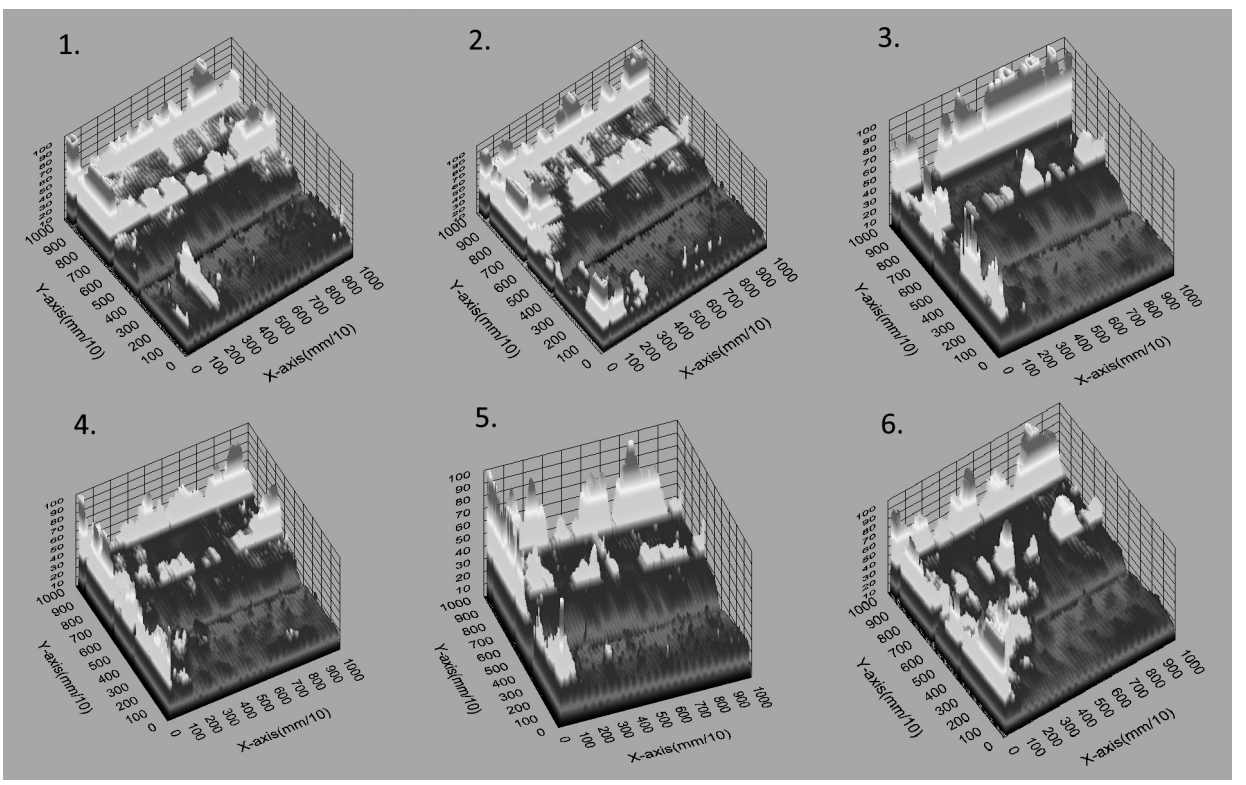

Fig. 5. 3D images of measured electrical results in analysed solar cells, where the numbers 1 to 6 correspond to each solar cell

Analyzing the values in Table 3 and Figure 5, it can be observed that the R_{cl} and R_c of the selected solar cells are non-uniform. This discrepancy likely arises from inconsistent conditions during the application of conductive pastes across all areas of the solar cell, as well as localized temperature differences during the contact co-firing process. Table 4 presents the parameters of the analysed solar cells, measured using a solar radiation simulator.

Tab. 4. Parameters of analysed solar cells

Solar cell number	U_{oc}, mV	I_{sc}, mA	V_m, mV	I_m, mA	P_m, mW	FF, -	E_{ff}, %
1	617.5	8302.7	476.4	7584.4	3613.3	0.705	15.25
2	612.7	8182.5	465.9	7539.4	3512.5	0.701	14.81
3	622.2	8280.9	481.1	7499.0	3607.8	0.700	15.24
4	614.5	8157.4	464.7	7436.8	3455.6	0.689	14.59
5	619.1	8256.1	468.9	7583.2	3557.8	0.696	15.01
6	614.2	7553.6	472.2	6666.5	3148.0	0.679	13.30

Examining Table 4 reveals that the open-circuit voltage (U_{oc}) for the analysed solar cells ranges between 612 mV and 620 mV, with short-circuit currents (I_{sc}) spanning from 7550 to 8300 mA. The V_m is between 464 mV and 482 mV, I_m is within 6666 mA and 7600 mA, and P_m is from 3100 mW to 3620 mW. The fill factor (FF) varies between 0.689 and 0.705, while the conversion efficiency (E_{ff}) ranges from 13.3% to 15.25%.

It is worth noting that the parameters of all solar cells are comparable. Solar cell number 6, which was damaged during testing, exhibits lower efficiency due to its reduced surface area, resulting in diminished short-circuit current and maximum power current. However, its maximum power voltage ranks as the third highest among all cells, indicating that the damage did not affect its voltage parameters.

The efficiencies achieved fall within the typical range for single-junction multicrystalline silicon solar cells, which is approximately 14 – 19 % [6][7]. The only exception is solar cell 6, whose reduced surface area accounts for its lower efficiency.

Figure 6 presents an example of the current-voltage characteristic for solar cell number 1, the most efficient among the tested samples.

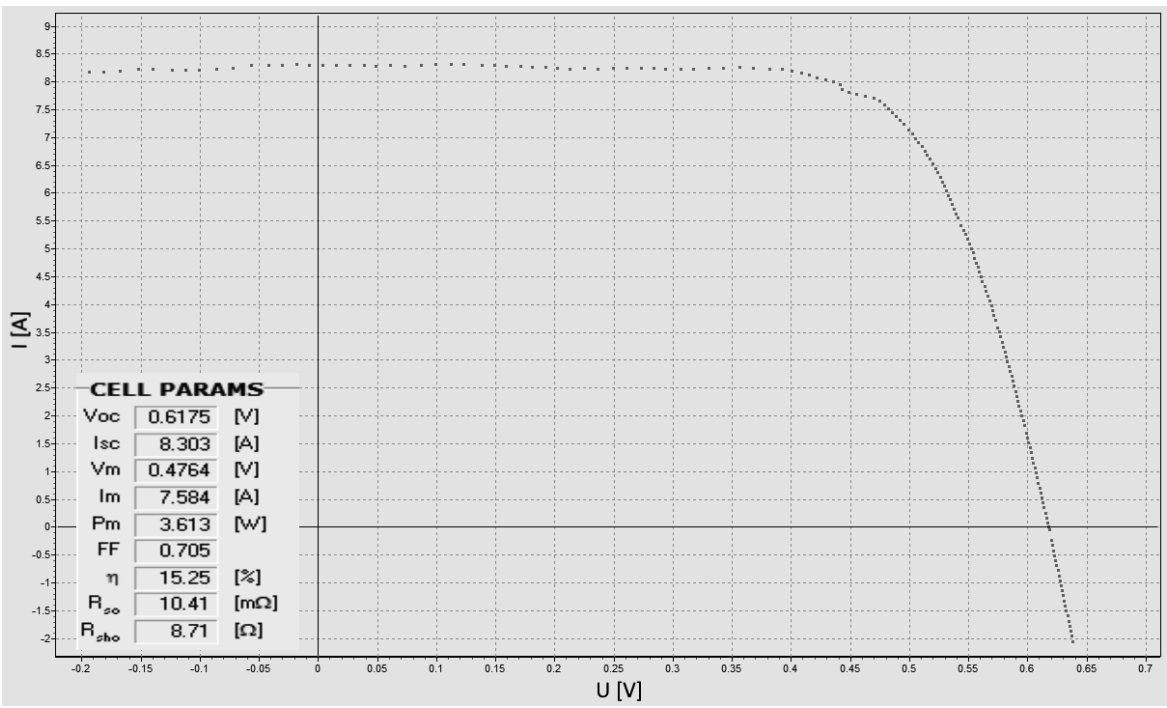

Fig. 6. Illuminated light current-voltage characteristic of solar cell (no 1)

4.2. Structural Properties Analysis

Figure 7 illustrates the topography of the front electrode of solar cell number 1. The image reveals that the electrode structure is porous and uneven.

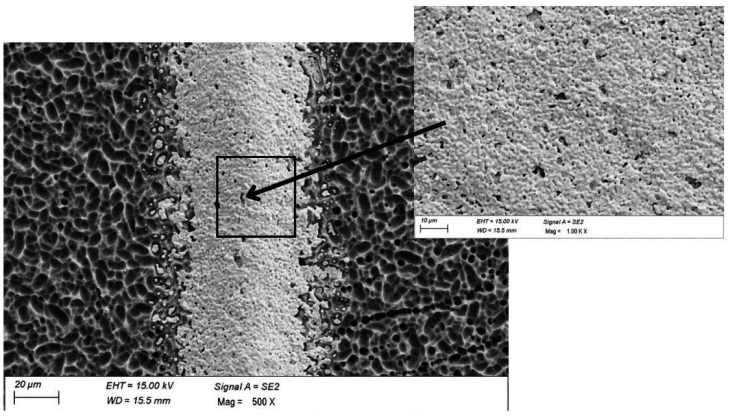

Fig. 7: Topography of the front electrode of solar cell (no 1)

Figure 8 illustrates the fractography of the front electrode, specifically a cross-sectional view of chosen solar cell. The structure is visibly porous and asymmetrical.

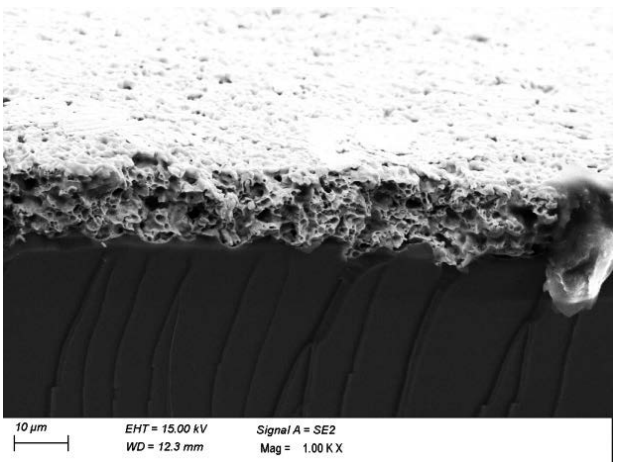

Fig. 8. Cross-section of solar cell number 1

EDS Analysis

Figure 9 illustrates the chemical composition of the silicon wafer surface and the busbar electrode of solar cell number 1. The results confirm that the chemical composition of the paste used to produce the collecting bars and paths is silver-based.

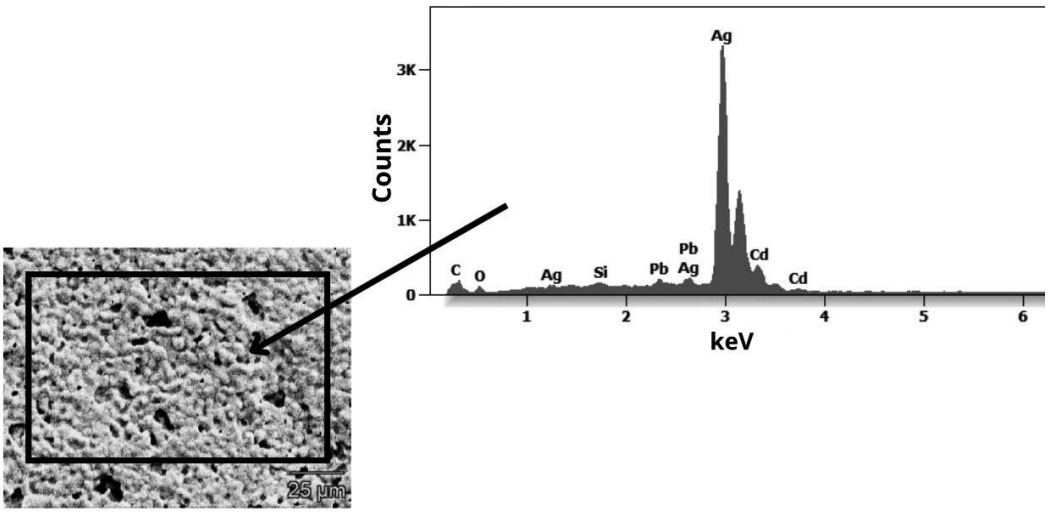

Fig. 9. Chemical Composition of the front electrode of solar cell (no 1)

5. SUMMARY

In the paper, an analysis of the illuminated current-voltage characteristics and the resulting efficiency of solar cells was conducted. Measurements and visualizations of line contact resistance and contact resistance were also performed. The investigation focused on structural properties such as topography, structure, and chemical composition.

The results indicate that while the current density measured in LBIC scan mode was uniform across all investigated samples, the electrical chosen parameters were inconsistent. This inconsistency may point to challenges in maintaining uniform manufacturing conditions for the contacts. It was found that the efficiencies of the investigated samples fall within the lower range of typical efficiencies for multicrystalline silicon-based cells, which is approximately 14 % to 19 % [2].

The only exception was solar cell number 6, whose surface area was reduced due to a broken fragment. Voltage parameters for this solar cell suggest that its efficiency before the damage would have been within the aforementioned range. Solar cell number 1 exhibited the highest efficiency, show casing the highest fill factor, short-circuit current, and maximum power current. However, its open-circuit voltage ranked third. The highest short-circuit current among the solar cells likely stems from the best-executed contacts in the investigated series.

Analysing topographic images from the scanning electron microscope, it was observed that the solar cells were manufactured using the screen-printing method. Additionally, chemical composition analysis (EDS) confirmed the use of silver paste in the production of the studied photovoltaic structures.

ACKNOWLEDGEMENTS

This work was completed as part of a project-based learning (PBL) initiative under the XI competition of the Excellence Initiative – Research University program at the Silesian University of Technology.

LITERATURE

1. Instytut Energetyki Odnawialnej, Rynek fotowoltaiki w Polsce, Edition XII, Warszawa, 2024.
2. Fraunhofer ISE: Photovoltaics Report, updated: 30 July 2024.
3. M. Fischer, M. Woodhouse, P. Baliozian, VDMA International Technology Roadmap for Photovoltaics (ITRPV), 15th edition, 2024.
4. L.A. Dobrzyński, M. Musztyfaga, A. Drygała, P. Panek, K Drabczyk, P. Zięba., Wytwarzanie ogniw fotowoltaicznych z wykorzystaniem metody sitodruku, 1. Krajowa Konferencja Fotowoltaiki, Krynica, 2009.
5. Corescan User Manual, Version 10.00 MRN-061-EN, 2008.
6. R. Figura, W. Zientarski, Analiza parametrów pracy modułu fotowoltaicznego, Autobusy: technika, eksploatacja, systemy transportowe, vol. 17, Issue 12, pp. 601-611, 2016.
7. K. Dyndał, G. Lewińska, K. Marszałek, Fotowoltaika, Open AGH e-podręczniki, pp. 81-82, 2021.

TalentDetector
31th January 2025
Gliwice, Poland
DEPARTMENT OF ENGINEERING MATERIALS AND BIOMATERIALS
FACULTY OF MECHANICAL ENGINEERING
SILESIAN UNIVERSITY OF TECHNOLOGY
INTERNATIONAL STUDENTS SCIENTIFIC CONFERENCE

Vplyv veľkosti plastickej deformácie na teplotu rekryštalizácie

Jozef Vicena[a], Milan Uhríčik[a], Mirosław Bonek[b]

[a] Žilinská univerzita v Žiline, Strojnícka fakulta, Katedra materiálového inžinierstva, Univerzitná 8215/1, 010 26 Žilina, Slovak Republic
[b] Silesian University of Technology, Faculty of Mechanical Engineering, Department of Engineering Materials and Biomaterials
email: vicena4@stud.uniza.sk, milan.uhricik@fstroj.uniza.sk

Abstract: This article represents the theoretical part of the author's bachelor's thesis, where the amount of plastic deformation at the recrystallization temperature was investigated. At the beginning of the article, the mechanical properties of materials are generally explained. Which includes an explanation of deformation as it occurs and its types. Heat treatment of metals and recrystallization are also mentioned.

Keywords: Recrystalization, Plastic/Elastic deformation, Heat treatment

1. ÚVOD

Plastická deformácia predstavuje zásadný proces v správaní sa materiálov, pri ktorom dochádza k trvalej zmene tvaru pod vplyvom vonkajších síl prekračujúcich elastický limit. Tento jav zohráva kľúčovú úlohu pri určovaní funkčnosti a trvanlivosti materiálov, ako sú kovy, keramika či polyméry. Na rozdiel od elastickej deformácie, pri ktorej sa materiál po uvoľnení zaťaženia vráti do pôvodného stavu, plastická deformácia spôsobuje trvalé posuny kryštálovej mriežky. Tento proces sa prejavuje aj v mikroštruktúre materiálu, kde dochádza k redistribúcii dislokácií a tvorbe nových zŕn, čo významne ovplyvňuje mechanické vlastnosti, ako sú pevnosť, tvrdosť a odolnosť voči ďalšej deformácii.

Rekryštalizácia je tepelný proces, ktorý umožňuje obnovenie pôvodnej mikroštruktúry materiálu po plastickej deformácii. Tento jav spočíva v tvorbe nových kryštálových zŕn, ktoré nahrádzajú zdeformované časti materiálu, čím dochádza k obnoveniu jeho pôvodných vlastností. Rekryštalizačné žíhanie je dôležité najmä pri spracovaní kovov, pretože umožňuje odstránenie následkov ťažkej plastickej deformácie za studena a optimalizáciu mechanických vlastností.

2. Mechanické vlastnosti materiálov

Mechanické vlastnosti materiálov sú kľúčové pre ich použitie v technických a priemyselných aplikáciách. Zohľadňujú reakciu materiálu na zaťaženie, vrátane pevnosti,

tvrdosti, húževnatosti, ťažnosti a pružnosti. Tieto vlastnosti určujú, ako materiál reaguje na rôzne typy zaťaženia, ako sú ťah, tlak, šmyk či ohyb [1].

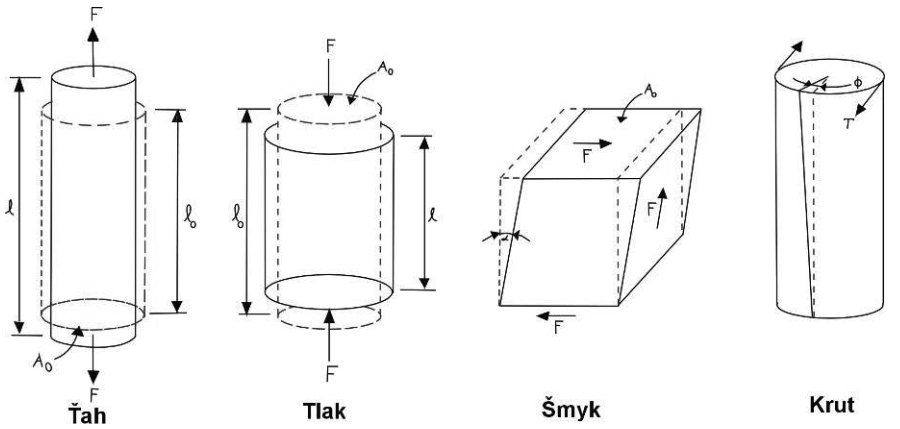

Obr. 1 Deformácia materilu pri zaťažení
Figure 1. Schematic representation of the action of forces

Pôsobenie vonkajších síl v materiáli spôsobí napätosť, ktorá sa potom prejaví určitým rozložením mechanického napätia (závisí od veľkosti, spôsobu, hlavne rozmerov a tvaru danej vzorky, na ktorú je sila upriamená). Napätie je definované ako sila pôsobiaca na jednotku plochy zaťažovaného prierezu vzorky, respektíve materiálu. Napätie získame z podielu sily a plochy, na ktorú sila pôsobí:

$$\sigma = \frac{F}{S} \quad [MPa] \tag{1}$$

Normálové napätie (σ) má smer kolmý k ploche zaťažovaného miesta, tangenciálne alebo aj inak nazývané ako šmykové (τ) pôsobí v zaťažovanej ploche. Normálové a tangenciálne (šmykové) predstavujú skutočné napätia v zaťažovanom priereze. Ako príklad je na obr. 2 popísaná krivka deformácie, t.j. závislosť normálového napätia od pomerného predĺženia [2 - 4].

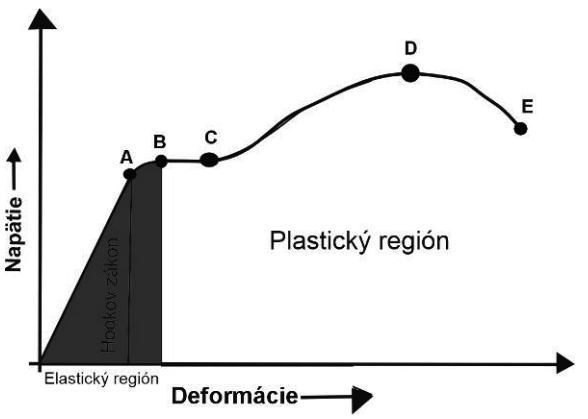

Obr. 2 Deformačná krivka
Figure 2. Deformation curve

Deformačnú krivku môžeme popísať nasledovne:

- 0-A - oblasť elastických (pružných) deformácií. Normálové napätie je priamo úmerné relatívnemu predĺženiu. Napätie, ktoré zodpovedá bodu A sa nazýva medza úmernosti. V oblasti po medzu úmernosti, t. j. pre malé napätia je závislosť lineárna a deformácia je priamo úmerná napätiu materiálu, materiál ešte dodržiava Hookov zákon. Po odstránení zaťaženia sa materiál vráti do pôvodných rozmerov bez trvalých zmien.

- Časť krivky A-B zodpovedá dopružovaniu. Keď prestanú na tyč pôsobiť vonkajšie sily, deformácia nezanikne hneď, ale až po istom čase. Jav dopružovania možno pozorovať napr. na gumovej hadici, ktorú zaťažíme. Po odstránení záťaže deformácia zmizne až po istom čase. Dopružovanie nastane v telesách, v ktorých nebolo vyvolané väčšie normálové napätie ako medza pružnosti. Medza úmernosti sa zväčša príliš neodlišuje od medze pružnosti; niektoré látky majú dokonca obe medze rovnako veľké a pri takých látkach dopružovanie nenastáva. diagram je tu lineárny, až po silu na medzi úmernosti, t. j. po bod B v obr. 2.

- Oblasť rovnomernej plastickej deformácie - po prekonaní prechodného javu v okolí síl na medzi kĺzu nastane rovnomerná trvalá - plastická deformácia v celom objeme tyče.

- Oblasť plastickej deformácie znázorňuje časť krivky BE. Úsek CD zodpovedá tzv. tečeniu materiálu, keď malej zmene normálového napätia prislúcha veľká zmena relatívneho predĺženia. Napätie, pri ktorom nastáva náhle predĺženie materiálu sa volá medza kĺzu (medza prieťažnosti).

- Úsek DE na krivke deformácie zodpovedá spevneniu materiálu, ktoré sa končí po dosiahnutí medze pevnosti. Po prekročení medze pevnosti sa poruší súdržnosť látky - tyč sa pretrhne.

$$\varepsilon = k.\sigma = \frac{1}{E}\sigma \qquad [MPa] \qquad (2)$$

Pre šmykové deformácie platí :

$$\gamma = k1.\tau = \frac{1}{G}\tau \qquad [MPa] \qquad (3)$$

2.1 Elastická deformácia

Nastáva vtedy, keď zaťaženie neprekročí určitú hranicu, nazývanú elastický limit. Tento typ deformácie je reverzibilný; po odstránení zaťaženia sa materiál vráti do pôvodného tvaru. Elastická deformácia je lineárna a popisuje ju Hookov zákon vzorcami (2) a (3) [3 - 4].

2.2 Plastická deformácia

Je trvalá zmena tvaru, ktorá nastáva pri prekročení medze sklzu materiálu. Tento proces zahŕňa pohyb dislokácií v kryštálovej mriežke, čím dochádza k reorganizácii vnútorných štruktúr materiálu. Dislokácie sa pohybujú v sklzových rovinách a smeroch, pričom proces je ovplyvnený kryštalografickou štruktúrou materiálu. Deformácia sklzom sa uskutočňuje iba v určitých kryštalografických rovinách a smeroch. Sklzové roviny a smery kĺzu niektorých kovov (Al, Cu, Fe_{α}, Zn) uvádza tab. 1 a ich grafické znázornenie v kryštálovej mriežke je na obr. 3 [3 - 4].

Tab.1 Sklzové roviny, smery klzu a počet sklzových systémov niektorých kovov
Table 1. Slip planes, slip directions and slip systems

Typ mriežky	**Kov**	**Sklzové roviny**	**Smery klzu**	**Počet sklzových systémov**
Kubická plošne centrovaná	Al, Cu	{111}	<101>	12
Kubická priestorovo centrovaná	Fe_{α}	{110} {112} {113}	<111>	12
Hexagonálna tesne usporiadaná	Zn	{0001}	<2 1 1 0 >	3

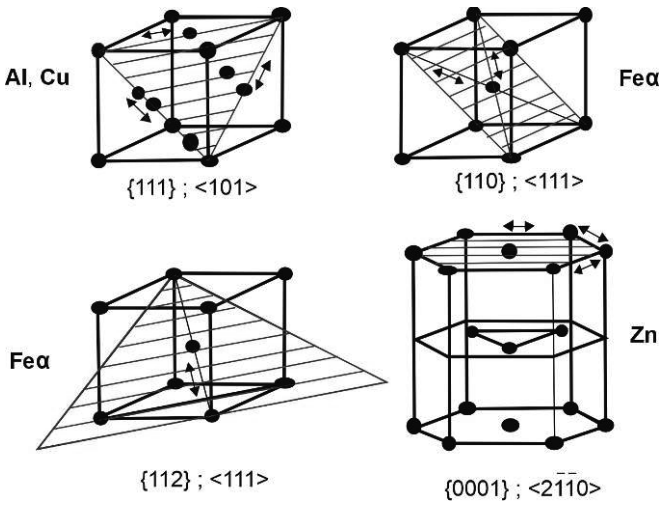

Obr. 3 Sklzové roviny a smery sklzu v kryštálových mriežkach
Figure 3. Slip planes and directions of individual crystallographic lattices

3. DEFORMÁCIA

Z obr. 4 je jasné, že dislokácia sa neodstráni, ale iba sa presunie po vhodne orientovaných rovinách, pokiaľ sa nedostanú na koniec kryštálu. Tým sa posunie časť kryštálu nad rovinou sklzu dislokácii oproti časti pod tou rovinou a vznikne elementárna trvalá deformácia o veľkosti rádu 10^{-10}m. Deformácia sklzom je rozdelená rovnomerne v celom zrne a sústreďuje sa v rovinách, kde je najmenej prekážok pre pohyb dislokácii [3 - 4].

Pri určitých podmienkach (napr. pri nízkej teplote, veľkej rýchlosti deformácie) sa kov môže trvalo deformovať dvojčatením. Pri dvojčatení (obr. 4) sa veľkou rýchlosťou pootočia rady atómov o určitý uhol vzhľadom na smer posunu. Nová mriežka v zdvojenej časti kryštálu má v porovnaní s pôvodnou mriežkou zrkadlovo súmernú orientáciu k určitej rovine, ktorú nazývame rovina dvojčatenia.

Na rozdiel od sklzového mechanizmu (pohyb úplných dislokácií) pri dvojčatení sa presunú atómy len o časť medziatómovej vzdialenosti (pohyb neúplných dislokácií). Schéma deformácie monokryštálu sklzom a dvojčatením je na obr. 5. [5].

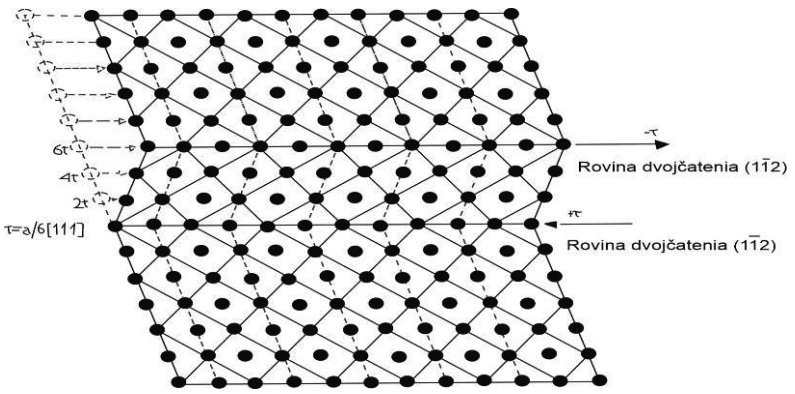

Obr. 4 Plastická deformácia dvojčatením
Figure 4. Plastic deformation by twinning

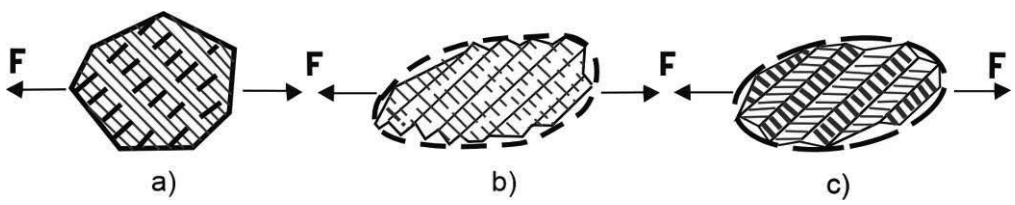

Obr. 5 Schéma deformácie monokryštálu: a - zrno pred deformáciou, b - zrno po deformácii sklzom, c - zrno po deformácii dvojčatením
Figure 5. Interpretation of deformation by slip and twinning on single crystals; a) grain before deformation; b) grain after deformation by slip; c) grain after def. twinning

4. REKRYŠTALIZÁCIA

Pri plastickej deformácii sa voľná entalpia materiálu zvyšuje, pretože sa ukladá deformačná energia spôsobená poruchami kryštálovej mriežky. Takýto materiál je z hľadiska termomechaniky považovaný za málo stabilný. Pri následnom žíhaní sa táto uložená energia postupne uvoľňuje, čo vedie k poklesu voľnej entalpie a zároveň k zmene mechanických vlastností materiálu.

Procesy, ktoré nastávajú počas uvoľňovania energie, sú zotavenie a rekryštalizácia. Zotavenie je charakteristické znižovaním počtu vakancií a reorganizáciou (premiestňovaním) zachytených dislokácií, čo obnovuje pôvodné hodnoty elektrického odporu, znižuje rezistivitu a eliminuje (znižujú sa) napätia v štruktúre.

Rekryštalizácia funguje odlišne. Na miestach s najvyššou energiou sa tvoria zárodky nových zŕn, ktoré postupne nahrádzajú zdeformované zrná bez akýchkoľvek známok predchádzajúcej deformácie. Rekryštalizácia je poháňaná energiou uvoľnenou pri deformácii. Rekryštalizované zrná nahradia postupne deformovanú štruktúru v celom objeme materiálu.

Je dôležité rozlišovať medzi rekryštalizáciou a prekryštalizáciou. Rekryštalizácia od prekryštalizácie (zmeny modifikácie) sa odlišuje tým, že v jej priebehu vznikajú kryštály s nezmeneným typom mriežky, pri prekryštalizácii sa mení kryštalografická mriežka materiálu.

Teplota rekryštalizácie je ovplyvnená čistotou materiálu - nečistoty a prímesi brzdia pohyb zŕn. Veľkosť nových zŕn závisí od predošlej deformácie a od teploty rekryštalizácie. Pri intenzívnej deformácii vzniká počas žíhania veľké množstvo zárodkov, čo vedie k jemnozrnnej štruktúre. Naopak, pri miernej deformácii rastú zrná z menšieho počtu zárodkov, čo vedie k ich výraznému zväčšeniu.

Rekryštalizáciou sa obnovujú pôvodné vlastnosti materiálu a jeho štruktúra, ako to ilustruje obr. 6. Pre čisté kovy je typická rekryštalizačná teplota v rozsahu 0,35- až 0,4-násobku teploty ich tavenia, čo hrá zásadnú úlohu pri určovaní procesov tvárnenia. Tvárnenie za studena prebieha pri teplotách nižších než rekryštalizačná teplota, zatiaľ čo tvárnenie za tepla prebieha pri teplotách vyšších než 0,7-násobok teploty tavenia, čím sa zaisťuje okamžitá rekryštalizácia bez spevnenia.

V priemyselnej praxi sa rekryštalizácia využíva pri výrobe tvárnených polovýrobkov, čo zlepšuje ich mechanické a mikroštrukturálne vlastnosti [3, 6].

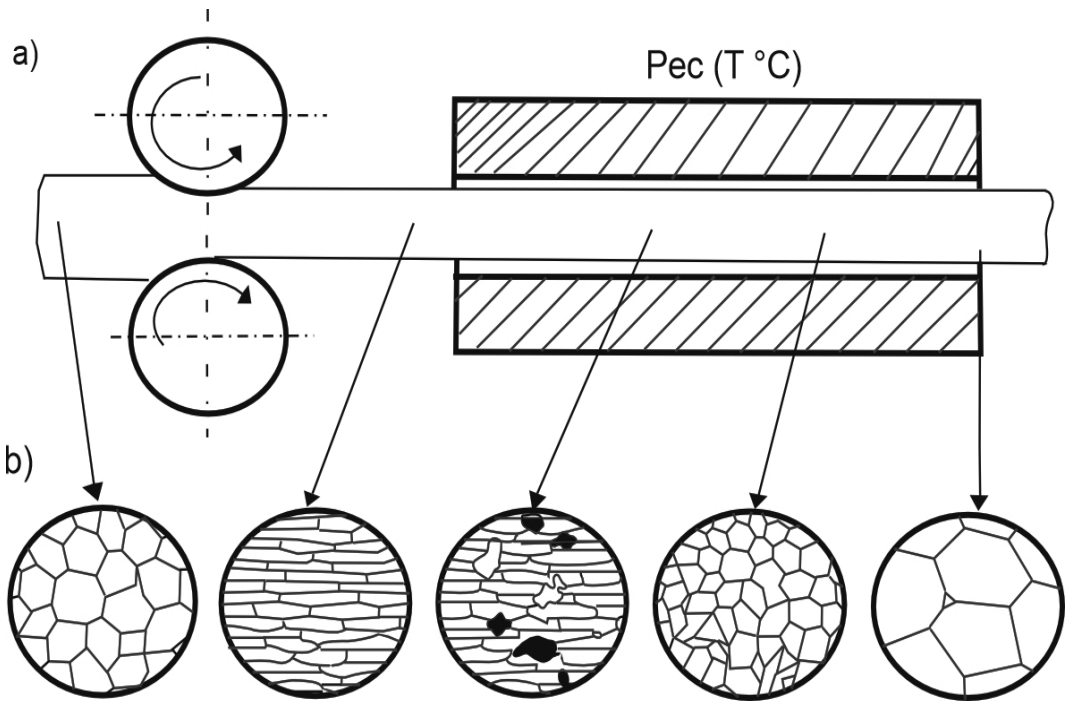

Obr. 6 Spevnenie a odpevnenie plasticky deformovaného polykryštalického kovového materiálu: a - schéma deformácie (valcovaním) a ohrevom (na teplotu °C), b - zmeny mikroštruktúry pri deformácii a ohreve deformovaného materiálu
Figure 6 Recrystallization of deformed polycrystalline material; a) Deformations by hot rolling; b) Microstructure changes during hot rolling

5. TEPELNÉ SPRACOVANIE

Tepelné spracovanie ocele kalením a popúšťaním je kľúčový proces, ktorý umožňuje dosiahnuť požadované mechanické vlastnosti materiálu, ako je tvrdosť, pevnosť, elasticita a plasticita. Tento proces sa zvyčajne používa na úpravu nástrojovej ocele a iných kovov, ktoré musia mať vynikajúcu odolnosť voči opotrebeniu a mechanickému poškodeniu.

5.1 Kalenie

Kalenie spočíva v zahrievaní ocele na teplotu, pri ktorej sa celá alebo časť štruktúry zmení na austenit (vysokoteplotná fáza ocele, kde je uhlík rozpustený v železe). Tento proces sa líši v závislosti od zloženia ocele:

- Nadeutektoidné ocele (s obsahom uhlíka do 0,8%) sa zahrievajú na teplotu, kde vzniká austenit (okolo 800 - 900 °C).
- Eutektoidné a nadeutektoidné ocele (s obsahom uhlíka nad 0,8% a do 1,35%) sa zahrievajú na vyššie teploty, približne 900 - 1000 °C.

Po zahriatí sa materiál rýchlo ochladí, aby sa zabránilo rozpusteniu uhlíka a dosiahla sa martenzitická alebo bainitická štruktúra. Proces ochladzovania sa vykonáva pomocou vody alebo oleja, pričom rýchlosť ochladzovania ovplyvňuje, či vznikne martenzit (pri veľmi rýchlom ochladzovaní) alebo bainit (pri mierne pomalšom ochladzovaní).

5.2. Popúšťanie

Po kalení je oceľ zvyčajne krehká, čo je spôsobené vysokou vnútornou napätosťou a metastabilnou štruktúrou martenzitu.

Preto je potrebné popúšťanie, pri ktorom sa oceľ opätovne zahrieva na určité teploty, čo spôsobuje prechod štruktúry z martenzitu na stabilnejšie formy, ako sú ferit alebo perlit. Teplota popúšťania ovplyvňuje vlastnosti materiálu:

- Nízke popúšťanie (100 - 250 °C) zvyšuje tvrdosť, ale aj krehkosť materiálu.
- Stredné popúšťanie (250 - 500 °C) zlepšuje elasticitu a plasticitu, čím sa materiál stáva menej krehkým.
- Vysoké popúšťanie (500 - 600 °C) spôsobuje zníženie tvrdosti, ale zvyšuje plasticitu a odolnosť proti nárazom.
- Popúšťanie sa často využíva aj po zváracích operáciách na zmiernenie vnútorných napätí a zabránenie prasklinám.

Tento proces je kľúčový pre výrobu komponentov, ktoré musia vykazovať vynikajúcu odolnosť voči opotrebeniu, ako sú nástroje, ložiská, čepele, a rôzne mechanické diely, ktoré podliehajú vysokým zaťaženiam [7].

5.3 Žíhanie

Tento proces sa využíva na zlepšenie mechanických vlastností materiálu, ako je zlepšenie jeho plasticity, zníženie vnútorných napätí alebo zmena štruktúry materiálu. Z technologického hľadiska pozostáva žíhanie z ohrevu na tzv. žíhaciu teplotu, výdrže na tejto teplote a ochladenia na teplotu okolia. Rýchlosť ohrevu na žíhaciu teplotu, podobne ako na požadovanú teplotu pri iných spôsoboch tepelného spracovania, môže byť rôzna. Ekonomicky najvýhodnejší je rýchly ohrev, ktorý sa realizuje napr. vložením súčiastok do pece vyhriatej na teplotu vyššiu, než je potrebná teplota tepelného spracovania. Teplota pece sa po určitej dobe zníži na požadovanú hodnotu v dôsledku výmeny tepla medzi pecou a vsádzkou. Zvýšenie rýchlosti ohrevu znamená skrátenie doby ohrevu, ale zároveň vyvoláva zvýšenie teplotného spádu v priereze súčiastok, a teda i zvýšenie tepelných napätí pri ohreve. Väčšie rýchlosti ohrevu nie je preto možné použiť pri oceliach s nízkou tepelnou vodivosťou (vysokouhlíkových a vysokolegovaných oceliach).

Podľa výšky žíhacej teploty zvykneme rozdeľovať druhy žíhania ocelí na žíhanie s prekryštalizáciou a bez prekryštalizácie. Najpoužívanejšie sú:

- Žíhanie na mäkko - cieľom žíhania na mäkko je zníženie pevnosti a tvrdosti a zlepšenie tvárnosti a obrábateľnosti, ktoré sa dosiahne sferoidizáciou lamelárneho perlitu na perlit globulárny.

- Normalizačné žíhanie - normalizačným žíhaním sa dosahuje zjemnenie a zrovnomernenie veľkosti zrna. Normalizačné žíhanie môže slúžiť ako predbežné tepelné spracovanie pred zušľachťovaním. Je základným druhom tepelného spracovania nízkouhlíkových ocelí zvyčajnej akosti.

- Žíhanie na odstránenie napätí má za cieľ znížiť hladinu vnútorných napätí, ktoré vznikajú v súčiastkach pri predchádzajúcom spracovaní. Podstata zníženia vnútorných napätí spočíva v premene pružnej deformácie na plastickú [8].

POĎAKOVANIE

Príspevok vznikol v rámci riešenia spoločného slovensko-poľského projektu Project Based Learning ako výsledok spolupráce medzi Politechnikou Slaskou, Gliwice a Žilinskou univerzitou v Žiline a projektov KEGA č. 004ŽU-4/2023 a KEGA č.009ŽU-4/2023.

BIBLIOGRAPHY

1. WILLIAM D. CALISTER,JR. *CuSn6P alloy at elevated temperatures*, Journal of Materials Processing Technology 162-163 (2005) 392-401.
2. X.SUNDAR. *Stress Strain Curve* | Stress Strain diagram. 2.9.2017 Dostupné na internete: https://extrudesign.com/stress-strain-curve/
3. SKOČOVSKÝ P. - et al. *Konštrukčné materiály*. Žilina: EDIS - vydavateľstvo Žilinskej Univerzity, 2000. ISBN 80-7100-608-4.
4. PUŠKÁR A. *Medzné stavy materiálov a súčastí*. Bratislava. 1985. ISBN: 108022400203. str. 299
5. Technická univerzita Liberec. Fakulta Strojní. Katedra strojírenské technologie. Oddelení tváření kovů a plastů. *Technologie tváření kovů.* Dostupná na internete: https://www.ksp.tul.cz
6. SEDLÁČEK V. *Zotavení a rekrystalizace*. Praha: Academia, 1985. Universal Decimal Class. No.:621.785.374.
7. MTMstal. *Procesy tepelného spracovania ocele*. Dostupné na internete: https://www.mtmstal.sk/blog/stale-do-ulepszania-cieplnego-charakterystyka
8. DUKÁ, M. et al. *Technológia tepelného spracovania materiálov*. 2014

TalentDetector
31th January 2025
Gliwice, Poland
DEPARTMENT OF ENGINEERING MATERIALS AND BIOMATERIALS
FACULTY OF MECHANICAL ENGINEERING
SILESIAN UNIVERSITY OF TECHNOLOGY
INTERNATIONAL STUDENTS SCIENTIFIC CONFERENCE

História, stavba kolenných endoprotéz a ich montáž

Richard Vidrich[a], Ronald Bašťovanský[b], Peter Palček[a]

[a] Žilinská univerzita v Žiline, Strojnícka fakulta, Katedra materiálového inžinierstva, Univerzitná 8215/1, 010 26 Žilina, Slovak Republic
[b] Žilinská univerzita v Žiline, Strojnícka fakulta, Katedra konštruovania a častí strojov, Univerzitná 8215/1, 010 26 Žilina, Slovak Republic
email: vidrich@stud.uniza.sk, ronald.bastovansky@fstroj.uniza.sk

Abstract: Kolenné endoprotézy predstavujú významný pokrok v oblasti ortopedickej chirurgie, umožňujúci efektívne riešenie degeneratívnych ochorení a poškodení kolenného kĺbu. Príspevok sumarizuje vývoj kolenných endoprotéz od prvých závesných modelov až po moderné stavebnicové systémy, ktoré kombinujú kovové a polyetylénové komponenty. Diskutuje sa použitie rôznych materiálov, najmä zliatin titánu, a ich vplyv na mechanické vlastnosti a životnosť implantátu. Podrobne sú rozpracované fázy implantácie, vrátane prípravy kosti, skúšobného procesu a osadenia endoprotézy. Osobitná pozornosť je venovaná problematike fixácie endoprotézy, ktorá zohráva kľúčovú úlohu v stabilite a životnosti náhrady.

Keywords: kolenná endoprotéza, zliatina Ti6Al4V, fixácia skrutkového spoja, opotrebenie materiálu

1. ÚVOD

Kolenný komplex je zložený kĺb a je najväčší a najzložitejší kĺb v ľudskom tele. Spája stehennú kosť s tibiou a najväčšiu sezamskú kosť tela, jabĺčko. Umožňuje pohyb dolnej časti nohy a tým chôdzu.

Medzi styčnými plochami kĺbu sú menisky, sú tam dva vonkajšie a štyri vnútorné väzy a kĺbové puzdro. Jabĺčko sa nachádza v prednej časti kolena a pri ohýbaní kĺže v stehennom kostnom zárezе. Koleno sa pri svojom pohybe nielen vystiera a ohýba, ale zároveň vykonáva viaceré jednoduché rotačné pohyby. Tvoria ho kĺby: tibiofemorálny a patelofemorálny. Základné postavenie kolenného kĺbu je extenzia, pri ktorej zviera pozdĺžna os stehennej kosti s pozdĺžnou osou tibie tupý uhol otvorený navonok. Hlavnou funkciou je mobilita a stabilita.

Kolenný kĺb pracuje v konjunkcii s bedrovým kĺbom a členkom a hlavnou funkciou je prenos záťaže (hmotnosť tela) vo vzpriamenej polohe. Dynamicky je kolenný komplex zodpovedný za pohyb a podporu tela počas rôznych bežných a iných aktivít. Kolenný kĺb napriek svojmu jednoduchému vzhľadu patrí medzi najkomplikovanejšie kĺby. Zároveň ide o najčastejšie poranený kĺb v ľudskom organizme.

Kolenné endoprotézy preto patria medzi najviac používané implantáty v oblasti ortopedickej chirurgie. Ich primárnou úlohou je nahradiť poškodený kolenný kĺb a obnoviť jeho funkčnosť, čím sa eliminuje bolesť a zlepšuje kvalita života pacienta. Vývoj endoprotéz prešiel dlhým procesom, od jednoduchých a nefyziologických modelov až po moderné systémy, ktoré rešpektujú biomechaniku kolena. Súčasné endoprotézy využívajú pokročilé materiály, ako sú zliatiny titánu a špeciálne polyetylénové komponenty, ktoré zabezpečujú ich dlhodobú životnosť a stabilitu. Napriek tomu stále existujú výzvy spojené s fixáciou a možnosťou lomu skrutky, ktoré sú predmetom detailného výskumu. Tento článok sa zameriava na analýzu histórie, stavby a montáže kolenných endoprotéz.

2. HISTÓRIA A SÚČASNÝ STAV KOLENNÝCH ENDOPROTÉZ

Endoprotéza je umelý kĺb navrhnutý na nahradenie poškodeného alebo opotrebovaného kĺbu, pričom jej hlavným cieľom je čo najvernejšie imitovať funkciu prirodzeného kĺbu. Medzi najčastejšie používané druhy patria endoprotézy ramenného, bedrového a kolenného kĺbu (obr. 1).

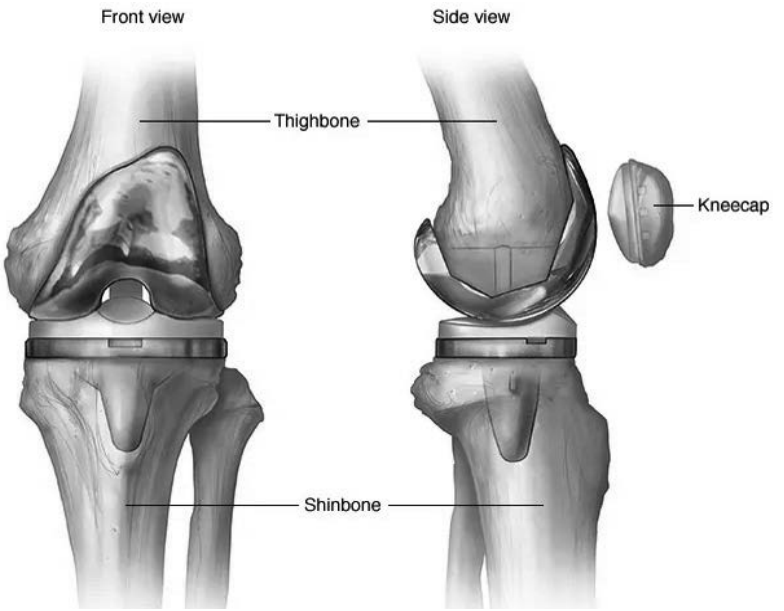

Obr. 1. Kolenná endoprotéza
Figure 1. Knee endoprosthesis

Vývoj totálnej endoprotézy kolenného kĺbu trval mnoho rokov, kým dosiahol svoju súčasnú podobu. Prvým typom bol kladkovitý implantát zo slonoviny vyrobený v 90. r. 19 storočia. Z r. 1951 pochádza závesná endoprotéza z akrylátu, ktorá však nezohľadňovala prirodzený pohyb kolenného kĺbu a mala tendenciu sa rýchlo uvoľňovať. Následné snahy viedli k vývoju funkčnejších modelov (napr. v r. 1958 endoprotéza z Co-Cr zliatiny), vrátane tých, ktoré nahrádzali iba časť kolenného kĺbu (obr. 2).

V Spojených štátoch boli navyše navrhnuté implantáty, ktoré predĺžili životnosť endoprotézy znížením zaťaženia na miestach kontaktu s kosťou. Intenzívny vývoj modernej endoprotézy kolenného kĺbu prebehol v 70 rokoch 20.st.

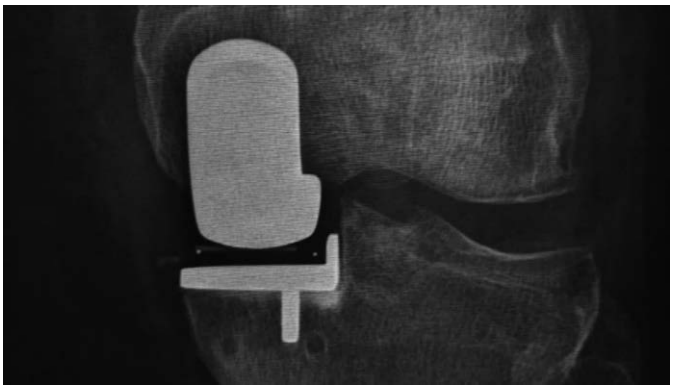

Obr. 2 Čiastočná endoprotéza kolena
Figure 2. Partial knee endoprosthesisa

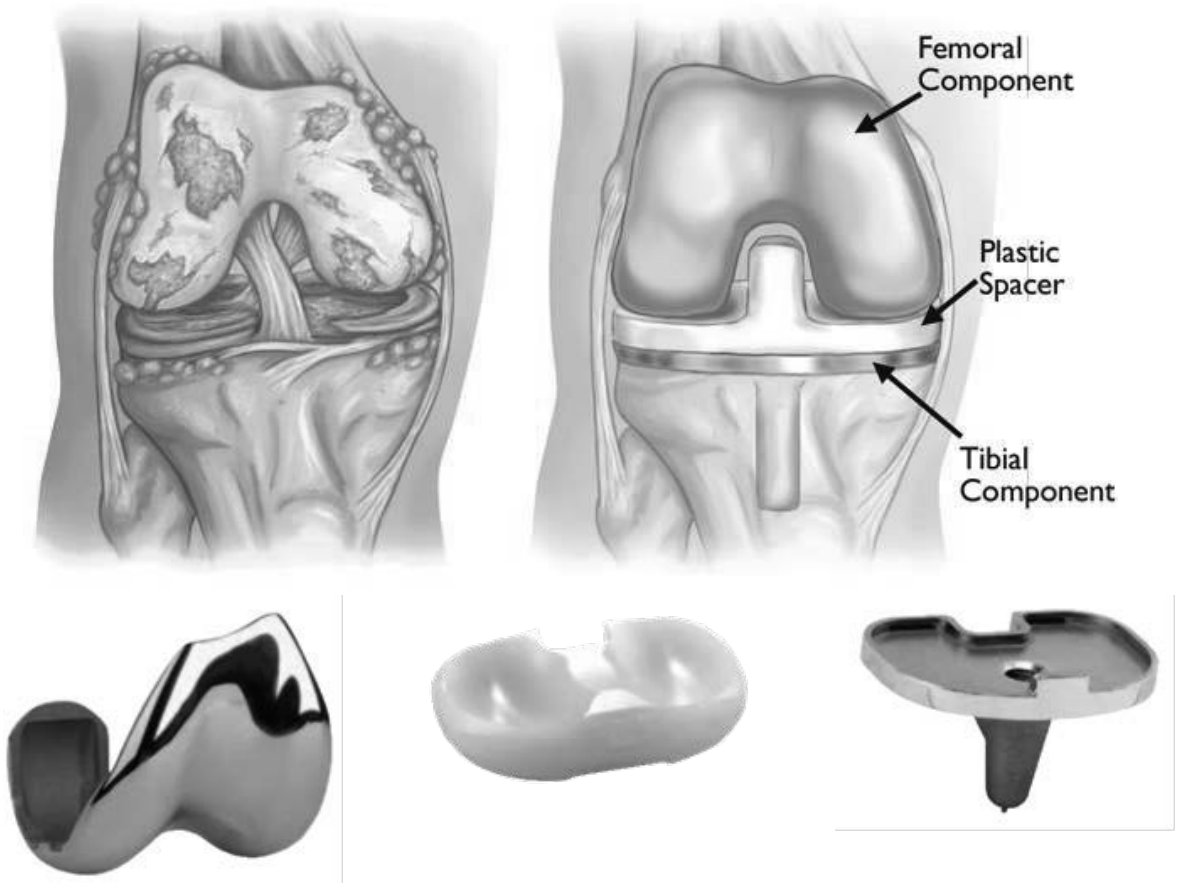

a) femorálna komponenta *b) polyetylénová vložka* *c) tibiálna komponenta*

Obr. 3 Kolenná endoprotéza s popisom jej súčastí
Figure 3. Knee endoprosthesis with a description of its components

V súčasnosti je väčšina endoprotéz (obr. 3) založená na tzv. kondylárnom - t. j. stavebnicovom systéme. Používajú sa kovové femorálne komponenty (obr. 3a) a tibiálne polyetylénové vložky (obr. 3b) vložené do kovovej kotviacej tibiálnej časti (obr. 3c). Životnosť

endoprotézy je individuálna (väčšinou viac ako 10 rokov). Najčastejšou príčinou zlyhania bývajú aseptické uvoľnenie a infekcia, príp. nestabilita, zlomenina, mechanické zlyhanie komponent, alebo nesprávna orientácia.

2.1 Materiály používané na kolenné endoprotézy

Základným predpokladom úspechu tak konštruktéra kĺbnych náhrad ako aj operatéra, je znalosť biomechaniky kĺbov. Na kĺbové náhrady sa kladú požiadavky z hľadiska statického namáhania (pevnosť, pružnosť), z hľadiska dynamického namáhania (únavová pevnosť, odolnosť proti oteru) a požiadavky tvarové (vyplnenie priestoru v mäkkých tkanivách, rozloženie tlakovej sily na kontaktných plochách jednotlivých kĺbnych komponentov).

Endoprotézy sa v súčasnosti vyrábajú predovšetkým z troch hlavných typov materiálov: plast, keramika a kov. Z kovov sú to chirurgická oceľ (obvykle AISI 316L), chrómkobaltová zliatina (CoCr) a komerčne čistý titán alebo jeho zliatiny s hliníkom (TiAl6V4), vanádom, nióbom a ostatnými kovmi. Najnovšie sa presadzujú v revíznej endoprotetike aj výplňové a fixačné implantáty z tantalu.

Kovové implantáty môžu byť cementované, necementované so špeciálnymi povrchmi, alebo hybridné. Cementové sú ku kosti fixované kostným cementom (väčšinou s obsahom antibiotík), čo umožňuje včasné zaťaženie končatiny. Fixácia necementových endoprotéz prebieha pomocou osteointegrácie, čo znamená priame vrastenie kosti do upraveného povrchu implantátu. Podmienkou necementovej fixácie je dobrá kvalita kosti. Výhodou necementových endoprotéz je dlhšia životnosť a väčšia odolnosť voči infekciám, nevýhodou je finančná náročnosť a náročnejšia rehabilitácia s dlhším odľahčením končatiny. Hybridné endoprotézy sú kombináciou cementovej a necementovej fixácie, kedy jeden komponent je fixovaný cementovým a jeden necementovým spôsobom.

Najvhodnejšia kombinácia sa vyberá na základe kvality kostného tkaniva, anatomických pomerov, perspektívy aktívneho života pacienta a pod.

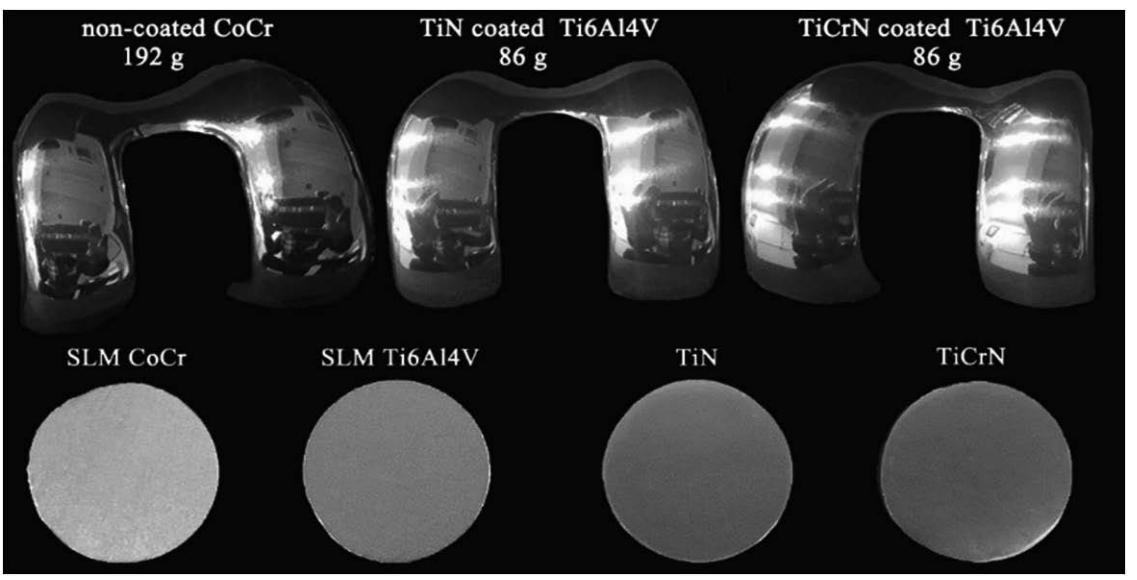

Obr. 2. Príklady materiálov používaných na výrobu kolenných endoprotéz
Figure 4. Examples of materials used for the manufacture of knee endoprostheses

Cementované sú zvyčajne implantáty z CoCr, prípadne z oceli, necementované bývajú hlavne implantáty z titánu alebo Ti-zliatiny.

CoCr zliatina má veľmi dobrú abrazívnu odolnosť, preto sa z nej vyrába femorálna komponenta kolena. Vykazuje ťažnosť až 8 %, je odolná voči koróznej únave a koróznemu praskaniu pod napätím a na rozdiel od ocele AISI 316 je odolnejšia aj voči únavovému lomu. Naopak titán a jeho zliatiny vykazujú zlú tribologickú odolnosť, na druhej strane majú veľmi dobré podmienky pre osteointegráciu a majú elasticitu podobnú spongióznej kosti. Preto sa z nich vyrába femorálny krk, ktorý potrebuje udržiavať zvýšené ohybové napätie a únavové zaťaženie, musí odolávať únave aj korózii a minimalizovať napätie. Najčastejšie sa Ti-endoprotézy, konkrétne ich kovové súčasti, zhotovujú zo zliatiny TiAl6V4, resp. TiAl6V4 ELI. Táto zliatina patrí medzi najrozšírenejšie titánové zliatiny, čo je spôsobené jej výbornými mechanickými vlastnosťami. V porovnaní s čistým titánom si zliatina zachováva rovnakú tuhosť a tepelné vlastnosti, no poskytuje vyššiu pevnosť a je biokompatibilná.

Životnosť endoprotézy býva 15 až 20 rokov. Pri pacientoch mladších ako 40 rokov je potrebné vyčerpať najskôr všetky konzervatívne alebo operačné liečebné možnosti, a až potom pristúpiť k totálnej endprotéze. Vo veku 45 - 55 rokov sa indikujú skôr necementované alebo hybridné endoprotézy, starším pacientom a pri reoperáciách necementovaných totálnych endoprotéz sú častejšie používané cementované totálne endoprotézy.

3. MONTÁŽ KOLENEJ ENDOPROTÉZY

Pri endoprotetickej náhrade kolenného kĺbu sa nahrádzajú obidva kĺbové komponenty - stehnový a predkolenný komponent s polyetylénovou vložkou. Pri implantovaní umelého kĺbu sa odstraňujú poškodené štruktúry kolena čím dochádza k eliminácii bolestivých klinických príznakov artrózy. Operáciou sa obnovuje fyziologická os končatiny a hybnosť.

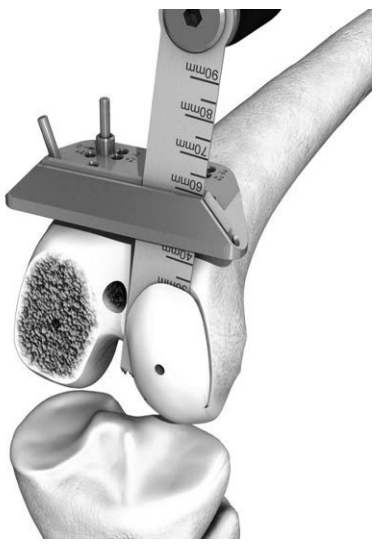

Obr. 5. Zrezanie stehennej kosti
Figure 5. Femur amputation

Obr. 6 Zrezanie kĺbových plôch
Figure 6. Cutting of articular surfaces

Prvým krokom pred samotnou inštaláciou kolennej endoprotézy je príprava biologického kĺbu na zákrok. Pomocou šablóny (obr. 5) sa stehenná kosť a kĺbne plochy presne zmerajú

podľa stanovených meracích postupov. Následne sa tieto časti upravia rezaním podľa uvedenej šablóny (obr. 6).

Po presnom zmeraní a upravení kosti sa stabilita kolena vyhodnotí pomocou meracieho zariadenia, pričom sa určí aj výška polyetylénovej vložky na základe šablóny (obr. 7). Následne sa nasadí skúšobná endoprotéza zodpovedajúca veľkosti podľa šablóny, ktorá umožňuje overiť správne postavenie, stabilitu a pohyblivosť kolena (obr. 8).

Obr. 7 Vyváženie stability
Figure 7. Balance of stability

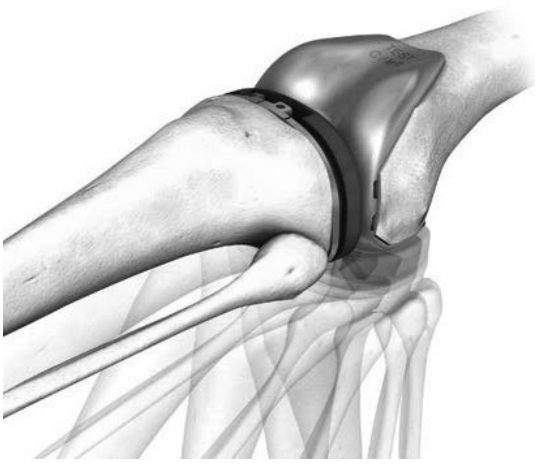

Obr. 8 Skúšobná endoprotéza
Figure 8. Trial endoprosthesis

Po overení parametrov pomocou skúšobnej endoprotézy sa pokračuje implantáciou finálnej endoprotézy (obr. 9).

Obr. 9 Implantácia kolennej endoprotézy
Figure 9. Knee endoprosthesis implantation

4. PROCES FIXÁCIE KOLENNEJ ENDOPROTÉZY

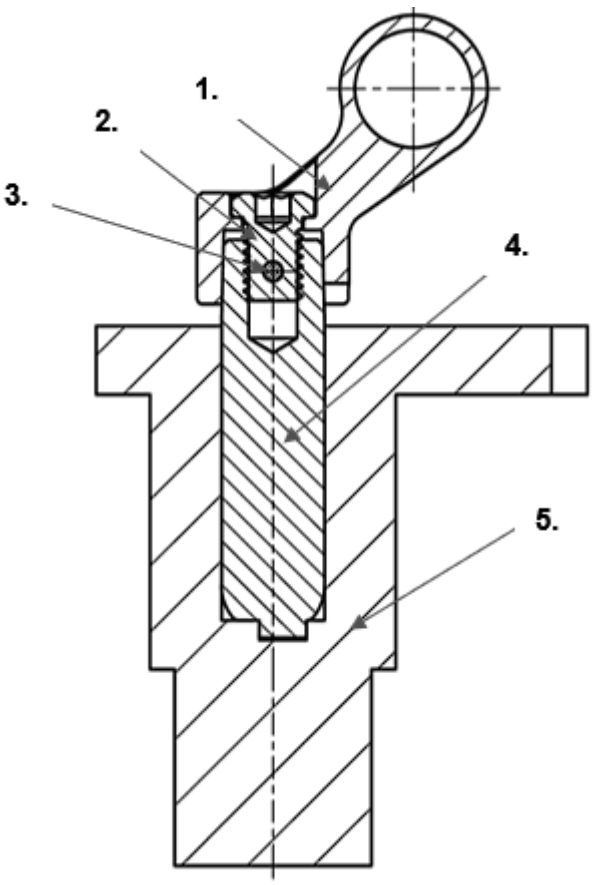

Obr. 10 Prierez zostavou kolennej endoprotézy
Figure 10. Cross-section of a knee endoprosthesis assembly

Proces fixácie kolennej endoprotézy je dokumentovaný na obr. 10. Zostava sa skladá z piatich častí: pánt kolennej endoprotézy (**1.**), skrutka M6 s otvorom pre poistný kolík (**2.**), poistný kolík (**3.**), driek s vnútorným závitom (**4.**) a púzdro (**5.**). Driek (**4.**) s vnútorným závitom sa vloží do púzdra (**5.**) a upevní sa pomocou momentového kľúča s uťahovacím momentom 10 Nm. Na vrch púzdra sa následne umiestni pánt (**1.**). Skrutka M6 (**2.**) sa prestrčí cez otvor v pánte (**1.**) a zaskrutkuje do drieku (**4.**) s použitím vopred určeného uťahovacieho momentu 5 Nm.

Po utiahnutí sa skrutka nastaví do polohy, ktorá umožní jej zabezpečenie poistným kolíkom (**3.**). Táto skrutka, ktorá nemá nosnú funkciu, slúži na uzatvorenie skrutkového spoja a umožňuje prepojenie medzi pántom (**1.**) a driekom (**4.**).

POĎAKOVANIE

Príspevok vznikol v rámci riešenia spoločného slovensko-poľského projektu Project Based Learning ako výsledok spolupráce medzi Politechnikou Slaskou, Gliwice a Žilinskou univerzitou v Žiline a projektov KEGA č. 004ŽU-4/2023 a KEGA č.009ŽU-4/2023.

BIBLIOGRAPHY

1. https://www.wikiskripta.eu/w/Totální_endoprotéza_kolenního_kloubu
2. https://clinicaorthopedica.sk/naco-menit-to-co-funguje/
3. https://en.wikipedia.org/wiki/Knee_replacement
4. https://www.mayoclinic.org/tests-procedures/knee-replacement/about/pac-20385276
5. https://orthoinfo.aaos.org/en/treatment/total-knee-replacement/
6. https://www.profvojtassak.sk/index.php/operacia?view=article&id=144:tep-genus-mathys&catid=40
7. http://www.mathysmedical.com/

TalentDetector
31th January 2025
Gliwice, Poland
DEPARTMENT OF ENGINEERING MATERIALS AND BIOMATERIALS
FACULTY OF MECHANICAL ENGINEERING
SILESIAN UNIVERSITY OF TECHNOLOGY
INTERNATIONAL STUDENTS SCIENTIFIC CONFERENCE

Welding of automotive structures made of DOCOL 1100M and DOCOL 1200M steel according to the new recommendations of the European Union

Tomasz Węgrzyn[a], Bożena Szczucka-Lasota[a], Małgorzata Musztyfaga-Staszuk[b], Abílio Manuel Pereira da Silva[c], Wojciech Tarasiuk[d], Artur Labus[e], Paweł Piotrowicz[e], Patrycja Lasota[f]

[a] Silesian University of Technology, Faculty of Transport and Aviation Engineering, Zygmunta Krasińskiego 8, 40-019 Katowice, Poland
[b] Silesian University of Technology, Department of Engineering Materials and Biomaterials, Konarskiego 18a, 44-100 Gliwice, Poland
email: malgorzata.musztyfaga@polsl.pl
[c] University Da Beira Interior, R. Marquês de Ávila e Bolama, 6201-001 Covilhã, Portugal
[d] Bialystok University of Technology, Wiejska 45A, 15-351, Białystok, Poland
[e]TUV SUD Polska, Podwale 17, 00-252 Warsaw, Poland
[f] Silesian University of Technology, Facultuy of Biomedical Engeering, Roosevelta 40, 41-800 Zabrze, Poland

Abstract: The article presents the results of tests on Metal Inert Gas (MAG) welding of DOCOL 1100 M and DOCOL 1200 M, which belong to the Advanced High Strength Steel (AHSS) group. This material is considered difficult to weld due to its predominantly martensitic structure, often resulting in cracks in the heat-affected zone (HAZ). Joints made from AHSS steel exhibit a tensile strength nearly twice that of the base material. Theweldability of these steels is influenced by the thickness of the welded components; thinner sections can be welded without preheating, while thicker ones may require preheating. In applications, it is crucial to achieve welded joints with high tensile strength and appropriate fatigue resistance. DOCOL 1100 M and DOCOL 1200 M are typically welded using the MAG process with a shielding gas mixture of argon and carbon dioxide. However, the EU recommends reducing CO_2 emissions to address the carbon footprint issue. This article explores the feasibility of creating joints from DOCOL 1100 M and DOCOL 1200 M steel using alternative shielding gases. The aim is to demonstrate that it is possible to produce a sound DOCOL steel joint without CO_2 additives in the shielding gas mixture. Additionally, the study examines the effect of using different electrode wires with varying chemical compositions. The impact of heating temperature was not investigated due to the nature of the thin-walled structure.

Keywords: welding, DOCOL steel, transport means, CO_2 emission

1. INTRODUCTION

In the automotive industry, there is a continual search for materials with increasing tensile strength and fatigue strength. Advanced High Strength Steels (AHSS) offer a tensile strength

exceeding 1000 MPa; however, their fatigue strength is relatively low, falling below 300 MPa. In contrast, steels from the DOCOL group are increasingly utilized in the construction of lift elements due to their high tensile strength and superior fatigue strength, which exceeds 400 MPa [1-4]. The DOCOL 1100 M and DOCOL 1200 M grades are primarily employed in thin-walled constructions that help reduce vehicle weight. Various welding processes can be applied to DOCOL 1100 M and DOCOL 1200 M steels, with the most commonly used method being MAG welding. Less frequently, these steels are welded using the TIG method, covered electrodes, or laser welding [5-7].

The DOCOL 1100 M and DOCOL 1200 M steels are known for their challenging weldability, as the tensile strength of the welded joint and its relative elongation are significantly lower than the strength of the base material. This issue is well documented in the technical literature. Most authors recommend limiting the linear energy input during welding [2], particularly for structures with wall thicknesses greater than 3 mm. The literature mentions welding thicker-walled structures made from DOCOL steel less frequently. The high strength of DOCOL 1100 M and DOCOL 1200 steels is attributed to their martensitic microstructure, which can be compromised by excessive heat input. Therefore, it is essential to employ low heat input and control the inter-pass temperature, which should not exceed 150°C. The aim of this article, and its novel contribution, is to develop a welding technology for joints made of DOCOL 1100 M and DOCOL 1200 M steel without the use of CO_2 as a shielding gas.

2. MATERIAL FOR INVESTIGATION

For non-destructive and destructive testing, DOCOL 1100 M and DOCOL 1200 M steels with a thickness of 1.8 mm were used. The mechanical properties and chemical composition of the steel in the delivered state are shown in Tables 1 and 2.

Table. 1. Mechanical properties of DOCOL 1100 M and DOCOL 1200 M

Grade	YS, MPa	UTS, MPa	Elongation A5, %
DOCOL 1100 M	975	1100	6.5
DOCOL 1200 M	1075	1200	5.7

The tensile strength and yield strength are at a high level, which is undoubtedly influenced by the martensitic structure and chemical composition of both steel grades (Table 2).

Table. 2. Chemical composition of tested materials

Grade	C, %	Si, %	Mn, %	P, %	S, %	Al., %	Nb, %	Ti, %
Docol 1100 M	0.11	0.19	2.1	0.009	0.002	0.038	0.011	0.013
Docol 1200 M	0.14	0.21	1.7	0.008	0.002	0.041	0.015	0.027

Table data indicate that both steel grades have a significantly higher titanium and aluminum content compared to classic non-alloy structural steels. For DOCOL 1100 M and DOCOL 1200 M steels, the objective is to ensure that the total content of titanium and niobium

does not exceed 0.45%. Additionally, it can be noted that DOCOL 1100 M and DOCOL 1200 M steels exhibit very low sulfur and phosphorus content (Table 2). Silicon enhances strength and promotes the stabilization of the microstructure, while the high manganese content increases strength and fracture resistance. The reduction of phosphorus and sulfur is crucial for improving ductility and minimizing the risk of cracking under welding conditions. This carefully selected chemical composition of DOCOL 1100 M and DOCOL 1200 M steels can guarantee high tensile strength while maintaining good plastic properties (refer to Table 1).

During the research, joints were produced using the MAG (Metal Active Gas) process, employing a standard mixture of Ar + 18% CO_2 and Ar + 2% O2 for comparison. Two electrode wires were chosen for welding the high-strength steels from the DOCOL group: UNION X96 (standardized wire designation: G 69 6 M Mn4Ni1.5CrMo) and UNION X90 (standardized wire designation: G 69 5 M Mn4Ni1.5CrMo). This designation complies with EN ISO 14341. The chemical composition of both electrode wires is presented in Table 3.

Table. 3. Weldig wires, chemical composition

UNION	C%	Si%	Mn%	P%	Cr%	Mo%	Ni%	Ti%
X90	0.10	0.75	1.8	0.01	0.35	0.6	2.35	0.005
X96	0.11	0.82	1.8	0.01	0.45	0.7	2.45	0.007

The data from the table suggest that the chemical composition of both wires is quite similar. The slight differences are related to the amounts of elements that influence the strength of the joint (such as carbon, chromium, and titanium) and those that contribute to favorable plastic properties (including nickel and molybdenum).

The welding parameters for the MAG process, which utilized two electrode wires (UNION X90 and UNION X96) and two shielding gas mixtures (Ar-18% CO_2 and Ar-2% O_2), were as follows:

- Wire diameter: 1 mm
- Arc voltage: 20.5 V
- Welding current: 121.5 A
- Direct current source (+) connected to the electrode
- Welding speed was varied at two rates: 325 mm/min and 425 mm/min.

To evaluate the weldability of DOCOL 1100 M and DOCOL 1200 M steels, sheets measuring 1.8 mm × 350 mm × 350 mm were used, and these sheets were not beveled.

3. METHODOLOGY

After the welded joints were completed, both non-destructive and destructive tests were conducted. In the area of non-destructive testing, the focus was on:

- Visual testing (VT) in accordance with the requirements of PN-EN ISO 17638, with assessment criteria according to EN ISO 5817.
- Magnetic particle testing (MT) according to PN-EN ISO 17638, with assessment of the tests conducted according to EN ISO 5817, using a magnetic flaw detector of type REM – 230.

In the area of destructive testing, the following tests were carried out:

- A bending test for specimens with a thickness of 1.8 mm. The parameters of the bending test were as follows: width of the specimen (b) = 20 mm, thickness of the specimen = 2.1 mm, mandrel diameter (d) = 15 mm, and bending angle = 180°.

Five measurements were made for each sample from both the ridge side and the face side using the INSTRON 3369 testing machine.

- Tensile strength testing of the joints was performed using the INSTRON 3369 testing machine.
- Observations were made under a light microscope.

After each type of test, the joints were evaluated, and samples were selected; only those welds of high quality were qualified for the next stages of testing.

4. RESEARCH RESULTS AND THEIR ANALYSIS

The method for determining the samples and the results of the non-destructive testing conducted on the DOCOL 1100M steel joint are presented in Table 4a, while those for the DOCOL 1200M steel are presented in Table 4b

Table. 4a. NDT test results for welds made with UNION X 90 and UNION X 96 wire for DOCOL 1100 steel

Sample	Wire	Shielding gas	Speed, mm/min	Observations
A1	Union X90	Ar + 18% CO_2	325	without defects
A2	Union X90	Ar + 18% CO_2	425	without defects
A3	Union X96	Ar + 18% CO_2	325	minor cracs
A4	Union X96	Ar + 18% CO_2	425	without defects
A5	Union X90	Ar + 2% O_2	325	without defects
A6	Union X90	Ar + 2% O_2	425	without defects
A7	Union X96	Ar + 2% O_2	325	minor cracs
A8	Union X96	Ar + 2% O_2	425	without defects

Table. 4b. NDT test results for joints made with UNION X 90 and UNION X 96 wire for DOCOL 1200 steel

Sample	Wire	**S**hielding gas	**S**peed, mm/min	Observations
B1	Union X90	Ar + 18% CO_2	325	without defects
B2	Union X90	Ar + 18% CO_2	425	without defects
B3	Union X96	Ar + 18% CO_2	325	minor cracs
B4	Union X96	Ar + 18% CO_2	425	without defects
B5	Union X90	Ar + 2% O_2	325	without defects
B6	Union X90	Ar + 2% O_2	425	without defects
B7	Union X96	Ar + 2% O_2	325	minor cracs
B8	Union X96	Ar + 2% O_2	425	without defects

The results of the tests presented in Tables 4a and 4b indicate that the selection of process parameters significantly impacts the quality of the joint. Improperly selected welding parameters led to the formation of small cracks (maximum of 4) in the joint, with each crack not exceeding 3 mm in length. The cause of the cracks in both DOCOL 1100 M and DOCOL 1200 M was found to be too low a welding speed. The next stage of the research involved assessing the quality of the joints through a bending test. Samples were taken only from those joints made with DOCOL 1100 M and DOCOL 1200 M (see Table 5) that did not exhibit defects in non-destructive testing. Joints A3, B3, A7, and B7 were rejected for further testing.

Table. 5. Bending test results

Sample	Observation from face side	Observation from root side
A1	positive	negative
A2	positive	positive
A4	positive	positive
A5	negative	positive
A6	positive	positive
A8	positive	positive
B1	positive	positive
B2	positive	positive
B4	positive	positive
B5	positive	negative
B6	positive	positive
B8	positive	positive

The table data confirm that the quality of the joint is strongly influenced by welding parameters, the most important of which appear to be the welding speed and the chemical composition of the electrode wire. After evaluating the joints in a bending test, it was decided to perform a tensile strength test. Again, only those joints that passed the bending test were eligible for this test. This time, the A1, A5, and B5 joints were rejected. The tests were carried out on an INSTRON 3369 machine. The results of the strength tests (average values from 3 measurements) are presented in Table 6. The ultimate tensile strength (UTS) and relative elongation (ε) were analyzed.

Table. 6. Results of strength tests of welded joints made of DOCOL 1100 M and DOCOL 1200 M steel

Sample	UTS	ε
A2	553	5.4
A4	754	5.5
A6	566	5.6
A8	585	5.6
B1	668	5.2
B2	672	5.2
B4	685	5.3
B6	694	5.3
B8	702	5.4

The table data showed that joints with good tensile strength were obtained, although their strength was much lower than that of the base material. For both DOCOL 1100 M steel (samples marked with the symbol A) and DOCOL 1200 M steel (marked with the symbol B), it was found that the highest tensile strength was achieved using the UNION X96 electrode wire, which contains a higher percentage of carbon and chromium compared to the UNION X90 electrode wire. Additionally, it was demonstrated that joints made in a gas-shielded Ar + 2% O_2 atmosphere exhibited slightly higher strength than those welded in an Ar + 18% CO_2 gas mixture.

Among all the tested joints made of DOCOL 1200 M steel, the B8 sample exhibited the best properties, with its structure illustrated in Figure 1.

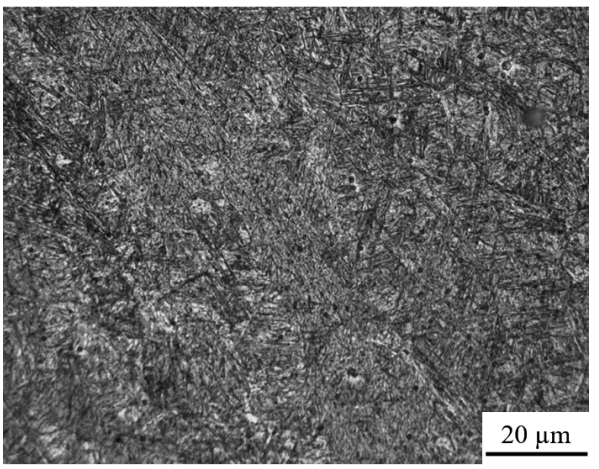

Figure 1. Microstructure of DOCOL 1200 M steel joint, B8 sample

The best properties of all tested joints made of DOCOL 1100 M steel are exhibited by the A8 sample, the structure of which is illustrated in Figure 2.

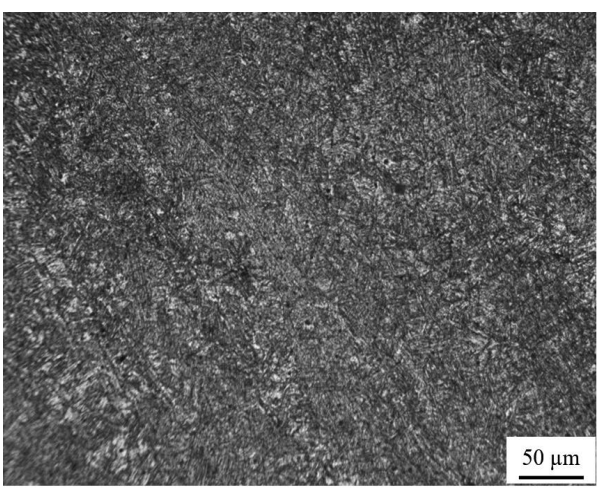

Fig. 2. Microstructure of DOCOL 1100 M steel joint, A8 sample

5. SUMMARY

Increasingly used materials in the construction of means of transport are high-strength steel DOCOL 1100 M and DOCOL 1200 M. Its high strength (approx. 1100-1200 MPa) is still much higher than the strength of a welded joint (approx. 550-700 MPa). The relative elongation of the joint obtained using the welding processes used so far is above 5%. New solutions are therefore sought to guarantee both the improvement of the weldability of DOCOL steel, allowing at the same time to increase the temporary tensile strength and to improve the elongation of the relative joint obtained. An important EU recommendation is to reduce CO_2 emissions, therefore the article shows that the use of a shielding gas mixture Ar-2% O_2 instead of Ar-18% CO_2 is justified and in line with EU expectations. The research presented in the article shows that in order to obtain the correct joint made of DOCOL 1100 M and DOCOL

1200 M steel with a thickness of 1.8 mm, the best results were obtained for the A8 joint (for DOCOL 110 M steel) and B8 for steel (DOCOL 1200 M) when the following were used at the same time:

- the electrode wire was used: UNION X 96, •
- the joints were welded at a higher speed of 425 mm/min.

The UNION X96 electrode wire contains more carbon and chromium than the UNION X90 electrode wire, which increases the strength. The welding speed of DOCOL 1200 M steel has a significant impact on the properties of the welded joint for both DOCOL 1200 M and DOCOL 110 M. Too low welding speed (325 mm/min) leads to an increase in the amount of heat introduced into the weld, which can lead to excessive growth of grains in the weld and in the heat-affected zone (HAZ). As a result, the joint becomes more brittle and mechanical properties such as strength and ductility can deteriorate. Higher welding speed (425 mm/min) leads to a reduction in heat input, which reduces grain growth in the weld seam and in the heat-affected zone (HAZ). It helps to maintain favorable mechanical properties. However, it is important to remember that welding too quickly can lead to incomplete penetration and the formation of defects such as blisters or discontinuities in the weld. Correctly selected welding parameters of DOCOL 1100 M and 1200 M steel ensure high quality of the joint and minimize the risk of defects.

ACKNOWLEDGMENTS

The article is related to the implementation of the university project 12/010/BK24/1155 of the international project: Aerospace Materials and Structures – AeroMaS Gropup of Cente for Mechanical and Aerospace Science and Technologies (Project UIDB/00151/2020)

BIBLIOGRAPHY

1. B. Skowrońska, J. Szulc, T. Chmielewski, D. Golański: Wybrane właściwości złączy spawanych stali S700 MC wykonanych metodą hybrydową plazma + MAG. Welding Technology Review, 2017, 89, 10, 104-111. http://dx.doi.org/10.26628/ps.v89i10.825.
2. Silva, B. Szczucka-Lasota, T. Węgrzyn, A. Jurek: MAG welding of S700MC steel used in transport means with the operation of low arc welding method. Welding Technology Review, 2019, 91, 3, 23-30.
3. L. Jaewson, A. Kamran, P. Jwo: Modeling of failure mode of laser welds in lap-shear specimens of HSLA steel sheets. Engineering Fracture Mechanics, 2011, 1, 347-396.
4. J. Darabi, K. Ekula: Development of a chip-integrated micro cooling device. Micro-electronics Journal, , 34, 11 (2016) 1067-1074. https://doi.org/10.1016/j.mejo.2003.09.010.
5. U. Prijanovič, M. Prijanovič Tonkovič, U. Trdan, M. Pleterski, M. Jezeršek, D. Klobčar: Remote Fibre Laser Welding of Advanced High Strength Martensitic Steel. Metals 2020, 10, 4, 533. https://doi.org/10.3390/met10040533.
6. D. Golański, T. Chmielewski, B. Skowrońska, D. Rochalski: Advanced Applications of Microplasma Welding. Biuletyn Instytutu Spawalnictwa w Gliwicach, 2018, 62, 5, 53-63. http://dx.doi.org/10.17729/ebis.2018.5/5.

7. B. Krupicz, W. Tarasiuk, V.G. Barsukov, A.I. Sviridenok: Experimental Evaluation of the Influence of Mechanical Properties of Contacting Materials on Gas Abrasive Wear of Steels in Sandblasting Systems. Journal of Friction and Wear, 2020, 41, 1,1-5.
8. V. L. Shwachko: Cold cracking of structural steel weldments as reversible hydrogen embrittlement effect. International Journal of Hydrogen Energy, 25, 2000, 473-480.
9. J. Łabanowski, D. Fydrych: Oznaczanie zawartości wodoru dyfundującego w stopiwie. Prace Naukowe Politechniki Warszawskiej, II Sympozjum Naukowe Zakładu Inżynierii Spajania Politechniki Warszawskiej, Warszawa 2008.
10. T. Lahtinen, P. Vilaça, P. Peura, S. Mehtonen: MAG Welding Tests of Modern High Strength Steels with Minimum Yield Strength of 700 MPa. Appl. Sci. 2019, 9,1031.
11. D. K. Matlock, J. G. Speer, E. de Moor: Recent AHSS Developments for Automotive Applications: Processing, Microstructures, and Properties, Addressing Key Technology Gaps in Implementing Advanced High-Strength Steels for Automotive Lightweighting, February 9 - 10, 2012, USCAR Offices, Southfield, MI.

TalentDetector

31th January 2025
Gliwice, Poland

DEPARTMENT OF ENGINEERING MATERIALS AND BIOMATERIALS
FACULTY OF MECHANICAL ENGINEERING
SILESIAN UNIVERSITY OF TECHNOLOGY

INTERNATIONAL STUDENTS SCIENTIFIC CONFERENCE

Research on the method of semantic segmentation of objects based on images obtained by multirotor platform

Jagoda Więcek [a], Michał Wieczorek[a], Kacper Matys[a], Patryk Mondry[a], Wojciech Cofalik[a]

[a] Silesian University of Technology, Virtual Flying Student Research Club
email: jw300503@student.polsl.pl

Abstract: This paper presents the results of implementing the segmentation_models.pytorch library in Python, focusing on the data normalisation process, the model learning scheme and the analysis of three selected variants with modified parameters. The main steps of database preparation are described (including image normalisation and standardisation), and the model training process is discussed in detail. As examples, three models are presented that differ in the loss functions used, the number of epochs and the use of data augmentation, allowing the impact of these parameters on the final semantic segmentation results to be analysed.

Keywords: model, binary semantic segmentation, RGB image, loss function

1. INTRODUCTION

Today, artificial intelligence algorithms are increasingly used for text generation and image analysis. Semantic segmentation is one of the most difficult tasks in the field of image analysis, it can identify objects in an image and assign each pixel to specific category e.g. cars or buildings. This algorithm provides a solution for automatic image analysis in various fields such as medicine, agriculture, security or autonomous vehicles.
The project was carried out using ready-made models available in the 'segmentation_models.pytorch' library written in Python. The aim of the project is the training of a binary semantic segmentation model for the recognition of a selected object on a map.

Figure 1. Bird's eye view of the town image

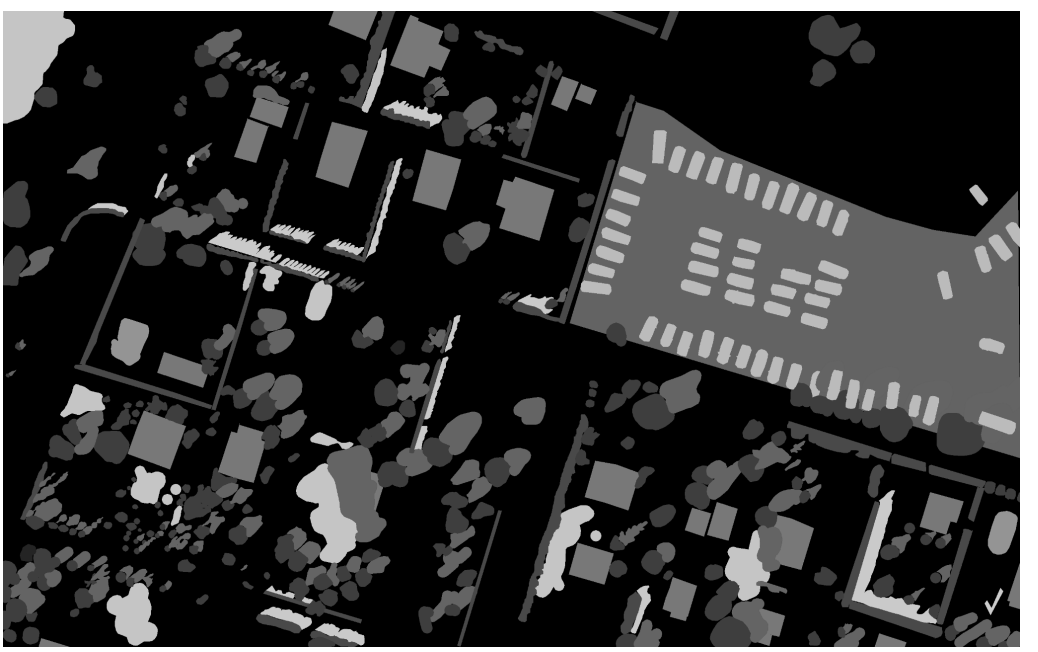

Figure 2. Image of bird's eye view of the town after segmentation

2. DATABASE AND NORMALIZATION

The database prepared for learning the model (for example of images and masks see Figure 1. and Figure 2.) needs to be normalised before it can be used, which is done using implemented functions. The database used in the project contains folders of RGB images and .json files containing information about the location of objects in the images as well as their contours. The first step was to read the data from the .json files and draw the contours of the objects in the image. For the masks, the contours were mapped with a value of 255, while the background

was given a value of 0. The generated images have measurements that match the corresponding originals.
To standardise the data for model learning, the original RGB images and their corresponding masks are cropped to a fixed size of 512x512 pixels. For larger images, the images are divided into several smaller fragments. Each fragment is adjusted accordingly to preserve the image context and ensure that the masks accurately represent the relevant areas in the image. This results in images of a normalized form, making the training process more efficient.
Once the masks have been generated and clipped, they are converted into matrices in which each pixel is represented as 0 (background) or 1 (foreground). The matrices are then saved to .pkl binary files using the pickle library in Python. This way of saving allows for compact and fast storage of the masks and their easy reading when training the semantic segmentation model. The .pkl format allows the masks to be stored in a form ready for use by the model, which significantly speeds up the process of loading the data at runtime.

3. LEARNING PROCESS

The binary semantic segmentation model requires carefully prepared input data to enable it to learn to recognise patterns relevant to pixel classification. Input images are represented as three-dimensional arrays of pixels, where, in the case of RGB images, the dimensions correspond to height, width and the three colour channels (red, green and blue). The pixel values are usually normalised, making it easier for the model to optimise and analyse the image features. During the learning process, the model also receives reference masks, which are two-dimensional binary matrices. These masks indicate which pixels belong to the object (foreground) and which belong to the background , acting as a benchmark to assess the correctness of the model. After image processing, the model generates an output binary prediction map, where each pixel is assigned to one of two classes. This output is then compared to a reference mask, allowing the error to be calculated using a loss function such as IOU (Intersection over Union) or Dice Coefficient. Based on this, the model weights are updated through a back-propagation process, allowing the model to improve its results. By repeating this scheme for a large number of training examples, the model learns to increasingly recognise the characteristic features of objects and segment them more effectively in new images, paying particular attention to edges and boundaries.

4. MODELS

Over the course of the project, several models were trained, combining key baseline parameters to ensure experimental consistency and allow comparison of results. All models used the U-Net architecture, which is commonly used in semantic segmentation tasks due to its ability to accurately detect objects and their boundaries. ResNet34 was chosen as the encoder, which provided a robust basis for extracting features from images, and the encoder weights were initialised against the ImageNet set, allowing transfer learning and faster model convergence. The batch size was set to 16, a trade-off between computational efficiency and accuracy of results in learning tasks. The images entered in each iteration were reordered, helping the model to pick up the pattern of images rather than learn them by heart. The optimisation of the network parameters was carried out using the ADAM algorithm (Adaptive Moment

Estimation), which allows stable and efficient training of the models thanks to the adaptive selection of the learning rate.

Model nr 1 - The first trained model was configured using the loss function nn.BCELoss() (Binary Cross Entropy Loss), which is commonly used in binary semantic segmentation tasks. The function calculates the difference between the model's output predictions and the expected values, as represented on the mask. This allows the model to refine the model weights, leading to better learning. The model was trained for 20 epochs without using augmentation on the images.

Model nr 2 - The second model was trained using the loss function nn.BCEWithLogitsLoss() (Binary Cross Entropy With Logits Loss), which integrates the mechanism of the sigmoid function. The use of this loss function allows the model to assign values of 0 or 1 more strongly, rather than generating intermediate values. Model 2, like model 1, was trained on 20 epochs without the use of augmentation. This approach allowed us to focus solely on the effect of changing the loss function on the quality of the prediction and the model's ability to identify important patterns in the data.

Table 1. Differences of presented models

	Model nr 1	Model nr 2	Model nr 3
loss function	nn.BCELoss()	nn.BCEWithLogitsLoss()	nn.BCELoss()
epoch amount	20	20	30
input data	static	static	augmented

Table 2. Learning outcomes in the last epoch

	Model nr 1	Model nr 2	Model nr 3
Training loss	0.04	0.68	0.3
Training accuracy	0.98	0.96	0.99
Validation loss	0.05	0.68	0.3
Validation accuracy	0.97	0.97	0.99
Training IOU	0.8	0.75	0.85
Training dice	0.84	0.78	0.91
Validation IOU	0.78	0.76	0.91
Validation dice	0.83	0.8	0.89

Model nr 3 - The third trained model was implemented using the loss function nn.BCELoss(), but unlike the previous variants, it used data augmentation. At each use, the input images were randomly modified, including by brightening or rotating, which increased the diversity of the training data. In addition, the model was trained for 30 epochs, allowing it to learn for longer and analyse a wider range of data variants. As a result, the model achieved better performance in processing variable input data.

5. CONCLUSION

The results obtained by the trained models and presented in Table 1. and Table 2. show that it is not necessary to change many parameters to get different results. The project can be developed further, for example by implementing new models with other changed parameters, such as increasing the batch size, changing the learning rate, or using a different optimiser than ADAM. The best results were achieved by model No. 3, indicating that the use of data augmentation and increasing the number of training epochs improves model performance.

BIBLIOGRAPHY

1. Guo, Y., Liu, Y., Georgiou, T. *et al.* A review of semantic segmentation using deep neural networks. *Int J Multimed Info Retr* **7**, 87–93 (2018). https://doi.org/10.1007/s13735-017-0141-z
2. Hongshan Yu, Zhengeng Yang, Lei Tan, Yaonan Wang, Wei Sun, Mingui Sun, Yandong Tang, Methods and datasets on semantic segmentation: A review,Neurocomputing, Volume 304, 2018, Pages 82-103, ISSN 0925-2312, https://doi.org/10.1016/j.neucom.2018.03.037. (https://www.sciencedirect.com/science/article/pii/S0925231218304077)
3. Shubhra Aich, William van der Kamp, Ian Stavness; Proceedings of the IEEE Conference on Computer Vision and Pattern Recognition (CVPR) Workshops, 2018, pp. 197-201
4. Fu, L.; Li, S. A New Semantic Segmentation Framework Based on UNet. *Sensors* **2023**, *23*, 8123. https://doi.org/10.3390/s23198123
5. Damkliang K, Thongsuksai P, Kayasut K, Wongsirichot T, Jitsuwan C, Boonpipat T. 2023. Binary semantic segmentation for detection of prostate adenocarcinoma using an ensemble with attention and residual U-Net architectures. *PeerJ Computer Science* 9:e1767 https://doi.org/10.7717/peerj-cs.1767

TalentDetector
31th January 2025
Gliwice, Poland
DEPARTMENT OF ENGINEERING MATERIALS AND BIOMATERIALS
FACULTY OF MECHANICAL ENGINEERING
SILESIAN UNIVERSITY OF TECHNOLOGY
INTERNATIONAL STUDENTS SCIENTIFIC CONFERENCE

Phase changes induced by corrosion of alkali-activated binders

Paulina Wiśniewska, Barbara Słomka-Słupik[a]

[a] Silesian University of Technology, Faculty Civil Engineering, Department of Building Structures
email: barbara.slomka-slupik@polsl.pl

Abstract:
The article describes the effect of ammonium chloride on cement paste, the matrix of which is considered to be weaker than the non-clinker matrix activated by alkali. This work is a continuation of the previously described research. Particular attention was paid to the phase transformations that occurred after the corrosion of AAM in NH_4Cl water solution. During corrosive attack, carbonation and the share of the amorphous phase increased.

Keywords: alkali activated materials (AAM), geopolymers, ammonium chloride, corrosion, phases changes

1. INTRODUCTION

Cement is a key building material, acting as a binder that combines aggregates into a homogeneous mass capable of carrying loads. Its properties result from the presence of silicates, aluminates and calcium oxides, which undergo hydration in reaction with water, creating a structure with high mechanical strength and resistance to compression [1].

However, the durability of cement depends on the quality of raw materials, the production process and operating conditions. Concrete containing cement is a porous material, which means that it can be penetrated by water and chemicals. In chemically aggressive environments, such as industrial or agricultural areas, where concrete is exposed to chlorides, sulphates or acids, the durability of the structure may be significantly reduced [2].

Ammonium chloride, an inorganic salt with the formula NH_4Cl, is a chemical compound that is commonly found in the natural environment and as a result of human activity. Its structure consists of ammonium cations (NH_4^+) and chloride anions (Cl^-), which completely dissociate in aqueous solutions. This property makes ammonium chloride a highly active chemical compound, capable of reacting with many building materials, including cement [3,6].

The natural occurrence of ammonium chloride mainly includes areas with increased volcanic activity. It is formed there as a by-product of geochemical processes, being released as steam and crystallizing in the colder layers of the Earth's crust. Mineralogically, it is known as ammonium chloride. Anthropogenic sources, on the other hand, include various branches of industry and human activity. In the chemical industry, ammonium chloride is a by-product of

the synthesis of soda using the Solvay method. In agriculture, it is found in nitrogen fertilizers, while in the energy industry it occurs in industrial gases, such as exhaust fumes from coal-fired power plants. Ammonium chloride is distinguished by several important chemical properties. It is a compound that is highly soluble in water, which allows the formation of solutions in an environment with high humidity. Due to its ionic structure, it easily penetrates porous materials, such as concrete. In addition, its aqueous solutions are slightly acidic, with a pH in the range of 4.5–5, which can intensify chemical reactions in the pores of concrete, affecting its durability [4]. When ammonium chloride penetrates the pores of concrete, a series of chemical reactions occur that lead to the degradation of the cement structure. The key step is the reaction of ammonium ions (NH_4^+) with calcium hydroxide ($Ca(OH)_2$), which is one of the main products of cement hydration. This reaction is described by the chemical equation:

$$NH_4Cl + Ca(OH)_2 \rightarrow CaCl_2 + NH_3\uparrow + H_2O.$$

As a result, calcium chloride ($CaCl_2$) is formed, which is highly soluble in water and easily washed out of concrete, which leads to decalcification of the cement matrix. At the same time, ammonia (NH_3) is released, which as a gas can affect the working environment and operation of the structure, and the resulting water additionally increases the humidity in the pores of concrete [8]. The effects of ammonium chloride on cement are complex and include several important processes. Decalcification, i.e. the leaching of calcium contained in cement hydrates, significantly weakens the structure of the cement matrix. In addition, chemical reactions lead to an increase in the porosity of concrete, which promotes further penetration of aggressive substances such as chloride ions (Cl^-). Additionally, the presence of these ions destabilizes the passive layer on the surface of steel reinforcement, initiating a corrosion process that can seriously affect the durability of the structure [4,6,7]. The action of ammonium chloride in concrete goes beyond the basic reactions with calcium hydroxide, also involving the degradation of calcium silicate hydrate (C-S-H), which plays a key role in ensuring the mechanical strength and durability of concrete. Chloride ions present in the concrete environment cause a reduction in the amount of calcium silicate hydrate, which results in a significant reduction in compressive strength. Concrete then becomes less resistant to loads, which can lead to a threat to the load-bearing capacity of the structure. Additionally, these changes contribute to the increased brittleness of the material, making it more susceptible to cracking, which in turn shortens the service life of concrete elements. Research on the mechanisms of cement degradation in the presence of ammonium chloride is important for the protection of structures exposed to aggressive chemical environments. Facilities such as sewage treatment plants, industrial plants, port infrastructure or bridges require special attention, because cement degradation can lead to [4,9]:

- reduction of the structure durability
- increase in maintenance and repair costs
- potential failures that threaten safety

In the case of cementless, alkali activated binders, the so-called geopolymer binders, the corrosion of the matrix, known as decalcification, practically does not occur. Geopolymer binders are alkali-activated aluminosilicates, which would not bind under the influence of water. However, it is not excluded, although less common, that the alkali activation of mixtures with higher calcium content is possible. We dealt with such materials in this work, so that the composition was not too different from cement clinker, and yet, that alkaline activation occurred, not only ordinary chemical binding. The most important hardened phase, constituting about 80% of the cement matrix, is the C-S-H gel, as already mentioned, formed as a result of the hydrolysis of calcium silicates. In the case of alkali-activated binders, the product is usually

the C-A-S-H gel: hydrated calcium aluminosilicates formed in geopolymerization reactions. In this work, we checked how ammonium chloride, in the form of an external solution, in which prepared mortars were immersed, affects the phases created as a result of geopolymerization, and not only hydration. The aim of this work was comparison of the results of pastes phase transformations, also changes in amorphous phase' amount after 16 months of corrosive immersion in NH_4Cl water solution.

2. MATERIALS AND METHODS

Many different ingredients were used to prepare samples of six alkaline-activated pastes. Their chemical composition are presented in Table 1 [10]. To determine the chemical composition, the XRF (X-ray fluorescence) method was involved. The composition of individual 6 pastes is shown in Table 2 [11].

Table 1. Chemical composition of components for preparation of binder mixtures [10]

Component (PL Abbreviation)	PV Glass (S1)	Kaolin Clay	Ground Granulated Blast Furnace Slag	Alumina-Lime Cement (CG-40)	Autoclaved Cellular Concrete (SOL.1)	Fly Ash from Coal Combustion (WR25.1)	Fly Ash from Biomass Combustion (PLB_T1)
Abbreviation used in this article	PVG	KC	GGBFS	ALC	ACC	FAC	FAB
				Content, wt.%			
Silica as SiO_2	72.39	47.46	40.43	3.05	67.45	43.53	60.25
Aluminium as Al_2O_3	1.10	36.75	7.88	42.52	2.32	25.30	5.87
Sodium as Na_2O	13.41	0.02	0.46	0.08	0.26	2.22	0.72
Calcium as CaO	9.01	0.23	43.27	35.87	17.26	4.42	11.47
Iron as Fe_2O_3	0.05	0.92	0.81	15.31	1.00	6.80	2.86
Magnesium as MgO	3.09	0.24	6.97	0.50	0.29	2.61	3.51
Potassium as K_2O	0.02	0.88	0.29	0.09	0.60	4.67	6.91
Titanium as TiO_2	0.02	0.24	0.28	2.01	0.06	1.39	0.39
Manganese as MnO	<0.01	0.02	0.16	0.07	0.02	0.07	0.37
Phosphorus as P_2O_5	<0.01	0.08	0.02	0.06	0.04	3.41	1.63
Chromium as Cr_2O_3	0.01	0.01	0.01	0.08	0.01	-	0.02
Zirconium as ZrO_2	<0.01	<0.01	<0.01	0.05	<0.01	-	0.04
LOI (550 °C)	0.31						
LOI (1025 °C)		13.35	0.46	0.29	10.44	26.31	5.88

Table 3, in turn, shows the method of testing mixtures over time. 2 weeks after forming, the bars were still damp and did not show much cohesion, so they were all placed in a dryer where they stayed at 105°C for 14 days. After 2 months of curing, they were placed in a water immersion of ammonium chloride in natural, outdoor conditions during 16 months. Reference samples were stored in bags at that time.

The study of the samples described in [11] focused on phase transformations, but especially related to carbonation reactions. In this paper, we show the remaining phase

transformations.The phase composition of non-corroded and corroded samples were examined by X-ray diffraction (XRD) method.

Table 2. Composition of dry components of binder mixtures, in %mas. [11]

Name of mixture / Components	CEM Al-Ca	GGBFS	GK-0	GK-1	PVG	PLB	SOL	PWR	NSH_5	NaOH
B1	30	30	15		5		5		5	10
B2	30	30		15	5			5	5	10
B3	30	30	15		5			5	5	10
C1	30	30	15		5	5			5	10
C2	30	30		15	5	5			5	10
C3	30	30		15	5		5		5	10

**CEM Al-Ca – clay-lime cement, *GGBFS – ground granulated blast furnace slag, *GK-0 – kaolin clay, *GK-1 – metakaolin, *PVG – glass from photovoltaic panels, *PLB – biomass ash, *SOL – ground autoclaved cellular concrete, *PWR – black ash with a large amount of unburned coal, *NSH_5 and NaOH – alkaline activators*

Table 3. Research schedule [11]

Actions	Time after preparation, in months
Preparation	0
Demoulding and drying	0,5
Immersion in a NH_4Cl saturated solution	2
Removal from solution	18
XRD examination	19

3. RESULTS WITH ANALYSIS

Figures 3 – 8 show the XRD results of phase composition for all six binders – not affected (designed: 0) and corroded (designed: C). In table 4, in turn, all phases in theirs amounts are listed. They were calculated using Rietveld method. The content of amorphous phase was calculated from the total amount of crystalline phase. As can be seen, in each dried corroded sample, NH_4Cl is present. It is a non-binding phase, not entering the binder matrix, but only deposited in the pores.

a) b)

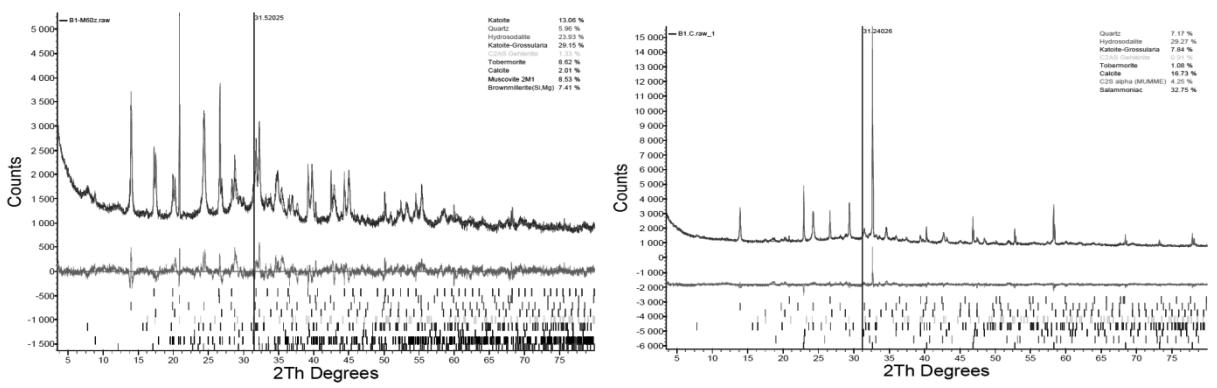

Figure 3. XRD pattern of a) B1.0 b) B1.C specimen

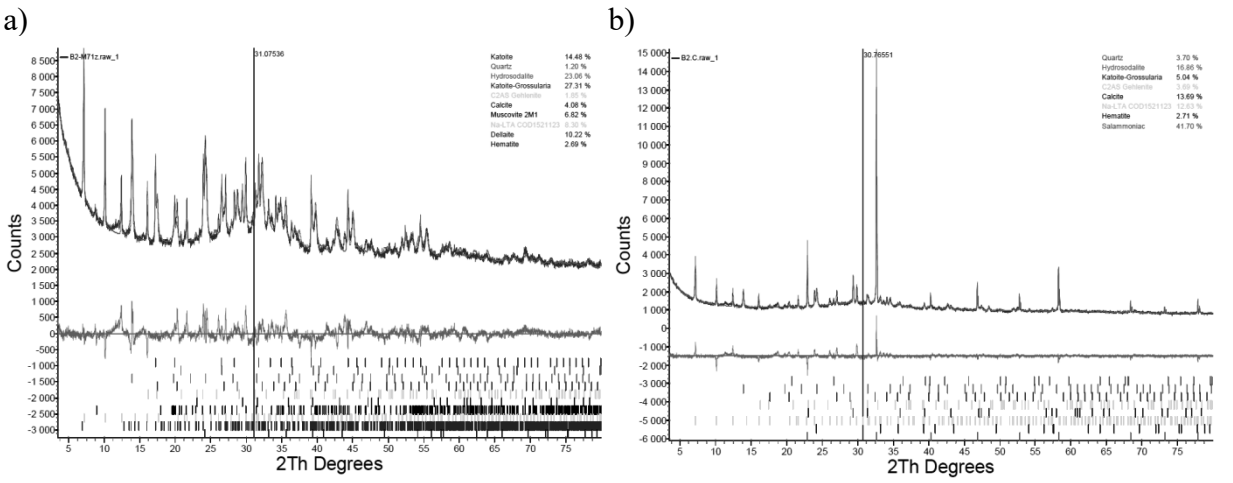

Figure 4. XRD pattern of a) B2.0 b) B2.C specimen

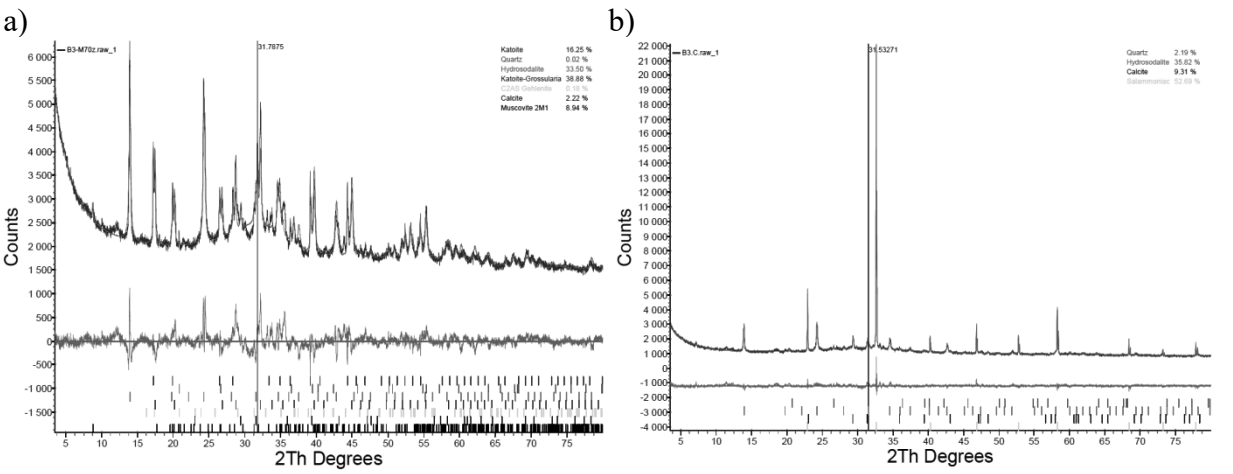

Figure 5. XRD pattern of a) B3.0 b) B3.C specimen

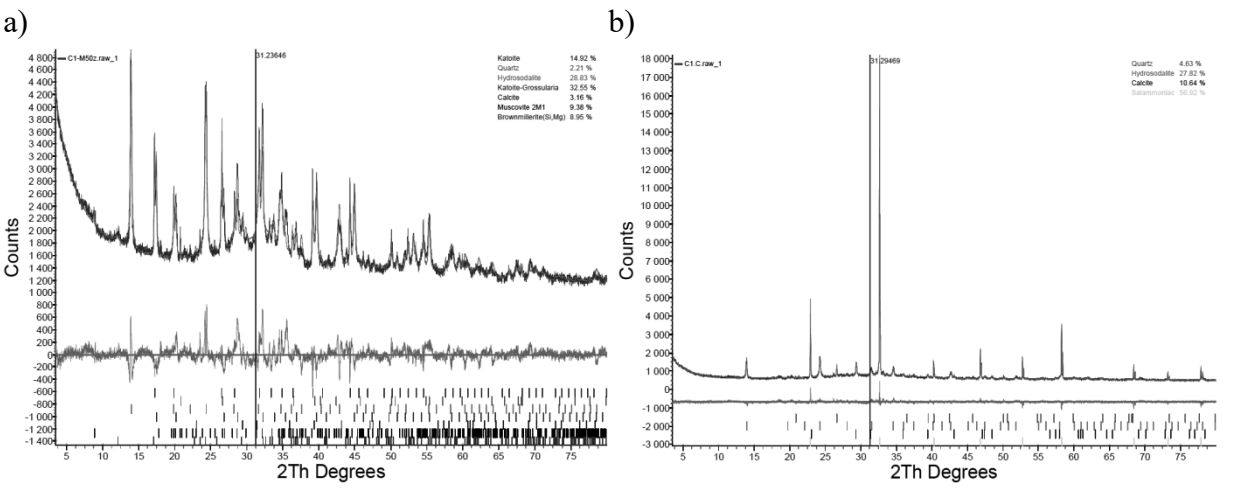

Figure 6. XRD pattern of a) C1.0 b) C1.C specimen

It can be assumed that the more of it there is, the greater the porosity of the AAM binder matrix was. To accurately quantitatively describe how ammonium chloride affected the amount of the amorphous phase, its content must be subtracted from the amounts of all phases.

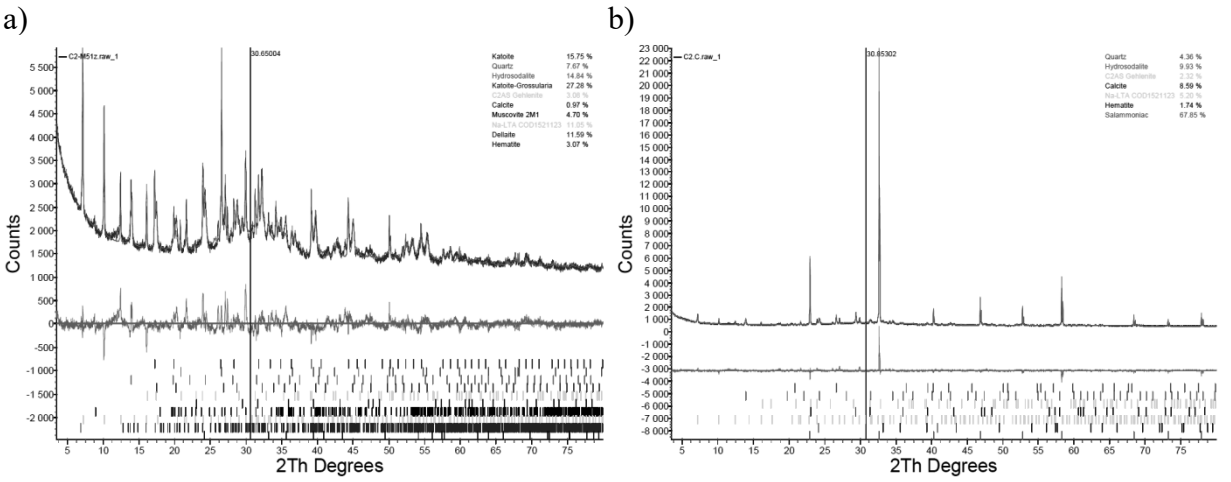

Figure 7. XRD pattern of a) C2.0 b) C2.C specimen

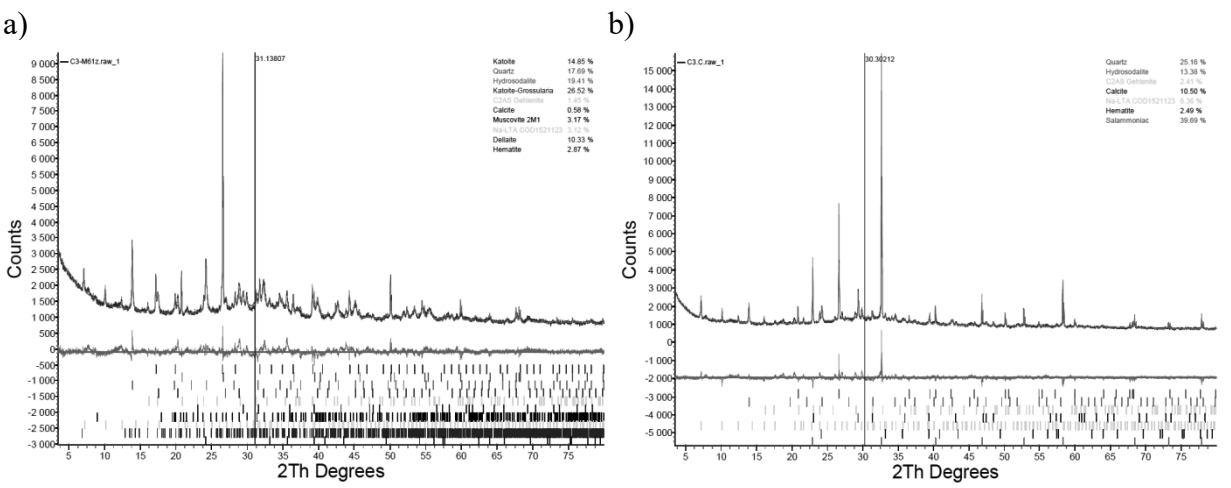

Figure 8. XRD pattern of a) C3.0 b) C3.C specimen

The exemplary calculation was performed for mixture B1. it turned out that the amount of crystalline phase decreased from 71% to 38.3%. When analyzing the diffraction spectra (Figs 3-8), it is very clear that there is a smaller number of crystalline phases in the corroded samples, because the spectra are poorer in the number of reflections. This also confirms the reduced proportion of crystalline phases. There are, however, mixtures in which the amount of the amorphous phase has been increased to a lesser extent, i.e. in B3 and C2. It is probably because a large proportion of the crystalline phase belongs to ammonium chloride that these calculations are so important. Comparing the share of crystalline phases, in turn, most of the aluminum phases were dissolved. Aluminum could have been washed out or entered the structures of the gel (amorphous) phase. The detected aluminate phases in hydrated and non-hydrated form come in particular from calcium aluminate cement and kaolin clay.
Brownmillerite is the unhydrated phase of calcium alumina cement and therefore has not been fully hydrated. The amount of calcite increased, which has already been demonstrated in [11]

work. However, the samples were isolated, so it is possible that the carbonation reactions occurred due to the carbon content in the amorphous phase, in the substrates, and in the components of the mixtures. Grossular and katoite are members of the grossular-katoite series, and can be described as $Ca_3Al_2(SiO_4)_{3-x}(OH)_{4x}$. For x = 3, only katoite is present, this end member, the species is also known as C_3AH_6 (tricalcium aluminate hydrate) in hydrated cement. Compositions where x < 0.2 were still considered grossular, whereas compositions where x > 1.5 were considered katoite [12].

Table 4. Phases content in examined 12 specimens - not affected (0) and corroded (C)

Name and Formula	B1.0	B1.C	B2.0	B2.C	B3.0	B3.C	C1.0	C1.C	C2.0	C2.C	C3.0	C3.C
Muscovite $KAl_2(AlSi_3)O_{10}(F,OH)_2$	6,1		4.2		4.8		5.7		2.8		1.8	
Brownmillerite $Ca_2(Al,Fe)_2O_5$	5.3						5.4					
Katoite $Ca_3Al_2(OH)_{12}$	9.3		9.0		8.7		9.0		9.3		8.4	
Grossular $Ca_3Al_2(SiO_4)_3$	20.7	3.8	17.0	2.4	20.7		19.7				15.0	
Quartz SiO_2	4.2	3.4	0.7	1.7		1.1	1.3	1.9	4.5	2.3	10.0	8.6
Hydrosodalite $Na_8[Cl_2(AlSiO_4)_6]$	17.0	14.1	14.3	7.9	17.9	17.6	17.4	11.3	8.7	5.2	11.0	4.6
Gehlenite $Ca_2Al[(Al,Si)_2O_7]$	0.9	0.4	1.3	1.7	0.1				16.1	1.2	0.8	0.8
Tobermorite $Ca_5Si_6O_{16}(OH)_2 \cdot 4H_2O$	6.1	0.5										
Calcite $CaCO_3$	1.4	8.0	2.5	6.4	1.2	4.6	1.9	4.3	0.6	4.5	0.3	3.6
α-Belite Ca_2SiO_4		2.0										
Ammonium chloride NH_4Cl		15.7		19.5		25.9		23.1		35.3		13.5
Amorphous phase -	29.0	52.0	38.0	54.0	47.0	51.0	40.0	60.0	42.0	48.0	44.0	66.0

4. SUMMARY AND CONCLUSIONS

The alkaline-activated matrices used in these studies contained large amounts of calcium, so only some structures could have been created by geopolymerization reactions, while others could have been created by hydration. The formation of phases of alkaline activated materials and their subsequent transformations in the presence of a corrosive medium are not easy problems to solve. The progress of corrosion processes is related not only to the durability of the given phases, but also to the porosity of the matrix, its diffusion properties. However, there are many factors [13, 14]. Brine, which can be very reactive and destructive to cement paste, will not necessarily have the same effect on geopolymer structures. In the chemistry of binders, the most important thing is the large share of the amorphous phase, which plays a decisive role in maintaining high strength values. As shown by the corrosion studies presented here, ammonium chloride solution disintegrates the matrix by destroying the crystals, but we are not sure whether the aluminum ions are incorporated into the gel structures or are leached out. To determine this, we plan to perform tests of the composition of the remaining solution and hard-

to-reach NMR (nuclear magnetic resonance) tests. As it is believed that calcium forms weak phases, in subsequent studies we want to limit the amount of calcium, using only enough of it to trigger pozzolanic reactions, and we will chemically activate the remaining amounts of aluminosilicates, leading to the formation of geopolymerization reactions.

BIBLIOGRAPHY

1. Giergiczny, Zbigniew. Składniki cementu i ich rola w kształtowaniu właściwości kompozytów cementowych. s.l. : SPC, 2016.
2. Website: „beton na dom" [Online] https://betonnadom.pl/zanim-kupisz-beton/czy-dany-element-konstrukcyjny-bedzie-eksploatowany-w-srodowisku-agresywnym.
3. B. Słomka-Słupik**,** A. Zybura, "Korozja zaczynów z cementów portlandzkich CEM I 42,5R i CEM I 42,5R-HSR/NA w roztworze chlorku amonu", *Cement Wapno Beton*, 2012..
4. B. Słomka-Słupik, A. Zybura, "Zmiany w czasie mikrostruktury zaczynu cementowego pod wpływem roztworu chlorku amonu", *Ochrona przed Korozją*, 2015, nr 1, s. 3-10.
5. M. Czapik, Badania właściwości cementów i betonu – stan obecny i perspektywy rozwoju, Dni Betonu, dostęp: https://www.dnibetonu.com/wp-content/pdfs/2016/czapik.pdf, 2016.
6. B. Słomka-Słupik, "Analiza zmian porowatości w zaczynach poddanych działaniu chlorku amonu", *Dni Betonu*, 2014.
7. B. Słomka-Słupik, A. Zybura, "Microstructure of decalcified cement paste", *ResearchGate*, 2016.
8. B. Słomka-Słupik, A. Zybura, "Laboratory Test and Geochemical Modeling of Cement Paste Degradation in Contact with Ammonium Chloride Solution", *Materials*, 2022, 15(8), 2930. Dostęp: https://www.mdpi.com/1996-1944/15/8/2930.
9. B. Słomka-Słupik, J. Podwórny, M. Staszuk, Corrosion of cement pastes made of CEM I and CEM III/A caused by a saturated water solution of ammonium chloride after 4 and 25 days of aggressive immersion, Construction and Building Materials, Volume 170, 2018, Pages 279-289, ISSN 0950-0618
10. B. Słomka-Słupik, P. Wiśniewska, W. Bargieł. Multicomponent low initial molar ratio of Si_{O2}/Al_{2O3} geopolymer mortars: pilot research. Materials, 2022, vol. 15, nr 17, s.1-20, Numer artykułu: 5943. DOI:10.3390/ma15175943
11. B. Słomka-Słupik, P. Wiśniewska. Analysis of corrosion changes in geopolymer binders. Carbonation. W: TalentDetector2024_Summer : International Students Scientific Conference, 17th - 19th June 2024 / Bonek Mirosław (red.), Prace Katedry Materiałów Inżynierskich i Biomedycznych, 2024, Gliwice, Katedra Materiałów Inżynierskich i Biomedycznych, s.469-474, ISBN 978-83-65138-41-5, https://pimib.polsl.pl/pdf/Talent-Detector-Summer-2024.pdf
12. Website: [Online] Katoite. https://www.mindat.org/min-2167.html
13. J.L. Provis, A. Palomo, C. Shi, Advances in understanding alkali-activated materials, Cement and Concrete Research 78, Part A (2015) 110-125.
14. B. Słomka-Słupik, P. Wiśniewska. Resistance of geopolymers to chemical aggression. Literature study. Ochrona przed Korozją, 2022, vol. 65, nr 12, s.378-392. DOI:10.15199/40.2022.12.2

TalentDetector

31th January 2025
Gliwice, Poland

DEPARTMENT OF ENGINEERING MATERIALS AND BIOMATERIALS
FACULTY OF MECHANICAL ENGINEERING
SILESIAN UNIVERSITY OF TECHNOLOGY

INTERNATIONAL STUDENTS SCIENTIFIC CONFERENCE

Characteristic properties decisive for the use of the material in industrial applications

Mateusz Woźniak[a], Borys Lipczyński[a], Judyta Drygała[b], Julia Popis[c], Sabina Lesz[c*]

[a] Upper-Secondary Schools of Communications in Gliwice
[b] Student, Silesian University of Technology, Faculty of Architecture
[c] Silesian University of Technology, Faculty of Mechanical Engineering, Department of Engineering Materials and Biomaterials
*email: sabina.lesz@polsl.pl

Abstract: The article presents the characteristic properties that are decisive for the use of the material in industrial applications. It also shows how to measure the hardness of materials and the calculation of hardness. The results indicated a correlation between strength with carbon content in the steel.

Keywords: materials, properties, hardness, strength

1. INTRODUCTION

Hardness measurements are important to determine the characteristic properties that are decisive for the use of a material in industrial applications. These measurements are widely used in testing metals, alloys, and plastics. The widespread use of this method for assessing mechanical properties stems from the ability to conduct quick and simple measurements while maintaining the non-destructive nature of the tests. The results of hardness measurements provide useful information for selecting engineering materials and technological processes. In turn, the selection of the appropriate engineering material along with the proper technological process is crucial for ensuring the reliability and quality of the product, minimizing production and operational costs, and meeting environmental requirements [1 – 3].
Hardness is a measure of the resistance of a material (solid body) to localized plastic deformation, produced on a small area of the test object, by mechanically pressing a second, harder body called an indenter into it, with a defined geometry, or by abrasion of the surface. The indenter is usually a steel ball, cone, or pyramid. The hardness of materials depends on the ductility, stiffness, ductility, formability, viscosity, and strength of the tested material [2, 3].

The most common methods used for measuring hardness are:

1.1. Rockwell hardness test

The Rockwell method involves measuring the depth of indentation made by a standard diamond cone with an apex angle of 120° and a rounding radius of 0.2 mm for the C, A, and N scales, or a hardened steel ball with a diameter of 1.5875 mm (1/16″) in methods B, F and T using appropriate load (Fig. 1,2, Table 1). This method is quick and easy to use, as the instrument is equipped with a sensor calibrated directly in hardness units. The Rockwell test leaves only a faint flaw on the test piece and can be used to inspect finished products [4 – 6].
The Rockwell hardness scale is a set of scales used to determine the hardness of metals based on a test made using a method based on measuring the difference in indentation at two test loads.

Table 1. Rockwell scale [4]

Rockwell scale	Indenter type	F_0 (initial load force) [N]	F_1 (main load force) [N]	F (total load force) [N]
B	steel ball	98.07	490.3	980.7
C	diamond cone	98.07	1373.0	1471.0

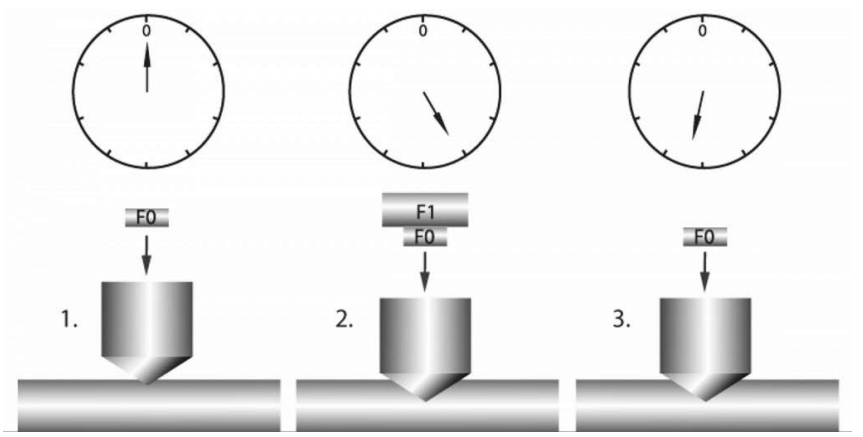

Fig. 1. Diagram of hardness measurement using the Rockwell method [6]

Fig. 2. Example of Rockwell hardness result for a sample of C45 steel

1.2. Vickers hardness test

The measurement of hardness by the Vickers method consists of indenting a quadrilateral regular diamond pyramid with an apex angle of 136° into the surface of the test material under static load F and then measuring the diagonals d of the resulting square-shaped imprint (Fig. 3). The numerical value of hardness expressed in Vickers HV is obtained by dividing the force F in kilograms of force (kgf) by the lateral area of the imprint A in square millimeters:

$$HV = \frac{F}{A} \qquad (1)$$

Where: A is the area of the imprint, calculated from the formula:

$$A = \frac{d^2}{2\,sin(\measuredangle/2)} \qquad (2)$$

- d - diagonal of the obtained imprint
- α - apex angle of the pyramid equal to 136°

It is very common to use the formula:

$$HV = \frac{F}{A} \approx \frac{1.8544F}{d^2} \qquad (3)$$

Where F is expressed in kilograms-force and d in mm.
Or in the SI system:

$$HV = \frac{F}{A} \approx \frac{0.1891F}{d^2} \qquad (4)$$

The Vickers hardness scale is a scale for determining the hardness of metals and carbides, which is derived from a test made by a method developed in 1924 by Smith and Sandland at Vickers Ltd. Hardness on the Vickers scale is designated HV [7,8].

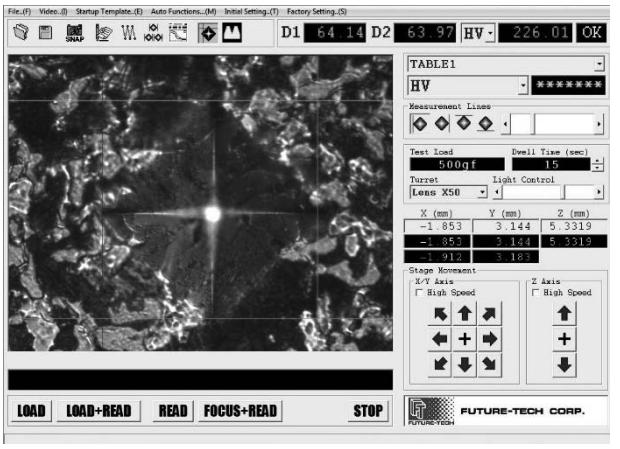

Fig. 3. The examples of data of Vickers hardness presented within the FT – ARS9000 software

1.3. Brinell hardness test

The Brinell hardness is designated by the most commonly used test standards [9]. It is defined as the ratio of the applied force to the surface area of the indentation. The unit of Brinell hardness is HBW, where H is hardness, B - Brinell, and W specifies the use of a tungsten carbide ball indenter. The upper limit of the Brinell hardness test range is 650HBW.
The Brinell method (Fig. 4) is one of the destructive tests due to the large imprint size. Brinell hardness is calculated from the formula:

$$HBW = 0.102\frac{2F}{\pi D(D-\sqrt{D^2-d^2})} \qquad (5)$$

where: F – load applied [N]
D – diameter of the ball indicator [mm]
d – impression diameter [mm].
The Brinell hardness scale is a scale for determining the hardness of metals based on a test made using a method developed by Swedish engineer Johan August Brinell in 1900 [9,10].

Fig. 4. The Brinell hardness tester [11]

2. MATERIALS AND METHODS

Hardness measurements were performed on high-purity **ARMCO Pure Iron** (steel with an iron content of at least 99.85% and very low impurities) and steel with varying carbon concentrations: 0,10%, 0,15%, 0,20%, 0,30%, 0,45%, 0,55%, 0,90%.
The test samples also included C45 steel in various technological states. The chemical composition of the samples is shown in Table 2.
Hardness tests were carried out using the Vickers, Brinell, and Rockwell methods according to standards [5, 7, 9].
In the Vickers hardness test, a load test of 500 gf and a dwell time of 15 s were used.
In the Brinell hardness test, a load force of F = 29420 N was applied and a dwell time of 15 s was used. The diameter of the ball indicator is D = 10 mm.

In the Rockwell hardness tests for scales B and C were done. The dwell times for F_0 and F were 1÷8 s and 2÷6 s, respectively.

Table 2. Chemical composition of C45 steel

Symbol classification	Element concentration [wt%]								
	C	Si	Mn	Cr	Ni	Mo	Cu	S	P
C45	0.45 ÷ 0.50	0.10 ÷ 0.40	0.50 ÷ 0.80	max ÷ 0.30	max ÷ 0.30	max ÷ 0.10	max ÷ 0.30	max ÷ 0.04	max ÷ 0.04

Hardness tests were carried out using the Vickers, Brinell, and Rockwell methods according to standards [5, 7, 9].
In the Vickers hardness test, a load test of 500 gf and a dwell time of 15 s were used.
In the Brinell hardness test, a load force of F = 29420 N was applied and a dwell time of 15 s was used. The diameter of the ball indicator is D = 10 mm.
In the Rockwell hardness tests for scales B and C were done. The dwell times for F_0 and F were 1÷8 s and 2÷6 s, respectively.

3. RESEARCH RESULT

The results of Vickers hardness measurements for C45 steel in the initial state, after normalization, and after hardening are shown in Figures 5÷7.

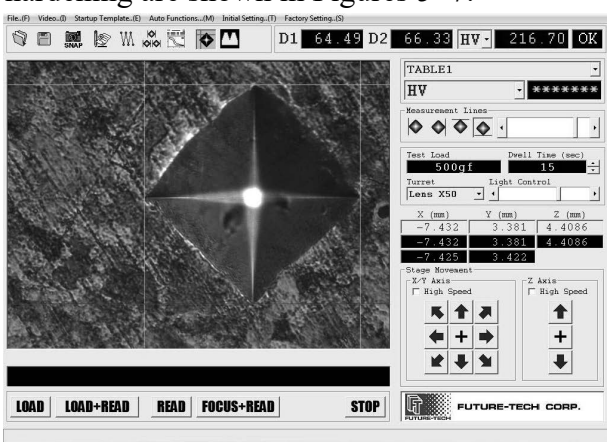

Fig. 5. Examples of Vickers hardness data of a sample in the initial state presented in FT - ARS9000 software

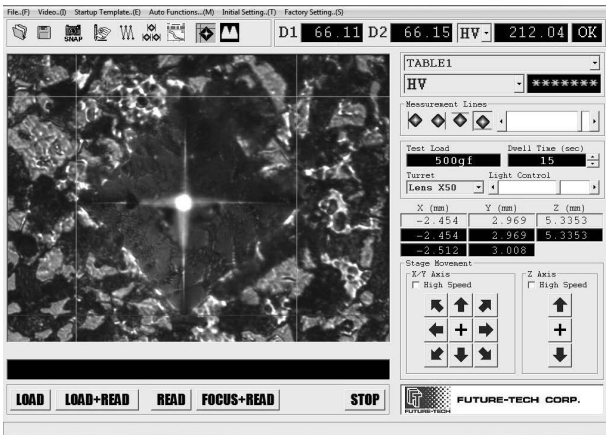

Fig. 6. Examples of Vickers hardness data of a sample after normalization presented in FT - ARS9000 software

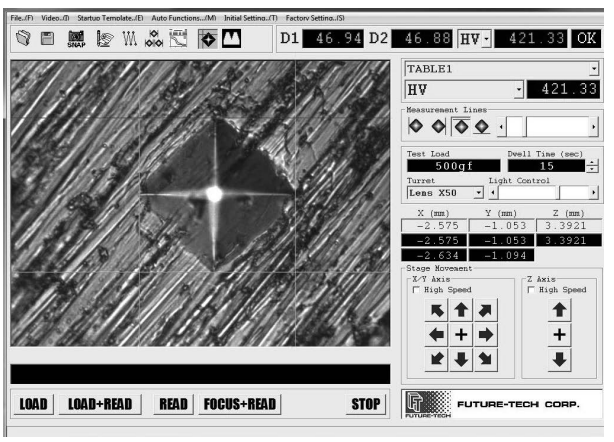

Fig. 7. Examples of Vickers hardness data of a hardening sample presented in FT - ARS9000 software

Brinell hardness measurements were made on iron and steel samples with different carbon concentrations (0.10%, 0.15%, 0.20%, 0.30%, 0.45%, 0.55%, 0.90%). Using a magnifying glass with a scale (in mm), the diameters of the imprints made with a 10 mm diameter sphere-shaped penetrator were measured.
The measured diameter values were then substituted into formula (5).
The results of the Brinell hardness measurements allowed the strength to be estimated from the relationship:

$$Rm = k \cdot HBW \qquad (6)$$

where k is a proportionality factor whose value depends on the material (Table 3).
Table 4 shows the results of imprint diameters, calculated HB hardness, and strength [12].

Table 3. The values of the proportionality coefficient k

Material	Proportionality factor k
Stal ($125 \leqslant HB \leqslant 175$)	3.33
Stal ($HB > 175$)	3.53

The Brinell hardness and strength results for steel with varying carbon concentrations are presented in Table 4 and Figure 8.

Table 4. The Brinell hardness and strength results for steel with varying carbon concentrations

The test samples	Impression diameter d [mm]	Hardness HBW	Strength [MPa]
A (pure iron)	5.2	130.9	435.9
C10 (steel containing approx. 0.1% carbon)	4.8	155.4	516.2
C15 (steel containing approx. 0.15% carbon)	4.5	178.7	630.8
C20 (steel containing approx. 0.2% carbon)	3.2	363.5	1283.2
C45 (steel containing approx. 0.45% carbon)	3.0	415.5	1466.7
C55 (steel containing approx. 0.55% carbon)	2.9	477.8	1686.6
N9 (steel containing approx. 0.9% carbon)	2.5	597.3	2108.5

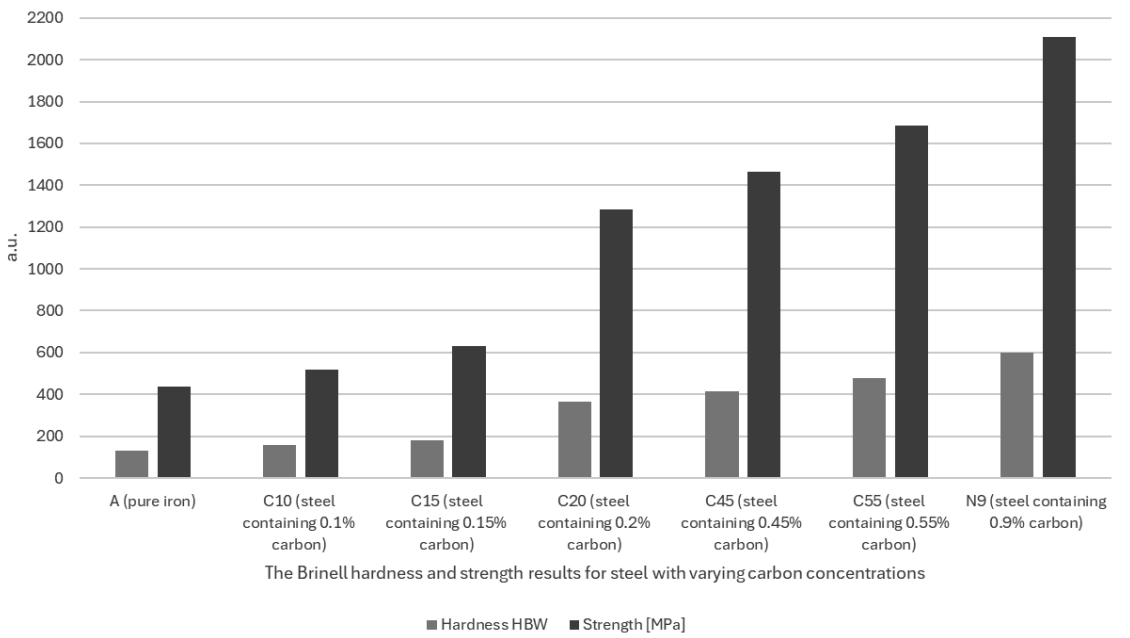

Fig. 8 . The Brinell hardness and strength results for steel with varying carbon concentrations

4. CONCLUSIONS

The following conclusions can be drawn from the research: the hardness of steel depends on its chemical composition, including carbon as the main component of steel. With the help of hardness testers, we can easily determine the hardness and strength of the tested material. The results of the Brinell hardness measurements allowed the strength to be estimated.

ACKNOWLEDGMENT

This paper is the result of a project carried out with secondary school students under the Excellence Initiative - Research University program (4th competition), Silesian University of Technology.

BIBLIOGRAPHY

1. L.A. Dobrzański, Materiały inżynierskie z podstawami technologii procesów materiałowych, Wydawnictwo Naukowe PWN, 2024.
2. G. Sundararajan, M. Roy, Hardness Testing, Encyclopedia of Materials: Science and Technology (Second Edition), Pages 3728-3736 (2001) DOI: https://doi.org/10.1016/B0-08-043152-6/00665-3.
3. S. R. Low, Rockwell Hardness Measurement of Metallic Materials, National Institute of Standards and Technology, 2001.
4. EN ISO 6508-1::2016-10 Metals – Metallic materials – Rockwell hardness test.
5. Website: https://pl.wikipedia.org/wiki/Skala_twardo%C5%9Bci_Rockwella.
6. Website: https://www.ita-polska.com.pl/baza-wiedzy/pomiary-twardosci/pomiary-twardosci-poradnik.
7. EN ISO 6507-1:2024-04. Metallic materials – Vickers hardness test.
8. Website: https://pl.wikipedia.org/wiki/Skala_twardo%C5%9Bci_Vickersa.
9. EN ISO 6506-1:2014-12. Metallic materials – Brinell hardness test.
10. Website: https://pl.wikipedia.org/wiki/Skala_twardo%C5%9Bci_Brinella.
11. Website: http://prazision.pl/pl/twardosciomierz-brinell/333-twardosciomierz-stacjonarne-przenosne-.html.
12. Website:https://pl.wikipedia.org/wiki/Skala_twardo%C5%9Bci_Brinella#:~:text=Skala%20twardo%C5%9Bci%20Brinella%20%E2%80%93%20skala%20oznaczania,zakresie%20od%203%20do%20650.

TalentDetector

31th January 2025
Gliwice, Poland

DEPARTMENT OF ENGINEERING MATERIALS AND BIOMATERIALS
FACULTY OF MECHANICAL ENGINEERING
SILESIAN UNIVERSITY OF TECHNOLOGY

INTERNATIONAL STUDENTS SCIENTIFIC CONFERENCE

Classification of polymer materials used in the manufacture of pressure pipes using computational classification models

Filip Ziarkowski[a], Rafał Honysz[b]

[a] Student of Automatic Control and Industrial Robotics, Silesian University of Technology, Faculty of Mechanical Engineering, Department of Engineering Materials and Biomaterials, email: filizia236@student.polsl.pl
[b] Silesian University of Technology, Faculty of Mechanical Engineering, Department of Engineering Materials and Biomaterials, email: rafal.honysz@polsl.pl

Abstract: The purpose of this study is to develop a computational classification model that, based on the physical properties of polymer materials such as density, tensile strength, hardness, elongation, flexural modulus, and Vicat softening temperature, classifies materials into appropriate categories (e.g., HDPE, MDPE, PP, ABS). Various classification techniques were used to build the model, such as fine tree, neural network, and ensemble, which were evaluated using errors such as standard deviation, spearman's correlation, and mean absolute error. The results indicate that the computational model can be effectively used for the classification of polymer materials depending on their mechanical and physical properties.

Keywords: materials, matlab, polimers

1. INTRODUCTION

MATLAB is a computational platform and programming language, primarily used in engineering, mathematical sciences, and data analysis. It offers advanced functions for performing computations, creating visualizations, and building models and simulations.[1]

The Classification Learner is an interactive tool available in MATLAB that enables the training, validation, and evaluation of machine learning models for classification task. Fine Tree is a classification algorithm that builds a decision tree by splitting data into groups based on significant features to predict outcomes. Ensemble is a method that integrates the results of multiple models, such as decision trees, to improve the accuracy and reliability of predictions. Neural Network is an algorithm inspired by the structure of the human brain, which uses a network of neurons to solve complicated classification and regression tasks.[4]

The database consists of various types of polymers and includes data on density, tensile strength, hardness, elongation, flexural modulus, and Vicat softening temperature. To evaluate the model's quality, errors such as Spearman's correlation, standard deviation, and mean absolute error are calculated.[2]

2. MATERIAL

The study utilized data on various polymer materials commonly used in the production of pressure pipes and other infrastructure components. Specifically, the following materials were considered: LDPE, HDPE, ABS, PE-UHMW, PP, PVC-U, PVC-C, PTFE, PC.[2] Each of these materials is characterized by specific physical and mechanical properties that influence their suitability for pressure pipe production.The mechanical and physical properties included in the model are:

- Density: Specifies the mass of a material per unit volume, affecting the weight and ease of transport of materials.
- Tensile Strength: Defines the material's ability to withstand tensile forces, which is critical for pipes exposed to mechanical forces.
- Hardness: Refers to the material's resistance to plastic deformation, significant in thecontext of resistance to mechanical damage.
- Elongation: It determines how much a material can stretch before it breaks. This is an important parameter in the analysis of material elasticity.
- Flexural Modulus: It refers to the stiffness of the material during bending, which is essential for ensuring the stability of the pipe structure under mechanical conditions.
- Vicat Softening Temperature: Specifies the temperature at which the material begins to lose its mechanical properties under heat.

The aim of the modeling was to assign a polymer material to one of the predefined categories (e.g., HDPE, MDPE, PP, ABS, PE-RT, PVC-U, PVC-C, PTFE, PC) based on its physical and mechanical properties. Such classification allows for better matching of materials to specific applications in pressure pipe production, where appropriate tensile strength, hardness, softening temperature, and elongation are key to ensuring durability and reliability.[2]

3.CONSTRUCTION OF THE COMPUTATIONAL MODEL

The process of building the model in MATLAB begins with loading the data into the environment, which can be done using the readtable function. After loading the data, it is necessary to prepare it for training. The dataset was divided into two parts: a training set 70% and a test set 30% using the cvpartition function, which allows for random data splitting. After preparing the data, the Classification Learner tool was launched. Model validation was performed using the 5-fold cross-validation method, which allowed the assessment of their effectiveness on different subsets of data.[1]

Three machine learning algorithms were used to develop classification models:

- Fine Tree: Based on decision trees and effective in simple classification tasks.
- Neural Network: A model inspired by the human brain, capable of handling nonlinear problems.
- Ensemble: A collective method that improves results through iterative learning from errors.

Subsequently, three different configuration settings were created for each algorithm, resulting in a total of nine configurations that enabled a more detailed analysis of their performance under various scenarios.

Fine Tree was divided into three different configurations.The first configuration assumed a maximum number of splits of 100 and applied a split criterion based on the Gini index.The second configuration reduced the maximum number of splits to 10 while retaining the Gini index criterion, simplifying the model and potentially preventing overfitting.The third configuration set the maximum number of splits to 25 but changed the split criterion to the twing rule.

Ensemble was configured as follows.The first configuration was based on boosted trees using the AdaBoost method, where the learner type was a decision tree with a maximum number of splits of 20.The second configuration was based on subspace discriminant, utilizing the Ensemble Subspace method and nearest neighbors. The number of learners was 10, and the subspace dimension was set to 1, providing high flexibility in classification.The third configuration also used the Subspace Discriminant method; however, in this case, the Ensemble method was changed to RUSBoost, and the learner type was decision trees with a maximum number of splits of 10, aimed at improving resistance to imbalanced data.

Neural Network was configured in three variants differing in the number of layers and the size of individual layers.The first configuration was a wide neural network with one fully connected layer of size 100, allowing for a more detailed representation of the data.The second configuration was a Narrow Neural Network with two fully connected layers, each of size 5, enabling more efficient modeling.The third configuration was also a Narrow Neural Network, but this time consisting of a single layer of size 5, allowing for fast and lightweight data processing.Such diverse configurations enabled a better understanding of the impact of various parameters on classification quality and allowed the selection of the most appropriate model.

After completing the training stage of the model, the next step was the evaluation of quality on the same dataset that was used for splitting into training and test sets. At this stage, the previously separated test data was used to verify the model's effectiveness in predicting outcomes. To assess the accuracy and quality of the model, the obtained results were compared with the actual label values in the test data by calculating appropriate metrics. Particular attention was paid to the following indicators:

- Standard deviation, which helps to understand the spread of the model's results and their distance from the mean, essential for evaluating prediction stability.
- Spearman's correlation, which assesses the extent to which the model's predictions correspond to a monotonic relationship with the actual values, verifying whether the model captured key patterns in the dataset.
- Mean absolute error, which shows the average difference between the model's predictions and the actual label values, providing a measure of accuracy.[7]

```
% Prediction using trained Model 1 (fine tree)
yfit1 = trainedModel2.predictFcn(X_test);

% Prediction using trained Model 2 (Essemble)
yfit2 = trainedModel22.predictFcn(X_test);

% Prediction using trained Model 3 (Neural Network)
yfit3 = trainedModel23.predictFcn(X_test);


 % Error calculation for model 1 (fine tree)
std_dev1 = std(y_test_num - grp2idx(yfit1));  % Standard deviation
mae1 = mean(abs(y_test_num - grp2idx(yfit1)));  % Mean absolute error
rho1 = corr(y_test_num, grp2idx(yfit1), 'Type', 'Spearman');  % Spearman correlation

% Error calculation for model 2 (Essemble)
std_dev2 = std(y_test_num - grp2idx(yfit2));  % Standard deviation
mae2 = mean(abs(y_test_num - grp2idx(yfit2)));  % Mean absolute error
rho2 = corr(y_test_num, grp2idx(yfit2), 'Type', 'Spearman');  % Spearman correlation

% Error calculation for model 3 (Neural Network)
std_dev3 = std(y_test_num - grp2idx(yfit3));  % Standard deviation
mae3 = mean(abs(y_test_num - grp2idx(yfit3)));  % Mean absolute error
rho3 = corr(y_test_num, grp2idx(yfit3), 'Type', 'Spearman');  % Spearman correlation

% Displaying results for each model
disp('Results for model 1 (fine tree):');
disp(['Standard deviation: ', num2str(std_dev1)]);
disp(['Mean absolute error: ', num2str(mae1)]);
disp(['Spearman correlation: ', num2str(rho1)]);
```

Figure 1. Matlab code fragment presenting error calculations

The error assessment process took place in the MATLAB environment, where previously exported models from the Classification Learner tool were used. The test data was processed by the trained models and their results were compared to the actual values to calculate the error.

4. EVALUATION OF THE QUALITY OF THE CALCULATION MODEL

After presenting the calculations in the MATLAB environment and performing the analysis in the Classification Learner tool, the following results were obtained:

Table 1. Results of error calculations for individual models

	Standard deviation	Spearman's correlation	Mean absolute error
Model Fine Tree No.1	16.505	0.51323	26.6441
Model Ensemle No.1	15.6879	0.82303	25.5763
Model Neural Network nr.1	15.8769	0.94608	26.4237
Model Fine Tree No.2	16.8401	0.4785	26.2881
Model Ensemle No.2	15.6011	0.92162	25.678
Network No.2	16.3297	0.37136	26.0678

Model Fine Tree No.3	16.3297	0.37136	26.0678
Model Ensemle No.3	15.69	0.67844	26.1186
Model Neural Network No.3	16.505	0.51323	26.6441

4.1 Results analysis

The results obtained for the selected models indicate differences in their performance and prediction accuracy. For the Fine Tree model No. 1, the standard deviation is 16.505, suggesting a greater divergence of predictions from the actual values. The Spearman correlation is 0.51323, indicating moderate alignment of the predictions with the actual values, and the mean absolute error is 26.6441.
The Ensemble model No. 1 achieved better results, with a standard deviation of 15.6879, a Spearman correlation of 0.82303, and a the mean absolute error is 25.5763. These results suggest higher accuracy and greater consistency of predictions compared to Fine Tree No. 1.
The Neural Network model No. 1 obtained a standard deviation of 15.8769, a Spearman correlation of 0.94608, and a mean absolute error of 26.4237, indicating even greater alignment of predictions with the actual values compared to the other models in the first group.

For the Fine Tree model No. 2, the standard deviation is 16.8401, the Spearman correlation is 0.4785, and the MAE is 26.2881, suggesting that the change in configuration did not significantly improve the results compared to the first version. However, the Ensemble model No. 2 demonstrates clearly better results, with a standard deviation of 15.6011, a Spearman correlation of 0.92162, and a MAE of 25.678, making it more accurate and consistent in this group. The Neural Network model No. 2 achieves a standard deviation of 15.9124, a Spearman correlation of 0.93514, and a MAE of 26.3729, once again indicating high prediction quality.

In the case of Fine Tree model No. 3, the standard deviation is 16.3297, the Spearman correlation is 0.37136, and the MAE is 26.0678, indicating relatively weak results in this group. The Ensemble model No. 3 achieves identical results, suggesting no performance differences compared to Fine Tree in this configuration. The Neural Network model No. 3 achieves a standard deviation of 15.69, a Spearman correlation of 0.67844, and a MAE of 26.1186, indicating better performance in this group.

The comparison of these methods allowed the identification of the model that most accurately reflected the characteristics of the test data, making it the most accurate and stable in its predictions.

5. CONCLUSIONS

As a result of the conducted analyses, classification models based on different algorithms, such as Fine Tree, Ensemble, and Neural Network, were built. The models were evaluated in terms of their performance using the 5-fold cross-validation method, which ensured the reliability of the results and the ability to assess their effectiveness on different data subsets.

The best results were obtained for Ensemble model nr 2, which featured the highest value of Spearman's correlation and the lowest standard deviation among all configurations. The results of this model indicate its high accuracy and stability in predicting values on the test data.

In summary, The analysis provided valuable conclusions regarding the effectiveness of the algorithms used effectiveness of the applied algorithms and their potential in practical applications.

BIBLIOGRAPHY

1. https://www.mathworks.com/ Accessed: 20 Oct 2024.
2. https://www.matweb.com/ Accessed: 20 Oct 2024.
3. Bishop, C. M. Pattern Recognition and Machine Learning., 2016.
4. Kamal I. M. Al-Malah ,Machine and Deep Learning Using MATLAB: Algorithms and Tools for Scientists and Engineers,2023.
5. Witten, I. H., Frank, E., Hall, M. A. Data Mining: Practical Machine Learning Tools and Techniques, 2016.
6. Goodfellow, I., Bengio, Y., Courville, A. Deep Learning , 2016.
7. Moore, D. S., McCabe, G. P., Craig, B. A. Introduction to the Practice of Statistics, 2016.
8. Chollet, F. Deep Learning with Python. Manning Publications, 2018.
9. Callister, W. D., Rethwisch, D. G. Materials Science and Engineering: An Introduction, 2018.
10. Osowski, S., Szmurło, R. Matematyczne modele uczenia maszynowego w językach MATLAB i PYTHON, 2024.

TalentDetector

31th January 2025
Gliwice, Poland

DEPARTMENT OF ENGINEERING MATERIALS AND BIOMATERIALS
FACULTY OF MECHANICAL ENGINEERING
SILESIAN UNIVERSITY OF TECHNOLOGY

INTERNATIONAL STUDENTS SCIENTIFIC CONFERENCE

Numerical analysis of the thermal strength of electrical insulators

Zuzanna Zielińska[a], Kajetan Kojm[b], Łukasz Lomania[b], Agata Śliwa[c], Marek Sroka[c], Wojciech Mikołejko[c]

[a] Student at the Silesian University of Technology, Faculty of Materials Engineering
email: zz304779@student.polsl.pl;
[b] Student of the Silesian University of Technology, Faculty of Electrical Engineering
e-mail: lukalom979@student.polsl.pl; kajekoj367@student.polsl.pl;
[c] Silesian University of Technology, Faculty of Mechanical Engineering, Institute of Engineering and Biomedical Materials,
email: agata.sliwa@polsl.pl; marek.sroka@polsl.pl; wojciech.mikolejko@polsl.pl

Abstract: The aim of this article is to present the effects of temperature on energy insulators using simulation programs such as SolidWorks and Ansys.

Keywords: Isolator, temperature, simulation.

1. INTRODUCTION

1.1. Finite Element Method (FEM)

The Finite Element Method (FEM) is one of the most widely used tools in engineering structural calculations, particularly in the context of using computer programs. It enables precise modeling of structural behavior under external influences, making it a preferred choice for material strength analyses. Thanks to its flexibility and intuitiveness, FEM is highly effective for analyzing systems with complex geometries, allowing accurate determination of stresses, displacements, and deformations. Its reliability makes it indispensable in engineering and other fields requiring precise modeling and analysis of structural behavior. [1]. The core principle of FEM involves transforming a structural model into a discrete mesh by dividing the structure into a finite number of elements. Stresses and other quantities are analyzed at the nodes of this mesh, providing detailed insights into processes within the structure and its reactions to variable loads over time. The accuracy of the analysis depends on properly defining boundary conditions and appropriately adjusting the mesh— densifying it in critical areas and simplifying it in less significant regions. Modern software, such as SolidWorks, significantly facilitates the use of FEM, offering extensive material libraries and the ability to define custom material parameters. This enables realistic modeling of the analyzed phenomena and achieving high simulation precision, making FEM a fundamental tool in modern engineering design [2].

1.2. Materials engineering of the energy insulator

Electrical insulators are a critical component of power systems, responsible for providing electrical separation between conductors and supporting structures or other network elements. They serve both an insulating function and bear mechanical loads, such as the weight of conductors or forces from wind, snow, and ice. Their applications include overhead lines, power stations, and switchgear across high, medium, and low-voltage systems. Thanks to their insulating properties, they protect against electric shock, prevent short circuits, and minimize energy losses. To meet technical requirements, insulators must be made of materials with high electrical and mechanical strength, as well as chemical and thermal resistance, ensuring reliability under variable environmental conditions. The production of insulators involves various materials with specific physical and electrical properties. Porcelain, a traditional insulating material, is noted for its high mechanical strength, resistance to moisture and contamination, and stability over a wide temperature range, up to 200°C. Tempered glass, primarily used in suspension and support insulators, features good mechanical strength, UV resistance, and the ability to facilitate visual inspection of damage. Its operational temperature range is -60°C to 150°C. Composite materials, such as fiberglass combined with elastomers or silicone resins, are increasingly popular due to their lightweight nature, flexibility, and resistance to corrosion, UV radiation, and ozone. Their thermal resistance reaches up to 250°C. The thermal endurance of power insulators is a key factor in ensuring reliability and operational safety. Each insulating material has a defined working temperature, which reflects its capacity to withstand heat generated by electric current without losing its mechanical and electrical properties. High temperatures can lead to material degradation, causing chemical changes, shrinkage, cracking, and, in extreme cases, total insulator failure. Insulators must be designed to resist short-term thermal overloads, which may occur due to faults or surges, as well as long-term thermal stresses from continuous operation under voltage. High temperatures must not compromise essential dielectric properties, such as surface and volume resistance. Resistance to sudden temperature changes, or thermal shocks, often encountered in overhead lines, is also crucial. Optimal material selection and insulator design, considering their thermal endurance, are essential for ensuring reliability, longevity, and safe operation of power equipment. Numerical analysis of thermal resistance allows precise determination of insulator behavior under extreme conditions, enabling the design of more efficient and durable solutions in the energy sector [3, 4].

2. PURPOSE OF THE WORK

The aim of this study is to simulate thermal actions on a modelled energy insulator in order to investigate the effect of temperature on its mechanical performance.

3. METHODOLOGY

To perform the numerical analysis, the insulator-conductor system was modeled in the SolidWorks environment (Fig. 1). The cad model was then imported into Ansys software where boundary conditions were prepared to calculate the temperature distribution. The first step in Ansys software was to prepare a 1[mm] finite element mesh for both components (Fig. 2). Then a bonded contact was added between the parts (Fig. 3). The next step was to add thermal loads

such as an ambient temperature of 22[°C] and a temperature on the wire of 1000[°C] (Fig. 4). The final step was to assign materials to the circuit such as copper and C-110 technical porcelain.

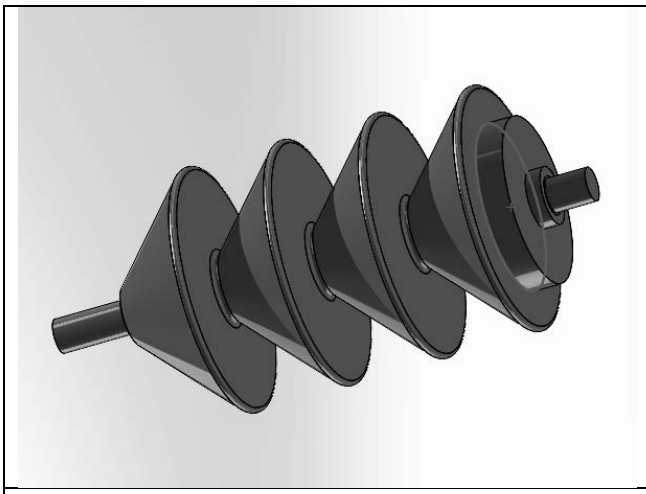

Figure 1. Energy insulator model.

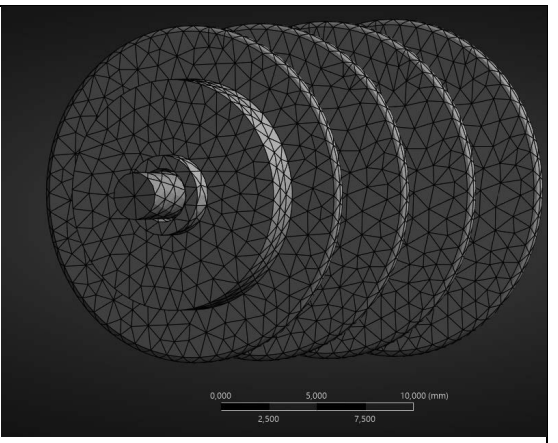

Figure 2. Model after grid application.

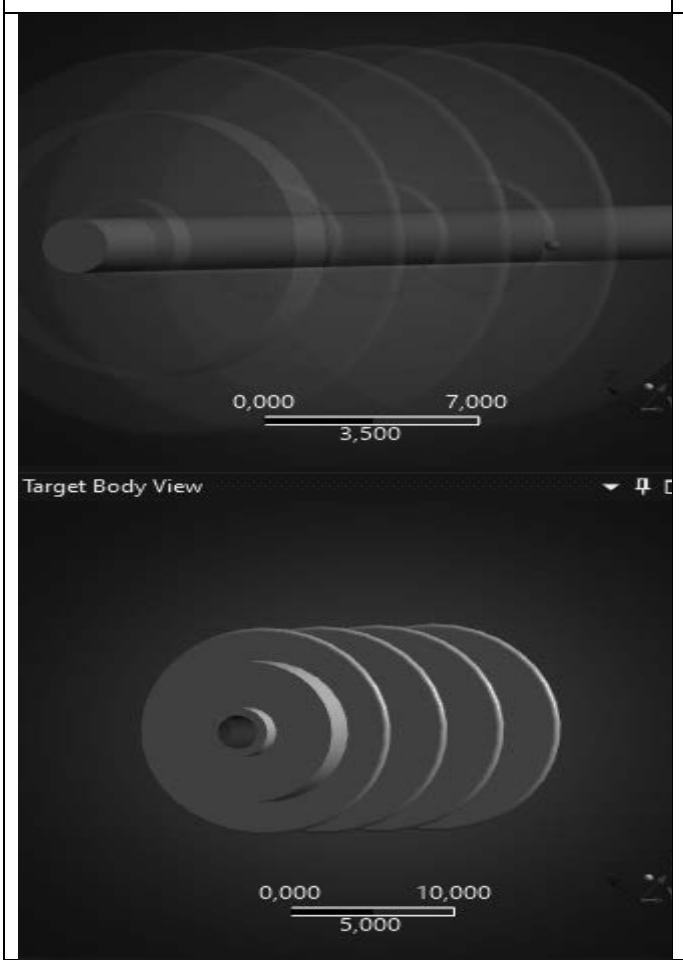

Figure 3. Contact surfaces between conductor and insulator

Figure 4. Temperature task site.

4. RESULTS AND DISCUSSION

Numerical analysis provided the result of the temperature distribution on the insulator model. This result shows the places from which the rapid temperature increase begins, and thus, in the case of ceramics, the places from which cracking resulting from thermal shock can initiate. Figures 5 and 6 show the temperature distribution of the insulator from different views. Numerical calculations in the thermal range of insulators can assist designers in terms of component operating temperatures, thermal shock resistance or indicate thermal conductivity properties.

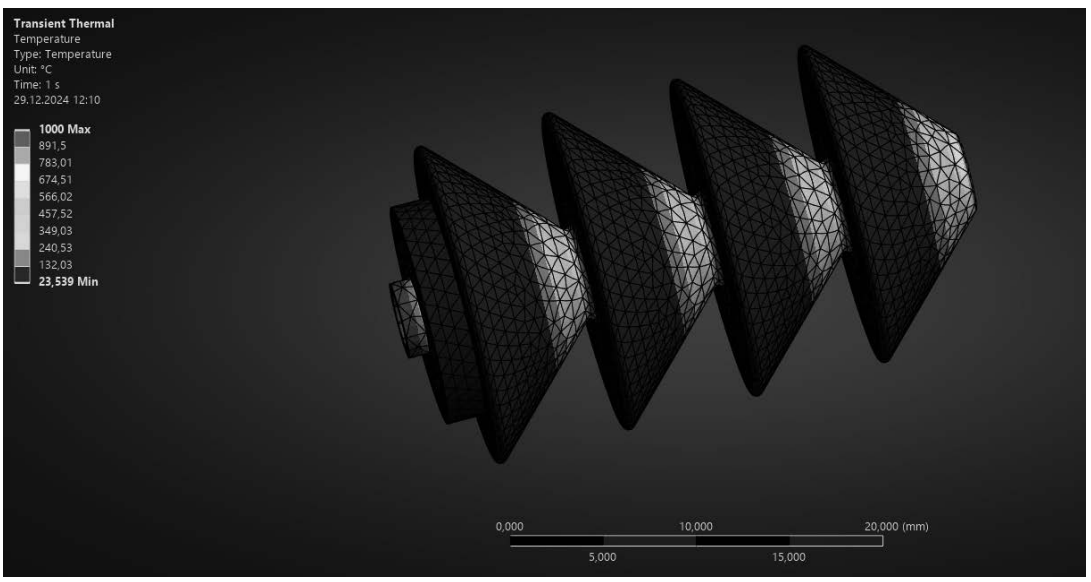

Figure 5. Temperature distribution result.

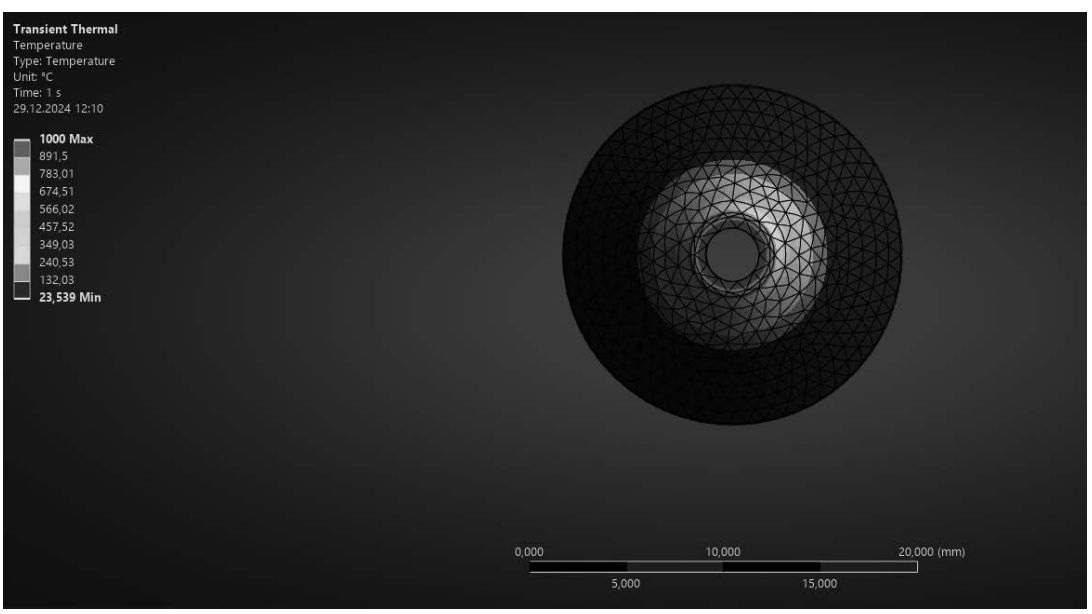

Figure 6. Temperature distribution result.

BIBLIOGRAPHY

[1] J. Zielnica, Wytrzymałość materiałów, Wyd. Pol. Poznańskiej, 1996.
[2] M. Sydor, Podstawy komputerowo wspomaganego projektowania Wprowadzenie do CAD., Warszawa: PWN, 2009
[3] B. Florkowska J. Furgał „Diagnostyka wysokonapięciowych układów izolacyjnych urządzeń elektroenergetycznych", Wydawnictwa AGH, Kraków 2009
[4] H. Markiewicz „Bezpieczeństwo w elektroenergetyce" Wydawnictwo WNT, 2017

TalentDetector

31th January 2025
Gliwice, Poland

DEPARTMENT OF ENGINEERING MATERIALS AND BIOMATERIALS
FACULTY OF MECHANICAL ENGINEERING
SILESIAN UNIVERSITY OF TECHNOLOGY

INTERNATIONAL STUDENTS SCIENTIFIC CONFERENCE

Numerical analysis of mechanical stresses acting on overhead line power cables

Zuzanna Zielińska[a], Kajetan Kojm[b], Łukasz Lomania[b], Agata Śliwa[c], Marek Sroka[c], Wojciech Mikołejko[c]

[a] Student at the Silesian University of Technology, Faculty of Materials Engineering
email: zz304779@student.polsl.pl;
[b] Student of the Silesian University of Technology, Faculty of Electrical Engineering
e-mail: lukalom979@student.polsl.pl; kajekoj367@student.polsl.pl;
[c] Silesian University of Technology, Faculty of Mechanical Engineering, Institute of Engineering and Biomedical Materials,
email: agata.sliwa@polsl.pl; marek.sroka@polsl.pl; wojciech.mikolejko@polsl.pl

Abstract: The article focuses on the issues related to power line cable sag. It outlines the capabilities of SolidWorks and Ansys in carrying out numerical analyses and determining the level of sag in question.

Keywords: Cable, overhang, simulation.

1. INTRODUCTION

1.1. Finite Element Method (FEM)

The Finite Element Method (FEM) is one of the most widely used tools in structural engineering calculations using computer software. It enables the precise modelling of the behaviour of structures under the influence of external factors, making it a popular choice for material strength simulations. Thanks to its flexibility and intuitiveness, FEM is applicable to the analysis of systems with complex geometries, allowing accurate determination of stresses, displacements and deformations. Its reliability makes it indispensable in engineering and other fields requiring precise modelling and analysis of structural behaviour.[1]

The basis of FE is the conceptual transformation of the model to a discretisation mesh, which means reducing the structure to a finite number of elements. Stresses are distributed along these elements and their values calculated at the nodes of the mesh. Such an analysis makes it possible to obtain important information about the processes taking place in structures and their response to varying forces over time. However, the accuracy of this method depends on the proper definition of the boundary conditions and the appropriate adjustment of the mesh - by thickening it in critical areas or diluting it in less important areas. Modern software, such as Solidworks, significantly supports the use of FEA by offering extensive material libraries and the ability to

define custom parameters for structural materials. This makes it possible to realistically model the analysed phenomenon and achieve maximum precision in simulations, making FEA one of the key tools in modern engineering design."[2]

1.2. Materials engineering for power cables

Materials engineering in the context of power cables plays a fundamental role in the processes of designing, manufacturing and maintaining their functionality and performance. Power cables used in overhead lines typically consist of conductors made of highly electrically conductive materials such as aluminium or copper. Increasingly, modern composite materials are also being used, which combine high mechanical strength with lower weight to reduce stresses and reduce cable sag. The overhang of power cables, i.e. the natural deflection of the cables due to their weight and external forces such as wind, ice or varying temperatures, is a key design parameter and aspect of the mechanical analysis of overhead lines. It directly affects the distribution of stresses in the cables and the stability of the entire line, so its proper design is fundamental to the safety and reliability of the electricity infrastructure.

The amount of sag depends on the mechanical properties of the material, span length, preload, ambient temperature and operating loads. Correct design requires consideration of both the geometrical parameters of the line and the material characteristics of the cables. This phenomenon is modelled using parabolic formulas or advanced chain curve equations that take into account dynamic changes in loads and operating conditions. Too little sag can lead to excessive stresses in the cable, increasing the risk of damage and reduced cable life, while too much sag can result in dangerous contact with the ground or other objects. To avoid such problems, advanced numerical tools such as the Finite Element Method (FEM) are increasingly being used in the overhead line design process. These allow for the accurate modelling of mechanical stresses and the prediction of cable behaviour under varying operating conditions, which makes it possible to optimise the design and increase the durability of the entire system.

The use of modern technologies and materials in the analysis of sag and stress in power cables allows more efficient management of the infrastructure. As a result, a higher level of safety and reliability of power transmission systems can be achieved, while extending their service life and reducing the risk of failure [3,4,5].

2. PURPOSE OF THE WORK

The aim of this study is to use the simulation programme ANSYS to determine the sag level of a power cable in order to check that the cable sag does not exceed the permissible standards associated with it.

3. METHODOLOGY

The AsXSn 0.6/1 kV 1x70mm2 power cable was modeled for analysis. The cable model was made in SolidWorks where the core and insulation of the cable were modeled and the models were positioned (Fig. 1 - 3). Simulations were carried out in Ansys software. In order to properly perform the numerical analysis, boundary conditions were implemented such as, a finite element mesh of 5[mm] for the cable insulation and 2[mm] for the cable core (Fig. 4). The effect of the

earth's attraction force was then added to the analysis (Fig. 5). The final step in preparing the numerical model was to take away all the degrees of freedom at both ends of the cable (Fig. 6) and apply a Bonded contact between the components of the system. The cable core is made from aluminium and the insulation from PVC.

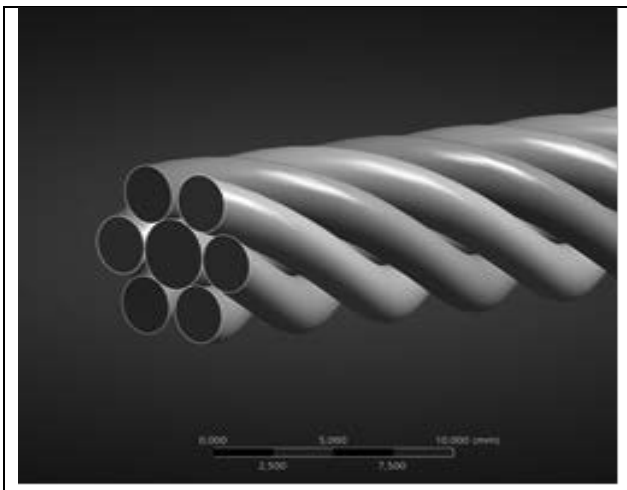

Figure 1. CAD model of cable core.

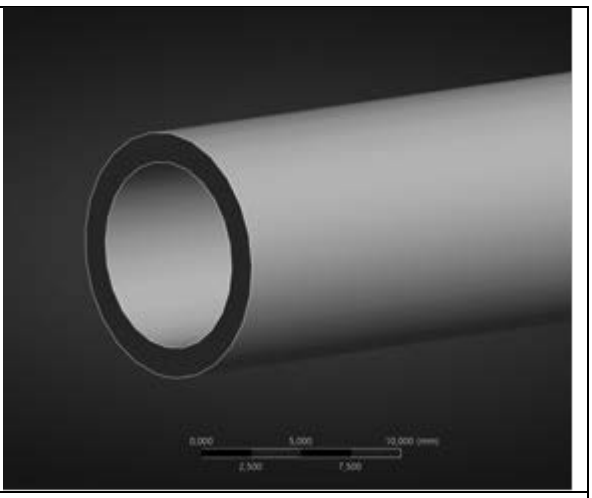

Figure 2. CAD model of cable insulation.

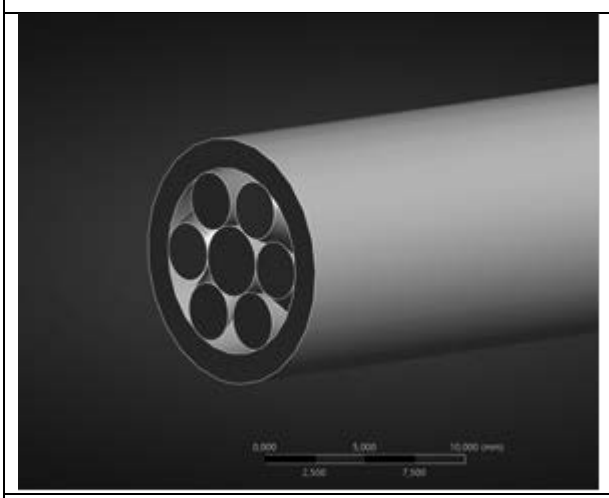

Figure 3. CAD model of cable

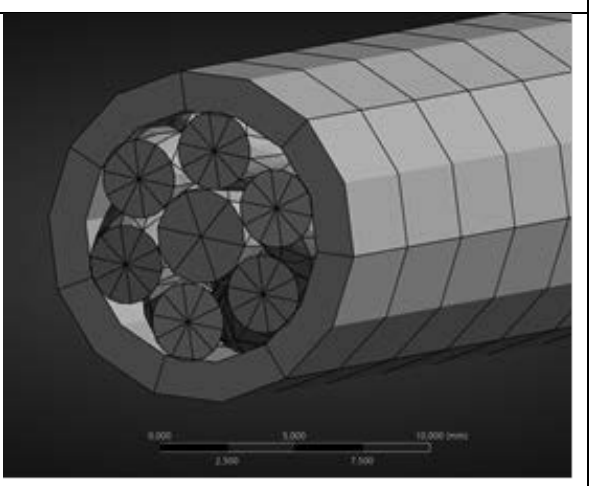

Figure 4. Model grid.

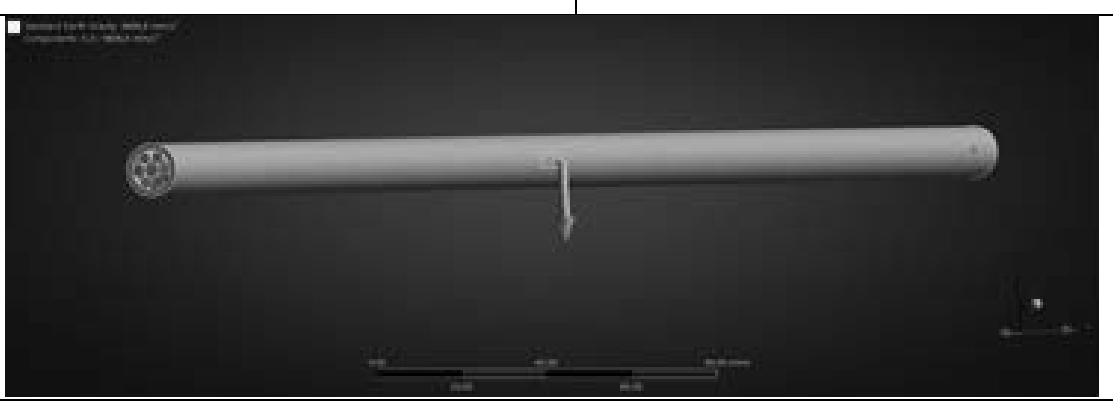

Figure 5. Direction of application of gravitational force.

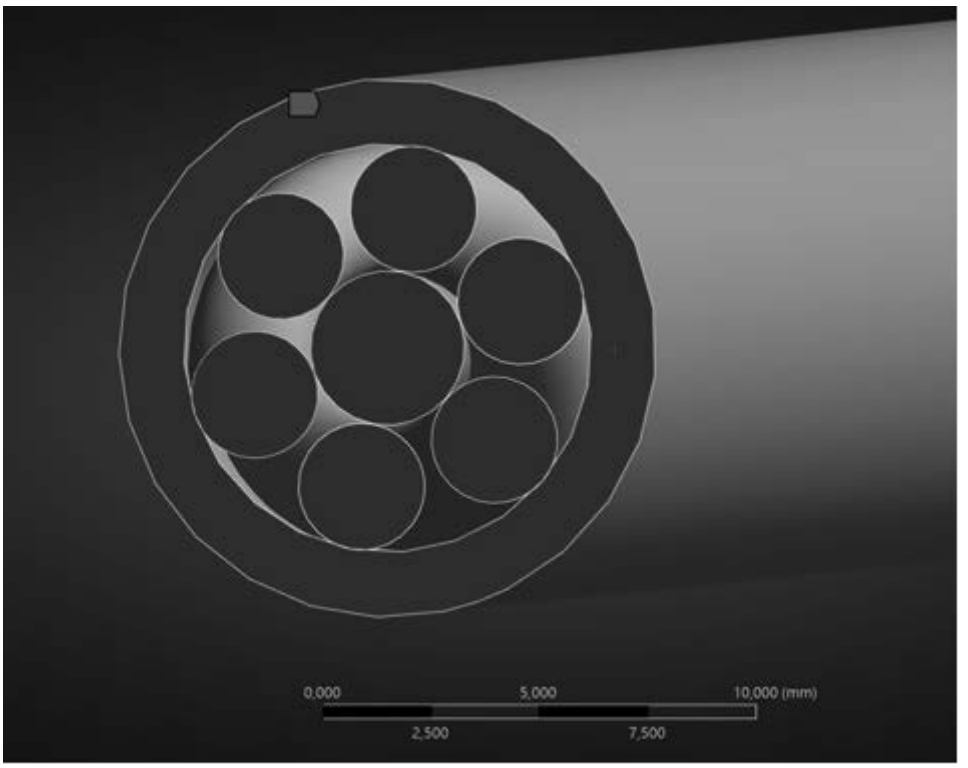

Figure 6. The place where degrees of freedom are taken away.

4. RESULTS AND DISCUSSION

As a result of the numerical analysis, the expected results of the displacement of the model (Table 1) of the cable under the action of its mass alone and the effect of the earth's gravitational force were obtained. After calculations, the displacement distribution was obtained (Fig. 7) and the same displacement distribution was compared with the undeformed result (Fig. 8). For the 0.5[m] cable used in the analysis, maximum displacements of 1.9523e-003[mm] were obtained. The prepared analysis presents a quick and easy way to prepare a model for cable sag calculations, which is helpful when designing an overhead cable line. Using a simulation program is much faster and more efficient than conducting physical experiments. As a result, it is possible to analyze many variations of cable lengths or other engineering materials in a short period of time. The simulation can be used in the design and maintenance of energy infrastructures, for example in determining the optimum spacing between poles, minimising the risk of cable breakage or optimising cable length according to operating conditions. With simulation analysis, potential problems can be detected, such as excessive stresses in the cable or insufficient ground clearance, which can lead to safety risks.

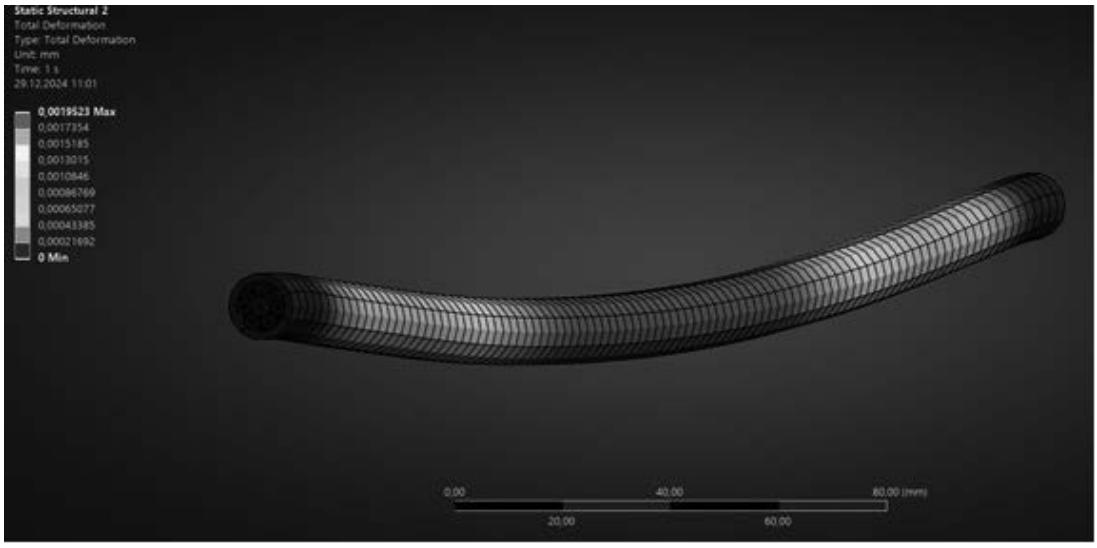

Figure 7. Distribution of cable displacements.

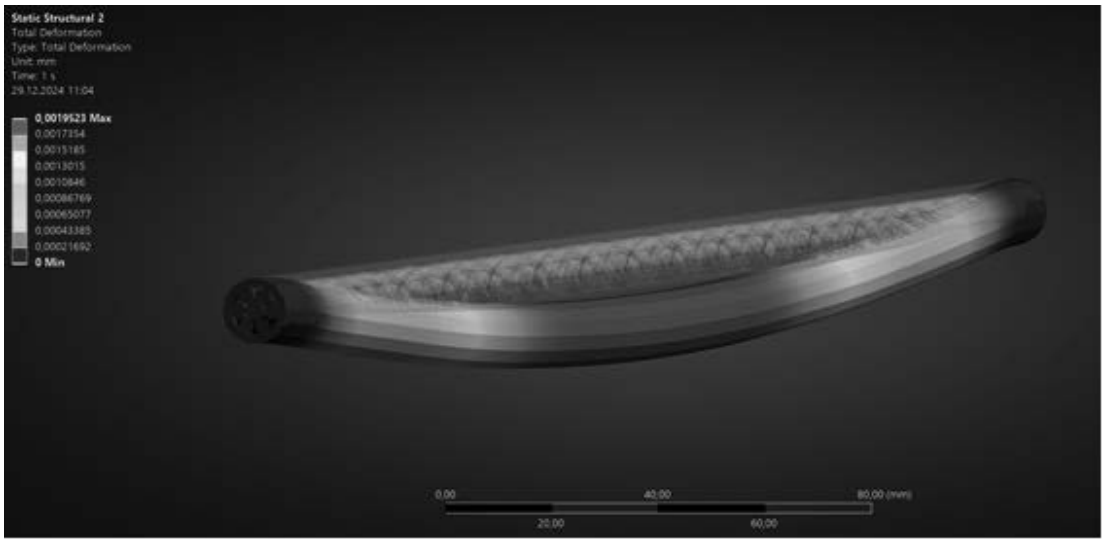

Figure 8. Distribution of cable displacements with view of undeformed cable.

Table 1. Results of cable displacement distribution.

	Time [s]	Minimum [mm]	Maximum [mm]	Average [mm]
1	1.	0.	1,9523e-003	1,1937e-003

BIBLIOGRAPHY

[1] J. Zielnica, Wytrzymałość materiałów, Wyd. Pol. Poznańskiej, 1996.
[2] M. Sydor, Podstawy komputerowo wspomaganego projektowania Wprowadzenie do CAD., Warszawa: PWN, 2009

[3] P. Zydroń, J. Roehrich, Pomiary i modelowanie wpływu parametrów konstrukcyjnych kabli elektroenergetycznych na występujące w nich zjawiska falowe. Wydział Elektrotechniki i Automatyki Politechniki Gdańskiej, 2010
[4] J. Grobicki, M. Germata, Przewody i kable elektroenergetyczne, PWN, 2019
[5] D. Złotecka, Nadmierne zwisy linii WN jako przyczyna awarii w systemach elektroenergetycznych. Politechnika Poznańska, Instytut Elektroenergetyk, 2018

TalentDetector

31th January 2025
Gliwice, Poland

DEPARTMENT OF ENGINEERING MATERIALS AND BIOMATERIALS
FACULTY OF MECHANICAL ENGINEERING
SILESIAN UNIVERSITY OF TECHNOLOGY

INTERNATIONAL STUDENTS SCIENTIFIC CONFERENCE

Key connections between Production Planning and Scheduling, Assembly Systems Organization, and Laser Processing

Dominik Towarnicki[a], Katarzyna Furman[a], Hubert Przybyszewski[a], Mirosław Bonek[b], Oleh Polishchuk[c], Boris Gitolendia[d]

[a] Silesian University of Technology, Faculty of Mechanical Engineering, email: katafur136@student.polsl.pl, domitow239@student.polsl.pl
[b] Silesian University of Technology, Faculty of Mechanical Engineering, Department of Engineering Materials and Biomaterials
[c] Khmelnitskyi National University, Faculty of Engineering, Transport and Architecture, Ukraine
[d] Georgian Technical University, Faculty of Transport Systems and Mechanical Engineering, Tibilisi, Georgia

Abstract: Laser processing technology, including cutting, welding, marking, and micromachining, is a highly precise and versatile method used in various industries such as automotive, aerospace, and medical. To maximize its efficiency, production planning, scheduling, and assembly system organization play crucial roles. These elements ensure optimal machine utilization, integration with advanced management systems, and seamless synchronization of processes, ultimately enhancing cost-effectiveness, quality, and flexibility in production systems.

Keywords: Laser processing, production planning, scheduling, assembly system organization, precision manufacturing, automation, ERP/MES integration, waste minimization.

1. INTRODUCTION

Production planning and scheduling, along with the organization of assembly systems, are fundamental management processes aimed at optimizing resource utilization and ensuring smooth order fulfillment. When integrated with advanced technologies like laser processing, these processes gain additional significance. Laser processing, encompassing precision techniques such as cutting, welding, marking, and micromachining, requires meticulous management to achieve maximum efficiency and quality. This document explores the key connections between production planning, assembly system organization, and laser processing, highlighting their combined impact on modern manufacturing.

1.1 The Connection Between Production Planning and Scheduling and Laser Processing

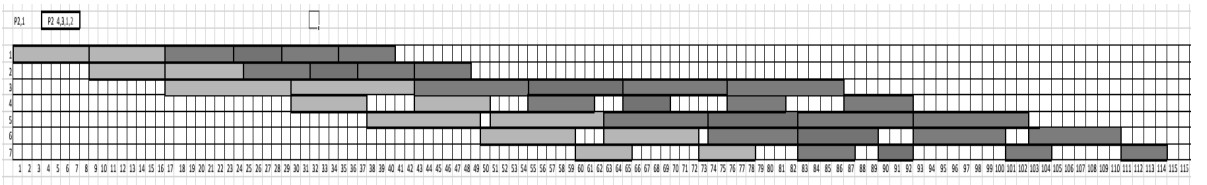

Figure 1 Gantt chart for a laser processing process

Production planning and scheduling involve key processes such as task prioritization, resource allocation, time management, and cost optimization. In the context of laser processing, precise planning is particularly crucial due to the following factors:

Optimal Machine and Resource Utilization
Laser processing machines are expensive to acquire and maintain. Effective planning minimizes machine downtime by organizing continuous operations and promptly addressing machine failures through task reallocation.

Sequencing of Production Orders
Laser processes vary based on material type, thickness, and required precision. Planning enables the grouping of tasks with similar technological requirements, reducing machine setup times and enhancing efficiency.

Time Management and Scheduling
Despite its precision, laser processing can be time-consuming for complex components. Scheduling predicts completion times for each stage, ensuring timely deliveries and overall production efficiency.

Integration with ERP/MES Systems
Modern enterprises use ERP (Enterprise Resource Planning) and MES (Manufacturing Execution System) tools. Laser processing integrates seamlessly with these systems, facilitating progress monitoring, quality control, and dynamic scheduling adjustments.

Waste Minimization and Quality Control
Laser technology significantly reduces material waste. Through planning, raw material utilization is optimized, for instance, by designing cutting patterns to minimize offcuts, thereby enhancing cost efficiency and sustainability.

1.2. The Connection Between Assembly System Organization and Laser Processing

The organization of assembly systems focuses on designing, implementing, and optimizing assembly processes, encompassing workstation layout, material flow management, and quality assurance. Laser processing aligns with these systems through the following key aspects:

Precision Preparation of Components
Laser processing delivers components with high dimensional accuracy, ensuring easier assembly, fewer corrections, and higher quality of final products.

Integrated Production Processes
In modern production lines, laser processing integrates with assembly systems via industrial robots that transport components between laser stations and assembly workstations, streamlining material flow and eliminating bottlenecks.

Automation and Robotics
Both laser processing and assembly systems often rely on robotics. System design ensures machine collaboration, process synchronization, and minimal downtime, enhancing productivity.

Modularity and Flexibility of Assembly Systems
Laser processing's adaptability to various materials and patterns supports modular assembly systems. This facilitates swift production changes, whether for new products or shifting market demands.

Real-Time Quality Control
The precision of laser technology ensures consistent component quality, simplifying real-time quality control. Advanced inspection systems integrated into both laser processing and assembly processes further enhance reliability.

Waste Reduction and Cost Optimization
Laser processing minimizes material loss, lowering component costs. In assembly systems, this translates to reduced raw material consumption and fewer defects, improving overall cost-efficiency.

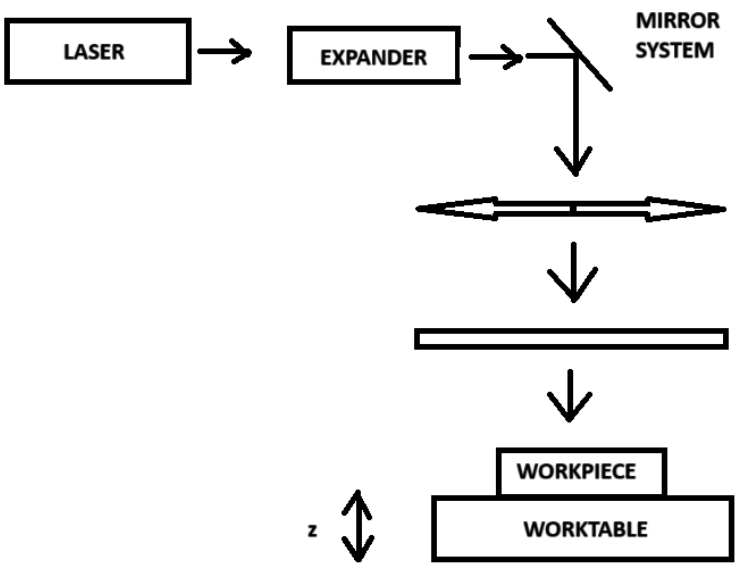

Figure 2 Diagram of the research setup for laser processing (own work)

1.3. The Connection Between System operation and reliability and Laser Processing

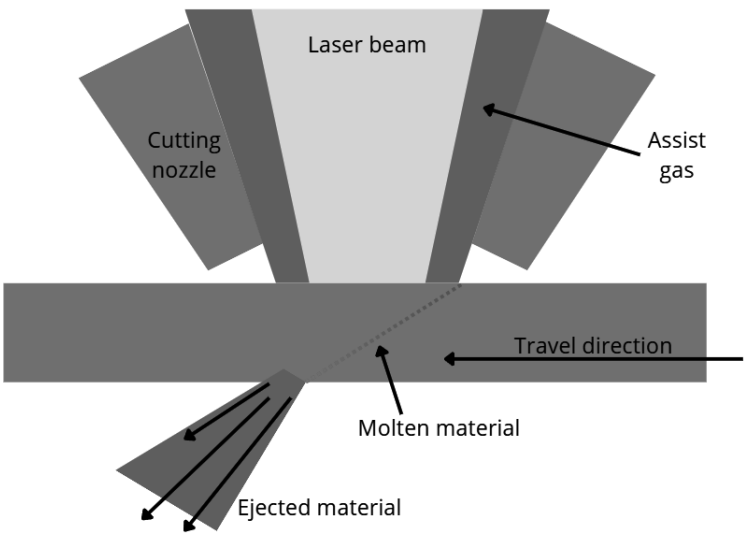

Figure 3 Laser Cutting

System Operation and Reliability
System operation ensures the efficient and uninterrupted functioning of production processes, while reliability focuses on maintaining consistent performance and minimizing downtime. Laser processing supports these goals through the following key aspects:

Improved System Performance
Laser processing ensures precise and repeatable operations, which reduces variability in production and stabilizes system performance. This leads to greater operational consistency.

Minimized Equipment Stress
The non-contact nature of laser processing minimizes mechanical wear and tear, reducing maintenance requirements and extending the lifespan of critical components, contributing to overall system reliability.

Higher Uptime Through Predictive Maintenance
Modern laser systems are equipped with sensors and monitoring tools that allow for predictive maintenance. By detecting potential faults early, they help prevent unexpected downtimes and ensure continuous system operation.

Enhanced Reliability of Production Outputs
The precision of laser technology minimizes defects and variability in processed components, ensuring that production outputs meet consistent quality standards, thereby increasing the reliability of the final products.

Integration into Reliable Production Systems
Laser processing integrates seamlessly with automated production systems, ensuring smooth workflows and synchronized operations. This avoids production delays and improves system reliability.

Automation Reduces Human Error
By automating complex or repetitive tasks, laser systems reduce human intervention and the potential for operator-related errors. This further enhances the reliability and consistency of system operation.

Real-Time Quality Control for Stability
Integrated inspection systems in laser processing enable real-time quality checks, ensuring consistent production quality. This proactive approach reduces waste, prevents defects, and maintains system stability.

2. CONCLUSION

Laser processing and the organization of production and assembly systems are complementary areas that significantly enhance manufacturing efficiency. By integrating laser precision with robust planning and assembly strategies, businesses can reduce costs, improve quality, and increase flexibility. The optimal combination of these technologies and management approaches is essential for thriving in today's competitive industrial landscape.

ACKNOWLEDGEMENTS

The work was created as part of project based learning - PBL, in the 11th competition under the Initiative of Excellence - Research University, Silesian University of Technology, Gliwice, Poland and as part of project of Students Scientific Circle of Laser Surface Treatment under the Initiative of Excellence - Research University, Silesian University of Technology, Gliwice, Poland.

BIBLIOGRAPHY

1. Groover, M. P. (2020). Automation, Production Systems, and Computer-Integrated Manufacturing. Pearson Education.
2. A comprehensive resource on advanced manufacturing technologies and the role of planning in their efficient implementation.
3. Steen, W. M., & Mazumder, J. (2010). Laser Material Processing. Springer.
4. An in-depth exploration of laser processing technologies and their applications in industrial manufacturing.
5. Chryssolouris, G. (2006). Manufacturing Systems: Theory and Practice. Springer.
6. A guide connecting manufacturing system theories with practical examples, including the use of laser technologies.

7. Slack, N., Brandon-Jones, A., & Johnston, R. (2021). Operations Management. Pearson Education.
8. Details production management processes, including scheduling, and their significance across various industries.
9. Sharma, S. (2019). Assembly Line Design: Balancing and Optimizing Performance. Springer.
10. Focuses on assembly system design and optimization, with examples incorporating advanced technologies.
11. Bozer, Y. A., & Hsieh, Y. Y. (2004). Material Handling Systems. Wiley.
12. Explains concepts of material flow design applicable to integrating laser processing with assembly systems.

TalentDetector
31th January 2025
Gliwice, Poland
DEPARTMENT OF ENGINEERING MATERIALS AND BIOMATERIALS
FACULTY OF MECHANICAL ENGINEERING
SILESIAN UNIVERSITY OF TECHNOLOGY
INTERNATIONAL STUDENTS SCIENTIFIC CONFERENCE

Surface Modification Analysis of Titanium Gyroid Scaffolds for Bone Implant Applications

Sichale Worku Fita[a], Mirosław Bonek[b], Sebastian Sławski[c], Anna Woźniak[d]

[a] Silesian University of Technology, Faculty of Mechanical Engineering, Department of Engineering Materials and Biomaterials, email: sichale.fita@gmail.com
[b] Silesian University of Technology, Faculty of Mechanical Engineering, Department of Engineering Materials and Biomaterials
[c] Silesian University of Technology, Faculty of Mechanical Engineering, Department of Theoretical and Applied Mechanics
[d] Silesian University of Technology, Faculty of Mechanical Engineering, Department of Engineering Materials and Biomaterials

Abstract: This research investigates how numerical methods can simulate the mechanical characteristics of titanium gyroid scaffolds employed in bone implants. The study examines stress distribution and deformation using advanced surface coatings like graphene oxide and hydroxyapatite under various loading conditions. Finite Element Analysis underscores the effect of coating thickness and material characteristics on scaffold performance, highlighting their significance in improving mechanical integrity. The results focus on enhancing scaffold design to achieve better load distribution.

Keywords: scaffold, , coating, stress analysis, deformation, finite element method

1. INTRODUCTION

Titanium and its alloys are commonly used in biomedical applications because of their mechanical strength and resistance to corrosion; however, their biological inertness needs surface modifications to improve cell interaction and integration with bone tissue. Numerical methods, such as e.g. finite element method (FEM), are capable of modeling the mechanical behavior of modified scaffolds when subjected to physiological loads, thus ensuring structural integrity. It can also simulate the interactions between the scaffolds.
The thickness of the coating and the type of material are crucial elements that affect stress distribution and mechanical integrity in titanium gyroid scaffolds used for bone implants. The FEM is widely utilized to examine these effects, offering valuable insights into the best coating configurations for improved implant performance. The relationship between coating thickness, material characteristics, and stress distribution is intricate, carrying important consequences for implants' mechanical stability and durability.
The thickness of the coating plays a crucial role in influencing the stress distribution throughout the coating-substrate system. Higher coating thickness can change both the location and

magnitude of maximum stress concentrations, which are essential for assessing the load-bearing capacity and identifying potential failure points of the implant [1]. Bone-coating relations, potentially enhancing the lifetime and mechanical integrity of the implant [2].

2. LITERATURE REVIEW

For investigating previous ideas reached by researchers, two keywords,**“** titanium gyroid scaffolds “ OR “ their applications in bone implants” was used. According to Web of Science data, till 2025 5771 Studies have been done. During the last 5 years, starting from 2019, 2084 Articles have been published. This shows the importance of this topic for future human bone replacement.

Those Titanium scaffolds, specifically constructed from Ti6Al4V, demonstrate a combination of higher porosity, flexible mechanical properties, and improved osteointegration, making them appropriate for orthopedic applications. According to C. M Suryawanshi et al. Gyroid structures show a significant decrease in effective elastic modulus, bringing it more in similarities to that of natural bone, thereby decreasing the stress shielding effect [3]. Additionally, Their Compression tests show these scaffolds are capable of supporting substantial loads while preserving their structural integrity, which is crucial for applications that need load-bearing capacities. While, Huo et al. indicate that the normalized Young’s modulus and yield stress are related to relative density, allowing modified mechanical properties [4].

Titanium gyroid scaffolds are now known as a strong choice for bone implants, due to their unique geometric and mechanical properties that improve osseointegration and minimize stress shielding. The porous structure of these scaffolds increases their integration with human bone, making them ideal for orthopedic applications. As an example studies show that Gyroid structures show flexible mechanical properties, indicating a normalized Young’s modulus ranging from 1.05% to 20.77% based on relative density, which helps in reducing stress shielding [4]. On the other hand, the elastic modulus of Ti-6Al-4V gyroid scaffolds can be modified to align with that of natural bone, improving osteointegration [3]. Additionally, Histological examinations show that titanium is the best metal implant because it was combined with its surrounding bone and dental tissues in human and animal models [5].

The purpose of this article is to analyze the effects of surface coatings on the mechanical behavior of titanium gyroid-structured scaffolds for bone implants to improve the challenge of suitability, mechanical strength, and load distribution by evaluating deformation properties and stress distribution.

3. METHODOLOGY AND MATERIAL

Finite Element Analysis (FEA) is a widely used computational technique that simulates mechanical behavior across different loading situations, offering helpful insights into stress distribution and deformation [6]. Many studies have used different titanium alloys, such as pure Ti, and Ti6Al4V [7], and TiZrNb with a focus on improving their wear resistance, hardness, and corrosion resistance using a coating mechanism.

3.1 Material and Structural Parameter Collection

Material properties such as Young modulus, Poisson's ratio, yield strength, and density have been collected from the met web of element property data, and the Book of Titanium alloy guide [8] and listed in Table 1.

Table 1. Basic mechanical properties of Titanium alloy

No.	Material	Young modulus [GPa]	Poisson's ratio	Yield strength [MPa]	Density [g/cm3]
1	Ti6Al4V	113.8	0.342	880	4.43
2	TiZrNb	80	0.31	910	6.12
3	Pure Ti	116	0.34	140	4.5

Graphene coatings (C= pure carbon) are the most effective coatings for improving mechanical performance and biocompatibility in biomedical implants and scaffolds. This coating is used for improving the mechanical properties of titanium alloys, and their wear resistance, and produce a lightweight, robust surface that promotes improved cell adhesion and proliferation. The second material used as a coating is bioceramic (calcium-based coating) specifically, hydroxyapatite, which facilitates osseointegration by creating a chemical connection with the surrounding tissue. Doped hydroxyapatite coatings improve biological performance and stability, successfully addressing the inertness of titanium surfaces [9].
From the met web of element property data, and book of Titanium alloy guide [8] the basic mechanical properties of selected coating materials have been possessed. Those properties are listed in Table 2.

Table 2. Basic mechanical properties of selected coating material.

No.	Coating material	Young modulus [GPa]	Poisson's ratio	Yield strength [MPa]	Density [g/cm3]
1	HA, hydroxyapatite	0.149	0.3	2.2	1.8
2	GO, graphene oxide	225	0.31	125	2.2

For HA, according to Gunawarman et al. coating thickness of approximately 10 μm implies it is effective, offering adequate bioactivity while maintaining mechanical integrity [10]. So, coatings at thicknesses of 10μm, 25μm, and 50 μm are used. GO coating thickness of around 3-5 μm is advised to enhance osseointegration and promote osteogenic differentiation, in addition to promoting mechanical stability. In the research coating thickness of 10μm,25μm, and 50μm have been investigated.

3.2 Geometry Design

To see constitutive behavior modeling and scaffold design, researchers recommended that the ideal design of a scaffold, i.e. its microarchitecture, has elements such as high porosity, appropriate connectivity of pore structures, and a sufficient specific surface area to facilitate cell attachment, segregation of new matrix, and proliferation [11].
For this analysis, R.V. i.e. single part of the gyroid which will be used as a general analysis for a large structure(as shown in Figure 1 below) was used. In this paper, only a single part of the

gyroidal structure has been analyzed. It is related to the aim of the paper which is an analysis of the coating impact on the mechanical response of the analyzed structure depending on the applied coating.
The suggested thickness for gyroid scaffolds used for bone replacement procedures commonly varies from 300 μm to 1 mm. A specific investigation demonstrates that a wall thickness of 300 μm is suitable for attaining better mechanical properties and porosity in gyroid scaffolds, crucial to allowing good osseointegration and load-bearing properties for orthopedic implants [12]. In this paper 300 μm (0.3mm) gyroid thickness is preferred.

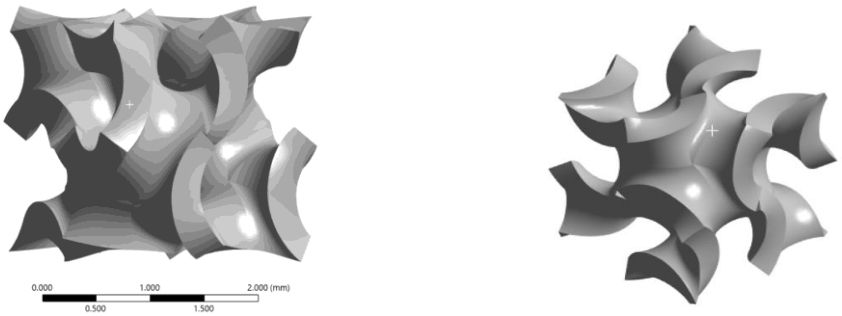

Figure 1. A single part of the gyroid from different view used for evaluation.

4. RESULTS

4.1. Main assumptions and stress analysis

Stress analysis of the single gyroid structure with two coatings has been performed with the use of the finite element method in commercially available ANSYS software. For boundary conditions, the surface was fixed from the reverse of the force application. The scaffold material is assumed to have homogeneity, isotropic behavior, linear elasticity, and the absence of viscoelastic or time-dependent deformation.
As in the actual biological setting, the model's fixed boundary conditions get in for the immovable components that reflect the physical limits. To avoid dynamic effects like impact forces, loads are often applied in a regulated manner, typically under static loading circumstances. Assumption, the scaffold and the bone do not move relative to each other once they touch. So, when pressure from outside sources is exerted, they respond as one solid body.
To calculate the force in Newtons required for a compressive load that simulates body weight it is crucial to take into account the material properties and the particular application context. The force is determined by the weight of the body being simulated, calculated as the product of mass and gravitational acceleration, which is roughly 9.81 m/s^2. However, because a single-cell model was used, it was found that, Applying tiny forces—specifically, 9.81 N, 50 N, and 100 N—in the opposite direction of the fixed support is the most effective.

4.2. Deformation and Stress Analysis

Analyzing stress and deformation is essential for improving the mechanical properties of bone scaffolds, which play a crucial role in effective bone tissue engineering.

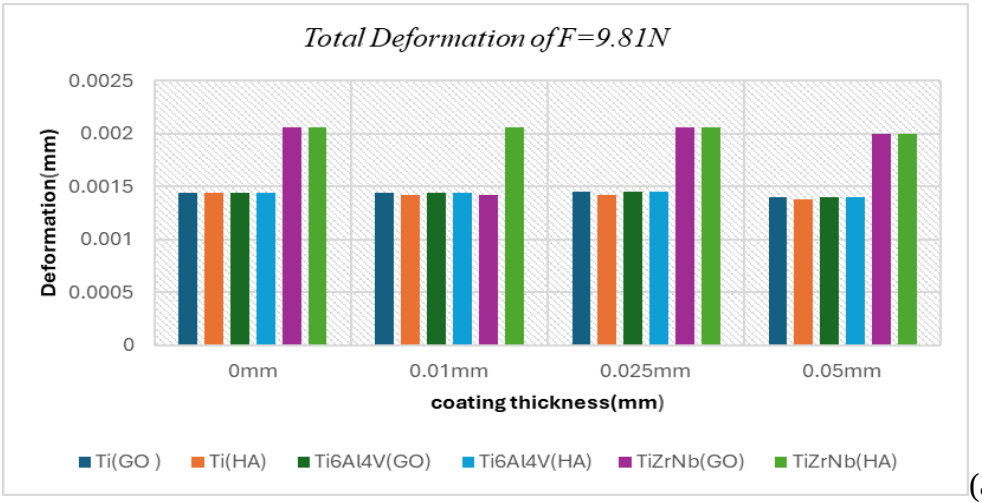

(a)

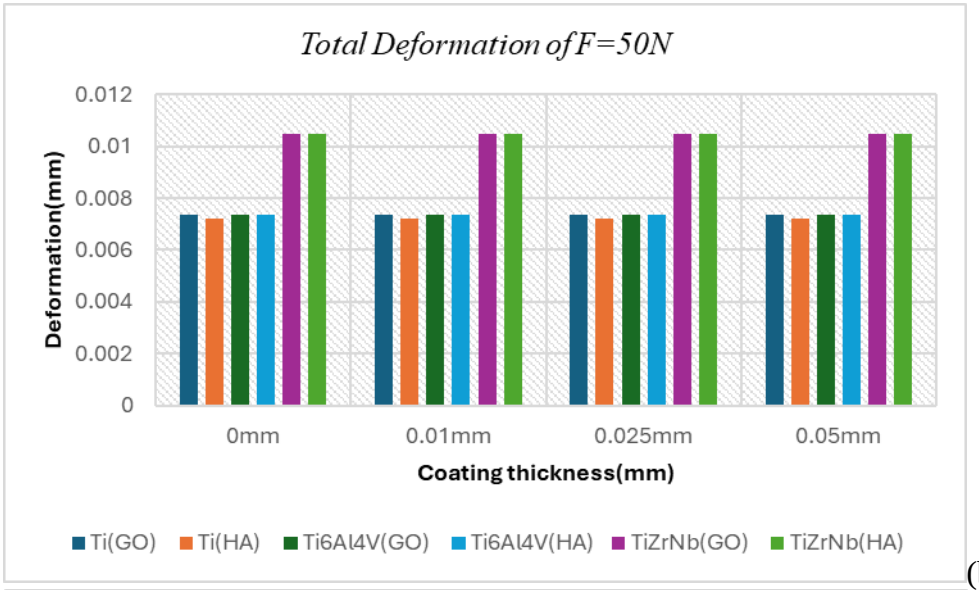

(b)

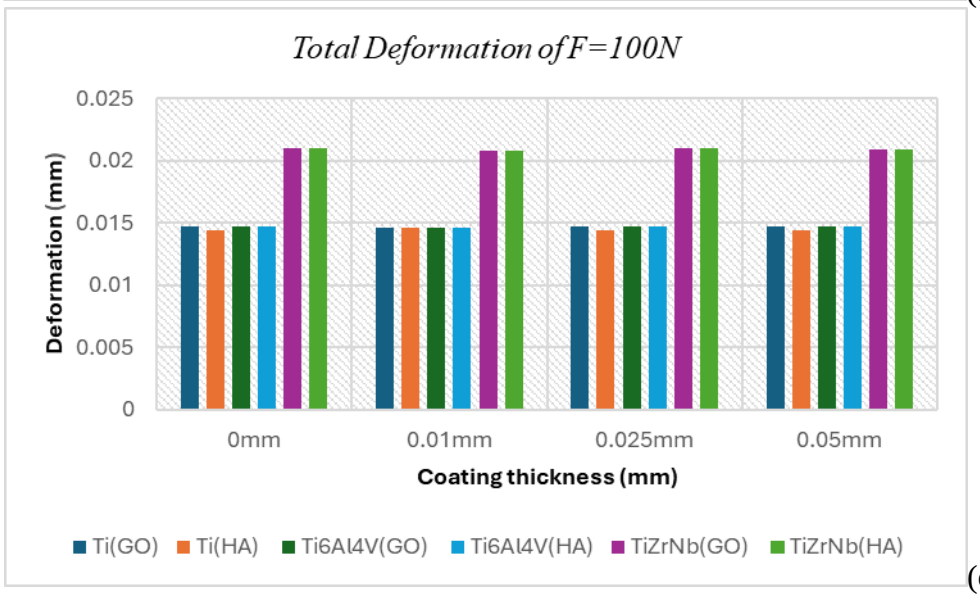

(c)

Figure 2(a-c) a. Ti alloy deformation with application of 9.81N b. Ti alloy deformation with the application of 50N c. Ti alloy deformation with the application of 100N.

This analysis provides an understanding of the response of scaffolds to mechanical loads, which in turn affects cell behavior and tissue regeneration. Stress analysis ensures that scaffolds are capable of efficiently transferring loads to cells, thus promoting differentiation and proliferation [13]. While stress analysis shows the connection between porosity and mechanical strength, providing the design of scaffolds with suitable pore structures for better performance [14].

Deformation: For the deformational behavior test, three Titanium alloys (Ti, Ti6Al4V, and TiZrNb) of non-coated(0.0mm), and coated with three different thicknesses of those two different coatings (Go and HA), and application of three different Forces (F1=9.81N, F2=50N, F3=100N) as listed below on figure 2(a-c) is applied. From this figure, it is clear that less deformational behavior is investigated on the first two types, Ti and Ti6Al4V alloy, while in TiZrNb, higher deformation was investigated. From two coatings, HA coating shows less deformational behavior on most coating of Titanium alloy. Also, Less force application shows less deformational behavior, which indicates scaffold can withstand physiological loads which helps to facilitate optimal bone growth and integration.

Stress: Similarly the same procedure was used for equivalent Stress (von- mises) stress analysis. Three titanium alloys were selected, 3 different force, two coating and non-coated analyses, and their stress behavior to analyze the ability of the scaffold to transfer loads to cells for the promotion of differentiation and proliferation. From this investigation, shown in Figure 3(a-c) stress value is concluded as follows. From Figure 3(a-b) , as coating thickness increases, equivalent stress(von -mises stress) decreases, this indicates that small thickness (< 0.01) [10] Is preferable for better value of stress and more bone growth promotion, even though it is better for failure, deformation, and biological disruption toleration. From this investigation, it is clear that there is no smooth relation between coating thickness and stress value, which that means sometimes as coating thickness increases, the stress of the material decreases and in some cases shows incrementation. In general, this can be concluded that, for both GO and HA coating, on 0.05mm thickness we investigate a decrease of stress value for all materials. Like deformation value, HA coating shows less stress value, except in some cases with 0.025mm coating which is useful to decrease failure, deformation, and biological disruption. Generally, like stress results, as force application increases equivalent stress also increases with a range of (49.104 MPa - 622.71MPa)

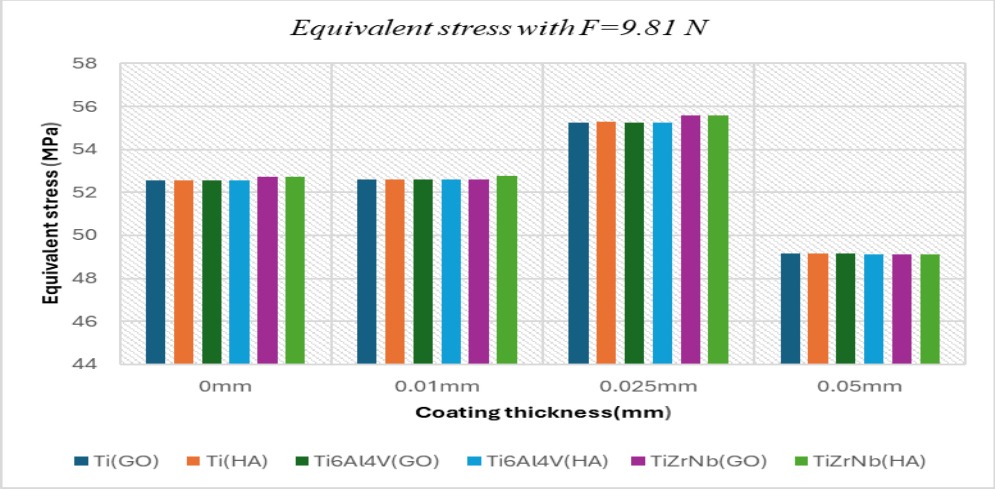

(a)

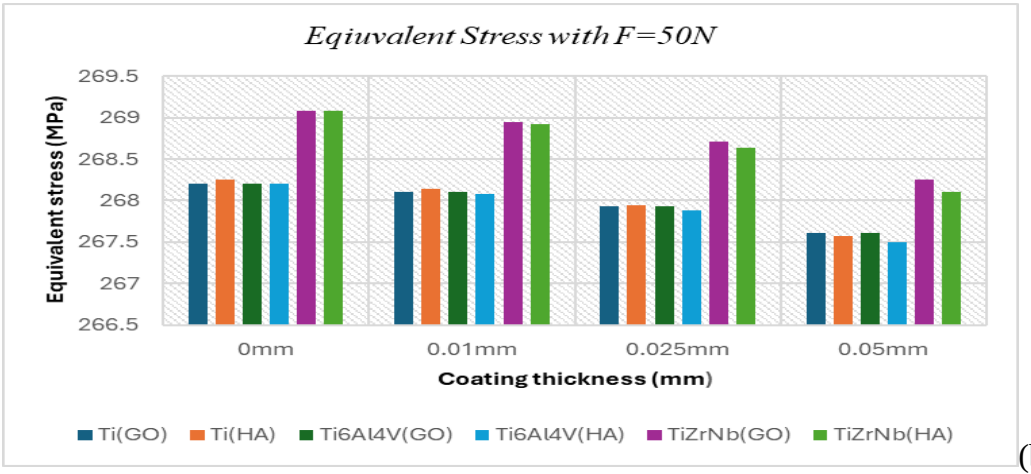

(b)

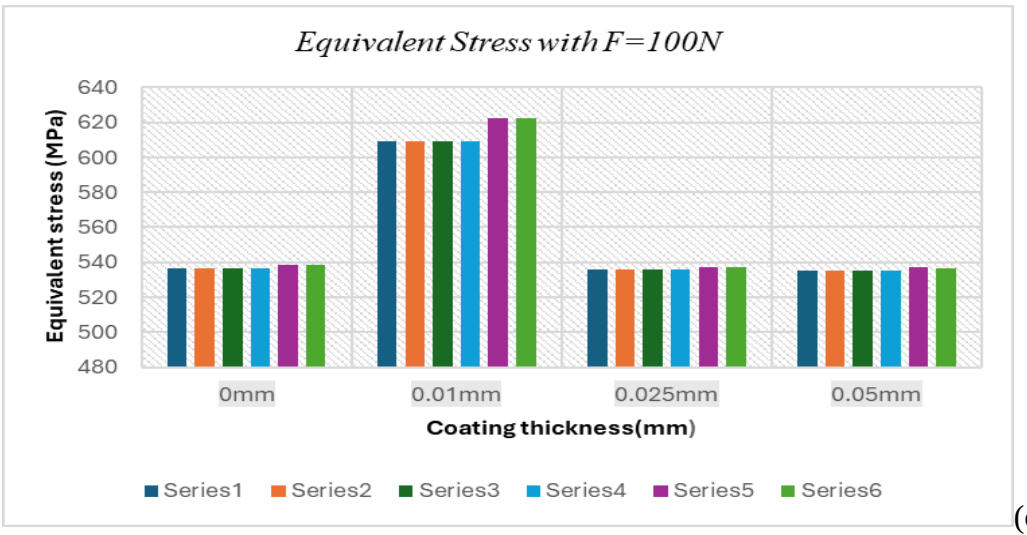

(c)

Figure 3(a-c) a. Ti alloy equivalent stress with application of 250N Force, b. Ti alloy equivalent stress with the application of 500N Force, c. Ti alloy equivalent stress with the application of 687N Force.

5. CONCLUSIONS

In summary, this research highlights the significant impact of surface coatings on improving the mechanical properties of titanium gyroid scaffolds used for bone implants. The study uses finite element analysis to show how coating materials like graphene oxide and hydroxyapatite, along with their different thicknesses, play an essential role in influencing stress distribution, and deformational properties. From the deformation test, it is clear that less deformation was investigated on Ti and Ti6Al4V titanium alloy for both coatings, and specifically, in HA coating less deformation value is evaluated. For stress (von-mises) as coating thickness increases, stress value decreases, specifically, a large decrease was evaluated on HA coating on Titanium alloy, so HA coating which is bioceramic coating is suggested by this research for better value of deformation and stress.

BIBLIOGRAPHY

[1]"Effect of residual stress on load bearing capacity of pvd coated surfaces," SciSpace - Paper. Accessed: Dec. 25, 2024. [Online]. Available: https://typeset.io/papers/effect-of-residual-stress-on-load-bearing-capacity-of-pvd-qn0yc8nurp
[2]"Investigation on the Stress Behaviour of Coating-Substrate Interface under Contact Loading," *Appl. Mech. Mater.*, pp. 1319–1323, Dec. 2013, doi: 10.4028/WWW.SCIENTIFIC.NET/AMM.465-466.1319.
[3]C. M. Suryawanshi, S. Sagar, R. Bhallamudi, and S. Mishra, "Effective design and mechanical response of Gyroid lattice scaffold for orthopedic implants," *Manuf. Lett.*, vol. 35, pp. 493–501, Aug. 2023, doi: 10.1016/j.mfglet.2023.07.015.
[4]C. Hou, M. Goris, D. Rosseel, B. Vrancken, and K. Denis, "Geometric and Mechanical Properties of Ti6Al4V Skeletal Gyroid Structures Produced by Laser Powder Bed Fusion for Biomedical Implants," *J. Manuf. Mater. Process.*, vol. 8, no. 6, p. 256, Nov. 2024, doi: 10.3390/jmmp8060256.
[5]I. Valdivia-Gandur, M. C. Manzanares-Céspedes, W. Astudillo-Rozas, O. Aceituno-Antezana, V. Tallón-Walton, and V. Beltrán, "Simultaneous Osseo- and Odontointegration of Titanium Implants: Description of Two Cases in Human and Animal Models and Review of Their Experimental and Clinical Implications," *Materials*, vol. 17, no. 22, p. 5555, Nov. 2024, doi: 10.3390/ma17225555.
[6]J. C. Castro-Sandoval, A. Chavez, J. Corona-Castuera, J. Henao, M. A. Rivera-Gil, and C. A. Poblano-Salas, "Additive manufactured gyroid-based cell structures under compression: design, testing and simulation for biomedical applications," *Comput. Methods Biomech. Biomed. Engin.*, vol. 27, no. 2, pp. 211–221, Jan. 2024, doi: 10.1080/10255842.2023.2179366.
[7]C. Polley, W. Radlof, F. Hauschulz, C. Benz, M. Sander, and H. Seitz, "Morphological and mechanical characterisation of three-dimensional gyroid structures fabricated by electron beam melting for the use as a porous biomaterial," *J. Mech. Behav. Biomed. Mater.*, vol. 125, p. 104882, Jan. 2022, doi: 10.1016/j.jmbbm.2021.104882.
[8]"BOOK TITANIUM ALLOY GUIDE.pdf."
[9]J. Li, T. Zhang, Z. Liao, Y. Wei, R. Hang, and D. Huang, "Engineered functional doped hydroxyapatite coating on titanium implants for osseointegration," *J. Mater. Res. Technol.*, vol. 27, pp. 122–152, Nov. 2023, doi: 10.1016/j.jmrt.2023.09.239.
[10] Gunawarman *et al.*, "Hydroxyapatite Coatings on Titanium Alloy TNTZ using Electrophoretic Deposition," *IOP Conf. Ser. Mater. Sci. Eng.*, vol. 602, no. 1, p. 012071, Aug. 2019, doi: 10.1088/1757-899X/602/1/012071.
[11] D. W. Hutmacher, "Scaffolds in tissue engineering bone and cartilage," *Biomaterials*, vol. 21, no. 24, pp. 2529–2543, 2000, Accessed: Dec. 08, 2024. [Online]. Available: https://www.sciencedirect.com/science/article/pii/S0142961200001216
[12] B. Ziaie, X. Velay, and W. Saleem, "Advanced porous hip implants: A comprehensive review," *Heliyon*, vol. 10, no. 18, p. e37818, Sep. 2024, doi: 10.1016/j.heliyon.2024.e37818.
[13] L. Moliner, C. Ruiz Wills, O. Camara, and A. L. Olivares, "The influence of scaffold deformation and fluid mechanical stimuli on bone tissue differentiation.," *bioRxiv*, pp. 2024–02, 2024, Accessed: Jan. 02, 2025. [Online]. Available: https://www.biorxiv.org/content/10.1101/2024.02.29.582717.abstract
[14] X. Wang, J. Chen, Y. Kang, and L. Sun, "Design and analysis of the mechanical properties of controllable porous scaffolds for bone tissue engineering," *Proc. Inst. Mech. Eng. [H]*, vol. 236, no. 5, pp. 748–760, May 2022, doi: 10.1177/09544119221086766.

TalentDetector
31th January 2025
Gliwice, Poland
DEPARTMENT OF ENGINEERING MATERIALS AND BIOMATERIALS
FACULTY OF MECHANICAL ENGINEERING
SILESIAN UNIVERSITY OF TECHNOLOGY
INTERNATIONAL STUDENTS SCIENTIFIC CONFERENCE

Microstructure of vacuum brazed joint of tool steels used in conformal inserts of injection molds

M. Grabowska[a], D. Dziurosz[a], Sz. Greń[a], Ł. Kaim[a], M. Prusko[b], J. Zarzycki[b], J. Mytnik[c], J. Mazurkiewicz[c], M. Król[c], W. Kołodziej[d]

[a] Students Faculty of Mechanical Engineering, Silesian University of Technology, [b] Students Faculty of Civil Engineering, Silesian University of Technology, [c] Department of Engineering Materials and Biomaterials, Faculty of Mechanical Engineering, Silesian University of Technology, [d] Student of the Mechanic-Electrical Technical School Chorzow
email: janusz.mazurkiewicz@polsl.pl

Abstract: This article presents the final research results of the PBL project entitled: "New technique for bonding SLM printed metal conformal inserts used in moulds for polymer products in construction and mechanical engineering " carried out within the framework of the "Initiative for Excellence - Research University" (IDUB) program at the Silesian University of Technology in Gliwice in the winter semester 2024/2025. The main task of the project was to analyse the influence of the production technology of maraging tool steel grade 1.2709 on the strength and structure of the vacuum furnace brazed joint. BNi2 nickel-based solders were used to braze SLM-printed 1.2709 steels and conventionally manufactured 1.2709 steels. The steels were prepared for soldering by shot-blasting and etching in hydrofluoric acid. Preparation of the samples for brazing was carried out at the Listemann Company in Krakow using their tooling and a Seco Warwick furnace. Powder steel samples were printed in the Scientific and Didactic Laboratory of Nanotechnology and Material Technologies, Faculty of Materials Engineering, Silesian University of Technology. The study showed the influence of surface preparation and fabrication technology on the strength of the brazed joint as well as its structure. It was found that the highest brazed joint strength was obtained for a pair of 1.2709 steels fabricated with different technologies, i.e. printed and conventional. The lowest brazed joint strength values were obtained for a pair of specimens fabricated using powder printing technology. Analysis of the structure of the solder joint breakthroughs and longitudinal cross-sections of the connection showed the influence of diffusion processes on the structure of the solder-steel boundary layers, which is directly responsible for the different strength values of the solder joints in the adopted compositions.

Keywords: High-temperature vacuum brazing, maraging steels, strength of brazed joints, etching of steel, structure of a brazed joint, diffusion of elements at the braze-steel interface.

1. INTRODUCTION

Welding joining technology is ideally suited to joining materials of the same type. Unfortunately, in mechanical engineering as well as in construction, it is often necessary to join materials with widely differing chemical compositions or produced using different technologies. From a technical point of view, the optimum method for joining such materials is, for example, soldering using high-temperature solders with high strength and good adhesion to the substrate. Nickel-based or copper-based solders are most commonly used. W niniejszej pracy wykorzystano do wykonania połączenia luty niklowe gatunku BNi2. In this study, nickel solder of grade BNi2 was used to make the joint. Crucial for a brazed joint are its strength properties, such as tensile strength, shear strength and compressive strength, depending on the mode of operation of the component to be brazed. Therefore, it is worth checking what the actual brazing capabilities of steels obtained using laser powder melting (SLM) technology are in relation to conventional steels obtained using traditional metallurgical technologies. The basis of this work will also be an analysis of how the surface treatment of the steel prior to brazing as a standard brazing technique will change the structure and strength of the brazed joint in correlation with the way the steel is produced. Of course, when considering the sense of investigating such a common material as steel, it can be confirmed with certainty that it is still a common and widely used material in construction and mechanical engineering. Ultimately, the brazing technology analysed and the combination of printed and conventional steel will be used to produce injection moulds with conformal inserts. Figure 1 below shows an example of the use of vacuum brazed printed conformal inserts in polymer injection moulding presented by Renishaw in its promotional material, using a Karcher pressure washer housing as an example.

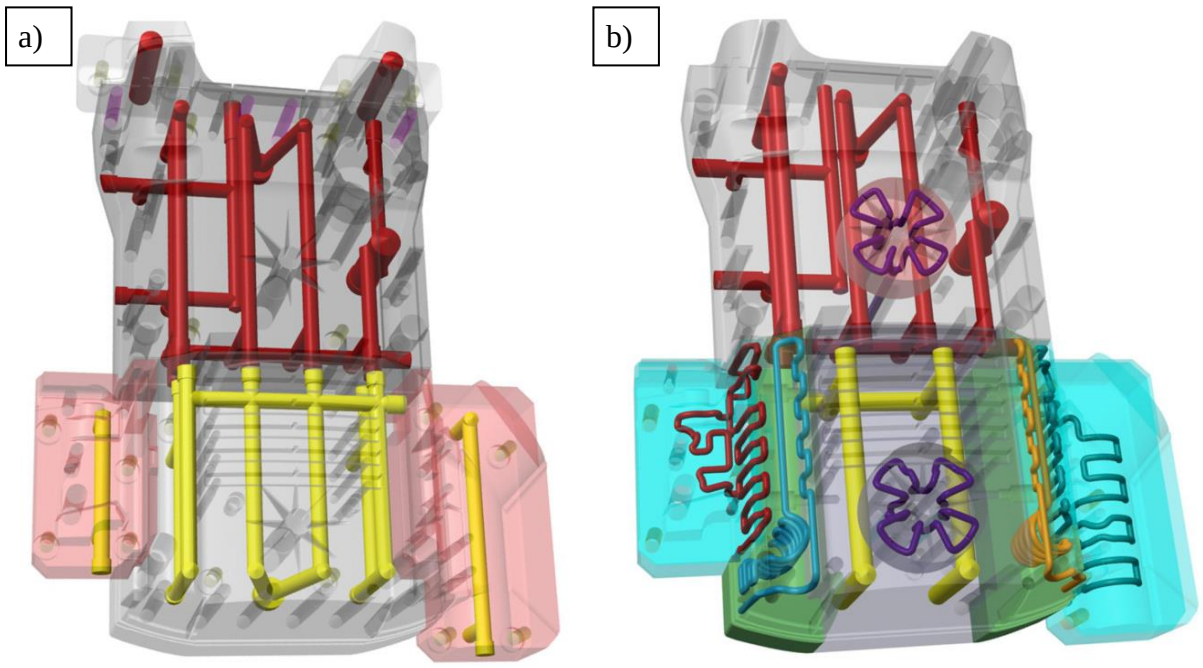

Fig. 1. a) Original design of the K2 rear yellow washer moulding tool, b) New conformal-cooled tool design for moulding the rear yellow housing of the K2 washer [6]

2. TEST METHODOLOGY AND TEST MATERIAL

The test specimens were prepared from maraging steel 1.2709 produced conventionally and from powder from the Bohler Company. The chemical composition of the steel and the steel powder is shown in Table 1, while the chemical composition of the brazing foil is shown in Table 2. 3 samples in the form of a cuboid from conventional steel and 3 from powder-printed steel with dimensions of 70x60x20 mm were prepared and, after surface preparation, brazed in a vacuum oven at 1050C. Fig.2 shows the test specimens produced after brazed and after the tensile strength test.

Tab. 1. Chemical composition of Maraging 1.2709 conventional steel and 1.2709 steel powder for 3D printing

Type of steel	Chemical composition by weight of maraging steel 1.2709 X3NiCoMoTi18-9-5 [%]								
	C	Si	Mn	Cr	Mo	Ni	Ti	Co	P and S
Conventionally manufactured	0.03	0.1	0.15	0.25	5.2	19.0	1.2	10.0	≤0.010
Powder for 3D printing 15 – 45 μm	0.03	0.1	0.15	-	4.9	18.0	1.1	9.3	≤0,01

Tab. 2. Chemical composition of 0.2 mm thick BNi2 solder foil

Type of steel	**Chemical composition by weight solder foil BNi2 [%]**					
	B	**Si**	**Cr**	**Fe**	**Ni**	**C**
Conventionally manufactured	3.1	4.5	7.0	3.0	82.3	0.06

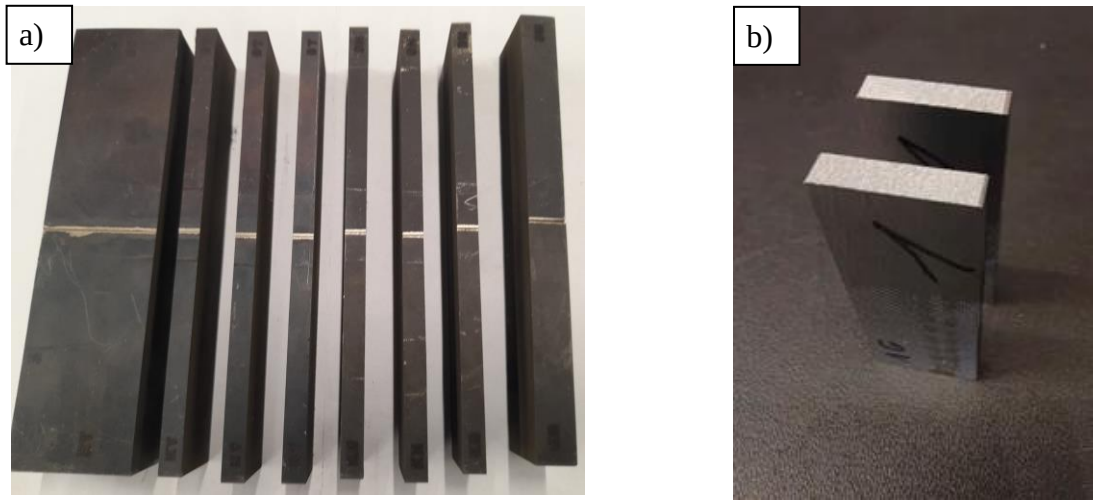

Fig. 2. a) View of KT-DT and KN-DN solder joint specimens for strength tests after electrospark cutting, b) Tensile view of a KT-DT brazed joint sample, brazed joint breakthroughs visible

Tensile tests on soldered joints were carried out on a Zwick ZSN 100 universal testing machine with hydraulic grips. A view of the testing machine and the specimens during the

strength test is shown in Figure 3. In the next stage of the study, the surface topography of the solder joints of each sample was analysed using a Leica DVM6 digital microscope. The specimens were analysed microscopically to reveal the structure of the solder joint and to assess the thickness of the solder using a Zeiss Axioobserver materialography light microscope and a Zeiss Supra 35 scanning electron microscope (SEM) and a Thermo Scientific EDS spectrometer.

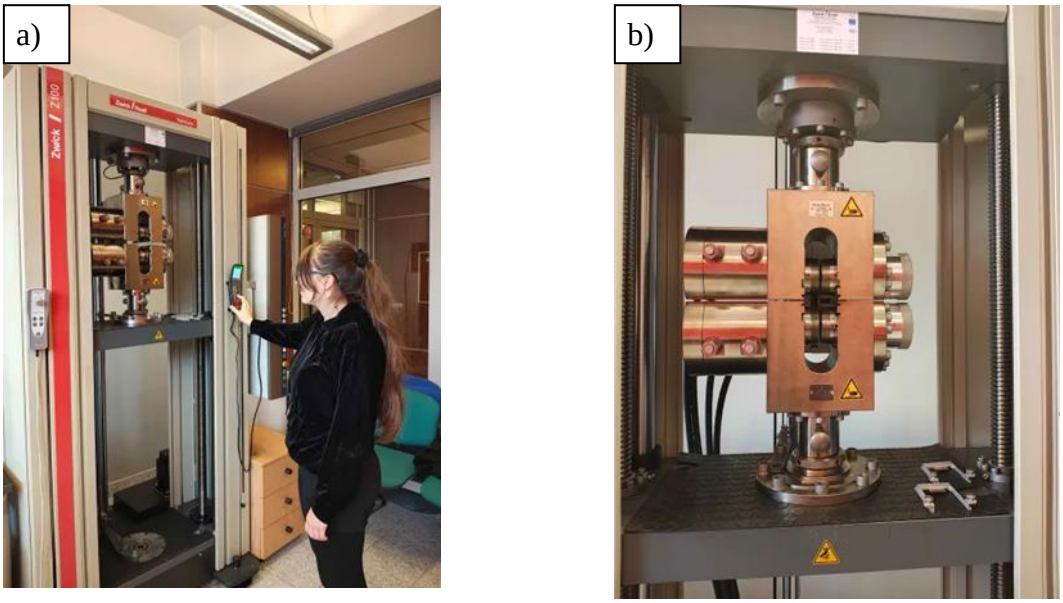

Fig. 3. a) Zwick ZSN 100 tensile testing machine during DT-DT tensile testing of a steel joint, b) Test specimens for strength testing of brazed joints when fixed in hydraulic fixtures

3. RESULTS OF THE STUDY

From the strength tests carried out on the brazed joints and the powder-printed steel specimens of 1.2709 steel, the solder strength results shown below in Figure 4e were obtained. Strength tests on the maraging steel itself confirmed that the conventional steel has a tensile strength Rm of up to 1120 MPa. In the case of powder-printed steels, depending on the variant of optimisation of the Renishaw AM 125 machine parameters in terms of parameter porosity, the strength of the steel was obtained in the range from 870-1050MPa. In the case of steel sample 1.2709, the highest brazed joint strength in the range 711-724 MPa was obtained for the conventional steel-powder-printed steel combination. In this case, the issue of etching the steel surface before brazing had virtually no effect on the strength result. Slightly lower strength values of approx. 8 % for the brazed joint were obtained for the conventional steel pair in the KT-KT and KN-KN system in the range 645-673 MPa, also rather without a clear influence of the surface preparation. The lowest, and clearly in relation to the other brazed joint variants described above (by about 17-30%), strength properties were obtained for the DT-DT and DN-DN sample arrangement in the range 502 to 580MPa. For this variant, the beneficial effect of etching the samples before brazing is also clearly visible, as the strength of the etched samples increased by approximately 14%. The results obtained show that only in the case of steels made from powders is there a significant effect of the etching process on the samples before brazing. This is in line with initial assumptions and reports in the literature. Why this is the case and what is the reason for this behaviour of printed steels will be the subject of an analysis of the

structure and diffusion processes carried out as part of the doctoral thesis of one of the authors of this work, Mr J. Mytnik.

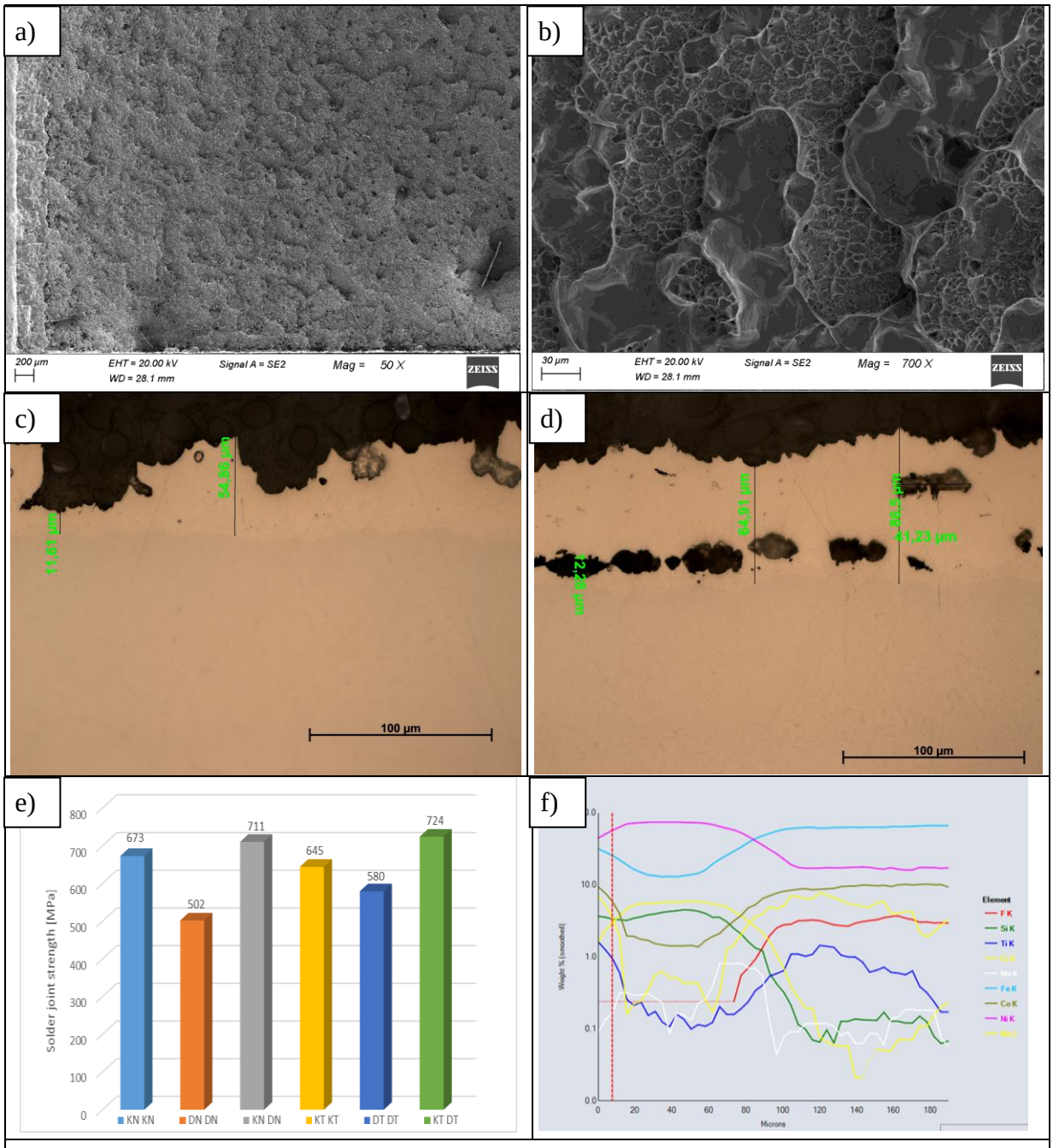

Fig. 4. a and b) Tensile fracture structure of the brazed joint of steel 1.2709 for the KT-KT joint, c) Tensile cross-section of the brazed joint for specimen KN, d) Tensile cross-section of the brazed joint for specimen DT, e) Tensile strength test results of steel 1.2709 for different variants of the brazed joint (designations adopted in the diagram: KN- conventional un-etched steel, KT - conventional etched steel, DN - powder-printed un-etched steel, DN - powder-printed etched steel), f) results of the change in elemental concentration on the tensile solder joint cross-section from the breakthrough surface towards the steel substrate.

In the analysed variants of surface preparation for solder joint, satisfactory results of solder joint strength were obtained, allowing an optimistic view of the continuation of research in this field. Digital microscopy and SEM examination of the surfaces of the strength breakthroughs confirmed that, over the entire cross-sectional area, the solder wetted the soldered surfaces well. The breakthrough morphologies seen in Fig. 4a and b confirm that the breakthroughs are of a mixed ductile-brittle nature.

Analysis of the results of metallographic examination of solder cross-sections after tensile testing confirms the presence of pores at the solder/steel interface. Often this type of defect is seen in solder joints of powder-printed steels (Fig. 4 c and d). Conventional steels show fewer pores and solder defects. When analysing the diffusion of the elements present in the steel towards the solder and the elements present in the solder (fig. 4f), it can be confirmed that the elements diffuse freely between the phases during high-temperature processes. Diffusion of Ni, Fe and Co between phases is particularly strongly observed. Crucial to good bonding is the concentration of Ti in the individual micro-areas. The results of the change in elemental concentration in Figure 4f are presented on a logarithmic scale to better illustrate the scale of elemental migration.

4. CONCLUSION

On the basis of the test results obtained for the brazed joints analysed, it was found that the highest brazed joint strength values were obtained for a pair of conventional specimens reaching strengths of more than 64% of the strength of the steel itself, which is a satisfactory result from the point of view of the application of this type of joint in injection moulding. The average joint strength of a pair of conventional specimens was around 717 MPa, while the lowest values were obtained for untreated powder-printed steel specimens, achieving an average joint strength of 502 MPa. The structure of all tensile breakthroughs observed on the digital microscope is homogeneous with isolated minor impurities from surface preparation processes prior to soldering. Analysis of the breakthroughs by scanning electron microscopy showed mixed breakthroughs with plastic and brittle micro-areas. The most interesting findings from a cognitive point of view are presented by the results of elemental diffusion processes in scanning electron microscopy using the EDS technique. The elements from the solder diffuse into the steel forming solid solutions at the interfacial boundaries. Boron contained in the solder forms compounds with chromium present in the micro-area of the solder. The element that shows a high tendency to diffuse towards the solder is cobalt. A more extensive discussion of the structural results was presented in the poster session of the conference and is planned to be presented in subsequent publications.

LITERATURE:

1. Winiowski A., Kuzio T., Rozwój możliwości zastosowania lutowania twardego w różnych gałęziach przemysłu, Biuletyn Instytutu Spawalnictwa Nr 5/2003 (in Polish);
2. Mazurkiewicz A., Nędzi B., Ocena jakości wykonania wybranego elementu z proszków metali metodą laserowego wytwarzania przyrostowego, Uniwersytet Technologiczno-Humanistyczny w Radomiu, Radom 2016 (in Polish);
3. Bochnia J., Wybrane właściwości fizyczne materiałów kształtowanych technologiami przyrostowymi, Politechnika Świętokrzyska, Kielce 2018 (in Polish);
4. Sha W. and Guo Z., Maraging steels: Modelling of microstructure, properties, and applications, Woodhead Publishing Limited, Cambridge, UK, 2009;

5. Davis J., Tool Materials, ASM Specialty Handbook, ASM International, 1995;
6. Mouritz, A., Introduction to Aerospace Materials, Woodhead Publishing, Cambridge, 2012;
7. Martin J., Materials for Engineering (Third Edition) Woodhead Publishing Limited, Cambridge, UK, 2006;
8. Strakosova A., Kubásek J., Michalcová A., Pruša F., Vojtech D. and Dvorsky D., High Strength X3NiCoMoTi 18-9-5 Maraging Steel Prepared by Selective Laser Melting from Atomized Powder, Materials MPDI, vol 12, No. 4174, 2019;
9. Renishaw promotional material, Use of conformal-cooling cores in moulds for the manufacture of plastic enclosures, https://www.renishaw.com/pl;

TalentDetector
31th January 2025
Gliwice, Poland
DEPARTMENT OF ENGINEERING MATERIALS AND BIOMATERIALS
FACULTY OF MECHANICAL ENGINEERING
SILESIAN UNIVERSITY OF TECHNOLOGY
INTERNATIONAL STUDENTS SCIENTIFIC CONFERENCE

Recycling opportunities - the second life of metallographic samples for light microscope studies in the form of QR code boards

M. Kiczyński[a], J. Ertel[a], J. Mazurkiewicz[b]

[a] Students Zabrze Centre for General and Vocational Education, Zabrze, [b] Department of Engineering Materials and Biomaterials, Faculty of Mechanical Engineering, Silesian University of Technology, Gliwice
email: janusz.mazurkiewicz@polsl.pl

Abstract: The article presents the results of a project carried out in collaboration between students Zabrze Centre for General and Vocational Education (ZCKOIZ) and the Faculty of Mechanical Engineering (MT) of the Silesian University of Technology in Gliwice. The project entitled: ”Development and production of interactive charts with qr codes for the websites of the school and the MT Faculty with metallographic samples used for testing engineering materials” was financed by the project “Polytechnic” carried out within the framework of the "Initiative for Excellence - Research University" (IDUB) program at the Silesian University of Technology in Gliwice in the summer semester 2023/2024. As part of the project, the pupils prepared two arrays constructed from sheets of glass in an aluminium frame and metallographic samples, which were samples used to test materials in several research units. Metallographic specimens, after structural testing has been carried out, are stored for a certain period of time for claim purposes and then disposed of. Here, the project uses the interesting and original idea of giving these no longer needed metallographic samples, which go to disposal, a second life by using them for educational purposes. The students prepared two 80x80 cm boards with QR codes of the websites of the school ZCKOIZ and the MT Faculty. The boards are backlit by LED strips installed in the frame, which makes it easier to read the QR codes shown on them with a mobile phone. For the construction of the boards, mainly waste samples were used, including 410 pieces for the MT board and 324 pieces for the ZCKOIZ board, in which more than 105 and 85 steel grades in the form of profiles, bars, pipes, sheets and strips, respectively, are embedded in resins. The project also included the preparation of some 45 new metallographic scales with lettering markings made of stainless steel, which were incorporated into the boards as project and contractor markings. The preparation of dozens of specimens provided an insight into the metallographic testing methodology, including the complex process of preparing metallographic specimens. The casts were made in the Materials Testing Laboratory of the Mechanical Engineering Department. Also, selected waste specimens that were not of good quality were corrected in order to obtain a good quality specimen structure. The metallographic samples on the prepared board were coated with a thin coat of epoxy varnish to protect them from corrosion. The charts are currently used as teaching aids in the school and department to present the study of material structures and the recycling of metallographic samples.

Keywords: recycling of metallographic samples, metallographic specimens, QR boards, Polytechnic project, preparation for the study of the structure of metallic materials.

1. INTRODUCTION

In the study of materials, especially their structure, the basic form of preparation is a metallographic specimen in the form of a hot or cold-encapsulated material sample in resin (Fig. 1). In the Materials Testing Laboratory at the Faculty of Mechanical Engineering, up to more than 200 such specimens are produced each month with the participation of students and staff, which, after a period of their use for research, become waste rather difficult to dispose of. During an Erasmus+ internship in 2023 in a country in Europe, the project supervisor was inspired to propose the theme of this project by a board prepared by an engineering graduate student at the local university, which allowed 314 useless metallographic samples to be used using waste from the laboratory, while also teaching and inspiring how diverse material structure research can be (Fig. 2). It is cognitively interesting to see how varied a form research samples can take.

The scientific objective of this project was to familiarise students with metallographic preparation techniques, including preparation without polymer resins, the study of the structure of materials using light microscopy, issues related to the adhesion of resins and the possibility of bonding this type of waste to glass, graphic design using Inventor, and issues of material recycling and the concept of Zero Waste.

The practical aim was to create two original boards that draw attention to the problem of waste in preparation of samples for metallographic tests, while generating interest in the study of the structure and properties of materials, materials engineering and websites presented in this original way.

The use of samples to build the QR boards is not a targeted and environmentally friendly way to dispose of them, but it draws the attention of the environment (pupils, students and academics) to the problem in this area with the use of resins that are difficult to recycle when combined with samples. The boards made will also inspire companies producing consumables for metallography to develop recycling facilities for this type of waste with the possibility of recovering and regranulating, for example, the frequently used thermoplastic resins for mounting. Currently, this type of equipment is not offered by manufacturers due to the lack of awareness of users of mounting resins and the downplaying of the waste problem in materialography.

It is not possible to purchase such aids in the form of inspirational boards and, arguably, these are the first original QR codes of their kind in Poland, and working with students to design, produce and assemble them was a great learning adventure for the authors.

Fig. 1. Structure test samples prepared as part of the project

Fig. 2. Blackboard prepared by a student as part of an engineering thesis in the Faculty of Materials Science and Technology in Trnava

2. TEST METHODOLOGY AND TEST MATERIAL

In the first stage of the project, the pupils learned about modern materials preparation, which is used at the Silesian University of Technology in the Materials Testing Laboratory, as well as about materials for preparation and the operation of preparation equipment. QR codes were then generated using free software in dots in the form of circles with a diameter of 25 mm, which, after graphic elaboration, form the backing for the metallographic samples. In the next stage, the students selected more than 700 metallographic samples from among several thousand waste metallographic samples that met the technical requirements to be used for the construction of the board. A 6 mm thick glass plate was chosen as the substrate for the board because of the possibility of illuminating the perimeter of its surface using led tape. The board's frame for hanging is made up of aluminium system mounting profiles. The samples were glued together using UV-curing glass adhesive.

Fig. 3. Preparation of additional samples using CitoPress is a high-performance hot mounting press

Fig. 4. Preparation of additional samples using Tegramin's integrated specimen mover, automated process control

Fig. 5. Stage of bonding samples to glass plates using UV-curable adhesive

3. RESULTS OF THE IMPLEMENTED PROJECT

The project resulted in two original and unique boards with QR codes directing to the school and faculty website (figs. 6 and 7). These boards not only have an informative function, but also inspire the interest of outside observers in the study of the structure and properties of engineering materials, and issues of material recycling. In the future, the boards will encourage people to study materials and technology at the Silesian University of Technology. The charts may also provide an incentive to manufacturers of materials and preparation equipment for the production of equipment for the recovery of thermoplastic resins from scrap. This type of equipment can be fully automated to recover metals and resins contained in the metallographic samples. The boards were installed with illumination at the Faculty of Mechanical Engineering and the Zabrze Centre for General and Vocational Education in Zabrze City. The use of many different types of materials and their various forms of manufacture makes for an excellent teaching board presenting not only the structure of the materials, but also the manufacturing technologies used in the mechanical engineering industry.

Fig. 6. Board prepared as part of the project presenting the QR code to website the Faculty MT

Fig. 2. Board prepared as part of the project presenting the QR code of the school's website ZCKOiZ

4. CONCLUSION

As a result of the Polytechnic project, the teaching and learning potential of the Project Team was used to carry out the novel task of preparing the QR code of web pages using metallographic specimens. In order to realise the set objective, it was necessary to familiarise and teach the Project Team with the methodology for preparing metallographic specimens. During the project, the students overcame technical difficulties encountered in the implementation of innovative science and teaching projects. The team had to select materials and tools to make arrays that met all requirements related to the safety of the made arrays. Also, the correct selection of electronic components for the lighting of the board substrate and the solution of the electrical power supply output testify to the Team's good preparation for

solving problems in the area of technology in terms of materials and technology. The students coped very well with the mechanical processing aspects of the board assembly elements and the aesthetic and fully safe execution of these prototype boards. The boards made will inspire interest in the world of mechanical engineering and materials engineering.

LITERATURE

1. Bjerregaard L., Geels K., Ottesen B., Rückert M., Metalog Guide, Your Guide to the Perfect Materialographic Structure, Published by Struers A/S, Rødovre, Denmark, 2002;
2. McCall J.M., William M. Mueller W.M., Metallographic Specimen Preparation, Optical and Electron Microscopy, Springer New York, USA, 2006;
3. Vander Voort G.F., Metallographic Practices Generally Applicable to All Metals, Metals Handbook Desk Edition, ASM International, 1998; https://doi.org/10.31399/asm.hb.mhde2.a0003244

TalentDetector
31th January 2025
Gliwice, Poland
DEPARTMENT OF ENGINEERING MATERIALS AND BIOMATERIALS
FACULTY OF MECHANICAL ENGINEERING
SILESIAN UNIVERSITY OF TECHNOLOGY
INTERNATIONAL STUDENTS SCIENTIFIC CONFERENCE

Using 3D FDM printing to build interactive educational models of elementary cells of crystal lattices

W. Kołodziej[a], J. Operskalski[a], M. Skoniczek[a], J. Mazurkiewicz[b], M. Król[b]

[a] Students Nikola Tesla Mechanical and Electrical Secondary School in Chorzow, [b] Department of Engineering Materials and Biomaterials, Faculty of Mechanical Engineering, Silesian University of Technology, Gliwice
email: janusz.mazurkiewicz@polsl.pl

Abstract: The article presents the results of a project carried out in collaboration between students Nikola Tesla Mechanical and Electrical Secondary School in Chorzow (TME) and the Faculty of Mechanical Engineering (MT) of the Silesian University of Technology in Gliwice. The project entitled: ”Development and production of 3d active models of elementary materials in engineering materials using SLA and FFF (FDM) printing” was financed by the project “Polytechnic” carried out within the framework of the "Initiative for Excellence - Research University" (IDUB) program at the Silesian University of Technology in Gliwice in the summer semester 2023/2024. The project developed the concept of interactive elementary cell models that can perform specific tasks related to the measurement or monitoring of variable parameters in the environment of the models. In the first stage of the two-stage project, three elemental cell models of materials such as calcium oxide CaO, fullerene C60 and the intermetallic phase LaNi5 were designed. Two of the designed models were planned with illuminated atoms (CaO and LaNi5) and fullerene C60 as a rotating and illuminated model. All three of the above-designed models were fabricated as spatial structures composed of 60 mm diameter spheres equivalent to atoms in the crystal lattice and connectors made of 6 mm diameter aluminium tubes with a wall thickness of 1 mm. The models of atoms in the form of spheres were finally made using the FDM technique from PLA filaments.

For the CaO and LaNi5 models, PLA filaments in white and orange were used. For the C60 model, a PLA filament in grey with glitter was used. Key to the stable construction of the models and the possibility of placing the led inside the sphere was the correct structural form. A solution based on a sphere with a division into two hemispheres was adopted for the illuminated models, glued together using cjanoacrylate glue after the wiring and LED were installed inside. For the fullerene model, the spheres were printed in their entirety. Guide sleeves were used to guide the connectors in the spheres properly, which were glued together with aluminium connectors after calibration. The atom models were installed at the Faculty of Mechanical Engineering in the leisure area for faculty students on the 3rd floor. Currently mounted under the ceiling, the models, ranging in size from 45-75 cm, provide inspiration for understanding the importance of the structure of materials in relation to their strength, chemical and physical properties.

Keywords: elementary cell models, FDM printing, atomic model design, C60 fullerene, LaNi5 atomic model, CaO atomic model, interactive atomic model.

1. INTRODUCTION

The issues related to the construction of crystal lattice models of various materials are rather difficult knowledge and are reluctantly taken up by young people as an area of interest. Nevertheless, it is important to remember that every compound and every engineering material is a combination of many often complex elementary structures. Knowledge of elementary cell structures allows us to follow phase transformations, chemical reaction processes and interpret the properties of individual materials and compounds.

The aim of the project undertaken was to encourage learning about elementary cell structures in a new unconventional way. In addition to the data presentation aspect of the prepared elementary cell models, the aim of the project is to inspire young people to develop their own original solutions for interactive models of further materials, which are currently crucial for the development of new technologies.

In this edition of the project, all the energy of the Project Team has been focused on the development and fabrication of the structures of selected models (fig. 1), and the next edition will follow the path of using the results of the first stage to build already fully active elementary cell structures. It is planned, among other things, to prepare a large model of fullerene C70 (approx. 80 cm in diameter), the atoms of which will be made using the 3D printing technique using the FDM method. and the linking of the atoms from polycarbonate tubes illuminated by a LED wire, which will imitate the 5 colours of the linking, linked to a coupled PM2.5 air pollution monitoring station around the school building, which will be prepared and installed by the students as part of the second stage of the project. A colour-changing model of C_{70} fullerene, suspended in the main entrance to the school, will draw pupils' attention to the state of the air and its importance to our health, as well as drawing their interest to physics, chemistry and materials engineering as a unique way of promoting related knowledge. The second interactive model to be prepared is a Borophene (fig. 2) model grid of 136 atoms, which will be progressively illuminated, and the number of illuminated atoms will be correlated with the school's water consumption on a given day (or, if this proves too difficult to implement, with the number of people passing through the corridor). This will draw attention to how much can be done for the environment by using clean water resources sparingly, something that seems seemingly indifferent and of no consequence to pupils and staff.

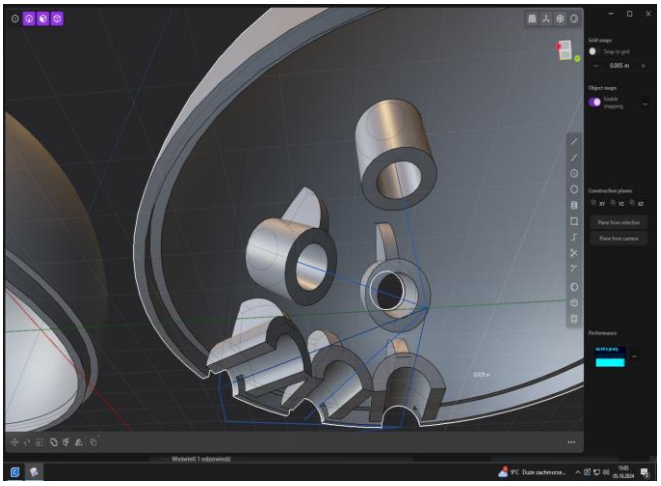

Fig. 1. Design, using CAD software, of the structural form of atomic models, including bonding stabilisation elements

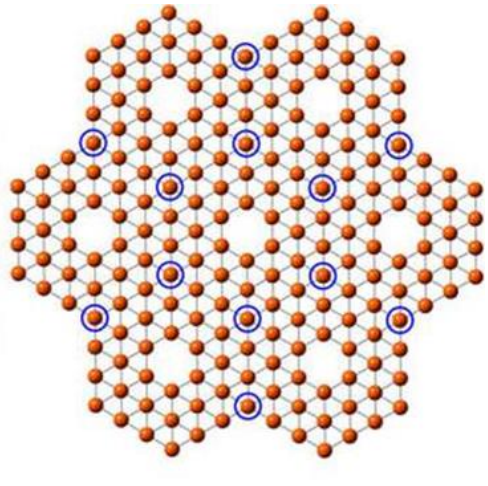

Fig. 2. Borophene lattice model planned as an inter-active elementary cell (wg. Lai-Sheng Wang, Brown University)

2. TEST METHODOLOGY AND TEST MATERIAL

As part of the project, the atomic models of the planned crystal lattices of the materials were optimised in a first step. As a first step, the diameter of the model was selected. Models with diameters ranging from 40 to 75 mm were made using the FDM printing method. In the end, it was assumed that the best solution in terms of the aesthetics of the model fabrication for connectors made of aluminium tubes with a diameter of 6 mm would be a ball with a diameter of 60 mm, imitating the atom model. In the next step, it was analysed how the material and printing technology affect the structure and light transmission through the wall of the atom model. Attempts to use liquid resin (SLA) printing technology were terminated due to the insufficient efficiency of this printing method and the relatively high cost of purchasing consumables. It was assumed that FDM technology guarantees good printing performance with good durability of the resulting prints. On the basis of several colours and filament materials, it was found that PLA filaments in white and orange best scattered the light of the LED without causing high light attenuation (Fig. 3). For the model fullerene atoms, which were not planned to be illuminated, a PLA filament with a graphite-coloured glitter was adopted. In the next step, the focus was on the construction of the atom (sphere) model and the dividing plane for the spheres folded in two halves in order to be able to mount the wiring and led in each atom model. Several different elements were considered to stabilise the two hemispheres of the atomic model in the form of pins, screws, snaps, etc. The final solution adopted was to divide the perimeter edge of the hemisphere into a male and female part, which would be glued together with cyanoacrylate glue after assembly. The determined lengths of aluminium connectors were pressed into the guide sleeves of the connectors in the spheres and stabilised by gluing. Suspension points were determined for each model in the three atoms and hanger links were installed to suspend the models to a rosette or turntable (for the fullerene model). The atom models were printed by optimising the printer output as a function of their surface quality (fig. 4.). Using Crystal Maker software, the angles of the fasteners in the atom models were determined and the models were assembled (Fig. 5).

Fig. 3. Optimisation of material colour and type of filament material as a function of light scattering quality

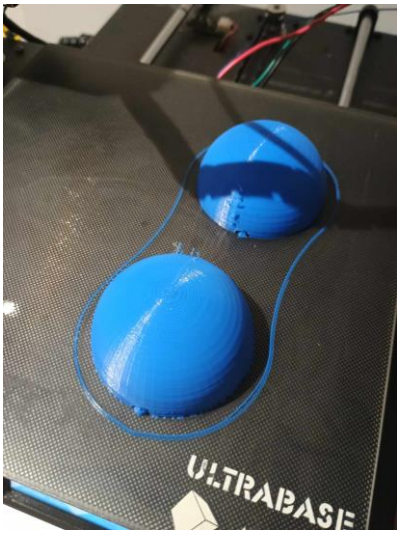

Fig. 4. Optimisation of printing parameters and support type as a function of the surface quality of the printed atom model

Fig. 5. Assembling linker atom models for the fullerene model C60

3. RESULTS OF THE IMPLEMENTED PROJECT

All three models planned to be made were designed and manufactured, and then assembled in the leisure area for the students of the Faculty of Mechanical Engineering. The models were connected to the mains via lighting sensors and timers to control the lighting and rotation of the models. The models were suspended from the ceiling using rosettes and a swivel in the case of the fullerene model. In addition, a chart presenting basic physical information for each model was prepared. Markers were also placed on the atomic models to denote the atoms in a given crystal lattice. The estimated lifetime of the models was set at 4-5 years. Due to the way the models are made, it is possible to periodically remove dust from the models. All atoms have been coated with antistatic agents to prevent them from becoming electrostatic and dirty. Currently, after 5 months of using the models, no problems have been found with their operation. The models inspire and encourage learning about materials, chemistry and physics, of which elementary cells are an integral part. As part of the second phase of the project, work is currently underway in another Team to build the interactive atomic network models indicated in the introduction to this article.

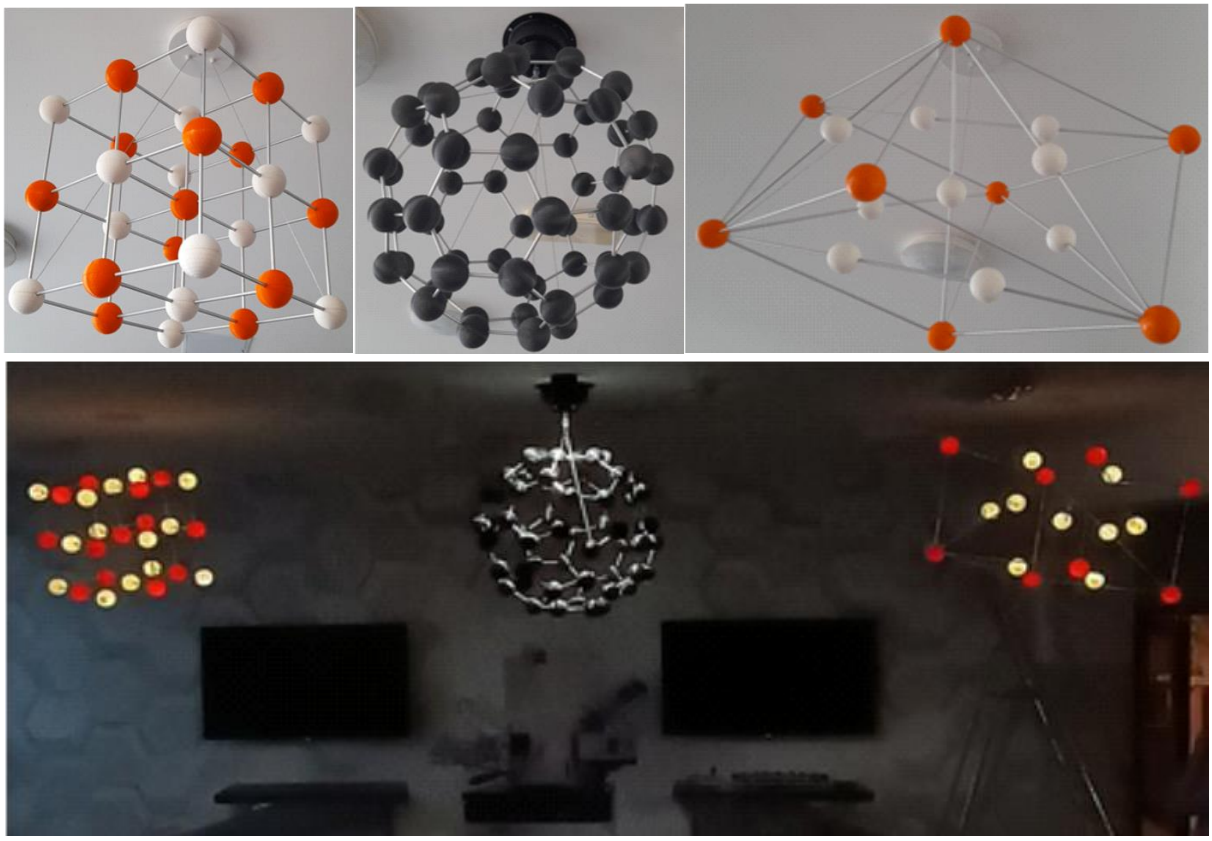

Fig. 6. Elemental cell models of CaO, C60 and LaNi5 made as part of the project, as well as an after-dark view of the mounted models in the rest area at the Faculty of Mechanical Engineering, Silesian University of Technology

LITERATURE

1. Velmurugan D., Elementary Crystallography, MJP Publisher, 2019;
2. Tilley R., Crystals and Crystal Structures, John Wiley & Sons Ltd, Chichester, 2006;
3. Maureen M. J., Foundations of crystallography with computer applications, CRC Press, 2008